CISM International Centre for Mechanical Sciences 550
Courses and Lectures

Jörg Schröder
Klaus Hackl

Plasticity and Beyond

Microstructures, Crystal-Plasticity and Phase Transitions

International Centre for Mechanical Sciences

Springer

CISM Courses and Lectures

Series Editors:

The Rectors
Friedrich Pfeiffer - Munich
Franz G. Rammerstorfer - Wien
Elisabeth Guazzelli - Marseille

The Secretary General
Bernhard Schrefler - Padua

Executive Editor
Paolo Serafini - Udine

The series presents lecture notes, monographs, edited works and proceedings in the field of Mechanics, Engineering, Computer Science and Applied Mathematics.
Purpose of the series is to make known in the international scientific and technical community results obtained in some of the activities organized by CISM, the International Centre for Mechanical Sciences.

International Centre for Mechanical Sciences

Courses and Lectures Vol. 550

For further volumes:
www.springer.com/series/76

Jörg Schröder · Klaus Hackl
Editors

Plasticity and Beyond:
Microstructures, Crystal-Plasticity and Phase Transitions

Springer

Editors

Jörg Schröder
University of Duisburg-Essen, Essen, Germany

Klaus Hackl
Ruhr University Bochum, Bochum, Germany

ISSN 0254-1971
ISBN 978-3-7091-1624-1 ISBN 978-3-7091-1625-8 (eBook)
DOI 10.1007/ 978-3-7091-1625-8
Springer Wien Heidelberg New York Dordrecht London

All contributions have been typeset by the authors
Printed in Italy

Printed on acid-free paper

Springer is part of Springer Science+Business Media (www.springer.com)

PREFACE

Many applications in mechanics, material science and technology require a comprehensive understanding and reliable representation of the elastoplastic behavior observed in a large class of engineering materials. In the last few decades several phenomenological theories have been developed on the macroscopic level. Extensions of these classic models taking into account the formation of microstructures and the microheterogeneity of multiphase materials have attracted a more pronounced scientific interest rather recently. The role of microstructures becomes more and more important with a decreasing size of the considered material specimen because then scale-effects play a dominant role. Microstructure is indeed crucial, since plastic behavior typically results from the interaction of complex substructures on several length scales. The macroscopic behavior is then determined by appropriate averages over the (evolving) microstructure.

The CISM course on "Plasticity and Beyond: Microstructures, Crystal-Plasticity and Phase Transitions", held in Udine from June 27 to July 1, 2011, was addressed to master students, doctoral students, post docs and experienced researchers in engineering, applied mathematics and material science who wished to broaden their knowledge in classical and extended continuum thermodynamics, incremental variational formulations, phase-field modeling, higher-order models like gradient plasticity or numerical multiscale approaches at finite deformations.

It is our pleasure to thank the lecturers of the CISM course Samuel Forest (Paris, France), Jan Kratochvil (Prague, Czech Republic), Mitsutoshi Kuroda (Yamagata, Japan), Valery Levitas (Ames, USA), as well as the additional contributors to these CISM lecture notes Kais Ammar (Paris, France), Benoît Appolaire (Châtillon, France), Daniel Balzani (Essen, Germany), Dominik Brands (Essen, Germany), Nicolas Cordero (Paris, France), Anaïs Gaubert (Châtillon, France), Ulrich Hoppe (Bochum, Germany), and Dennis Kochmann (Pasadena, USA). We furthermore thank the 47 participants from 9 countries who made the course a success. Finally, we extend our thanks to the Rectors, the Board, and the staff of CISM for the excellent support and kind help.

Jörg Schröder and Klaus Hackl

CONTENTS

A numerical two-scale homogenization scheme: the FE^2-method

Jörg Schröder

Institute of mechanics, Dept. Civil Engineering, Fac. of Engineering,
University of Duisburg-Essen
Corresponding author: j.schroeder@uni-due.de

Abstract A wide class of micro-heterogeneous materials is designed to satisfy the advanced challenges of modern materials occurring in a variety of technical applications. The effective macroscopic properties of such materials are governed by the complex interaction of the individual constituents of the associated microstructure. A *sufficient* macroscopic phenomenological description of these materials up to a certain order of accuracy can be very complicated or even impossible. On the contrary, a whole resolution of the fine scale for the macroscopic boundary value problem by means of a classical discretization technique seems to be too elaborate.

Instead of developing a macroscopic phenomenological constitutive law, it is possible to attach a representative volume element ($\mathcal{RVE}$) of the microstructure at each point of the macrostructure; this results in a two-scale modeling scheme. A discrete version of this scheme performing finite element (FE) discretizations of the boundary value problems on both scales, the macro- and the micro-scale, is denoted as the FE^2-method or as the multilevel finite element method. The main advantage of this procedure is based on the fact that we do not have to define a macroscopic phenomenological constitutive law; this is replaced by suitable averages of stress measures and deformation tensors over the microstructure.

Details concerning the definition of the macroscopic quantities in terms of their microscopic counterparts, the definition/construction of boundary conditions on the $\mathcal{RVE}$ as well as the consistent linearization of the macroscopic constitutive equations are discussed in this contribution.

Furthermore, remarks concerning stability problems on both scales as well as their interactions are given and representative numerical examples for elasto-plastic microstructures are discussed.

J. Schröder, K. Hackl (Eds.), *Plasticity and Beyond*, CISM International Centre for Mechanical Sciences, DOI 10.1007/978-3-7091-1625-8_1, © CISM, Udine 2014

1 Introduction

For the analysis of micro-heterogeneous materials, we define two different scales, the macroscopic scale (coarse scale) and the microscopic scale (fine scale). The fine scale is assumed to be the scale of the heterogeneities of characteristic length l, whereas the characteristic length of the coarse scale is denoted by L. If we assume that the domain size at the fine scale is sufficient for homogenization requirements, then the *separation of scales* expressed by

$$l \ll L \tag{1}$$

has to hold. A homogenized – that means effective macroscopic – description of the micro-heterogeneous material requires the definition of a representative volume element ($\mathcal{RVE}$) or a *statistically homogeneous volume element*, which is here assumed to be possible. In classical works, effective quantities of micro-heterogeneous media, such as stiffness or compliance tensors, have been discussed by Voigt (1910) and Reuss (1929). The arithmetical mean value of Voigt and the harmonic mean value of Reuss were shown later to be upper and lower bounds of effective parameters, see Hill (1965b, 1964a,b, 1963). However, the gap between these approximations can be quite wide, see e.g. Babuska (1976). General procedures for the derivation of inequalities between various moduli of mixtures have been discussed by Hill (1963) and Kröner (1971). A variety of methods for the computation of overall properties of micro-heterogeneous materials are documented in the monograph Nemat-Nasser and Hori (1999).
A fundamental assumption for the scale-transition is the *macro-homogeneity condition*, also denoted as *Hill condition* or *Hill-Mandel condition*, which asserts the equality of the virtual work between both scales, see Hill (1965a, 1963), Mandel and Dantu (1963), Mandel (1972). There are several "additive" mechanical quantities which could be averaged over the representative volume element when transferred to the macro-scale, e.g. the mass, internal energy, entropy and dissipation. Furthermore, macroscopic measures of plastic work for micro-heterogeneous materials have been analyzed in Hill (1971).

A suitable framework for the solution of two-scale problems is the mathematical homogenization theory. There, it is usually assumed that the microstructure is locally built by the spatial repetition of a suitable, very small part of the whole microstructure, a unit cell. Thus, it is assumed that the morphology and the distribution of the material properties are periodic functions of the microscopic spatial parametrization y. As an introductionary example we consider a simple one-dimensional bar. For this purpose, let

the periodic function $EA(y)$ denote the axial stiffness of a bar, $u(\overline{x}, y)$ the axial displacement, $\overline{x}$ the parametrization of the coarse scale, and $n(\overline{x})$ the distributed axial load, then the axial displacements of the bar are described by the differential equation

$$\frac{d}{d\overline{x}} N(\overline{x}, y) + n(\overline{x}) = 0 \quad \text{with} \quad N(\overline{x}, y) := EA(y) \, \frac{du(\overline{x}, y)}{d\overline{x}} \, . \tag{2}$$

The mathematical homogenization theory is based on the double scale asymptotic expansion of the yet unknown y-periodic field variable $u(\overline{x}, y)$, i.e.,

$$u(\overline{x}, y) = u^{(0)}(\overline{x}, y) + \epsilon \, u^{(1)}(\overline{x}, y) + \epsilon^2 \, u^{(2)}(\overline{x}, y) + \cdots \, , \tag{3}$$

where ϵ, defined as the microscopic to macroscopic dimension ratio (l/L), is a very small number. The asymptotic expansion (3) has to be substituted into the underlying partial differential equation with oscillating coefficients. Applying the chain rule, i.e.,

$$\frac{d}{d\overline{x}} N(\overline{x}, y) = \frac{\partial N(\overline{x}, y)}{\partial \overline{x}} + \epsilon^{-1} \frac{\partial N(\overline{x}, y)}{\partial y} \, , \tag{4}$$

yields a set of equations with factors in powers of ϵ. Equating the terms of the different orders of ϵ with zero yields the set of differential equations, which have to be solved. Fundamentals of this framework can be found in Bensoussan et al. (1978), Sanchez-Palencia and Zaoui (1986) and Bakhvalov and Panasenko (1984). Based on this approach, a computational homogenization framework in the field of linear elasticity as well as the application of adaptive finite element methods has been proposed in Guedes and Kikuchi (1990). Extensions of this method to locally non-periodic microheterogeneous media are given by Fish and Wagiman (1993). A framework of a two-scale homogenization technique using a Voronoi cell finite element formulation has been proposed by Ghosh et al. (1995). Generalized convergence arguments for the interpretation of the homogenized variational equations have been used by Terada and Kikuchi (2001). An extension of the latter simultaneous two-scale method to geometrical nonlinear formulations of the associated two-scale boundary value problems in a material and a spatial setting has been developed in Terada et al. (2003). Several mathematical aspects of homogenization theory are discussed in Tartar (2000). For the treatment of finite thermoelasticity in this scheme, we refer to Temizer (2012).

A homogenization technique without recourse to the two-scale asymptotic expansion is governed by the above mentioned *Hill-Mandel condition*.

Here, the boundary value problems on the macro- and on the micro-scale are prescribed by the balance of linear and angular momentum and suitable boundary conditions on both scales, where the micro-scale is approximated by means of a representative volume element. A summary of recent developments in this field of applied computational mechanics of the overall description of micro-heterogeneous materials up to the mid 1980's is given in Suquet (1987). In this context we also refer to Michel et al. (1999) where the boundary value problem on the micro-scale is solved using the Finite-Element-Method (FEM) and, alternatively, using a Fast Fourier Transformation. The authors also discuss the constraints on discrete unknown displacements arising when periodic boundary conditions are used.
A multilevel finite element method (FE^2-method) for nonlinear heterogeneous systems has been discussed by Smit et al. (1998), where the authors implemented their algorithms in an Updated Lagrange environment. Another FE^2-method for the analysis of the elasto-viscoplastic behavior of fiber-reinforced composite materials was presented by Feyel and Chaboche (2000), where the tangent matrix has been approximated by a perturbation method. A framework for geometrically and/or physically linear/nonlinear homogenization techniques in the sense of the FE^2-method has been developed by Miehe et al. (1999a,b), including a closed-form representation of the macroscopic (homogenized) tangent moduli. In order to design "deformation-driven" microstructures, Miehe and Koch (2002) proposed a Lagrangian multiplier method for the computational treatment of the constraints arising from the different boundary conditions: i) linear displacements, ii) constant tractions, and iii) periodic displacements in combination with antiperiodic tractions; for the discussion of the distinct boundary conditions, see also van der Sluis et al. (2000), Terada et al. (2000), Kouznetsova et al. (2001), Miehe and Bayreuther (2007) and Perić et al. (2011). A family of algorithms and matrix representations of overall stresses and tangent moduli of discretized micro-heterogeneous materials at finite strains is descriped in Miehe (2003). Different methods for the computation of the macroscopic tangent, e.g. the penalty method, have been investigated in Temizer and Wriggers (2008).

The nature of finite deformation continuum mechanics is the non-uniqueness of solutions at specific thermodynamic states. As an example, this can be associated to stability problems like buckling of columns under compressive loadings. Although in micro-heterogeneous materials, like aligned fiber-reinforced composites, cellular solids or in general arbitrary arrangements of inhomogeneities, buckling phenomena may occur on the micro-scale. A challenging issue in homogenization schemes at finite strains is the ana-

lysis of instabilities at the macro- and micro-scale and their interactions. In general, we distinguish between structural instabilities and material instabilities: structural instabilities are associated to the non-uniqueness of the underlying boundary value problem, whereas material instabilities are understood as the violation of the Legendre-Hadamard-condition (loss of rank-one convexity) of the free-energy. Nevertheless, there exits a relation between material instabilities on the macro-scale and specific structural instabilities on the micro-scale. Abeyaratne and Triantafyllidis (1984) studied the macroscopic material instability occuring in nonlinear elastic composites with periodically arranged voids. It was shown that a homogenized material instability occurs although the matrix material was polyconvex in the sense of Ball (1977b). Bifurcation modes of fiber-reinforced composites as well as possible macroscopic material instabilities have been analyzed in Triantafyllidis and Maker (1985). Structural instability problems on the micro-scale are associated to the homogenization of a nonconvex boundary value problem on the micro-scale, see Müller (1987). The main challenge here is the a priori unknown size of the $\mathcal{RVE}$. A systematic investigation of the problems pointed out in Abeyaratne and Triantafyllidis (1984) and Triantafyllidis and Maker (1985) is given in Geymonat et al. (1993). Applying a Bloch-wave ansatz to a fiber-reinforced composite, the authors showed that the onset of a bifurcation on the micro-scale corresponding to the long-wavelength limit (infinite wavelength) leads to a macroscopic material instability. A detailed computational homogenization analysis of structural instabilities on the micro-scale and possible material instabilities on the macro-scale as well as their interactions is performed in Miehe et al. (2002), in this context see also Agoras et al. (2009) and Aubert et al. (2008). A microscopic bifurcation condition of cellular solids, like elastic cellular honeycombs, have been presented in Ohno et al. (2002). A procedure, based on a block-diagonalization method for periodic microstructures, for the estimation of the number of unit cells necessary for the definition of a $\mathcal{RVE}$ of cellular solids in microscopic bifurcation problems has been proposed in Saiki et al. (2002). In the context of homogenization of non-convex integral functionals and especially for the relation between linearization and homogenization in finite elasticity, we refer to Müller and Neukamm (2011). For the treatment of localized failure with softening in this multi-scale approach see Hautefeuille et al. (2012).

If the classical assumption of scale separation does not hold or if it is necessary to capture size dependency, then in general higher-order homogenization techniques can be applied. A second-order homogenization scheme, implying a second gradient continuum on the macro-scale and a remaining classical continuum on the micro-scale, has been proposed by Geers et al.

(2001, 2003) and Kouznetsova et al. (2004). A multilevel finite element method coupling a classical continuum, a Cauchy continuum, on the fine scale with a Cosserat continuum at the coarse scale has been proposed by Feyel (2003). A critical analysis of the two-scale homogenization of macroscopic second gradient and micromorphic models based on a Cauchy continuum on the fine scale with emphasis on non-homogeneous boundary conditions is given by Forest and Trinh (2011), in this context see also Forest (2002) and Jänicke et al. (2009). An application of the computational homogenization scheme for structured thin sheets has been proposed by Geers et al. (2007) and Gruttmann and Wagner (2013). Here, the $\mathcal{RVE}$ resolves the full thickness of the thin sheet and the nature of the coupling of deformation between the shell-type macro-scale and the microstructure is of second-order.
Another non-classical approach, denoted as a multi-scale strategy for *strongly coupled scales*, has been proposed by Ibrahimbegović and Markovič (2003). Here, the authors attach a part of the microstructure at each finite element of the macro-scale, for details see Markovic et al. (2005) and Niekamp et al. (2009). This is in contrast to the *weakly coupled scales*, where we attach an $\mathcal{RVE}$ of the microstructure at each point of the macrostructure, i.e., at each Gauss point in the discrete version obtained from the FE^2-method.

Recent developments are concerned with direct two-scale homogenization techniques for thermo-mechanically coupled problems, Özdemir et al. (2008), and for electro-mechanically coupled problems concerning the general localization and homogenization scheme, Schröder (2009), as well as the numerical treatment Schröder and Keip (2011, 2012).
Another important topic is the characterization of random microstructures, Ohser and Mücklich (2000), and the identification of statistically representative volume elements, see e.g. Kanit et al. (2003), Stroeven and Askes (2004), Temizer and Zohdi (2007). From the computational point of view, the application of statistically similar representative volume elements, which have less complexity than the original random microstructure, could lead to a significant reduction in computation time. Basic considerations for the definition and optimization procedures based on suitable statistical measure are discussed in Povirk (1995), Ostoja-Starzewski (2006), Balzani et al. (2009, 2010), Schröder et al. (2010), Ambrozinski et al. (2012), in this context see also Swaminathan et al. (2006) and Zohdi and Wriggers (2005). Details on the construction of statistically similar representative volume elements are presented in the contribution by Balzani et al. in this book.

2 Direct Micro-Macro Transition Approach

For the analysis of micro-heterogeneous materials, where we want to take into account the microstructure directly, the transition between the macro- and the micro scale has to be defined, cf. Fig. 1. The direct micro-macro homogenization scheme, based on the finite element discretization of both scales, allows for the computation of macroscopic boundary value problems in consideration of $\mathcal{RVE}s$, which should represent the main characteristics of the associated micro-continuum.

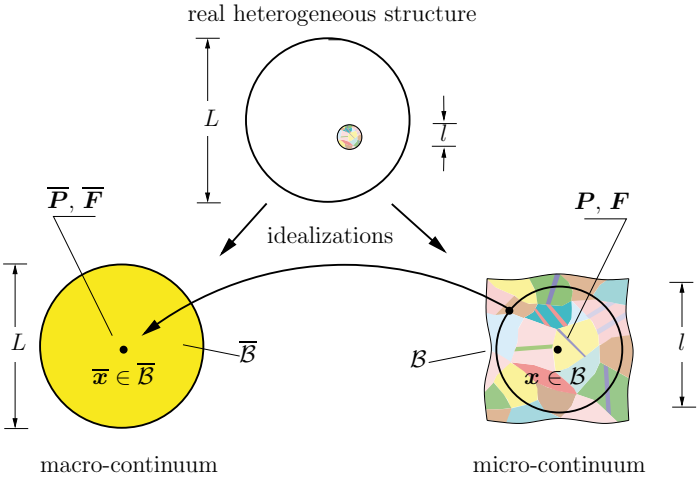

Figure 1. Schematic illustration of the direct homogenization procedure. Notation: macroscopic first Piola-Kirchhoff stresses $\overline{\boldsymbol{P}}$ and deformation gradient $\overline{\boldsymbol{F}}$; their microscopic counterparts are denoted by $\boldsymbol{P}$ and $\boldsymbol{F}$, taken from Schröder et al. (2010)

Since the definition of the individual scales, like macro-, meso- and micro-scale, is somewhat arbitrary, we denote the coarse and fine scale as the macro- and micro-scale, respectively. The main technical ingredients for the two-scale homogenization procedure for mechanical problems are:

- Definition of a $\mathcal{RVE}$ and choosing suitable boundary conditions: The boundary conditions for the microscopic boundary value problem are in general not given a priori. Suitable boundary conditions can be derived by the Hill-Mandel condition, which equates the virtual macroscopic work with the averaged virtual work performed within the $\mathcal{RVE}$.
- Discretization of the microscopic boundary value problem.
- Discretization of the macroscopic boundary value problem.

The main advantage of a direct two-scale homogenization scheme is that we do not have to define a macroscopic phenomenological constitutive law; this is replaced by suitable averages over the $\mathcal{RVE}$. Nevertheless, we have to set up constitutive models for the individual phases on the fine scale. If the local distributions of the deformation and stress measures within the $\mathcal{RVE}$ are computed, we can calculate their macroscopic counterparts by suitable surface or volume integrals over the representative volume element, which are attached at each macroscopic point. Therefore, the numerical micro-to-macro procedure is based on the following consecutive steps:

a) *Localization step, boundary value problem on the micro-scale*: computation of the local distribution of the deformation and stress measures within the $\mathcal{RVE}$ by solving the weak form of the balance of linear momentum.

b) *Homogenization step*: computation of the macroscopic quantities, e.g. the first Piola-Kirchhoff stresses, by means of suitable averages.

c) *Boundary value problem on the macro-scale*: solving the weak form of balance of linear momentum on the coarse scale.

These steps have to be repeated until convergence on both scales is obtained.

2.1 Boundary value problem on the macro-scale

Let the reference configuration of the body of interest on the macroscopic scale $\overline{\mathcal{B}}_0 \subset R^3$ be parameterized in $\overline{\boldsymbol{X}}$. The macroscopic nonlinear deformation map is denoted as $\overline{\boldsymbol{\varphi}}_t(\overline{\boldsymbol{X}})$; it maps points $\overline{\boldsymbol{X}}$ of the reference configuration onto points $\overline{\boldsymbol{x}}$ of the actual configuration $\overline{B}_t$, see Figure 2. The fundamental deformation measure is the macroscopic deformation gradient, defined by

$$\overline{\boldsymbol{F}}(\overline{\boldsymbol{X}}) := \mathrm{Grad}_{\overline{X}}[\overline{\boldsymbol{\varphi}}_t(\overline{\boldsymbol{X}})] \quad \text{with} \quad \overline{F}^a{}_A := \frac{\partial \overline{x}^a}{\partial \overline{X}^A}\,, \tag{5}$$

which maps macroscopic infinitesimal line elements $d\overline{\boldsymbol{X}}$ from the reference configuration to the current configuration, i.e.,

$$d\overline{\boldsymbol{x}} = \overline{\boldsymbol{F}}\, d\overline{\boldsymbol{X}}\,. \tag{6}$$

Let $d\overline{\boldsymbol{A}} = \overline{\boldsymbol{N}}\, d\overline{A}$ and $d\overline{\boldsymbol{a}} = \overline{\boldsymbol{n}}\, d\overline{a}$ denote the infinitesimal vectorial area elements with respect to the reference and current configuration, repectively. The transformation between the quantities is

$$d\overline{\boldsymbol{a}} = [\mathrm{Cof}\, \overline{\boldsymbol{F}}]\, d\overline{\boldsymbol{A}} \quad \text{with} \quad \mathrm{Cof}\, \overline{\boldsymbol{F}} = \overline{J}\, \overline{\boldsymbol{F}}^{-T}\,, \tag{7}$$

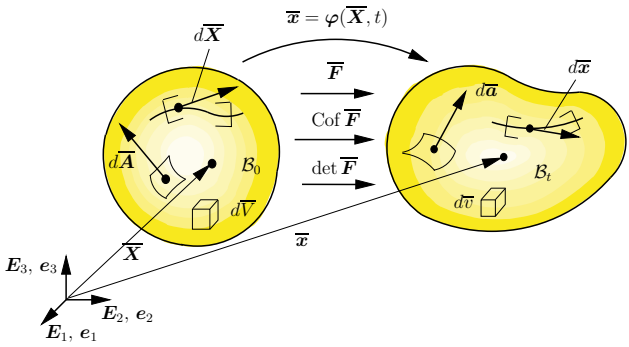

Figure 2. Mapping of infinitesimal line-, vectorial area- and volume-elements from the reference to the actual configuration at the macro-scale.

using Nanson's formula and the abbreviation $\overline{J} = \det \overline{\boldsymbol{F}}$ for their Jacobian determinant. The relation between the macroscopic infinitesimal volume elements $d\overline{V}$ of the reference and $d\overline{v}$ of the current configuration reads

$$d\overline{v} = \overline{J}\, d\overline{V}\,. \tag{8}$$

As a suitable deformation measure, we introduce the macroscopic right Cauchy-Green tensor

$$\overline{\boldsymbol{C}} := \overline{\boldsymbol{F}}^T \overline{\boldsymbol{F}}\,. \tag{9}$$

With the first Piola-Kirchhoff stress tensor $\overline{\boldsymbol{P}}$ the Kirchhoff stresses, the Cauchy stresses and the second Piola-Kirchhoff stresses can be computed by

$$\overline{\boldsymbol{\tau}} = \overline{\boldsymbol{P}}\,\overline{\boldsymbol{F}}^T\,, \quad \overline{\boldsymbol{\sigma}} = \frac{1}{\overline{J}}\,\overline{\boldsymbol{P}}\,\overline{\boldsymbol{F}}^T \quad \text{and} \quad \overline{\boldsymbol{S}} = \overline{\boldsymbol{F}}^{-1}\,\overline{\boldsymbol{P}}\,, \tag{10}$$

respectively. The balance of linear momentum at the macroscopic scale, neglecting acceleration terms, requires

$$\mathrm{Div}_{\overline{X}}\overline{\boldsymbol{P}} + \overline{\boldsymbol{f}} = \boldsymbol{0}\,. \tag{11}$$

Furthermore, the macroscopic balance of moment of momentum, i.e.,

$$\overline{\boldsymbol{P}}\,\overline{\boldsymbol{F}}^T = \overline{\boldsymbol{F}}\,\overline{\boldsymbol{P}}^T \tag{12}$$

is assumed to be satisfied a priori by symmetry requirements of the macroscopic Kirchhoff stress tensor.

2.2 Boundary value problem on the micro-scale

In analogy to the description of the mechanical quantities on the macro-scale, we parametrize the reference placement of the $\mathcal{RVE}$ on the micro-scale $\mathcal{B}_0 \subset \mathbb{R}^3$ with $\boldsymbol{X}$. The nonlinear deformation map on the micro-scale is denoted as $\boldsymbol{\varphi}_t(\boldsymbol{X})$, which maps points $\boldsymbol{X}$ of the reference placement onto points $\boldsymbol{x}$ of the current placement B_t.

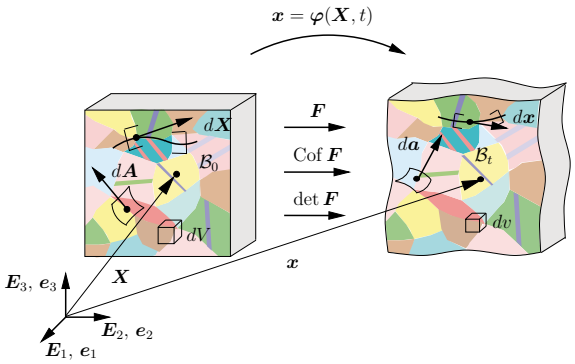

Figure 3. Transport theorems at the micro-scale: Mapping of infinitesimal geometrical elements from the reference to the actual configuration.

The microscopic deformation gradient is defined by

$$\boldsymbol{F}(\boldsymbol{X}) := \mathrm{Grad}_X[\boldsymbol{\varphi}_t(\boldsymbol{X})] \quad \text{with} \quad F^a{}_A := \frac{\partial x^a}{\partial X^A}\,, \tag{13}$$

which maps microscopic infinitesimal line elements $d\boldsymbol{X}$ from the reference configuration to the current configuration, i.e.,

$$d\boldsymbol{x} = \boldsymbol{F}\, d\boldsymbol{X}\,. \tag{14}$$

The transformation of the infinitesimal vectorial area elements of the reference configuration $d\boldsymbol{A} = \boldsymbol{N}\, dA$ to the area elements of the current configuration $d\boldsymbol{a} = \boldsymbol{n}\, da$ is given by

$$d\boldsymbol{a} = [\mathrm{Cof}\, \boldsymbol{F}]d\boldsymbol{A} \quad \text{with} \quad \mathrm{Cof}\, \boldsymbol{F} = J\, \boldsymbol{F}^{-T}\,, \tag{15}$$

using the abbreviation $J = \det \boldsymbol{F}$. The microscopic infinitesimal volume elements dV and dv of the reference and current configuration, respectively, transform with

$$dv = J\, dV\,. \tag{16}$$

As further deformation measures, we introduce the microscopic right Cauchy-Green tensor and the microscopic Finger tensor

$$\boldsymbol{C} := \boldsymbol{F}^T \boldsymbol{F} \quad \text{and} \quad \boldsymbol{b} := \boldsymbol{F} \boldsymbol{F}^T , \tag{17}$$

respectively. Starting from the microscopic first Piola-Kirchhoff stress tensor $\boldsymbol{P}$, we can compute the microscopic Kirchhoff-, Cauchy- and second Piola-Kirchhoff stresses by

$$\boldsymbol{\tau} = \boldsymbol{P} \boldsymbol{F}^T , \quad \boldsymbol{\sigma} = \frac{1}{J} \boldsymbol{\tau} \quad \text{and} \quad \boldsymbol{S} = \boldsymbol{F}^{-1} \boldsymbol{P} , \tag{18}$$

respectively. The balance of linear momentum, neglecting body forces, is given by

$$\mathrm{Div}_X \boldsymbol{P} = \boldsymbol{0} \quad \text{or} \quad \mathrm{div}_x \boldsymbol{\sigma} = \boldsymbol{0} , \tag{19}$$

with respect to the reference and actual placement, respectively. Equation $(19)_2$ is derived from $(19)_1$ by setting $\boldsymbol{P} = \boldsymbol{\sigma} \mathrm{Cof} \boldsymbol{F}$ and applying the Piola identity

$$\mathrm{Div}_X [\mathrm{Cof} \boldsymbol{F}] = \boldsymbol{0} . \tag{20}$$

The balance of moment of momentum

$$\boldsymbol{P} \boldsymbol{F}^T = \boldsymbol{F} \boldsymbol{P}^T . \tag{21}$$

is assumed to be satisfied a priori by symmetry requirements of the Kirchhoff stress tensor, which are guaranteed by the constitutive modeling.

2.3 Macro-variables and microscopic counterparts

An extension of the micro-macro transition framework from small to finite strains has been given in Hill (1972). The determinant $\overline{J}$ of the macroscopic deformation gradient is related to its microscopic counterpart by the volume averages

$$\overline{J} = \frac{1}{V} \int_{\mathcal{B}_0} J \, dV = \frac{1}{V} \int_{\mathcal{B}_t} dv = \frac{v}{V} , \tag{22}$$

here V denotes the reference and v the actual volume of the $\mathcal{RVE}$. Let us assume that the $\mathcal{RVE}$ in its reference placement has a hole $\mathcal{L}_0$ with boundary $\partial \mathcal{L}_0$, then the volume average of deformation gradient can be expressed by

$$\frac{1}{V} \int_{\mathcal{B}_0} \boldsymbol{F} \, dV = \frac{1}{V} \int_{\partial \mathcal{B}_0} \boldsymbol{x} \otimes \boldsymbol{N} \, dA + \frac{1}{V} \int_{\partial \mathcal{L}_0} \boldsymbol{x} \otimes \boldsymbol{N} \, dA . \tag{23}$$

Furthermore, the volume average of the first Piola-Kirchhoff stress tensor is then given by the surface integrals

$$\frac{1}{V}\int_{\mathcal{B}_0} \boldsymbol{P}\, dV = \frac{1}{V}\int_{\partial\mathcal{B}_0} \boldsymbol{t}_0 \otimes \boldsymbol{X}\, dA + \frac{1}{V}\int_{\partial\mathcal{L}_0} \boldsymbol{t}_0 \otimes \boldsymbol{X}\, dA\,, \tag{24}$$

with $\boldsymbol{t}_0 = \boldsymbol{P}\boldsymbol{N}$ and the outward unit normal $\boldsymbol{N}$. In order to get a simple correlation of the macroscopic quantities in terms of suitable integrals over the $\mathcal{RVE}$ with experimental set-ups, we define the macroscopic deformation gradient and the first Piola-Kirchhoff stress tensor in terms of surface integrals over the boundary $\partial\mathcal{B}_0$ of the $\mathcal{RVE}$:

$$\overline{\boldsymbol{F}} = \frac{1}{V}\int_{\partial\mathcal{B}_0} \boldsymbol{x} \otimes \boldsymbol{N}\, dA\,, \qquad \overline{\boldsymbol{P}} = \frac{1}{V}\int_{\partial\mathcal{B}_0} \boldsymbol{t}_0 \otimes \boldsymbol{X}\, dA\,. \tag{25}$$

By analogy with the previous relations, we obtain

$$\dot{\overline{\boldsymbol{F}}} = \frac{1}{V}\int_{\partial\mathcal{B}_0} \dot{\boldsymbol{x}} \otimes \boldsymbol{N}\, dA\,, \qquad \dot{\overline{\boldsymbol{P}}} = \frac{1}{V}\int_{\partial\mathcal{B}_0} \dot{\boldsymbol{t}}_0 \otimes \boldsymbol{X}\, dA\,. \tag{26}$$

In the following, we neglect holes $\mathcal{L}_0$, then the surface integrals (25, 26) are identical to their volume averages. Similar arguments have to be applied if singular surfaces are taken into account, see e.g. Schröder (2000).

For the following algebraic manipulations we introduce an additive decomposition of the microscopic deformation gradient in a constant and a fluctuation part, i.e.,

$$\boldsymbol{F} = \overline{\boldsymbol{F}} + \widetilde{\boldsymbol{F}}\,. \tag{27}$$

Integration of (27) over the representative volume element yields

$$\overline{\boldsymbol{F}} = \frac{1}{V}\int_{\mathcal{B}_0} \boldsymbol{F}\, dV = \frac{1}{V}\int_{\mathcal{B}_0} (\overline{\boldsymbol{F}} + \widetilde{\boldsymbol{F}})\, dV = \overline{\boldsymbol{F}} + \frac{1}{V}\int_{\mathcal{B}_0} \widetilde{\boldsymbol{F}}\, dV\,. \tag{28}$$

The implication of the latter relation is that the volume averages of the fluctuation part $\widetilde{\boldsymbol{F}}$ vanish, i.e.,

$$\frac{1}{V}\int_{\mathcal{B}_0} \widetilde{\boldsymbol{F}}\, dV = \boldsymbol{0}\,. \tag{29}$$

If we further assume that the fluctuation part of the microscopic deformation gradient can be computed by $\widetilde{\boldsymbol{F}} = \mathrm{Grad}_X\, \widetilde{\boldsymbol{w}}$, where $\widetilde{\boldsymbol{w}}$ represents the fluctuation part of the deformation field on the micro-scale, then the following condition holds:

$$\frac{1}{V}\int_{\partial\mathcal{B}_0} \widetilde{\boldsymbol{w}} \otimes \boldsymbol{N}\, dA = \boldsymbol{0}\,. \tag{30}$$

By analogy with the decomposition of the microscopic deformation gradient, we introduce an additive decomposition of the microscopic first Piola-Kirchhoff stresses in a constant and a fluctuation part, i.e.,

$$\boldsymbol{P} = \overline{\boldsymbol{P}} + \widetilde{\boldsymbol{P}} \,. \tag{31}$$

The evaluation of the integral of the decomposition (31) over the $\mathcal{RVE}$ yields

$$\overline{\boldsymbol{P}} = \frac{1}{V} \int_{\mathcal{B}_0} \boldsymbol{P} \, dV = \frac{1}{V} \int_{\mathcal{B}_0} (\overline{\boldsymbol{P}} + \widetilde{\boldsymbol{P}}) \, dV = \overline{\boldsymbol{P}} + \frac{1}{V} \int_{\mathcal{B}_0} \widetilde{\boldsymbol{P}} \, dV \,, \tag{32}$$

which implies

$$\frac{1}{V} \int_{\mathcal{B}_0} \widetilde{\boldsymbol{P}} \, dV = \boldsymbol{0} \,. \tag{33}$$

Based on the definition of the traction vector $\boldsymbol{t}_0 = \boldsymbol{P}\boldsymbol{N} = (\overline{\boldsymbol{P}} + \widetilde{\boldsymbol{P}})\boldsymbol{N}$ we introduce the abbreviation $\boldsymbol{t}_0 = \overline{\boldsymbol{t}}_0 + \widetilde{\boldsymbol{t}}_0$ with $\overline{\boldsymbol{t}}_0 = \overline{\boldsymbol{P}}\boldsymbol{N}$ and $\widetilde{\boldsymbol{t}}_0 = \widetilde{\boldsymbol{P}}\boldsymbol{N}$. Inserting these quantities in $(25)_2$ yields

$$\overline{\boldsymbol{P}} = \frac{1}{V} \int_{\partial \mathcal{B}_0} (\overline{\boldsymbol{t}}_0 + \widetilde{\boldsymbol{t}}_0) \otimes \boldsymbol{X} \, dA \,. \tag{34}$$

From one part of the surface integral we derive the relation

$$\frac{1}{V} \int_{\partial \mathcal{B}_0} \overline{\boldsymbol{t}}_0 \otimes \boldsymbol{X} \, dA = \frac{1}{V} \int_{\partial \mathcal{B}_0} (\overline{\boldsymbol{P}}\boldsymbol{N}) \otimes \boldsymbol{X} \, dA = \overline{\boldsymbol{P}} \, \frac{1}{V} \int_{\partial \mathcal{B}_0} \boldsymbol{N} \otimes \boldsymbol{X} \, dA \,, \tag{35}$$

which yields with the relation $\dfrac{1}{V} \displaystyle\int_{\partial \mathcal{B}_0} \boldsymbol{N} \otimes \boldsymbol{X} \, dA = \boldsymbol{1}$ the identity

$$\frac{1}{V} \int_{\partial \mathcal{B}_0} \overline{\boldsymbol{t}}_0 \otimes \boldsymbol{X} \, dA = \overline{\boldsymbol{P}} \,. \tag{36}$$

Therefore, we conclude from (34) that for an equilibrium state

$$\frac{1}{V} \int_{\partial \mathcal{B}_0} \widetilde{\boldsymbol{t}}_0 \otimes \boldsymbol{X} \, dA = \boldsymbol{0} \tag{37}$$

holds. In general, other macroscopic quantities are defined by the standard transformations using the macroscopic stress- and deformation tensors. Thus, the macroscopic Kirchhoff stresses $\overline{\boldsymbol{\tau}}$ are defined as

$$\overline{\boldsymbol{\tau}} = \overline{\boldsymbol{P}} \, \overline{\boldsymbol{F}}^T = \frac{1}{V} \int_{\mathcal{B}_0} \boldsymbol{P} \, dV \quad \left(\frac{1}{V} \int_{\mathcal{B}_0} \boldsymbol{F} \, dV \right)^T \,. \tag{38}$$

In a similar way, we define the macroscopic Cauchy stresses by the transformation

$$\overline{\boldsymbol{\sigma}} = \frac{1}{\overline{J}} \overline{\boldsymbol{P}}\, \overline{\boldsymbol{F}}^T = \frac{1}{\overline{J}} \overline{\boldsymbol{\tau}} = \frac{1}{\overline{J}} \left(\frac{1}{V} \int_{\mathcal{B}_0} \boldsymbol{P}\, dV \right) \left(\frac{1}{V} \int_{\mathcal{B}_0} \boldsymbol{F}\, dV \right)^T . \tag{39}$$

Also the definition of the macroscopic Cauchy-Green tensor is based on the product of the macroscopic deformation gradient, i.e.,

$$\overline{\boldsymbol{C}} = \overline{\boldsymbol{F}}^T \overline{\boldsymbol{F}} = \left(\frac{1}{V} \int_{\mathcal{B}_0} \boldsymbol{F}\, dV \right)^T \left(\frac{1}{V} \int_{\mathcal{B}_0} \boldsymbol{F}\, dV \right) , \tag{40}$$

A simple volume averaging of the microscopic Cauchy-Green tensor

$$\frac{1}{V} \int_{\mathcal{B}_0} \boldsymbol{C}\, dV = \frac{1}{V} \int_{\mathcal{B}_0} \boldsymbol{F}^T \boldsymbol{F}\, dV , \tag{41}$$

leads with the decomposition $\boldsymbol{F} = \overline{\boldsymbol{F}} + \widetilde{\boldsymbol{F}}$ to the expression

$$\begin{aligned} \frac{1}{V} \int_{\mathcal{B}_0} (\overline{\boldsymbol{F}} + \widetilde{\boldsymbol{F}})^T (\overline{\boldsymbol{F}} + \widetilde{\boldsymbol{F}})\, dV = \;& \overline{\boldsymbol{F}}^T \overline{\boldsymbol{F}} + \frac{1}{V} \int_{\mathcal{B}_0} \widetilde{\boldsymbol{F}}^T \widetilde{\boldsymbol{F}}\, dV \\ + \;& \frac{1}{V} \int_{\mathcal{B}_0} (\widetilde{\boldsymbol{F}}^T \overline{\boldsymbol{F}} + \overline{\boldsymbol{F}}^T \widetilde{\boldsymbol{F}})\, dV . \end{aligned} \tag{42}$$

The integral term on the right-hand side

$$\int_{\mathcal{B}_0} (\widetilde{\boldsymbol{F}}^T \overline{\boldsymbol{F}} + \overline{\boldsymbol{F}}^T \widetilde{\boldsymbol{F}})\, dV = \int_{\mathcal{B}_0} \widetilde{\boldsymbol{F}}^T\, dV\, \overline{\boldsymbol{F}} + \overline{\boldsymbol{F}}^T \int_{\mathcal{B}_0} \widetilde{\boldsymbol{F}}\, dV \tag{43}$$

vanishes obviously, thus the remaining expression of (41) is

$$\frac{1}{V} \int_{\mathcal{B}_0} \boldsymbol{C}\, dV = \overline{\boldsymbol{F}}^T \overline{\boldsymbol{F}} + \frac{1}{V} \int_{\mathcal{B}_0} \widetilde{\boldsymbol{F}}^T \widetilde{\boldsymbol{F}}\, dV , \tag{44}$$

which differs from (40) by the integral term on the right-hand side in (44).

Equivalences between the definitions (38) and (39) and direct averages of $\boldsymbol{\tau}$ and $\boldsymbol{\sigma}$ with respect to the volume of the $\mathcal{RVE}$ in the reference and actual placement, respectively, i.e.

$$\overline{\boldsymbol{\tau}} \equiv \frac{1}{V} \int_{\mathcal{B}_0} \boldsymbol{\tau}\, dV , \qquad \overline{\boldsymbol{\sigma}} \equiv \frac{1}{v} \int_{\mathcal{B}_t} \boldsymbol{\sigma}\, dv \tag{45}$$

hold only for specific boundary conditions and geometries, see e.g. de Souza Neto and Feijoo (2008). If the conditions are satisfied, we obtain for the Kirchhoff stresses and by analogy for the Cauchy stresses, assuming (19):

$$\frac{1}{V} \int_{\mathcal{B}_0} \boldsymbol{\tau}\, dV = \frac{1}{V} \int_{\partial \mathcal{B}_0} \boldsymbol{t}_0 \otimes \boldsymbol{x}\, dA , \qquad \frac{1}{v} \int_{\mathcal{B}_t} \boldsymbol{\sigma}\, dv = \frac{1}{v} \int_{\partial \mathcal{B}_t} \boldsymbol{t} \otimes \boldsymbol{x}\, da \tag{46}$$

with $\boldsymbol{t} = \boldsymbol{\sigma}\boldsymbol{n}$ and the outward unit normal $\boldsymbol{n}$ on $\partial\mathcal{B}_t$. Useful relations for further kinematical quantities and stress measures in finite deformation plasticity are given in Nemat-Nasser (1999); for the elastoplasticity of polycrystals see Clayton and McDowell (2003).

2.4 Macro-homogeneity condition

One of the most important relations in micro-macro transition schemes is the *macro-homogeneity condition* (also denoted as Hill's condition or Hill-Mandel condition), Hill (1965a) and Mandel (1972). In the finite strain setting, we define the condition as

$$\overline{\boldsymbol{P}} : \dot{\overline{\boldsymbol{F}}} = \frac{1}{V} \int_{\partial\mathcal{B}_0} \boldsymbol{t}_0 \cdot \dot{\boldsymbol{x}} \, dA \,, \tag{47}$$

which leads with the algebraic manipulations

$$\frac{1}{V} \int_{\partial\mathcal{B}_0} \boldsymbol{t}_0 \cdot \dot{\boldsymbol{x}} \, dA = \frac{1}{V} \int_{\partial\mathcal{B}_0} (\boldsymbol{P}\boldsymbol{N}) \cdot \dot{\boldsymbol{x}} \, dA = \frac{1}{V} \int_{\partial\mathcal{B}_0} \boldsymbol{P} : \dot{\boldsymbol{x}} \otimes \boldsymbol{N} \, dA$$

and the application of the Gaussian integral theorem

$$\int_{\partial\mathcal{B}_0} \boldsymbol{P} : \dot{\boldsymbol{x}} \otimes \boldsymbol{N} \, dA = \int_{\mathcal{B}_0} \mathrm{Div}_X [\dot{\boldsymbol{x}} \boldsymbol{P}] \, dV = \int_{\mathcal{B}_0} (\boldsymbol{P} : \mathrm{Grad}_X \dot{\boldsymbol{x}} + \dot{\boldsymbol{x}} \mathrm{Div}_X \boldsymbol{P}) \, dV$$

and taking into account the equilibrium condition (19) to the volume average

$$\overline{\boldsymbol{P}} : \dot{\overline{\boldsymbol{F}}} = \frac{1}{V} \int_{\mathcal{B}_0} \boldsymbol{P} : \dot{\boldsymbol{F}} \, dV \,, \tag{48}$$

with $\dot{\boldsymbol{F}} = \mathrm{Grad}_X \dot{\boldsymbol{x}}$. It should be noted that the macro-homogeneity condition of Hill and Mandel is written as the volume average of the scalar product of first Piola-Kirchhoff stresses and the deformation gradient with respect to the parametrization of the $\mathcal{RVE}$ in the reference placement.

2.5 Constraint/Boundary conditions on the micro-scale

Following the explanations of Hill (1984), we write the identity

$$\frac{1}{V} \int_{\mathcal{B}_0} \boldsymbol{P} : \dot{\boldsymbol{F}} \, dV - \overline{\boldsymbol{P}} : \dot{\overline{\boldsymbol{F}}} = \frac{1}{V} \int_{\mathcal{B}_0} ((\boldsymbol{P} - \overline{\boldsymbol{P}}) : (\dot{\boldsymbol{F}} - \dot{\overline{\boldsymbol{F}}})) \, dV \,. \tag{49}$$

If the right-hand side of the latter equation vanishes, the theorem of product averages (48) is satisfied. Two simple solutions are obtained by setting

$$\boldsymbol{P} = \overline{\boldsymbol{P}} \quad \forall \boldsymbol{X} \in \mathcal{B}_0 \quad \text{or} \quad \dot{\boldsymbol{F}} = \dot{\overline{\boldsymbol{F}}} \quad \forall \boldsymbol{X} \in \mathcal{B}_0 \,, \tag{50}$$

where the first assumption of constant stresses over the $\mathcal{RVE}$ is associated to the estimate of Reuss and the second of a constant deformation gradient to the estimate of Voigt. In the following, we denote the implications in (50) as constraint conditions.

Let us now consider the right-hand side of (49); with the definition of the microscopic deformation gradient (13) and the relation $\mathrm{Grad}_X \boldsymbol{X} = \mathbf{1}$, we obtain

$$\int_{\mathcal{B}_0} (\boldsymbol{P} - \overline{\boldsymbol{P}}) : (\mathrm{Grad}_X \dot{\boldsymbol{x}} - \dot{\overline{\boldsymbol{F}}}\, \mathrm{Grad}_X \boldsymbol{X})\, dV\,. \tag{51}$$

With the equilibrium requirement $\mathrm{Div}_X(\boldsymbol{P} - \overline{\boldsymbol{P}}) = \mathbf{0}$ and the Cauchy theorem $\boldsymbol{t}_0 = \boldsymbol{P}\boldsymbol{N}$, we derive the following equivalent expression of (48):

$$\int_{\partial\mathcal{B}_0} (\boldsymbol{t}_0 - \overline{\boldsymbol{P}}\boldsymbol{N}) \cdot (\dot{\boldsymbol{x}} - \dot{\overline{\boldsymbol{F}}}\boldsymbol{X})\, dA = 0\,. \tag{52}$$

The above relations do not only hold for $\mathrm{Grad}_X \dot{\boldsymbol{x}} = \dot{\boldsymbol{F}}$, but also for $\delta\boldsymbol{F}$ as well as for $\boldsymbol{F}$, etc.; therefore, we can replace $\dot{\overline{\boldsymbol{F}}}$ by $\delta\overline{\boldsymbol{F}}$ and $\overline{\boldsymbol{F}}$. *Dirichlet boundary conditions* are defined by setting the second bracket term in (52) equal to zero, it follows

$$\boldsymbol{x} = \overline{\boldsymbol{F}}\boldsymbol{X} \quad \forall \boldsymbol{X} \in \partial\mathcal{B}_0\,. \tag{53}$$

Analogously, enforcing the first bracket term in (52) to be zero yields the *Neumann boundary conditions*

$$\boldsymbol{t}_0 = \overline{\boldsymbol{P}}\boldsymbol{N} \quad \forall \boldsymbol{X} \in \partial\mathcal{B}_0\,. \tag{54}$$

For the derivation of *periodic boundary conditions* we decompose the boundary of the microstructure ∂B_0 into two associated parts

$$\partial\mathcal{B}_0 = \partial\mathcal{B}_0^- \cup \partial\mathcal{B}_0^+\,. \tag{55}$$

Every point $\boldsymbol{X}^+ \in \partial\mathcal{B}^+$ is assumed to have an associated point $\boldsymbol{X}^- \in \partial\mathcal{B}^-$ with outward unit normals $\boldsymbol{N}^+$ and $\boldsymbol{N}^-$, respectively. Since $\overline{\boldsymbol{F}}$ as well as $\boldsymbol{X}$ are assumed to be given quantities, we define the fluctuation field

$$\widetilde{\boldsymbol{w}} := \boldsymbol{x} - \overline{\boldsymbol{F}}\boldsymbol{X}\,. \tag{56}$$

Thus, the macro-homogeneity condition (52) appears as

$$\begin{aligned}\int_{\partial\mathcal{B}_0} (\boldsymbol{t}_0 - \overline{\boldsymbol{P}}\boldsymbol{N}) \cdot \widetilde{\boldsymbol{w}}\, dA = &\int_{\partial\mathcal{B}_0^+} (\boldsymbol{t}_0^+ - \overline{\boldsymbol{P}}\boldsymbol{N}^+) \cdot \widetilde{\boldsymbol{w}}^+\, dA \\ &+ \int_{\partial\mathcal{B}_0^-} (\boldsymbol{t}_0^- - \overline{\boldsymbol{P}}\boldsymbol{N}^-) \cdot \widetilde{\boldsymbol{w}}^-\, dA\,.\end{aligned} \tag{57}$$

Table 1. constraint conditions & boundary conditions (bcs)

Reuss	$\boldsymbol{P} = \overline{\boldsymbol{P}}$	$\forall \boldsymbol{X} \in \mathcal{B}_0$
Voigt	$\boldsymbol{F} = \overline{\boldsymbol{F}}$	$\forall \boldsymbol{X} \in \mathcal{B}_0$
Dirichlet bcs	$\boldsymbol{x} = \overline{\boldsymbol{F}}\boldsymbol{X}$	$\forall \boldsymbol{X} \in \partial\mathcal{B}_0$
Neumann bcs	$\boldsymbol{t}_0 = \overline{\boldsymbol{P}}\boldsymbol{N}$	$\forall \boldsymbol{X} \in \partial\mathcal{B}_0$
periodic bcs	$\widetilde{\boldsymbol{w}} = \boldsymbol{x} - \overline{\boldsymbol{F}}\boldsymbol{X}$ $\widetilde{\boldsymbol{w}}^+ = \widetilde{\boldsymbol{w}}^-$ $\boldsymbol{t}_0^+ = -\boldsymbol{t}_0^-$	$\forall \boldsymbol{X}^+ \in \partial\mathcal{B}_0^+$ and $\boldsymbol{X}^- \in \partial\mathcal{B}_0^-$

A periodic fluctuation field is characterized by $\widetilde{\boldsymbol{w}}^+ = \widetilde{\boldsymbol{w}}^-$ at associated points, with the essential requirement $\boldsymbol{N}^+ = -\boldsymbol{N}^-$ it follows

$$\int_{\partial\mathcal{B}_0^+} \left\{ (\boldsymbol{t}_0^+ - \overline{\boldsymbol{P}}\boldsymbol{N}^+) \cdot \widetilde{\boldsymbol{w}}^+ + (\boldsymbol{t}_0^- + \overline{\boldsymbol{P}}\boldsymbol{N}^+) \cdot \widetilde{\boldsymbol{w}}^+ \right\} dA = \int_{\partial\mathcal{B}_0^+} (\boldsymbol{t}_0^+ + \boldsymbol{t}_0^-) \cdot \widetilde{\boldsymbol{w}}^+ \, dA \,. \tag{58}$$

The latter expression is identical to zero if $\boldsymbol{t}_0^+ = -\boldsymbol{t}_0^-$ holds.

An appropriate requirement for the type of the boundary condition to be used can be rephrased as follows

- Suquet (1987): *"The boundary conditions must reproduce, as closely as possible, the in situ state of the $\mathcal{RVE}$ inside the material".*

It should be noted that linear boundary displacements yield an energetically upper bound, whereas uniform boundary tractions provide a lower bound of the homogenized system. Nevertheless, the choice of the boundary condition influences the mechanical response in many cases:

- Xia et al. (2003): *"... 'homogeneous boundary conditions' are not only over-constrained but they may also violate the boundary traction periodicity conditions.".*

For periodic media, a natural course of action are periodic boundary conditions. They can be realized in a *strong format*, i.e., one part of the discretized boundary of the $\mathcal{RVE}$ (the *image boundary*, e.g. $\partial\mathcal{B}_0^-$) must be completely mirrored to the nodes on the associated part of the boundary (the *mirror boundary* $\partial\mathcal{B}_0^+$). Alternatively, a *weak format* of the periodic boundary conditions is proposed in Larsson et al. (2011). In this context, we also refer to Miehe and Bayreuther (2007).

In order to discuss the influence of the different boundary conditions on the mechanical response, we consider a periodic microstructure with stiff inclusions embedded in a weak matrix, as shown in Fig. 4a.

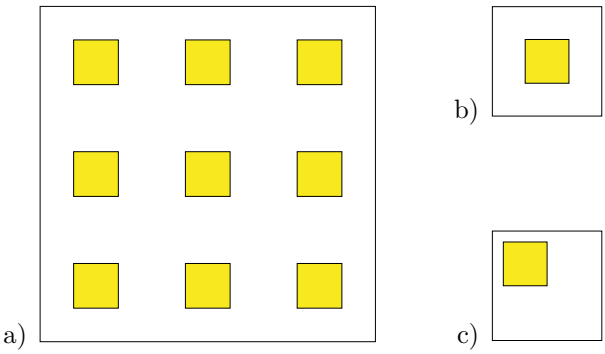

Figure 4. Periodic microstructure: a) Continuous matrix with periodically distributed inclusions. $\mathcal{RVE}s$ with b) a centric and c) an eccentric inclusion, see Schröder (2000).

For the analysis we choose unit cells which are discretized with 20×20 equal-sized quadrilateral elements, the inclusion is discretized with 8×8 elements. We choose a unit cell with a centric inclusion, as depicted in Fig. 4b and one unit cell with an eccentric inclusion, cf. Fig. 4c. The simulation is carried out for small strains under plain strain conditions and we apply an isotropic constitutive law for both, the weak matrix and the stiffer inclusion material. As mentioned above, for the considered periodic media the natural choice are periodic boundary conditions. That means, that for both unit cells, cf. Fig. 4b,c, the periodic boundary conditions must yield identical results. For the macroscopic loading

$$\overline{\boldsymbol{F}} = \text{diag}[\, 1.0005 \,;\; 1.0 \,;\; 1.0 \,]\,, \tag{59}$$

we obtain the stress distribution as depicted in Fig. 5. In both cases, the macroscopic Cauchy stress tensor has only non-vanishing and identical diagonal components, as expected; the values of the components of the stress tensor (in consistent units) are

$$\overline{\boldsymbol{\sigma}}^{per} = \text{diag}[\, 837.4 \,;\; 490.7 \,;\; 530.7 \,]\,. \tag{60}$$

These stress values will be applied to the unit cells when we analyze the Neumann boundary conditions. The stress response for the Dirichlet boundary conditions is depicted in Fig. 6. For the unit cell with centered inclusion, the macroscopic stress tensor is also diagonal and the values differ

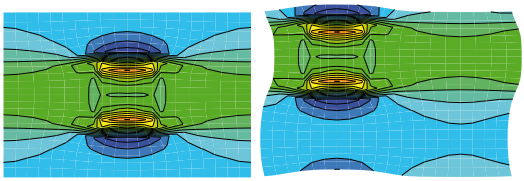

Figure 5. Stress σ_{11} in the unit cells with centric (left) and eccentric (right) inclusion under periodic boundary conditions, see Schröder (2000).

approximately by 1% compared to (60) and the local stress distribution is comparable to the ones in Fig. 5. Considering the unit cell with the eccentric inclusion, we observe a symmetry-break in the stress distribution. Nevertheless, the stress components deviate from the components in (60) by approx. 3%, in addition the off-diagonal element of $\overline{\boldsymbol{\sigma}}$ is not vanishing.

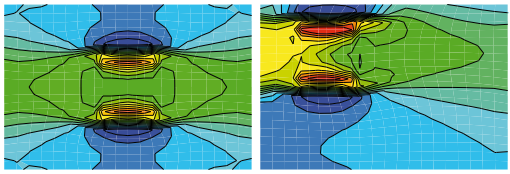

Figure 6. Stress σ_{11} in the unit cells with centric (left) and eccentric (right) inclusion under Dirichlet boundary conditions, see Schröder (2000).

Applying the stress values of (60) as loading conditions for the Neumann boundary conditions, we get the results shown in Fig. 7. The macroscopic deformation gradient should be close to (59). The deviation for both unit cells is approximately up to 8% and again we observe a symmetry-break in the local stress distribution for the unit cell with the eccentric inclusion.
Sum up: As expected, periodic boundary conditions yield the best results.

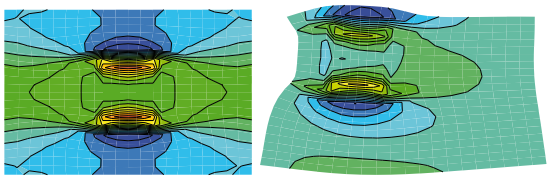

Figure 7. Stress σ_{11} in the unit cells with centric (left) and eccentric (right) inclusion under Neumann boundary conditions, see Schröder (2000).

2.6 Remarks on the Choice of the $\mathcal{RVE}$

The choice of the representative volume element ($\mathcal{RVE}$) for the application to a two-scale homogenization scheme is an ongoing research topic. In general, the $\mathcal{RVE}$ should be a partial volume of the material, which is statistically homogeneous from the macroscopic point of view. Furthermore, the choice of a $\mathcal{RVE}$ is not unique, see Fig. 8.

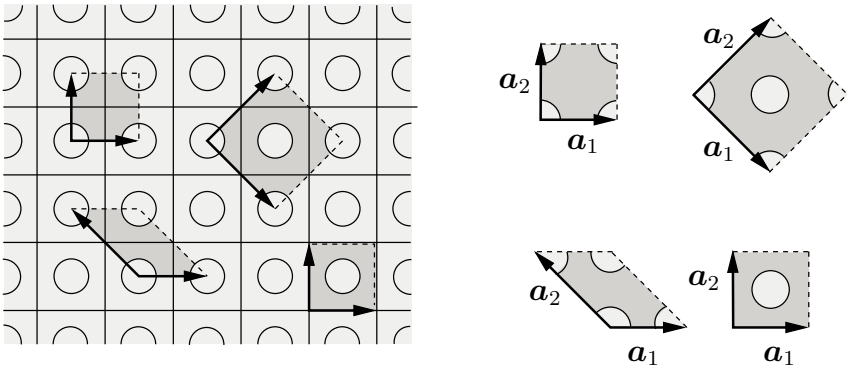

Figure 8. Non-uniqueness of the $\mathcal{RVE}$s of a periodically arranged microstructure. The dashed boxed regions represent four possible $\mathcal{RVE}$s, see Schröder (2000).

In Zeman (2003), several properties for the definition of a $\mathcal{RVE}$, taken from the literature, are summarized:

- Hill (1963): *"This phrase (the $\mathcal{RVE}$) will be used when referring to a sample that (a) is structurally entirely typical of the whole structure on average, and (b) contains sufficient number of inclusions for the apparent overall moduli to be effectively independent of the surface value of traction and displacement, so long as these values are "macroscopically uniform""*

- Hashin (1983): *"The RVE is a model of the material to be used to determine the corresponding effective properties of the homogenized macroscopic model. The RVE should be large enough to contain sufficient information about the microstructure in order to be representative, however it should be much smaller than the macroscopic body."*

- Drugan and Willis (1996): *"The RVE is the smallest material volume element of the composite for which the usual spatially constant "over-*

all modulus" macroscopic constitutive representation is a sufficiently accurate model to represent the mean constitutive response."

- Ostoja-Starzewski (2001): *"The RVE is very clearly defined in two situations only: (i) it is a unit cell of a periodic microstructure, and (ii) volume containing a very large set of micro-scale elements, possessing statistically homogeneous and ergodic properties."*

- Stroeven et al. (2002): *"The determination of the RVE size is by no means straightforward. It depends on the material under consideration, but also on the structure sensitivity of the physical quantity that is measured. Normally, elastic moduli are taken as the governing parameter, however, other quantities can also be taken, such as energy dissipation in case of microstructural cracking."*

A note on periodic unit cells: In periodic media, typically unit cells, which are translationally symmetric, are used as $\mathcal{RVE}$s. In order to design (sub-) unit cells with a lower number of degrees of freedom, Ohno et al. (2001) exploited the point symmetrical distribution of the mechanical field quantities with respect to the center of the considered unit cell. Substantial savings in computer time can also be realized when the unit cell possesses further special symmetries, see Flores and de Souza Neto (2010).

A note on random microstructures: Capturing the random nature of microstructures is a challenge in homogenization (effective macroscopic description). The lack of microstructural periodicity implies that we have to analyze statistical volume elements ($\mathcal{SVE}s$) instead of $\mathcal{RVE}s$. Mathematical tools for the characterization of random microstructures are discussed in Ohser and Mücklich (2000). A brief introduction of basic morphological measurements for a quantitative characterization of the geometry of random microstructures is given in Jeulin and Ostoja-Starzewski (2001). From the viewpoint of stochastical mechanics, we could consider ensemble averages over several realizations of the microstructure. From the practical point of view, we are interested in only one realization of the microstructure in order to achieve a sufficient estimate of the macroscopic mechanical response. Furthermore, the interchangeability of the ensemble averaging and volume averaging (in general for sufficiently large microstructures) is a key assumption in this field, which is based on the concepts of statistical homogeneity and ergodicity, see Jeulin and Ostoja-Starzewski (2001) and Ostoja-Starzweski (2008).

3 Algorithmic Treatment

This chapter concerns the theoretical and numerical treatment of a discrete two-scale homogenization scheme, also known as the FE^2-method or direct micro-macro transition approach. A major role plays the coupled numerical solution of the boundary value problems on both scales. Especially the consistent linearization of the effective macroscopic response function can be seen as a crucial part in this numerical scheme. In the following, the (matrix) approximations of the field quantities are denoted by a superscript h, e.g., the discrete counterpart of $\boldsymbol{x}$ is denoted as $\boldsymbol{x}^h$.

3.1 Boundary Value Problems on the Macro- and Micro-Scale

The *balance of linear momentum at the macro-scale* (11) can be written in its weak form as

$$\overline{G} = -\int_{\overline{\mathcal{B}}_0} \delta\overline{\boldsymbol{x}} \cdot \left(\mathrm{Div}_{\overline{X}}\overline{\boldsymbol{P}} + \overline{\boldsymbol{f}}\right) \, dV \tag{61}$$

with $\overline{G} = 0$ at the equilibrium state. Application of the relation

$$\delta\overline{\boldsymbol{x}} \cdot \mathrm{Div}_{\overline{X}}\,\overline{\boldsymbol{P}} = \mathrm{Div}_{\overline{X}}[\delta\overline{\boldsymbol{x}}\,\overline{\boldsymbol{P}}] - \mathrm{Grad}_{\overline{X}}\delta\overline{\boldsymbol{x}} : \overline{\boldsymbol{P}} \tag{62}$$

and the Gauss integral theorem yields the modified expression

$$\overline{G} = \underbrace{\int_{\overline{\mathcal{B}}_0} \delta\overline{\boldsymbol{F}} : \overline{\boldsymbol{P}} \, dV}_{=:\,\overline{G}^{int}} - \underbrace{\left\{\int_{\overline{\mathcal{B}}_0} \delta\overline{\boldsymbol{x}} \cdot \overline{\boldsymbol{f}} \, dV + \int_{\partial\overline{\mathcal{B}}_0} \delta\overline{\boldsymbol{x}} \cdot \overline{\boldsymbol{t}}_0 \, dA\right\}}_{=:\,\overline{G}^{ext}} \tag{63}$$

with $\overline{\boldsymbol{t}}_0 = \overline{\boldsymbol{P}}\,\overline{\boldsymbol{N}}$. For the discretization of the *macroscopic boundary value problem*, we apply the following discretizations for the actual, virtual and incremental deformation within a typical finite element

$$\overline{\boldsymbol{x}}^h = \overline{\boldsymbol{X}}^h + \mathbb{N}^e\overline{\boldsymbol{d}}\,, \quad \delta\overline{\boldsymbol{x}}^h = \mathbb{N}^e\delta\overline{\boldsymbol{d}}\,, \qquad \Delta\overline{\boldsymbol{x}}^h = \mathbb{N}^e\Delta\overline{\boldsymbol{d}}\,, \tag{64}$$

respectively. Here the matrix $\mathbb{N}^e$ contains the classical ansatz-functions and the vectors $\{\overline{\boldsymbol{d}}\,, \delta\overline{\boldsymbol{d}}\,, \Delta\overline{\boldsymbol{d}}\}$ represent the actual, virtual and incremental nodal displacements. With the $\mathbb{B}^e$-matrices containing the partial derivatives of the ansatz functions with respect to reference coordinates, we define the approximations of the actual, virtual and incremental deformation tensors

$$\overline{\boldsymbol{F}}^h = \mathbf{1}^h + \mathbb{B}^e\overline{\boldsymbol{d}}\,, \qquad \delta\overline{\boldsymbol{F}}^h = \mathbb{B}^e\delta\overline{\boldsymbol{d}}\,, \qquad \Delta\overline{\boldsymbol{F}}^h = \mathbb{B}^e\Delta\overline{\boldsymbol{d}}\,. \tag{65}$$

Inserting the approximations for the virtual fields (64) and (65) in Eq. (63) yields the approximation of $\overline{G}(\overline{\boldsymbol{x}}, \delta\overline{\boldsymbol{x}})$ by $\overline{G}^h(\overline{\boldsymbol{x}}^h, \delta\overline{\boldsymbol{x}}^h)$, i.e.

$$\overline{G}^h = \sum_e \overline{G}^e(\overline{\boldsymbol{x}}^h, \delta\overline{\boldsymbol{x}}^h) = \sum_e \overline{G}^{e,int}(\overline{\boldsymbol{x}}^h, \delta\overline{\boldsymbol{x}}^h) - \sum_e \overline{G}^{e,ext}(\overline{\boldsymbol{x}}^h, \delta\overline{\boldsymbol{x}}^h) \,. \quad (66)$$

If the weak form (63) is associated with a typical finite element, we get the expressions for the internal and external parts

$$\overline{G}^{e,int}(\overline{\boldsymbol{x}}^h, \delta\overline{\boldsymbol{x}}^h) = \delta\overline{\boldsymbol{d}}^T \underbrace{\int_{\overline{\mathcal{B}}_0^e} \mathbb{B}^{eT} \overline{\boldsymbol{P}}^h \, dV}_{=:\,\overline{\boldsymbol{r}}^{e,int}} \,, \quad (67)$$

and

$$\overline{G}^{e,ext}(\overline{\boldsymbol{x}}^h, \delta\overline{\boldsymbol{x}}^h) = \delta\overline{\boldsymbol{d}}^T \underbrace{\left\{ \int_{\overline{\mathcal{B}}_0^e} \mathbb{N}^e \overline{\boldsymbol{f}}^h \, dV + \int_{\partial\overline{\mathcal{B}}_0^e} \mathbb{N}^e \overline{\boldsymbol{t}}_0^h \, dA \right\}}_{=:\,\overline{\boldsymbol{r}}^{e,ext}} \,. \quad (68)$$

With this, the element residual vector $\overline{\boldsymbol{r}}^e$ is computed by $\overline{\boldsymbol{r}}^e = \overline{\boldsymbol{r}}^{e,int} - \overline{\boldsymbol{r}}^{e,ext}$. To solve the nonlinear weak form $\overline{G}^h(\overline{\boldsymbol{x}}^h, \delta\overline{\boldsymbol{x}}^h)$ we apply the Newton-Raphson iteration scheme. Therefore, the linerization of $\overline{G}^h(\overline{\boldsymbol{x}}^h, \delta\overline{\boldsymbol{x}}^h)$ at $\overline{\boldsymbol{x}}^h = \overline{\boldsymbol{x}}^{h*}$ has to be computed:

$$\mathrm{Lin}\, \overline{G}^h(\overline{\boldsymbol{x}}^{h*}, \delta\overline{\boldsymbol{x}}^h, \Delta\overline{\boldsymbol{x}}^h) = \overline{G}^h(\overline{\boldsymbol{x}}^{h*}, \delta\overline{\boldsymbol{x}}^h) + \Delta\overline{G}^h(\overline{\boldsymbol{x}}^{h*}, \delta\overline{\boldsymbol{x}}^h, \Delta\overline{\boldsymbol{x}}^h) \,. \quad (69)$$

The linear increment is defined as the directional derivative of $\overline{G}^h$ at $\overline{\boldsymbol{x}}^h$ in the direction of the incremental deformation $\Delta\overline{\boldsymbol{x}}^h$, i.e.,

$$\Delta\overline{G}^h(\overline{\boldsymbol{x}}^{h*}, \delta\overline{\boldsymbol{x}}^h, \Delta\overline{\boldsymbol{x}}^h) = \frac{d}{d\epsilon} \left[\overline{G}^h(\overline{\boldsymbol{x}}^{h*} + \epsilon\Delta\overline{\boldsymbol{x}}^h, \delta\overline{\boldsymbol{x}}^h) \right] \Big|_{\epsilon=0} \,. \quad (70)$$

For dead-loaded systems the linear increment of the discrete form of $\overline{G}$ is formally given by

$$\Delta\overline{G}^h = \sum_e \Delta\overline{G}^{e,int} \quad (71)$$

and the linear increment for a typical element is calculated by

$$\Delta\overline{G}^{e,int} = \int_{\overline{\mathcal{B}}_0^e} \delta\overline{\boldsymbol{F}}^{hT} \overline{\mathbb{A}}^h \Delta\overline{\boldsymbol{F}}^h \, dV = \delta\overline{\boldsymbol{d}}^T \underbrace{\int_{\overline{\mathcal{B}}_0^e} \mathbb{B}^{eT} \overline{\mathbb{A}}^h \mathbb{B}^e \, dV}_{=:\,\overline{\boldsymbol{k}}^e} \Delta\overline{\boldsymbol{d}} \,. \quad (72)$$

For the computation of the stiffness matrix $\overline{\boldsymbol{k}}^e$ for a macroscopic element, we need the macroscopic (overall) algorithmic consistent moduli $\overline{\mathbb{A}}$, which is formally defined by the partial derivative

$$\overline{\mathbb{A}} = \frac{\partial \overline{\boldsymbol{P}}}{\partial \overline{\boldsymbol{F}}} \quad \text{with} \quad \overline{\boldsymbol{P}} = \frac{1}{V} \int_{\mathcal{B}_0} \boldsymbol{P}(\boldsymbol{F})\, dV \ . \tag{73}$$

This fourth-order tensor cannot be computed directly, becauce we have no explicit expression of the macroscopic first Piola-Kirchhoff stress tensor $\overline{\boldsymbol{P}}$ as a function of its work-conjugated variable, the macroscopic deformation gradient $\overline{\boldsymbol{F}}$. An efficient algorithmic treatment of handling this is presented in the next chapter; therefore, we assume the algorithmic consistent moduli $\overline{\mathbb{A}}$ as known at this point. Thus, the linearization yields

$$\sum_{e=1}^{\overline{num}_{ele}} \left\{ \delta \overline{\boldsymbol{d}}^T \left(\overline{\boldsymbol{k}}^e \Delta \overline{\boldsymbol{d}} + \overline{\boldsymbol{r}}^e \right) \right\} = 0 \ , \tag{74}$$

where $\overline{num}_{ele}$ denotes the number of macroscopic finite elements. The application of the assembling procedure yields the system of equations

$$\overline{\boldsymbol{K}} \Delta \overline{\boldsymbol{D}} = -\overline{\boldsymbol{R}} \quad \text{with} \quad \overline{\boldsymbol{K}} = \mathop{\mathsf{A}}_{e=1}^{\overline{num}_{ele}} \overline{\boldsymbol{k}}^e \quad \text{and} \quad \overline{\boldsymbol{R}} = \mathop{\mathsf{A}}_{e=1}^{\overline{num}_{ele}} \overline{\boldsymbol{r}}^e \, , \tag{75}$$

where A denote the standard assembling operators. The solution of the latter system of equations yields an increment of the actual deformation field. This procedure has to be repeated until an equilibrium state of the macroscopic boundary value problem has been reached, i.e. $\overline{G}^h(\overline{\boldsymbol{x}}, \delta\overline{\boldsymbol{x}}) \approx 0$.

The weak form of the *balance of linear momentum at the microscale*, based on the expression $(19)_1$, is given by

$$G = -\int_{\mathcal{B}_0} \delta \boldsymbol{x} \cdot \mathrm{Div}_X \boldsymbol{P}\, dV \tag{76}$$

with $G = 0$. Here, we are neglecting the volume acceleration and inertia terms. Taking into account the additive split of the deformation into a linear map $\overline{\boldsymbol{F}}\boldsymbol{X}$ and a fluctuation part $\widetilde{\boldsymbol{w}}$, we obtain the following representation of the microscopic deformation tensor $\boldsymbol{F} = \mathrm{Grad}_X\, \boldsymbol{x}$:

$$\boldsymbol{F} = \overline{\boldsymbol{F}} + \widetilde{\boldsymbol{F}} \quad \text{with} \quad \widetilde{\boldsymbol{F}} = \mathrm{Grad}_X\, \widetilde{\boldsymbol{w}} \ . \tag{77}$$

With this in hand, we get the modified expression

$$G = \int_{\mathcal{B}_0} \delta \widetilde{\boldsymbol{F}} : \boldsymbol{P}\, dV \ . \tag{78}$$

Note that the part $\overline{\boldsymbol{F}}$ of the microscopic deformation gradient $\boldsymbol{F}$ is given and constant over the $\mathcal{RVE}$.

For the discretization of the *microscopic boundary value problem*, we apply the following discretizations for the actual, virtual and incremental fluctuation within a typical finite element

$$\widetilde{\boldsymbol{w}}^h = \mathbb{N}^e \widetilde{\boldsymbol{d}}, \qquad \delta\widetilde{\boldsymbol{w}}^h = \mathbb{N}^e \delta\widetilde{\boldsymbol{d}}, \qquad \Delta\widetilde{\boldsymbol{w}}^h = \mathbb{N}^e \Delta\widetilde{\boldsymbol{d}}, \tag{79}$$

respectively. Here, the matrix $\mathbb{N}^e$ contains the classical ansatz-functions and the vectors $\{\widetilde{\boldsymbol{d}}, \delta\widetilde{\boldsymbol{d}}, \Delta\widetilde{\boldsymbol{d}}\}$ represent the actual, virtual and incremental nodal fluctuations. With the $\mathbb{B}^e$-matrices containing the partial derivatives of the ansatz functions with respect to reference coordinates, we define the approximations of the actual, virtual and incremental deformation tensors

$$\widetilde{\boldsymbol{F}}^h = \mathbb{B}^e \widetilde{\boldsymbol{d}}, \qquad \delta\widetilde{\boldsymbol{F}}^h = \mathbb{B}^e \delta\widetilde{\boldsymbol{d}}, \qquad \Delta\widetilde{\boldsymbol{F}}^h = \mathbb{B}^e \Delta\widetilde{\boldsymbol{d}}\,. \tag{80}$$

Inserting the approximations for the virtual fields (79) and (80) in (78) leads to the discrete counterpart G^h of G:

$$G^h(\boldsymbol{x}^h, \delta\boldsymbol{x}^h) = \sum_e G^e(\boldsymbol{x}^h, \delta\boldsymbol{x}^h) \tag{81}$$

with

$$G^e(\boldsymbol{x}^h, \delta\boldsymbol{x}^h) = \delta\boldsymbol{d}^T \underbrace{\int_{\mathcal{B}_0^e} \mathbb{B}^{eT} \boldsymbol{P}^h \, dV}_{=:\,\boldsymbol{r}^e}\,. \tag{82}$$

To solve the nonlinear discrete weak form $G^h(\boldsymbol{x}^h, \delta\boldsymbol{x}^h)$, we apply the Newton-Raphson iteration scheme and apply the linerization analogously to the procedure at the macro-scale described above. Finally, we obtain the linear increment for a typical microscopic finite element

$$\Delta G^e = \int_{\mathcal{B}_0^e} \delta\widetilde{\boldsymbol{F}}^{h\,T} \mathbb{A}^h \Delta\widetilde{\boldsymbol{F}}^h \, dV = \delta\widetilde{\boldsymbol{d}}^T \underbrace{\int_{\mathcal{B}_0^e} \mathbb{B}^{eT} \mathbb{A}^h \mathbb{B}^e \, dV}_{=:\,\boldsymbol{k}^e} \Delta\widetilde{\boldsymbol{d}}\,. \tag{83}$$

The application of the standard assembling operator, cf. Eq. (75), to the microscopic stiffness matrices and the residual vectors result in the system of equations

$$\boldsymbol{K}\Delta\widetilde{\boldsymbol{D}} + \boldsymbol{R} = 0\,. \tag{84}$$

From this system of equations, we obtain an update of the discrete fluctuation field and evaluate the discrete weak form (82). If the euclidian norm of $\boldsymbol{R}$ is higher than a given tolerance, we apply further Newton iteration steps until convergence is achieved.

3.2 Computation of Algorithmic Consistent Overall Moduli

In the previous section, we assumed that the macroscopic overall moduli $\overline{\mathbb{A}}$ was given during the solution process at the macro-scale. However, in contrast to the macroscopic stress tensor $\overline{\boldsymbol{P}}$, which can be calculated directly as the volume average of the microscopic counterparts, the macroscopic moduli cannot be consistently computed solely by volumetric averaging. Starting from the incremental constitutive relation at the macro-scale

$$\Delta\overline{\boldsymbol{P}} = \left\{ \frac{1}{V} \frac{\partial}{\partial \overline{\boldsymbol{F}}} \int_{\mathcal{B}} \boldsymbol{P}(\boldsymbol{F})\, dV \right\} : \Delta\overline{\boldsymbol{F}} =: \overline{\mathbb{A}} : \Delta\overline{\boldsymbol{F}} \,, \tag{85}$$

we define the overall (effective) nominal moduli as follows

$$\overline{\mathbb{A}} = \frac{1}{V} \int_{\mathcal{B}} \frac{\partial}{\partial \overline{\boldsymbol{F}}} \boldsymbol{P}(\boldsymbol{F})\, dV = \frac{1}{V} \int_{\mathcal{B}} \frac{\partial \boldsymbol{P}(\boldsymbol{F})}{\partial \boldsymbol{F}} : \frac{\partial \boldsymbol{F}}{\partial \overline{\boldsymbol{F}}}\, dV \,. \tag{86}$$

Let us now exploit the additive decomposition of $\boldsymbol{F}$ into a constant and a fluctuating part. Substituting

$$\boldsymbol{F} = \overline{\boldsymbol{F}} + \widetilde{\boldsymbol{F}} \,, \tag{87}$$

in Equation (86) yields

$$\overline{\mathbb{A}} = \frac{1}{V} \int_{\mathcal{B}} \frac{\partial \boldsymbol{P}(\boldsymbol{F})}{\partial \boldsymbol{F}} : \frac{\partial (\overline{\boldsymbol{F}} + \widetilde{\boldsymbol{F}})}{\partial \overline{\boldsymbol{F}}}\, dV \,. \tag{88}$$

Thus, we obtain with the abbreviation $\mathbb{A} := \partial_F \boldsymbol{P}(\boldsymbol{F})$

$$\overline{\mathbb{A}} = \frac{1}{V} \int_{\mathcal{B}} \mathbb{A}\, dV + \frac{1}{V} \int_{\mathcal{B}} \mathbb{A} : \frac{\partial \widetilde{\boldsymbol{F}}}{\partial \overline{\boldsymbol{F}}}\, dV \,. \tag{89}$$

In the latter equation, the computation of the sensitivity of $\widetilde{\boldsymbol{F}}$ with respect to $\overline{\boldsymbol{F}}$ is the crucial part. Starting from the weak form of the balance of linear momentum at the micro-scale (78) at an equilibrium state, i.e., $G = 0$, then the linearization yields

$$\int_{\mathcal{B}} \delta\widetilde{\boldsymbol{F}} : \mathbb{A} : \Delta\boldsymbol{F}\, dV = 0 \,. \tag{90}$$

Substituting the additive split (87) in (90) yields

$$\underbrace{\int_{\mathcal{B}_0} \delta\widetilde{\boldsymbol{F}} : \mathbb{A} : \Delta\overline{\boldsymbol{F}}\, dV}_{\int_{\mathcal{B}_0} \delta\widetilde{\boldsymbol{F}} : \mathbb{A}\, dV \; : \Delta\overline{\boldsymbol{F}}} + \int_{\mathcal{B}_0} \delta\widetilde{\boldsymbol{F}} : \mathbb{A} : \Delta\widetilde{\boldsymbol{F}}\, dV = 0 \,. \tag{91}$$

The discrete counterpart of the latter equation appears after inserting the approximations of the fluctuation part of the deformation gradient (80) as

$$\sum_{e=1}^{num_{ele}} \delta\widetilde{\boldsymbol{d}}^T \left\{ \underbrace{\int_{\mathcal{B}_0^e} \mathbb{B}^{eT} \mathbb{A}^h \, dV}_{\boldsymbol{l}^e} \, \Delta\overline{\boldsymbol{F}}^h + \underbrace{\int_{\mathcal{B}_0^e} \mathbb{B}^{eT} \mathbb{A}^h \mathbb{B}^e \, dV}_{\boldsymbol{k}^e} \, \Delta\widetilde{\boldsymbol{d}} \right\} = 0 \,, \tag{92}$$

where num_{ele} denotes the number of microscopic finite elements, $\boldsymbol{k}^e$ the element stiffness matrices, see also (83), and $\boldsymbol{l}^e$ the matrices, which take into account the sensitivity of the moduli of the individual finite elements. Thus, in contracted matrix notation, we obtain

$$\sum_{e=1}^{num_{ele}} \left\{ \delta\widetilde{\boldsymbol{d}}^T \left(\boldsymbol{l}^e \, \Delta\overline{\boldsymbol{F}}^h + \boldsymbol{k}^e \Delta\widetilde{\boldsymbol{d}} \right) \right\} = 0 \,. \tag{93}$$

Application of a standard assembling procedure, cf. Eq. (75), yields

$$\delta\widetilde{\boldsymbol{D}}^T \left(\boldsymbol{K} \Delta\widetilde{\boldsymbol{D}} + \boldsymbol{L} \, \Delta\overline{\boldsymbol{F}} \right) = 0 \,. \tag{94}$$

The global stiffness matrix $\boldsymbol{K}$ and the generalized right hand sides $\boldsymbol{L}$ are defined as

$$\boldsymbol{K} = \mathop{\mathsf{A}}_{e=1}^{num_{ele}} \boldsymbol{k}^e \,, \qquad \boldsymbol{L} = \mathop{\mathsf{A}}_{e=1}^{num_{ele}} \boldsymbol{l}^e \,. \tag{95}$$

Formally, the solution of Eq. (94) is achieved by

$$\Delta\widetilde{\boldsymbol{D}} = -\boldsymbol{K}^{-1} \boldsymbol{L} \, \Delta\overline{\boldsymbol{F}}^h \,, \tag{96}$$

which represents the incremental fluctuation field as a consequence of an incremental macroscopic deformation gradient. Inserting the elementwise solutions $\Delta\widetilde{\boldsymbol{d}}$ of (96) in $(80)_3$ and substituting this result into Eq. (89) yields

$$\overline{\mathbb{A}}^h = \underbrace{\frac{1}{V} \sum_{e=1}^{num_{ele}} \int_{\mathcal{B}^e} \mathbb{A}^h \, dV}_{\mathbb{A}^{\text{Voigt}}} + \frac{1}{V} \sum_{e=1}^{num_{ele}} \int_{\mathcal{B}^e} \mathbb{A}^h \, \frac{\partial(\mathbb{B}^e \Delta\widetilde{\boldsymbol{d}})}{\partial\overline{\boldsymbol{F}}^h} \, dV \,, \tag{97}$$

where $\mathbb{A}^{\text{Voigt}}$ denotes the (numerical approximation of the) Voigt upper bound. The second integral term in (97) can be reformulated as

$$\frac{1}{V} \sum_{e=1}^{num_{ele}} \int_{\mathcal{B}^e} \mathbb{A}^h \, \frac{\partial(\mathbb{B}^e \Delta\widetilde{\boldsymbol{d}})}{\partial\overline{\boldsymbol{F}}^h} \, dV = \frac{1}{V} \sum_{e=1}^{num_{ele}} \underbrace{\int_{\mathcal{B}^e} \mathbb{A}^h \mathbb{B}^e \, dV}_{\boldsymbol{l}^{e\star}} \frac{\partial\Delta\widetilde{\boldsymbol{d}}}{\partial\overline{\boldsymbol{F}}^h} \,, \tag{98}$$

where $\boldsymbol{l}^{e\star} = \boldsymbol{l}^{eT}$ if $\mathbb{A}$ fullfills the major symmetries, i.e., $\mathbb{A}_{ijkl} = \mathbb{A}_{klij}$. This symmetry relation is provided in the following. After assembling the discrete form, we get with (96) and the linear increment

$$\Delta\overline{\boldsymbol{F}}^h = \overline{\boldsymbol{F}}^h - \overline{\boldsymbol{F}}^h_n \,, \tag{99}$$

based on the nomenclature

$$\overline{\boldsymbol{F}}^h = \overline{\boldsymbol{F}}^h(t_{n+1}) \quad \text{and} \quad \overline{\boldsymbol{F}}^h_n = \overline{\boldsymbol{F}}^h(t_n) \,, \tag{100}$$

the algebraic expression

$$\frac{1}{V}\boldsymbol{L}^T \frac{\partial \Delta\widetilde{\boldsymbol{D}}}{\partial \overline{\boldsymbol{F}}^h} = -\frac{1}{V}\boldsymbol{L}^T\, \boldsymbol{K}^{-1}\boldsymbol{L}\, \frac{\partial \Delta\overline{\boldsymbol{F}}}{\partial \overline{\boldsymbol{F}}^h} = -\frac{1}{V}\boldsymbol{L}^T\, \boldsymbol{K}^{-1}\boldsymbol{L} \,. \tag{101}$$

Thus, the final result for the algorithmic consistent overall moduli is

$$\boxed{\overline{\mathbb{A}} = \mathbb{A}^{\text{Voigt}} - \frac{1}{V}\boldsymbol{L}^T\boldsymbol{K}^{-1}\boldsymbol{L} \quad \text{with} \quad \mathbb{A}^{\text{Voigt}} = \frac{1}{V}\sum_e \int_{\mathcal{B}^e} \mathbb{A}^h \, dV} \,, \tag{102}$$

see Miehe et al. (1999a,b).

In general, huge computational costs in typical direct nonlinear homogenization schemes are governed by using the Newton-Raphson iteration on both scales at each quadrature point. For the efficient computation of the second term in $(102)_1$, we identify

$$\boldsymbol{L}^T\boldsymbol{K}^{-1}\boldsymbol{L} = \boldsymbol{L}^T\mathbb{X}. \tag{103}$$

Here, $\mathbb{X}$ is the solution of a system of equations with several, e.g. nine in 3D, right hand sides which are organized in the matrix $\boldsymbol{L}$:

$$\boldsymbol{K}\mathbb{X} = \boldsymbol{L} \,. \tag{104}$$

For the solution of (103) as well as for the solutions of the weak forms, the sparse structure of all matrices is taken into account.
A study of efficient two-scale homogenization algorithms for nonlinear problems using approximations of the Schur-Complement of the microscopic stiffness matrix based on e.g. LU factorizations is presented in Okada et al. (2010). Several works in the literature are concerned with the derivation of the overall tangent moduli as well as with different approaches (associated to Schur complement computation, perturbation techniques, penalty formulations, Lagrange multiplier methods) useful for efficient computations, in this context we refer to Miehe et al. (1999a), Schröder (2000), Kouznetsova et al. (2001), Miehe and Koch (2002), Miehe (2003), Miehe and Bayreuther (2007), Temizer and Wriggers (2008) and Schröder and Keip (2012).

4 Stability Problems at Different Scales

A challenge in two-scale homogenization techniques is the consideration of instability problems on the different scales, cf. Abeyaratne and Triantafyllidis (1984), Triantafyllidis and Maker (1985), Müller (1987), Geymonat et al. (1993), Miehe et al. (2002), Schröder (2010). In the following, we restrict ourselves to hyperelastic materials and distinguish between structural instabilities and material instabilities. Let

$$\overline{\Pi}(\overline{\boldsymbol{x}}) = \overline{\Pi}^{int}(\overline{\boldsymbol{F}}) + \overline{\Pi}^{ext}(\overline{\boldsymbol{x}}) \tag{105}$$

be the total potential energy of the body of interest on the macro-scale, with

$$\overline{\Pi}^{int}(\overline{\boldsymbol{F}}) = \int_{\overline{\mathcal{B}}_0} \overline{\psi}(\overline{\boldsymbol{F}})\, dV \tag{106}$$

and

$$\overline{\Pi}^{ext}(\overline{\boldsymbol{x}}) = -\int_{\overline{\mathcal{B}}_0} \overline{\boldsymbol{x}} \cdot \overline{\boldsymbol{f}}\, dV - \int_{\partial\overline{\mathcal{B}}_{0,t}} \overline{\boldsymbol{x}} \cdot \overline{\boldsymbol{t}}_0\, dA\ . \tag{107}$$

An equilibrium state, denoted by $\overline{\boldsymbol{x}}^{eq}$, is characterized by an infimum of the total potential energy in the space of admissible functions. The deformation state $\overline{\boldsymbol{x}}^{eq}$ is stable if the inequality

$$\overline{\Pi}(\overline{\boldsymbol{x}}^{ka}) \geq \overline{\Pi}(\overline{\boldsymbol{x}}^{eq}) \quad \forall \text{ kinematically admissible } \overline{\boldsymbol{x}}^{ka} \tag{108}$$

holds and the equality sign only holds for some $\overline{\boldsymbol{x}}^{ka} \neq \overline{\boldsymbol{x}}^{eq}$, see Ogden (1984). The inequality (108) is a sufficient (global) condition for the stability of the equilibrium state $\overline{\boldsymbol{x}}^{eq}$.

For a more suitable criterion, especially from the computational point of view, we restrict our analysis to kinematically admissible functions in the vicinity of $\overline{\boldsymbol{x}}^{eq}$. This means that Eq. (108) becomes an infinitesimal stability criterion, see Truesdell and Noll (1965), chapter 68. The deviation of the total potential energy between an equilibrium state $\overline{\boldsymbol{x}}^{eq}$ and $\overline{\boldsymbol{x}}^{ka}$ is

$$\Delta\overline{\Pi} := \overline{\Pi}(\boldsymbol{x}^{ka}) - \overline{\Pi}(\overline{\boldsymbol{x}}^{eq})\ . \tag{109}$$

For the following remarks, let us recapitulate the first directional derivative of $\overline{\Pi}$ in the direction of $\delta\overline{\boldsymbol{x}}$

$$\frac{d}{d\epsilon}\overline{\Pi}(\overline{\boldsymbol{x}}^{eq} + \epsilon\, \delta\overline{\boldsymbol{x}})\bigg|_{\epsilon=0} =: \overline{G}(\overline{\boldsymbol{x}}^{eq}, \delta\overline{\boldsymbol{x}}^{eq})\ . \tag{110}$$

The second directional derivative of $\overline{\Pi}$, or equivalently the directional derivative of $\overline{G}$, is

$$\frac{d}{d\epsilon}\overline{G}(\overline{\boldsymbol{x}}^{eq}, \delta\overline{\boldsymbol{x}}, \epsilon\, \Delta\overline{\boldsymbol{x}})\bigg|_{\epsilon=0} := \Delta\overline{G}(\overline{\boldsymbol{x}}^{eq}, \delta\overline{\boldsymbol{x}}, \Delta\overline{\boldsymbol{x}})\ . \tag{111}$$

Let us now write $\Delta\overline{\Pi}$, see (109), in terms of a classical Taylor expansion, then we obtain

$$\Delta\overline{\Pi} = \overline{G}(\overline{\boldsymbol{x}}^{eq}, \delta\overline{\boldsymbol{x}}) + \frac{1}{2!}\Delta G(\overline{\boldsymbol{x}}^{eq}, \delta\overline{\boldsymbol{x}}, \Delta\overline{\boldsymbol{x}}) + \frac{1}{3!}\dots \,. \tag{112}$$

In an equilibrium state, $\overline{G}$ is per definition identical to zero, thus, the equilibrium state is stable if

$$\Delta\overline{G}(\overline{\boldsymbol{x}}^{eq}, \delta\overline{\boldsymbol{x}}^{eq}, \Delta\overline{\boldsymbol{x}}) = \int_{\overline{\mathcal{B}}_0} \delta\overline{\boldsymbol{F}} : \overline{\mathbb{A}} : \Delta\overline{\boldsymbol{F}} > 0 \tag{113}$$

holds. More general overviews in this field can be found e.g. in Pflüger (1975) and Thompson and Hunt (1984).

Generalized Convexity Conditions play a major role for the proofs of the existence of minimizing deformations $\boldsymbol{x}$ of the elastic free energy $\psi(\boldsymbol{F})$ of boundary value problems subjected to specific boundary value conditions. A sufficient condition for the existence of minimizers is the sequential-weak lower semicontinuity (s.w.l.s.) and the coercivity of the free energy function. Morrey (1952, 1966) introduced the concept of quasiconvexity, which is formulated as an integral inequality over an arbitrary domain subjected to affine Dirichlet boundary conditions:

[Definition of Quasiconvexity] An elastic stored energy is quasiconvex whenever for all $\mathcal{B} \subset \mathbb{R}^3$, all constant deformation gradients $\overline{\boldsymbol{F}} \in \mathbb{R}^{3\times3}$ and all superposed fluctuation fields $\boldsymbol{w} \in C_0^\infty(\mathcal{B})$ (i.e. with $\boldsymbol{w} = \boldsymbol{0}$ on $\partial\mathcal{B}$) the integral inequality

$$\int_{\mathcal{B}} W(\overline{\boldsymbol{F}} + \mathrm{Grad}\boldsymbol{w})\, dV \geq \int_{\mathcal{B}} W(\overline{\boldsymbol{F}})\, dV = W(\overline{\boldsymbol{F}}) \times \mathrm{Vol}(\mathcal{B}) \tag{114}$$

is valid, Morrey (1952). □

The sequential-lower semicontinuity condition is ensured if the elastic stored energy is quasiconvex and an additional growth condition is fulfilled.

Another very important concept is the polyconvexity introduced by Ball (1977a,b):

[Definition of Polyconvexity] $\boldsymbol{F} \mapsto W(\boldsymbol{F})$ is polyconvex if and only if there exists a function $P : \mathbb{R}^{3\times3} \times \mathbb{R}^{3\times3} \times \mathbb{R} \mapsto \mathbb{R}$ (in general non-unique) such that

$$W(\boldsymbol{F}) = P(\boldsymbol{F}, \mathrm{Cof}\boldsymbol{F}, \det\boldsymbol{F}) \tag{115}$$

and the function $(\boldsymbol{F}, \mathrm{Cof}\boldsymbol{F}, \det\boldsymbol{F}) \in \mathbb{R}^{19} \mapsto P(\boldsymbol{F}, \mathrm{Cof}\boldsymbol{F}, \det\boldsymbol{F}) \in \mathbb{R}$ is convex for all points $\boldsymbol{X} \in \mathbb{R}^3$. □

Polyconvex functions are always s.w.l.s.. Finally, let us recapitulate the notion of Rank-one-convexity and ellipticity:

[Definition of Rank-one convexity] An elastic stored energy is rank-one convex whenever

$$W(\boldsymbol{F} + \lambda \boldsymbol{m} \otimes \boldsymbol{N}_0) \leq \lambda W(\boldsymbol{F} + \boldsymbol{m} \otimes \boldsymbol{N}_0) + (1 - \lambda) W(\boldsymbol{F}) \tag{116}$$

holds for all $\lambda \in [0, 1]$, $\boldsymbol{F} \in \mathbb{R}^{3\times3}$ and all $\boldsymbol{m} \in \mathbb{R}^3, \boldsymbol{N}_0 \in \mathbb{R}^3$ with $\det(\boldsymbol{F} + \lambda \boldsymbol{m} \otimes \boldsymbol{N}_0) > 0$. □

[Definition of Ellipticity] We say that the stored energy $W(\boldsymbol{F}) = \psi(\boldsymbol{C})$ leads to a uniformly elliptical equilibrium system whenever the uniform Legendre-Hadamard condition

$$\exists\, c^+ > 0\,, \forall\, \boldsymbol{F} \in \mathbb{R}^{3\times3}\,, \forall\, \boldsymbol{m}, \boldsymbol{N}_0 \in \mathbb{R}^3 \backslash \{\boldsymbol{0}\} : \\ (\boldsymbol{m} \otimes \boldsymbol{N}_0) : \mathbb{A} : (\boldsymbol{m} \otimes \boldsymbol{N}_0) \geq c^+ \, \|\boldsymbol{m}\|^2 \|\boldsymbol{N}_0\|^2$$

holds. We state that W gives rise to an (strictly) elliptical system if and only if the Legendre-Hadamard condition is valid:

$$\forall\, \boldsymbol{F} \in \mathbb{R}^{3\times3}\,, \forall\, \boldsymbol{m}, \boldsymbol{N}_0 \in \mathbb{R}^3 \backslash \{\boldsymbol{0}\} : \; (\boldsymbol{m} \otimes \boldsymbol{N}_0) : \mathbb{A} : (\boldsymbol{m} \otimes \boldsymbol{N}_0) \geq 0 \; (> 0). \; \square$$

Note that for smooth stored energy functions W strict rank-one convexity implies the strict Legendre-Hadamard condition. A physical interpretation of the aforementioned conditions can be obtained in the context in the field of wave propagation, for more details we refer e.g. to Schröder (2010).

A free energy is materially stable if it is elliptic. A reformulation of the Legendre-Hadamard condition yields

$$(\boldsymbol{m} \otimes \boldsymbol{N}_0) : \mathbb{A} : (\boldsymbol{m} \otimes \boldsymbol{N}_0) = \boldsymbol{m} \cdot \overline{\boldsymbol{Q}}(\boldsymbol{N}_0)\boldsymbol{m} > 0\,, \tag{117}$$

with the accoustic tensor $\overline{\boldsymbol{Q}}$, which is given in index notation by

$$\overline{Q}^{ab} = \mathbb{A}^{aBbD} N_{0B} N_{0D}\,. \tag{118}$$

This means that the accoustic tensor must be positive definite if we want to ensure material stability.

The non-uniqueness of solutions is an inherent feature in finite deformation continuum mechanics. Such problems could occur on both scales, the micro- and the macro-scale. In the following, we focus on microscopic structural instabilities, i.e. on non-stable equilibrium states on the micro-scale, in the context of the micro to macro transition. These phenomena are

associated to convexity properties of the boundary value problems on both scales and their interactions. Following Müller (1987) and Geymonat et al. (1993), we summarize that (i) in case of convex functionals we compute macroscopic energies by

$$\overline{\psi}(\overline{\boldsymbol{F}}) := \inf_{\widetilde{\boldsymbol{w}}} \frac{1}{V_0} \int_{\overline{B}_0} \psi(\overline{\boldsymbol{F}} + \nabla \widetilde{\boldsymbol{w}})\, dV\,, \tag{119}$$

with the fluctuation field $\widetilde{\boldsymbol{w}}$ on *one* unit cell $\mathcal{B}_0$. (ii) Structural instability problems on the micro-scale are associated to the homogenization of a nonconvex boundary value problem on the micro-scale. However, for non-convex functions we have to find in addition the critical size of the representative volume element $\mathcal{B}_0^{crit}$, i.e.

$$\overline{\psi}(\overline{\boldsymbol{F}}) := \inf_{\mathcal{B}_0^{crit}} \left\{ \inf_{\widetilde{\boldsymbol{w}}} \frac{1}{V_0^{crit}} \int_{\mathcal{B}_0^{crit}} \psi(\overline{\boldsymbol{F}} + \nabla \widetilde{\boldsymbol{w}}) dV \right\}\,, \tag{120}$$

with the fluctuation field $\widetilde{\boldsymbol{w}}$ on the representative volume element $\mathcal{B}_0^{crit}$ of critical size. It should be noted that for micro-heterogeneous structures, e.g. for fiber-reinforced matrix materials, the concept of quasiconvexity may not hold. As an illustrative example, we consider the system depicted in Fig. 9 and assume Dirichlet boundary conditions at the outer boundary. Even under affine boundary deformations, as indicated in Fig. 9, we are not able to expect an infimum of the stored energy of the whole system for a constant deformation gradient. On the contrary, we observe a buckling of the fiber for a specific compression state in horizontal direction, which should represent a post-critical stable deformation state.

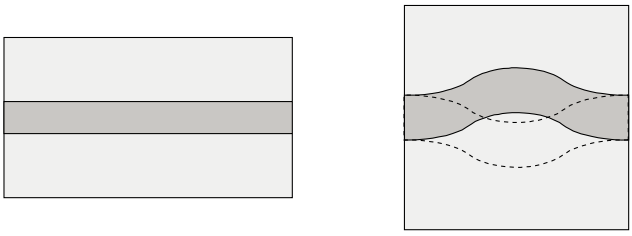

Figure 9. Fiber-reinforced matrix material: Unloaded reference configuration (left) versus buckling of the elastically bedded rod under horizontal compression (right), cf. Marsden and Hughes (1983).

In the following we analyze the influence of the size of the representative volume element (RVE) of a fiber-reinforced microstructure on the macroscopic response at microscopic buckling problems, as discussed in Schröder (2000). A more detailed analysis of instabilities on both scales as well as their interactions are given in Miehe et al. (2002). We consider a homogeneous deformation state at the macro-scale. The considered microstructure consists of a weak matrix (volume faction 80%) with fibers, which are reinforced in horizontal direction, as depicted in Fig. 10a. We expect two classical bifurcation modes, an out-of-phase buckling (Fig. 10b) and an in-phase buckling (Fig. 10c) of the fibers.

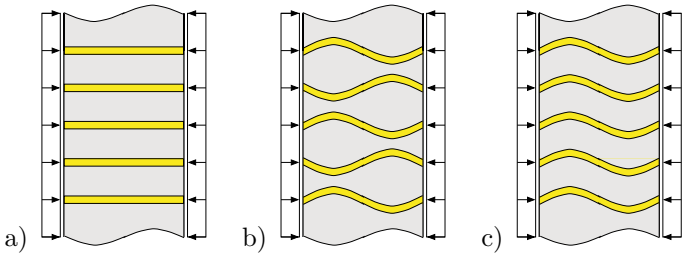

Figure 10. Horizontally loaded fiber reinforced composites: a) reference configuration, b) symmetric (out-of-phase) and c) unsymmetric (in-phase) buckling of the fibers, cf. Schröder (2000).

For simplicity, we apply a standard isotropic St. Venant-Kirchhoff material for the matrix and the fibers and apply periodic boundary conditions. The matrix material has a compression modulus of $\kappa_M = 49.98\, N/mm^2$ and a shear modulus of $\mu_M = 74.97\, N/mm^2$; for the reinforcement we consider the parameters $\kappa_I = 10^4\, \kappa_M$ and $\mu_I = 10^4\, \mu_M$. Applying the macroscopic deformation gradient $\overline{\boldsymbol{F}}$ with

$$\bar{\boldsymbol{F}} = \begin{bmatrix} 1-\lambda & 0 & 0 \\ 0 & 1 & 0 \\ 0 & 0 & 1 \end{bmatrix} \tag{121}$$

represents a horizontal compression state. For the considered compression case, we distinguish, as mentioned above, between two characteristic failure modes: buckling of the reinforcement in-phase (unsymmetric case) and buckling out-of-phase (symmetric case). For the unsymmetric case, we consider a finite-element discretization of an $\mathcal{RVE}$ with one fiber and for the symmetric case a finite-element discretization of an $\mathcal{RVE}$ with two fibers arranged in parallel. The crucial part is the yet unknown size of the $\mathcal{RVE}s$.

Thus, in order to find the critical load value as a function of the length of the discretized microstructure we have to modify the length of the $\mathcal{RVE}s$. For the finite element simulation of the in-phase buckling we discretize the system with 120×20 and for the out-of-phase buckling with 60×40 four-noded standard displacement elements. We start the simulation with a length of $l = 12$ (in consistent units) and increase the length by increments of $\Delta l = 12$ until the value $l = 60$ is reached. Two typical post-critical deformation states for the lengths $l = 6$ and $l = 2$ at the compressions $\lambda = 0.04$ and $\lambda = 0.01$, respectively, are shown in Fig. 11a,b.

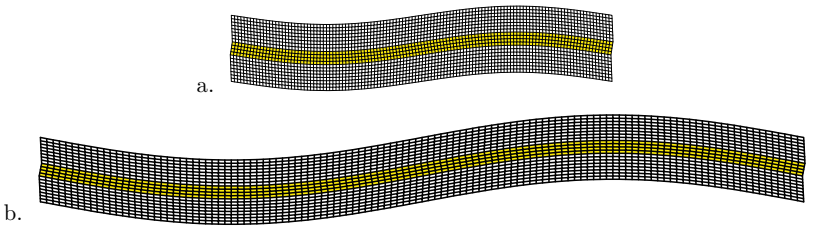

Figure 11. In-phase buckling of the fiber: post-critical deformation state of a) $l = 6$ at a compression parameter $\lambda = 0.04$ and b) $l = 12$ at a compression parameter $\lambda = 0.01$, see Schröder (2000).

The macroscopic Kirchhoff-stresses $\overline{\tau}_{11}$ with respect to the compression parameter λ are depicted in Fig. 12 for different lengths l. With increasing length l, the load-displacement curves are decreasing. Fig. 12b represents the critical stress components $\overline{\tau}_{11,crit}$ at the onset of the microscopic instability. The critical load converges against the lower bound.

For the stability analysis of the out-of-phase buckling mode, we start the simulation with a length $l = 3$ and increase the length stepwise using the increment $\Delta l = 1$ until $l = 12$ is reached.
Fig. 13a shows the macroscopic Kirchhoff-stresses $\overline{\tau}_{11}$ versus the loading paramter λ for eight different lengths. In contrast to the previously discussed in-phase buckling mode, the change of the characteristic curve shape is significant with increasing length. In Fig. 13b, the critical macroscopic stresses $\overline{\tau}_{11,crit}$ are depicted for the onset of the buckling of the fibers. The minimum of the critical stress $\overline{\tau}_{11,crit}$ is obtained at approximately $l = 7$.
Postcritical deformation states for the $\mathcal{RVE}$ of length $l = 5$ at the compression values $\lambda = 0.02$ and $\lambda = 0.03$ are depicted in Fig. 14a,b. A sequence of deformation states for the length $l = 12$ is documented in Fig. 15a–c, for

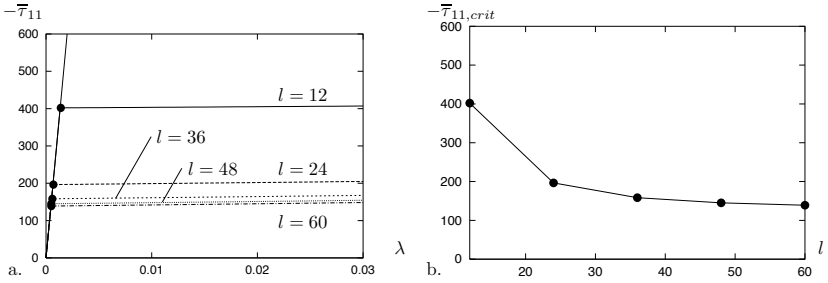

Figure 12. In-phase buckling of the fiber: a) macroscopic Kirchhoff-stresses $\overline{\tau}_{11}$ versus the compression parameter λ and b) critical stress $\overline{\tau}_{11,crit}$ at the onset of the structural instability at the micro-scale versus the length l of the considered microstructure, see Schröder (2000).

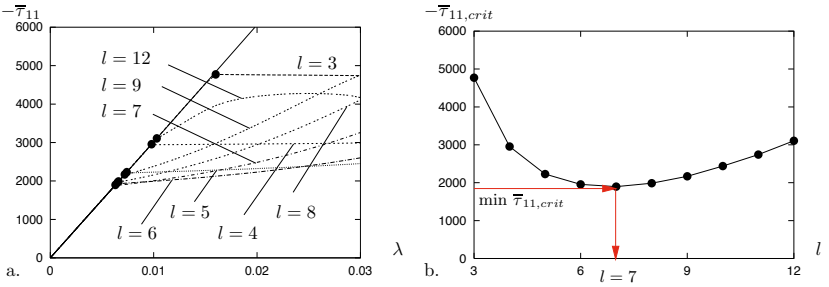

Figure 13. Out-of-phase buckling of the fibers: a) macroscopic Kirchhoff-stresses $\overline{\tau}_{11}$ versus the compression parameter λ for different lengths l and b) critical stress $\overline{\tau}_{11,crit}$ at the onset of the structural instability versus the length l, see Schröder (2000).

the load parameters $\lambda = 0.011, 0.017$ and 0.035, respectively. Additionally, Fig. 15c shows that higher-order buckling modes occur in the case where the length $\mathcal{RVE}$ becomes large enough. Here, three repeating characteristic deformation patterns are observable within the $\mathcal{RVE}$.

The two classical bifurcation modes, in-phase and out-of-phase, show different characteristics in the postcritical regime. In case of the out-of-phase buckling, the fibers support each other at a specific misalignment,

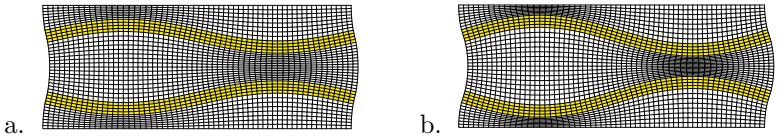

Figure 14. Out-of-phase buckling of the fibers: Post-critical deformation states for $l = 5$ at a compression parameter a) $\lambda = 0.02$ and b) $\lambda = 0.03$, see Schröder (2000).

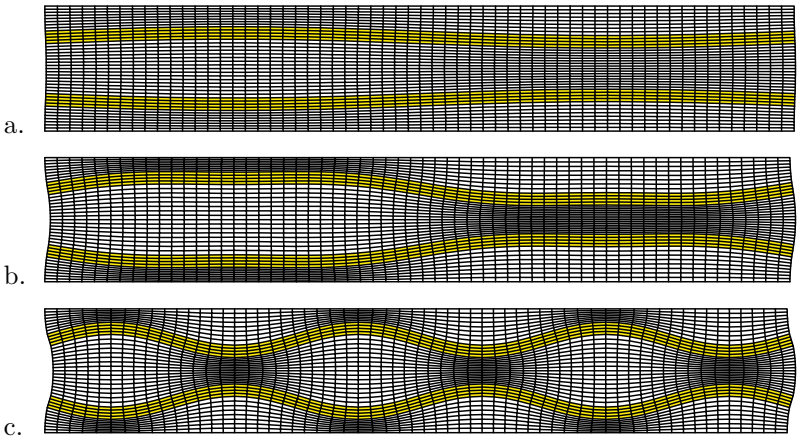

Figure 15. Out-of-phase buckling of the fibers: Post-critical deformation states for length $l = 12$ at a compression parameter a) $\lambda = 0.011$, b) $\lambda = 0.017$ and c) $\lambda = 0.035$, see Schröder (2000).

which leads to an increasing load-deflection curve. Thus, the out-of-phase buckling of the fibers could result in a stabilizing effect, this is in contrast to the postcritical behavior of the in-phase buckling of the fibers.

For a detailed analysis of possible bifurcation modes on the micro-scale as well as associated possible macroscopic material instabilities, we refer to Triantafyllidis and Maker (1985), Müller (1987), Abeyaratne and Triantafyllidis (1984), Triantafyllidis and Maker (1985), Geymonat et al. (1993), Miehe et al. (2002), Aubert et al. (2008), and Agoras et al. (2009) and the references therein.

5 Numerical Studies for Elasto-Plastic $\mathcal{RVE}$s

An important class of micro-heterogeneous materials are modern dual- and multi-phase steels. They exhibit a complex elasto-plastic mechanical response due to the interaction of the different phases in the microstructure. A micrograph of a typical dual-phase steel, a ferrite-perlite steel, is shown in Fig. 16a. The corresponding finite element discretization of this microstructure is depicted in Fig. 16b.

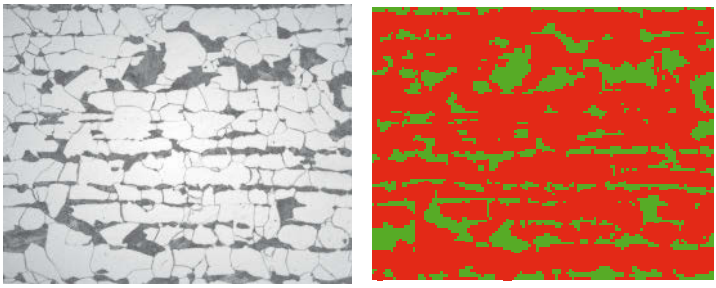

a) b)

Figure 16. Ferrite-Perlite Steel: a) micrograph and b) finite element discretization with 125×100 four noded quadrilateral elements.

In order to demonstrate the complexity of the distribution of the individual fields within the micro-heterogeneous composite, we consider a macroscopic simple tension test under plane strain conditions and apply periodic boundary conditions. For the individual phases, we apply an isotropic J_2-plasictiy model. Fig. 17a,b depict the distributions of the microscopic equivalent

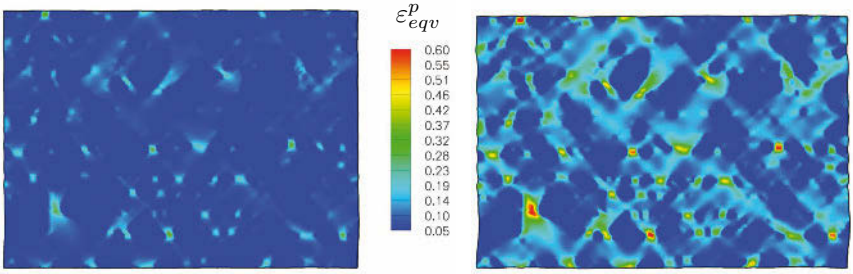

a) b)

Figure 17. Ferrite-Perlite Steel: distribution of equivalent plastic strains under horizontal elongation of a) 5% and b) 10%.

plastic strains for a horizontal elongation of 5% and 10%, respectively.

In this section, we discuss several examples illustrating the influence of different microscopic properties to the macroscopic response, where the numerical analysis is performed with FE^2-simulations.

5.1 Finite J_2-Plasticity Model

The elasto-plastic behavior of the individual constituents at the microscale is described by isotropic finite elasto-plasticity formulations based on the multiplicative decomposition of the deformation gradient

$$\boldsymbol{F} = \boldsymbol{F}^e \, \boldsymbol{F}^p \, , \tag{122}$$

where $\boldsymbol{F}^e$ denotes the elastic and $\boldsymbol{F}^p$ the plastic parts, see Kröner (1960), Lee (1969). For details of the thermodynamical formulation as well as for the numerical treatment, we refer to Simo (1988, 1992), Simo and Miehe (1992), Perić et al. (1992), Miehe and Stein (1992), and Miehe (1993). The strain energy function is assumed to be of the form

$$\psi = \psi^e(\boldsymbol{b}^e) + \psi^p(\alpha) \, , \tag{123}$$

wherein $\boldsymbol{b}^e$ denotes the elastic finger tensor and α the equivalent plastic strains. The elastic finger tensor is defined as

$$\boldsymbol{b}^e = \boldsymbol{F}^e \, (\boldsymbol{F}^e)^T = \sum_{A=1}^{3} (\lambda_A^e)^2 \boldsymbol{n}_A \otimes \boldsymbol{n}_A \tag{124}$$

with the eigenvectors $\boldsymbol{n}_A$ and eigenvalues $(\lambda_A^e)^2$ of the elastic finger tensor $\boldsymbol{b}^e$. Following Simo (1992), we define the strain energy function as

$$\psi^e = \frac{\lambda}{2}[\epsilon_1^e + \epsilon_2^e + \epsilon_3^e]^2 + \mu[(\epsilon_1^e)^2 + (\epsilon_2^e)^2 + (\epsilon_3^e)^2] \tag{125}$$

in terms of the logarithmic elastic strains $\epsilon_A^e = \log(\lambda_A^e)$; λ and μ are the Lamé constants. An exponential-type hardening of the individual phases is modeled by the well-known function

$$\psi^p = y_\infty \alpha - \frac{1}{\eta}(y_0 - y_\infty) \exp(-\eta\alpha) + \frac{1}{2} \, h \, \alpha^2 \, . \tag{126}$$

Herein, y_0 is the initial yield strength, y_∞ and η describe an exponential hardening behavior and h is the slope of a superimposed linear hardening. The yield criterion, formulated in terms of the Kirchhoff stresses

$$\boldsymbol{\tau} = \sum_{A=1}^{3} \tau_A \, \boldsymbol{n}_A \otimes \boldsymbol{n}_A \quad \text{with} \quad \tau_A = \frac{\partial \psi_e}{\partial \epsilon_A^e} \, , \tag{127}$$

is given by the expression

$$\phi = ||\mathrm{dev}\,\boldsymbol{\tau}|| - \sqrt{\frac{2}{3}}\beta \leq 0\,, \tag{128}$$

with

$$\beta = \frac{\partial \psi^p(\alpha)}{\partial \alpha} = y_0 + (y_\infty - y_0)(1 - \exp(-\eta\alpha)) + h\,\alpha\,. \tag{129}$$

The flow rule and the evolution equation for the internal plastic quantity are given by

$$\frac{1}{2}\mathcal{L}(\boldsymbol{b}^e)\boldsymbol{b}^{e\,-1} = -\lambda\frac{\partial\phi}{\partial\boldsymbol{\tau}} \quad \text{and} \quad \dot{\alpha} = \lambda\frac{\partial\phi}{\partial\beta}\,, \tag{130}$$

respectively. Here, $\mathcal{L}$ denotes the Lie time derivative and λ the scalar-valued Lagrange multiplier. The flow rule is integrated using an exponential update algorithm, which preserves plastic incompressibility (Weber and Anand (1990), Simo (1992), and Miehe and Stein (1992)). For the numerical implementation, we follow the algorithmic formulation in a material setting as proposed in Klinkel (2000).

5.2 Shear Test: Comparative Study of Different $\mathcal{RVE}s$.

In the following examples, we consider a (homogeneous) macroscopic pure shear test and analyze the stress-strain relation at the macro-scale for different combinations of constitutive equations of the matrix and the inclusion phase for an artificial $\mathcal{RVE}$. At the macro-scal,e a homogeneous pure shear situation is prescribed by the macroscopic deformation gradient

$$\overline{\boldsymbol{F}} = \begin{bmatrix} 1 & \overline{F}_{12} & 0 \\ \overline{F}_{21} & 1 & 0 \\ 0 & 0 & 1 \end{bmatrix} \quad \text{with} \quad \overline{F}_{12} = \overline{F}_{21}\,. \tag{131}$$

During the simulation, the coefficient $\overline{F}_{12}$ oscillates stepwise between -0.1 and 0.1 in order to simulate a cyclic loading process. It starts with $\overline{F}_{12} = 0.0$ with an increase of the component up to 0.1, this marks the first inflection point. Afterwards the loading is switched and the coefficient is stepwise decreased to -0.1, where the second inflection point is reached. Again, $\overline{F}_{12}$ is increased to 0.1, the next inflection point, and the procedure is repeated. The whole process is controlled by a linear modification of the coefficient $\overline{F}_{12}$ between the coordinates

$$\overline{F}_{12} : 0.0 \rightarrow +0.1 \rightarrow -0.1 \rightarrow +0.1 \rightarrow -0.1 \rightarrow +0.1\,. \tag{132}$$

At the micro-scale, an artificial microstructure is considered, where the inclusion geometry is a *smiley* embedded in a matrix phase. To study

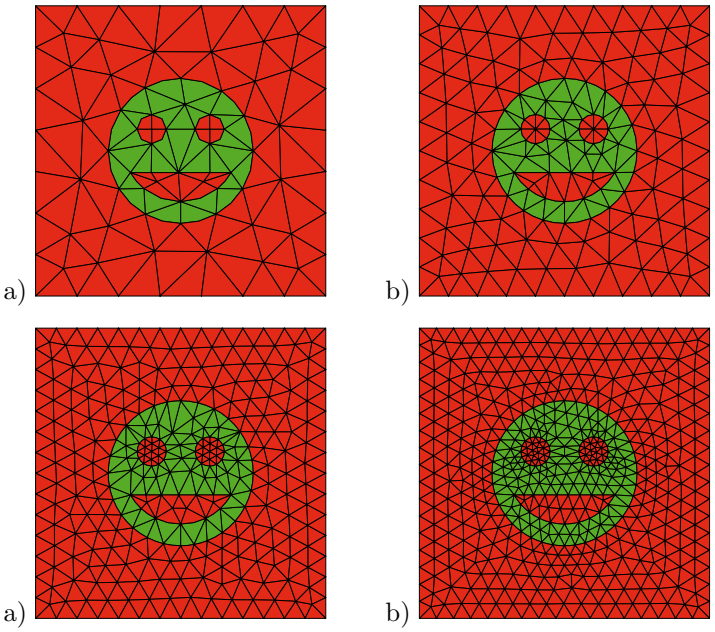

Figure 18. Artificial microstructure with different finite element discretizations: a) 140, b) 292, c) 538 and d) 970 triangular elements with quadratic ansatz functions.

the convergence of the simulation with respect to the element size, four different discretization levels at the micro-scale are used, which consist of 140, 292, 558 and 970 triangular elements with quadratic ansatz functions, cf. Figure 18.

Elastic Matrix and Elastic Inclusion In a first setup, we consider both phases, matrix and inclusion, to be described by a purely elastic material behavior. Thereby, the instantaneous elasticity modulus of the inclusion is assumed to be 1000 times higher than the one of the matrix material; the elasticity parameters for the matrix material are set to

$$\lambda = 118.85 \text{ MPa} \quad \text{and} \quad \mu = 79.230 \text{ MPa} \,. \tag{133}$$

In order to study the influence of the finite element mesh density, we consider the four different discretization levels at the micro-scale depicted in Figure 18.

For the study of the microscopic stress distribution based on the four different discretization levels, the coefficient σ_{12} of the microscopic Cauchy stresses are shown in Figure 19. In the matrix region, no significant differences of the stress distributions are observable. Nevertheless, in the regions close to the inclusion as well as inside the inclusion the stress distributions differ.

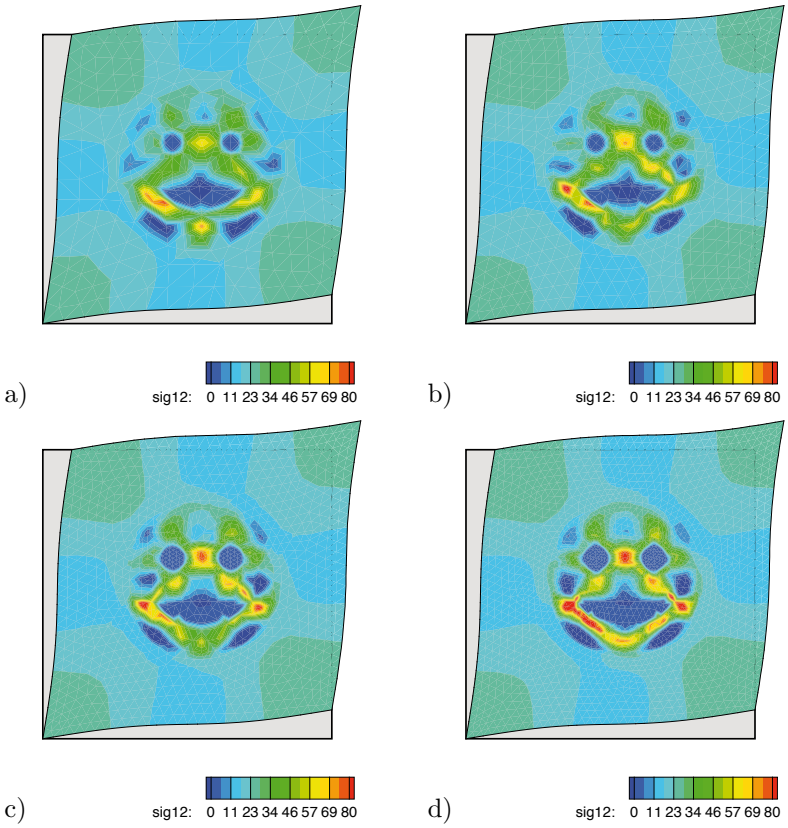

Figure 19. Distribution of the stresses σ_{12} at $\overline{F}_{12} = 0.1$ for different discretizations: a) 140, b) 292, c) 558 and d) 970 elements.

Figure 20a depicts the Cauchy stress σ_{12} versus the shear strain F_{12} for the matrix and the inclusion phase. The macroscopic stress strain curves are practically not influenced by the different mesh densities, see Figure 20b, although at the micro-scale deviations between the simulations can be ob-

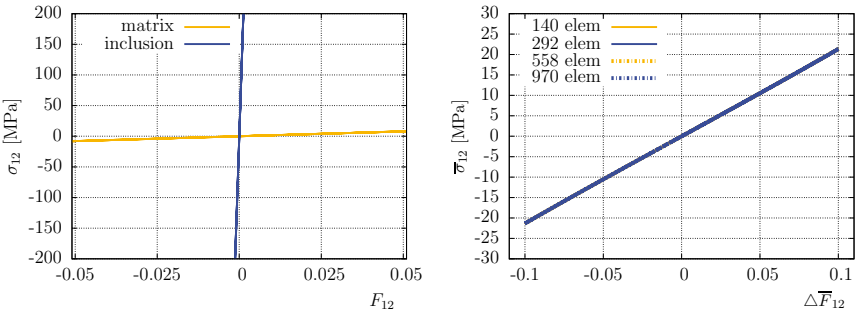

Figure 20. Cauchy stresses versus shear strain: a) σ_{12} versus F_{12} for the individual phases and b) $\overline{\sigma}_{12}$ versus $\overline{F}_{12}$ for the four mesh densities.

served (in this simple example). Therefore, in the following examples we will consider the macroscopic stress-strain relations for all four discretization levels and the local stress distribution at the micro-scale is only depicted for the finest mesh density.

The relative deviation, defined as $e_{\overline{\sigma}_{12}} = (\overline{\sigma}_{12} - \overline{\sigma}_{12}^{[970\ \text{elem}]})/\overline{\sigma}_{12}^{[970\ \text{elem}]}$ for $\overline{\sigma}_{12}^{[970\ \text{elem}]} \neq 0$, of the macroscopic Cauchy stresses with respect to the one obtained using the finest discretization level (970 elements) are depicted in Figure 21. As expected, the deviation of the stresses is decreased along an increasing number of finite elements; nevertheless, the relative error is lower than 0.2%

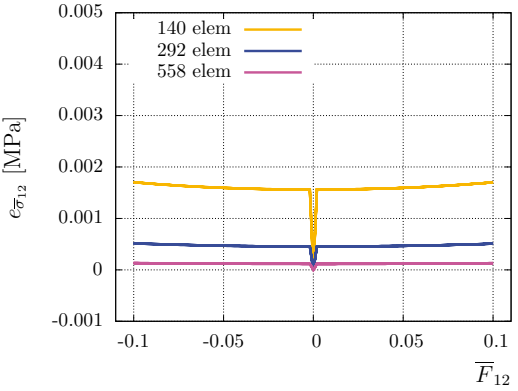

Figure 21. Relative error $e_{\overline{\sigma}_{12}}$ for different discretizations at the micro-scale with respect to the finest discretization level (970 elements).

Elasto-Plastic Matrix and Elastic Inclusion In the following example, we consider again a pure shear test at the macro-scale and also an elastic behavior of the inclusion. With contrast to the previous example, the matrix behavior is now considered to be elasto-plastic. In the elastic domain the same instantaneous elasticity modulus is considered for both phases and for the elasto-plastic behavior of the matrix phase the finite J_2-plasticity model is applied. The material parameters for the matrix material are given in Table 2. The stress-strain relations for the matrix and the inclusion material for the pure shear test are depicted in Figure 22f.

Table 2. Material parameters of the matrix phase.

phase	λ [MPa]	μ [MPa]	y_0 [MPa]	y_∞ [MPa]	η [-]	h [-]
matrix	118,846.2	79,230.77	300.0	300.0	0.0	500.0

The simulations are performed again for the four discretization levels under the pure shear condition described by Eq. (131) and (132). As mentioned in the previous example of pure elastic phases, we represent the distribution of the local fields only for the finest discretization of the $\mathcal{RVE}$ with 970 elements.

Since the matrix phase behaves elasto-plastically, we study the evolution of the equivalent plastic strains α inside this microscopic phase. In Fig. 22a-e, these quantities are shown at the inflection points of the loading. The plastic strains in the matrix phase increase during the whole loading process and in the final state nearly the complete region around the "smiley" exhibits plastic deformation. But inside the "eyes" and the "mouth" the equivalent plastic strains remain at a comparatively low level. This behavior is obvious, since the shape of the inclusion remains nearly undeformed due to its larger stiffness.

In Figure 23a-e, the distribution of the microscopic Cauchy stress coefficient σ_{12} is shown for different loading states, which are obtained by the macroscopic pure shear condition due to the macroscopic deformation tensor given by Equation (131). The macroscopic stress response is nearly the same for all different microscopic discretization levels, cf. Figure 23f. In the inflection points of the loading the microscopic stress components σ_{12} inside most parts of the inclusion phase is larger compared to the matrix phase. Only the region near the "cheeks" of the "smiley" shows lower stress levels.

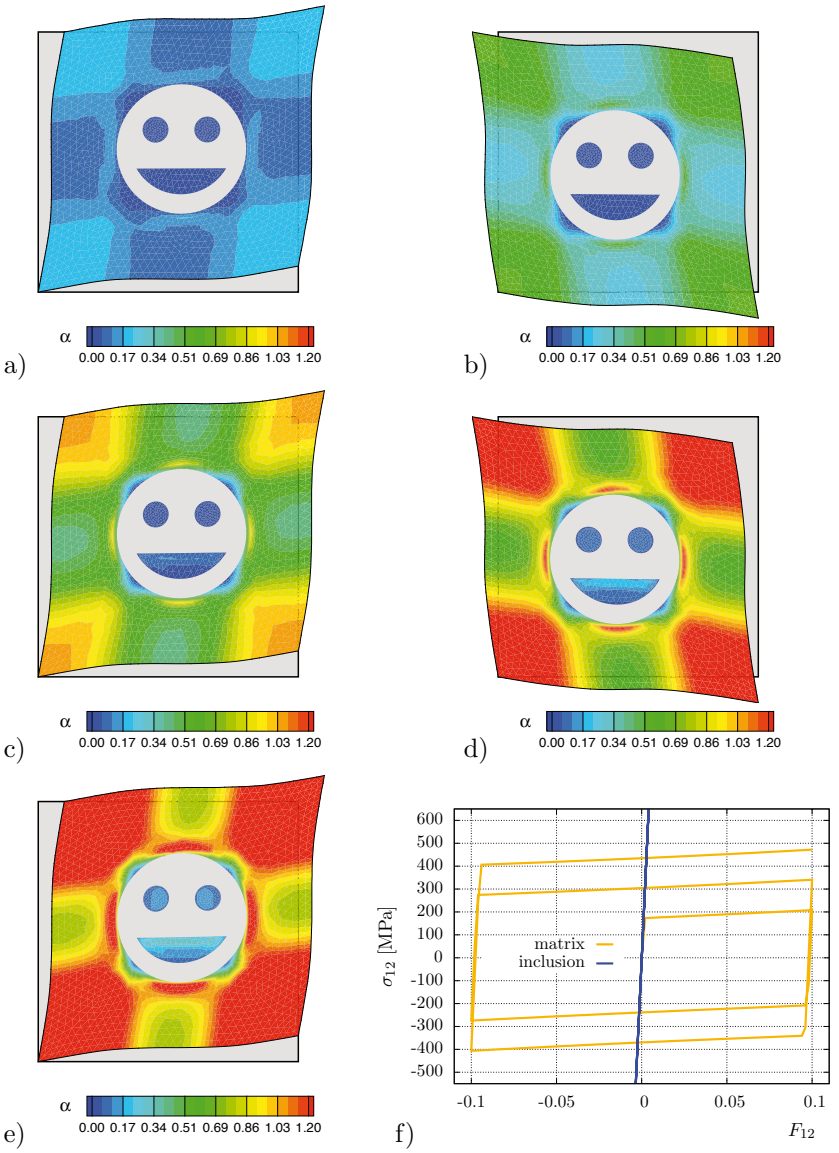

Figure 22. Distribution of the equivalent plastic strains α at the micro-scale (970 elements) with macroscopic deformation gradient coefficient a) $\overline{F}_{12} = 0.1$ in 1^{st} load cycle (l.c.), b) $\overline{F}_{12} = -0.1$ in 1^{st} l.c., c) $\overline{F}_{12} = 0.1$ in 2^{nd} l.c., d) $\overline{F}_{12} = -0.1$ in 2^{nd} l.c., e) $\overline{F}_{12} = 0.1$ in 3^{rd} l.c. The inclusion phase is blanked due to its purely elastic behavior. f) Cauchy stress σ_{12} versus F_{12} for the individual phases.

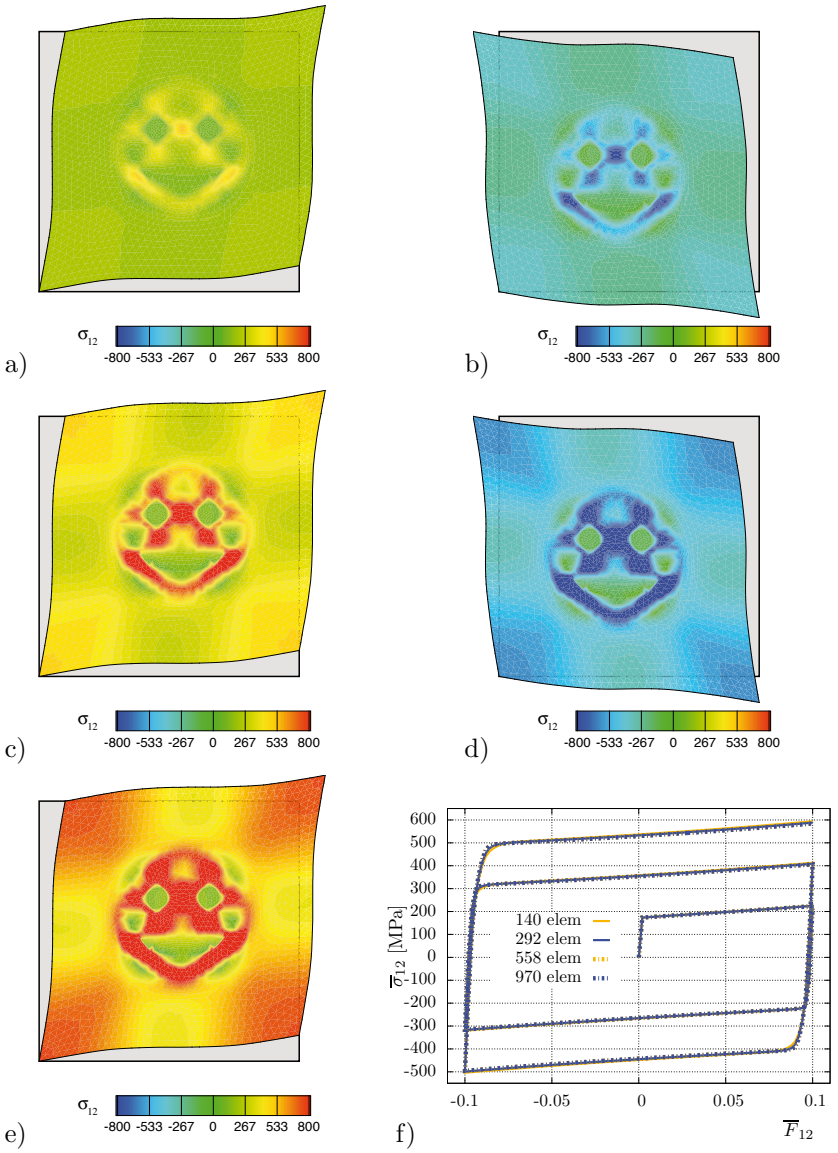

Figure 23. Distribution of the Cauchy stress σ_{12} at the micro-scale (970 elements) with macroscopic deformation gradient coefficient a) $\overline{F}_{12} = 0.1$ in 1st load cycle (l.c.), b) $\overline{F}_{12} = -0.1$ in 1st l.c., c) $\overline{F}_{12} = 0.1$ in 2nd l.c., d) $\overline{F}_{12} = -0.1$ in 2nd l.c., e) $\overline{F}_{12} = 0.1$ in 3rd l.c. and f) macroscopic Cauchy stress $\overline{\sigma}_{12}$ versus $\overline{F}_{12}$ obtained with all microscopic discretization levels.

Elasto-Plastic Matrix and Elasto-Plastic Inclusion Considering the same pure shear situation with a cyclic loading, we study the macroscopic and microscopic mechanical response of the "smiley"-microstructure when both phases, the matrix and the inclusion, behave elasto-plastically. The material model is again described by the set of equations (125)-(127) used with the material parameters given in Table 3. The individual material response of the phases in the pure shear situation is shown in Figure 24f. Note that the parameters are chosen for the inclusion phase such that almost no hardening is obtained during the loading process.

Table 3. Material parameters of the individual phases.

phase	λ [MPa]	μ [MPa]	y_0 [MPa]	y_∞ [MPa]	η [-]	h [-]
matrix	118,846.2	79,230.77	300.0	300.0	0.0	500.0
inclusion	118,846.2	79,230.77	600.0	1000.0	0.0	10.0

Using the four meshes shown in Fig. 18 for the discretization of the "smiley" at the micro-scale, four cyclic loading processes are performed. In Fig. 24a-e, the evolution of the equivalent plastic strains α at the micro-scale is shown in the inflection points and the final state of the loading. At the second and third inflection point the plastic strains are lower almost everywhere in the inclusion phase than in the matrix phase and in the next point this aspect is switched. The reason for this observation becomes obvious if one takes a closer look at the behavior of the individual phases in Fig. 24f. Until the third inflection point, the yield stresses inside the matrix phase are lower than the ones of the inclusion phase, due to the low hardening rate of the inclusion phase. After this point, the relation turns and the plastic strains in the inclusion phase increase. Thus, in the final state the (local averaged) equivalent plastic strains are higher in the inclusion phase than in the matrix phase. The macroscopic mechanical response of the microstructure obtained by the computations using the different discretization levels is depicted in Fig. 25f. The distribution of the microscopic stress components σ_{12} is shown in Fig. 25a-e for all inflection points, where the results of the finest discretization level is used. Again, the different mesh densities provide an almost equal macroscopic response. The microscopic stress distribution correlates inversely to the equivalent plastic strains at the micro-scale. Until the third inflection point, the stress component in the inclusion is higher than in the matrix phase. Afterwards, it turns and the stress distribution in the matrix shows larger values. This effect is also caused by the different hardening properties of the individual phases.

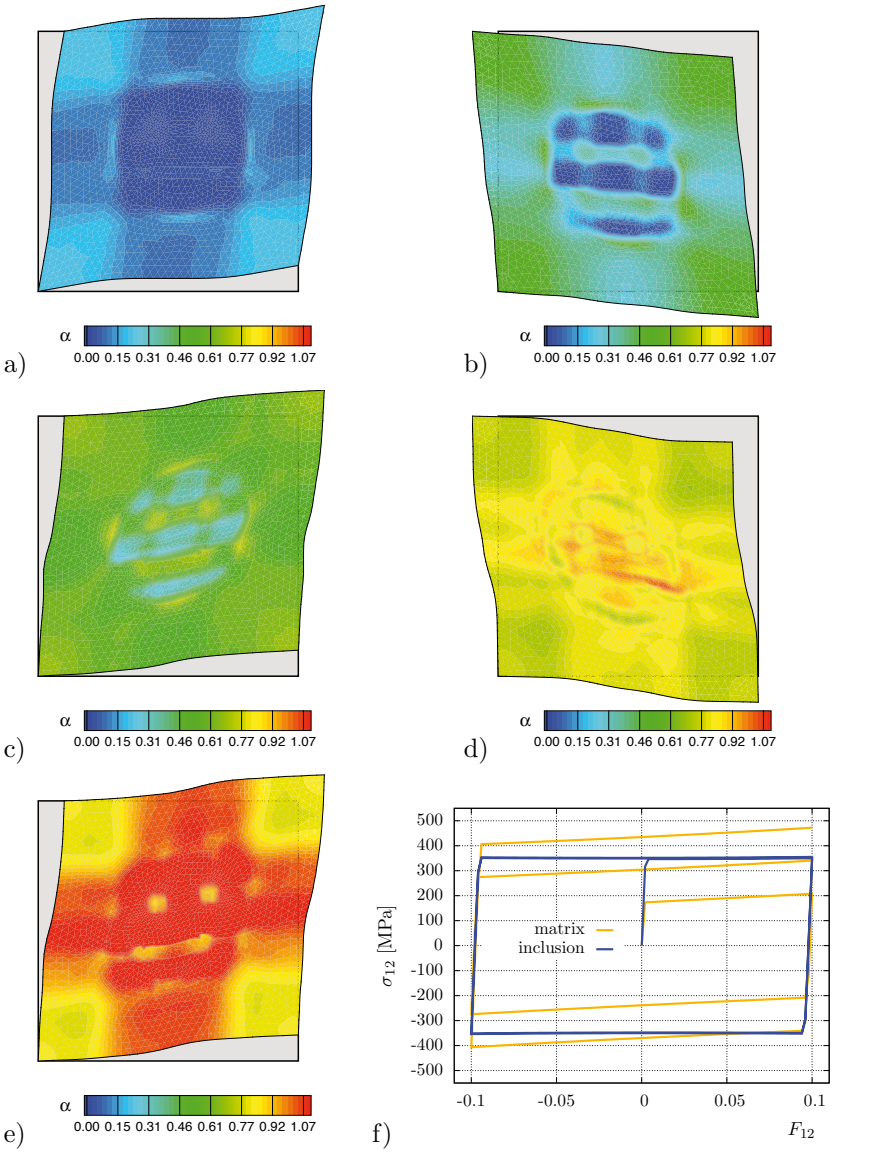

Figure 24. Distribution of the equivalent plastic strains α at the micro-scale (970 elements) with macroscopic deformation gradient coefficient a) $\overline{F}_{12} = 0.1$ in 1st load cycle (l.c.), b) $\overline{F}_{12} = -0.1$ in 1st l.c., c) $\overline{F}_{12} = 0.1$ in 2nd l.c., d) $\overline{F}_{12} = -0.1$ in 2nd l.c., e) $\overline{F}_{12} = 0.1$ in 3rd l.c., and f) Cauchy stress σ_{12} versus F_{12} obtained for the individual phases.

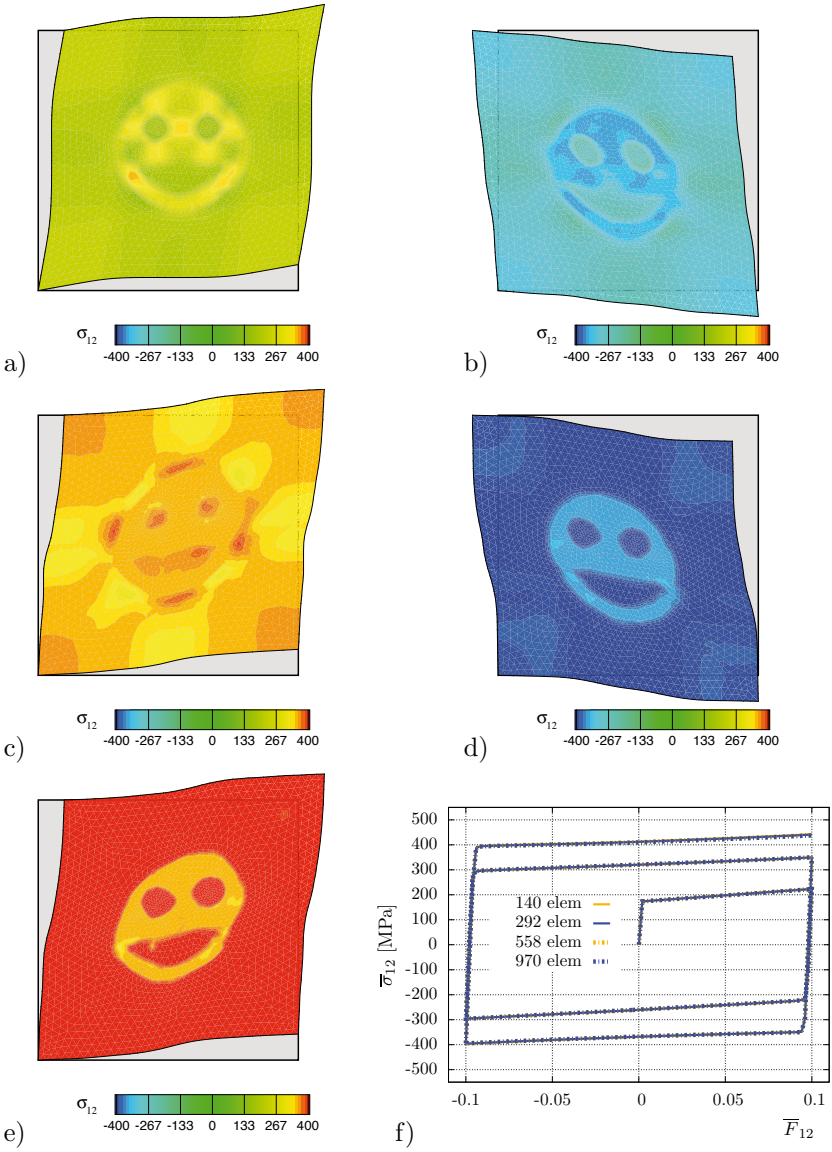

Figure 25. Distribution of the Cauchy stress σ_{12} at the micro-scale (970 elements) with macroscopic deformation gradient coefficient a) $\overline{F}_{12} = 0.1$ in 1st load cycle (l.c.), b) $\overline{F}_{12} = -0.1$ in 1st l.c., c) $\overline{F}_{12} = 0.1$ in 2nd l.c., d) $\overline{F}_{12} = -0.1$ in 2nd l.c., e) $\overline{F}_{12} = 0.1$ in 3rd l.c. and f) macroscopic Cauchy stress $\overline{\sigma}_{12}$ versus $\overline{F}_{12}$ obtained with all microscopic discretization levels.

5.3 Influence of Inclusion Size

The Bauschinger effect, a general phenomenon observed in a variety of polycrystalline metals, describes a yield strength characteristic, denoted as kinematic hardening, as a result of the distribution of the microscopic stress fields. As an example, if the tensile yield strength increases due to tensile loading, the compressive yield strength decreases: we observe a translational movement of the elastic region in stress space. The micromechanical motivation is the assistance of the dislocation movement in reverse loading direction by local back stresses. For the definition of a quantity measuring the Bauschinger, effect several parameters can be found in the literature. Here, a suitable Bauschinger factor is defined as

$$\overline{f}_B = \frac{|\overline{\sigma}^I| - \overline{\sigma}^{II}}{|\overline{\sigma}^I|} \,, \tag{134}$$

for the definition of the individual stress values cf. Fig. 26. This factor is zero for the case where no kinematic hardening occurs and it increases for an increasing kinematic hardening.

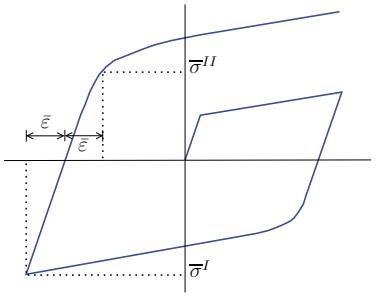

Figure 26. Illustration for the definition of the Bauschinger factor.

In this section, the influence of the inclusion phase fraction on the Bauschinger effect is studied. Thereby, the matrix phase has an elasto-plastic mechanical behavior using the parameters given in Table 4.

Table 4. Material parameters of the matrix phase.

phase	λ [MPa]	μ [MPa]	y_0 [MPa]	y_∞ [MPa]	η [-]	h [-]
matrix	118,846.2	79,230.77	200.0	200.0	0.0	10000.0

The inclusion phase behaves purely elastic with the same instantaneous elasticity modulus as the matrix phase in the elastic domain.

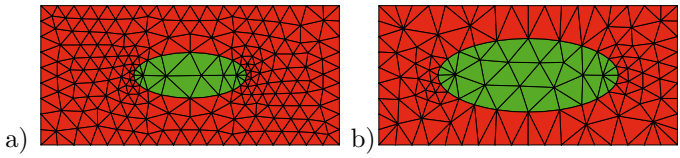

Figure 27. Discretization of the microstructures with a) 10% and b) 25% inclusion phase fraction.

A cyclic tension-compression test is performed at the macro-scale, cf. Fig. 26, and at the micro-scale three different microstructures are considered. The microstructures differ from each other in the phase fraction of the inclusion phase: 0%, 10% and 25%. Consequently, the first configuration is a homogeneous material built from the matrix phase and identical to a purely macroscopic computation using the material parameters of the matrix phase. The inclusion geometry of the second and third one is described by an ellipse. Their discretizations result in two meshes with 386 and 200 triangular finite elements with quadratic shape functions, respectively, cf. Fig. 27a,b.

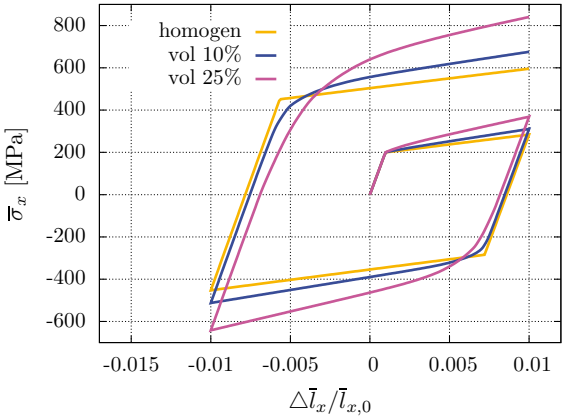

Bauschinger factors:

homogen:
$\overline{f}_B = \frac{450-450}{450} = 0.0$

10% inclusion:
$\overline{f}_B = \frac{510-420}{510} = 0.18$

25% inclusion:
$\overline{f}_B = \frac{640-440}{640} = 0.31$

Figure 28. Macroscopic stress-strain response of the compression-tension test of the homogeneous material and the microstructure with 0%, 10% and 25% inclusion phase fraction and the computed Bauschinger factors, for the definitions cf. Fig. 26.

The macroscopic load scenario involves compression up to $\Delta\bar{l}/\bar{l}_0 = -0.05$, tension back to $\Delta\bar{l}/\bar{l}_0 = 0$ and then further tensile loading. The resulting stress-strain diagrams and the Bauschinger factors computed from that are displayed in Fig. 28. In the homogeneous case, i.e. 0% inclusion phase fraction, the Bauschinger factor is zero, since the material model of the matrix phase does not take into account any kinematic hardening. With an increasing phase fraction of the inclusion phase, the Bauschinger factor also increases to 0.18 and 0.31, respectively, see Fig. 28. Consequently, a significant macroscopic kinematic hardening is observed although no kinematic hardening is considered in the individual phases.

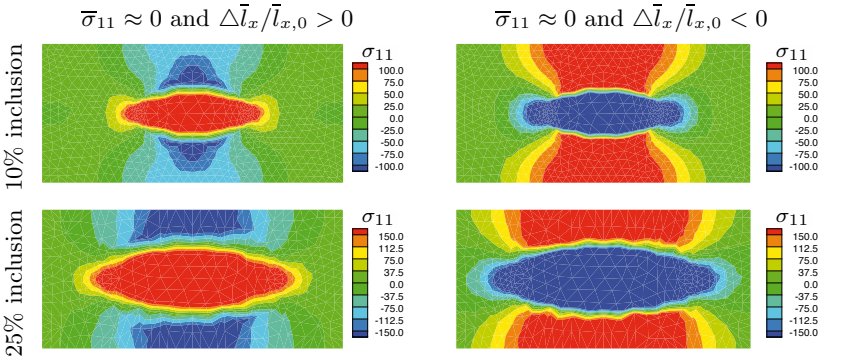

Figure 29. Distribution of the σ_{11}-stress in the macroscopic zero stress states for the microstructures with 10% (bottom row) and 25% (top row) inclusion phase fraction.

To analyze this effect, we take a look at the distribution of the microscopic stress component σ_{11} at the loading point, where the macroscopic stress response is nearly zero, see Fig. 29. These distributions show that in the macroscopic zero stress state the microscopic stresses remain due to the elasto-plastic behavior of the matrix phase. These eigenstresses play a major role for the macroscopic kinematic hardening.

5.4 Notched Rod under Tension

In this section, the mechanical response of a notched rod is analyzed under tensile loading. Thus, we consider now an inhomogeneous boundary value problem on the macro-scale. The geometry of the rod and the boundary conditions are shown in Fig. 30. Associated to the geometric quantities defined therein, we set the length $l = 4.2\,\text{mm}$, the notch radius $r = 0.7\,\text{mm}$, the distance between the notches $d = 1.1\,\text{mm}$ and thus, the height of the rod yields $D = 2.5\,\text{mm}$.

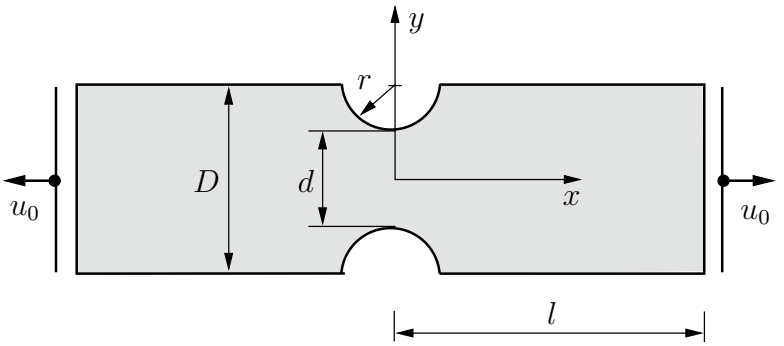

Figure 30. Macroscopic boundary value problem of a notched rod under tensile loading. The vertical degree of freedom of the nodes on the left and right end of the rod are constrained.

Here, a two-dimensional analysis is performed considering plane-strain conditions. The micro-heterogeneity of the underlying material is considered by applying a $\mathcal{RVE}$ at the micro-scale and using the FE^2-method. For this purpose, a real microstructure obtained by image analysis of a micrograph of a Dual-Phase steel as shown in Fig. 31 serves as the $\mathcal{RVE}$. The individual phases (here martensitic island-like inclusions in a ferritic matrix) are modeled by the finite J_2-plasticity model described above incorporating exponential isotropic hardening. The material parameters are chosen such that the matrix and inclusion phase behave similarly to the typical behavior of ferrite and martensite, respectively. As can be seen in Table 5, the elastic Lamé parameters λ and μ are assumed to be the same for both phases and only the plastic parameters are different. At the micro-scale, we consider a discretization with 1548 triangular finite elements, cf. Fig. 31. Linear displacement boundary conditions are taken into account for simplicity. However, a reasonably large $\mathcal{RVE}$ is considered and therefore the impact of the type of boundary conditions should neither significantly influence the macroscopic response, nor the microscopic fields in a reasonable distance from the boundary.

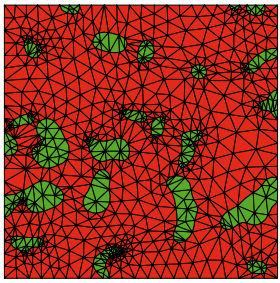

Figure 31. Discretization of the microstructure ($\mathcal{RVE}$) with 1548 quadratic triangular finite elements.

Table 5. Material parameters of the individual phases.

phase	λ [MPa]	μ [MPa]	y_0 [MPa]	y_∞ [MPa]	η [-]	h [-]
matrix	118,846.2	79,230.77	260.0	580.0	9.0	70.0
inclusion	118,846.2	79,230.77	1000.0	2750.0	35.0	10.0

At the macro-scale, the rod is discretized with 528 triangular finite elements, also with quadratic shape functions. The displacements at the macroscopic boundary, as shown in Fig. 30, are increased stepwise until a maximum external displacement of $u_0 = 0.175\,\text{mm}$ is obtained. In total, 2092 load steps are calculated and for each step an average number of 5-7 macroscopic Newton iterations are required. The notched rod in its final deformed configuration is depicted in Fig. 32. In more detail, the von Mises stress distribution is shown indicating the maximum stress values in the center of the rod. At three different macroscopic locations, in the center of the rod, at the boundary of the notch and at the transition of the notch and the rod, local distributions of the equivalent plastic strains are depicted at the microscopic level, see Fig. 32. The locations of those macroscopic integration points are marked by geometric symbols. Whereas the distribution of equivalent plastic strains in the first two microscopic problems are strongly localized with maximum strains of up to 1.2, the third position at the transition between the notch and the straight edge does not exhibit significant plastic strains. Note that a microscopic calculation is run for every macroscopic integration point in a coupled manner and the three microscopic strain distributions shown in Fig. 32 are just three elected situations.

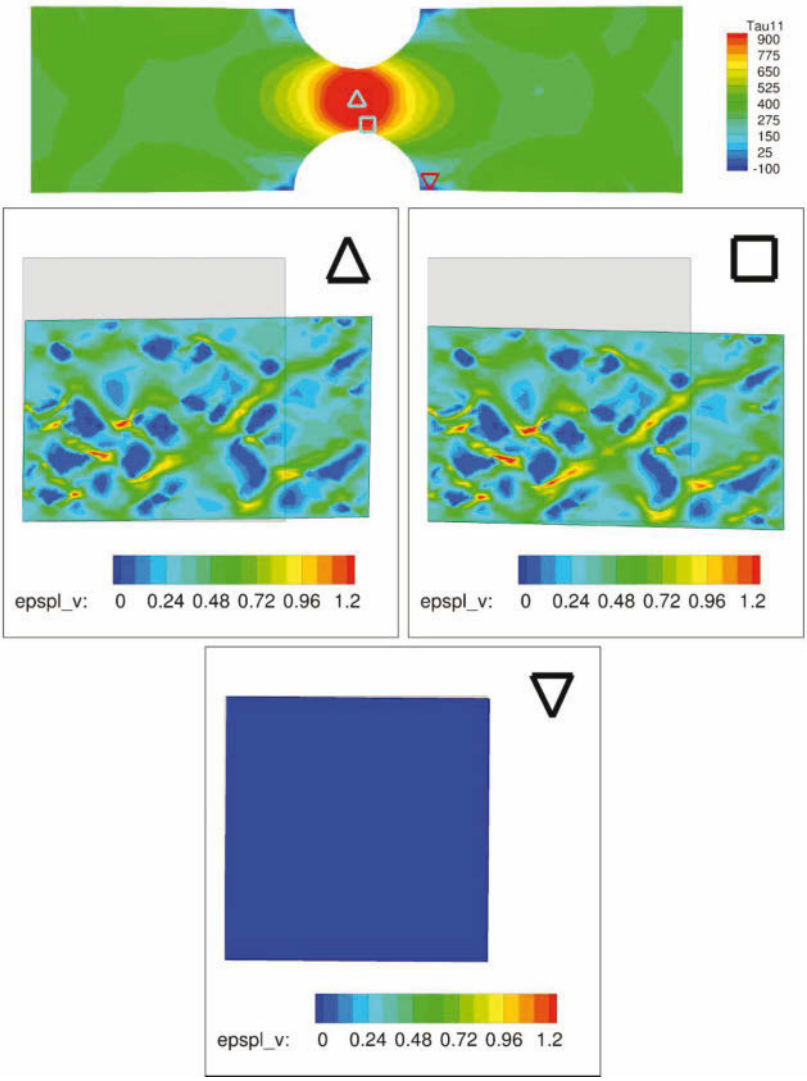

Figure 32. FE^2-simulation: Macroscopic von Mises stress (top), distribution of equivalent plastic strains in the microstructures associated with the three marked macroscopic integration points.

6 Summary and Outlook

In this contribution, we have discussed a direct two-scale homogenization technique, denoted as the FE^2-method or as the multilevel finite element method, for the numerical solution of coupled micro-macro boundary value problems. The presented first-order homogenization scheme seems to be sufficient if the concept of *separation of scales* holds. A fundamental advantage of this scheme is that we do not have to develop (complex) macroscopic constitutive models. Instead of developing such macroscopic phenomenological constitutive laws , we attach representative volume elements ($\mathcal{RVE}$s), reflecting the main characteristics of the underlying microstructure as close as possible, at each point of the macrostructure. In consequence, the macroscopic phenomenological quantities of interest, like stress measures and deformation tensors, are replaced by suitable averages over the microstructure. For this reason we cannot directly compute the macroscopic (overall) algorithmic tangent moduli by the partial derivative of the macroscopic first Piola-Kirchhoff stresses with respect to the macroscopic deformation gradient. In fact, we have to compute this sensitivity in an implicit manner; here we followed the closed-form representation of the macroscopic tangent moduli derived by Miehe et al. (1999a,b).
This general numerical procedure has a wide range of capabilities in the field of classical micro to macro transition problems. In order to demonstrate the performance of this method, we analyzed simple unit cell problems with different stress-strain characteristics for the individual phases of the microstructure. Especially the analysis of complicated processes on the microstructure, taking into account microscopic stress fields, which are responsible for the Bauschinger effect, can be incorporated into the direct homogenization scheme. Furthermore, we have given some remarks concerning structural instabilities on the microstructure and material instabilities on the macrostructure as well as their interactions. In these cases, the size of the attached microstructure plays a crucial role. It was also shown that the procedure solves inhomogeneous macroscopic boundary value problems.

7 Acknowledgements:

Parts of work presented in this contribution are taken from my habilitation thesis and other parts from joint studies with Daniel Balzani and Dominik Brands. The author greatly appreciates the “Deutsche Forschungsgemeinschaft” (DFG) for the financial support under the research grant SCHR 570/8-2 within the research group on “Analysis and Computation of Microstructure in Finite Plasticity”.

Bibliography

R. Abeyaratne and N. Triantafyllidis. An investigation of localization in a porous elastic material using homogenization theory. *Journal of Applied Mechanics*, 51:481–486, 1984.

M. Agoras, O. Lopez-Pamies, and P. Ponte Castañeda. Onset of macroscopic instabilities in fiber-reinforced elastomers at finite strain. *Journal of the Mechanics and Physics of Solids*, 57:1828–1850, 2009.

M. Ambrozinski, K. Bzowski, L. Rauch, and M. Pietrzyk. Application of statistically similar representative volume element in numerical simulations of crash box stamping. *Archives of Cicvil and Mechanical Engineering*, 12:126–132, 2012.

P. Aubert, C. Licht, and S. Pagano. Some numerical simulations of large deformations of heterogeneous hyperelastic materials. *Computational Mechanics*, 41:739–746, 2008.

I. Babuska. Homogenisation approach in engineering. In *Lecture Notes in Economics and Math. Systems*, volume 134, pages 137–153. Springer Verlag, 1976.

N. Bakhvalov and G. Panasenko. *Homogenisation: Averaging processes in periodic media*. Kluwer Academic Publishers, 1984.

J.M. Ball. Convexity conditions and existence theorems in nonlinear elasticity. *Archive for Rational Mechanics and Analysis*, 63:337–403, 1977a.

J.M. Ball. Constitutive inequalities and existence theorems in nonlinear elastostatics. In R. J. Knops, editor, *Symposium on Non-Well Posed Problems and Logarithmic Convexity*, volume 316. Springer-Lecture Notes in Math., 1977b.

D. Balzani, J. Schröder, and D. Brands. FE^2-simulation of microheterogeneous steels based on statistically similar RVEs. In *Proceedings of the IUTAM Symposium on Variational Concepts with applications to the mechanics of materials, September 22-26, 2008, Bochum, Germany*, 2009.

D. Balzani, D. Brands, J. Schröder, and C. Carstensen. Sensitivity analysis of statistical measures for the reconstruction of microstructures based on the minimization of generalized least-square functionals. *Technische Mechanik*, 30:297–315, 2010.

A. Bensoussan, J.L. Lions, and G. Papanicolaou. *Asymptotic Analysis for Periodic Structures*. North-Holland Publishing Company, 1978.

J.D. Clayton and D.L. McDowell. A multiscale multiplicative decomposition for elastoplasticity of polycrystals. *International Journal of Plasticity*, 19:1401–1444, 2003.

E. A. de Souza Neto and R.A. Feijoo. On the equivalence between spatial and material volume averaging of stress in large strain multi-scale solid constitutive models. *Mechanics of Materials*, 40:803–811, 2008.

W.J. Drugan and J.R. Willis. A micromechanics-based nonlocal constitutive equation and estimates of representative volume element size for elastic composites. *Journal of the Mechanics and Physics of Solids*, 44:497–524, 1996.

F. Feyel. A multilevel finite element method (FE^2) to describe the response of highly non-linear structures using generalized continua. *Computer Methods in Applied Mechanics and Engineering*, 192:3233–3244, 2003.

F. Feyel and J.-L. Chaboche. FE^2 multiscale approach for modelling the elastoviscoplastic behavior of long fibre SiC/Ti composite materials. *Computer Methods in Applied Mechanics and Engineering*, 183:309–330, 2000.

J. Fish and A. Wagiman. Multiscale finite element method for a locally nonperiodic heterogeneous medium. *Computational Mechanics*, 12:164–180, 1993.

E. I. Saavedra Flores and E. A. de Souza Neto. Remarks on symmetry conditions in computational homogenisation problems. *International Journal for Computer-Aided Engineering and Software*, 27:551–575, 2010.

S. Forest. Homogenization methods and the mechanics of generalized continua, part 2. *Theoretical and Applied Mechanics*, 28–29:113–143, 2002.

S. Forest and D. K. Trinh. Generalized continua and non-homogeneous boundary conditions in homogenisation methods. *Zeitschrift für angewandte Mathematik und Mechanik*, 91:90–109, 2011.

M.G.D. Geers, V. Kouznetsova, and W.A.M. Brekelmans. Gradient-enhanced computational homogenization for the micro-macro scale transition. *Journal de Physique IV*, 11:145–152, 2001.

M.G.D. Geers, V. Kouznetsova, and W.A.M. Brekelmans. Multi-scale first-order and second-order computational homogenization of microstructures towards continua. *International Journal for Multiscale Computational Engineering*, 1:371–386, 2003.

M.G.D. Geers, E.W.C. Coenen, and V. Kouznetsova. Multi-scale computational homogenization of structured thin sheets. *Modelling and Simulation in Material Science and Engineering*, 15:393–404, 2007.

G. Geymonat, S. Müller, and N. Triantafyllidis. Homogenization of nonlinearly elastic materials, microscopic bifurcation and macroscopic loss of rank-one convexity. *Archive for Rational Mechanics and Analysis*, 122: 231–290, 1993.

S. Ghosh, K. Lee, and S. Moorthy. Multiple scale analysis of heterogeneous elastic structures using homogenization theory and voronoi cell finite element method. *International Journal of Solids and Structures*, 32:27–62, 1995.

F. Gruttmann and W. Wagner. A coupled two-scale shell model with applications to layered structures. *International Journal for Numerical Methods in Engineering*, 2013. accepted for publication.

J.M. Guedes and N. Kikuchi. Preprocessing and postprocessing for materials based on the homogenization method with adaptive finite element methods. *Computer Methods in Applied Mechanics and Engineering*, 83: 143–198, 1990.

Z. Hashin. Analysis of composite materials - a survey. *Journal of Applied Mechanics*, 50:481–505, 1983.

M. Hautefeuille, J.-B. Colliat, A. Ibrahimbegović, H.G. Matthies, and P. Villon. A multi-scale approach to model localized failure with softening. *Computers and Structures*, 94-95:83–95, 2012.

R. Hill. Elastic properties of reinforced solids: some theoretical principles. *Journal of the Mechanics and Physics of Solids*, 11:357–372, 1963.

R. Hill. Theory of mechanical properties of fibre-strengthened materials 1. elastic behaviour. *Journal of the Mechanics and Physics of Solids*, 12: 199–212, 1964a.

R. Hill. Theory of mechanical properties of fibre-strengthened materials 2. inelastic behaviour. *Journal of the Mechanics and Physics of Solids*, 12: 213–218, 1964b.

R. Hill. A self–consistent mechanics of composite materials. *Journal of the Mechanics and Physics of Solids*, 13:213–222, 1965a.

R. Hill. Theory of mechanical properties of fibre-strengthened materials 3. self-consistent model. *Journal of the Mechanics and Physics of Solids*, 13:189–198, 1965b.

R. Hill. On macroscopic measures of plastic work and deformation in microheterogeneous media. *Journal of Applied Mathematics and Mechanics*, 35:31–39, 1971.

R. Hill. On constitutive macro-variables for heterogeneous solids at finite strain. *Proceedings of the Royal Society London A*, 326:131–147, 1972.

R. Hill. On macroscopic effects of heterogeneity in elastoplastic media at finite strain. *Mathematical Proceedings of the Cambridge Philosophical Society*, 95:481–494, 1984.

A. Ibrahimbegović and D. Markovič. Strong coupling methods in multiphase and multi-scale modeling of inelastic behavior of heterogeneous structures. *Computer Methods in Applied Mechanics and Engineering*, 192:3089–3107, 2003.

R. Jänicke, S. Diebels, H. G. Sehlhorst, and A. Düster. Two-scale modeling of micromorphic continua. *Continuum Mechanics and Thermodynamics*, 21:297–315, 2009.

D. Jeulin and M. Ostoja-Starzewski, editors. *Mechanics of random and multiscale microstructures*. Springer, 2001.

T. Kanit, S. Forest, I. Galliet, V. Mounoury, and D. Jeulin. Determination of the size of the representative volume element for random composites: statistical and numerical approach. *International Journal of Solids and Structures*, 40:3647–3679, 2003.

S.O. Klinkel. *Theorie und Numerik eines Volumen-Schalen-Elementes bei finiten elastischen und plastischen Verzerrungen.* PhD thesis, Universität Fridericiana zu Karlsruhe, 2000.

V. Kouznetsova, W.A.M. Brekelmans, and Baaijens F.P.T. An approach to micro-macro modeling of heterogeneous materials. *Computational Mechanics*, 27:37–48, 2001.

V. Kouznetsova, M.G.D. Geers, and W.A.M. Brekelmans. Multi-scale second-order computational homogenization of multi-phase materials: a nested finite element solution strategy. *Computer Methods in Applied Mechanics and Engineering*, 193(48-51):5525–5550, 2004.

E. Kröner. Allgemeine Kontinuumstheorie der Versetzung und Eigenspannung. *Archive of Rational Mechanics and Analysis*, 4:273–334, 1960.

E. Kröner. Statistical continuum mechanics. In *CISM Courses and Lectures*, volume 92. Springer-Verlag, Wien, New-York, 1971.

F. Larsson, K. Runesson, S. Saroukhani, and R. Vafadari. Computational homogenization based on a weak format of micro-periodicity for RVE-problems. *Computer Methods in Applied Mechanics and Engineering*, 200:11–26, 2011.

E.H. Lee. Elasto-plastic deformation at finite strains. *Journal of Applied Mechanics*, 36:1–6, 1969.

J. Mandel. *Plasticité cassique et Viscoplasticité.* Number 97 in CISM lecture notes. Springer, 1972.

J. Mandel and P. Dantu. Contribution à l'étude théorique et expérimentale du coefficient d'élasticité d'un milieu hétérogène mais statistiquement homogène. *Anales des Ponts et Chaussées Paris*, 133(2):115–146, 1963.

D. Markovic, R. Niekamp, A. Ibrahimbegovic, H.G. Matthies, and R.L. Taylor. Multi-scale modeling of heterogeneous structures with inelastic constitutive behaviour: Part I - physical and mathematical aspects. *Engineering Computations*, 22(5-6):664–683, 2005.

J.E. Marsden and J.R. Hughes. *Mathematical Foundations of Elasticity.* Prentice-Hall, 1983.

J.C. Michel, H. Moulinec, and P. Suquet. Effective properties of composite materials with periodic microstructure: a computational approach. *Computer Methods in Applied Mechanics and Engineering*, 172:109–143, 1999.

C. Miehe. *Kanonische Modelle multiplikativer Elasto-Plastizität. Thermodynamische Formulierung und Numerische Implementation.* 1993. Habilitationsschrift.

C. Miehe. Computational micro-to-macro transitions for discretized microstructures of heterogeneous materials at finite strains based on the minimization of averaged incremental energy. *Computer Methods in Applied Mechanics and Engineering*, 192:559–591, 2003.

C. Miehe and C.G. Bayreuther. On mutiscale FE analyses of heterogeneous structures: from homogenization to multigrid solvers. *International Journal for Numerical Methods in Engineering*, 71:1135–1180, 2007.

C. Miehe and A. Koch. Computational micro-to-macro transitions of discretized microstructures undergoing small strains. *Archive of Applied Mechanics*, 72(4):300–317, 2002.

C. Miehe and E. Stein. A canonical model of multiplicative elasto-plasticity formulation and aspects of the numerical implementation. *European Journal of Mechanics, A/Solids*, 11:25–43, 1992.

C. Miehe, J. Schotte, and J. Schröder. Computational micro-macro transitions and overall moduli in the analysis of polycrystals at large strains. *Computational Materials Science*, 16(1-4):372–382, 1999a.

C. Miehe, J. Schröder, and J. Schotte. Computational homogenization analysis in finite plasticity. Simulation of texture development in polycrystalline materials. *Computer Methods in Applied Mechanics and Engineering*, 171(3-4):387–418, 1999b.

C. Miehe, J. Schröder, and M. Becker. Computational homogenization analysis in finite elasticity: Material and structural instabilities on the micro- and macro-scales of periodic composites and their interaction. *Computer Methods in Applied Mechanics and Engineering*, 191:4971–5005, 2002.

C.B. Morrey. Quasi-convexity and the lower semicontinuity of multiple integrals. *Pacific Journal of Mathematics*, 2:25–53, 1952.

C.B. Morrey. *Multiple integrals in the calculus of variations.* Springer, 1966.

S. Müller. Homogenization of nonconvex integral functionals and cellular elastic materials. *Archive for Rational Mechanics and Analysis*, 99:189–212, 1987.

S. Müller and S. Neukamm. On the commutability of homogenization and linearization in finite elasticity. *Archive for Rational Mechanics and Analysis*, 201:465–500, 2011.

S. Nemat-Nasser. Averaging theorems in finite deformation plasticity. *Mechanics of Materials*, 31:493–523, 1999.

S. Nemat-Nasser and M. Hori. *Micromechanics: Overall Properties of Heterogeneous Materials.* North Holland, 2 edition, 1999.

R. Niekamp, D. Markovic, A. Ibrahimbegovic, H.G. Matthies, and R.L. Taylor. Multi-scale modelling of heterogeneous structures with inelastic constitutive behavior: Part II - software coupling implementation aspects. *Engineering Computations*, 26(1/2):6–28, 2009.

R.W. Ogden. *Non-linear elastic deformations.* Dover Publications, 1984.

N. Ohno, T. Matsuda, and X. Wu. A homogenization theory for elastic-viscoplastic composites with point symmetry of internal distributions. *International Journal of Solids and Structures*, 38:2867–2878, 2001.

N. Ohno, D. Okumura, and H. Noguchi. Microscopic symmetric bifurcation condition of cellular solids based on a homogenization theory of finite deformation. *Journal of the Mechanics and Physics of Solids*, 50:1125–1153, 2002.

J. Ohser and F. Mücklich. *Statistical analysis of microstructures in materials science*. J Wiley & Sons, 2000.

J. Okada, T. Washio, and T. Hisada. Study of efficient homogenization algorithms for nonlinear problems – approximation of a homogenized tangent stiffness to reduce computational cost. *Computational Mechanics*, 46:247–258, 2010.

M. Ostoja-Starzewski. Material spatial randomness: From statistical to representative volume element. *Probabilistic Engineering Mechanics*, 21: 112–132, 2006.

M. Ostoja-Starzewski. The use, misuse, and abuse of stochastic random media. In *Proceedings of European Conference on Computational Mechanics*, 2001.

M. Ostoja-Starzweski. *Microstructural randomness and scaling in mechanics of materials*. CRC Series: Modern mechanics and mathematics. Chapman & Hall, 2008.

I. Özdemir, W.A.M. Brekelmans, and M.G.D. Geers. Computational homogenization for heat conduction in heterogeneous solids. *International Journal for Numerical Methods in Engineering*, 73:185–204, 2008.

D. Perić, D.R.J. Owen, and M.E. Honnor. A model for finite strain elasto-plasticity based on logarithmic strains: Computational issues. *Computer Methods in Applied Mechanics and Engineering*, 94:35–61, 1992.

D. Perić, E.A. de Souza Neto, R.A. Feijóo, M. Partovi, and A.J. Carneiro Molina. On micro-to-macro transitions for multi-scale analysis of non-linear heterogeneous materials: unified variational basis and finite element implementation. *International Journal for Numerical Methods in Engineering*, 87:149–170, 2011.

A. Pflüger. *Stabilitätsprobleme in der Elastostatik*. Springer-Verlag, 1975.

G.L. Povirk. Incorporation of microstructural information into models of two-phase materials. 43/8:3199–3206, 1995.

A. Reuss. Berechnung der Fließgrenze von Mischkristallen auf Grund der Plastizitätsbedingung für Einkristalle. *Zeitschrift für angewandte Mathematik und Mechanik*, 9(1):49–58, 1929.

I. Saiki, K. Terada, K. Ikeda, and M. Hori. Appropriate number of unit cells in a representative volume element for micro-structural bifurcation encountered in a multi-scale modeling. *Computer Methods in Applied Mechanics and Engineering*, 191:2561–2585, 2002.

E. Sanchez-Palencia and A. Zaoui. *Lecture notes in physics: Homogenization techniques for composite media*. Springer–Verlag, Berlin, 1986.

J. Schröder. *Homogenisierungsmethoden der nichtlinearen Kontinuumsmechanik unter Beachtung von Stabilitätsproblemen*. Bericht aus der Forschungsreihe des Instituts für Mechanik (Bauwesen), Lehrstuhl I, Universität Stuttgart, 2000. Habilitation.

J. Schröder. Derivation of the localization and homogenization conditions for electro-mechanically coupled problems. *Computational Materials Science*, 46(3):595–599, 2009.

J. Schröder. Anisotropic polyconvex energies. In J. Schröder and P. Neff, editors, *Poly-, Quasi- and Rank-One Convexity in Applied Mechanics*, number 516 in CISM Courses and Lectures, pages 53–105. Springer-Verlag, 2010.

J. Schröder and M.-A. Keip. Multiscale modeling of electro-mechanically coupled materials: homogenization procedure and computation of overall moduli. In M. Kuna and A. Ricoeur, editors, *IUTAM Symposium on Multiscale Modelling of Fatigue, Damage and Fracture in Smart Materials*, volume 24 of *IUTAM Bookseries*, pages 265–276. Springer, Netherlands, 2011. ISBN 978-90-481-9887-0.

J. Schröder and M.-A. Keip. Two-scale homogenization of electromechanically coupled boundary value problems – consistent linearization and applications. *Computational Mechanics*, 50(2):229–244, 2012.

J. Schröder, D. Balzani, and D. Brands. Approximation of random microstructures by periodic statistically similar representative volume elements based on lineal-path functions. *Archive of Applied Mechanics*, 81 (7):975–997, 2010.

J.C. Simo. A framework for finite strain elastoplasticity based on maximum plastic dissipation and the multiplicative decomposition: Part I. continuum formulation. *Computer Methods in Applied Mechanics and Engineering*, 66:199–219, 1988.

J.C. Simo. Algorithms for static and dynamic multiplicative plasticity that preserve the classical return mapping schemes of the infinitesimal theory. *Computer Methods in Applied Mechanics and Engineering*, 99:61–112, 1992.

J.C. Simo and C. Miehe. Associative coupled thermoplasticity at finite strains: formulation, numerical analysis and implementation. *Computer Methods in Applied Mechanics and Engineering*, 96:133–171, 1992.

R.J.M. Smit, W.A.M. Brekelmans, and H.E.H. Meijer. Prediction of the mechanical behavior of nonlinear heterogeneous systems by multi-level finite element modeling. *Computer Methods in Applied Mechanics and Engineering*, 155:181–192, 1998.

M. Stroeven and L.J. Askes, H. Sluys. Numerical determination of representative volumes for granular materials. *Computer Methods in Applied Mechanics and Engineering*, 193:3221–3238, 2004.

M. Stroeven, H. Askes, and L.J. Sluys. A numerical approach to determine representative volumes for granular materials. In *Fifth World Congress on Computational Mechanics (WCCM V)*. Vienna University of Technology, 2002.

P.M. Suquet. Elements of homogenization for inelastic solid mechanics. In *Homogenization techniques for composite materials*, Lecture notes in physics 272, chapter 4, pages 193–278. Springer–Verlag, 1987.

S. Swaminathan, S. Ghosh, and N.J. Pagano. Statistically equivalent representative volume elements for unidirectional composite microstructures: part i - without damage. *Journal of Composite Materials*, 40:583–604, 2006.

L. Tartar. *The general theory of homogenization*. Lecture notes of the unione mathematica italiana. Springer–Verlag, 2000.

I. Temizer. On the asymptotic expansion treatment of two-scale finite thermoelasticity. *International Journal of Engineering Science*, 53:74–84, 2012.

I. Temizer and P. Wriggers. On the computation of the macroscopic tangent for multiscale volumetric homogenization problems. *Computer Methods in Applied Mechanics and Engineering*, 198:495–510, 2008.

I. Temizer and T.I. Zohdi. A numerical method for homogenization in nonlinear elasticity. *Computational Mechanics*, 40:281–298, 2007.

K. Terada and N. Kikuchi. A class of general algorithms for multi-scale analyses of heterogeneous media. *Computer Methods in Applied Mechanics and Engineering*, 190(40-41):5427–5464, 2001.

K. Terada, M. Hori, T. Kyoya, and N. Kikuchi. Simulation of the multi-scale convergence in computational homogenization approach. *International Journal of Solids and Structures*, 37:2285–2311, 2000.

K. Terada, I. Saiki, K. Matsui, and Y. Yamakawa. Two-scale kinematics and linearization for simultaneous two-scale analysis of periodic heterogeneous solids at finite strain. *Computer Methods in Applied Mechanics and Engineering*, 192(31-32):3531–3563, 2003.

J.M.T. Thompson and G.W. Hunt. *Elastic Instability Phenomena*. John Wiley & Sons Ltd., 1984.

N. Triantafyllidis and B.N. Maker. On the comparison between microscopic and macroscopic instability mechanisms in a class of fiber-reinforced composites. *Journal of Applied Mechanics*, 52:794–800, 1985.

C. Truesdell and W. Noll. The nonlinear field theories of mechanics. In S. Flügge, editor, *Encyclopedia of Physics*, volume III/3. Springer, 1965.

O. van der Sluis, P.J.G. Schreurs, W.A.M. Brekelmans, and H.E.H. Meijer. Overall behavior of heterogeneous elastoviscoplastic materials: effect of microstructural modelling. *Mechanics of Materials*, 32:449–462, 2000.

W. Voigt. *Lehrbuch der Kristallphysik*. Teubner, 1910.

G. Weber and L. Anand. Finite deformation constitutive equations and a time integration procedure for isotropic, hyperelastic-viscoelastic solids. *Computer Methods in Applied Mechanics and Engineering*, 79:173–202, 1990.

Z. Xia, Y. Zhang, and F. Ellyin. A unified periodical boundary conditions for representative volume elements of composites and applications. *International Journal of Solids and Structures*, 40:1907–1921, 2003.

J. Zeman. *Analysis of Composite Materials with Random Microstructure*. PhD thesis, University of Prague, 2003.

T.I. Zohdi and P. Wriggers. *Introduction to Computational Micromechanics*, volume 20 of *Lecture Notes in Applied and Computational Mechanics*. Springer, 2005.

Variational modeling of microstructures in plasticity

Klaus Hackl [1†], Ulrich Hoppe [1], and Dennis M. Kochmann [2]

[1] Ruhr-Universität Bochum, Institut für Computational Engineering, Lehrstuhl für Mechanik – Materialtheorie, D-44780 Bochum, Germany

[2] California Institute of Technology, Graduate Aerospace Laboratories, 1200 E. California Blvd., MC 205-45, Pasadena, CA 91125, U.S.A.

[†] Corresponding author: klaus.hackl@rub.de

Abstract The analysis and simulation of microstructures in solids has gained crucial importance, virtue of the influence of all microstructural characteristics on a material's macroscopic, mechanical behavior. In particular, the arrangement of dislocations and other lattice defects to particular structures and patterns on the microscale as well as the resultant inhomogeneous distribution of localized strain results in a highly altered stress-strain response. Energetic models predicting the mechanical properties are commonly based on thermodynamic variational principles. Modeling the material response in finite-strain crystal plasticity very often results in a nonconvex variational problem so that the minimizing deformation fields are no longer continuous but exhibit small-scale fluctuations related to probability distributions of deformation gradients to be calculated via energy relaxation. This results in fine structures which can be interpreted as the observed microstructures.

This manuscript is supposed to give an overview of the available methods and results in this field. We start by discussing the underlying variational principles for inelastic materials, derive evolution equations for internal variables, and introduce the concept of condensed energy. As a mathematical prerequisite we review the variational calculus of nonconvex potentials and the notion of relaxation. We use these instruments in order to study the initiation of plastic microstructures. Here we focus on a model of single-slip crystal plasticity. Afterward we move on to model the evolution of microstructures. We introduce the concept of essential microstructures and the corresponding relaxed energies and dissipation potentials, and derive evolution equations for microstructure parameters.

J. Schröder, K. Hackl (Eds.), *Plasticity and Beyond*, CISM International Centre for Mechanical Sciences, DOI 10.1007/978-3-7091-1625-8_2, © CISM, Udine 2014

We then present a numerical scheme by means of which the microstructure development can be computed, and show numerical results for particular examples in single- and double-slip plasticity. We discuss the influence of hardening and of slip system orientations in the present model.

1 Variational framework for inelastic materials

1.1 Constitutive setting and variational principles

The macroscopic mechanical behavior of a material deforming inelastically under the action of external forces reflects the aggregate of all physical mechanisms occurring on smaller scales. The state of the microstructure is commonly described in terms of so-called internal or history variables. Thus, we describe the state of a general inelastic material in an isothermal setting by its deformation gradient $\mathbf{F} = \boldsymbol{\nabla}\phi$, where $\phi(\mathbf{X})$ represents the deformation field, and a collection of internal variables $\mathbf{z}(\mathbf{X})$, which might be scalars, vectors, tensors, or combinations of those, capturing all microstructural characteristics. We propose that inelastic deformation is predominantly dictated by the concepts of energy and dissipation. In the sequel we denote the specific Helmholtz free energy density by $\Psi(\boldsymbol{\nabla}\phi, \mathbf{z})$ so that the total energy of the deformed body reads

$$\mathcal{I}(t, \phi, \mathbf{z}) = \int_\Omega \Psi(\boldsymbol{\nabla}\phi, \mathbf{z})\, \mathrm{d}V - \ell(t, \phi) \tag{1}$$

where $\ell(t, \phi)$ represents the potential of external forces and Ω is the domain in space occupied by the material body. Let us introduce thermodynamically conjugate stresses by defining

$$\mathbf{P} = \frac{\partial \Psi}{\partial \mathbf{F}}, \qquad \mathbf{q} = -\frac{\partial \Psi}{\partial \mathbf{z}}. \tag{2}$$

Here, of course, $\mathbf{P}$ is the first Piola-Kirchhoff stress tensor. The evolution of the internal variables $\mathbf{z}$ is now governed either by a so-called inelastic potential $J(\mathbf{z}, \mathbf{q})$ or its Legendre transform, the dissipation functional, Carstensen et al. (2002),

$$\Delta(\mathbf{z}, \dot{\mathbf{z}}) = \sup \big\{\, \dot{\mathbf{z}} : \mathbf{q} - J(\mathbf{z}, \mathbf{q}) \;\big|\; \mathbf{q} \,\big\}. \tag{3}$$

Here, the nature of the inner product $\dot{\mathbf{z}} : \mathbf{q}$ depends of course on the type of internal variables involved and essentially corresponds to a contraction over all components. Evolution equations for the internal variables are then given in the two equivalent forms, Carstensen et al. (2002),

$$\dot{\mathbf{z}} \in \frac{\partial J}{\partial \mathbf{q}}, \qquad \mathbf{q} \in \frac{\partial \Delta}{\partial \dot{\mathbf{z}}}. \tag{4}$$

With the above framework we can employ the variational principles of thermodynamics to describe the time-continuous change of microstructures in a deformed solid. According to the principle of minimum potential energy, Truesdell and Noll (1965), the actual displacement field follows from

$$\phi = \operatorname{argmin} \left\{ \mathcal{I}(t, \phi, \mathbf{z}) \,\middle|\, \phi = \phi_0 \text{ on } \Gamma_{\mathbf{u}} \right\} \tag{5}$$

where $\Gamma_{\mathbf{u}}$ denotes a subset of the body's boundary $\partial\Omega$. The internal (plastic) variables can be obtained from the principle of maximum dissipation, Simo (1988a,b),

$$\dot{\mathbf{z}} = \operatorname{argmax} \left\{ \mathcal{D}(\mathbf{q}, \dot{\mathbf{z}}) \,\middle|\, \mathbf{q} \;:\; \mathcal{D} = \mathbf{q} \cdot \dot{\mathbf{z}} \right\}. \tag{6}$$

Alternatively the internal variables can be computed, following (4), from the principle of minimum dissipation potential, Carstensen et al. (2002),

$$\dot{\mathbf{z}} = \operatorname{argmin} \left\{ \mathcal{L}(\mathbf{z}, \dot{\mathbf{z}}) \,\middle|\, \dot{\mathbf{z}} \right\}, \tag{7}$$

where we introduced the Lagrange functional

$$\mathcal{L}(\mathbf{z}, \dot{\mathbf{z}}) = \frac{\mathrm{d}}{\mathrm{d}t} \Psi(\boldsymbol{\nabla}\phi, \mathbf{z}) + \Delta(\mathbf{z}, \dot{\mathbf{z}}), \tag{8}$$

and the dot denotes differentiation with respect to time. This Lagrange functional consists of the sum of elastic power and dissipation due to changes of the internal state of the material, Hackl (1997); Carstensen et al. (2002); Ortiz and Repetto (1999). Minimization of the Lagrange functional hence determines the changes of the internal variables. Hackl and Fischer (2008) investigated the interrelation between the principles (6) and (7) and proved that they coincide as long as the dissipation potential is homogeneous, see also Hackl et al. (2011a), for a generalization to the non-isothermal case. For problems in rate-independent plasticity as those considered in the sequel, the dissipation potential is homogeneous of degree 1 so that the (more convenient) principle of minimum dissipation potential (7) will be applied.

Example 1.1. Linear visco-elasticity

We assume a small-strain setting, hence an additive decomposition of the strain-tensor in an elastic and an inelastic part, $\varepsilon = \varepsilon_{\mathbf{e}} + \varepsilon_{\mathbf{i}}$, and a quadratic free energy, $\Psi = \frac{1}{2}\, \varepsilon_{\mathbf{e}} : \mathbf{C} : \varepsilon_{\mathbf{e}}$. The thermodynamically conjugate stresses are now

$$\sigma = \frac{\partial \Psi}{\partial \varepsilon} = \mathbf{C} : (\varepsilon - \varepsilon_{\mathbf{i}}), \qquad \mathbf{q} = -\frac{\partial \Psi}{\partial \varepsilon_{\mathbf{i}}} = \sigma. \tag{9}$$

Clearly we have the correspondences $\mathbf{z} = \varepsilon_{\mathbf{i}}$ and $\mathbf{q} = \sigma$ which will also apply to subsequent examples involving an additive decomposition. Let us assume a quadratic inelastic potential of the form $J = \frac{1}{2}\, \mathbf{q} : \mathbf{A} : \mathbf{q}$, where

A is assumed to be positive definite, leading to a viscoelastic evolution equation of the form

$$\dot{\mathbf{z}} = \frac{\partial J}{\partial \mathbf{q}} = \mathbf{A} : \mathbf{q}. \tag{10}$$

By a straight-forward calculation on obtains the dissipation potential

$$\Delta = \sup \left\{ \dot{\mathbf{z}} : \mathbf{q} - \frac{1}{2}\mathbf{q} : \mathbf{A} : \mathbf{q} \,\middle|\, \mathbf{q} \right\} = \frac{1}{2}\dot{\mathbf{z}} : \mathbf{A}^{-1} : \dot{\mathbf{z}}, \tag{11}$$

giving the inverse evolution equation

$$\mathbf{q} = \frac{\partial \Delta}{\partial \dot{\mathbf{z}}} = \mathbf{A}^{-1} : \mathbf{q}. \tag{12}$$

Example 1.2. Ideal plasticity

Let us now consider a dissipation potential which is homogeneous of order one as $\Delta = (\dot{\mathbf{z}} : \mathbf{B} : \dot{\mathbf{z}})^{1/2}$, where $\mathbf{B}$ is assumed to be positive definite. Now clearly Δ is not differentiable at the origin, hence (4) becomes a true differential inclusion. For this purpose let us introduce the *subdifferential* of a convex functional f at a point $\mathbf{x}_0$. This is defined as the set of all hyperplanes containing $\mathbf{x}_0$ situated below f. To be strict

$$\partial f(\mathbf{x}_0) = \left\{ \mathbf{y} \,\middle|\, \mathbf{y} : (\mathbf{x} - \mathbf{x}_0) \leq f(\mathbf{x} - \mathbf{x}_0) \quad \forall \mathbf{x} \right\}. \tag{13}$$

In our case we have

$$\partial \Delta(\mathbf{0}) = \left\{ \mathbf{y} \,\middle|\, \mathbf{y} : \dot{\mathbf{z}} \leq (\dot{\mathbf{z}} : \mathbf{B} : \dot{\mathbf{z}})^{1/2} \quad \forall \dot{\mathbf{z}} \right\}. \tag{14}$$

The substitution $\mathbf{x} = \mathbf{B}^{1/2} : \dot{\mathbf{z}}$ gives

$$\partial \Delta(\mathbf{0}) = \left\{ \mathbf{y} \,\middle|\, \mathbf{y} : \mathbf{B}^{-1/2} : \mathbf{x} \leq \|\mathbf{x}\| \quad \forall \mathbf{x} \right\} = \left\{ \mathbf{y} \,\middle|\, \|\mathbf{B}^{-1/2} : \mathbf{y}\| \leq 1 \right\}. \tag{15}$$

In summary, and by squaring the inequality in (15) we obtain the following differential inclusion determining the evolution of $\mathbf{z}$:

$$\mathbf{q} \in \partial \Delta(\dot{\mathbf{z}}) = \begin{cases} \left\{ \dfrac{\mathbf{B} : \dot{\mathbf{z}}}{(\dot{\mathbf{z}} : \mathbf{B} : \dot{\mathbf{z}})^{1/2}} \right\} & \text{for} \quad \dot{\mathbf{z}} \neq \mathbf{0} \\ \left\{ \mathbf{y} \,\middle|\, \mathbf{y} : \mathbf{B}^{-1} : \mathbf{y} \leq 1 \right\} & \text{for} \quad \dot{\mathbf{z}} = \mathbf{0} \end{cases}. \tag{16}$$

The inclusion (16) can now be interpreted as ideally plastic behavior. The second case defines a yield-condition of the form $\mathbf{q} : \mathbf{B}^{-1} : \mathbf{q} \leq 1$. The first case gives the flow-law

$$\dot{\mathbf{z}} = \lambda \mathbf{B}^{-1}\mathbf{q}, \qquad \lambda > 0. \tag{17}$$

Note that the consistency parameter λ cannot be determined directly from (16). However, assuming that $\dot{\mathbf{z}} \neq \mathbf{0}$ for t in an entire interval, we obtain from the first case in (16) that $\mathbf{q} : \mathbf{B}^{-1} : \mathbf{q} = 1$ on the same interval. Differentiation with respect to time then gives

$$\dot{\mathbf{q}} : \mathbf{B}^{-1} : \mathbf{q} = 0. \tag{18}$$

Substitution of (2) and (17) finally allows to determine λ.

Let us now have a look at the dual formulation. We derive the inelastic potential as Legendre transform of the dissipation potential

$$J(\mathbf{q}) = \sup \left\{ \dot{\mathbf{z}} : \mathbf{q} - \Delta(\dot{\mathbf{z}}) \,\middle|\, \dot{\mathbf{z}} \right\}. \tag{19}$$

Once again the substitution $\mathbf{x} = \mathbf{B}^{1/2} : \dot{\mathbf{z}}$ gives

$$J(\mathbf{q}) = \sup \left\{ \mathbf{x} : \mathbf{B}^{-1/2} : \mathbf{q} - \|\mathbf{x}\| \,\middle|\, \mathbf{x} \right\} = \begin{cases} 0 & \text{for} \quad \|\mathbf{B}^{-1/2} : \mathbf{q}\| \leq 1 \\ \\ \infty & \text{for} \quad \|\mathbf{B}^{-1/2} : \mathbf{q}\| > 1 \end{cases}. \tag{20}$$

Squaring the inequalities in (20) we obtain the evolution equations as subdifferential

$$\dot{\mathbf{z}} \in \partial J(\mathbf{q}) = \begin{cases} \{\mathbf{0}\} & \text{for} \quad \mathbf{q} : \mathbf{B}^{-1} : \mathbf{q} \leq 1 \\ \\ \left\{ \lambda \mathbf{B}^{-1} : \mathbf{q} \,\middle|\, \lambda > 0 \right\} & \text{for} \quad \mathbf{q} : \mathbf{B}^{-1} : \mathbf{q} > 1 \end{cases}. \tag{21}$$

Immediately we recognize yield condition and flow law.

Example 1.3. Crystal plasticity

We return to a finite-deformation setting. The split of the deformation gradient into an elastic part $\mathbf{F}_\mathrm{e}$ and an irreversible, plastic part $\mathbf{F}_\mathrm{p}$ yields the standard multiplicative decomposition $\mathbf{F} = \mathbf{F}_\mathrm{e}\mathbf{F}_\mathrm{p}$. In the following, we study a material with free energy density $\Psi_\mathrm{el}(\mathbf{F}_\mathrm{e})$.

Plastic deformation is accommodated by dislocation gliding along specific active slip systems. Each slip system is characterized by its unit vectors $\mathbf{s}$ and $\mathbf{m}$ ($|\mathbf{s}| = |\mathbf{m}| = 1$, $\mathbf{s} \cdot \mathbf{m} = 0$), where $\mathbf{s}$ characterizes the slip direction and $\mathbf{m}$ denotes the unit vector normal to the slip plane. For a total of n active slip systems plastic flow is given in the form

$$\dot{\mathbf{F}}_\mathrm{p}\mathbf{F}_\mathrm{p}^{-1} = \sum_i^n \dot{\gamma}_i \; \mathbf{s}_i \otimes \mathbf{m}_i \tag{22}$$

with plastic slip rates $\dot{\gamma}_i$ and the initial conditions $\gamma_i(0) = 0$. Time-integration then yields the plastic contribution to the deformation gradient

tensor. If we assume that all slip directions lie within the same slip plane, i.e. $\mathbf{m}_i = \mathbf{m}$, we infer from $\mathbf{s}_i \cdot \mathbf{m} = 0$ that

$$\mathbf{F}_{\mathrm{p}}^{-1} = \boldsymbol{I} - \sum_{i}^{n} \gamma_i \, \mathbf{s}_i \otimes \mathbf{m}. \tag{23}$$

Many recent approaches, see e.g. Carstensen et al. (2008); Miehe et al. (2004), were based on only one active slip system (single-slip plasticity). In this case the above condition further reduces to

$$\mathbf{F}_{\mathrm{p}}^{-1} = \boldsymbol{I} - \gamma \, \mathbf{s} \otimes \mathbf{m}. \tag{24}$$

To account for work hardening, we introduce internal hardening history variables p_i, Carstensen et al. (2002), one such hardening variable for each active slip system. The hardening variables enter what is often termed the plastic (intrinsic) contribution to the energy, Carstensen et al. (2008), $\Psi_p(\mathbf{p})$, so that

$$\Psi(\mathbf{F}_{\mathrm{e}}, \mathbf{p}) = \Psi_{\mathrm{el}}(\mathbf{F}_{\mathrm{e}}) + \Psi_{\mathrm{p}}(\mathbf{p}), \tag{25}$$

where $\mathbf{p} = \{p_1, \ldots, p_n\}$ summarizes the hardening variables. In the sequel we will make use of the formulation

$$\Psi_{\mathrm{p}}(\mathbf{p}) = \sum_{i} \sum_{j} \kappa_{ij} \, |p_i \, p_j|^{\alpha/2}, \tag{26}$$

where $\kappa_{ij} > 0$ are the components of a hardening modulus tensor of the material and α is commonly 2 (linear hardening) or 4. Self-hardening along the given slip systems is characterized by the diagonal components κ_{ii} whereas latent hardening (slip system interactions due to cross-slip etc.) involves the off-diagonal components κ_{ij} $(i \neq j)$. Experiments confirm that the off-diagonal entries should dominate. A common but less physical approximation, Kochmann and Hackl (2010a), assumes that $\kappa_{ii} = \kappa$ and $\kappa_{ij} = 0$ else, so that $\Psi_{\mathrm{p}}(\mathbf{p}) = \kappa \sum_i^n p_i^\alpha$. As the evolution law, we consider the following flow rule, Carstensen et al. (2002), for the internal hardening variables p_i

$$\dot{p}_i = |\dot{\gamma}_i| \tag{27}$$

with the initial condition $p_i(0) = 0$ (virgin initial state). Note that often infinite latent hardening is assumed, which means that, as soon as one slip system becomes active, the remaining slip systems are blocked, so that only single-slip domains form. The above formulation allows for a practical treatment of infinite as well as finite latent hardening.

Dissipation occurs as a result of dislocation motion and is hence linked to changes of the plastic slips γ_i. For the dissipation functional with only

one active slip system we simply assume, Carstensen et al. (2002); Hackl and Kochmann (2008),

$$\Delta(\dot\gamma) = r\,|\dot\gamma|, \tag{28}$$

with a positive constant r, the critical resolved shear stress. If several slip systems are active, the definition of the dissipation potential becomes more involved. A common definition (for von Mises plasticity) follows with $\gamma = \{\gamma_1, \dots, \gamma_n\}$ from

$$\Delta(\dot\gamma) = r\,\|\dot{\mathbf{F}}_\mathrm{p}\mathbf{F}_\mathrm{p}^{-1}\|, \tag{29}$$

where we imply the Euclidean norm $\|\mathbf{F}\|^2 = \mathrm{tr}\,(\mathbf{F}^T\mathbf{F})$. For n active slip systems within the same glide plane we infer

$$\Delta(\dot\gamma) = r\,\sqrt{\sum_i^n \sum_j^n \dot\gamma_i\,\dot\gamma_j\,\mathbf{s}_i\cdot\mathbf{s}_j}. \tag{30}$$

In subsequent sections we will apply this formulation to only two active slip systems where we conclude

$$\Delta(\dot\gamma_1, \dot\gamma_2) = r\,\sqrt{\dot\gamma_1^2 + \dot\gamma_2^2 + 2\dot\gamma_1\dot\gamma_2\,\mathbf{s}_1\cdot\mathbf{s}_2}. \tag{31}$$

For two or more active slip systems it is hard to integrate (30) in general. For two slip systems which are aligned symmetrically with respect to the applied deformation one may conclude that with $\gamma_1 = \gamma_2 = \gamma$ it follows that $\Delta(\dot\gamma) = r\,|\gamma|\sqrt{2(1+\cos\psi)}$, where ψ denotes the angle enclosed by the two slip directions $\mathbf{s}_1$ and $\mathbf{s}_2$. (E.g., for identical slip systems with $\mathbf{s}_1 = \mathbf{s}_2$ it follows that $\Delta(\dot\gamma) = 2\,r\,|\dot\gamma|$.) A practical alternative to (30), which corresponds to a flow rule of the Tresca-type, to be integrated directly is:

$$\Delta(\dot\gamma) = r\,\sum_i^n |\dot\gamma_i|. \tag{32}$$

The internal variables of our model are now comprised as $\mathbf{z} = (\gamma_1, \dots, \gamma_n, p_1, \dots, p_n)$. Let us denote the conjugate stresses as $\mathbf{q} = (\tau_1, \dots, \tau_n, q_1, \dots, q_n)$. We immediately obtain

$$q_i = -\frac{\partial\Psi_\mathrm{p}}{p_i} = -\frac{\alpha}{2}\,\sum_j \kappa_{ij}\,|p_i\,p_j|^{\alpha/2}p_i^{-1}. \tag{33}$$

The calculation of the τ_i is more complicated, because, in general, the dependence of $\mathbf{F}_\mathrm{p}$ on the γ_i is only implicitly known. However, it holds

$$\frac{\partial\Psi_\mathrm{el}}{\partial\mathbf{F}_\mathrm{p}} : \dot{\mathbf{F}}_\mathrm{p} = \sum_i \frac{\partial\Psi_\mathrm{el}}{\partial\gamma_i}\,\dot\gamma_i = -\sum_i \tau_i\dot\gamma_i. \tag{34}$$

A straight-forward matrix-calculation gives

$$\frac{\partial \Psi_{\mathrm{el}}}{\partial \mathbf{F}_{\mathrm{p}}} = -\mathbf{F}_{\mathrm{p}}^{-\mathsf{T}} \mathbf{F}^{\mathsf{T}} \frac{\partial \Psi_{\mathrm{el}}}{\partial \mathbf{F}_{\mathrm{e}}} \mathbf{F}_{\mathrm{p}}^{-\mathsf{T}} = -\mathbf{F}_{\mathrm{e}}^{\mathsf{T}} \mathbf{P}. \tag{35}$$

Using (35) and (22) in (34) gives

$$\tau_i = \mathbf{s}_i \cdot \mathbf{F}_{\mathrm{e}}^{\mathsf{T}} \mathbf{P} \mathbf{F}_{\mathrm{p}}^{\mathsf{T}} \mathbf{m}_i \tag{36}$$

constituting the well-known Schmid stress or resolved shear stress of the slip system.

Let us derive the corresponding evolution-equations now. The functional (8) can be specified as

$$\mathcal{L}(\mathbf{z}, \dot{\mathbf{z}}) = \frac{\mathrm{d}}{\mathrm{d}t} \Psi(\boldsymbol{\nabla}\phi, \mathbf{z}) + \Delta(\mathbf{z}, \dot{\mathbf{z}}) = \frac{\partial \Psi}{\partial \mathbf{F}} : \dot{\mathbf{F}} - \sum_i \tau_i \dot{\gamma}_i - \sum_i q_i \dot{p}_i + \Delta(\mathbf{z}, \dot{\mathbf{z}}). \tag{37}$$

Furthermore let us for simplicity specify the dissipation functional (32). Substituting the constraints (27) we obtain

$$\mathcal{L}(\gamma_i, p_i, \dot{\gamma}_i) = \frac{\partial \Psi}{\partial \mathbf{F}} : \dot{\mathbf{F}} - \sum_i \tau_i \dot{\gamma}_i - \sum_i q_i \, |\dot{\gamma}_i| + r \sum_i^n |\dot{\gamma}_i|. \tag{38}$$

Note that the subdifferential of the modulus-function $|\xi|$ is given by $\partial|\xi| = \operatorname{sign} \xi$, where the set-valued sign-function is defined as

$$\operatorname{sign} \xi = \begin{cases} \{-1\} & \text{for} \quad \xi < 0 \\ [-1, 1] & \text{for} \quad \xi = 0 \\ \{1\} & \text{for} \quad \xi > 0 \end{cases} . \tag{39}$$

The stationarity condition $\mathbf{0} \in \partial\mathcal{L}$ with respect to the slip rates reads as

$$\tau_i \in (r - q_i) \operatorname{sign} \dot{\gamma}_i. \tag{40}$$

Hence the differential inclusion (40) gives both, the Schmid yield-condition

$$|\tau_i| \leq r - q_i, \tag{41}$$

and the flow-rule

$$\dot{\gamma}_i = \lambda_i \tau_i, \qquad \lambda_i > 0. \tag{42}$$

Note that $-q_i$, which is positive via (33), plays the role of a back-stress introducing hardening.

The inelastic potential can be calculated as

$$J(\tau_i, q_i) = \sup \Big\{ \sum_i \dot{\gamma}_i : \tau_i + \sum_i q_i \, |\dot{\gamma}_i| - r \sum_i^n |\dot{\gamma}_i| \;\Big|\; \dot{\gamma}_i \Big\}. \tag{43}$$

A straight-forward investigation gives

$$J(\tau_i, q_i) = \begin{cases} 0 & \text{if} \quad |\tau_i| \leq r - q_i \quad \forall i \\ \\ \infty & \text{else} \end{cases}, \tag{44}$$

defining an admissible stress space bounded by multiple yield surfaces.

1.2 Time-incremental formulation

Approaches to model microstructural patterns must account for the two crucial problems of the initiation of a microstructure and the ensuing evolution of the newly-formed structure. The initiation of microstructure usually follows from a loss of stability. At the material point local instability corresponds to a state where the crystal can reduce its energy by breaking up the homogeneous deformation state into fine structures. For details on the differences between local and global stability for related problems see e.g. Miehe et al. (2004). Here, we resort to the common approach that a microstructure may form as soon as it becomes energetically preferable (i.e. as soon as the material becomes locally unstable).

By considering associated potentials in a time-incremental setting, numerous authors have investigated the initiation of microstructures by using a so-called condensed energy functional, see e.g. Bartels et al. (2004); Carstensen et al. (2008); Conti and Theil (2005); Lambrecht et al. (2003); Mielke (2004); Ortiz and Repetto (1999), which is derived as follows. For rate-independent materials principle (7) allows to account for instantaneous changes of the value of $\mathbf{z}$, as it can be integrated to yield the balance law

$$\Psi(\boldsymbol{\nabla}\phi, \mathbf{z}_1) - \Psi(\boldsymbol{\nabla}\phi, \mathbf{z}_0) = -D(\mathbf{z}_0, \mathbf{z}_1), \tag{45}$$

where

$$D(\mathbf{z}_0, \mathbf{z}_1) = \inf \Big\{ \int_0^1 \Delta(\mathbf{z}(s), \dot{\mathbf{z}}(s)) \, \mathrm{d}s \;\Big|\; \mathbf{z}(0) = \mathbf{z}_0, \mathbf{z}(1) = \mathbf{z}_1 \Big\} \tag{46}$$

is the so-called dissipation distance, Mielke (2002). When applied to a finite time-increment $[t_n, t_{n+1}]$, Eq. (45) allows for an approximate formulation, where ϕ_{n+1} and $\mathbf{z}_{n+1}$ at time t_{n+1} are determined for given loading at time

t_{n+1} and the known value of the internal variables $\mathbf{z}_n$ at time t_n via the following principle, Carstensen et al. (2002); Mielke (2002):

$$\{\phi_{n+1}, \mathbf{z}_{n+1}\} = \operatorname{argmin}\Big\{ \int_\Omega [\Psi(\boldsymbol{\nabla}\phi, \mathbf{z}) + D(\mathbf{z}_n, \mathbf{z})]\, \mathrm{d}V - \ell(t_{n+1}, \phi) \,\Big|\, \phi, \mathbf{z} \Big\}. \tag{47}$$

Carrying out the minimization with respect to $\mathbf{z}$ in (47) beforehand gives the aforementioned condensed energy

$$\Psi^{\mathrm{cond}}_{\mathbf{z}_n}(\mathbf{F}) = \inf\Big\{ \Psi(\mathbf{F}, \mathbf{z}) + D(\mathbf{z}_n, \mathbf{z}) \,\Big|\, \mathbf{z} \Big\} \tag{48}$$

which has been used in the literature to calculate the onset of microstructure. However, many applications based on the condensed energy rely upon the assumption that no microstructures exists at the beginning of the time step (therefore, it is suitable to model the onset of microstructure formation only).

The formulation at hand allows to split the problem of inelastic evolution into a purely elastic step,

$$\phi_{n+1} = \operatorname{argmin}\Big\{ \int_\Omega \Psi^{\mathrm{cond}}_{\mathbf{z}_n}(\boldsymbol{\nabla}\phi)\, \mathrm{d}V - \ell(t_{n+1}, \phi) \,\Big|\, \phi \Big\}, \tag{49}$$

followed by an update of the internal variables

$$\mathbf{z}_{n+1} = \operatorname{argmin}\Big\{ \Psi(\boldsymbol{\nabla}\phi_{n+1}, \mathbf{z}) + D(\mathbf{z}_n, \mathbf{z}) \,\Big|\, \mathbf{z} \Big\}. \tag{50}$$

Example 1.4. Ideal plasticity, continued

For the dissipation potential of Example 1.2 the dissipation-distance is given by

$$D(\mathbf{z}_0, \mathbf{z}_1) = ((\mathbf{z}_1 - \mathbf{z}_0) : \mathbf{B} : (\mathbf{z}_1 - \mathbf{z}_0))^{1/2}, \tag{51}$$

and the condensed energy can be calculated as

$$\Psi^{\mathrm{cond}}_{\mathbf{z}_n}(\varepsilon) = \inf\Big\{ \frac{1}{2}\,(\varepsilon - \mathbf{z}) : \mathbf{C} : (\varepsilon - \mathbf{z}) + ((\mathbf{z} - \mathbf{z}_n) : \mathbf{B} : (\mathbf{z} - \mathbf{z}_n))^{1/2} \Big| \mathbf{z} \Big\}. \tag{52}$$

We apply the substitution $\mathbf{x} = \mathbf{B}^{1/2} : (\mathbf{z} - \mathbf{z}_n)$ and obtain

$$\Psi^{\mathrm{cond}}_{\mathbf{z}_n}(\varepsilon) = \inf\Big\{ \frac{1}{2}\,(\varepsilon - \mathbf{B}^{-1/2} : \mathbf{x} - \mathbf{z}_n) : \mathbf{C} : (\varepsilon - \mathbf{B}^{-1/2} : \mathbf{x} - \mathbf{z}_n) + \|\mathbf{x}\| \,\Big|\, \mathbf{x} \Big\}. \tag{53}$$

The stationarity condition reads

$$\mathbf{0} \in -\mathbf{B}^{-1/2} : \mathbf{C} : (\varepsilon - \mathbf{B}^{-1/2} : \mathbf{x} - \mathbf{z}_n) + \operatorname{sign}\mathbf{x}. \tag{54}$$

Note that the set-valued sign-function in the vectorial or tensorial case is defined as

$$\operatorname{sign} \mathbf{x} = \begin{cases} \{ \mathbf{v} \mid \|\mathbf{v}\| \leq 1 \} & \text{for} \quad \mathbf{x} = \mathbf{0} \\ \{\mathbf{x}/\|\mathbf{x}\|\} & \text{for} \quad \mathbf{x} \neq \mathbf{0} \end{cases} . \tag{55}$$

In order to be able to proceed further let us specialize this example to isotopic, isochoric plasticity. Hence, we assume $\mathbf{z}$ to be trace-free, $\operatorname{tr}\mathbf{z} = 0$. The free energy can then be written in the form

$$\Psi = \frac{K}{2}(\operatorname{tr}\varepsilon)^2 + \mu \| \operatorname{dev} \varepsilon - \mathbf{z}\|^2, \tag{56}$$

where $\operatorname{dev}\varepsilon = \varepsilon - 1/3\operatorname{tr}\varepsilon\mathbf{I}$, K denotes the bulk and μ the shear modulus. Let us further specify $\Delta = r\|\dot{\mathbf{z}}\|$ which yield a dissipation distance of the form

$$D(\mathbf{z}_0, \mathbf{z}_1) = r \, \|\mathbf{z}_1 - \mathbf{z}_0\|. \tag{57}$$

This gives

$$\Psi^{\text{cond}}_{\mathbf{z}_n}(\varepsilon) = \frac{K}{2}(\operatorname{tr}\varepsilon)^2 + \inf \{ \, \mu \| \operatorname{dev} \varepsilon - \mathbf{z}\|^2 + r \, \|\mathbf{z} - \mathbf{z}_n\| \mid \mathbf{z} \, \}. \tag{58}$$

The stationarity condition reads

$$\mathbf{0} \in -2\mu(\operatorname{dev}\varepsilon - \mathbf{z}) + r \operatorname{sign}(\mathbf{z} - \mathbf{z}_n). \tag{59}$$

The differential inclusion (59) can be solved explicitly. Let us do this in general for later reference:

The differential inclusion

$$\mathbf{0} \in \alpha\mathbf{x} + \beta \operatorname{sign}\mathbf{x} + \mathbf{b} \tag{60}$$

has the unique solution

$$\mathbf{x} = -\frac{1}{\alpha} \left(\|\mathbf{b}\| - \beta\right)_+ \operatorname{sign}\mathbf{b} \tag{61}$$

where $(\xi)_+ = \max\{0, \xi\}$ denotes the positive part of an expression. The proof follows by simple inspection.

Applying this result to (59), with $\mathbf{x} = \mathbf{z} - \mathbf{z}_n$ gives

$$\mathbf{z}_{n+1} = \mathbf{z} = \mathbf{z}_n + \frac{1}{2\mu} \left(2\mu \| \operatorname{dev}\varepsilon - \mathbf{z}_n\| - r\right)_+ \operatorname{sign}(\operatorname{dev}\varepsilon - \mathbf{z}_n). \tag{62}$$

Substitution of (62) into (58) gives

$$\begin{aligned}\Psi^{\text{cond}}_{\mathbf{z}_n}(\varepsilon) &= \frac{K}{2}(\text{tr}\varepsilon)^2 + \mu\|\operatorname{dev}\varepsilon - \mathbf{z}_n\|^2 \\ &\quad - (2\mu\|\operatorname{dev}\varepsilon - \mathbf{z}_n\| - r)_+(\operatorname{dev}\varepsilon - \mathbf{z}_n) : \operatorname{sign}(\operatorname{dev}\varepsilon - \mathbf{z}_n) \\ &\quad + \frac{1}{4\mu}(2\mu\|\operatorname{dev}\varepsilon - \mathbf{z}_n\| - r)_+^2 + r\frac{1}{2\mu}\,(2\mu\|\operatorname{dev}\varepsilon - \mathbf{z}_n\| - r)_+ \\ &= \frac{K}{2}(\text{tr}\varepsilon)^2 + (2\mu\|\operatorname{dev}\varepsilon - \mathbf{z}_n\| - r)_+\Big[- \|\operatorname{dev}\varepsilon - \mathbf{z}_n\| \\ &\quad + \frac{1}{2}\,\|\operatorname{dev}\varepsilon - \mathbf{z}_n\| - \frac{r}{4\mu} + \frac{r}{2\mu}\Big] \\ &= \frac{K}{2}(\text{tr}\varepsilon)^2 + \mu\|\operatorname{dev}\varepsilon - \mathbf{z}_n\|^2 - \frac{1}{4\mu}\,(2\mu\|\operatorname{dev}\varepsilon - \mathbf{z}_n\| - r)_+^2.\end{aligned} \tag{63}$$

Note that for $2\mu\|\operatorname{dev}\varepsilon - \mathbf{z}_n\| > r$, i.e. in the case of plastic flow, we have $\Psi^{\text{cond}}_{\mathbf{z}_n}(\varepsilon) = \frac{K}{2}(\text{tr}\varepsilon)^2 + r\|\operatorname{dev}\varepsilon - \mathbf{z}_n\| - \frac{r^2}{4\mu}$ which means linear growth in ε.

Example 1.5. Crystal plasticity, continued

Let us investigate the model of 1.3 further. The dissipation distance for a time step $[t_n, t_{n+1}]$ is obtained from

$$D(\gamma_{n+1}, \gamma_n) = r\,\inf_{\gamma(t)}\left\{\int_{t_n}^{t_{n+1}} \Delta(\dot\gamma)\;\mathrm{d}t\;:\;\gamma(t_n) = \gamma_n, \gamma(t_{n+1}) = \gamma_{n+1}.\right\}, \tag{64}$$

For the dissipation potential (32) this is specified as

$$D(\gamma_{n+1}, \gamma_n) = r\,\sum_i |\gamma_{i,n+1} - \gamma_{i,n}|, \tag{65}$$

and in particular for a single active slip system

$$D(\gamma_{n+1}, \gamma_n) = r\,|\gamma_{n+1} - \gamma_n|. \tag{66}$$

The condensed energy now takes the form

$$\Psi^{\text{cond}}_{\gamma_n, \mathbf{p}_n}(\mathbf{F}) = \inf\left\{\Psi(\mathbf{F}\mathbf{F}_{\text{p}}^{-1}(\gamma), \mathbf{p}) + D(\gamma)\;\Big|\;\gamma\,;\,p_i = p_{i,n} + |\gamma_i - \gamma_{i,n}|\right\}, \tag{67}$$

which for a single active slip system ($n = 1$) for a single time step as employed e.g. in Carstensen et al. (2008) reduces to

$$\Psi^{\text{cond}}_{\gamma_n, p_n}(\mathbf{F}) = \inf\left\{\Psi(\mathbf{F}(\boldsymbol{I} - \gamma\mathbf{s}\otimes\mathbf{m}), p_n + |\gamma - \gamma_n|) + r\,|\gamma - \gamma_n|\;\Big|\gamma\right\}. \tag{68}$$

In the following, let us study a neo-Hookean material with free energy density

$$\Psi_{\rm el}(\mathbf{F}_{\rm e}) = U(j) + \frac{\mu}{2}\left(\operatorname{tr}\mathbf{F}_{\rm e}^{\mathsf{T}}\mathbf{F}_{\rm e} - 3\right), \tag{69}$$

with

$$U(j) = \frac{\lambda}{4}\left[j^2 - 2\left(1 + 2\frac{\mu}{\lambda}\right)\ln\ j - 1\right], \tag{70}$$

where $j = \det\mathbf{F}_{\rm e}$ denotes the elastic volumetric change, and $\mu > 0$ and $\lambda > 0$ are the Lamé elastic moduli. Let us further choose $\Psi_{\rm p}(p) = \frac{\kappa}{2}\,p^2$. Then the condensed energy reads

$$\begin{aligned}\Psi^{\rm cond}_{\gamma_n,p_n}(\mathbf{F}) = \inf\Big\{&U(j) + \frac{\mu}{2}(\operatorname{tr}\mathbf{F}^{\mathsf{T}}\mathbf{F} - 2\gamma C_{sm} + \gamma^2 C_{ss})\\ &+\frac{\kappa}{2}\left(p_n + |\gamma - \gamma_n|\right)^2 + r\,|\gamma - \gamma_n|\ \Big|\gamma\Big\}.\end{aligned} \tag{71}$$

Here, $C_{ss} = \mathbf{s}\cdot\mathbf{F}^{\mathsf{T}}\mathbf{F}\mathbf{s}$ and $C_{sm} = \mathbf{s}\cdot\mathbf{F}^{\mathsf{T}}\mathbf{F}\mathbf{m}$ denote the corresponding components of the Cauchy–Green strain–tensor $\mathbf{C} = \mathbf{F}^{\mathsf{T}}\mathbf{F}$ in the directions given by $\mathbf{s}$ and $\mathbf{m}$.

The stationarity condition reads

$$0 \in -\mu C_{sm} + \mu\gamma C_{ss} + \kappa(\gamma - \gamma_n) + (r + \kappa p_n)\operatorname{sign}(\gamma - \gamma_n). \tag{72}$$

Applying (60) and (61) we get

$$\gamma = \gamma_n + \frac{(\mu|C_{sm} - \gamma_n C_{ss}| - r - \kappa p_n)_+}{\mu C_{ss} + \kappa}\operatorname{sign}(C_{sm} - \gamma_n C_{ss}). \tag{73}$$

Substitution of (73) into (71) gives

$$\begin{aligned}\Psi^{\rm cond}_{\gamma_n,p_n}(\mathbf{F}) = U(j) &+ \frac{\mu}{2}(\operatorname{tr}\mathbf{F}^{\mathsf{T}}\mathbf{F} - 2\gamma_n C_{sm} + \gamma_n^2 C_{ss})\\ &-\frac{1}{2(\mu C_{ss} + \kappa)}\left(\mu|C_{sm} - \gamma_n C_{ss}| - r - \kappa p_n\right)_+^2.\end{aligned} \tag{74}$$

To investigate the convexity properties of the potential $\Psi^{\rm cond}_{\gamma_n,p_n}$, we consider the special case $\gamma_n = 0$, $p_n = 0$, i.e., we look at a time–increment at the beginning of which the body is completely elastic. Let us specify $\mathbf{F}$ as

$$\mathbf{F} = \boldsymbol{I} + \frac{a}{2}\,(\mathbf{s} + \mathbf{m}) \otimes (\mathbf{m} - \mathbf{s}). \tag{75}$$

Note that (1.5) constitutes a rank–one family of matrices parameterized by α; $\mathbf{F}$ represents a simple shear under an angle of 45 degrees with respect

to the plastic slip–system given. Substitution of (1.5) into $\Psi_{0,0}^{\text{cond}}$ yields the energy

$$W = \mu + \frac{\mu}{2}\, a^2 - \frac{(\frac{\mu}{2}\, a^2 - r)_+^2}{2a + \mu(2 - 2a + a^2)}. \tag{76}$$

The graph of W is depicted in Figure 1. For the case $\alpha = 4$ the condensed energy can be calculated via numerical minimization. For this case the graph of Ψ^{cond} for a plane-strain simple-shear test and a tension-compression test is illustrated in Fig. 2, where the in-plane orientation of the laminate interface normal vector is defined by $\mathbf{b} = (\cos\varphi, \sin\varphi, 0)^T$. Note that the appearing non-convexity depends on the choice of the active slip system. In Fig. 2a we demonstrate the non-convex energy for various slip system orientations for a simple shear test ($\mathbf{F} = \boldsymbol{I} + \gamma\, \mathbf{e}_1 \otimes \mathbf{e}_2$). It becomes apparent that the non-convexity appears during positive loading ($\gamma > 0$) if $\varphi > 90°$, and during negative loading if $\varphi < 90°$, see also Conti and Theil (2005). The influence of the hardening parameter κ is shown in Fig. 2b for tension-compression ($\mathbf{F} = (1+\delta)\, \mathbf{e}_1 \otimes \mathbf{e}_1 + \frac{1}{1+\delta} \mathbf{e}_2 \otimes \mathbf{e}_2$) with $\alpha = 4$ (in both graphics). With increasing hardening the second energy well is lifted considerably. In all of these cases the energy is clearly non-convex giving rise to instability and hence to the formation of microstructure as has already been discussed e.g. in Carstensen et al. (2002); Hackl and Kochmann (2008); Kochmann and Hackl (2010a); Lambrecht et al. (2003).

Based on the constitutive framework outlined above we now investigate the formation of microstructures. Many authors have employed a condensed energy functional for a single time step only, see e.g. Bartels et al. (2004); Carstensen et al. (2008), which may be appropriate for monotonic loading.

2 Nonconvex energies and microstructures

2.1 Quasiconvexity

The essential condition for the existence of minima of the functional $\mathcal{I}(t, \phi, \mathbf{z})$, see (1), is *quasiconvexity* of the free energy $\Psi(\mathbf{F}, \mathbf{z})$ with respect to $\mathbf{F}$. (There are also some growth conditions). For a detailed exposition of this topic, see Dacorogna (1989).

We call a functional ψ quasiconvex, if and only if

$$\Psi(\mathbf{A}) \leq \frac{1}{w} \int_w \Psi(\mathbf{A} + \boldsymbol{\nabla}\boldsymbol{\varphi})\, \mathrm{d}V \quad \text{(QC)}, \tag{77}$$

for every bounded domain ω and every vector-field $\boldsymbol{\varphi}$ with $\boldsymbol{\varphi} = \mathbf{0}$ on $\partial\omega$.

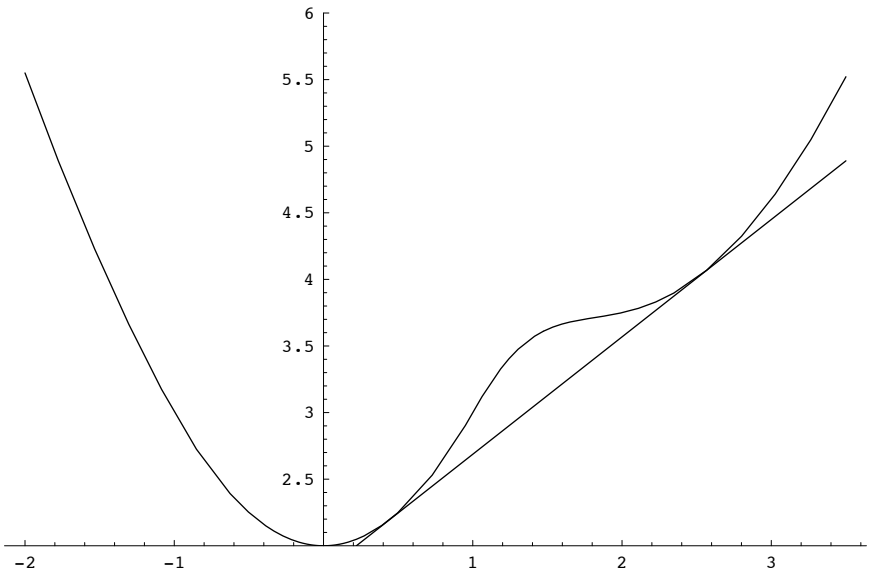

Figure 1. Condensed energy W for $\mu = 2$, $\kappa = 0$, $r = 1$. The energy is clearly not convex. (Originally published in Carstensen et al. (2002).)

There a two remarks:

1. If (QC) holds for a certain bounded domain ω, then it holds for every bounded domain.
2. Ψ is quasiconvex if and only if

$$\Psi(\mathbf{A}) \leq \int\limits_{[0,1]^d} \Psi(\mathbf{A} + \boldsymbol{\nabla}\boldsymbol{\varphi}) \, \mathrm{d}V \tag{78}$$

for all periodic continuous vector-fields $\boldsymbol{\varphi}$ on the unit-cube $[0,1]^d$.

Example 2.1. martensitic microstructures

Some metals posses a high-temperature phase called *austenite* with high symmetry which can undergo a phase-transformation to a low-temperature phase called *martensite* with lower symmetry, see Figure 3. For more details on martensitic microstructures and the application of relaxation concepts to this topic, see Ball and James (1987, 1992); Bhattacharya (2003); Chu and James (1995); Govindjee et al. (2003, 2007); Hackl and Heinen

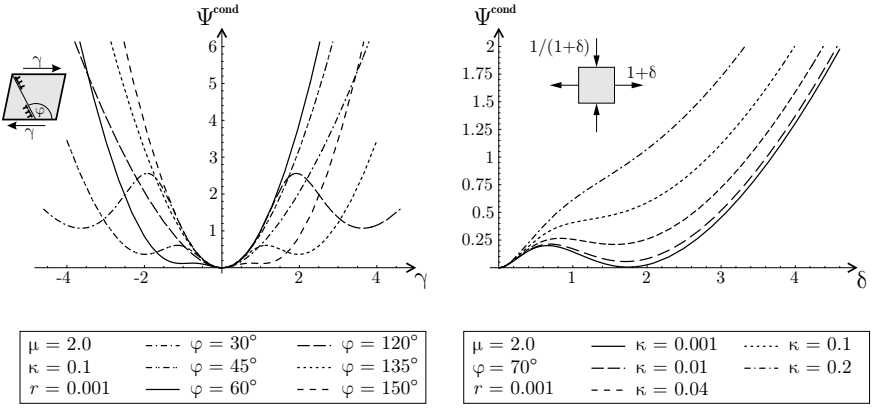

Figure 2. Unrelaxed condensed energy of a homogeneous single crystal with one active slip system ($\alpha = 4$). The energy is clearly not convex. a) Condensed energy during a simple shear test for fixed hardening and varying slip system orientation, b) condensed energy during a tension-compression test for fixed slip system orientation and varying hardening parameter values. (Originally published in Kochmann and Hackl (2011).)

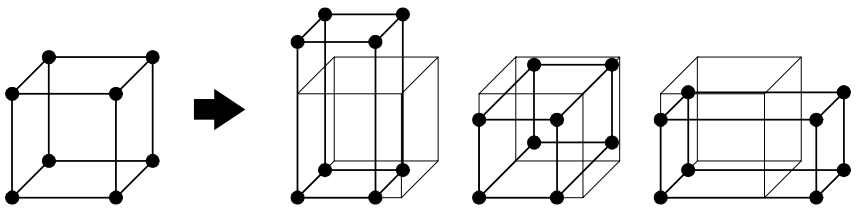

Figure 3. Austenite and martensite phases

(2007, 2008a,b); Hackl et al. (2003); Junker nad Hackl (2011); Hackl et al. (2011b).

We will return to a small strain formulation now. The martensite is characterized by a transformation strain, which for simplicity in this example we assume to be:

$$\mathbf{T} = \begin{pmatrix} \beta & 0 & 0 \\ 0 & 0 & 0 \\ 0 & 0 & 0 \end{pmatrix}. \tag{79}$$

Hence we have

$$\|\mathbf{T}\| = \beta. \tag{80}$$

Let the strain be given as $\varepsilon = \frac{1}{2}(\boldsymbol{\nabla}\mathbf{u} + \boldsymbol{\nabla}\mathbf{u}^T) = \frac{1}{2}(\mathbf{A} + \mathbf{A}^{\mathsf{T}})$. Then we assume the potential energy to be given as the minimum of the energies of two martensite phases:

$$\Psi(\mathbf{A}) = \alpha \min\left\{\|\varepsilon - \mathbf{T}\|^2, \|\varepsilon + \mathbf{T}\|^2\right\}. \tag{81}$$

This energy is not quasiconvex as we are going to show. Obviously we have

$$\Psi(\mathbf{0}) = \alpha\beta^2. \tag{82}$$

It is, however, possible for the material to lower its energy further by forming a microstructure given by a fluctuation field given by the following construction:

Let an RVE be subdivided into regions named a, b, c, d, as shown in Figure 4. Now define

$$\boldsymbol{\varphi}_n = \begin{pmatrix} \varphi_n \\ 0 \\ 0 \end{pmatrix}, \quad \text{such that} \tag{83}$$

$$\boldsymbol{\nabla}\boldsymbol{\varphi}_n = \mathbf{T} \quad \text{in} \quad a, \tag{84}$$

$$\boldsymbol{\nabla}\boldsymbol{\varphi}_n = -\mathbf{T} \quad \text{in} \quad b, \tag{85}$$

$$\boldsymbol{\nabla}\boldsymbol{\varphi}_n = \begin{pmatrix} 0 & -\beta & 0 \\ 0 & 0 & 0 \\ 0 & 0 & 0 \end{pmatrix} \quad \text{in} \quad c, \tag{86}$$

$$\boldsymbol{\nabla}\boldsymbol{\varphi}_n = \begin{pmatrix} 0 & \beta & 0 \\ 0 & 0 & 0 \\ 0 & 0 & 0 \end{pmatrix} \quad \text{in} \quad d. \tag{87}$$

It now holds

$$\begin{aligned} \int_\omega \Psi(\mathbf{0} + \boldsymbol{\nabla}\boldsymbol{\varphi}_n)\, \mathrm{d}V &= \alpha \left\| \begin{pmatrix} \beta & \pm\beta/2 & 0 \\ \pm\beta/2 & 0 & 0 \\ 0 & 0 & 0 \end{pmatrix} \right\|^2 \frac{l^2}{n} h \\ &= \frac{3}{2}\alpha\beta^2 l^2 h \frac{1}{n} < \omega\, \Psi(\mathbf{0}) = \alpha\beta^2 l^2 h. \end{aligned} \tag{88}$$

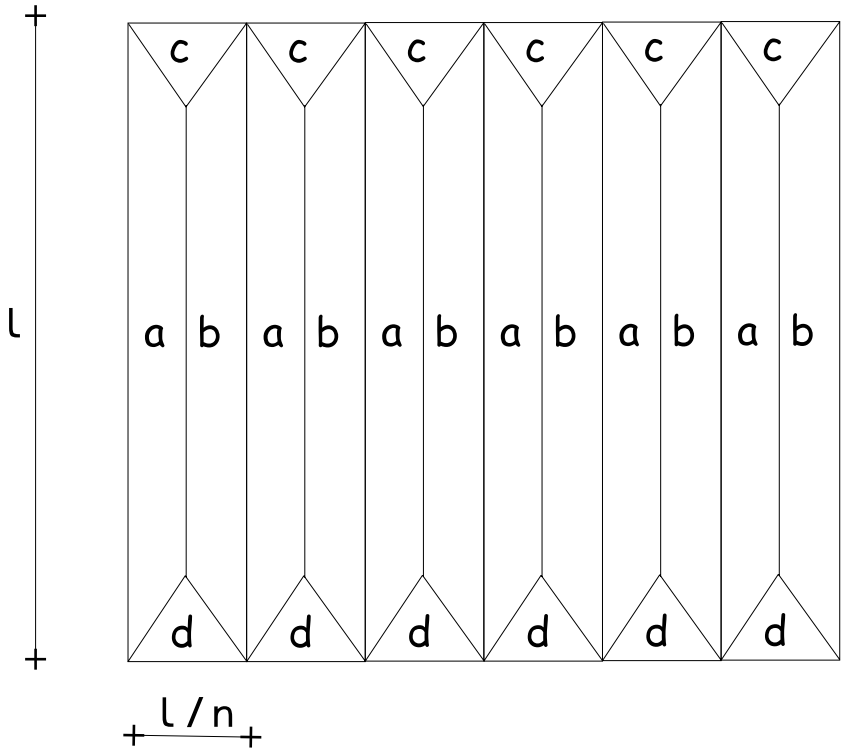

Figure 4. Laminated microstructure

This means that Ψ is not quasiconvex. Moreover we have

$$\Pi(\boldsymbol{\varphi}_n) \to 0. \tag{89}$$

This limit value however cannot be reached because $\boldsymbol{\varphi}_n$ does not converge to a continuous displacement for $n \to \infty$. The minimum does not exist. The microstructure in Figure 4 is very typical and called *laminate*.

2.2 Alternative notions of convexity

The notion of quasiconvexity is very difficult to handle mathematically. Therefore one tries to replace it by various concepts which are more accessible.

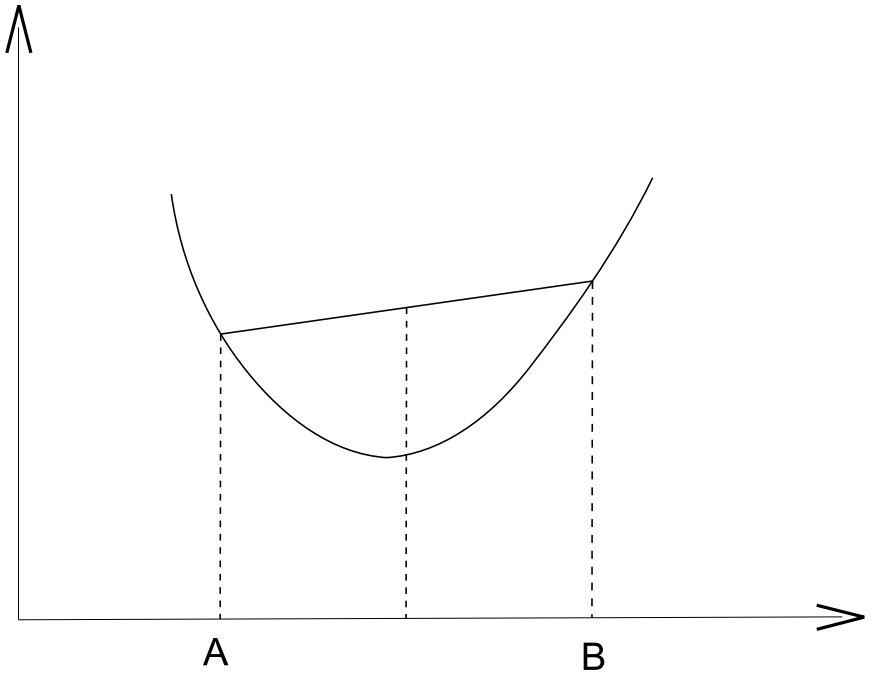

Figure 5. Convex function

Ψ convex: For all $\mathbf{A}$, $\mathbf{B}$ and $0 \leq \lambda \leq 1$ it holds

$$\Psi(\lambda\mathbf{A} + (1-\lambda)\mathbf{B})) \leq \lambda\Psi(\mathbf{A}) + (1-\lambda)\Psi(\mathbf{B}), \tag{90}$$

or alternatively

$$\Psi(\mathbf{A}) \leq \lambda\Psi(\mathbf{A} + (1-\lambda)\mathbf{B}) + (1-\lambda)\Psi(\mathbf{A} - \lambda\mathbf{B}), \tag{91}$$

compare Figure 5.

Ψ rank-1-convex: (90) or (91) holds for all $\mathbf{A}, \mathbf{B}$ with $\mathrm{Rank}(\mathbf{A} - \mathbf{B}) \leq 1$, that means

$$\mathbf{B} = \mathbf{A} + \mathbf{a} \otimes \mathbf{b}, \tag{92}$$

for vectors $\mathbf{a}$ and $\mathbf{b}$.

Ψ polyconvex: there is a *convex* function $f = \mathbb{R}^{d\times d} \times \mathbb{R}^{d\times d} \times \mathbb{R} \to \mathbb{R}$ with:

$$\Psi(\mathbf{A}) = f(\mathbf{A}, \mathrm{cof}\mathbf{A}, \det \mathbf{A}), \tag{93}$$

where

$$\operatorname{cof}\mathbf{A} = (\det \mathbf{A})\mathbf{A}^{-\mathsf{T}} \tag{94}$$

denotes the cofactor matrix corresponding to $\mathbf{A}$.

It holds:

Ψ convex $\Rightarrow$ Ψ polyconvex $\Rightarrow$ Ψ quasiconvex $\Rightarrow$ Ψ rank-1-convex.

The opposite does not hold in general.

We are going to look into the notion of rank-1-convexity a little more closely. Let us once again look at a fluctuation field which is a laminate. This can in the most general form be written as follows:

Let us introduce a scalar function by

$$\psi(x) = \begin{cases} \dfrac{x}{\lambda}, & 0 \le x \le \lambda \\ \\ \dfrac{1-x}{1-\lambda}, & \lambda \le x \le 1 \end{cases} \quad , \quad \text{periodically repeated,} \tag{95}$$

see Figure 6.

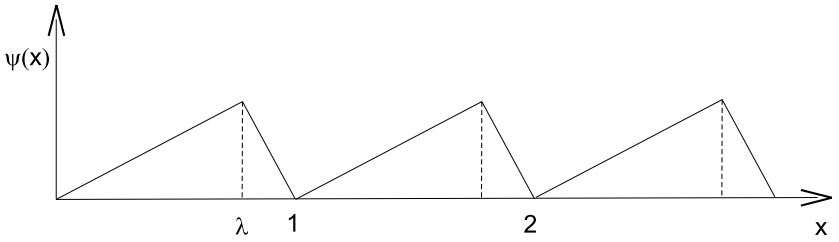

Figure 6. scalar function $\psi(x)$

We define our fluctuation field as

$$\boldsymbol{\varphi}(\mathbf{x}) = \mathbf{a}\,\psi(\mathbf{b}\cdot\mathbf{x}) \quad , \quad |\mathbf{b}| = 1, \tag{96}$$

which corresponds to the laminate depicted in Figure 7. The gradient of $\boldsymbol{\varphi}$ is then alternating between two values:

$$\boldsymbol{\nabla}\boldsymbol{\varphi}(x) = \begin{cases} \dfrac{1}{\lambda}\,\mathbf{a}\otimes\mathbf{b} & 1. \\ -\dfrac{1}{1-\lambda}\,\mathbf{a}\otimes\mathbf{b} & 2. \end{cases} , \tag{97}$$

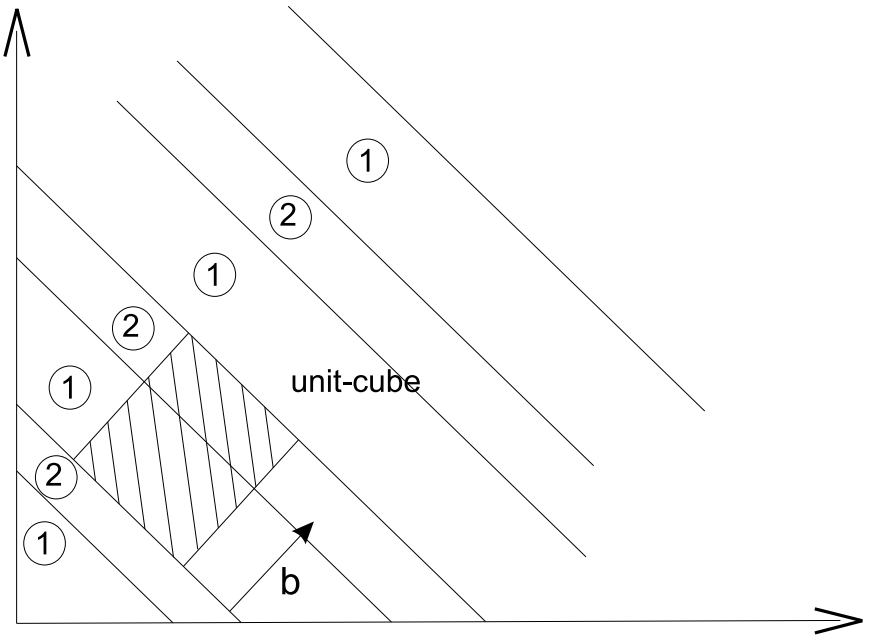

Figure 7. Laminate of 1. order and RVE

compare Figure 7.

Without restriction we can adjust our RVE now to have edges aligned with the laminate as in Figure 7. The definition of quasiconvexity in equation (78) then reduces to

$$\Psi(\bar{\mathbf{A}}) \leq \int\limits_{[0,1]^d} \Psi(\bar{\mathbf{A}} + \boldsymbol{\nabla}\boldsymbol{\varphi})\, \mathrm{d}V$$
$$= \lambda \Psi \underbrace{\left(\bar{\mathbf{A}} + \frac{1}{\lambda}\mathbf{a}\otimes\mathbf{b}\right)}_{\mathbf{A}} + (1-\lambda)\underbrace{\left(\bar{\mathbf{A}} - \frac{1}{1-\lambda}\mathbf{a}\otimes\mathbf{b}\right)}_{\mathbf{B}}, \quad (98)$$

which is exactly the definition of rank-1-convexity. Hence rank-1-convexity is nothing more than quasiconvexity restricted to laminates as possible fluctuation fields.

3 Relaxed potentials

3.1 Basic concepts

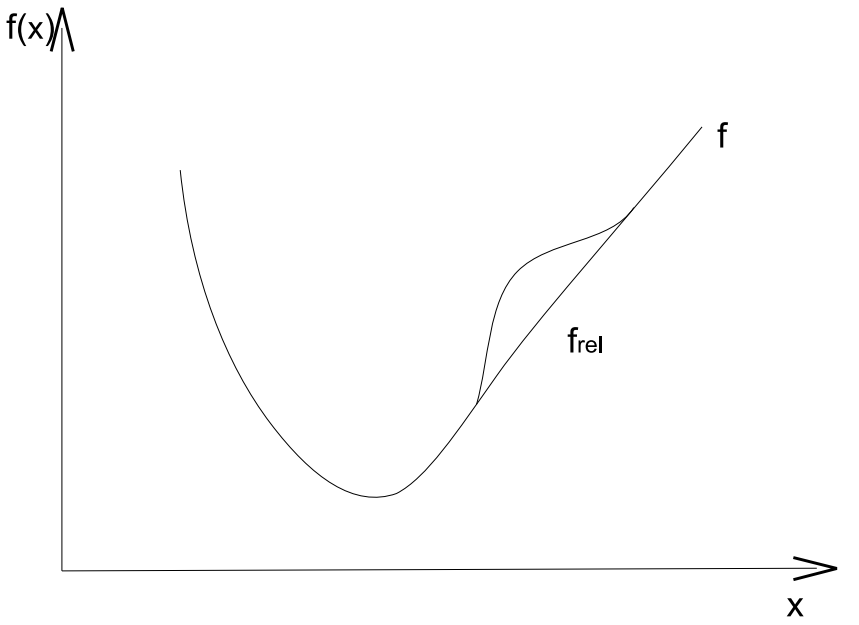

Figure 8. Relaxed potential

Let us explain the basic concept of relaxation via the one-dimensional potential $f(x)$ shown in Figure 8. If we take the infimum over all fluctuation-fields, this amounts in the one-dimensional case to the convexification of the potential indicated in Figure 8. Thus we can define a relaxed potential of the form

$$f_{\text{rel}}(x) = \inf\{\lambda_1 f(x_1) + \lambda_2 f(x_2); \quad \lambda_1 + \lambda_2 = 1, \quad \lambda_1 x_1 + \lambda_2 x_2 = x\}\,. \tag{99}$$

The generalization to higher dimensions is most easily performed by switching to an abstract description. Let us define an ordering for potentials by

$$f \leq g \Leftrightarrow f(x) \leq g(x), \quad \forall x. \tag{100}$$

Then f_{rel} of equation (99) can also be given in the form

$$f_{\text{rel}}(x) = \sup\{g \leq f; \quad g \quad \text{convex}\}\,. \tag{101}$$

This notion can now be easily extended to various concepts of so-called envelopes. We have for a potential $\Psi(\mathbf{A})$ the

convex envelope:

$$C\,\Psi = \sup\{\phi \leq \Psi; \quad \phi \quad \text{convex}\}, \tag{102}$$

polyconvex envelope:

$$P\,\Psi = \sup\{\phi \leq \Psi; \quad \phi \quad \text{polyconvex}\}, \tag{103}$$

quasiconvex envelope:

$$Q\,\Psi = \sup\{\phi \leq \Psi; \quad \phi \quad \text{quasiconvex}\}, \tag{104}$$

Rank-1-convex envelope:

$$R\,\Psi = \sup\{\phi \leq \Psi; \quad \phi \quad \text{rank}-1-\text{convex}\}. \tag{105}$$

It holds

$$C\,\Psi \leq P\,\Psi \leq Q\,\Psi \leq R\,\Psi \leq \Psi. \tag{106}$$

3.2 Calculation of envelopes

There exist specific formulas for all envelopes except for the quasiconvex envelope, which we are going to give here now. For $C\,\Psi$ and $P\,\Psi$ the formulas consist of a minimization problem involving a finite number of matrices (= displacement gradients), called *atoms*. The number of atoms n depends on the dimension $d = 1, 2, 3$ of the problem.

$$C\,\Psi(\mathbf{A}) = \inf\left\{\sum \lambda_i \Psi(\mathbf{A}_i); \quad \lambda_i,\, \mathbf{A}_i, \quad \sum \lambda_i = 1,\, \sum \lambda_i \mathbf{A}_i = \mathbf{A}\right\}. \tag{107}$$

$$n = d^2 + 1. \tag{108}$$

$$P\,\Psi(\mathbf{A}) = \inf\Big\{\sum \lambda_i \Psi(\mathbf{A}_i);\quad \lambda_i,\quad \mathbf{A}_i,\quad \sum \lambda_i = 1,\quad \sum \lambda_i \mathbf{A}_i = \mathbf{A}\ ,\\ \sum \lambda_i \mathrm{cof}\mathbf{A}_i = \mathrm{cof}\mathbf{A},\quad \sum \lambda_i \det\,\mathbf{A}_i = \det\,\mathbf{A}\Big\}. \tag{109}$$

$$\begin{aligned} d=2 \quad &: \quad n = 4+1 = 5 \\ d=3 \quad &: \quad n = 9+9+1 = 19. \end{aligned} \tag{110}$$

$$Q\,\Psi(\mathbf{A}) = \inf\left\{\frac{1}{\omega}\int\limits_{\omega} \Psi(\mathbf{A}+\boldsymbol{\nabla}\boldsymbol{\phi})\,\mathrm{d}V;\quad \boldsymbol{\phi},\quad \boldsymbol{\phi}=0\quad \text{on}\quad \partial\omega\right\}. \tag{111}$$

The characterization of the rank-1-convex envelope is more involved, but very instructive. We start by relaxation with respect to all first-order laminates:

$$R_1\,\Psi(\mathbf{A}) = \inf\Big\{\lambda_1\Psi(\mathbf{A}_1)+\lambda_2\Psi(\mathbf{A}_2);\quad \lambda_i,\quad \mathbf{A}_i,\quad \sum\lambda_i = 1\ ,\\ \sum\lambda_i\mathbf{A}_i = \mathbf{A},\quad \mathrm{Rank}(\mathbf{A}_1-\mathbf{A}_2)\le 1\Big\}, \tag{112}$$

which can alternatively be written in the form

$$R_1\,\Psi(\mathbf{A}) = \inf\{\lambda\Psi(\mathbf{A}+(1-\lambda)\mathbf{a}\otimes\mathbf{b}+(1-\lambda)\Psi(\mathbf{A}-\lambda\mathbf{a}\otimes\mathbf{b}))\ ;\\ \lambda,\quad \mathbf{a},\quad \mathbf{b},\quad 0\le\lambda\le 1,\quad |\mathbf{a}|=1\}. \tag{113}$$

Surprisingly it turns out that $R_1\,\Psi$ is not rank-1-convex. This means that we can repeat the procedure and calculate the rank-1-convex envelope of $R_1\,\Psi$ in turn:

$$R_1(R_1\,\Psi) = R_1^2\Psi = R_2\Psi. \tag{114}$$

Now in general $R_2\,\Psi$ will not be rank-1-convex either. Theoretically one has to repeat the procedure an infinite number of times in order to finally reach the rank-1-convex envelope:

$$R_k\,\Psi = R_1^k\Psi, \tag{115}$$

$$R\,\Psi = \lim_{k\to\infty} R_k\Psi. \tag{116}$$

In most cases, however, it will be possible to stop after a finite number of iterations.

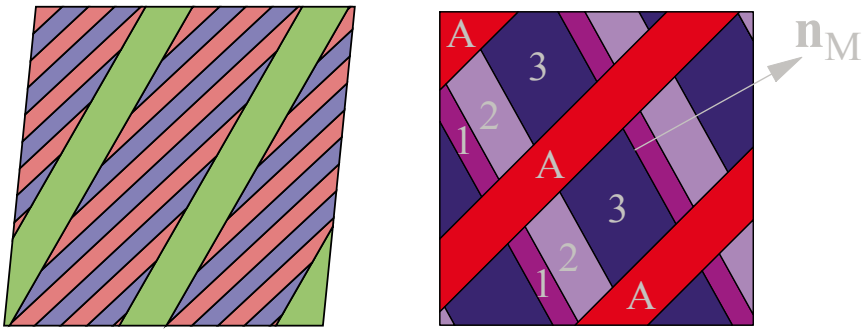

Figure 9. Laminates of higher order

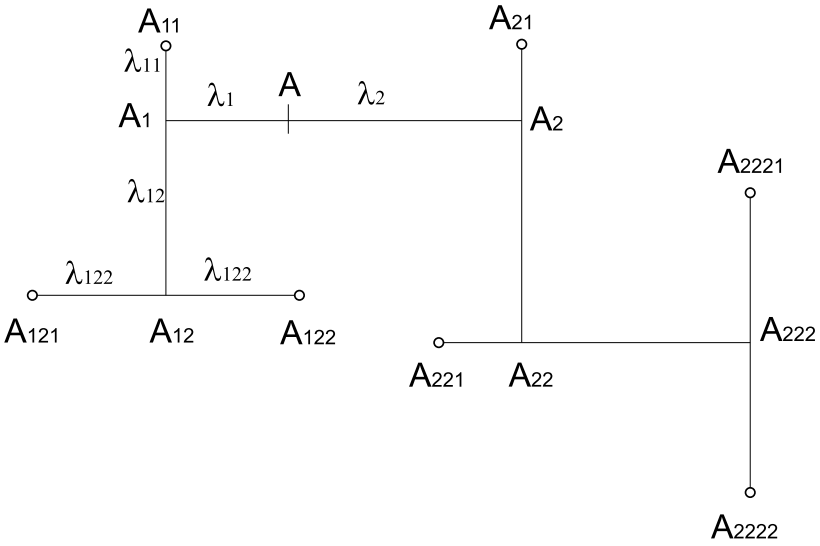

Figure 10. Tree-diagram

The envelope then corresponds to relaxation with respect to *laminates of higher order k*. Examples of such laminates are shown in Figure 9. A nice way to picture such laminates are so-called *tree-diagrams*, see Figure 10:

Every atom used corresponds to a node of the diagram. Rank-1-connected matrices are joined by line segments. The length of sub-segments then cor-

respond to the volume ratios with which two atoms are mixed to form the laminate. The atoms and volume rations have to obey the following rules:

$$A_{i_1....i_n} = \lambda_{i_1....i_n\,1} A_{i_1....i_n\,1} + \lambda_{i_1....i_n\,2} A_{i_1....i_n\,2}, \tag{117}$$

$$Rank(A_{i_1....i_n\,1} - A_{i_1....i_n\,2}) \leq 1. \tag{118}$$

4 Single-slip elastoplasticity, initiation of microstructures

We are now going to apply the concepts developed in Section 3 to the condensed energy given by (74) in order to describe the initiation of plastic microstructures.

For a particular range of material parameters the condensed energy fails to be rank-one convex, as can be seen from Figures 1 and 2, and, hence, fails to be quasiconvex. As a consequence, microstructures may be obtained as solutions of boundary value problems. The occurrence of microstructures can be demonstrated by direct finite element simulation using representative volume elements under periodic boundary conditions, cf. Hackl and Hoppe (2002). Figure 11 shows two typical results of these simulations: Oscillations in the plastic slip field γ, forming first and second-order laminates. These oscillations are highly mesh dependent. The number of laminates grows towards infinity when the mesh becomes finer and finer.

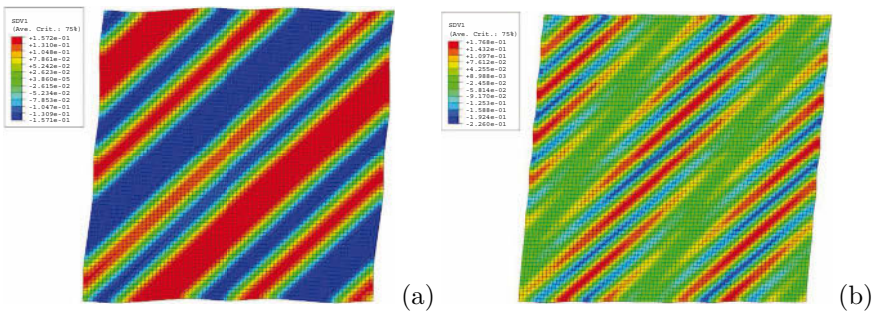

Figure 11. Single-slip plasticity (a) first-order laminates and (b) second-order laminates, assuming periodic boundary conditions.

The mesh dependency and the accompanying material instability phenomena can be avoided by replacing the nonconvex condensed energy by a suitable relaxed energy. Because of its simple algorithmic structure and its

ability to provide sufficient information to reconstruct the microstructure, we use the rank-one relaxation $R^{(k)}\Psi^{\mathrm{cond}}(\mathbf{F})$ as the underlying relaxation technique. The numerical algorithm can be formulated as a restricted optimization problem. For example, in the 2–dimensional case and $k = 1$ the objective function

$$\tilde{\Psi}^{\mathrm{cond}}(\mathbf{x}, \mathbf{F}) := (1-\lambda)\Psi^{\mathrm{cond}}(\mathbf{F} - \lambda \mathbf{a} \otimes \mathbf{b}) + \lambda \Psi^{\mathrm{cond}}(\mathbf{F} + (1-\lambda)\mathbf{a} \otimes \mathbf{b}) \quad (119)$$

depends on 4 optimization variables, for example,

$$\mathbf{x} = (\lambda, \rho, \alpha, \beta), \qquad \text{representing} \quad \mathbf{a} = \rho \begin{pmatrix} \cos(\alpha) \\ \sin(\alpha) \end{pmatrix}, \quad \mathbf{b} = \begin{pmatrix} \cos(\beta) \\ \sin(\beta) \end{pmatrix}. \quad (120)$$

The vectors $\mathbf{a}$ and $\mathbf{b}$ form the rank–one matrix $\mathbf{a} \otimes \mathbf{b}$ and the scalar λ determines the volume fraction of the two phases of the first-order laminate. The relaxed energy is obtained by solving the minimization problem

$$R^1\Psi^{\mathrm{cond}}(\mathbf{F}) = \inf \left\{ \tilde{\Psi}^{\mathrm{cond}}(\mathbf{x}, \mathbf{F}) \,\middle|\, \mathbf{x} \in \mathcal{B} \right\} \quad (121)$$

for a given deformation gradient $\mathbf{F}$ and a domain $\mathcal{B}$ of $\mathbf{x}$ defined by

$$\begin{aligned} \mathcal{B} = \{ \mathbf{x} \in \mathbb{R}^4 \mid & 0 \le \lambda \le 1,\ 0 \le \rho,\ 0 \le \alpha \le \pi,\ 0 \le \beta \le 2\pi, \\ & \det(\mathbf{F} - \lambda \mathbf{a} \otimes \mathbf{b}) > 0,\ \det(\mathbf{F} + (1-\lambda)\mathbf{a} \otimes \mathbf{b}) > 0 \}. \end{aligned} \quad (122)$$

Corresponding minimization problems can be set up for higher order laminations. Although the realization of an algorithm for higher order laminates is straight forward, the exponentially growing number of optimization variables strongly limits its practical application. Already for low order laminates the numerical search for the minimizer of (121) turns out to be difficult, because the objective function may have several local extrema Fig. 13(a) and the inequalities in (122) impose nonlinear constraints, which require a special treatment. Different procedures have been used to solve the minimization problem numerically. Probabilistic global search procedures have shown to be efficient and sufficiently robust. But applying a local search several times starting from randomly chosen sampling points leads to an inefficient global search, because the same local minimum may be identified over and over. As an improvement, clustering methods attempt to avoid this inefficiency by carefully selecting points at which the local search is initiated. The following algorithm was presented in Bartels et al. (2004)

Algorithm 4.0.1 (Clustering method)**.**
Input F, initial population $x_i \in \mathcal{B}$ of n starting points, tolerance ε.
(a) (Sampling and reduction): Sample the objective function of (119) at x_i and reduce population taking the m best points giving the least value.
(b) (Clustering): Identify clusters, such that the points inside a cluster are 'close' to each other, and the clusters are 'separated' from each other.
(c) (Center of attraction): Identify a center of attraction in each cluster.
(d) (Local search): Start a local search from the center of attraction and stop when a minimum is reached within the tolerance ε.
Output the value of $R^{(1)}\Psi(F)$.

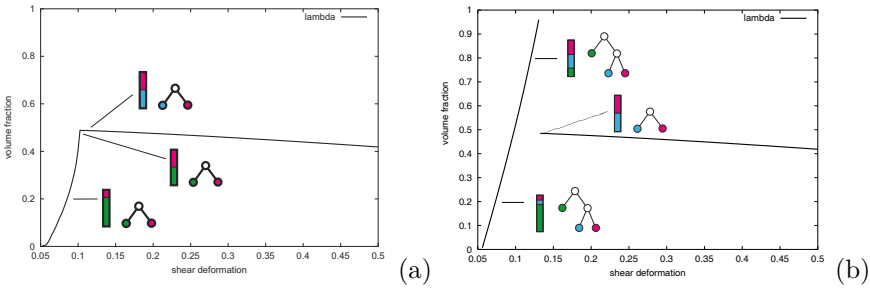

Figure 12. Evolution of the volume fraction parameter λ for a first-order (a) and a second-order (b) laminate. (Originally published in Bartels et al. (2004).)

The final local search step is done by a quasi-Newton algorithm (unconstrained) or a sequential quadratic programming algorithm. The latter is used to handle nonlinear constraints near the boundary of the feasible domain. The rank-one relaxation of the simple shear problem has been computed using first-order and second-order laminates. In a finite element framework the above mentioned algorithm has to be performed in every material point (e.g. Gauss point) and within every time step. As a result of the numerical rank-one relaxation not only the energy and the volume fractions, but also the rank-one matrices are obtained from which sufficient information about the orientation of the laminar microstructure can be gathered. Figure 12(a) shows the evolution of the volume fraction λ for the first-order laminate. At each time step the initial internal parameters $\gamma_0 = p_0 = 0$ have been fixed, which corresponds to an algorithm with a single–step update of the internal variables. Initially, the material is in a homogeneous elastic state. Then a plastic phase shows up and grows until it reaches 50% volume fraction. At that state the remaining elastic phase becomes

plastic, too, but with an opposite plastic slip. Both plastic phases then progress with slowly varying volume fractions. Solving the problem with second-order laminates gives a qualitatively different result: Now, a $N = 3$–type laminate shows up in the first stage of the deformation, comprising an elastic state and a mixture of two opposite–slip plastic states, Fig. 12(b). The volume fraction of the elastic phase starts at 100% and then decreases continuously until it vanishes at a deformation of 0.13. The further process coincides with the results of the first-order laminate relaxation.

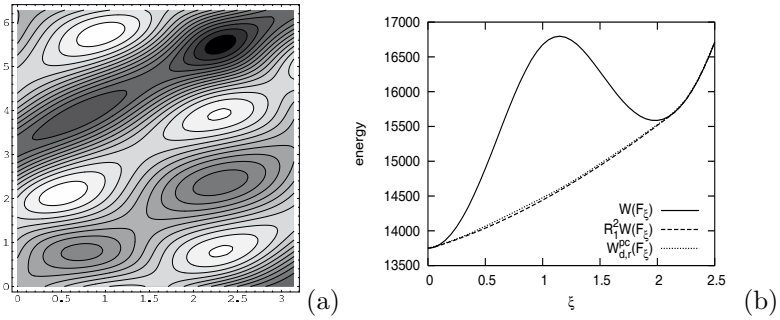

Figure 13. (a) Isolines of the functional $\tilde{\Psi}^{\mathrm{cond}}$; (b) Polyconvex envelope and second-order laminate hull for the condensed energy density in single-slip plasticity. (Originally published in Bartels et al. (2004).)

Figure 13(b), finally, compares approximations of the polyconvex hull $\Psi^{pc}_{\delta,r}(F)$ and the second-order laminate hull $R^{(2)}\Psi(F)$, realized by the algorithm described above. Both approximations almost coincide and significantly lower the energy. The good agreement suggests that the quasiconvex hull of $\Psi^{\mathrm{cond}}_{z_0}$ can be realized by second-order laminates.

5 Evolution of microstructures

5.1 Essential microstructures

The theory outlined in the previous section, centered around the notion of condensed energy, has proven successful in calculating the onset of microstructure. However, many applications based on the condensed energy rely upon the assumption that no microstructure exists at the beginning of the time step (therefore, it is suitable to model the onset of microstructure formation only). Yet in order to model the time-continuous evolution of microstructures, we need to account for the dissipation required to change from one state in time to the next. Hence, the incremental update of the in-

ternal variables will depend on the state of the internal variables at the end of the preceding time step so that use of the condensed energy functional looses physical meaning.

To overcome this problem, let us assume that the material behavior takes place within a closed class of microstructures. These evolve within this class but do not leave it, for example by refinement. Experimental evidence suggests the existence of such classes.

We denote this class *essential microstructures*. In general they can be given as spatial distributions of deformation field ϕ and internal variables $\mathbf{z}$, parametrized in the form

$$\phi = \hat{\phi}(\mathbf{x}, \mathbf{z}_{\text{ess}}, \mathbf{z}_{\text{mar}}), \quad \mathbf{z} = \hat{\mathbf{z}}(\mathbf{x}, \mathbf{z}_{\text{ess}}, \mathbf{z}_{\text{mar}}). \tag{123}$$

Here we distinguish between *essential parameters* $\mathbf{z}_{\text{ess}}$, which can only be altered by inelastic deformation, for example volume fractions, normal directions, values of internal variables, and *marginal parameters* $\mathbf{z}_{\text{mar}}$, which can be relaxed elastically, for example amplitudes of fluctuation fields, or do not influence any effective quantities, for example position of interfaces.

By selecting an appropriate *representative volume element* Ω_{rep}, for example respecting a periodicity of the microstructure, we are able to define relaxed quantities by volumetric averaging: a relaxed energy

$$\begin{aligned}&\Psi^{\text{rel}}(\mathbf{F}, \mathbf{z}_{\text{ess}})\\ &= \inf \Big\{ \frac{1}{|\Omega_{\text{rep}}|} \int_{\Omega_{\text{rep}}} \Psi(\mathbf{F} + \nabla\hat{\phi}(\mathbf{x}, \mathbf{z}_{\text{ess}}, \mathbf{z}_{\text{mar}}), \hat{\mathbf{z}}(\mathbf{x}, \mathbf{z}_{\text{ess}}, \mathbf{z}_{\text{mar}}))\, \mathrm{d}V \;\Big|\; \mathbf{z}_{\text{mar}} \Big\},\end{aligned} \tag{124}$$

and a relaxed dissipation functional:

$$\Delta^{\text{rel}}(\dot{\mathbf{z}}_{\text{ess}}, \mathbf{z}_{\text{ess}}) = \inf \Big\{ \frac{1}{|\Omega_{\text{rep}}|} \int_{\Omega_{\text{rep}}} \Delta(\frac{d}{dt}\, \hat{\mathbf{z}}(\mathbf{x}, \mathbf{z}_{\text{ess}}, \mathbf{z}_{\text{mar}}))\, \mathrm{d}V \;\Big|\; \mathbf{z}_{\text{mar}}, \dot{\mathbf{z}}_{\text{mar}} \Big\}. \tag{125}$$

Note that we now have a variational structure which is identical to that one introduced in Section 1, where Ψ, Δ, and $\mathbf{z}$ are replaced by Ψ^{rel}, Δ^{rel}, and $\mathbf{z}_{\text{ess}}$. This may provide a substantial simplification, because usually $\mathbf{z}$ is a continuum variable while $\mathbf{z}_{\text{ess}}$ is just a finite set of parameters. Applying the minimum principle (7) we obtain equations describing the evolution of essential microstructures in the form:

$$\mathbf{0} \in \frac{\partial \Psi^{\text{rel}}}{\partial \mathbf{z}_{\text{ess}}} + \frac{\partial \Delta^{\text{rel}}}{\partial \dot{\mathbf{z}}_{\text{ess}}}. \tag{126}$$

5.2 Relaxation via lamination

For a most general microstructure, expressions (124) and (126) will be hard to compute. One possible approximation is via so-called lamination. Applications of this procedure to the time-incremental problem can be found in Bartels et al. (2004); Hackl and Kochmann (2008); Kochmann and Hackl (2010a). For conciseness we will restrict ourselves to first-order laminates. Everything stated in subsequent sections can be extended to general laminates in an essentially straightforward manner, but the presentation of the intricate details would exceed the scope of this paper.

A laminate of first-order is characterized by N volume fractions λ_i separated by parallel planes with normal vector $\mathbf{b}$, as sketched in Fig. 14. To every volume fraction i there corresponds a value $\mathbf{z}_i$ of the internal variables. Moreover, in every volume fraction we have a deformation gradient $\mathbf{F}_i$ which we write as

$$\mathbf{F}_i = \mathbf{F}(\boldsymbol{I} + \mathbf{a}_i \otimes \mathbf{b}). \tag{127}$$

This formulation ensures that deformation gradients differ only by tensors of rank one, enforcing compatibility at laminate interfaces and hence ensuring the existence of a corresponding deformation field ϕ. We need to impose the volume average of the deformation gradient

$$\sum_{i=1}^{N} \lambda_i \, \mathbf{F}_i = \mathbf{F}, \tag{128}$$

which is equivalent to

$$\sum_{i=1}^{N} \lambda_i \, \mathbf{a}_i = \mathbf{0}. \tag{129}$$

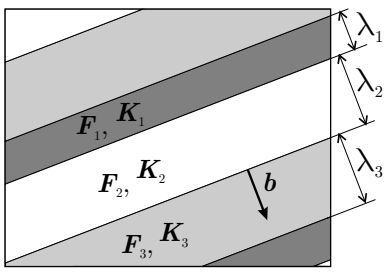

Figure 14. first-order laminate for $N = 3$ with normal vector $\mathbf{b}$. (Originally published in Hackl and Kochmann (2008).)

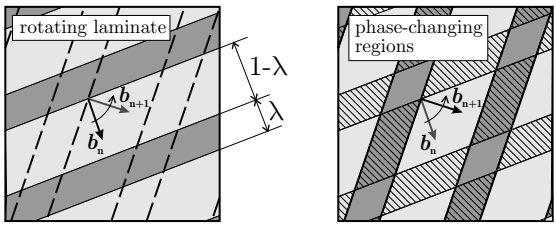

Figure 15. Rotation of the original laminate (for simplicity with only two domains with volume fractions λ and $1-\lambda$) from the old normal vector $\mathbf{b}_n$ to the new normal vector $\mathbf{b}_{n+1}$. The right graphic highlights the hatched regions which have changed their domain membership upon rotation and hence caused dissipation. (Originally published in Kochmann and Hackl (2011).)

Let us consider the normal vector $\mathbf{b}$ as ingrained into the material since any change of $\mathbf{b}$ would require a change of the internal variables and thus lead to dissipation. The amplitudes $\mathbf{a}_i$ on the other hand can be changed purely elastically. This suggests to define a semi-relaxed energy by

$$\Psi^{\mathrm{rel}}(\mathbf{F},\lambda,\mathbf{z},\mathbf{b}) = \inf\Big\{ \sum_{i=1}^{N} \lambda_i \Psi(\mathbf{F}_i,\mathbf{z}_i) \;\Big|\; \mathbf{a}_i,\ \sum_{i=1}^{N} \lambda_i \mathbf{a}_i = \mathbf{0}\Big\}, \tag{130}$$

where we introduced the abbreviations $\lambda = \{\lambda_1,\dots,\lambda_N\}$ and $\mathbf{z} = \{\mathbf{z}_1,\dots,\mathbf{z}_N\}$. Note that the energy is only partially relaxed since full relaxation would require further minimization with respect to the internal variables (and in particular with respect to $\mathbf{b}$). If we assume that the lamination respects the ordering $\{1,\dots,N\}$ and that the normal vector $\mathbf{b}$ remains fixed, the relaxation of the dissipation is given by

$$\begin{aligned}\Delta^*(\lambda,\mathbf{z},\dot\lambda,\dot{\mathbf{z}}) = \sum_{i=1}^{N} \lambda_i\, \Delta(\mathbf{z}_i,\dot{\mathbf{z}}_i) + \inf\Big\{ \sum_{i,j=1}^{N} \Delta\lambda_{ij}\, D(\mathbf{z}_i,\mathbf{z}_j) \;\Big|\; \Delta\lambda_{ij},\\ \sum_{i=1}^{N}\Delta\lambda_{ij} = \dot\lambda_j, \sum_{j=1}^{N}\Delta\lambda_{ij} = \dot\lambda_i, \Delta\lambda_{ij} = 0 \text{ for } |(i-j) \bmod N| \neq 1\Big\}.\end{aligned} \tag{131}$$

Now once again from (7) we obtain evolution equations for λ and $\mathbf{z}$ for fixed $\mathbf{b}$. As can be seen from Fig. 15, a change of the laminate orientation (i.e., a change of $\mathbf{b}$) results in changes of the plastic slip in certain regions

of the deformed body and is hence associated with a specific amount of dissipation given by

$$D_{\mathbf{b}}(\lambda, \mathbf{z}) = \sum_{i,j=1}^{N} \lambda_i \lambda_j D(\mathbf{z}_i, \mathbf{z}_j). \tag{132}$$

The dissipation $D_{\mathbf{b}}$ is proportional to the area of those regions which change their domain membership upon rotation and to the dissipation distance required to turn a region of domain i into a part of domain j. We assume that a jump in orientation will take place as soon as it becomes energetically favorable. This gives

$$\inf \left\{ \Psi^{\mathrm{rel}}(\mathbf{F}, \lambda, \mathbf{z}, \mathbf{b}_{n+1}) - \Psi^{\mathrm{rel}}(\mathbf{F}, \lambda, \mathbf{z}, \mathbf{b}_n) \,\middle|\, \mathbf{b}_{n+1},\ |\mathbf{b}_{n+1}| = 1 \right\} + D_{\mathbf{b}}(\lambda, \mathbf{z}) \leq 0 \tag{133}$$

for given $\mathbf{b}_n, \lambda, \mathbf{z}$. Eq. (133) completes the description of the inelastic evolution of a first-order laminate. In the sequel, this formal concept will be applied to model problems of crystal plasticity, where we follow ideas of Carstensen et al. (2002); Hackl and Kochmann (2008); Kochmann and Hackl (2010a).

6 Model problem: crystal plasticity

6.1 Relaxed potentials

Due to the non-quasiconvex energy of a homogeneous single crystal, microstructures arise as energy minimizers. Let us assume a first-order laminate microstructure with N domains having interfaces with unit normal $\mathbf{b}$. We define the deformation gradient in domain i according to (127). To every volume fraction i there correspond values of the internal variables γ_{ij} and p_{ij} for each active slip system j. To ensure incompressibility of each laminate domain, we must enforce that for every domain i we have $\det \mathbf{F}_i = 1$, which is equivalent to

$$\mathbf{a}_i \cdot \mathbf{b} = 0. \tag{134}$$

We assume once again a Neo-Hookean material with an elastic free energy density $\Psi_{\mathrm{el}}(\mathbf{F}_{\mathrm{e}}) = \frac{\mu}{2}\left(\operatorname{tr} \mathbf{F}_{\mathrm{e}}^T \mathbf{F}_{\mathrm{e}} - 3\right)$. Taking into account the constraints (129) and (134) by introducing Lagrange multipliers $\mathbf{\Lambda}$ and ρ_i, the semi-

relaxed energy can be written as

$$\begin{aligned}&\Psi^{\mathrm{rel}}(\mathbf{F},\lambda_i,\gamma_{ij},p_{ij},\mathbf{b})\\&=\inf\Big\{\,\frac{\mu}{2}\sum_i^N\lambda_i\,[\,\mathrm{tr}\,\mathbf{C}_{\mathrm{e},i}-3-2\boldsymbol{\Lambda}\cdot\mathbf{a}_i-2\rho_i\mathbf{a}_i\cdot\mathbf{b}]+\sum_i^N\lambda_i\Psi_{\mathrm{p}}(p_{ij})\;\Big|\;\mathbf{a}_i\,\Big\}\end{aligned}\tag{135}$$

where an appropriate choice of Ψ_{p} is assumed. We denote by $\mathbf{C}_{\mathrm{e},i}=\mathbf{F}_{\mathrm{e},i}^{\mathsf{T}}\mathbf{F}_{\mathrm{e},i}$ the elastic right Cauchy-Green tensor in domain i with, following (23) and (127),

$$\mathbf{F}_{\mathrm{e},i}=\mathbf{F}_i\mathbf{F}_{\mathrm{p},i}^{-1}=\mathbf{F}(\boldsymbol{I}+\mathbf{a}_i\otimes\mathbf{b})(\boldsymbol{I}-\sum_j^n\gamma_{ij}\mathbf{s}_j\otimes\mathbf{m}),\tag{136}$$

Let us define

$$\mathbf{b}_i=\mathbf{b}\cdot\mathbf{F}_{\mathrm{p},i}^{-1}\mathbf{F}_{\mathrm{p},i}^{-T}.\tag{137}$$

Minimization in (135) with respect to the unknown quantities $\mathbf{a}_i$ yields the stationarity condition

$$\mathbf{a}_i\;\mathbf{b}_i\cdot\mathbf{b}=\mathbf{C}^{-1}\boldsymbol{\Lambda}+\rho_i\,\mathbf{C}^{-1}\mathbf{b}-\mathbf{b}_i,\tag{138}$$

where $\mathbf{C}=\mathbf{F}^{\mathsf{T}}\mathbf{F}$ denotes the overall right Cauchy-Green tensor. Via some algebraic manipulation we finally arrive at

$$\begin{aligned}\rho_i&=\frac{\mathbf{b}_i\cdot\mathbf{b}}{\mathbf{b}\cdot\mathbf{C}^{-1}\mathbf{b}},\\\mathbf{C}^{-1}\boldsymbol{\Lambda}&=\frac{1}{\sum_i\frac{\lambda_i}{\mathbf{b}_i\cdot\mathbf{b}}}\left(\sum_i\frac{\lambda_i}{\mathbf{b}_i\cdot\mathbf{b}}\mathbf{b}_i-\frac{1}{\mathbf{b}\cdot\mathbf{C}^{-1}\mathbf{b}}\mathbf{C}^{-1}\mathbf{b}\right),\\\mathbf{a}_i&=\frac{1}{\mathbf{b}_i\cdot\mathbf{b}}\mathbf{C}^{-1}\boldsymbol{\Lambda}+\frac{1}{\mathbf{b}\cdot\mathbf{C}^{-1}\mathbf{b}}\mathbf{C}^{-1}\mathbf{b}-\frac{1}{\mathbf{b}_i\cdot\mathbf{b}}\mathbf{b}_i.\end{aligned}\tag{139}$$

Application of (139) to (135) yields the relaxed energy in the form

$$\begin{aligned}&\Psi^{\mathrm{rel}}(\mathbf{F},\lambda_i,\gamma_{ij},p_{ij},\mathbf{b})\\&=\sum_i^N\lambda_i\Psi_{\mathrm{p}}(p_{ij})+\frac{\mu}{2}\left[\frac{1}{\sum_i^N\frac{\lambda_i}{\mathbf{b}_i\cdot\mathbf{b}}}\left(\sum_j^N\sum_k^N\frac{\lambda_j\lambda_k\mathbf{b}_j\cdot\mathbf{C}\mathbf{b}_k}{\mathbf{b}_j\cdot\mathbf{b}\;\mathbf{b}_k\cdot\mathbf{b}}-\frac{1}{\mathbf{b}\cdot\mathbf{C}^{-1}\mathbf{b}}\right)\right.\\&\qquad\left.+\sum_i^N\lambda_i\left(\frac{\mathbf{b}_i\cdot\mathbf{b}}{\mathbf{b}\cdot\mathbf{C}^{-1}\mathbf{b}}-\frac{\mathbf{b}_i\cdot\mathbf{C}\mathbf{b}_i}{\mathbf{b}_i\cdot\mathbf{b}}\right)+\sum_i^N\lambda_i\,\mathrm{tr}\,\left(\mathbf{F}_{\mathrm{p},i}^{-T}\mathbf{C}\mathbf{F}_{\mathrm{p},i}^{-1}\right)-3\right].\end{aligned}\tag{140}$$

The most general case to be treated analytically presumes that all active slip systems within one laminate domain lie within the same common glide plane (but this common glide plane may well differ between domains). In the sequel we will make use of this simplification, i.e. $\mathbf{m}_{ij} = \mathbf{m}_i$ within each domain i. In this case we obtain the neat formulation

$$\mathbf{b}_i = \mathbf{b} - \sum_j^n \gamma_{ij}(\mathbf{b}\cdot\mathbf{m}_i\,\mathbf{s}_{ij} + \mathbf{b}\cdot\mathbf{s}_{ij}\,\mathbf{m}_i) + \sum_j^n \gamma_{ij}^2\,\mathbf{b}\cdot\mathbf{s}_{ij}\,\mathbf{s}_{ij}, \tag{141}$$

and the last term in (140) reduces to

$$\text{tr}\,\left(\mathbf{F}_{\text{p},i}^{-T}\mathbf{C}\mathbf{F}_{\text{p},i}^{-1}\right) = \sum_j^n \left(\gamma_{ij}^2\,\mathbf{s}_{ij}\cdot\mathbf{C}\mathbf{s}_{ij} - 2\,\gamma_{ij}\,\mathbf{s}_{ij}\cdot\mathbf{C}\mathbf{m}_i\right). \tag{142}$$

From this general case several simpler ones can be deduced. On the one hand, if only one slip system $(\mathbf{s}_i, \mathbf{m}_i)$ is active within each domain i of the laminate but the active slip systems may differ between domains, then the above solution holds with

$$\mathbf{b}_i = \mathbf{b} - \gamma_i(\mathbf{b}\cdot\mathbf{m}_i\,\mathbf{s}_i + \mathbf{b}\cdot\mathbf{s}_i\,\mathbf{m}_i) + \gamma_i^2\mathbf{b}\cdot\mathbf{s}_i\,\mathbf{s}_i. \tag{143}$$

This is the typical case of infinite latent hardening in each domain but differing orientations between domains. The interfaces are then formed as so-called dipolar dislocation walls. Finally, the case of only one single active slip system $(\mathbf{s}, \mathbf{m})$ throughout the entire crystal (i.e. equal active slip systems in all laminate domains) has been studied Hackl and Kochmann (2008); Kochmann and Hackl (2010a). This assumption reduces the above form to

$$\mathbf{b}_i = \mathbf{b} - \gamma_i(\mathbf{b}\cdot\mathbf{m}\;\mathbf{s} + \mathbf{b}\cdot\mathbf{s}\;\mathbf{m}) + \gamma_i^2\mathbf{b}\cdot\mathbf{s}\;\mathbf{s}. \tag{144}$$

For instructiveness of the following examples, let us finally reduce the present model to a two-domain laminate ($N = 2$) and define the volume fraction of domain 2 by λ. Taking into account (28), the dissipation potential, defined in (131), may be written for a single active slip system within each domain in the form

$$\Delta^*(\lambda, \gamma_i, \dot\lambda, \dot\gamma_i) = r\left((1-\lambda)\,|\dot\gamma_1| + \lambda\,|\dot\gamma_2| + \left|\dot\lambda(\gamma_1 - \gamma_2)\right|\right). \tag{145}$$

and the Lagrange functional reads

$$\mathcal{L}(\mathbf{F}, \lambda, \gamma_i, p_i, \dot\lambda, \dot\gamma_i, \mathbf{b}) = \frac{\mathrm{d}}{\mathrm{d}t}\,\Psi^{\text{rel}}(\mathbf{F}, \lambda, \gamma_i, p_i, \mathbf{b}) + \Delta^*(\lambda, \gamma_i, \dot\lambda, \dot\gamma_i). \tag{146}$$

Here, one of the major differences of the present model to previous approaches becomes apparent from the last term in (145): a change of the volume fractions (here, of λ) causes dissipation. However, we do not consider the dissipation required to transform some region with originally no plastic history into a part of the increasing domain (an increase of domain 2 would then mean $\dot{\lambda} > 0$ and $\Delta^* = r|\dot{\lambda}\,\gamma_2|$). Instead, we correctly account for the transformation of some part originally belonging to domain 1 into a part of the increasing domain 2. Therefore, the amount of dissipation depends on the microstructure at the beginning of each time step.

For multiple active slip systems within each domain a careful choice must be made for the form of the dissipation potential (see the discussion above) as integration of (30) to the dissipation distance can hardly be done analytically, such that the dissipation due to changes of the volume fractions is still a key open question. A possible approximation Kochmann and Hackl (2010a) can be formulated when assuming that the dissipation from volumetric changes results from the sum of the amounts of dissipation required to change the plastic states along each active slip system independently. For two active slip systems we hence write, using (32),

$$\Delta^*(\lambda, \gamma_{ij}, \dot{\lambda}, \dot{\gamma}_{ij}) = r\left[(1-\lambda)\Delta(\dot{\gamma}_{11}, \dot{\gamma}_{12}) + \lambda\,\Delta(\dot{\gamma}_{21}, \dot{\gamma}_{22}) + \left|\dot{\lambda}(|\gamma_{11} - \gamma_{21}| + |\gamma_{12} - \gamma_{22}|)\right|\right]. \tag{147}$$

6.2 Evolution equations

Via the principle given in (7) we arrive at evolution equations for λ and γ_{ij}, i.e., the stationarity conditions from minimizing the above Lagrange functional, which read

$$0 \in \frac{\partial \Psi^{\mathrm{rel}}}{\partial \lambda} + \frac{\partial \Delta^*}{\partial \dot{\lambda}}, \tag{148}$$

$$0 \in \frac{\partial \Psi^{\mathrm{rel}}}{\partial \gamma_{ij}} + \frac{\partial \Psi^{\mathrm{rel}}}{\partial p_{ij}} \operatorname{sign} \dot{\gamma}_{ij} + \frac{\partial \Delta^*}{\partial \dot{\gamma}_{ij}}, \text{ for } 1 \le i \le N,\ 1 \le j \le n. \tag{149}$$

With our goal of computing the evolution of plastic microstructures in mind, we need to find an incremental formulation to be solved numerically, using finite deformation increments $[\mathbf{F}_n, \mathbf{F}_{n+1}]$ with known initial conditions $\mathbf{F}_n$, $\gamma_{ij,n}$, λ_n, $p_{ij,n}$ and the known deformation $\mathbf{F}_{n+1}$ at the end of the time step. Then, (148) and (149) can be used to compute the updates $\Delta\gamma_{ij} = \gamma_{ij,n+1} - \gamma_{ij,n}$, $\Delta\lambda = \lambda_{n+1} - \lambda_n$ and $\Delta p_{ij} = p_{ij,n+1} - p_{ij,n}$ for given $\Delta\mathbf{F} = \mathbf{F}_{n+1} - \mathbf{F}_n$.

Before outlining the numerical scheme, we need to discuss three important aspects of the present model. Firstly, any change of λ results in mixing

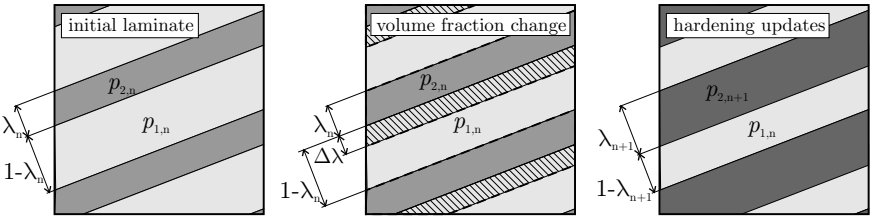

Figure 16. Schematic view of the update procedure: as the volume fractions change in the initial laminate (here, the volume fraction of domain 2, λ, increases), the updated, internal hardening parameters are obtained from energetic averaging of the initial values. (Originally published in Kochmann and Hackl (2011).)

the formerly pure domains in a small part of the body; e.g. an increase of λ in the two-domain laminate will raise the volume fraction of domain 2 (with history variables p_{2j}) by adding certain regions which were previously associated with domain 1 and hence exhibited history variable values p_{1j}. As a consequence, the hardening histories p_{2j} should be updated to account for a mixture of the two domains (see Fig. 16). We propose to obtain the updated p_{ij}-values by computing the energetic average of the original values weighted by the volume fractions. For example for a single active slip system and for $\lambda_{n+1} = \lambda_n + \Delta\lambda$ and $\Delta\lambda > 0$ we have

$$(\lambda_n + \Delta\lambda)p^\alpha_{2,n+1} = \lambda_n\, p^\alpha_{2,n} + \Delta\lambda\, p^\alpha_{1,n}, \qquad p_{1,n+1} = p_{1,n}, \tag{150}$$

and analogously for $\Delta\lambda < 0$

$$(1 - \lambda_n - \Delta\lambda)p^\alpha_{1,n+1} = (1 - \lambda_n)p^\alpha_{1,n} - \Delta\lambda\, p^\alpha_{2,n}, \qquad p_{2,n+1} = p_{2,n}. \tag{151}$$

The corresponding formulations for multiple active slip systems are analogous and assume no interaction between the different slip systems at this step (cross-hardening is accounted for by the choice of Ψ_{p}). So, we omit these lengthy equations here for conciseness; see Kochmann (2009); Kochmann and Hackl (2010a) for details.

Secondly, once a laminate microstructure exists, changes of the orientation vector $\mathbf{b}$ will be treated using the criterion given in (133). We check for each load increment whether or not a rotation of the laminate is energetically admissible. From (132) (see also Fig. 16) it follows for a single active slip system that

$$D_{\mathbf{b}}(\lambda, \gamma_1, \gamma_2) = 2r\lambda(1 - \lambda)|\gamma_1 - \gamma_2|. \tag{152}$$

For multiple active slip systems the same discussion as above applies since the dissipation distance cannot be determined in a simple way. Therefore, we make use of the approximation (32) for a double-slip material Kochmann and Hackl (2010a):

$$D_{\mathbf{b}}(\lambda, \gamma_{ij}) = 2r\lambda(1-\lambda)\left(|\gamma_{11} - \gamma_{21}| + |\gamma_{12} - \gamma_{22}|\right). \tag{153}$$

Then, we obtain $\mathbf{b}_{n+1}$ from

$$\begin{aligned}\min\big\{\Psi^{\mathrm{rel}}(\mathbf{F}_n, \lambda_n, \gamma_{ij,n}, p_{ij,n}, \mathbf{b}_{n+1}) - \Psi^{\mathrm{rel}}(\mathbf{F}_n, \lambda_n, \gamma_{ij,n}, p_{ij,n}, \mathbf{b}_n) \\ + D_{\mathbf{b}}(\lambda, \gamma_{ij,n}) \mid \mathbf{b}_{n+1},\, |\mathbf{b}_{n+1}| = 1\big\} \leq 0.\end{aligned} \tag{154}$$

Thirdly, a crucial issue is the initiation of the laminate microstructure from the originally uniform crystal. On the one hand, it is possible to numerically compute the condensed semi-relaxed energy, e.g. for a single-slip laminate

$$\begin{aligned}\Psi_{n+1}^{\mathrm{cond,rel}}(\mathbf{F}_{n+1}) = \min\Big\{\Psi^{\mathrm{rel}}(\mathbf{F}_{n+1}, \gamma_{1,n}, \gamma_2, \lambda, \mathbf{b}) + r\,|\lambda(\gamma_2 - \gamma_{1,n})| \;\Big|\; \\ \gamma_2, \lambda, \mathbf{b},\, p_2 = |\gamma_2|,\; 0 \leq \lambda \leq 1,\; |\mathbf{b}| = 1\Big\}\end{aligned} \tag{155}$$

and check whether or not $\Psi_{n+1}^{\mathrm{cond,rel}} \leq \Psi_{n+1}^{\mathrm{cond}}$, i.e. if the formation of a laminate can reduce the energy below that of the homogeneous crystal, accounting for the dissipation to create the new domain. If $\Psi_{n+1}^{\mathrm{cond,rel}} \leq \Psi_{n+1}^{\mathrm{cond}}$ then a laminate forms with $(\gamma_2, \lambda, \mathbf{b}) = \mathrm{argmin}\Psi_{n+1}^{\mathrm{cond,rel}}$ from (155). On the other hand, one can treat the laminate initiation as follows. At the beginning of each time increment, one computes the driving force $q_\lambda = -\partial\Psi/\partial\lambda$ on the volume fractions in the limit of a marginal amount of domain 2, i.e. for single-slip

$$q_0(\mathbf{F}, \gamma_1, \gamma_2, p_1, p_2, \mathbf{b}) = \lim_{\lambda \to 0} q_\lambda(\mathbf{F}, \lambda, \gamma_1, \gamma_2, p_1, p_2, \mathbf{b}). \tag{156}$$

Maximizing this driving force with respect to $\mathbf{b}_{n+1}$ and $\gamma_{2,n+1}$, one can determine the energetically favored values of these quantities in the arising domain 2, i.e.

$$\begin{aligned}(\mathbf{b}_{n+1}, \gamma_{2,n+1}) = \mathrm{argmax}\,\Big\{q_0(\mathbf{F}_{n+1}, \gamma_{1,n}, \gamma_{2,n+1}, p_{1,n}, p_{2,n+1}, \mathbf{b}_{n+1}) \;\Big|\; \\ p_{2,n+1} = |\gamma_{2,n+1}|,\; |\mathbf{b}_{n+1}| = 1\,\Big\}.\end{aligned} \tag{157}$$

One then determines the actual value of λ_{n+1} by solving

$$\begin{aligned}r\,|\gamma_{1,n} - \gamma_{2,n+1}| \\ = q_\lambda(\mathbf{F}_{n+1}, \lambda_{n+1}, \gamma_{1,n}, \gamma_{2,n+1}, p_{1,n}, p_{2,n+1} = |\gamma_{2,n+1}|, \mathbf{b}_{n+1}).\end{aligned} \tag{158}$$

If there exists a solution λ_{n+1}, a laminate forms with domain 2 having the determined values of λ_{n+1}, $\gamma_{2,n+1}$ and $\mathbf{b}_{n+1}$.

6.3 Numerical scheme

Our numerical scheme computes the microstructure evolution by incrementally minimizing the Lagrange functional. As we use the relaxed energy and dissipation functional, this constitutes in principle a well-posed problem and we can resort to solving the stationarity conditions. We here demonstrate the general procedure for single-slip plasticity, i.e. we compute the updates of the plastic slips $\Delta\gamma_{ij}$, the history variable updates Δp_i, and the volume fraction update $\Delta\lambda$ from the stationarity conditions (148) and (149). For a given load increment $[\mathbf{F}_n, \mathbf{F}_{n+1}]$, each step starts with the current state as initial values $\lambda_n, \gamma_{i,n}, p_{i,n}$, and solves the stationarity conditions in order to update all internal variables at time t_{n+1} with known load $\mathbf{F}_{n+1}$. For the initially homogeneous material the interface normal $\mathbf{b}_{n+1}$ as well as the internal variables of the originating second laminate domain, λ_{n+1}, $\gamma_{2,n+1}$ and $p_{2,n+1}$, are determined from (157). Once a laminate has formed, the evolution of the internal variables λ, γ_i and p_i is computed using a staggered scheme. In a first step a time-discretized version of (148) is solved for the increment $\Delta\lambda$ for fixed γ_1 and γ_2. Afterwards, p_1 and p_2 are updated via (150) or (151). Then, in a second step, (149) are solved for the increments $\Delta\gamma_1$ and $\Delta\gamma_2$ for fixed λ. Finally, the updated values of $\lambda, \gamma_1, \gamma_2, p_1, p_2$ are transfered to the next time-step. This procedure is summarized in Table 1.

For multiple active slip systems the numerical procedure is analogous and involves additional internal variables (the plastic slips γ_{ij} on all active slip systems). As the only modification we solve for the updates of the plastic slips also in a staggered manner instead of solving for all values $\Delta\gamma_{ij}$ at the same time. Other than that, the algorithm takes the form summarized above.

Note that the order of solving the stationarity conditions is only of minor importance as long as the the load increment is kept small, which we tacitly assume. With increasing load increments the order of solution gains influence; in particular, the initial laminate formation requires very small increments to capture the actual onset of lamination and thus the correct variables in the newly forming laminate domain.

(a) incremental load update: $\mathbf{F}_{n+1} = \mathbf{F}_n + \Delta\mathbf{F}$

(b) find λ_{n+1} (assume $\gamma_i = \gamma_{i,n} = const.$):

- for the initially uniform single-crystal ($\lambda_n = 0$) find $\mathbf{b}_{n+1}$, $\gamma_{2,n+1}$ and λ_{n+1} from (155), i.e.

$$
\begin{aligned}
&(\mathbf{b}_{n+1}, \gamma_{2,n+1}, \lambda_{n+1}) \\
&= \operatorname{argmin} \Big\{ \Psi^{\mathrm{rel}}(\mathbf{F}_{n+1}, \gamma_{1,n}, \gamma_2, \lambda, \mathbf{b}) + r\,|\lambda(\gamma_2 - \gamma_{1,n})| \Big| \gamma_2, \lambda, \mathbf{b} \ : \\
&\qquad\qquad p_2 = |\gamma_2|,\ 0 \le \lambda \le 1,\ |\mathbf{b}| = 1 \Big\} \\
&\qquad\qquad \Rightarrow \quad \text{if } 0 < \lambda_{n+1} \le 1, \text{ update } \ \lambda_{n+1}, \gamma_{2,n+1}, \mathbf{b}_{n+1}
\end{aligned}
$$

- for an existing laminate microstructure ($\lambda_n > 0$) solve:

$$
\begin{aligned}
q_\lambda(\mathbf{F}_{n+1}, \lambda_n + \Delta\lambda, \gamma_{i,n}, p_{i,n}) \operatorname{sign} \Delta\lambda &= r\,|\gamma_{1,n} - \gamma_{2,n}| \\
\Rightarrow \quad \lambda_{n+1} &= \lambda_n + \Delta\lambda
\end{aligned}
$$

and check for a laminate rotation by finding $\mathbf{b}_{n+1}$ such that:

$$
\min_{\mathbf{b}_{n+1}} \Psi^{\mathrm{rel}}(\mathbf{b}_{n+1}) - \Psi^{\mathrm{rel}}(\mathbf{b}_n) + 2r\lambda_{n+1}(1 - \lambda_{n+1})\,|\gamma_{1,n} - \gamma_{2,n}| \overset{?}{\le} 0
$$

- if $\lambda_{n+1} \neq \lambda_n$: update $p_{i,n+1}$ according to (150) or (151)

(c) find $\gamma_{i,n+1}$ (assume $\lambda = \lambda_{n+1} = const.$) by solving:

$$
\left[
\begin{aligned}
&\frac{\partial \Psi^{\mathrm{rel}}}{\partial \gamma_1} + \frac{\partial \Psi^{\mathrm{rel}}}{\partial p_1} \operatorname{sign} \Delta\gamma_1 \Big|_{\substack{\gamma_{i,n} + \Delta\gamma_i \\ p_{i,n} + |\Delta\gamma_i|}} = -r\,(1 - \lambda_{n+1}) \operatorname{sign} \Delta\gamma_1 \\
&\frac{\partial \Psi^{\mathrm{rel}}}{\partial \gamma_2} + \frac{\partial \Psi^{\mathrm{rel}}}{\partial p_2} \operatorname{sign} \Delta\gamma_2 \Big|_{\substack{\gamma_{i,n} + \Delta\gamma_i \\ p_{i,n} + |\Delta\gamma_i|}} = -r\,\lambda_{n+1} \operatorname{sign} \Delta\gamma_2
\end{aligned}
\right.
$$

$$
\Rightarrow \quad \gamma_{i,n+1} = \gamma_{i,n} + \Delta\gamma_i, \quad p_{i,n+1} = p_{i,n} + |\Delta\gamma_i|
$$

Table 1. Incremental solution for a single active slip system

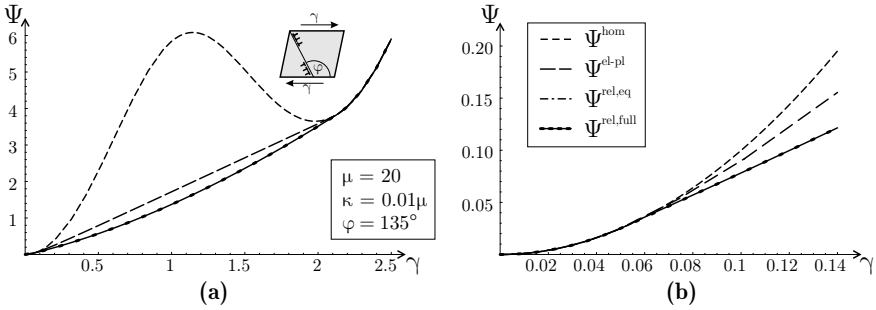

Figure 17. Original energy Ψ^{hom} and possible relaxations $\Psi^{\text{el-pl}}$, $\Psi^{\text{rel,eq}}$ and $\Psi^{\text{rel,full}}$ as defined in Section 6.4. The right image shows a magnification of the initial section of the left one. (Originally published in Kochmann and Hackl (2011).)

6.4 Numerical full relaxation and comparison with the convex lower bound

As a first result it is interesting to present the fully relaxed energy obtained from minimizing the partially relaxed functional (140) with respect to the internal variables λ, γ_i, p_i and $\mathbf{b}$. As the energy is semi-relaxed with respect to the amplitudes $\mathbf{a}_i$ already, minimization with respect to the remaining unknowns can conveniently be performed numerically. Approximations of the relaxed energy can be determined for specific microstructures, for which a solution is simple to find, Carstensen et al. (2008). The unrelaxed energy Ψ^{hom} for a homogeneous deformation state (which is clearly non-convex) is illustrated in Fig. 17 along with a comparison of several relaxation results based on the present energy formulation. The energy path corresponds to a plane-strain simple shear test with overall deformation gradient $\mathbf{F} = \gamma\, \mathbf{e}_1 \otimes \mathbf{e}_2$ with a single active slip system aligned under the angle $\varphi = 135°$. The fully relaxed energy is obtained from

$$\Psi^{\text{rel,full}}(\mathbf{F}) = \min \left\{ \Psi^{\text{rel}}(\mathbf{F}, \lambda, \gamma_i, p_i, \mathbf{b}) \;\middle|\; \gamma_i, \lambda, \mathbf{b} \;:\; p_i = |\gamma_i| \,, \; 0 \le \lambda \le 1, \; |\mathbf{b}| = 1 \right\}, \tag{159}$$

which has been used in the literature in different settings to compute laminate microstructures, see e.g. Bartels et al. (2004); Carstensen et al. (2008).

The highest of the approximate relaxed energy curves in Fig. 17 is obtained from mixing one purely elastic domain with one elasto-plastic domain ($\gamma_1 = 0$, $\gamma_2 \neq 0$), i.e. by assuming a spatial separation of elastic and plastic

deformation:

$$\Psi^{\text{el-pl}}(\mathbf{F}) = \min \Big\{ \Psi^{\text{rel}}(\mathbf{F}, \lambda, \gamma_i, p_i, \mathbf{b}) \; \Big| \lambda, \gamma_2, \mathbf{b} \; : \; \gamma_1 = p_1 = 0, \; p_2 = |\gamma_2|, \\ 0 \leq \lambda \leq 1, \; |\mathbf{b}| = 1 \big\} \,. \tag{160}$$

Another possible relaxation corresponds to a laminate approximation where both domains are elasto-plastic but with equal amounts of plastic slip of opposite signs ($\gamma_1 = -\gamma_2 = \gamma$):

$$\Psi^{\text{rel,eq}}(\mathbf{F}) = \min \big\{ \Psi^{\text{rel}}(\mathbf{F}, \lambda, \gamma_i, p_i, \mathbf{b}) \; \big| \, \lambda, \gamma, \mathbf{b} \; : \; \gamma_2 = -\gamma_1 = \gamma, \\ p_1 = p_2 = |\gamma|, \; 0 \leq \lambda \leq 1, \; |\mathbf{b}| = 1 \big\} \,. \tag{161}$$

A comparison of all three energy curves together with the unrelaxed curve is shown in Fig. 17. Clearly, the elastic-plastic energy $\Psi^{\text{el-pl}}$ lies higher than the relaxed condensed energy $\Psi^{\text{rel,full}}$ as well as the energy curve of $\Psi^{\text{rel,eq}}$ (the latter two almost coincide). Note that results in this subsection are for linear hardening ($\alpha = 2$) to allow for a comparison with literature results as e.g. in Carstensen et al. (2008).

The quality of the relaxed energy can be estimated by comparison with the convex energy lower bound. A convex energy hull be defined by

$$\Psi^{\text{conv}}(\mathbf{F}, \lambda, \gamma_i, p_i) = \min \big\{ (1-\lambda)\Psi(\mathbf{F}_1, \gamma_1, p_1) + \lambda \Psi(\mathbf{F}_2, \gamma_2, p_2) \big| \, \mathbf{F}_1, \mathbf{F}_2, \\ \det \mathbf{F}_1 = \det \mathbf{F}_2 = 1, \; (1-\lambda)\mathbf{F}_1 + \lambda \mathbf{F}_2 = \mathbf{F} \big\} \,, \tag{162}$$

Unlike in the case of the laminate energy hulls (with additional constraint $\text{rank}(\mathbf{F}_1 - \mathbf{F}_2) \leq 1$) deformation gradients in the two domains of the convex energy hull do not have to satisfy compatibility.

Exemplary comparisons of the convex and the fully relaxed energy curves are illustrated in Fig. 18 for the given values of the internal variables. Examples comprise a tension-compression test with the overall deformation gradient $\mathbf{F}_a$ and a mixed tension-compression-shear test with $\mathbf{F}_b$ with slip system orientations defined according to the sketch included in Fig. 18.

$$\mathbf{F}_a = \begin{pmatrix} 1+\delta & 0 & 0 \\ 0 & 1/(1+\delta) & 0 \\ 0 & 0 & 1 \end{pmatrix}, \qquad \mathbf{F}_b = \begin{pmatrix} e^{\delta} & \delta & 0 \\ 0 & e^{-\delta} & 0 \\ 0 & 0 & 1 \end{pmatrix} \tag{163}$$

For the chosen straining paths and internal variables the difference between the relaxed and the convex energy curve is small. An overview of the deviation $\Delta\Psi(\mathbf{F}) = \Psi^{\text{rel,full}}(\mathbf{F}) - \Psi^{\text{conv}}(\mathbf{F})$ for the above two examples is illustrated in Fig. 18d. For the example in Fig. 18a the relative deviation of the relaxed energy from the convex hull is less than 3% everywhere and

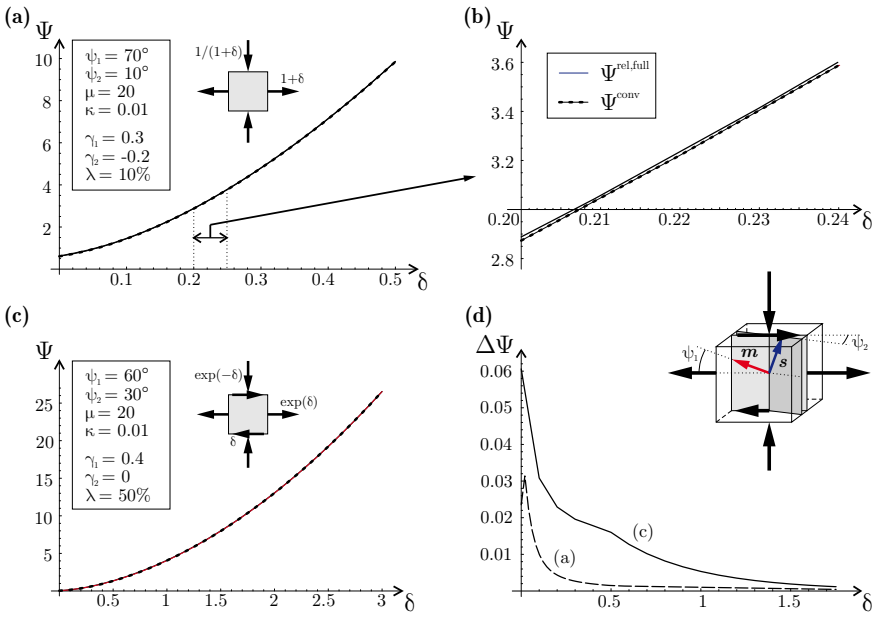

Figure 18. Comparison of the numerically relaxed energy and the convex hull lower bound of the energy for given straining paths with fixed internal variables. (Originally published in Kochmann and Hackl (2011).)

quickly decays to below 0.2% with increasing strain (and, of course, the relaxed energy lies above the convex hull). The example in Fig. 18c exhibits a larger relative error (in particular for small strains δ) of less than 6% everywhere. With increasing strain δ the deviation rapidly decreases to less than 1%, which hints at a good approximation of the quasiconvex envelope by the (semi-)relaxed energy, since the quasiconvex energy hull ist bounded from above and below by the laminate approximation of the rank-one-convex hull and the convex hull, respectively. Other examples for various three-dimensional deformation paths and slip system orientations confirm only little deviation of the laminate upper bound as compared to the convex lower bound.

It is theorized that the larger difference at smaller strains results from the necessity to account for higher-order laminates. Previous works have shown, see e.g. Bartels et al. (2004), that the formation of higher-order laminates indeed lowers the laminate energy compared to the energy of a

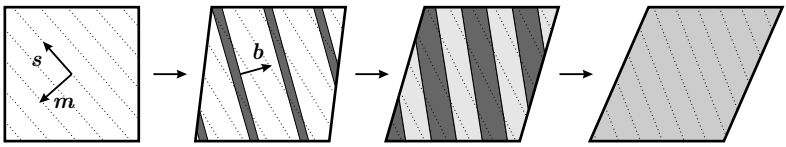

Figure 19. Microstructure development of a first-order laminate for a simple shear test with a single active slip system. Two bifurcated laminate domains arise with common surface normal **b**. The newly nucleated domain 2 exhibits finite plastic slip already at the onset of lamination whereas the original domain 1 remains elastic first and eventually yields plastically, too. Volume fractions develop to finally recover the crystal in a stable homogeneous state with uniform plastic slip. (Originally published in Kochmann and Hackl (2011).)

first-order laminate. At larger strains the higher-order laminates collapse to only first-order laminates so that the difference decreases with increasing load.

6.5 Laminate evolution for single-slip plasticity

The numerical scheme outlined above can be applied to arbitrary examples, for which the relaxed energy density is known. As the relaxed energy density derived in the preceding requires incompressible material behavior, we restrict our following examples to volume-preserving deformation paths only. We present results from applying the algorithm in Table 1 to different exemplary problems with varying hardening parameters and active slip systems. For simplicity, we use for all results $\mu = 2$ and $r = 0.001$, and we name results obtained from this method *relaxed*, compared to the *unrelaxed* solution presuming homogeneous deformations. Unless otherwise noted, all subsequent results will be computed with $\alpha = 4$. The active slip systems are characterized for plane problems by the orientation angle φ denoting the angle of the slip direction $\mathbf{s}$ with the x-axis, and for three-dimensional problems according to the characterization of angles introduced in Fig. 18.

Fig. 19 illustrates the general nature of solutions obtained for those problems considered here: First, the crystal behaves in a homogeneous elastic manner. At the onset of lamination, a second domain arises out of the originally uniform single crystal. This newly nucleated domain exhibits a finite amount of plastic slip already, whereas the original domain may still evolve elastically, and it occupies only a small volume fraction of the crystal. (De-

pending on the non-aligned slip system, plastic flow may also occur before the onset of lamination.) Upon further loading both domains eventually exhibit plastic flow and all internal variables evolve. Finally, only one domain remains at the recovery of convexity of the unrelaxed energy, leaving the crystal in a homogeneous stable state with uniform plastic slip and uniform hardening variables.

The first example investigates the microstructure evolution during a plane-strain simple shear test parametrized by the macroscopic deformation gradient

$$\mathbf{F} = \begin{pmatrix} 1 & \gamma & 0 \\ 0 & 1 & 0 \\ 0 & 0 & 1 \end{pmatrix}. \tag{164}$$

Results in Fig. 20 are for $\kappa = 0$ (no hardening) and $\kappa = 0.1$, computed with constant load increments of $\Delta\gamma = 5 \cdot 10^{-4}$ up to a maximum of $\gamma_{\max} = 2.8$. The exact step size of the load increment is of minor importance as long as the increment is kept small. (This is of particular importance for finding the initial laminate.) The slip system is oriented under an angle of $\varphi = 135°$. Because of the non-aligned slip system the material stability of the homogeneous deformation is lost and microstructures arise. Due to the convexity of the unrelaxed energy Ψ^{unrel} for $\gamma < 0$, no microstructures form with negative strain γ. In Fig. 20 we summarize the evolution of the laminate microstructure by illustrating the paths of the energy, the evolution of the volume fraction λ of domain 2, the plastic slips γ_i and the Cauchy shear stress σ_{12} upon straining. Also included is a sketch of the originating laminate and the resultant normal vector $\mathbf{b}$. Note that for simple shear without hardening ($\kappa = 0$) the orientation of the laminate (i.e. the orientation of $\mathbf{b}$ with the x-axis) results under an angle of approximately $-27.59°$, whereas in the case of non-zero hardening ($\kappa = 0.1$) the orientation changes to $-23.49°$. The exemplary evolution of the laminate microstructure during the simple shear test is illustrated in Fig. 21.

As a second example we investigate the microstructure evolution for a plane-strain tension-compression test with the macroscopic deformation gradient

$$\mathbf{F} = \begin{pmatrix} 1+\delta & 0 & 0 \\ 0 & 1/(1+\delta) & 0 \\ 0 & 0 & 1 \end{pmatrix}. \tag{165}$$

Computations were carried out with $\kappa = 0.01$ and with constant load increments $\Delta\delta = 2 \cdot 10^{-4}$ up to the maximum load of $\delta_{\max} = 2.5$. The slip system is oriented under an angle of $\varphi = 70°$. Again, due to the loss of rank-one convexity, the homogeneous deformation state becomes unstable

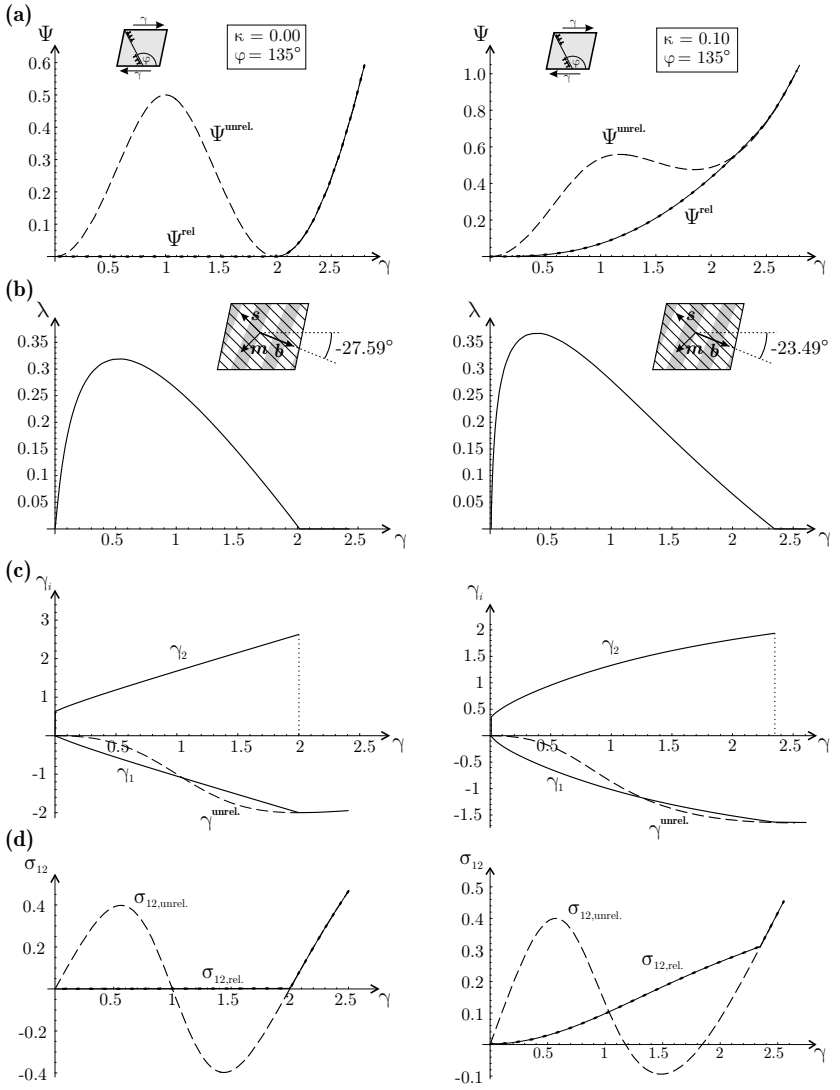

Figure 20. Plane-strain simple shear test for zero and non-zero hardening ($\kappa = 0$ and $\kappa = 0.1$, respectively): (a) comparison of unrelaxed and relaxed energy (i.e., the path of energy obtained from the present incremental approach), (b) origin and evolution of the volume fraction λ of domain 2, (c) evolution of the plastic slips γ_i for both laminate domains compared to the unrelaxed slip, (d) comparison of unrelaxed and relaxed Cauchy shear stress. (Originally published in Kochmann and Hackl (2011).)

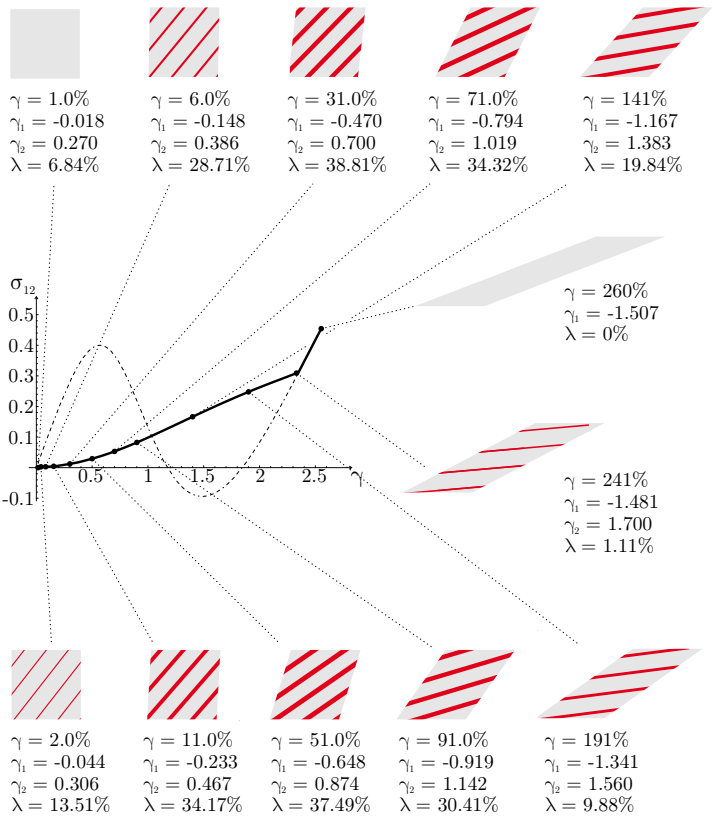

Figure 21. Illustration of the evolving laminate domains during a plane-strain simple shear test. (Originally published in Kochmann and Hackl (2011).)

and decomposes into micro-deformations. The microstructure evolution, including the evolution of plastic slips, volume fractions, and Cauchy stress along with the path of energy upon straining, is summarized in Fig. 22.

In the above examples the body behaves elastically first, until a second domain with finite, non-zero slip γ_2 originates from the uniform ground state till finally domain 1 exhibits plastic flow, too (cf. Fig. 19). Once the laminate has formed with a distinct orientation vector $\mathbf{b}$, we do not

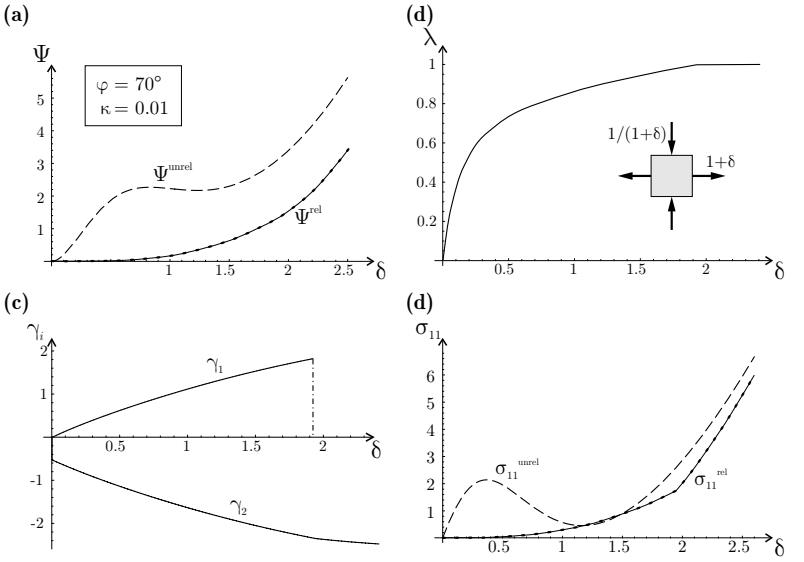

Figure 22. Plane-strain tension-compression test: (a) path of the energy as compared to the unrelaxed solution, (b) evolution of the volume fraction λ of domain 2, (c) evolution of plastic slips γ_i for both domains, (d) comparison of condensed and relaxed Cauchy stress component σ_{11}. (Originally published in Kochmann and Hackl (2011).)

observe laminate rotations due to the large amount of dissipation assumed to be necessary for a rotation. Rotation commonly only occurs when the body is in an almost uniform state (i.e. if $\lambda \approx 0$ or $\lambda \approx 1$). For a detailed investigation of the forming laminate specifics and the correlation between the material parameters and the initial laminate orientation see Hackl and Kochmann (2010); Kochmann (2009).

6.6 Comparison of energy paths and hardening history

Having illustrated the results obtained from the present approach, it is interesting to compare the results obtained here with those obtained from the approach of minimizing a condensed energy functional for a single time step, see e.g. Carstensen et al. (2008). For our purposes the condensed energy functional for the two-domain laminate (now employing the relaxed laminate energy density derived above) can be given for a single time step

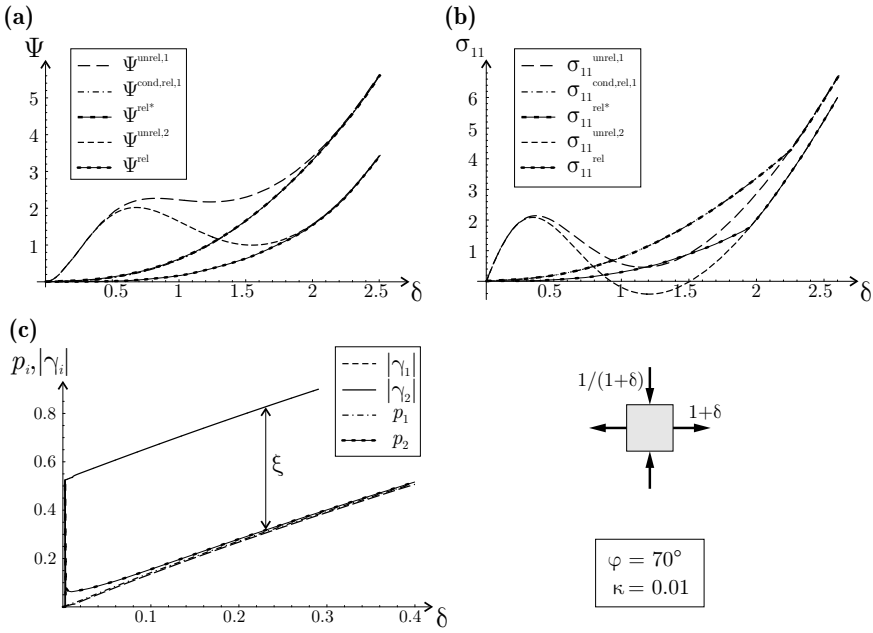

Figure 23. Difference between the present approach and results from energy condensation for a single time step: Comparison of the energy paths, the Cauchy stress component σ_{11} and the developing plastic slips γ_i and hardening variables p_i. (Originally published in Kochmann and Hackl (2011).)

as

$$\Psi^{\mathrm{cond,rel}}(\mathbf{F}) = \min \left\{ \Psi^{\mathrm{rel}}(\mathbf{F}, \lambda, \gamma_i, p_i, \mathbf{b}) + r(1-\lambda)|\gamma_1| + r\,\lambda|\gamma_2| \middle| \gamma_i, \lambda, \mathbf{b}, \right.$$
$$\left. p_i = |\gamma_i|\,,\ 0 \le \lambda \le 1,\ |\mathbf{b}| = 1 \right\}. \tag{166}$$

To avoid confusion about the influence of the dissipation term in the condensed relaxed energy, we can compare the actual paths of energy from both approaches, i.e. we plot the free energy as a function of the applied load. Both approaches determine the evolution of microstructures via minimum energy states, therefore a direct comparison of the energy paths can give a hint at the physical interpretation. A very important aspect of the present model is the updating procedure for the internal hardening variables p_i. In the literature the condensed energy functional is often used for a single time

step only to model the entire course of microstructure evolution, i.e. one assumes no microstructure at the beginning of the time step. As for the hardening variables, these models presume that $p_i = |\gamma_i|$ at each time step, cf. (166). In reality, however, changes of the volume fractions result in a mixture of domains and hence a mixture of previous p_i-values. The present approach accounts for this mixture by the energetic averaging, see (150) and (151).

We have already seen in Fig. 22 that the energy obtained from the present approach may lie considerably below the unrelaxed energy path even beyond the recovery of convexity. We conclude that this energy reduction occurs predominantly due to the updating procedure of the hardening variables, Hackl and Kochmann (2010). To investigate this behavior, let us discuss Fig. 23. The top two images show the energy curves ($\Psi^{\mathrm{unrel},1}$ and Ψ^{rel}) and the curves of the Cauchy stress components ($\sigma_{11}^{\mathrm{unrel},1}$ and $\sigma_{11}^{\mathrm{rel}}$) from Fig. 22, now compared to the condensed solution for the energy and the Cauchy stress, $\Psi^{\mathrm{cond,rel},1}$ and $\sigma_{11}^{\mathrm{cond,rel},1}$, respectively, obtained from condensation of the relaxed energy for a single time step. We see that the latter curves fit perfectly to the unrelaxed solutions at the recovery of convexity and that both the energy and the stress from the present approach attain considerably lower values. The bottom image explains the causal mechanism. The image depicts the evolution of (the absolute value of) the plastic slips γ_i compared to the hardening parameters p_i. It becomes obvious that we still have $p_1 \cong |\gamma_1|$, but – due to the chosen updating procedure – p_2 rapidly decreases from the initial value $|\gamma_2|$ (in the forming laminate) to lower values to finally approach approximately the value of p_1. As the final homogeneous material after lamination contains only domain 2 (see the course of λ in Fig. 22), the homogeneous body exhibits values γ_2 and p_2 where p_2 is $|\gamma_2| - \xi$ (here, ξ is approximately 0.5122). Assuming $p_2 = |\gamma_2| - \xi$ in the unrelaxed (condensed) energy functional results in the curves of $\Psi^{\mathrm{unrel},2}$ and $\sigma_{11}^{\mathrm{unrel},2}$, which very well fit into the picture. Therefore, it becomes apparent that the present approach can reduce the material's energy during lamination considerably below the energy predicted by using the condensed energy functional in a single time step.

If, in contrast, we suppress the energetic averaging of the hardening variables in the present incremental scheme we obtain the curves of Ψ^{rel^*} and $\sigma_{11}^{\mathrm{rel}^*}$ in Fig. 23. These curves almost perfectly match those obtained from the condensation of a single time step, i.e., the results from the present approach without averaged hardening updates seem to coincide with those from the condensed approach).

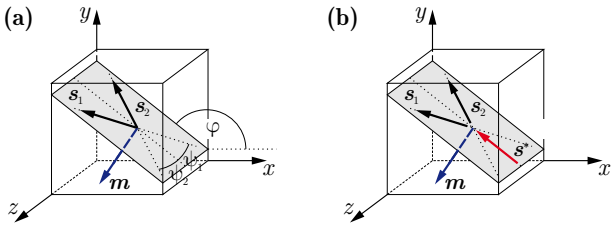

Figure 24. Definition of the active slip system orientations and auxiliary slip system. (Originally published in Kochmann and Hackl (2011).)

6.7 Results for double-slip plasticity

As an example for more than one active slip system we analyze double-slip plasticity in this section. We assume the two active slip systems to lie within the same glide plane to ensure the applicability of (23). As we have pointed out before, analytical integration of the dissipation potential (31) for two active slip systems is not directly possible. In a time-continuous setting, however, where we assume small changes of the internal variables during each time step (except during the particular step during which the initial laminate forms), we can employ (30) in its discrete form. Therefore, a comparison with a corresponding condensed solution is not directly possible. An approximate condensed solution for a single time step (beginning at $\gamma_1 = \gamma_2 = 0$) may be obtained (and is plotted for a comparison in what follows) from assuming $D(\gamma_1, \gamma_2) = r\sqrt{\gamma_1^2 + \gamma_2^2 + 2\gamma_1\gamma_2\,\mathbf{s}_1 \otimes \mathbf{s}_2}$. Another important novelty compared to the previous single-slip problems is the choice of Ψ_p as in (26), which governs the hardening behavior of the material through the κ_{ij}-values. As before, all computations are performed with $\mu = 2$, $r = 0.001$ and $\alpha = 4$.

Let us investigate a simple-shear test with slip system orientations defined by the angles in Fig. 24a, where φ locates the glide plane and ψ_1 and ψ_2 denote the orientation of the two slip directions within the glide plane. Let the macroscopic deformation gradient again be given by $\mathbf{F} = \gamma\,\mathbf{e}_1 \otimes \mathbf{e}_2$. The first example in Fig. 25 is for symmetric active slip systems having $\psi_1 = \psi_2 = \psi = 30°$. As may be expected, the plastic slip along both active slip system is identical due to the symmetric alignment. It is often argued that such symmetric slip systems can by combination provide a new (compound) slip system, here e.g. characterized by the slip direction $\mathbf{s}^*$ in Fig. 24b. The sum of the identical Burgers' vectors on each of the symmetric slip systems jointly provides a Burgers' vector in the new slip system

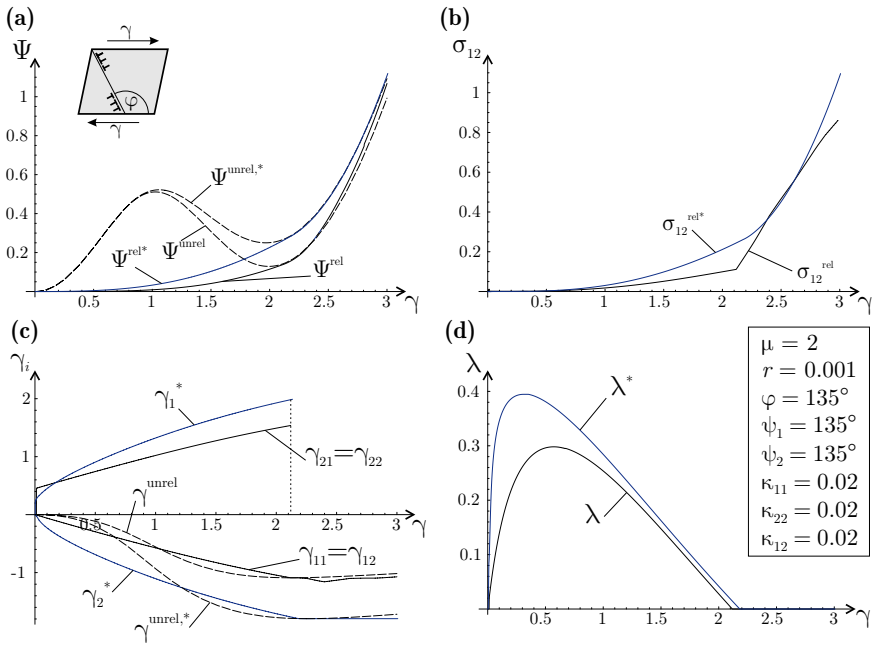

Figure 25. Energy paths compared to the unrelaxed solutions, Cauchy shear stresses, plastic slips compared to the unrelaxed solutions, and volume fractions for a simple-shear test with two symmetrically aligned active slip systems. The *-curves are for the equivalent single-slip problem. (Originally published in Kochmann and Hackl (2011).)

$(\mathbf{s}^*, \mathbf{m})$. Although the overall plastic slip can then be assumed to be equivalent, the hardening behavior should not. Indeed, depending on the choice of the hardening parameters κ_{ij} and the slip system orientation ψ, the present approach reveals a different hardening behavior of the material for the two active slip systems compared to only one active slip system with orientation $(\mathbf{s}^*, \mathbf{m})$. This can easily be seen by inspection of the energy curves, the evolving internal variables and the Cauchy shear stress in Fig. 25.

As the symmetric angle ψ changes, the material hardening also changes as can be seen in Fig. 26, where we compare the above results of the energy and the Cauchy shear stress for $\psi = 30°$ with the corresponding solutions for 45° and 60°.

The second example comprises a simple-shear test with non-symmetric

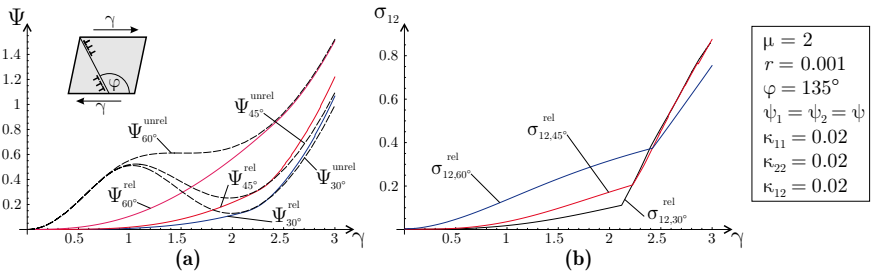

Figure 26. Comparison of (a) the paths of energy and (b) the Cauchy shear stress during a simple shear test with symmetric slip system orientations with $\psi_1 = \psi_2 = \psi$ for $\psi = 30°,\ 45°, 60°$ as indicated. (Originally published in Kochmann and Hackl (2011).)

active slip systems exhibiting $\psi_1 = 30°$ and $\psi_2 = 60°$. The results are summarized in Fig. 27. As a consequence of the loss of symmetry of the slip directions, plastic slips γ_i are no longer identical along the two slip systems. In this problem the influence of latent hardening is important and becomes obvious from Fig. 27b, where the ratio κ_{11}/κ_{12} is varied between 0 and 8 (while keeping $\kappa_{11} = \kappa_{22} = 0.02\mu$). The increased amount of latent hardening manifests in Fig. 27a in terms of the rising energy curves with increasing κ_{12}, and in Fig. 27b in terms of the increasing hardening rate.

7 Microstructure formation during cyclic loading

It has been reported, Hackl and Kochmann (2010), that the present model gives rise to interesting effects when applied to cyclic loading of single-crystals in terms of an elastic shakedown, i.e. the stress-strain behavior has been shown to rapidly reduce within a few number of cycles (less than four) to almost elastic behavior with an almost steady laminate. However, it has been argued that this short number of cycles until the steady state is reached is rather unphysical. Therefore, we investigate here the influence of work hardening on the cyclic loading of single-crystals by computing the stress-strain behavior at the material point level.

7.1 Cyclic loading in single-slip plasticity

Let us first analyze the cyclic load response of a crystal in two dimensions with only a single active slip system, whose orientation is defined by

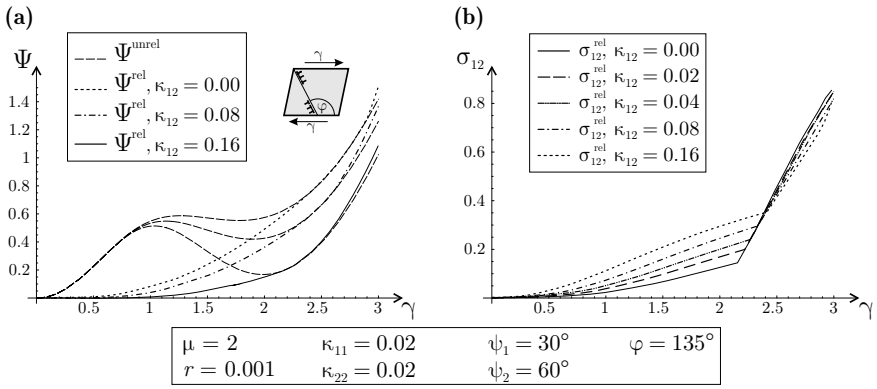

Figure 27. Comparison of the energy paths and the Cauchy shear stresses for non-symmetric active slip systems with different latent hardening parameters κ_{12}. (Originally published in Kochmann and Hackl (2011).)

the angle φ through $\mathbf{s} = (\cos\varphi, \sin\varphi, 0)^T$, $\mathbf{m} = (-\sin\varphi, \cos\varphi, 0)^T$. The material is subject to the homogeneous deformation

$$\mathbf{F}(\gamma) = \begin{pmatrix} 1 & \gamma & 0 \\ 0 & 1 & 0 \\ 0 & 0 & 1 \end{pmatrix}, \tag{167}$$

so that we can study the evolution of the microstructure, of the energy and, of course, of the shear stress as functions of the shear strain γ. It becomes apparent from Figure 28 that hardening does indeed considerably affect the cyclic load behavior: Without hardening ($\kappa = 0$) the stress-strain hysteresis remains unaltered for all cycles. Note that the nonconvexity of the free energy density for the chosen slip system orientation of $\varphi = 135°$ appears only for $\gamma > 0$ such that we observe microstructure formation and the typical corresponding stress plateau only in that region, whereas for $\gamma < 0$ the body deforms homogeneously and no microstructure forms. With an increasing amount of hardening ($\kappa > 0$) the stress-strain behavior changes essentially. For higher load cycles, the hysteresis becomes narrower and the stresses increase. The final elastic shakedown becomes visible for high hardening parameters (see e.g. the curves for $\kappa = 0.01\mu$ and $\kappa = 0.02\mu$). Here, one can clearly state that the amount of hardening essentially affects the progressive degeneration of the stress-strain hysteresis by altering the number of load cycles required until the final steady state is reached. For

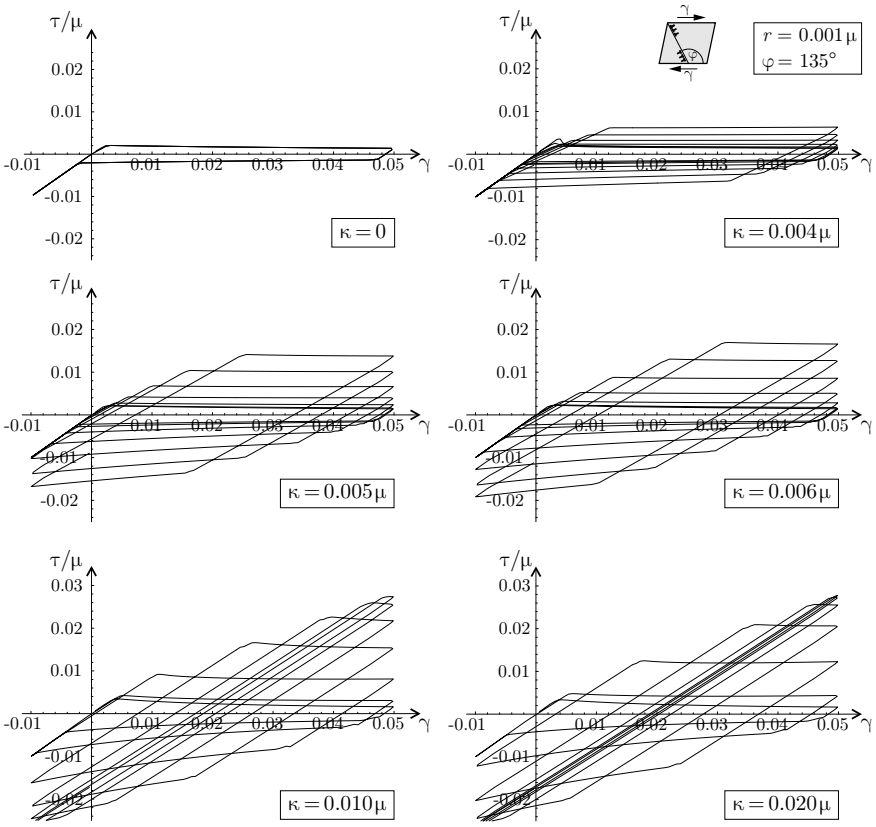

Figure 28. Stress-strain curves for a cyclic shear test for various hardening moduli κ and fixed remaining properties (shown are the first seven complete cycles). (Originally published in Kochmann and Hackl (2010b).)

moderate hardening it may hence take a large number of load cycles until the elastic shakedown occurs.

The observed stress-strain behavior can be linked to microstructural mechanisms by inspection of the evolving internal variables. Figure 29 illustrates the evolution of the plastic slips, the volume fractions and the stored energy as functions of the applied shear strain for little hardening only ($\kappa = 0.004\mu$), whereas Figure 30 illustrates the course of the same quantities for strong hardening ($\kappa = 0.02\mu$). In Figure 29 the paths of the

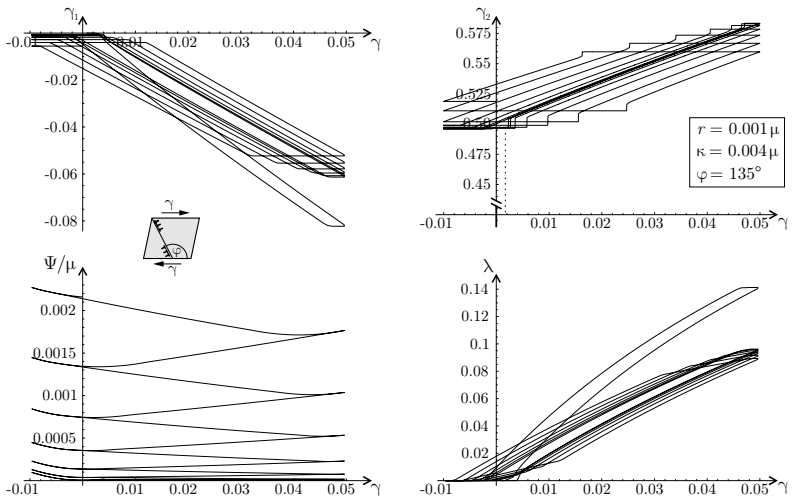

Figure 29. Evolution of the internal variables (i.e., the plastic slips γ_1 and γ_2, and the volume fraction λ of phase 2) and of the energy during a cyclic shear test for little hardening ($\kappa = 0.004\mu$); shown are the first seven complete cycles. (Originally published in Kochmann and Hackl (2010b).)

internal variables of the first cycle considerably differ from those of subsequent cycles, but the changes between subsequent cycles after the first cycle are relatively small. Note that the plastic slips in both phases, γ_1 and γ_2, show distinct cyclic changes for the entire load path investigated here. Also, the volume fraction λ changes cyclically between 0 and approximately 10%. Hence, a laminate microstructure forms with both domains deforming plastically, which forms and vanishes cyclically. As a result, the stored energy increases moderately from cycle to cycle due to the increasing amount of intrinsically stored energy captured in the monotonously increasing plastic hardening variables p_i.

In contrast, Figure 30 indicates a different behavior for large hardening (here, $\kappa = 0.02\mu$). Again, we observe that the evolution of the internal variables changes with an increasing number of load cycles, and the plot of the evolving plastic slip γ_2 in the second laminate domain is almost identical to the one of Figure 29. However, two crucial differences become obvious: now, the plastic slip γ_1 in the initial laminate domain transforms within a few load cycles to reach a steady value of about 5%, which hardly changes during subsequent load cycles, i.e. the initial laminate domain transforms

into a steady, elastic state after a few cycles only. Besides, the evolution of the volume fraction λ also indicates a drastic change. In constrast to the periodic changes in Figure 29, the volume fraction λ here very soon reaches an approximately steady state with only minor changes during subsequent cycles (viz., λ tends to change cyclically between about 10 and 12% only). The laminate thus considerably deviates from the one observed for small hardening only. Here, within a few cycles an approximately steady laminate is developed with hardly changing volume fractions, and only the smaller, newly-formed domain 2 exhibiting plastic flow. As a result, the stored energy increases notably faster than before and the elastic shakedown is reached after fewer load cycles.

Finally, let us complete the description of results by underlining the influence of the specific hardening formulation chosen here. To this end, we inspect the evolution of the hardening variables, as illustrated in Figure 31, where the evolution of p_1 and p_2 is plotted exemplarily for a laminate loaded cyclically in single-slip with the given set of material parameters. The graphic highlights two particular characteristics during the evolution of the

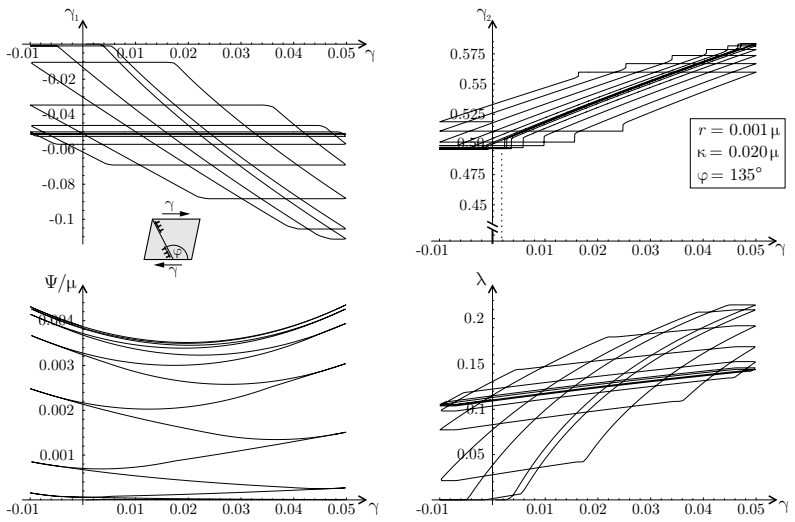

Figure 30. Evolution of the internal variables (i.e., the plastic slips γ_1 and γ_2, and the volume fraction λ of phase 2) and of the energy during a cyclic shear test for high hardening ($\kappa = 0.02\mu$); shown are the first seven complete cycles. (Originally published in Kochmann and Hackl (2010b).)

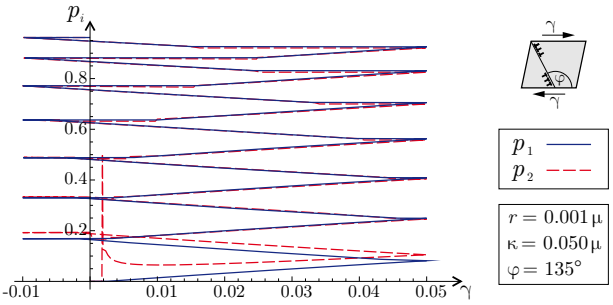

Figure 31. Evolution of the hardening variables p_1 and p_2 during cyclic loading in single-slip. (Originally published in Kochmann and Hackl (2010b).)

hardening variables, which shall be discussed briefly.

On the one hand, the impact of the update procedure for the hardening variables becomes apparent from the evolution of p_2 upon laminate nucleation, as has been reported e.g. in Hackl and Kochmann (2010); Kochmann and Hackl (2011). During the initial positive loading of the first load cycle, we have $p_1 \cong |\gamma_1|$ due to the present flow rule and the monotonically increasing load. As the second laminate phase forms during the first load cycle, we observe that p_2 first assumes the value $|\gamma_2|$ upon laminate initiation, but then rapidly decreases from its initial value and gradually approaches the evolving p_1-value due to the evolution of the volume fractions and the corresponding updates of the hardening variables. At the end of the first cycle, both hardening variables show approximately equal values, from where on we observe uniform hardening in both laminate phases.

On the other hand, we can observe in Figure 31 how both hardening variables increase with subsequent load cycles, i.e. with repeated plastic deformation, which gives rise to the observed cyclic hardening and eventually to the elastic shakedown of the stress-strain hysteresis. This is a major advantage of the present variational formulation, which allows for the study of cyclic loading, while the literature approach, based on condensed energy functionals, accounts for monotonic loading. Here, the values of the hardening variables gradually increase during each load cycle, leading to higher stresses and the reported cyclic hardening. Note that the orientation (characterized by vector $\mathbf{b}$) shows hardly any changes during load cycles due to the large amount of dissipation required to rearrange the rotated laminate. Therefore, the nucleated laminate microstructures predominantly remains

in its initial orientation, which results from the energetically optimal state upon laminate formation.

7.2 Cyclic loading in double-slip plasticity

When more than one slip system is active, latent hardening due to interaction mechanisms (such as cross slip) plays an essential role, increasing the amount of work hardening considerably. To illustrate this effect, we show results for a cyclic shear test with two active slip systems within the same slip plane, so that (23) holds. For comparison with the single-slip results, we locate the slip plane under an angle of $\varphi = 135°$ and align the two active slip systems under angles ψ_1 and ψ_2 with respect to the direction of shear, as depicted in the schematic view included in Figure 32. The particular hardening characteristics are described in terms of the hardening parameters κ_{ij} in (26).

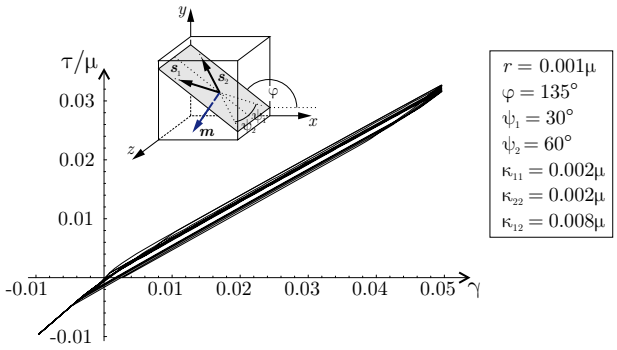

Figure 32. Cyclic stress-strain response for double-slip plasticity with low hardening (shown are the first seven load cycles) for non-symmetric active slip systems. (Originally published in Kochmann and Hackl (2010b).)

Figure 32 illustrates the stress-strain behavior for two active slip systems with low (self- and latent) hardening. We observe the typical stress-strain hysteresis with only little cyclic deviations, as has already been noted for the single-slip problem with a low hardening parameter κ (see Figure 28). Here, the asymmetrically aligned slip systems ($\psi_1 \neq \psi_2$) locates the resultant slip out-of-plane (and so is the laminate orientation), which gives rise to the enormous increase of the stress even for low values of the hardening parameters κ_{ij}.

In contrast, Figure 33 shows the analogous stress-strain curve with higher

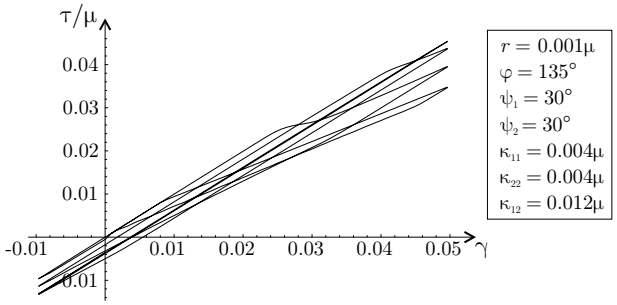

Figure 33. Cyclic stress-strain response for double-slip plasticity with high hardening (shown are the first seven load cycles) for symmetric active slip systems. (Originally published in Kochmann and Hackl (2010b).)

hardening parameters κ_{ij}. Here, the stress-strain curve shows a similar hysteresis loop, which, however, is not completely recovered but, upon further load cycles, deviates gradually. Within a few load cycles the typical, aforementioned elastic shakedown appears due to the increase of energy as a consequence of work hardening and, in particular, latent hardening of the two active slip systems. In conclusion, the presence of hardening, as for the examples in single-slip plasticity, considerably effects the cyclic stress-strain behavior and determines the number of cycles required before the laminate microstructure degenerates to approach a close to elastic mechanical behavior.

8 Discussion and Conclusions

We have outlined an incremental strategy to model the time-continuous evolution of laminate microstructures in finite-strain plasticity by employing partially relaxed approximations of the nonconvex potentials involved. For an incompressible Neo-Hookean material we have derived a closed-form, semi-relaxed energy which corresponds to a laminate of first-order. Partial relaxation implies that the relaxation of the laminate energy is carried out only with respect to those variables that change purely elastically, in our case the amplitudes of the deformation gradient in each domain. The course of all remaining unknowns is determined from dissipative evolution equations, where we employ the principle of minimum dissipation potential, Carstensen et al. (2002); Ortiz and Repetto (1999). Full relaxation can be

performed numerically, and results indicate only little deviation from the convex energy lower bound such that usage of the chosen approximation of the rank-one-convex hull is justified (note that the energy hull obtained from the present approach will gain accuracy when modified for second-order laminates which, however, goes beyond the scope of this paper). In case of several active slip systems the outlined relaxed energy is applicable only if all active slip systems within each laminate domain lie within the same glide plane.

In contrast to earlier approaches in the literature we pursued an incremental strategy that captures the actual microstructural changes during each time step and allows for a more general application. Many reported examples, Bartels et al. (2004); Carstensen et al. (2008); Miehe et al. (2004) were for conciseness restricted to single-slip plasticity (and often to two dimensions only). The present approach accounts for, in principle, arbitrarily many active slip systems in three-dimensional problems, while the numerical examples outlined in this work involve two active slip systems. As a crucial difference to those approaches based on condensed energy functionals, see e.g. Bartels et al. (2004); Carstensen et al. (2008), we account for the actual changes of the microstructure during each time step and the associated amount of dissipation (for a different incremental approach, see e.g. Miehe et al. (2004)). This becomes particularly important in two cases: first, when dealing with non-monotonic loading as in cyclic tests, which can easily be performed using the present approach, Kochmann and Hackl (2010a); and second, when the dissipation distance can no longer be given in an analytical form. As soon as more than one slip system is active, it is hard (if not impossible) to obtain a closed-form solution for the dissipation distance that only depends on the final states of the internal variables. Therefore, one can no longer use the condensed energy functional without making approximate assumptions on the dissipation distance. In the outlined incremental setting this troublesome issue reduces to only one time step, viz. the one during which the laminate forms. Here, the present approach still requires knowledge about the dissipation distance to form the laminate, and we have proposed approximate formulations. However, once the laminate has formed, the complete evolution in time can be treated by usage of the dissipation potential only, so that computations can be accurately performed without the necessity of a given dissipation distance. Besides, the present approach also accounts for the actual amount of dissipation required to change not only the plastic slips but also the volume fractions during each time step (this amount of dissipation depends on the existing internal variables at the beginning of the time step).

As most of the aforementioned approaches in the literature were for

single-slip, a comparison of the results with the present method is possible when the outlined strategy is applied to a single active slip system only. In this case it has been shown that the present incremental strategy considerably reduces the stored energy during a given straining path even beyond the recovery of convexity of the unrelaxed solution, Kochmann and Hackl (2010a). This behavior has been observed to be mainly due to the particular form of the updates of the internal hardening variables upon changes of the volume fractions. We have proposed an energetically-reasoned formulation for the changes of the hardening variables, which is based on energetic averages of the initial values and which gives rise to the observed energy reduction. Without this updating procedure (or for only negligible hardening) the solution exhibits high agreement with approaches based on condensed energy functionals for monotonic loading.

Finally, we have discussed the influence of latent hardening, which becomes important as soon as more than one active slip system is considered. We have made use of a very simple but sensible ansatz to account for self-hardening as well as latent hardening. Numerical results for two active slip systems exemplarily show the influence of the self-hardening term on the stress-strain behavior and the evolving internal variables. Generalizations of the outlined method in several directions are underway.

Bibliography

Ball, J. M.: Convexity conditions and existence theorems in nonlinear elasticity. Arch. Rat. Mech. Anal. **63**, 337-403 (1977).

Ball, J. M., and James, R. D.: Fine phase mixtures as minimizer of energy. Arch. Rat. Mech. Anal. **100**, 13–52 (1987).

Ball, J., James, R.:Proposed experimental tests of a theory of Dne microstructures and the 2-well problem. Philos. Trans. R. Soc. Lond. A **338**, 389-450 (1992).

Bartels, S., Carstensen, C., Hackl, K., Hoppe, U.: Effective relaxation for microstructure simulation: algorithms and applications. Comp. Meth. Appl. Mech. Eng. **193**, 5143–5175 (2004).

Bhattacharya, K.: Microstructure of martensite. Why it forms and how it gives rise to the shape-memory effect. Oxford University Press, Oxford (2003).

Canadinc, D., Sehitoglu, H., Maier, H. J., Chumlyakov, Y. I.: Strain hardening behavior of aluminum alloyed Hadfield steel single crystals. Acta Mater. **53**, 1831-1842 (2005).

Carstensen, C., Hackl, K., Mielke, A.: Non-convex potentials and microstructures in finite-strain plasticity. Proc. R. Soc. Lond. A **458**, 299–317 (2002).

Carstensen, C., Conti, S., Orlando, A.: Mixed analytical-numerical relaxation in finite single-slip crystal plasticity. Continuum Mech. Thermodyn. **20**, 275–301 (2008).

Christian, J. W., Mahajan, S.: Deformation twinning. Progr. Mater. Sci. **39**, 1–157 (1995).

Chu, C., James, R. D.: Analysis of microstructures in Cu-14.0%Al-3.9%Ni by energy minimization. Journal de Physique III – Colloque C8 **5**, 143–149 (1995).

Conti, S., Ortiz, M.: Minimum principles for the trajectories of systems governed by rate problems. J. Mech. Phys. Solids **56**, 1885–1904 (2008).

Conti, S., Theil, F.: Single-slip elastoplastic microstructures. Arch. Rat. Mech. Anal. **178**, 125–148 (2005).

Dacorogna, B.: Direct Methods in the Calculus of Variations. Springer, Berlin (1989).

Dmitrieva, O., Dondl, P., Müller, S., Raabe, D., 2009. Lamination microstructure in shear deformed copper single crystals. Acta Mater. 57, 3439-3449.

Ericksen, J. L.: Equilibrium of bars. J. Elasticity **5**, 191–201 (1975).

Govindjee, S., Mielke, A., Hall, G.J.: The free energy of mixing for n-variant martensitic phase transformations using quasi-convex analysis. J. Mech. Phys. Solids **51**, 1–26 (2003).

Govindjee, S., Hackl, K., Heinen, R.: An upper bound to the free energy of mixing by twin-compatible lamination for n-variant martensitic phase transformations. Cont. Mech. and Thermodyn. **18**, 443–453 (2007).

Hackl, K.: Generalized standard media and variational principles in classical and finite strain elastoplasticity. J. Mech. Phys. Solids **45**, 667-688 (1997).

Hackl, K.: Relaxed potentials and evolution equations. In: Gumbsch, P. (Ed.), Third International Conference on Multiscale Materials Modeling. Fraunhofer IRB Verlag (2006).

Hackl, K., Fischer, F. D.: On the relation between the principle of maximum dissipation and inelastic evolution given by dissipation potentials. Proc. R. Soc. Lond. A **464**, 117-132 (2008).

Hackl, K., Fischer, F. D., Svoboda, J.: A study on the principle of maximum dissipation for coupled and non-coupled non-isothermal processes in materials. Proc. R. Soc. Lond. A **467**, 1186–1196 (2011).

Hackl, K., Heinen, R.: On the calculation of energy-minimizing phase fractions in shape memory alloys. Comput. Meth. Appl. Mech. Eng. **196**, 2401–2412 (2007).

Hackl, K., Heinen, R.: A micromechanical model for pretextured polycrystalline shape-memory alloys including elastic anisotropy. Continuum Mech. Thermodyn. **19**, 499–510 (2008).

Hackl, K., Heinen, R.: An upper bound to the free energy of n-variant polycrystalline shape memory alloys. J. Mech. Phys. Solids **56**, 2832–2843 (2008).

Hackl K., Hoppe U.: On the calculation of microstructures for inelastic materials using relaxed energies. In Miehe C. (Eds.), IUTAM Symposium on Computational Mechanics of Solid Materials at large Strains, Kluwer, 77–86 (2002).

Variational modeling of shape memory alloys-an overview. Int. J. Mat. Res. **102**, 643–651 (2011).

Hackl, K., Kochmann, D. M.: Relaxed potentials and evolution equations for inelastic microstructures. In: Daya Reddy, B. (ed.), Theoretical, Computational and Modelling Aspects of Inelastic Media, IUTAM Bookseries, Springer, 27–39 (2008).

Hackl, K., Kochmann, D. M.: An incremental strategy for modeling laminate microstructures in finite plasticity – energy reduction, laminate orientation and cyclic behavior. In: de Borst, R., Ramm, E. (Eds.), Multiscale Methods in Computational Mechanics, Springer, 117–134 (2010).

Hackl, K., Schmidt-Baldassari, M., Zhang, W.: A micromechanical model for polycrystalline shape-memory alloys. Mat. Sci. Eng. A **378**, 503–506 (2003).

Junker, P., Hackl, K.: Finite element simulations of poly-crystalline shape memory alloys based on a micromechanical model. Computational Mechanics **47**, 505–517 (2011).

Kochmann, D. M.: Mechanical Modeling of Microstructures in Elasto-Plastically Deformed Crystalline Solids. Ph.D. Thesis (2009). Ruhr-University Bochum, Germany.

Kochmann, D. M., Hackl, K.: Time-continuous evolution of microstructures in finite plasticity. In: Hackl, K. (Ed.), Variational Concepts with Applications to the Mechanics of Materials, IUTAM Bookseries, Springer, 117–130 (2010).

Kochmann, D. M., Hackl, K.: Influence of hardening on the cyclic behavior of laminate microstructures in finite crystal plasticity. Tech. Mech. 30, 384–400 (2010).

Kochmann, D. M., Hackl, K.: The evolution of laminates in finite plasticity: a variational approach. Continuum Mech. Thermodyn. 23, 63–85 (2011).

Lambrecht, M., Miehe, C., Dettmar, J.: Energy relaxation of non-convex incremental stress potentials in a strain-softening elastic-plastic bar. Int. J. Sol. Struct. **40**, 1369–1391 (2003).

Lukáš, P., Kunz, L., Svoboda, M.: Stress-strain response and fatigue life of copper single crystals cyclically loaded with a positive mean stress. Mat. Sci. Eng. A **272**, 31–37 (1999).

Miehe, C., Lambrecht, E., Gürses, E.: Analysis of material instabilities in inelastic solids by incremental energy minimization and relaxation methods: evolving deformation microstructures in finite plasticity. J. Mech. Phys. Solids **52**, 2725–2769 (2004).

Miehe, C., Schotte, J., Lambrecht, M.: Homogenization of inelastic solid materials at finite strains based on incremental minimization principles. Application to the texture analysis of polycrystals. J. Mech. Phys. Solids **50**, 2123–2167 (2002).

Mielke, A.: Finite elastoplasticity, Lie groups and geodesics on SL(d). In: Newton, P., Weinstein, A., Holmes, P. (Eds.), Geometry, Dynamics, and Mechanics. Springer, Berlin (2002).

Mielke, A.: Deriving new evolution equations for microstructures via relaxation of variational incremental problems. Comp. Meth. Appl. Mech. Eng. **193**, 5095–5127 (2004).

Mielke, A., Ortiz, M.: A class of minimum principles for characterizing the trajectories and the relaxation of dissipative systems. ESAIM: Control, Optimization and Calculus of Variations **14**, 494–516 (2007).

Ortiz, M., Repetto, E. A.: Nonconvex energy minimization and dislocation structures in ductile single crystals. J. Mech. Phys. Solids **47**, 397–462 (1999).

Simo, J. C.: A framework for finite strain elastoplasticity based on maximum plastic dissipation and the multiplicative decomposition. I. Continuum formulation. Comput. Meth. Appl. Mech. Eng. **66**, 199–219 (1988a).

Simo, J. C.: A framework for finite strain elastoplasticity based on maximum plastic dissipation and the multiplicative decomposition. II. Computational Aspects. Comput. Meth. Appl. Mech. Eng. **68**, 1–31 (1988b).

Truesdell, C., Noll, W.: The nonlinear field theories of mechanics. In: Flügge, S. (ed.), Encyclopedia of Physics III/3, Springer, Berlin (1965).

Truskinovsky, L.: Finite Scale Microstructures in Nonlocal Elasticity. J. Elasticity 59, 319–355 (2000).

Truskinovsky, L., Zanzotto, G.: Finite-scale microstructures and metastability in one-dimensional elasticity. Meccanica **30**, 577–589 (1995).

Young, L. C.: Lectures on the Calculus of Variations and Optimal Control Theory. AMS Chelsea Publications, New York (1980).

Micromorphic approach to crystal plasticity and phase transformation

Samuel Forest [*†], Kais Ammar [*], Benoît Appolaire [**], Nicolas Cordero [*], and Anaïs Gaubert [***],

[*] MINES ParisTech, Centre des matériaux, CNRS UMR 7633, Evry, France
[**] Laboratoire d'étude des microstructures, CNRS/ONERA, Châtillon, France
[***] Dept. of Metallic Materials and Structures, ONERA, Châtillon, France
[†] Corresponding author: samuel.forest@mines-paristech.fr

Abstract Continuum crystal plasticity models are extended to incorporate the effect of the dislocation density tensor on material hardening. The approach is based on generalized continuum mechanics including strain gradient plasticity, Cosserat and micromorphic media. The applications deal with the effect of precipitate size in two–phase single crystals and to the Hall-Petch grain size effect in polycrystals. Some links between the micromorphic approach and phase field models are established. A coupling between phase field approach and elastoviscoplasticity constitutive equations is then presented and applied to the prediction of the influence of viscoplasticity on the kinetics of diffusive precipitate growth and morphology changes.

1 Introduction

Continuum crystal plasticity is a special class of anisotropic elastoviscoplastic behaviour of materials. It relies on the precise knowledge of the kinematics of plastic slip according to crystallographic slip systems and of the driving force for activation of plastic slip, namely the corresponding resolved shear stress. When the number of dislocations inside the material volume element is high enough, a continuum description of plastic deformation and hardening can be formulated as settled in (Mandel, 1965, 1971, 1973) and (Teodosiu and Sidoroff, 1976).

The objectives of this contribution is first to establish the continuum mechanical framework for the formulation of constitutive equations for single crystals including the effect of the dislocation density tensor. We show then than this model class can be used to predict size effects in the response of polycrystals. The considered plastic deformation mechanism is

J. Schröder, K. Hackl (Eds.), *Plasticity and Beyond*, CISM International Centre for Mechanical Sciences, DOI 10.1007/978-3-7091-1625-8_3,

crystallographic slip but the formulation can serve as a basis for extensions to climb or twinning since thermomechanical balances and most kinematic considerations are still valid.

There exists an extreme variety of possible constitutive equations for single crystals derived in the last 40 years but the thermomechanical foundation is quite unique and now clearly settled Estrin (1996). We will consider this variety of constitutive laws by introducing generic internal variables without making specific choices. Only generic examples of evolution laws for such internal variables are provided and the reader is referred to (Fivel and Forest, 2004a), and references quoted therein, for a detailed discussion of best–suited constitutive laws for metal single crystals. Also the transition from single to polycrystal behaviour is shortly addressed here but fundamentals for modelling polycrystals can be found in (Fivel and Forest, 2004b; Besson et al., 2009).

The most relevant internal variables for describing the work–hardening of single crystals are undoubtedly dislocation densities, ρ^s, defined as the total length of dislocations belonging to a slip system s divided by the volume of the material volume element. Evolution equations for dislocations densities can be found in (Fivel and Forest, 2004a). In the present contribution, we introduce general isotropic and kinematic hardening variables accounting for monotonic and cyclic responses of crystals. Dislocation densities are generally related to isotropic hardening through forest hardening but recent contributions also aim at establishing dislocation based kinematic hardening dislocation rules.

Another characterisation of the dislocation distribution is the dislocation density tensor introduced by (Nye, 1953). It is defined in section 2.3 and contributes to many size effects observed in crystalline solids: grain size or Hall–Petch effect, precipitate size effect, etc. The dislocation density tensor cannot be handled as a usual internal variable because it is related to the gradient of the plastic deformation field. As a result, higher order partial differential equations arise when hardening laws involve the dislocation density tensor. The development of constitutive models involving the dislocation density tensor is the realm of strain gradient plasticity. Even for the much too simple constitutive equations presented in this work, the model shows that the dislocation density tensor is responsible for a size–dependent kinematic hardening component in the material behaviour.

The final part of this chapter draws a parallel between the micromorphic approach which consists in introducing additional degrees of freedom in the mechanical framework, and the phase field approach dedicated to the simulation of evolution of microstructures. The comparison enables us to combine the elastoviscoplastic behaviour of constitutents and the phase field

model in order to address the question of the influence of nonlinear deformation on the kinetics and morphology evolution during phase transformation (Ammar et al., 2011).

Notations Vectors, second, third and fourth rank tensors are denoted by $\underline{\boldsymbol{a}}, \underline{\underline{\boldsymbol{a}}}, \underline{\underline{\underline{\boldsymbol{a}}}}, \underline{\underline{\underline{\underline{\boldsymbol{a}}}}}$, respectively. The initial and current positions of the material point are denoted by $\underline{\boldsymbol{X}}$ and $\underline{\boldsymbol{x}}$, respectively. Throughout this work, the initial configuration of the body is V_0 whereas V denotes the current one. The associated smooth boundaries are ∂V_0 and ∂V with normal vector $\underline{\boldsymbol{N}}$ and $\underline{\boldsymbol{n}}$. The gradient operators with respect to initial and current coordinates are called $\boldsymbol{\nabla}_X$ and $\boldsymbol{\nabla}_x$ respectively. Similarily, the divergence and curl operators are Div, div and Curl, curl whether they are computed with respect to initial or current positions, respectively. Intrinsic notation is used in general but it is sometimes complemented or replaced by the index notation for clarity. A Cartesian coordinate system is used throughout with respect to the orthonormal basis $(\underline{\boldsymbol{e}}_1, \underline{\boldsymbol{e}}_2, \underline{\boldsymbol{e}}_3)$. The notations for double contraction and gradient operations are:

$$\underline{\underline{\boldsymbol{A}}} : \underline{\underline{\boldsymbol{B}}} = A_{ij}B_{ij}, \quad \underline{\boldsymbol{u}} \otimes \boldsymbol{\nabla}_X = \frac{\partial u_i}{\partial X_j}\, \underline{\boldsymbol{e}}_i \otimes \underline{\boldsymbol{e}}_j \tag{1}$$

2 Crystal plasticity and the dislocation density tensor

2.1 Thermomechanics of single crystal behaviour

Balance equations. Mechanical equilibrium can be expressed in the form of the principle of virtual power

$$-\int_{\mathcal{D}} \underline{\underline{\boldsymbol{\sigma}}} : \underline{\underline{\boldsymbol{D}}}^*\, dv + \int_{\mathcal{D}} \rho(\underline{\boldsymbol{f}} - \underline{\boldsymbol{a}}) \cdot \underline{\boldsymbol{v}}^*\, dv + \int_{\partial\mathcal{D}} \underline{\boldsymbol{t}} \cdot \underline{\boldsymbol{v}}^*\, ds = 0 \tag{2}$$

for all virtual velocity fields and all subdomains, $\mathcal{D}$, of the current configuration Ω of the body. The Cauchy stress tensor is $\underline{\underline{\boldsymbol{\sigma}}}$ and $\underline{\underline{\boldsymbol{D}}}$ is the strain rate tensor. Volume and acceleration forces are denoted by $\underline{\boldsymbol{f}}$ and $\underline{\boldsymbol{a}}$, respectively, whereas $\underline{\boldsymbol{t}}$ is the traction vector. The principle of virtual power implies the following balance of momentum equation

$$\operatorname{div} \underline{\underline{\boldsymbol{\sigma}}} + \rho \underline{\boldsymbol{f}} = \rho \underline{\boldsymbol{a}} \tag{3}$$

The energy balance is the purpose of the first principle of thermodynamics

$$\int_{\mathcal{D}} \rho \dot{e}\, dv - \int_{\mathcal{D}} \rho(\underline{\boldsymbol{a}} - \underline{\boldsymbol{f}}) \cdot \underline{\boldsymbol{v}}\, dv = \int_{\partial\mathcal{D}} \underline{\boldsymbol{t}} \cdot \underline{\boldsymbol{v}}\, ds + \mathcal{Q} \tag{4}$$

or equivalently, after implementing the balance of momentum principle,

$$\int_{\mathcal{D}} \rho \dot{e}\, dv = \int_{\mathcal{D}} \underset{\sim}{\boldsymbol{\sigma}} : \underset{\sim}{\boldsymbol{D}}\, dv + \mathcal{Q} \tag{5}$$

where ρe is the volume density of internal energy. The heat production rate is assumed to take the form

$$\mathcal{Q} = -\int_{\partial\mathcal{D}} \underline{\boldsymbol{q}} \cdot \underline{\boldsymbol{n}}\, ds \tag{6}$$

The local form of the energy principle is then

$$\rho \dot{e} = \underset{\sim}{\boldsymbol{\sigma}} : \underset{\sim}{\boldsymbol{D}} - \operatorname{div} \underline{\boldsymbol{q}} \tag{7}$$

The second principle of thermodynamics stipulates that

$$\int_{\mathcal{D}} \rho \dot{\eta}\, dv + \int_{\partial\mathcal{D}} \frac{\underline{\boldsymbol{q}}}{T} \cdot \underline{\boldsymbol{n}}\, ds \geq 0 \tag{8}$$

where η is the mass density of entropy and T the temperature field. The validity of this principle with respect to all subdomain $\mathcal{D}$ leads to the local form of the entropy principle

$$\rho \dot{\eta} + \operatorname{div} \frac{\underline{\boldsymbol{q}}}{T} \geq 0 \tag{9}$$

Introducing the free energy density $\Psi := e - T\eta$ and taking the balance of energy into account, we are lead to the Clausius inequality

$$\underset{\sim}{\boldsymbol{\sigma}} : \underset{\sim}{\boldsymbol{D}} - \rho \dot{\Psi} - \rho \eta \dot{T} - \underline{\boldsymbol{q}} \cdot \frac{\boldsymbol{\nabla} T}{T} \geq 0 \tag{10}$$

Kinematics of single crystals. It is based on the multiplicative decomposition of the deformation gradient, $\underset{\sim}{\boldsymbol{F}}$, into an elastic part, $\underset{\sim}{\boldsymbol{E}}$, and a plastic part, $\underset{\sim}{\boldsymbol{P}}$:

$$\underset{\sim}{\boldsymbol{F}}(\underline{\boldsymbol{X}}) = \underset{\sim}{\mathbf{1}} + \frac{\partial \underline{\boldsymbol{u}}}{\partial \underline{\boldsymbol{X}}} = \underset{\sim}{\mathbf{1}} + \underline{\boldsymbol{u}} \otimes \boldsymbol{\nabla}_X, \quad \underset{\sim}{\boldsymbol{F}}(\underline{\boldsymbol{X}}) = \underset{\sim}{\boldsymbol{E}}(\underline{\boldsymbol{X}}).\underset{\sim}{\boldsymbol{P}}(\underline{\boldsymbol{X}}) \tag{11}$$

The initial coordinates of the material point in the reference configuration are denoted by $\underline{\boldsymbol{X}}$ and $\boldsymbol{\nabla}_X$ denotes the gradient operator with respect to initial coordinates. The current position of the material point in the current configuration is $\underline{\boldsymbol{x}}$. The displacement vector is $\underline{\boldsymbol{u}} = \underline{\boldsymbol{x}} - \underline{\boldsymbol{X}}$. The multiplicative decomposition (11) is associated with the definition of an intermediate

configuration for which elastic strain is unloaded, see figure 1. The intermediate released configuration is uniquely determined up to a rigid body rotation which is chosen such that the lattice orientation in the intermediate configuration is the same as the initial one. Mandel called it the *isoclinic* intermediate configuration. As a result, lattice rotation and distortion during elastoplastic deformation are contained in the elastic deformation part $\underset{\sim}{\boldsymbol{E}}$, as examined at the end of this section.

The multiplicative decomposition leads to the following partition of the velocity gradient

$$\underline{\boldsymbol{v}} \otimes \boldsymbol{\nabla} = \dot{\underset{\sim}{\boldsymbol{F}}} \cdot \underset{\sim}{\boldsymbol{F}}^{-1} = \dot{\underset{\sim}{\boldsymbol{E}}} \cdot \underset{\sim}{\boldsymbol{E}}^{-1} + \underset{\sim}{\boldsymbol{E}} \cdot \dot{\underset{\sim}{\boldsymbol{P}}} \cdot \underset{\sim}{\boldsymbol{P}}^{-1} \cdot \underset{\sim}{\boldsymbol{E}}^{-1} \tag{12}$$

We introduce the Cauchy–Green and Green–Lagrange elastic strain measures

$$\underset{\sim}{\boldsymbol{C}}^e := \underset{\sim}{\boldsymbol{E}}^T \cdot \underset{\sim}{\boldsymbol{E}}, \quad \underset{\sim}{\boldsymbol{E}}^e = \frac{1}{2}(\underset{\sim}{\boldsymbol{C}}^e - \underset{\sim}{\boldsymbol{1}}) \tag{13}$$

and note that

$$\begin{aligned} \dot{\underset{\sim}{\boldsymbol{E}}}^e &= \frac{1}{2}(\dot{\underset{\sim}{\boldsymbol{E}}}^T \cdot \underset{\sim}{\boldsymbol{E}} + \underset{\sim}{\boldsymbol{E}}^T \cdot \dot{\underset{\sim}{\boldsymbol{E}}}) = \frac{1}{2}\dot{\underset{\sim}{\boldsymbol{C}}}^e \\ &= \frac{1}{2}\underset{\sim}{\boldsymbol{E}}^T \cdot (\underset{\sim}{\boldsymbol{E}}^{-T} \cdot \dot{\underset{\sim}{\boldsymbol{E}}}^T + \dot{\underset{\sim}{\boldsymbol{E}}} \cdot \underset{\sim}{\boldsymbol{E}}^{-1}) \cdot \underset{\sim}{\boldsymbol{E}} = \underset{\sim}{\boldsymbol{E}}^T \cdot \left(\dot{\underset{\sim}{\boldsymbol{E}}}^e \cdot \underset{\sim}{\boldsymbol{E}}^{-1}\right)^{sym} \cdot \underset{\sim}{\boldsymbol{E}} \end{aligned}$$

where *sym* operator takes the symmetric part of the quantity in brackets. The mass density of the material point with respect to the current (resp. intermediate) configuration is denoted by ρ (resp. ρ_e). The volume density of internal forces with respect to the intermediate configuration is

$$\begin{aligned} J_e \underset{\sim}{\boldsymbol{\sigma}} : \underset{\sim}{\boldsymbol{D}} &= J_e \underset{\sim}{\boldsymbol{\sigma}} : (\dot{\underset{\sim}{\boldsymbol{F}}} \cdot \underset{\sim}{\boldsymbol{F}}^{-1}) = J_e \underset{\sim}{\boldsymbol{\sigma}} : (\dot{\underset{\sim}{\boldsymbol{E}}} \cdot \underset{\sim}{\boldsymbol{E}}^{-1}) + J_e \underset{\sim}{\boldsymbol{\sigma}} : (\underset{\sim}{\boldsymbol{E}} \cdot \dot{\underset{\sim}{\boldsymbol{P}}} \cdot \underset{\sim}{\boldsymbol{P}}^{-1} \cdot \underset{\sim}{\boldsymbol{E}}^{-1}) \\ &= J_e \underset{\sim}{\boldsymbol{\sigma}} : (\dot{\underset{\sim}{\boldsymbol{E}}} \cdot \underset{\sim}{\boldsymbol{E}}^{-1})^{sym} + J_e \underset{\sim}{\boldsymbol{\sigma}} : (\underset{\sim}{\boldsymbol{E}} \cdot \dot{\underset{\sim}{\boldsymbol{P}}} \cdot \underset{\sim}{\boldsymbol{P}}^{-1} \cdot \underset{\sim}{\boldsymbol{E}}^{-1}) \\ &= \underset{\sim}{\boldsymbol{\Pi}}^e : \dot{\underset{\sim}{\boldsymbol{E}}}^e + \underset{\sim}{\boldsymbol{M}} : \dot{\underset{\sim}{\boldsymbol{P}}}.\underset{\sim}{\boldsymbol{P}}^{-1} \end{aligned} \tag{14}$$

where $J_e = \det \underset{\sim}{\boldsymbol{E}}$ is the volume change from the intermediate to the current configuration, $\underset{\sim}{\boldsymbol{\Pi}}^e$ is the second Piola–Kirchhoff stress tensor with respect to the isoclinic intermediate configuration, and $\underset{\sim}{\boldsymbol{M}}$ is the Mandel stress tensor defined as :

$$\underset{\sim}{\boldsymbol{\Pi}}^e = J_e \underset{\sim}{\boldsymbol{E}}^{-1}.\underset{\sim}{\boldsymbol{\sigma}}.\underset{\sim}{\boldsymbol{E}}^{-T}, \quad \underset{\sim}{\boldsymbol{M}} = J_e \underset{\sim}{\boldsymbol{E}}^T.\underset{\sim}{\boldsymbol{\sigma}}.\underset{\sim}{\boldsymbol{E}}^{-T} = \underset{\sim}{\boldsymbol{C}}^e \cdot \underset{\sim}{\boldsymbol{\Pi}}^e \tag{15}$$

Plastic deformation is the result of slip processes according to N slip systems characterised by the slip direction, $\underline{\boldsymbol{m}}^s$, and the normal to the slip plane, $\underline{\boldsymbol{n}}^s$, in the intermediate configuration :

$$\dot{\underset{\sim}{\boldsymbol{P}}}.\underset{\sim}{\boldsymbol{P}}^{-1} = \sum_{s=1}^{N} \dot{\gamma}^s \underline{\boldsymbol{m}}^s \otimes \underline{\boldsymbol{n}}^s \tag{16}$$

Note that plastic deformation induced by dislocation glide is isochoric so that

$$J_p = \det \underset{\sim}{\boldsymbol{P}} = 1, \quad J_e = J = \det \underset{\sim}{\boldsymbol{F}} \tag{17}$$

Constitutive equations Constitutive equations for elastoviscoplastic materials are based on the definition of two potential functions, namely the free energy density function and the dissipation potential. The specific energy density, $\Psi(\underset{\sim}{\boldsymbol{E}}^e, T, \alpha)$, is a function of elastic strain, temperature and internal variables accounting for hardening properties. Writing the Clausius–Duhem inequality (10) with respect to the intermediate isoclinic configuration amounts to multiplying (10) by $\rho_e/\rho = J_e$

$$J_e \underset{\sim}{\boldsymbol{\sigma}} : \underset{\sim}{\boldsymbol{D}} - \rho_e \dot{\Psi} - \rho_e \eta \dot{T} - \underline{\boldsymbol{Q}} \cdot \frac{\boldsymbol{\nabla}_X T}{T} \geq 0 \tag{18}$$

where $\underline{\boldsymbol{Q}} = J_e \underset{\sim}{\boldsymbol{F}}^{-T} \cdot \underline{\boldsymbol{q}}$. Expanding the time derivative of the free energy density, we obtain

$$\left(\underset{\sim}{\boldsymbol{\Pi}}^e - \rho_e \frac{\partial \Psi}{\partial \underset{\sim}{\boldsymbol{E}}^e} \right) : \dot{\underset{\sim}{\boldsymbol{E}}}^e - \rho_e (\eta + \frac{\partial \Psi}{\partial T}) \dot{T} + \underset{\sim}{\boldsymbol{M}} : \dot{\underset{\sim}{\boldsymbol{P}}} \cdot \underset{\sim}{\boldsymbol{P}}^{-1} - \rho_e \frac{\partial \Psi}{\partial \alpha} \dot{\alpha} - \underline{\boldsymbol{Q}} \cdot \frac{\boldsymbol{\nabla}_X}{\partial T} \geq 0 \tag{19}$$

The following state laws provide the hyperelasticity relation and the entropy density :

$$\underset{\sim}{\boldsymbol{\Pi}}^e = \rho_e \frac{\partial \Psi}{\partial \underset{\sim}{\boldsymbol{E}}^e} = \underset{\approx}{\boldsymbol{C}} : \underset{\sim}{\boldsymbol{E}}^e, \quad \eta = -\frac{\partial \Psi}{\partial T}, \quad X = \rho_e \frac{\partial \Psi}{\partial \alpha} \tag{20}$$

where a quadratic potential for elasticity has been proposed, thus introducing the fourth rank tensor of elasticity moduli, $\underset{\approx}{\boldsymbol{C}}$. Such an assumption is realistic for metals since elastic strain usually remains small, as discussed in the next subsection. The thermodynamic forces associated with the internal variables α are called X. The residual dissipation rate is

$$\underset{\sim}{\boldsymbol{M}} : \dot{\underset{\sim}{\boldsymbol{P}}} \cdot \underset{\sim}{\boldsymbol{P}}^{-1} - X \dot{\alpha} - \underline{\boldsymbol{Q}} \cdot \frac{\boldsymbol{\nabla}_X T}{T} \geq 0 \tag{21}$$

The first term is the plastic power. Part of it is stored due to the second contribution whereas the third one denotes thermal dissipation.

At this stage, a dissipation potential $\Omega(\underset{\sim}{\boldsymbol{M}}, X)$ is introduced from which the flow rule and the evolution equation for internal variables are derived

$$\dot{\underset{\sim}{\boldsymbol{P}}} . \underset{\sim}{\boldsymbol{P}}^{-1} = \frac{\partial \Omega}{\partial \underset{\sim}{\boldsymbol{M}}}, \quad \dot{\alpha} = -\frac{\partial \Omega}{\partial X} \tag{22}$$

Positivity of dissipation rate is ensured if the dissipation potential $\Omega(\underset{\sim}{\boldsymbol{M}}, X)$ exhibits specific convexity properties with respect to its arguments (convex with respect to $\underset{\sim}{\boldsymbol{M}}$ and concave with respect to X) and if a Fourier type of heat conduction is chosen

$$\underline{\boldsymbol{Q}} = -\underset{\sim}{\boldsymbol{K}} \cdot \boldsymbol{\nabla}_X(\log T) \tag{23}$$

The dissipation potential is assumed to depend on $\underset{\sim}{\boldsymbol{M}}$ and X via the Schmid yield function

$$f^s(\underset{\sim}{\boldsymbol{M}}, X) = |\tau^s - x^s| - \tau_c^s, \quad \text{with} \quad \tau^s = \underset{\sim}{\boldsymbol{M}} : \underline{\boldsymbol{m}}^s \otimes \underline{\boldsymbol{n}}^s \tag{24}$$

where τ_c^s is the critical resolved shear stress for slip system s, which may evolve due to isotropic hardening. Kinematic hardening is accounted for by means of back-stress components x^s attached to each slip system. The resolved shear stress $\tau^s = \underline{\boldsymbol{m}}^s.\underset{\sim}{\boldsymbol{M}}.\underline{\boldsymbol{n}}^s$ on slip system s is the driving force for activation of slip. This corresponds to the specific choice of hardening variables: $X = (\tau_c^s, x^s)$. So we consider a function

$$\Omega(\underset{\sim}{\boldsymbol{M}}, X) = \sum_{s=1}^{N} \Omega^s(f^s(\underset{\sim}{\boldsymbol{M}}, X)) \tag{25}$$

It follows that

$$\dot{\underset{\sim}{\boldsymbol{P}}}.\underset{\sim}{\boldsymbol{P}}^{-1} = \frac{\partial \Omega}{\partial \underset{\sim}{\boldsymbol{M}}} = \sum_{s=1}^{N} \frac{\partial \Omega^s}{\partial f^s} \frac{\partial f^s}{\partial \underset{\sim}{\boldsymbol{M}}} = \sum_{s=1}^{N} \dot{\gamma}^s \underline{\boldsymbol{m}}^s \otimes \underline{\boldsymbol{n}}^s \tag{26}$$

where the slip rate is computed as

$$\dot{\gamma}^s = \frac{\partial \Omega^s}{\partial f^s} \ \text{sign}\,(\tau^s - x^s) \tag{27}$$

Accordingly, the kinematics (16) is retrieved from the normality rule, showing that the crystal slip kinematics is associated with the Schmid law. Let us call (ρ^s, α^s) internal variables associated with the isotropic and kinematic hardening variables (τ_c^s, x^s). The hardening rules in (22) become

$$\dot{\rho}^s = -\frac{\partial \Omega}{\partial \tau_c^s} = \frac{\partial \Omega^s}{\partial f^s} = |\dot{\gamma}^s|, \quad \dot{\alpha}^s = -\frac{\partial \Omega}{\partial x^s} = \frac{\partial \Omega^s}{\partial f^s} \ \text{sign}\,(\tau^s - x^s) = \dot{\gamma}^s \tag{28}$$

It is worth computing the plastic power after taking the previous relations into account

$$\underset{\sim}{\boldsymbol{M}} : \dot{\underset{\sim}{\boldsymbol{P}}}.\underset{\sim}{\boldsymbol{P}}^{-1} = \sum_{s=1}^{N} \tau^s \dot{\gamma}^s \tag{29}$$

Specific hardening laws including evolution equations for dislocation densities can be found for example in Fivel and Forest (2004a). As an example, we consider here a power law potential

$$\dot{\gamma}^s = \frac{\partial \Omega}{\partial \tau^s} = \left\langle \frac{|\tau^s - x^s| - \tau_c}{K} \right\rangle^n \operatorname{sign}(\tau^s) \tag{30}$$

$$\Omega(\tau^s) = \sum_{s=1}^{N} \frac{K}{n+1} \left\langle \frac{|\tau^s - x^s| - \tau_c}{K} \right\rangle^{n+1} \tag{31}$$

The brackets $\langle x \rangle$ denote the positive part of x. Viscosity parameters are K and n in (31). They can be chosen such that plastic processes are almost rate–independent in a given range of applied strain rates. As an example, we give here simple nonlinear evolution rules for the isotropic and kinematic variables that are used for practical computations

$$\tau_c^s = \tau_c + q \sum_{r=1}^{N} h^{sr} (1 - \exp(-b v^r)), \quad \dot{\alpha}^s = \dot{\gamma}^s - d \dot{v}^s \alpha^s \tag{32}$$

where q, b, d are material parameters. An interaction matrix h^{rs} is necessary to account for interaction between dislocations and is responsible for latent hardening Fivel and Forest (2004a).

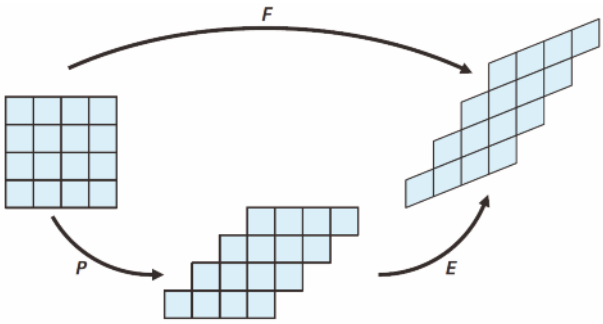

Figure 1. Multiplicative decomposition of the deformation gradient into elastic and plastic parts.

Lattice rotation. The previous continuum mechanical approach makes it possible to distinguish between the transformation of material and lattice

directions. Material lines are made of material points that are subjected to the motion $\underline{\boldsymbol{u}}(\underline{\boldsymbol{X}})$. The tangent to a material line at $\underline{\boldsymbol{X}}$ is a material direction $\underline{\boldsymbol{d}}$ in the reference configuration that transforms into the material direction $\underline{\boldsymbol{d}}'$ in the current configuration by means of the deformation gradient:

$$\underline{\boldsymbol{d}}'(\underline{\boldsymbol{X}}) = \underset{\sim}{\boldsymbol{F}}(\underline{\boldsymbol{X}}) \cdot \underline{\boldsymbol{d}}(\underline{\boldsymbol{X}}) \tag{33}$$

In contrast, lattice directions are not material insofar as they are not necessarily made of the same material points (atoms) in the initial and current configurations due to the passing of dislocations, but keep the same crystallographic meaning. According to the concept of isoclinic configuration, lattice directions are unchanged from the initial to the intermediate configuration of figure 1. Glide of dislocations through, and thus leaving, the material volume element do not distort nor rotate the lattice, although material lines are sheared. According to the continuum theory of dislocations, statistically stored dislocations accumulating in the material volume element affect material hardening but do not change the element shape. Accordingly, an initial lattice direction $\underline{\boldsymbol{d}}^\sharp$ is transformed into $\underline{\boldsymbol{d}}^{\sharp\prime}$ by means of the elastic deformation:

$$\underline{\boldsymbol{d}}^{\sharp\prime}(\underline{\boldsymbol{X}}) = \underset{\sim}{\boldsymbol{E}}(\underline{\boldsymbol{X}}).\underline{\boldsymbol{d}}^\sharp(\underline{\boldsymbol{X}}) \tag{34}$$

The kinematics of elastoplastic deformation recalled in section 2.1 can be expanded in the case of small strains and small rotations, based on the polar decompositions of total, elastic and plastic deformations:

$$\underset{\sim}{\boldsymbol{E}} = \underset{\sim}{\boldsymbol{R}}^e.\underset{\sim}{\boldsymbol{U}}^e \simeq (\underset{\sim}{\mathbf{1}} + \underset{\sim}{\boldsymbol{\omega}}^e).(\underset{\sim}{\mathbf{1}} + \underset{\sim}{\boldsymbol{\varepsilon}}^e) \simeq \underset{\sim}{\mathbf{1}} + \underset{\sim}{\boldsymbol{\varepsilon}}^e + \underset{\sim}{\boldsymbol{\omega}}^e \tag{35}$$

$$\underset{\sim}{\boldsymbol{P}} = \underset{\sim}{\boldsymbol{R}}^p.\underset{\sim}{\boldsymbol{U}}^p \simeq (\underset{\sim}{\mathbf{1}} + \underset{\sim}{\boldsymbol{\omega}}^p).(\underset{\sim}{\mathbf{1}} + \underset{\sim}{\boldsymbol{\varepsilon}}^p) \simeq \underset{\sim}{\mathbf{1}} + \underset{\sim}{\boldsymbol{\varepsilon}}^p + \underset{\sim}{\boldsymbol{\omega}}^p \tag{36}$$

where $\underset{\sim}{\boldsymbol{R}}^e, \underset{\sim}{\boldsymbol{R}}^p$ and $\underset{\sim}{\boldsymbol{U}}^e, \underset{\sim}{\boldsymbol{U}}^p$ are rotations and symmetric stretch tensors, respectively. Accordingly, $\underset{\sim}{\boldsymbol{\varepsilon}}^e, \underset{\sim}{\boldsymbol{\omega}}^e$ (resp. $\underset{\sim}{\boldsymbol{\varepsilon}}^p, \underset{\sim}{\boldsymbol{\omega}}^p$) represent small elastic (resp. plastic) strain and rotation. The elastic rotation accounts for lattice rotation, as follows from the proposed kinematics of plastic slip. Similarly, the following holds for the total deformation:

$$\underset{\sim}{\boldsymbol{F}} = \underset{\sim}{\boldsymbol{R}}.\underset{\sim}{\boldsymbol{U}} = (\underset{\sim}{\mathbf{1}} + \underset{\sim}{\boldsymbol{\omega}}).(\underset{\sim}{\mathbf{1}} + \underset{\sim}{\boldsymbol{\varepsilon}}) \simeq \underset{\sim}{\mathbf{1}} + \underset{\sim}{\boldsymbol{\varepsilon}} + \underset{\sim}{\boldsymbol{\omega}} \tag{37}$$

so that

$$\underset{\sim}{\boldsymbol{\varepsilon}} = \underset{\sim}{\boldsymbol{\varepsilon}}^e + \underset{\sim}{\boldsymbol{\varepsilon}}^p, \quad \underset{\sim}{\boldsymbol{\omega}} = \underset{\sim}{\boldsymbol{\omega}}^e + \underset{\sim}{\boldsymbol{\omega}}^p \tag{38}$$

where all strain tensors are symmetric whereas all ω tensors are skew–symmetric.

In metals, elastic strain remains small whereas lattice rotations can become very large. That is why the kinematics of crystallographic slip is very often approximated as

$$\underset{\sim}{\boldsymbol{F}} \simeq \underset{\sim}{\boldsymbol{R}}^e \cdot \underset{\sim}{\boldsymbol{P}} \tag{39}$$

especially for the simulation of metal forming processes. Lattice rotation is then directly given by $\underset{\sim}{\boldsymbol{R}}^e$.

Let us consider also rotation rates by introducing the material spin tensor $\underset{\sim}{\boldsymbol{W}}$ which is the skew–symmetric part of the velocity gradient

$$\dot{\underset{\sim}{\boldsymbol{F}}} \cdot \underset{\sim}{\boldsymbol{F}}^{-1} = \underset{\sim}{\boldsymbol{D}} + \underset{\sim}{\boldsymbol{W}} = \dot{\underset{\sim}{\boldsymbol{E}}} \cdot \underset{\sim}{\boldsymbol{E}}^{-1} + \underset{\sim}{\boldsymbol{E}} \cdot \dot{\underset{\sim}{\boldsymbol{P}}} \cdot \underset{\sim}{\boldsymbol{P}}^{-1} \cdot \underset{\sim}{\boldsymbol{E}}^{-1} = \underset{\sim}{\boldsymbol{D}}^e + \underset{\sim}{\boldsymbol{W}}^e + \underset{\sim}{\boldsymbol{D}}^p + \underset{\sim}{\boldsymbol{W}}^p \tag{40}$$

where the elastic and plastic contributions have been split into their symmetric and skew–symmetric parts. The elastic spin tensor is therefore defined as

$$\underset{\sim}{\boldsymbol{W}}^e = \left(\dot{\underset{\sim}{\boldsymbol{E}}} \cdot \underset{\sim}{\boldsymbol{E}}^{-1} \right)^{skew} = \left(\dot{\underset{\sim}{\boldsymbol{R}}}^e \cdot \underset{\sim}{\boldsymbol{R}}^{e-1} + \underset{\sim}{\boldsymbol{R}}^e \cdot \dot{\underset{\sim}{\boldsymbol{U}}}^e \cdot \underset{\sim}{\boldsymbol{U}}^e \cdot \underset{\sim}{\boldsymbol{R}}^{e-1} \right)^{skew} \tag{41}$$

$$\simeq \dot{\underset{\sim}{\boldsymbol{R}}}^e \cdot \underset{\sim}{\boldsymbol{R}}^{e-1} = \dot{\underset{\sim}{\boldsymbol{R}}}^e \cdot \underset{\sim}{\boldsymbol{R}}^{eT} \tag{42}$$

where the exponent *skew* denotes the skew–symmetric part of the tensor in brackets. The latter approximation is valid when elastic strain rates can be neglected compared to rotation rates, which is generally the case for metals at sufficiently high total strains. Note that for any rotation $\underset{\sim}{\boldsymbol{Q}}$, the rotation rate $\dot{\underset{\sim}{\boldsymbol{Q}}} \cdot \underset{\sim}{\boldsymbol{Q}}^{-1} = \dot{\underset{\sim}{\boldsymbol{Q}}} \cdot \underset{\sim}{\boldsymbol{Q}}^{T}$ is a skew–symmetric tensor due to the fact that a rotation is an orthogonal tensor[1]. The plastic spin rate is

$$\begin{aligned}
\underset{\sim}{\boldsymbol{W}}^p &= \left(\underset{\sim}{\boldsymbol{E}} \cdot \left(\sum_{s=1}^{N} \dot{\gamma}^s \underline{\boldsymbol{m}}^s \otimes \underline{\boldsymbol{n}}^s \right) \cdot \underset{\sim}{\boldsymbol{E}}^{-1} \right)^{skew} \\
&\simeq \left(\underset{\sim}{\boldsymbol{R}}^e \cdot \left(\sum_{s=1}^{N} \dot{\gamma}^s \underline{\boldsymbol{m}}^s \otimes \underline{\boldsymbol{n}}^s \right) \cdot \underset{\sim}{\boldsymbol{R}}^{eT} \right)^{skew} \\
&\simeq \underset{\sim}{\boldsymbol{R}}^e \cdot \left(\sum_{s=1}^{N} \dot{\gamma}^s \left(\underline{\boldsymbol{m}}^s \otimes \underline{\boldsymbol{n}}^s \right)^{skew} \right) \cdot \underset{\sim}{\boldsymbol{R}}^{eT}
\end{aligned}$$

In the case of small elastic strain and rotations, the expressions simplify

[1] meaning that $\underset{\sim}{\boldsymbol{Q}} \cdot \underset{\sim}{\boldsymbol{Q}}^T = \underset{\sim}{\boldsymbol{Q}}^T \cdot \underset{\sim}{\boldsymbol{Q}} = \underset{\sim}{\boldsymbol{1}}$

and we obtain

$$\underset{\sim}{\boldsymbol{D}}^p \simeq \underset{\sim}{\dot{\boldsymbol{\varepsilon}}}^p = \sum_{s=1}^{N} \dot{\gamma}^s \left(\underline{\boldsymbol{m}}^s \otimes \underline{\boldsymbol{n}}^s\right)^{sym} \tag{43}$$

$$\underset{\sim}{\boldsymbol{W}}^p \simeq \underset{\sim}{\dot{\boldsymbol{\omega}}}^p = \sum_{s=1}^{N} \dot{\gamma}^s \left(\underline{\boldsymbol{m}}^s \otimes \underline{\boldsymbol{n}}^s\right)^{skew} \tag{44}$$

$$\underset{\sim}{\boldsymbol{D}}^e \simeq \underset{\sim}{\dot{\boldsymbol{\varepsilon}}}^e = \underset{\sim}{\dot{\boldsymbol{\varepsilon}}} - \underset{\sim}{\dot{\boldsymbol{\varepsilon}}}^p, \quad \underset{\sim}{\dot{\boldsymbol{W}}}^e \simeq \underset{\sim}{\dot{\boldsymbol{\omega}}}^e = \underset{\sim}{\dot{\boldsymbol{\omega}}} - \underset{\sim}{\dot{\boldsymbol{\omega}}}^p \tag{45}$$

2.2 Elements of tensor analysis

The Euclidean space is endowed with an arbitrary coordinate system characterizing the points $M(q^i)$. The basis vectors are defined as

$$\underline{\boldsymbol{e}}_i = \frac{\partial M}{\partial q^i} \tag{46}$$

The reciprocal basis $(\underline{\boldsymbol{e}}^i)_{i=1,3}$ of $(\underline{\boldsymbol{e}}_i)_{i=1,3}$ is the unique triad of vectors such that

$$\underline{\boldsymbol{e}}^i \cdot \underline{\boldsymbol{e}}_j = \delta^i_j \tag{47}$$

If a Cartesian orthonormal coordinate system is chosen, then both bases coincide.

The gradient operator for a tensor field $T(\underline{\boldsymbol{X}})$ of arbitrary rank is then defined as

$$\operatorname{grad} T = T \otimes \boldsymbol{\nabla} := \frac{\partial T}{\partial q^i} \otimes \underline{\boldsymbol{e}}^i \tag{48}$$

The gradient operation therefore increases the tensor rank by one.

The divergence operator for a tensor field $T(\underline{\boldsymbol{X}})$ of arbitrary rank is then defined as

$$\operatorname{div} T = T \cdot \boldsymbol{\nabla} := \frac{\partial T}{\partial q^i} \cdot \underline{\boldsymbol{e}}^i \tag{49}$$

The divergence operation therefore decreases the tensor rank by one.

The curl operator[2] for a tensor field $T(\underline{\boldsymbol{X}})$ of arbitrary rank is then defined as

$$\operatorname{curl} T = T \wedge \boldsymbol{\nabla} := \frac{\partial T}{\partial q^i} \wedge \underline{\boldsymbol{e}}^i \tag{50}$$

where the vector product is $\wedge$. The curl operation therefore leaves the tensor rank unchanged. The vector product on an oriented Euclidean space is

$$\underline{\boldsymbol{a}} \wedge \underline{\boldsymbol{b}} = \epsilon_{ijk} a_j b_k \, \underline{\boldsymbol{e}}_i = \underset{\sim}{\boldsymbol{\epsilon}} : (\underline{\boldsymbol{a}} \otimes \underline{\boldsymbol{b}}) \tag{51}$$

[2] or rotational operator.

The component ϵ_{ijk} of the third rank permutation tensor is the signature of the permutation of $(1,2,3)$.

With respect to a Cartesian orthonormal basis, the previous formula simplify. We give the expressions for a second rank tensor $\underset{\sim}{\boldsymbol{T}}$

$$\operatorname{grad} \underset{\sim}{\boldsymbol{T}} = T_{ij,k}\, \underline{\boldsymbol{e}}_i \otimes \underline{\boldsymbol{e}}_j \otimes \underline{\boldsymbol{e}}_k \tag{52}$$

$$\operatorname{div} \underset{\sim}{\boldsymbol{T}} = T_{ij,j}\, \underline{\boldsymbol{e}}_i \tag{53}$$

We consider then successively the curl of a vector field and of a second rank vector field, in a Cartesian orthonormal coordinate frame

$$\operatorname{curl} \underline{\boldsymbol{u}} = \frac{\partial \underline{\boldsymbol{u}}}{\partial X_j} \wedge \underline{\boldsymbol{e}}_j = u_{i,j}\, \underline{\boldsymbol{e}}_i \wedge \underline{\boldsymbol{e}}_j = \epsilon_{kij} u_{i,j}\, \underline{\boldsymbol{e}}_k \tag{54}$$

$$\operatorname{curl} \underset{\sim}{\boldsymbol{A}} = \frac{\partial \underset{\sim}{\boldsymbol{A}}}{\partial x_k} \wedge \underline{\boldsymbol{e}}_k = A_{ij,k} \underline{\boldsymbol{e}}_i \otimes \underline{\boldsymbol{e}}_j \wedge \underline{\boldsymbol{e}}_k = \epsilon_{mjk} A_{ij,k}\, \underline{\boldsymbol{e}}_i \otimes \underline{\boldsymbol{e}}_m \tag{55}$$

We also recall the Stokes formula for a vector field for a surface $\mathcal{S}$ with unit normal vector $\underline{\boldsymbol{n}}$ and oriented closed border line $\mathcal{L}$:

$$\oint_{\mathcal{L}} \underline{\boldsymbol{u}} \cdot \underline{\boldsymbol{dl}} = -\int_{\mathcal{S}} (\operatorname{curl} \underline{\boldsymbol{u}}) \cdot \underline{\boldsymbol{n}}\, ds, \quad \oint_{\mathcal{L}} u_i dl_i = -\epsilon_{kij} \int_{\mathcal{S}} u_{i,j} n_k\, ds \tag{56}$$

Applying the previous formula to $u_j = A_{ij}$ at fixed i leads to the Stokes formula for a tensor field of rank 2:

$$\oint_{\mathcal{L}} \underset{\sim}{\boldsymbol{T}} \cdot \underline{\boldsymbol{dl}} = -\int_{\mathcal{S}} (\operatorname{curl} \underset{\sim}{\boldsymbol{T}}) \cdot \underline{\boldsymbol{n}}\, ds, \quad \oint_{\mathcal{L}} A_{ij} dl_i = -\epsilon_{kij} \int_{\mathcal{S}} A_{ij,k} n_m\, ds \tag{57}$$

2.3 Dislocation density tensor

In continuum mechanics, the previous differential operators are used with respect to the initial coordinates $\underline{\boldsymbol{X}}$ or with respect to the current coordinates $\underline{\boldsymbol{x}}$ of the material points. In the latter case, the notation $\boldsymbol{\nabla}, \operatorname{grad}, \operatorname{div}$ and curl are used but in the former case we adopt $\boldsymbol{\nabla}_X, \operatorname{Grad}, Div$ and Curl. For instance,

$$\underset{\sim}{\boldsymbol{F}} = \underset{\sim}{\mathbf{1}} + \operatorname{Grad} \underline{\boldsymbol{u}} \quad \Longrightarrow \quad \operatorname{Curl} \underset{\sim}{\boldsymbol{F}} = 0 \tag{58}$$

This result expresses the fact that the deformation gradient is a compatible field which derives from the displacement vector field. This is generally not the case for elastic and plastic deformation:

$$\operatorname{Curl} \underset{\sim}{\boldsymbol{E}} \neq 0, \quad \operatorname{Curl} \underset{\sim}{\boldsymbol{P}} \neq 0 \tag{59}$$

Elastic and plastic deformations are generally incompatible tensor fields, even though the product $\underset{\sim}{\boldsymbol{F}} = \underset{\sim}{\boldsymbol{E}} \cdot \underset{\sim}{\boldsymbol{P}}$ is compatible. It may happen incidentally that elastic deformation be compatible for instance when plastic or elastic deformation is homogeneous.

A consequence of the incompatibility of the elastic deformation is that, for an oriented surface $\mathcal{S} \subset \Omega$ of the body, with border $\mathcal{L}$, the vector $\underline{\boldsymbol{B}}$ belonging to the intermediate isoclinic configuration

$$\underline{\boldsymbol{B}} = \oint_{\mathcal{L}} \underset{\sim}{\boldsymbol{E}}^{-1} \cdot \underline{\boldsymbol{dl}} = -\int_{\mathcal{S}} (\operatorname{curl} \underset{\sim}{\boldsymbol{E}}^{-1}) \cdot \underline{\boldsymbol{n}}\, ds \tag{60}$$

does not vanish in general. It can be interpreted as the continuum Burgers vector for the circuit $\mathcal{L}$. It represents a generalization of the concept of Burgers vector for dislocations. This geometric definition was introduced by Bilby et al. (1957); Teodosiu (1970); Kröner and Teodosiu (1972) within the context of the continuum theory of dislocations. The previous calculation leads to the definition of the dislocation density tensor

$$\underset{\sim}{\boldsymbol{\alpha}} := -\operatorname{curl} \underset{\sim}{\boldsymbol{E}}^{-1} = -\epsilon_{jkl} E^{-1}_{ik,l}\, \underline{\boldsymbol{e}}_i \otimes \underline{\boldsymbol{e}}_j \tag{61}$$

which is used to compute the resulting Burgers vector for dislocations crossing the surface $\mathcal{S}$:

$$\underline{\boldsymbol{B}} = \int_{\mathcal{S}} \underset{\sim}{\boldsymbol{\alpha}} \cdot \underline{\boldsymbol{n}}\, ds \tag{62}$$

The Burgers vector can also be computed by means of a closed circuit $\mathcal{L}_0 \subset \Omega_0$ convected from $\mathcal{L} \subset \Omega$:

$$\underline{\boldsymbol{B}} = \oint_{\mathcal{L}} \underset{\sim}{\boldsymbol{E}}^{-1} \cdot \underline{\boldsymbol{dx}} = \oint_{\mathcal{L}_0} \underset{\sim}{\boldsymbol{E}}^{-1} \cdot \underset{\sim}{\boldsymbol{F}} \cdot \underline{\boldsymbol{dX}} = \oint_{\mathcal{L}_0} \underset{\sim}{\boldsymbol{P}} \cdot \underline{\boldsymbol{dX}} \tag{63}$$

$$= \int_{\mathcal{S}_0} (\operatorname{Curl} \underset{\sim}{\boldsymbol{P}}) \cdot \underline{\boldsymbol{dS}} = \int_{\mathcal{S}} (\operatorname{Curl} \underset{\sim}{\boldsymbol{P}}) \cdot \underset{\sim}{\boldsymbol{F}}^T \cdot \frac{\underline{\boldsymbol{dS}}}{J} \tag{64}$$

Nanson's formula[3] has been used. We obtain the alternative definition of the dislocation density tensor

$$\underset{\sim}{\boldsymbol{\alpha}} = \operatorname{curl} \underset{\sim}{\boldsymbol{E}}^{-1} = \frac{1}{J} (\operatorname{Curl} \underset{\sim}{\boldsymbol{P}}) \cdot \underset{\sim}{\boldsymbol{F}}^T \tag{65}$$

The present modern treatment of the dislocation density tensor was settled by Cermelli and Gurtin (2001); Svendsen (2002). A statistical mechanics perspective of the dislocation density tensor can be found in Kröner (1969).

It can be noticed that the relation (65) implies

$$J(\operatorname{curl} \underset{\sim}{\boldsymbol{E}}^{-1}) \cdot \underset{\sim}{\boldsymbol{E}}^{-T} = (\operatorname{Curl} \underset{\sim}{\boldsymbol{P}}) \cdot \underset{\sim}{\boldsymbol{P}}^T \tag{66}$$

which is a consequence of (58), $\operatorname{curl} \underset{\sim}{\boldsymbol{F}} = \operatorname{curl}(\underset{\sim}{\boldsymbol{E}} \cdot \underset{\sim}{\boldsymbol{P}}) = 0$.

[3] $\underline{\boldsymbol{ds}} = J \underset{\sim}{\boldsymbol{F}}^{-T} \cdot \underline{\boldsymbol{dS}}$

Within the small perturbation framework, we introduce the notations

$$\underset{\sim}{\boldsymbol{H}} = \operatorname{Grad} \underline{\boldsymbol{u}} = \underset{\sim}{\boldsymbol{H}}^e + \underset{\sim}{\boldsymbol{H}}^p, \quad \text{with} \quad \underset{\sim}{\boldsymbol{H}}^e = \underset{\sim}{\boldsymbol{\varepsilon}}^e + \underset{\sim}{\boldsymbol{\omega}}^e, \quad \underset{\sim}{\boldsymbol{H}}^p = \underset{\sim}{\boldsymbol{\varepsilon}}^p + \underset{\sim}{\boldsymbol{\omega}}^p \tag{67}$$

We have

$$\underset{\sim}{\boldsymbol{E}}^{-1} \simeq \underset{\sim}{\mathbf{1}} - \underset{\sim}{\boldsymbol{H}}^e \tag{68}$$

so that the dislocation density tensor can be computed as

$$\underset{\sim}{\boldsymbol{\alpha}} \simeq \operatorname{Curl} \underset{\sim}{\boldsymbol{H}}^e = -\operatorname{Curl} \underset{\sim}{\boldsymbol{H}}^p \tag{69}$$

since $\operatorname{Curl} \underset{\sim}{\boldsymbol{H}} = 0$ due to the compatibility of the deformation gradient.

2.4 Lattice curvature

Experimental techniques like EBSD provide the field of lattice orientation and, consequently, of lattice rotation $\underset{\sim}{\boldsymbol{R}}^e$ during deformation. Since

$$\underset{\sim}{\boldsymbol{\alpha}} = -\operatorname{curl} \underset{\sim}{\boldsymbol{E}}^{-1} = -\operatorname{curl}(\underset{\sim}{\boldsymbol{U}}^{e-1} \cdot \underset{\sim}{\boldsymbol{R}}^{eT}) \tag{70}$$

the hypothesis of small elastic strain implies

$$\underset{\sim}{\boldsymbol{\alpha}} \simeq -\operatorname{curl} \underset{\sim}{\boldsymbol{R}}^{eT} \tag{71}$$

If, in addition, elastic rotations are small, we have

$$\underset{\sim}{\boldsymbol{\alpha}} \simeq -\operatorname{curl}(\underset{\sim}{\mathbf{1}} - \underset{\sim}{\boldsymbol{\omega}}^e) = \operatorname{curl} \underset{\sim}{\boldsymbol{\omega}}^e \tag{72}$$

The small rotation axial vector is defined as

$$\overset{\times}{\underline{\boldsymbol{\omega}}}{}^e = -\frac{1}{2} \underset{\approx}{\boldsymbol{\epsilon}} : \underset{\sim}{\boldsymbol{\omega}}^e, \quad \underset{\sim}{\boldsymbol{\omega}}^e = -\underset{\approx}{\boldsymbol{\epsilon}} \cdot \overset{\times}{\underline{\boldsymbol{\omega}}}{}^e \tag{73}$$

or, in matrix notations,

$$[\underset{\sim}{\boldsymbol{\omega}}^e] = \begin{bmatrix} 0 & \omega_{12}^e & -\omega_{31}^e \\ -\omega_{12}^e & 0 & \omega_{23}^e \\ \omega_{31}^e & -\omega_{23}^e & 0 \end{bmatrix} = \begin{bmatrix} 0 & -\overset{\times}{\omega}{}_3^e & \overset{\times}{\omega}{}_2^e \\ \overset{\times}{\omega}{}_3^e & 0 & -\overset{\times}{\omega}{}_1^e \\ -\overset{\times}{\omega}{}_2^e & \overset{\times}{\omega}{}_1^e & 0 \end{bmatrix} \tag{74}$$

The gradient of the lattice rotation field delivers the lattice curvature tensor. In the small deformation context, the gradient of the rotation tensor is represented by the gradient of the axial vector:

$$\underset{\sim}{\boldsymbol{\kappa}} := \overset{\times}{\underline{\boldsymbol{\omega}}}{}^e \tag{75}$$

One can establish a direct link between $\operatorname{curl}\underset{\sim}{\boldsymbol{\omega}}^e$ and the gradient of the axial vector associated with $\underset{\sim}{\boldsymbol{\omega}}$. For that purpose, the matrix form of $\operatorname{curl}\underset{\sim}{\boldsymbol{\omega}}^e$ is derived according to (55):

$$[\operatorname{curl}\underset{\sim}{\boldsymbol{\omega}}^e] = \begin{bmatrix} \omega^e_{12,3} + \omega^e_{31,2} & -\omega^e_{31,1} & -\omega^e_{12,1} \\ -\omega^e_{23,2} & \omega^e_{12,3} + \omega^e_{23,1} & -\omega^e_{12,2} \\ -\omega^e_{23,3} & -\omega^e_{31,3} & \omega^e_{23,1} + \omega^e_{31,2} \end{bmatrix} \tag{76}$$

or equivalently

$$[\operatorname{curl}\underset{\sim}{\boldsymbol{\omega}}^e] = \begin{bmatrix} -\overset{\times}{\omega}{}^e_{3,3} - \overset{\times}{\omega}{}^e_{2,2} & \overset{\times}{\omega}{}^e_{2,1} & \overset{\times}{\omega}{}^{}_{3,1} \\ \overset{\times}{\omega}{}^e_{1,2} & -\overset{\times}{\omega}{}^e_{3,3} - \overset{\times}{\omega}{}^e_{1,1} & \overset{\times}{\omega}{}^{e}_{3,2} \\ \overset{\times}{\omega}{}^e_{1,3} & \overset{\times}{\omega}{}^e_{2,3} & -\overset{\times}{\omega}{}^e_{1,1} - \overset{\times}{\omega}{}^e_{2,2} \end{bmatrix} \tag{77}$$

from which it becomes apparent that

$$\underset{\sim}{\boldsymbol{\alpha}} = \underset{\sim}{\boldsymbol{\kappa}}^T - (\operatorname{trace}\underset{\sim}{\boldsymbol{\kappa}})\underset{\sim}{\mathbf{1}}, \quad \underset{\sim}{\boldsymbol{\kappa}} = \underset{\sim}{\boldsymbol{\alpha}}^T - \frac{1}{2}(\operatorname{trace}\underset{\sim}{\boldsymbol{\alpha}})\underset{\sim}{\mathbf{1}} \tag{78}$$

This is a remarkable relation linking, with the context of small elastic strains[4] and rotations, the dislocation density tensor to lattice curvature. It is known as Nye's formula Nye (1953).

3 Micromorphic crystal plasticity

The links between the micromorphic continuum and the plasticity of crystalline materials has been recognized very early by Eringen himself (Claus and Eringen, 1969; Eringen and Claus, 1970). Lattice directions in a single crystal can be regarded as directors that rotate and deform as they do in a micromorphic continuum. The fact that lattice directions can be rotated and stretched in a different way than material lines connecting individual atoms, especially in the presence of static or moving dislocations, illustrates the independence between directors and material lines in a micromorphic continuum, even though their deformations can be related at the constitutive level.

The identification of a micromorphic continuum from the discrete atomic single crystal model is possible based on proper averaging relations proposed in (Chen and Lee, 2003a,b). These works contain virial formula for

[4] and in fact of small gradient of elastic strain.

the higher order stress tensors arising in the micromorphic theory. This atomistic–based approach can be used to predict phonon dispersion relations (Chen and Lee, 2003c). Claus and Eringen (1971) also studied the dispersion of waves in a dislocated crystal.

Analytical solutions have been provided that give the generalized stress fields around individual screw or edge dislocations embedded in an elastic generalized continuum medium, like the micromorphic medium. The physical meaning of such a calculation is the account of non–local elasticity at the core of dislocations that may suppress or limit the singularity of the stress fields. For instance, non singular force and couple stress were determined by (Lazar and Maugin, 2004) for a screw dislocation embedded in a gradient micropolar medium that combines the first strain gradient with independent rotational degrees of freedom. The unphysical singularities at the core of straight screw and edge dislocations are also removed when the second gradient of strain is introduced in the theory, while the first strain gradient is not sufficient, see (Lazar et al., 2006). Other crystal defects in a large range of microcontinua were analysed by Lazar and Maugin (2007).

The next step is to consider the collective behaviour of dislocations in a single crystal by means of the continuum theory of dislocations. The material volume element is now assumed to contain a large enough number of dislocations for the continuum theory of dislocation to be applicable. Non–homogeneous plastic deformations induce material and lattice incompatibilities that are resolved by a suitable distribution of the dislocation density tensor field which is a second rank statistical mean for a population of arbitrary dislocations inside a material volume element (Kröner, 1969; Cermelli and Gurtin, 2001). Nye's fundamental relation linearly connects the dislocation density tensor to the lattice curvature field of the crystal. This fact has prompted many authors to treat a continuously dislocated crystal as a Cosserat continuum (Günther, 1958; Kröner, 1963; Schäfer,H., 1969; Forest et al., 2000). The Cosserat approach records only the lattice curvature of the crystal but neglects the effect of the rotational part of the elastic strain tensor, which is a part of the total dislocation density tensor (Cordero et al., 2010). Full account of plastic incompatibilities is taken in strain gradient plasticity theories, starting from the original work by Aifantis (1984) up to recent progress by Gurtin (2002). Formulation of crystal plasticity within the micromorphic framework is more recent and was suggested by Clayton et al. (2005) for a large spectrum of crystal defects, including point defects and disclinations. Limiting the discussion to dislocation density tensor effects, also called geometrically necessary dislocation (GND) effects, Cordero et al. (2010) showed, within a small deformation setting, how the micromorphic model can be used to predict grain and precipitate

size effects in laminate crystalline materials. In particular, the micromorphic model is shown to deliver more general scaling laws than conventional strain gradient plasticity. These models represent extensions of the conventional crystal plasticity theory, see for instance (Teodosiu and Sidoroff, 1976), that accounts for single crystal hardening and lattice rotation but does not incorporate the effect of the dislocation density tensor.

The objective of the present work is, first, to formulate a finite deformation micromorphic extension of conventional crystal plasticity to account for GND effects in single crystals, and, second, to show that the micromorphic approach can also be used to introduce cleavage induced damage in a single crystal model. The first part, see Section 3, represents an extension to finite deformation of the model proposed by Aslan et al. (2011). It also provides new analytical predictions of size effects on the yield stength and kinematic hardening of laminate microstructures made of an elastic layer and an elastic–plastic single crystal layer undergoing single slip. The theory is called the *microcurl* model because the evaluation of the curl of the microdeformation, instead of its full gradient, is sufficient to account for the effect of the dislocation density tensor.

The models proposed in this work for single crystals fall in the class of anisotropic elastoviscoplastic micromorphic media for which constitutive frameworks at finite deformations have been proposed in (Forest and Sievert, 2003; Lee and Chen, 2003; Grammenoudis and Tsakmakis, 2009; Sansour et al., 2010; Regueiro, 2010). The introduction of damage variables was performed in (Grammenoudis et al., 2009). In fact, the micromorphic approach can be applied not only to the total deformation by introducing the micro–deformation field, but can also be restricted to plastic deformation, for specific application to size effects in plasticity, or to damage variables for application to regularized simulation of crack propagation, as proposed in (Forest, 2009; Hirschberger and Steinmann, 2009).

3.1 Model formulation

Balance equations. The degrees of freedom of the proposed theory are the displacement vector $\underline{\boldsymbol{u}}$ and the microdeformation variable $\underset{\sim}{\hat{\boldsymbol{\chi}}}^p$, a generally non–symmetric second rank tensor. The field $\underset{\sim}{\hat{\boldsymbol{\chi}}}^p(\underline{\boldsymbol{X}})$ is generally not compatible, meaning that it does not derive from a vector field. The exponent ^{p} indicates, in advance, that this variable will eventually be constitutively related to plastic deformation occurring at the material point. In particular, the microdeformation $\underset{\sim}{\hat{\boldsymbol{\chi}}}^p$ is treated as an invariant quantity with respect to rigid body motion. The constitutive model will eventually ensure this invariance property. This is in contrast to the general microdeforma-

tion degrees of freedom of the original micromorphic theory. A first gradient theory is considered with respect to the degrees of freedom. However, the influence of the microdeformation gradient is limited to its curl part because of the aimed relation to the dislocation density tensor associated with the curl of plastic distortion. The following sets of degrees of freedom and of their gradients are therefore defined:

$$DOF = \{\underline{\boldsymbol{u}}, \quad \underset{\sim}{\hat{\boldsymbol{\chi}}}^p\}, \quad GRAD = \{\underset{\sim}{\boldsymbol{F}} := \underset{\sim}{\mathbf{1}} + \underline{\boldsymbol{u}} \otimes \boldsymbol{\nabla}_X, \quad \underset{\sim}{\boldsymbol{K}} := \mathrm{Curl}\, \underset{\sim}{\hat{\boldsymbol{\chi}}}^p\} \tag{79}$$

The following definition of the Curl operator is adopted:

$$\mathrm{Curl}\, \underset{\sim}{\hat{\boldsymbol{\chi}}}^p := \frac{\partial \underset{\sim}{\hat{\boldsymbol{\chi}}}^p}{\partial X_k} \times \underline{\boldsymbol{e}}_k, \quad K_{ij} := \epsilon_{jkl} \frac{\partial \hat{\chi}^p_{ik}}{\partial X_l} \tag{80}$$

where ϵ_{ijk} is the permutation tensor.
The method of virtual power is used to derive the balance and boundary conditions, following (Germain, 1973b). For that purpose, we define the power density of internal forces as a linear form with respect to the velocity fields and their Eulerian gradients:

$$p^{(i)} = \underset{\sim}{\boldsymbol{\sigma}} : (\dot{\underline{\boldsymbol{u}}} \otimes \boldsymbol{\nabla}_x) + \underset{\sim}{\boldsymbol{s}} : \dot{\underset{\sim}{\hat{\boldsymbol{\chi}}}}^p + \underset{\sim}{\boldsymbol{M}} : \mathrm{curl}\, \dot{\underset{\sim}{\hat{\boldsymbol{\chi}}}}^p, \quad \forall \underline{\boldsymbol{x}} \in V \tag{81}$$

where the conjugate quantities are the Cauchy stress tensor $\underset{\sim}{\boldsymbol{\sigma}}$, which is symmetric for objectivity reasons, the microstress tensor, $\underset{\sim}{\boldsymbol{s}}$, and the generalized couple stress tensor $\underset{\sim}{\boldsymbol{M}}$. The curl of the microdeformation rate is defined as

$$\mathrm{curl}\, \dot{\underset{\sim}{\hat{\boldsymbol{\chi}}}}^p := \epsilon_{jkl} \frac{\partial \dot{\hat{\chi}}^p_{ik}}{\partial x_l} \underline{\boldsymbol{e}}_i \otimes \underline{\boldsymbol{e}}_j = \dot{\underset{\sim}{\boldsymbol{K}}} \cdot \underset{\sim}{\boldsymbol{F}}^{-1} \tag{82}$$

The form of the power density of internal forces dictates the form of the power density of contact forces:

$$p^{(c)} = \underline{\boldsymbol{t}} \cdot \dot{\underline{\boldsymbol{u}}} + \underset{\sim}{\boldsymbol{m}} : \dot{\underset{\sim}{\hat{\boldsymbol{\chi}}}}^p, \quad \forall \underline{\boldsymbol{x}} \in \partial V \tag{83}$$

where $\underline{\boldsymbol{t}}$ is the usual simple traction vector and $\underset{\sim}{\boldsymbol{m}}$ the double traction tensor. The principle of virtual power is stated in the static case and in the absence of volume forces for the sake of brevity:

$$-\int_D p^{(i)}\, dV + \int_{\partial D} p^{(c)}\, dS = 0 \tag{84}$$

for all virtual fields $\dot{\underline{\boldsymbol{u}}}, \dot{\underset{\sim}{\hat{\boldsymbol{\chi}}}}^p$, and any subdomain $D \subset V$. By application of Gauss divergence theorem, assuming sufficient regularity of the fields, this

statement expands into:

$$\int_V \frac{\partial \sigma_{ij}}{\partial x_j}\dot{u}_i\, dV + \int_V \left(\epsilon_{kjl}\frac{\partial M_{ik}}{\partial x_l} - s_{ij}\right)\dot{\chi}^p_{ij}\, dV$$
$$+ \int_{\partial V}(t_i - \sigma_{ij}n_j)\,\dot{u}_i\, dS + \int_{\partial V}(m_{ik} - \epsilon_{jkl}M_{ij}n_l)\,\dot{\chi}^p_{ik}\, dS = 0, \quad \forall \dot{u}_i, \forall \dot{\chi}^p_{ij}$$

which leads to the two field equations of balance of momentum and generalized balance of moment of momentum:

$$\operatorname{div} \underset{\sim}{\boldsymbol{\sigma}} = 0, \quad \operatorname{curl} \underset{\sim}{\boldsymbol{M}} + \underset{\sim}{\boldsymbol{s}} = 0, \quad \forall \underline{\boldsymbol{x}} \in V \tag{85}$$

and two boundary conditions

$$\underline{\boldsymbol{t}} = \underset{\sim}{\boldsymbol{\sigma}} \cdot \underline{\boldsymbol{n}}, \quad \underset{\sim}{\boldsymbol{m}} = \underset{\sim}{\boldsymbol{M}} \cdot \underset{\approx}{\boldsymbol{\epsilon}} \cdot \underline{\boldsymbol{n}}, \quad \forall \underline{\boldsymbol{x}} \in \partial V \tag{86}$$

the index notation of the latter relation being $m_{ij} = M_{ik}\epsilon_{kjl}n_l$.

Constitutive equations. The deformation gradient is decomposed into elastic and plastic parts in the form

$$\underset{\sim}{\boldsymbol{F}} = \underset{\sim}{\boldsymbol{F}}^e \cdot \underset{\sim}{\boldsymbol{F}}^p \tag{87}$$

The isoclinic intermediate configuration is defined in a unique way by keeping the crystal orientation unchanged from the initial to the intermediate configuration following (Mandel, 1973). The plastic distortion $\underset{\sim}{\boldsymbol{F}}^p$ is invariant with respect to rigid body motions that are carried by $\underset{\sim}{\boldsymbol{F}}^e$. The current mass density is ρ whereas the mass density of the material element in the intermediate configuration is ρ_i, such that $\rho_i/\rho = J_e := \det \underset{\sim}{\boldsymbol{F}}^e$. The elastic strain is defined as

$$\underset{\sim}{\boldsymbol{E}}^e := \frac{1}{2}(\underset{\sim}{\boldsymbol{F}}^{eT} \cdot \underset{\sim}{\boldsymbol{F}}^e - \underset{\sim}{\mathbf{1}}) \tag{88}$$

The microdeformation is linked to the plastic deformation via the introduction of a relative deformation measure defined as

$$\underset{\sim}{\boldsymbol{e}}^p := \underset{\sim}{\boldsymbol{F}}^{p-1} \cdot \underset{\sim}{\hat{\boldsymbol{\chi}}}^p - \underset{\sim}{\mathbf{1}} \tag{89}$$

It measures the departure of the microdeformation from the plastic deformation, which will be associated with a cost in the free energy potential. When $\underset{\sim}{\boldsymbol{e}}^p \equiv 0$, the microdeformation coincides with the plastic deformation. The state variables are assumed to be the elastic strain, the relative deformation, the curl of microdeformation and some internal variables, α:

$$STATE := \{\underset{\sim}{\boldsymbol{E}}^e, \quad \underset{\sim}{\boldsymbol{e}}^p, \quad \underset{\sim}{\boldsymbol{K}}, \quad \alpha\} \tag{90}$$

The specific Helmholtz free energy density, ψ, is assumed to be a function of this set of state variables. In particular, in this simple version of the model, the curl of microdeformation is assumed to contribute entirely to the stored energy. In more sophisticated models, as proposed in (Forest and Sievert, 2003, 2006; Forest, 2009; Gurtin and Anand, 2009), the relative deformation, the microdeformation and its gradient can be split into elastic plastic parts. This is not necessary for the size effects to be described in the present work.

When the internal constraint $\underset{\sim}{\boldsymbol{e}}^p \equiv 0$ is enforced, the plastic microdeformation coincides with the plastic deformation so that the curl of the plastic microdformation is directly related to the dislocation density tensor:

$$\underset{\sim}{\boldsymbol{K}} := \mathrm{Curl}\,\underset{\sim}{\hat{\boldsymbol{\chi}}}^p \equiv \mathrm{Curl}\,P = J\underset{\sim}{\boldsymbol{\alpha}} \cdot \underset{\sim}{\boldsymbol{F}}^{-T} \tag{91}$$

The micromorphic model then reduces to strain gradient plasticity according to Gurtin (2002).

The dissipation rate density is the difference:

$$D := p^{(i)} - \rho\dot{\psi} \geq 0 \tag{92}$$

which must be positive according to the second principle of thermodynamics. When the previous strain measures are introduced, the power density of internal forces takes the following form:

$$\begin{aligned} p^{(i)} &= \underset{\sim}{\boldsymbol{\sigma}} : \dot{\underset{\sim}{\boldsymbol{F}}}^e \cdot \underset{\sim}{\boldsymbol{F}}^{e-1} + \underset{\sim}{\boldsymbol{\sigma}} : \underset{\sim}{\boldsymbol{F}}^e \cdot \dot{\underset{\sim}{\boldsymbol{F}}}^p \cdot \underset{\sim}{\boldsymbol{F}}^{p-1} \cdot \underset{\sim}{\boldsymbol{F}}^{e-1} \\ &+ \underset{\sim}{\boldsymbol{s}} : (\underset{\sim}{\boldsymbol{F}}^p \cdot \dot{\underset{\sim}{\boldsymbol{e}}}^p + \dot{\underset{\sim}{\boldsymbol{F}}}^p \cdot \underset{\sim}{\boldsymbol{e}}^p) + \underset{\sim}{\boldsymbol{M}} : \dot{\underset{\sim}{\boldsymbol{K}}} \cdot \underset{\sim}{\boldsymbol{F}}^{-1} \\ &= \frac{\rho}{\rho_i}\underset{\sim}{\boldsymbol{\Pi}}^e : \dot{\underset{\sim}{\boldsymbol{E}}}^e + \frac{\rho}{\rho_i}\underset{\sim}{\boldsymbol{\Pi}}^M : \dot{\underset{\sim}{\boldsymbol{F}}}^p \cdot \underset{\sim}{\boldsymbol{F}}^{p-1} \\ &+ \underset{\sim}{\boldsymbol{s}} : (\underset{\sim}{\boldsymbol{F}}^p \cdot \dot{\underset{\sim}{\boldsymbol{e}}}^p + \dot{\underset{\sim}{\boldsymbol{F}}}^p \cdot \underset{\sim}{\boldsymbol{e}}^p) + \underset{\sim}{\boldsymbol{M}} : \dot{\underset{\sim}{\boldsymbol{K}}} \cdot \underset{\sim}{\boldsymbol{F}}^{-1} \end{aligned} \tag{93}$$

where $\underset{\sim}{\boldsymbol{\Pi}}^e$ is the second Piola–Kirchhoff stress tensor with respect to the intermediate configuration and $\underset{\sim}{\boldsymbol{\Pi}}^M$ is the Mandel stress tensor:

$$\underset{\sim}{\boldsymbol{\Pi}}^e := J_e\underset{\sim}{\boldsymbol{F}}^{e-1} \cdot \underset{\sim}{\boldsymbol{\sigma}} \cdot \underset{\sim}{\boldsymbol{F}}^{e-T}, \quad \underset{\sim}{\boldsymbol{\Pi}}^M := J_e\underset{\sim}{\boldsymbol{F}}^{eT} \cdot \underset{\sim}{\boldsymbol{\sigma}} \cdot \underset{\sim}{\boldsymbol{F}}^{e-T} = \underset{\sim}{\boldsymbol{F}}^{eT} \cdot \underset{\sim}{\boldsymbol{F}}^e \cdot \underset{\sim}{\boldsymbol{\Pi}}^e \tag{94}$$

On the other hand,

$$\rho\dot{\psi} = \rho\frac{\partial\psi}{\partial\underset{\sim}{\boldsymbol{E}}^e} : \dot{\underset{\sim}{\boldsymbol{E}}}^e + \rho\frac{\partial\psi}{\partial\underset{\sim}{\boldsymbol{e}}^p} : \dot{\underset{\sim}{\boldsymbol{e}}}^p + \rho\frac{\partial\psi}{\partial\underset{\sim}{\boldsymbol{K}}} : \dot{\underset{\sim}{\boldsymbol{K}}} + \rho\frac{\partial\psi}{\partial\alpha}\dot{\alpha} \tag{95}$$

We compute

$$\begin{aligned} J_e D &= (\underset{\sim}{\boldsymbol{\Pi}}^e - \rho_i \frac{\partial \psi}{\partial \underset{\sim}{\boldsymbol{E}}^e}) : \dot{\underset{\sim}{\boldsymbol{E}}}^e + (J_e \underset{\sim}{\boldsymbol{F}}^{pT} \cdot \underset{\sim}{\boldsymbol{s}} - \rho_i \frac{\partial \psi}{\partial \underset{\sim}{\boldsymbol{e}}^p}) : \dot{\underset{\sim}{\boldsymbol{e}}}^p \\ &+ (J_e \underset{\sim}{\boldsymbol{M}} \cdot \underset{\sim}{\boldsymbol{F}}^{-T} - \rho_i \frac{\partial \psi}{\partial \underset{\sim}{\boldsymbol{K}}}) : \dot{\underset{\sim}{\boldsymbol{K}}} \\ &+ (\underset{\sim}{\boldsymbol{\Pi}}^M + J_e \underset{\sim}{\boldsymbol{s}} \cdot \underset{\sim}{\hat{\boldsymbol{\chi}}}^{pT}) : \dot{\underset{\sim}{\boldsymbol{F}}}^p \cdot \underset{\sim}{\boldsymbol{F}}^{p-1} - \rho_i \frac{\partial \psi}{\partial \alpha} \dot{\alpha} \geq 0 \end{aligned} \tag{96}$$

Assuming that the processes associated with $\dot{\underset{\sim}{\boldsymbol{E}}}^e$, $\dot{\underset{\sim}{\boldsymbol{e}}}^p$ and $\dot{\underset{\sim}{\boldsymbol{K}}}$ are non–dissipative, the state laws are obtained:

$$\underset{\sim}{\boldsymbol{\Pi}}^e = \rho_i \frac{\partial \psi}{\partial \underset{\sim}{\boldsymbol{E}}^e}, \quad \underset{\sim}{\boldsymbol{s}} = J_e^{-1} \underset{\sim}{\boldsymbol{F}}^{p-T} \cdot \rho_i \frac{\partial \psi}{\partial \underset{\sim}{\boldsymbol{e}}^p}, \quad \underset{\sim}{\boldsymbol{M}} = J_e^{-1} \rho_i \frac{\partial \psi}{\partial \underset{\sim}{\boldsymbol{K}}} \cdot \underset{\sim}{\boldsymbol{F}}^T \tag{97}$$

The residual dissipation rate is

$$J_e D = (\underset{\sim}{\boldsymbol{\Pi}}^M + J_e \underset{\sim}{\boldsymbol{s}} \cdot \underset{\sim}{\hat{\boldsymbol{\chi}}}^{pT}) : \dot{\underset{\sim}{\boldsymbol{F}}}^p \cdot \underset{\sim}{\boldsymbol{F}}^{p-1} - R\dot{\alpha} \geq 0, \quad \text{with} \quad R := \rho_i \frac{\partial \psi}{\partial \alpha} \tag{98}$$

At this stage, a dissipation potential, function of stress measures, $\Omega(\underset{\sim}{\boldsymbol{\mathcal{S}}}, R)$, is introduced in order to formulate the evolution equations for plastic flow and internal variables:

$$\dot{\underset{\sim}{\boldsymbol{F}}}^p \cdot \underset{\sim}{\boldsymbol{F}}^{p-1} = \frac{\partial \Omega}{\partial \underset{\sim}{\boldsymbol{\mathcal{S}}}}, \quad \text{with} \quad \underset{\sim}{\boldsymbol{\mathcal{S}}} := \underset{\sim}{\boldsymbol{\Pi}}^M + J_e \underset{\sim}{\boldsymbol{s}} \cdot \underset{\sim}{\hat{\boldsymbol{\chi}}}^{pT} \tag{99}$$

$$\dot{\alpha} = -\frac{\partial \Omega}{\partial R} \tag{100}$$

where R is the thermodynamic force associated with the internal variable α, and $\underset{\sim}{\boldsymbol{\mathcal{S}}}$ is the effective stress conjugate to plastic strain rate, the driving force for plastic flow.

In the case of crystal plasticity, a generalized Schmid law is adopted for each slip system s in the form:

$$f^s(\underset{\sim}{\boldsymbol{\mathcal{S}}}, \tau_c^s) = |\underset{\sim}{\boldsymbol{\mathcal{S}}} : \underset{\sim}{\boldsymbol{P}}^s| - \tau_c^s \geq 0, \quad \text{with} \quad \underset{\sim}{\boldsymbol{P}}^s = \underline{\boldsymbol{l}}^s \otimes \underline{\boldsymbol{n}}^s \tag{101}$$

for activation of slip system s with slip direction, $\underline{\boldsymbol{l}}^s$, and normal to the slip plane, $\underline{\boldsymbol{n}}^s$. We call $\underset{\sim}{\boldsymbol{P}}^s$ the orientation tensor. The critical resolved shear stress is τ_c^s which may be a function of R in the presence of isotropic hardening. The kinematics of plastic slip follows from the choice of a dissipation potential, $\Omega(f^s)$, that depends on the stress variables through the yield function itself, f^s:

$$\dot{\underset{\sim}{\boldsymbol{F}}}^p \cdot \underset{\sim}{\boldsymbol{F}}^{p-1} = \sum_{s=1}^{N} \frac{\partial \Omega}{\partial f^s} \frac{\partial f^s}{\partial \underset{\sim}{\boldsymbol{\mathcal{S}}}} = \sum_{s=1}^{N} \dot{\gamma}^s \underset{\sim}{\boldsymbol{P}}^s, \quad \text{with} \quad \dot{\gamma}^s = \frac{\partial \Omega}{\partial f^s} \text{sign}(\underset{\sim}{\boldsymbol{\mathcal{S}}} : \underset{\sim}{\boldsymbol{P}}^s) \tag{102}$$

A possible viscoplastic potential is then:

$$\Omega(f^s) = \frac{K}{n+1} < \frac{f^s}{K} >^{n+1} \tag{103}$$

where K, n are viscosity parameters associated with viscoplastic slip, and the brackets stand for $< \cdot >= Max(0, \cdot)$. The generalized resolved shear stress can be decomposed into two contributions:

$$\underset{\sim}{\boldsymbol{\mathcal{S}}} : \underset{\sim}{\boldsymbol{P}}^s = \tau^s - x^s, \quad \text{with} \quad \tau^s = \underset{\sim}{\boldsymbol{\Pi}}^M : \underset{\sim}{\boldsymbol{P}}^s \quad \text{and} \quad x^s = -\underset{\sim}{\boldsymbol{s}} \cdot \underset{\sim}{\hat{\boldsymbol{\chi}}}^{pT} : \underset{\sim}{\boldsymbol{P}}^s \tag{104}$$

The usual resolved shear stress is τ^s whereas x^s can be interpreted as an internal stress or back–stress leading to kinematic hardening. The fact that the introduction of the effect of the dislocation density tensor or, more generally, of gradient of plastic strain tensor, leads to the existence of internal stresses induced by higher order stresses has already been noticed by (Steinmann, 1996), see also (Forest, 2008). The back–stress component is induced by the microstress $\underset{\sim}{\boldsymbol{s}}$ or, equivalently, by the curl of the generalized couple stress tensor, $\underset{\sim}{\boldsymbol{M}}$, via the balance equation (85).

When deformations and rotations remain sufficiently small, the previous equations can be linearized as follows:

$$\underset{\sim}{\boldsymbol{F}} = \underset{\sim}{\boldsymbol{1}} + \underset{\sim}{\boldsymbol{H}} \simeq \underset{\sim}{\boldsymbol{1}} + \underset{\sim}{\boldsymbol{H}}^e + \underset{\sim}{\boldsymbol{H}}^p, \quad \underset{\sim}{\boldsymbol{H}}^e = \underset{\sim}{\boldsymbol{\varepsilon}}^e + \omega^e, \quad \underset{\sim}{\boldsymbol{H}}^p = \underset{\sim}{\boldsymbol{\varepsilon}}^p + \omega^p \tag{105}$$

where $\underset{\sim}{\boldsymbol{\varepsilon}}^e, \underset{\sim}{\boldsymbol{\omega}}^e$ (resp. $\underset{\sim}{\boldsymbol{\varepsilon}}^p, \underset{\sim}{\boldsymbol{\omega}}^p$) are the symmetric and skew–symmetric parts of $\underset{\sim}{\boldsymbol{F}}^e - \underset{\sim}{\boldsymbol{1}}$ (resp. $\underset{\sim}{\boldsymbol{F}}^p - \underset{\sim}{\boldsymbol{1}}$). When microdeformation is small, the relative deformation is linearized as

$$\underset{\sim}{\boldsymbol{e}}^p = (\underset{\sim}{\boldsymbol{1}} + \underset{\sim}{\boldsymbol{H}}^p)^{-1} \cdot (\underset{\sim}{\boldsymbol{1}} + \underset{\sim}{\boldsymbol{\chi}}^p) - \underset{\sim}{\boldsymbol{1}} \simeq \underset{\sim}{\boldsymbol{\chi}}^p - \underset{\sim}{\boldsymbol{H}}^p, \quad \text{with} \quad \underset{\sim}{\boldsymbol{\chi}}^p = \underset{\sim}{\hat{\boldsymbol{\chi}}}^p - \underset{\sim}{\boldsymbol{1}} \tag{106}$$

When linearized, the state laws (97) become:

$$\underset{\sim}{\boldsymbol{\sigma}} = \rho \frac{\partial \psi}{\partial \underset{\sim}{\boldsymbol{\varepsilon}}^e}, \quad \underset{\sim}{\boldsymbol{s}} = \rho \frac{\partial \psi}{\partial \underset{\sim}{\boldsymbol{e}}^p}, \quad \underset{\sim}{\boldsymbol{M}} = \rho \frac{\partial \psi}{\partial \underset{\sim}{\boldsymbol{K}}} \tag{107}$$

The evolution equations read then:

$$\dot{\underset{\sim}{\boldsymbol{\varepsilon}}}^p = \frac{\partial \Omega}{\partial (\underset{\sim}{\boldsymbol{\sigma}} + \underset{\sim}{\boldsymbol{s}})}, \quad \dot{\alpha} = -\frac{\partial \Omega}{\partial R} \tag{108}$$

We adopt the most simple case of a quadratic free energy potential:

$$\rho\psi(\underset{\sim}{\boldsymbol{\varepsilon}}^e, \underset{\sim}{\boldsymbol{e}}^p, \underset{\sim}{\boldsymbol{K}}) = \frac{1}{2} \underset{\sim}{\boldsymbol{\varepsilon}}^e : \underset{\approx}{\boldsymbol{C}} : \underset{\sim}{\boldsymbol{\varepsilon}}^e + \frac{1}{2} H_\chi \underset{\sim}{\boldsymbol{e}}^p : \underset{\sim}{\boldsymbol{e}}^p + \frac{1}{2} A \underset{\sim}{\boldsymbol{K}} : \underset{\sim}{\boldsymbol{K}} \tag{109}$$

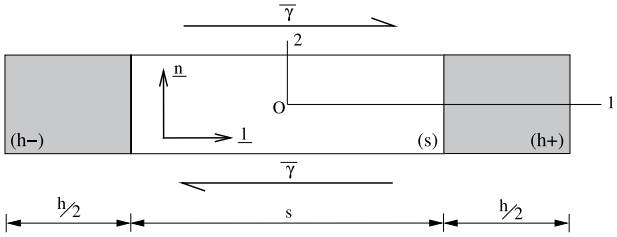

Figure 2. Single slip in a periodic two–phase single crystal laminate under simple shear: the grey phase (h) displays a purely linear elastic behaviour whereas the inelastic deformation of the white elasto–plastic phase (s) is controlled by a single slip system $(\underline{\boldsymbol{n}}, \underline{\boldsymbol{l}})$.

The usual four–rank tensor of elastic moduli is denoted by $\underset{\approx}{\boldsymbol{C}}$. The higher order moduli have been limited to only two additional parameters: H_χ (unit MPa) and A (unit MPa.mm^2). Their essential impact on the prediction of size effect will be analyzed in the next section. It follows that:

$$\underset{\sim}{\boldsymbol{\sigma}} = \underset{\approx}{\boldsymbol{C}} : \underset{\sim}{\boldsymbol{\varepsilon}}^e, \quad \underset{\sim}{\boldsymbol{s}} = H_\chi \underset{\sim}{\boldsymbol{e}}^p, \quad \underset{\sim}{\boldsymbol{M}} = A\underset{\sim}{\boldsymbol{K}} \tag{110}$$

Large values of H_χ ensure that $\underset{\sim}{\boldsymbol{e}}^p$ remains small so that $\hat{\underset{\sim}{\boldsymbol{\chi}}}^p$ remains close to $\underset{\sim}{\boldsymbol{H}}^p$ and $\underset{\sim}{\boldsymbol{K}}$ is close to the dislocation density tensor. The yield condition for each slip system becomes:

$$f^s = |\tau^s - x^s| - \tau_c^s \tag{111}$$

with

$$x^s = -\underline{\boldsymbol{s}} : \underset{\sim}{\boldsymbol{P}}^s = (\operatorname{curl} \underset{\sim}{\boldsymbol{M}}) : \underset{\sim}{\boldsymbol{P}}^s = A(\operatorname{curl}\operatorname{curl} \underset{\sim}{\boldsymbol{\chi}}^p) : \underset{\sim}{\boldsymbol{P}}^s \tag{112}$$

3.2 Size effects in a two-phase single crystal laminate

Let us consider a periodic two–phase single crystal laminate under simple shear as in (Forest and Sedláček, 2003), (Forest, 2008) and (Cordero et al., 2010). This microstructure is described in Fig. 2; it is composed of a hard elastic phase (h) and a soft elasto–plastic phase (s) where one slip system with slip direction normal to the interface between (h) and (s) is considered. A mean simple glide $\bar{\gamma}$ is applied in the crystal slip direction of the phase (s). We consider a displacement and microdeformation fields of the form:

$$u_1 = \bar{\gamma} x_2, \quad u_2(x_1), \quad u_3 = 0, \quad \chi^p_{12}(x_1), \quad \chi^p_{21}(x_1) \tag{113}$$

within the context of small deformation theory. It follows that

$$\left[\underset{\sim}{\boldsymbol{H}}\right] = \begin{bmatrix} 0 & \bar{\gamma} & 0 \\ u_{2,1} & 0 & 0 \\ 0 & 0 & 0 \end{bmatrix}$$

$$\left[\underset{\sim}{\boldsymbol{H}}^p\right] = \begin{bmatrix} 0 & \gamma & 0 \\ 0 & 0 & 0 \\ 0 & 0 & 0 \end{bmatrix} \quad \left[\underset{\sim}{\boldsymbol{H}}^e\right] = \begin{bmatrix} 0 & \bar{\gamma}-\gamma & 0 \\ u_{2,1} & 0 & 0 \\ 0 & 0 & 0 \end{bmatrix}$$

$$\left[\underset{\sim}{\boldsymbol{\chi}}^p\right] = \begin{bmatrix} 0 & \chi^p_{12}(x_1) & 0 \\ \chi^p_{21}(x_1) & 0 & 0 \\ 0 & 0 & 0 \end{bmatrix} \quad \left[\operatorname{curl}\underset{\sim}{\boldsymbol{\chi}}^p\right] = \begin{bmatrix} 0 & 0 & -\chi^p_{12,1} \\ 0 & 0 & 0 \\ 0 & 0 & 0 \end{bmatrix}$$

The resulting stress tensors are:

$$\left[\underset{\sim}{\boldsymbol{\sigma}}\right] = \mu \begin{bmatrix} 0 & \bar{\gamma}-\gamma+u_{2,1} & 0 \\ \bar{\gamma}-\gamma+u_{2,1} & 0 & 0 \\ 0 & 0 & 0 \end{bmatrix}$$

$$\left[\underset{\sim}{\boldsymbol{s}}\right] = -H_\chi \begin{bmatrix} 0 & \gamma-\chi^p_{12} & 0 \\ -\chi^p_{21} & 0 & 0 \\ 0 & 0 & 0 \end{bmatrix}$$

$$\left[\underset{\sim}{\boldsymbol{M}}\right] = \begin{bmatrix} 0 & 0 & -A\chi^p_{12,1} \\ 0 & 0 & 0 \\ 0 & 0 & 0 \end{bmatrix} \quad \left[\operatorname{curl}\underset{\sim}{\boldsymbol{M}}\right] = \begin{bmatrix} 0 & -A\chi^p_{12,11} & 0 \\ 0 & 0 & 0 \\ 0 & 0 & 0 \end{bmatrix}$$

These forms of matrices are valid for both phases, except that $\gamma \equiv 0$ in the hard elastic phase. Each phase possesses its own material parameters, H_χ and A, the shear modulus, μ, being assumed for simplicity to be identical in both phases. The balance equation, $\underset{\sim}{\boldsymbol{s}} = -\operatorname{curl}\underset{\sim}{\boldsymbol{M}}$, gives $\chi^p_{21} = 0$ and the plastic slip:

$$\gamma = \chi^p_{12} - \frac{A}{H_\chi}\chi^p_{12,11}. \tag{114}$$

In the soft phase, the plasticity criterion stipulates that

$$\sigma_{12} + s_{12} = \tau_c + H\gamma_{cum}, \tag{115}$$

where H is a linear hardening modulus considered in this phase and γ_{cum} is the accumulated plastic slip as $\dot{\gamma}_{cum} = |\dot{\gamma}|$. The following analytical resolution is done for the first loading branch, under monotonic loading. The slip direction, $\underline{\boldsymbol{l}}$, has been chosen such that $\gamma > 0$ for this first loading branch, so that we have: $\gamma_{cum} = \gamma$. Considering Eqs. (114) and (115),

we obtain the second order differential equation for the microdeformation variable in the soft phase, χ_{12}^{ps},

$$\frac{1}{\omega^{s2}}\,\chi_{12,11}^{ps} - \chi_{12}^{ps} = \frac{\tau_c - \sigma_{12}}{H}, \quad \text{with} \quad \omega^s = \sqrt{\frac{H_\chi^s H}{A^s\left(H_\chi^s + H\right)}}. \tag{116}$$

where $1/\omega^s$ is the characteristic length of the soft phase for this boundary value problem. The force stress balance equation requires σ_{12} to be uniform. It follows that the non–homogeneous part of the differential equation is constant and then the hyperbolic profile of χ_{12}^{ps} takes the form:

$$\chi_{12}^{ps} = C^s \cosh\left(\omega^s x\right) + D, \tag{117}$$

where C^s and D are constants to be determined. Symmetry conditions $(\chi_{12}^{ps}(-s/2) = \chi_{12}^{ps}(s/2))$ have been taken into account.
In the elastic phase, where the plastic slip vanishes, an hyperbolic profile of the microdeformation variable, χ_{12}^{ph}, is also obtained:

$$\chi_{12}^{ph} = C^h \cosh\left(\omega^h\left(x \pm \frac{s+h}{2}\right)\right), \quad \text{with} \quad \omega^h = \sqrt{\frac{H_\chi^h}{A^h}}, \tag{118}$$

where, again, C^h is a constant to be determined and symmetry conditions have been taken into account. It is remarkable that the plastic microvariable, χ_{12}^{ph}, does not vanish in the elastic phase, close to the interfaces, although no plastic deformation takes place. This is due to the transmission of double traction. Such a transmission has been shown in (Cordero et al., 2010) to be essential for size effects to occur. This point will be discussed in section 3.3. The meaning of the linear constitutive equation for the double stress tensor in (110) can be interpreted, for the elastic phase, as non–local elasticity. That is why the corresponding characteristic length, $1/\omega^h$, will be kept of the order of nanometer in the presented simulation.

Note that the same boundary value problem was handled in (Cordero et al., 2010) in the case of a perfectly plastic phase (s), i.e., without linear isotropic hardening. It showed that χ_{12}^{ps} has a parabolic profile over (s), the profile of χ_{12}^{ph} remaining hyperbolic in the hard phase (h). In the following of this section we will show how the additional isotropic hardening affects the local and macroscopic behaviors while the main effects of the *microcurl* model as presented in (Cordero et al., 2010) remain.
The coefficients C^s, D and C^h can be identified using the interface and periodicity conditions:

- Continuity of χ_{12}^p at $x = \pm s/2$:

$$C^s \cosh\left(\omega^s \frac{s}{2}\right) + D = C^h \cosh\left(\omega^h \frac{h}{2}\right). \tag{119}$$

- Continuity of the double traction, as given in Eq. (86), $m_{12} = -M_{13}$ at $x = \pm s/2$:

$$A^s \omega^s C^s \sinh\left(\omega^s \frac{s}{2}\right) = -A^h \omega^h C^h \sinh\left(\omega^h \frac{h}{2}\right). \tag{120}$$

- Periodicity of displacement component u_2. We have the constant stress component

$$\sigma_{12} = \mu(\bar{\gamma} - \gamma + u_{2,1}) \tag{121}$$

whose value is obtained from the plasticity criterion in the soft phase (Eq. 115):

$$\sigma_{12} = \tau_c + H\gamma_{cum} - A^s \chi_{12,11}^{ps}. \tag{122}$$

Still considering the first loading branch for which $\gamma_{cum} = \gamma$, it follows that

$$u_{2,1}^s = \frac{\sigma_{12}}{\mu} - \bar{\gamma} + \gamma = \frac{\tau_c}{\mu} - \bar{\gamma} + \frac{A^s \omega^{s2} C^s}{H} \cosh(\omega^s x) + \frac{H+\mu}{\mu} D \tag{123}$$

in the soft phase and

$$u_{2,1}^h = \frac{\sigma_{12}}{\mu} - \bar{\gamma} = \frac{\tau_c}{\mu} - \bar{\gamma} + \frac{H}{\mu} D \tag{124}$$

in the hard phase. The average on the whole structure,

$$\int_{-(s+h)/2}^{(s+h)/2} u_{2,1}\, dx = 0, \tag{125}$$

must vanish for periodicity reasons and gives

$$\left(\frac{\tau_c}{\mu} - \bar{\gamma}\right)(s+h) + \frac{2A^s \omega^s C^s}{H} \sinh\left(\omega^s \frac{s}{2}\right) + \frac{H(s+h) + \mu s}{\mu} D = 0 \tag{126}$$

The resolution of Eqs. (119), (120) and (126) gives

$$C^s = \left(\frac{\tau_c}{\mu} - \bar{\gamma}\right) \left[\frac{A^s \omega^s \sinh\left(\omega^s \frac{s}{2}\right)}{s+h} \right.$$

$$\left(\frac{H\,(s+h)+\mu s}{\mu} \left(\frac{\coth\left(\omega^s \dfrac{s}{2}\right)}{A^s\omega^s} + \frac{\coth\left(\omega^h \dfrac{h}{2}\right)}{A^h\omega^h} \right) - \frac{2}{H} \right)^{-1} \tag{127}$$

$$D = -A^s\omega^s C^s \sinh\left(\omega^s \frac{s}{2}\right) \left(\frac{\coth\left(\omega^s \dfrac{s}{2}\right)}{A^s\omega^s} + \frac{\coth\left(\omega^h \dfrac{h}{2}\right)}{A^h\omega^h} \right) \tag{128}$$

$$C^h = -C^s \frac{A^s\omega^s \sinh\left(\omega^s \dfrac{s}{2}\right)}{A^h\omega^h \sinh\left(\omega^h \dfrac{h}{2}\right)}. \tag{129}$$

Fig. 3 shows the profiles of plastic microdeformation and double traction in the two–phase laminate for different sets of material parameters and for a fraction of soft phase (s), $f_s = 0.7$. These profiles clearly show the continuity of χ^p_{12} and m_{12} at the interfaces. The different shapes presented are obtained for various values of the modulus A^s, the other material parameters being fixed and given in Table 1. Varying A^s modifies the mismatch with respect to the modulus A^h of the phase (h). Without mismatch the profile of χ^p_{12} is smooth at interfaces while stronger mismatches lead to sharper transitions between the phases. Varying A^s also changes the intrinsic length scale $1/\omega^s$ of the phase (s). When the intrinsic length scale is small compared to the size of the microstructure, the microdeformation gradient can develop inside the phase (s) which leads to a rounded profile of the plastic microdeformation χ^{ps}_{12} and to a double traction m_{12} localized at the interfaces. When the intrinsic length scale increases, the value of the double traction also increases at the interfaces (or equivalently, when decreasing the microstructure length scale, $l = s + h$, for a fixed intrinsic length scale). When the intrinsic length scale becomes of the order of the size of the microstructure or even larger, the model starts to saturate so that χ^{ps}_{12} becomes quasi–homogeneous (flat profile) and the double traction is not localized anymore (linear profile). χ^{ps}_{12} is affected by A^s in the same way as in (Cordero et al., 2010) where the hardening modulus, H, was not considered; in this latter case, the plastic microdeformation profile was parabolic, so that m_{12}, as a linear function of $\chi^{ps}_{12,1}$, always displayed a linear evolution in the phase (s), even for very small intrinsic length scales.

From Eq. (122) we derive the expression of the macroscopic stress tensor component, Σ_{12}, defined as the mean value of the stress component σ_{12} over

Table 1. Set of material parameters used in the simulations. The intrinsic length scales, defined as $1/\omega^{h,s}$, induced by these parameters is of the order of 10 nm for the elastic phase (h) and 500 nm for the plastic phase (s).

	μ [MPa]	τ_c [MPa]	H [MPa]	H_χ [MPa]	A [MPa.mm^2]
Phase (s)	35000	40	5000	500000	1.10^{-3}
Phase (h)	35000	-	-	500000	5.10^{-5}

the microstructure size, $l = (s + h)$:

$$\Sigma_{12} =< \sigma_{12} >= \frac{1}{l}\int_{-\frac{l}{2}}^{\frac{l}{2}} \sigma_{12}\, dx = \tau_c + \frac{H}{f_s}\langle\gamma^{cum}\rangle - \frac{A^s}{f_s}\langle\chi^{ps}_{12,11}\rangle, \tag{130}$$

where brackets <> denote the average values over the microstructure unit cell. We obtain the mean plastic slip for the first loading branch from Eq. (114):

$$\langle\gamma\rangle = \left\langle \chi^{ps}_{12} - \frac{A^s}{H^s_\chi}\chi^{ps}_{12,11}\right\rangle = \frac{2A^s\omega^s C^s \sinh\left(\omega^s\dfrac{f_s l}{2}\right)}{Hl} + f_s D \tag{131}$$

where f_s is the fraction of soft phase. From this we obtain alternative expressions of C^s and D as functions of $\langle\gamma\rangle$,

$$C^s = -\langle\gamma\rangle\left[A^s\omega^s \sinh\left(\omega^s\frac{f_s l}{2}\right)\right.$$
$$\left.\left(f_s\left(\frac{\coth\left(\omega^s\dfrac{f_s l}{2}\right)}{A^s\omega^s} + \frac{\coth\left(\omega^h\dfrac{(1-f_s)\,l}{2}\right)}{A^h\omega^h}\right) - \frac{2}{Hl}\right)\right]^{-1} \tag{132}$$

$$D = \langle\gamma\rangle\left[f_s - \frac{2}{Hl}\left(\frac{\coth\left(\omega^s\dfrac{f_s l}{2}\right)}{A^s\omega^s} + \frac{\coth\left(\omega^h\dfrac{(1-f_s)\,l}{2}\right)}{A^h\omega^h}\right)^{-1}\right]^{-1} \tag{133}$$

which contain contributions from both the back–stress and the isotropic hardening. The macroscopic stress takes the form:

$$\Sigma_{12} = \tau_c + HD. \tag{134}$$

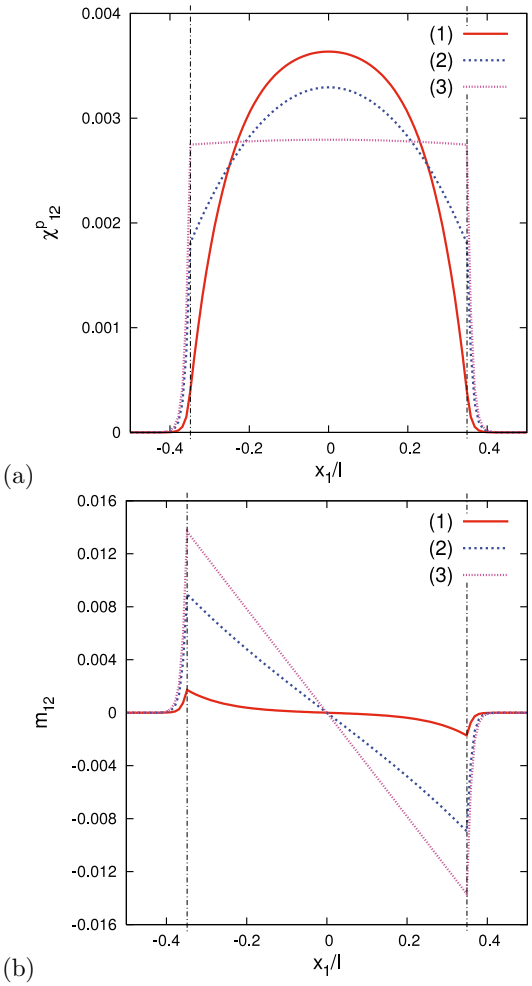

Figure 3. Profiles of (a) plastic microdeformation χ^p_{12} and (b) double traction m_{12} in the two–phase microstructure with the *microcurl* model at 0.2% overall plastic strain obtained with the set of material parameters given in Table 1 and: (1) with no mismatch between the moduli of the two phases, $A^h = A^s = 5.10^{-5}$ MPa.mm^2, (2) with a stronger mismatch, $A^h = 5.10^{-5}$ MPa.mm^2 and $A^s = 1.10^{-3}$ MPa.mm^2 and (3) $A^h = 5.10^{-5}$ MPa.mm^2 and $A^s = 5.10^{-2}$ MPa.mm^2. The associated intrinsic length scales, $1/\omega^s$, are respectively: 100 nm, 449 nm and 3.2 μm. In all three cases, the fraction of soft phase $f_s = 0.7$ and the microstructure size is fixed, $l = 1$ μm. The vertical lines indicate the position of interfaces.

The hardening produced by the model is a combination of the kinematic hardening arising from the higher order back–stress component and the linear isotropic hardening introduced in (115). Its modulus, H^{tot}, is size–dependent and is obtained using Eqs. (133) and (134):

$$H^{tot} = H\left[f_s - \frac{2}{Hl}\left(\frac{\coth\left(\omega^s \frac{f_s l}{2}\right)}{A^s\omega^s} + \frac{\coth\left(\omega^h \frac{(1-f_s)\,l}{2}\right)}{A^h\omega^h}\right)^{-1}\right]^{-1} \tag{135}$$

The macroscopic stress–strain curves shown in Fig. 4 illustrate the additional hardening predicted by the *microcurl* model in comparison to a conventional crystal plasticity theory. One cycle of deformation $\bar{\gamma}$ has been considered to illustrate the kinematic hardening effects. The first loading branch is described by the previous analytical solution, whereas the remaining of the loop has been computed numerically. In the absence of gradient effects (classical case, dashed line), only isotropic hardening is visible. The *microcurl* model leads to an additional kinematic hardening component. When the size of the elasto-plastic phase (s) becomes large compared to the intrinsic length scale $1/\omega_s$, strain gradient effect is small and the kinematic hardening arising from the *microcurl* model tends to vanish. Then the model reduces to conventional crystal plasticity theory and the limit of the 0.2% macroscopic flow stress is:

$$\lim_{l\to\infty} \Sigma_{12|0.2} = \tau_c + \frac{H}{f_s}\langle\gamma^{cum}\rangle. \tag{136}$$

In contrast, the maximum extra–stress, $\Delta\Sigma$, predicted by the model at small microstructure sizes can be computed as:

$$\Delta\Sigma = \lim_{l\to 0} \Sigma_{12}(<\gamma>) - \lim_{l\to\infty} \Sigma_{12|0.2} = \frac{1-f_s}{f_s} H_\chi \,\langle\gamma\rangle\,. \tag{137}$$

Fig. 5 presents the predicted evolution of the macroscopic flow stress $\Sigma_{12|0.2}$ at 0.2% plastic strain (obtained by setting $\langle\gamma\rangle = 0.002$) as a function of the microstructure length scale l in a log–log diagram. This evolution is plotted using the material parameters given in Table 1 and for various values of the coupling modulus, $H^s_\chi = H^h_\chi = H_\chi$. The four lower curves are obtained for finite values of the modulus H_χ, they exhibit a *tanh*–shape with saturation for large ($l > 10^{-2}$ mm) and small ($l < 10^{-5}$ mm) values of l. These saturations can be characterized by the limit given in Eq. (136) and the maximum extra–stress, $\Delta\Sigma$, given in Eq. (137) respectively. A transition

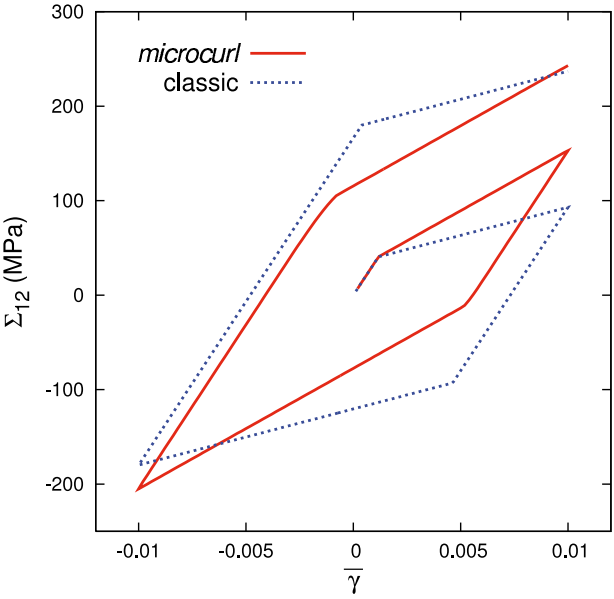

Figure 4. Macroscopic stress–strain response of the two–phase microstructure under cyclic shear loading conditions: comparison between the behaviour from a conventional crystal plasticity theory and the behaviour according to the *microcurl* model in which an additional kinematic hardening is predicted. Results obtained by finite element simulations for: $l = 1\mu$m, $f_s = 0.7$ and the material parameters given in Table 1.

domain with strong size dependence is observed between these two plateaus. The limits and the maximum extra–stress, the position of the transition zone and the scaling law exponent in the size dependent domain (slope in the log–log diagram) are directly related to the material parameters used in the model. In fact, the position of the size dependent domain is controlled by the moduli $A^{h,s}$ (not illustrated here) while the maximum extra–stress and the scaling law exponent are both controlled by the modulus H_χ, both increasing for higher values of H_χ as suggested by Fig. 5.
When H_χ is very small, we can deduce from Eq. (137) that $\Delta\Sigma$ vanishes and consequently the scaling law exponent will tend to 0. The upper curve is obtained for $H_\chi \to \infty$, it no longer exhibits a *tanh*–shape as no saturation occurs for small values of l, the limit $\Delta\Sigma \to \infty$ follows. This limit case will

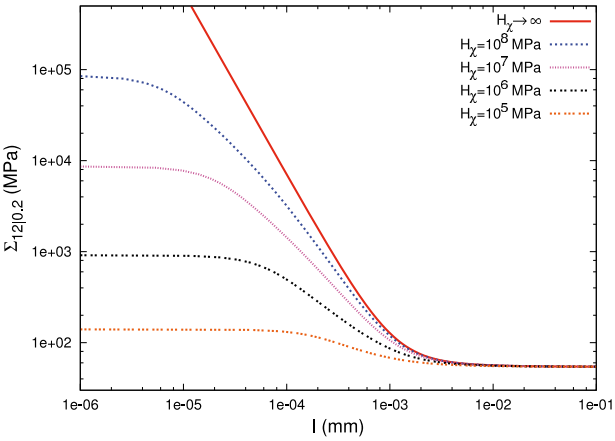

Figure 5. Evolution of the macroscopic flow stress $\Sigma_{12|0.2}$ at 0.2% plastic strain as a function of the microstructure length scale l, plotted for different coupling moduli H_χ ($= H^s_\chi = H^h_\chi$). The other material parameters are given in Table 1 and $f_s = 0.7$.

be described in next subsection, it will be shown that in that case a scaling law exponent of -2 is reached. Finally the *microcurl* model can produce scaling law exponents ranging from 0 to -2.

3.3 Strain gradient plasticity as a limit case

In the proposed *microcurl* model, the modulus H_χ introduces a coupling between micro and macro variables. A high value of H_χ forces the plastic microdeformation $\underset{\sim}{\boldsymbol{\chi}}^p$ to remain as close as possible to the macro plastic deformation $\underset{\sim}{\boldsymbol{H}}^p$. Consequently, it enforces the condition that $\underset{\sim}{\boldsymbol{K}}$ coincides with the dislocation density tensor. In this case, the *microcurl* model degenerates into the strain gradient plasticity model by (Gurtin, 2002). When applied to the laminate microstructure, the strain gradient plasticity model leads to the indeterminacy of the double traction vector at the interfaces, due to the fact that no strain gradient effect occurs in the elastic phase, see (Cordero et al., 2010). The *microcurl* model can then be used to derive the missing interface condition to be applied at the interface, by means of a limit process in the previous solution of the boundary value problem.
The limit $H_\chi \to \infty$ of the *microcurl* model can be used to determine the

value of the double traction to be imposed at the interface.

$$\begin{aligned}\lim_{H_\chi\to\infty} m_{12}(s/2) &= \lim_{H_\chi\to\infty} A^s\chi^{ps}_{12,1}(s/2)\\ &= \lim_{H_\chi\to\infty} A^s\omega^s \sinh\left(\omega^s\frac{f_s l}{2}\right) C^s\end{aligned}$$

$$= \lim_{H_\chi\to\infty}\langle\gamma\rangle\left[\frac{2}{Hl} - f_s\left(\frac{\coth\left(\omega^s\frac{f_s l}{2}\right)}{A^s\omega^s} + \frac{\coth\left(\omega^h\frac{(1-f_s)\,l}{2}\right)}{A^h\omega^h}\right)\right]^{-1}$$

Since $H_\chi\to\infty$, $1/\omega^h\to 0$ and $\coth\left(\omega^h h/2\right)\to 1$. Moreover, $\omega^s_\infty := \omega^s \to \sqrt{H/A^s}$. Consequently,

$$\lim_{H_\chi\to\infty} m_{12}(s/2) = \langle\gamma\rangle\left[\frac{2}{Hl} - f_s\frac{\coth\left(\omega^s_\infty\frac{f_s l}{2}\right)}{A^s\omega^s_\infty}\right]^{-1} \tag{138}$$

Accordingly, the double traction is found to depend on the mean plastic slip. The characteristic length in the soft phase for the strain gradient plasticity model is found to be related to the ratio between the hardening modulus and the higher order modulus, A^s.

The limiting process can also be used to predict the response of the strain gradient plasticity model in the size effect zone. For that purpose, let us consider the limit of $\Sigma_{12|0.2}$, when H_χ goes to infinity. Indeed, when H_χ tends to infinity, the expression of D in Eq. (133) can be simplified. We consider sizes of the microstructures in the size effect zone, i.e. intermediate values of l. Since H_χ is very high, the term $\tanh\left(\omega^h(1-f_s)l/2\right)$ tends to 1. Considering that l is small enough, the term $l\left(\tanh\left(\omega_s f_s l/2\right)\right)$ can be approximated by its Taylor expansion at the order 2, which leads to D of the form:

$$D \approx \frac{al+b}{cl^2+dl+e} \tag{139}$$

where

$$a = \frac{\langle\gamma\rangle f_s}{2\sqrt{H_\chi}}, \quad b = \langle\gamma\rangle f_s A^h\left(1+\frac{H}{H_\chi}\right) \tag{140}$$

$$c = -\frac{f_s^3 H\sqrt{A^h}}{12}, \quad d = \frac{f_s^2 H}{2\sqrt{H_\chi}}, \quad e = -\frac{f_s\sqrt{A^h}H}{H_\chi} \tag{141}$$

The terms a, d and e tend to 0 when $H_\chi \to \infty$, so that

$$D \approx \frac{12 A_s \langle \gamma \rangle}{f_s^3 H l^2} \tag{142}$$

and for the macroscopic stress:

$$\Sigma_{12} \approx \tau_c + \frac{12 A_s \langle \gamma \rangle}{f_s^3 l^2} \tag{143}$$

This expression is the same as that found in the absence of isotropic hardening in (Cordero et al., 2010). It indicates a l^{-2} scaling law for the strain gradient plasticity model. This scaling law differs from Hall–Petch relation, $l^{-1/2}$, typical for grain size effects, and from Orowan's law, l^{-1}, valid for precipitate size effects.

4 Continuum modelling of size effects in polycrystals

The model is now applied to simulate the response of polycrystals and the effects of grain size.

The interface conditions at grain boundaries play a major role in the simulated size effects in the polycrystal behaviour. No special interface law is considered in this work, although such physically motivated interface conditions exist in the literature, see (Gurtin and Anand, 2008). Instead we consider the canonical interface conditions that arise from the formulation of the balance equations of the *microcurl* continuum model. These conditions are the continuity of displacement, $\underline{\boldsymbol{u}}$, and the continuity of plastic micro–deformation, $\underset{\sim}{\boldsymbol{\chi}}^p$. These conditions also include the continuity of the simple and double tractions, $\underline{\boldsymbol{t}}$ and $\underset{\sim}{\boldsymbol{M}}$, described in Eq. (86). Continuity of displacement excludes grain boundary cracking and sliding. Continuity of plastic micro–deformation is reminiscent of the fact that dislocations generally do not cross grain boundaries, especially for such random grain boundaries. Note that in the *microcurl* model, only the kinematic degrees of freedom $\underset{\sim}{\boldsymbol{\chi}}^p$ are continuous. This is not the case of the plastic deformation, $\underset{\sim}{\boldsymbol{H}}^p$, which is treated here as an internal variable. However, due to the internal constraint discussed in section 3.1, $\underset{\sim}{\boldsymbol{H}}^p$ closely follows the plastic micro–deformation, so that it is quasi–continuous at grain boundaries when the penalty coefficient, H_χ, is high enough. Conversely, lower values of H_χ may allow slightly discontinuous plastic deformation, which may be tentatively interpreted as dislocation sinking inside grain boundaries. The continuity of the associated tractions expresses the transmission of classical and generalised internal forces from one grain to another through grain

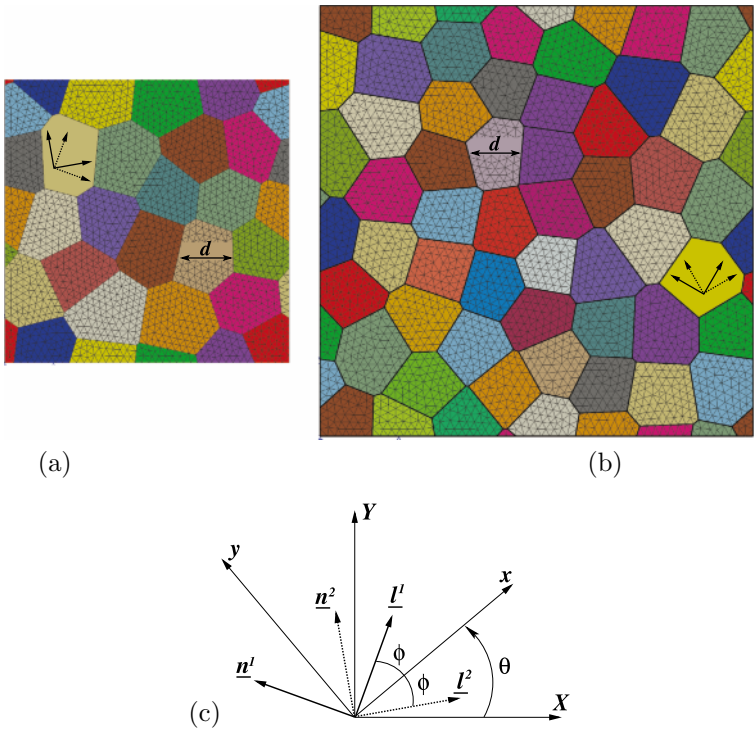

Figure 6. Periodic meshes of the 2D periodic aggregates used in the finite element simulations: (a) 24 grains, (b) 52 gains. Two slip systems are taken into account in each randomly oriented grain. Various mean grain sizes, d, ranging from tens of nanometers to hundreds of microns, are investigated. (c) Description of the two effective slip systems for 2D planar double slip.

boundaries. Such continuum models are then able to mimic in that way the development of dislocation pile–ups at grain boundaries (Forest and Sedláček, 2003).

4.1 Boundary value problem for polycrystals

The size effects exhibited by the solution of the boundary value problem are linked to an intrinsic length scale, l_s, introduced through the generalised

moduli H_χ and A of Eq. (110) and defined as:

$$l_s = \sqrt{\frac{A}{H_\chi}}. \tag{144}$$

This intrinsic length scale has to be consistent with the fact that plasticity effects occur at scales ranging from hundreds of nanometers to a few microns. In addition, as stated in section 3.1, the coupling modulus, H_χ, has to be chosen high enough to ensure that $\underset{\sim}{\boldsymbol{\chi}}^p$ and $\underset{\approx}{\boldsymbol{H}}^p$ are close. H_χ also determines the scaling law exponent. These requirements are guidelines for the choice of relevant generalised moduli H_χ and A. The sets of material parameters used in this paper are chosen in that way.

The finite element simulations have been made on periodic 2D meshes of periodic polycrystalline aggregates generated by a method based on Voronoi tessellations (Fig. 6(a)(b)). The integration order of elements is quadratic. The Voronoi polyhedra represent the grains, the random distribution of their centers has been controlled so that their sizes are sensibly the same, that is why we can reasonably assume that the mean grain size, d, is sufficient to characterise the microstructure of our aggregates. A random orientation is assigned to each grain and two slip systems are taken into account. In 2D, the plastic behaviour of f.c.c. crystals can be simulated with 2D planar double slip by considering two effective slip systems separated by an angle of 2ϕ (Asaro, 1983; Bennett and McDowell, 2003). Figure 6(c) describes the geometry. The slip system pair is oriented by the angle θ which is the grain orientation randomly fixed for each grain. For a f.c.c. crystal $\phi = 35.1°$, it corresponds to the orientation of the close–packed planes in the crystal lattice of the grain.

Periodic homogenization for generalised continua is used to predict the effective response of the polycrystal. The displacement field is assumed to be of the form

$$\underline{\boldsymbol{u}}\,(x) = \underset{\sim}{\boldsymbol{E}}.\underline{\boldsymbol{x}} + \underline{\boldsymbol{v}}\,(x), \tag{145}$$

with the fluctuation $\underline{\boldsymbol{v}}$ periodic, meaning that it takes identical values at homologous points of the unit cell (Forest et al., 2001). The plastic micro–deformation field, $\underset{\sim}{\boldsymbol{\chi}}^p$, is assumed to be periodic, meaning that no rotational macroscopic plastic deformation is imposed to the unit cell. Its components are equal at homologous opposite nodes. According to periodic homogenization, the simple and double tractions $\underline{\boldsymbol{t}}$ and $\underset{\sim}{\boldsymbol{m}}$ are anti–periodic at homologous points of the unit cell.

Polycrystals are random materials so that the periodicity constraint may lead to a bias in the estimation of the effective properties. This boundary

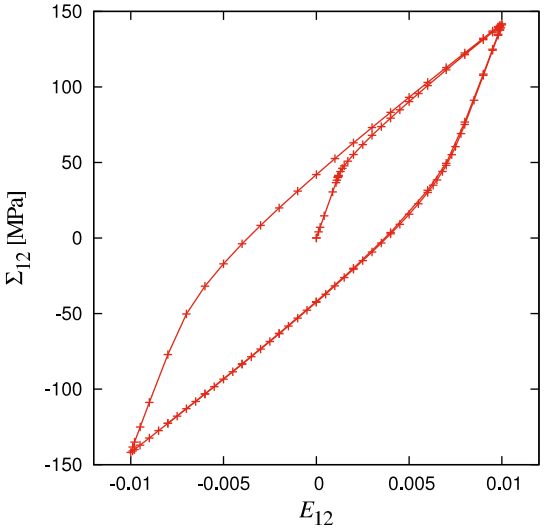

Figure 7. Macroscopic stress–strain response of the 24–grain aggregate under cyclic simple shear loading conditions with a mean gain size $d \approx 0.2\mu$m. The set of material parameters used is labelled (c) in Table 2.

effect can be alleviated by considering several realization of the microstructure and performing ensemble averaging (Zeghadi et al., 2007).

4.2 Overall cyclic response of a polycrystalline aggregate

The finite element simulations of the boundary value problem presented previously have been conducted under generalised plane strain conditions on aggregates with a relatively small number of grains. The aim here is not to obtain a representative response but to catch the grain size effects and to explore qualitatively the impact of different sets of material parameters. In this section, a virtual material is considered with various intrinsic length scales. The macroscopic stress–strain curve shown in Fig. 7 is obtained by applying a cyclic simple shear loading controlled by the average stress component E_{12} on the aggregate of 24 grains with $d = 0.2\mu$m and the set of material parameters labelled (c) in Table 2. The mean stress component Σ_{12} is then computed:

$$\Sigma_{12} = \frac{1}{V}\int_V \sigma_{12}\, dV, \quad E_{12} = \frac{1}{V}\int_V \varepsilon_{12}\, dV, \tag{146}$$

Table 2. Sets of material parameters used in the 24–grain aggregate case (Fig 6(a)). The intrinsic length scale, $l_s = \sqrt{A/H_\chi}$, is given for each set.

Set	μ [MPa]	τ_c [MPa]	H_χ [MPa]	A [MPa mm^2]	l_s [μm]
a	35000	40	$3.0\,10^6$	$1.0\,10^{-2}$	$5.8\,10^{-2}$
b	35000	40	$1.0\,10^6$	$1.0\,10^{-2}$	$1.0\,10^{-1}$
c	35000	40	$3.5\,10^5$	$1.0\,10^{-2}$	$1.7\,10^{-1}$
d	35000	40	$8.8\,10^4$	$1.0\,10^{-3}$	$1.1\,10^{-1}$

where V denotes each polycrystal unit cell. The simulated response illustrates the kinematic hardening produced by the *microcurl* model. The stress–strain curves obtained in the next case (see Fig. 9) show that this kinematic hardening is size dependent: it increases for smaller grains. Note that the observed overall kinematic hardening has two distinct sources: the intragranular back–stress induced by plastic strain gradients, and the intergranular internal stress that originate from the grain to grain plastic strain incompatibilities. The latter contribution is also predicted by classical crystal plasticity models.

Figure 8 presents the effect of the mean grain size, d, on the macroscopic flow stress at 1% plastic strain in the 24–grain aggregate in a log–log diagram for different intrinsic length scales, l_s, introduced through the sets of material parameters (labelled a, b, c and d) given in Table 2. The curves exhibit two plateaus for large ($d > 20\mu$m) and small ($d < 0.1\mu$m) mean grain sizes with a transition domain in between. This *tanh*–shape indicates that when d is large compared to the intrinsic length scale, l_s, strain gradient effects are small and the kinematic hardening arising from the *microcurl* model vanishes. The model saturates when d is of the order of l_s or smaller. The transition domain exhibits a strong size dependence, the polycrystalline aggregate becoming harder for decreasing grain sizes. The position of the transition zone, the maximum extra–stress (the distance between the two plateaus) and the scaling law exponent, m, in the size dependent domain are controlled by the material parameters used in the model. The two latter effects are controlled by the coupling modulus, H_χ, they both increase for higher values of H_χ as shown in Fig. 8. The scaling exponent is defined as the slope in the log–log diagram in the inflection domain, reflecting the scaling law:

$$\Sigma_{12} \propto d^m. \tag{147}$$

It is obtained with the sets of material parameters given in Table 2. The found values range from -0.26 to -0.64 including the well–known Hall–

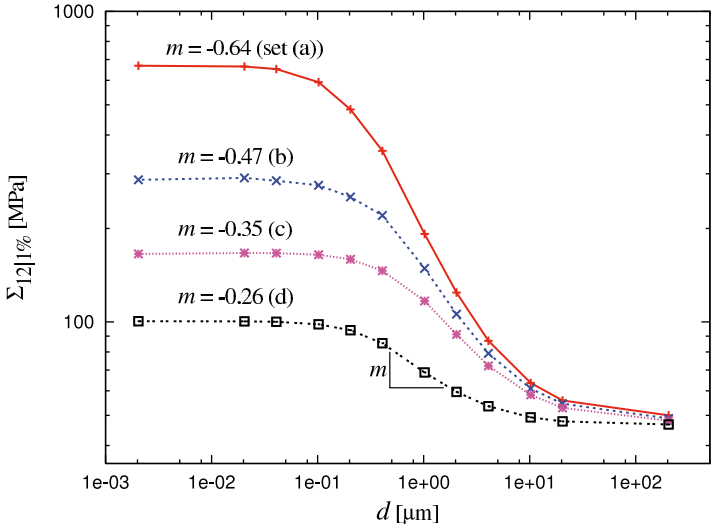

Figure 8. Effect of the mean grain size, d, on the macroscopic flow stress, $\Sigma_{12|1\%}$, at 1% plastic strain. The results are obtained for the 24–grain aggregate using the different sets of material parameters given in Table 2. The scaling law exponent, m, is identified in each case.

Petch exponent $m = -0.5$. In fact it was shown in (Cordero et al., 2010) that values of m ranging from 0 to -2 can be simulated with the *microcurl* model in the case of two–phase microstructures. In each case, these values are obtained without classical isotropic hardening, meaning that the linear kinematic hardening produced by the model is able to reproduce a wide range of scaling laws. Note that conventional strain gradient plasticity models do not lead to *tanh*–shape curves but rather to unbounded stress increase for vanishingly small microstructures (Cordero et al., 2010).

4.3 Grain size effects in idealised aluminium polycrystals

Similar finite element simulations have been performed on idealised aluminium aggregates of 52 grains shown in Fig. 6(b). An additional isotropic hardening component is added as in (Méric et al., 1991) to obtain a more realistic response of large aluminium grains. The size–independent hardening

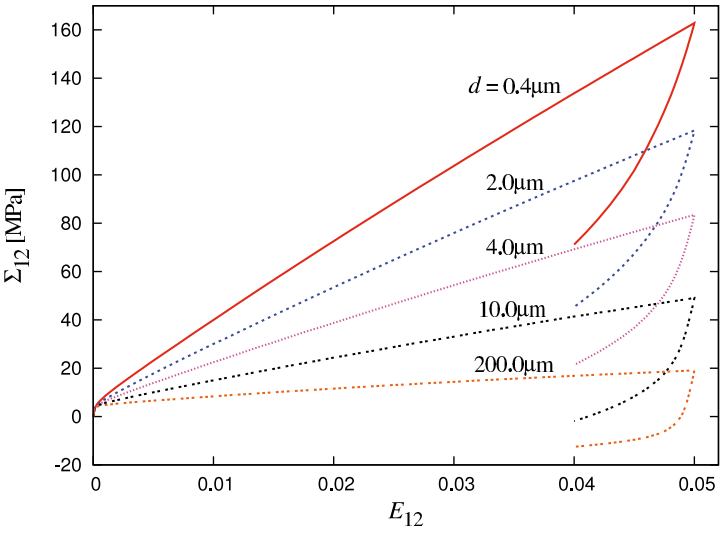

Figure 9. Macroscopic stress–strain response of the 52–grain aggregate under simple shear for various mean grain sizes, d. The set of material parameters used is labelled (g) in Table 3.

law reads:

$$R^\alpha = \tau_c + Q \sum_\beta^n h^{\alpha\beta} \left(1 - \exp\left(-b\,\gamma^\beta_{\rm cum}\right)\right), \tag{148}$$

where n is the number of slip systems (here $n = 2$), Q and b are material coefficients defining non–linear isotropic hardening, $h^{\alpha\beta}$ is the interaction matrix and $\gamma^\beta_{\rm cum}$ is the accumulated micro–plastic slip on the slip system β. Cumulative plastic slip results from the integration of the differential equation $\dot\gamma^\beta_{\rm cum} = |\dot\gamma^\beta|$. The material parameters used in these simulations are given in Table 3. The macroscopic stress–strain curves presented in Fig. 9 are obtained by applying a simple shear loading controlled by the average strain component E_{12} on the 52–grain aggregate with various mean grain sizes, d, taken in the size dependent domain. The chosen set of material parameters has the label (g) in Table 3. These parameters are such that an acceptable description of aluminium polycrystals is obtained for large grains and that a Hall–Petch–like behaviour is found in a plausible range of grain sizes. However we did not attempt to calibrate the amplitude of the extra–hardening so that simulation predictions remain qualitative. The

Table 3. Sets of material parameters used in the 52–grain aggregate case (Fig 6(b)).

Set	μ [MPa]	τ_c [MPa]	Q [MPa]	b	$h^{\alpha\alpha}$	$h^{\alpha\beta,\,\alpha\neq\beta}$
e	27000	0.75	7.9	10.2	1	4.4
f	27000	0.75	7.9	10.2	1	4.4
g	27000	0.75	7.9	10.2	1	4.4

Set	H_χ [MPa]	A [MPa mm^2]	l_s [μm]
e	$1.0\,10^6$	$1.0\,10^{-2}$	$1.0\,10^{-1}$
f	$3.5\,10^5$	$1.0\,10^{-2}$	$1.7\,10^{-1}$
g	$5.0\,10^4$	$1.0\,10^{-2}$	$4.5\,10^{-1}$

curves of Fig. 9 show again that the kinematic hardening produced by the model is strongly size dependent. The evolution of the macroscopic flow stress at 1% plastic strain in the 52–grain aggregate is shown in Fig. 10 in the same way as it was done in Fig. 8. The set of material parameters (g) of Table 3 gives the ideal Hall–Petch scaling law exponent $m = -0.5$.

An important output of the simulations is the dependence of the stress and strain fields in the grains of the polycrystal on grain size. Figures 11 and 12 show the contour plots of the field of accumulated plastic slip, computed as

$$\dot{p} = \sqrt{\frac{2}{3}\underset{\sim}{\dot{\varepsilon}}^p : \underset{\sim}{\dot{\varepsilon}}^p}, \tag{149}$$

where $\underset{\sim}{\varepsilon}^p$ is the symmetric part of the plastic deformation, $\underset{\sim}{\boldsymbol{H}}^p$, and the contour plots of the norm Γ of the dislocation density tensor,

$$\Gamma = \sqrt{\underset{\sim}{\boldsymbol{\Gamma}} : \underset{\sim}{\boldsymbol{\Gamma}}}, \tag{150}$$

respectively. The considered grain sizes are taken in the size dependent domain where the evolution of the fields is assumed to be physically relevant. The chosen set of material parameters has the label (g) in Table 3, it corresponds to an intrinsic length scale $l_s = 0.45\mu$m and gives a scaling law exponent $m = -0.5$. The mean value of the accumulated plastic slip is the same in every case, only its distribution varies with the size of the microstructure as shown in Fig. 11.

The first contour plot of each figure is obtained for $d = 200\mu\text{m} \gg l_s = 0.45\mu$m, at the very beginning of the size–dependent behaviour domain according to Fig. 10. At this size, the simulated fields show that p is quite inhomogeneous and that some deformation bands appear; Γ is localised at

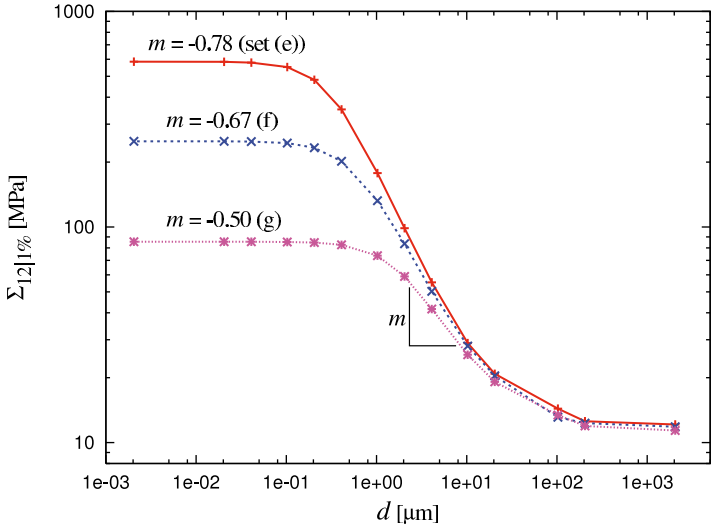

Figure 10. Effect of the mean grain size, d, on the macroscopic flow stress, $\Sigma_{12|1\%}$, at 1% plastic strain. The results are obtained for the 52–grain aggregate using the different sets of material parameters given in Table 3. The scaling law exponent, m, is identified in each case.

the grain boundaries and almost vanishes in the grain cores. The contour plots obtained for 2μm$< d < 20\mu$m show a significant evolution of both fields. One observes the progressive building of a network of strain localization bands. These bands are slip bands as they are parallel to the slip plane directions represented on the 1μm contour plot of Fig. 11. They compensate the larger blue zones where plastic strain cannot develop due to the higher energy cost associated with its gradient. Plastic strain becomes stronger inside the localization bands. This is due to the fact that the contour plots are given for fixed mean value of p, which implies that the applied total strain is higher for small grain sizes as suggested by Fig. 9. The field of the norm of the dislocation density tensor is still high close to grain boundaries and spreads over the grain cores. The last contour plot of each figure is obtained for $d = 1\mu$m, a size close to l_s. Here the model starts to saturate, which can be seen from the simulated fields. The field of p does not evolve anymore and Γ decreases. In fact, as l_s controls the strain gradient effects, strong strain gradients cannot develop because they become energetically too expensive when the microstructure size is too small.

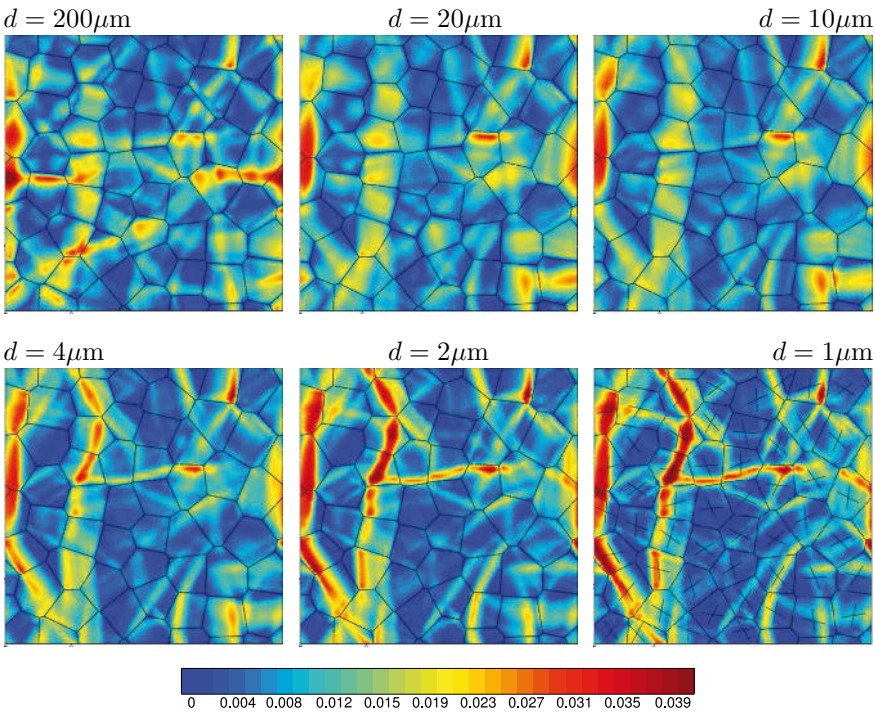

Figure 11. Grain size effect on the accumulated plastic slip. These contour plots are obtained with the 52–grain aggregate for the same mean value of $p = 0.01$. The set of material parameters (g) of Table 3 is used. The pairs of slip plane directions are represented for each grain on the 1μm contour plot.

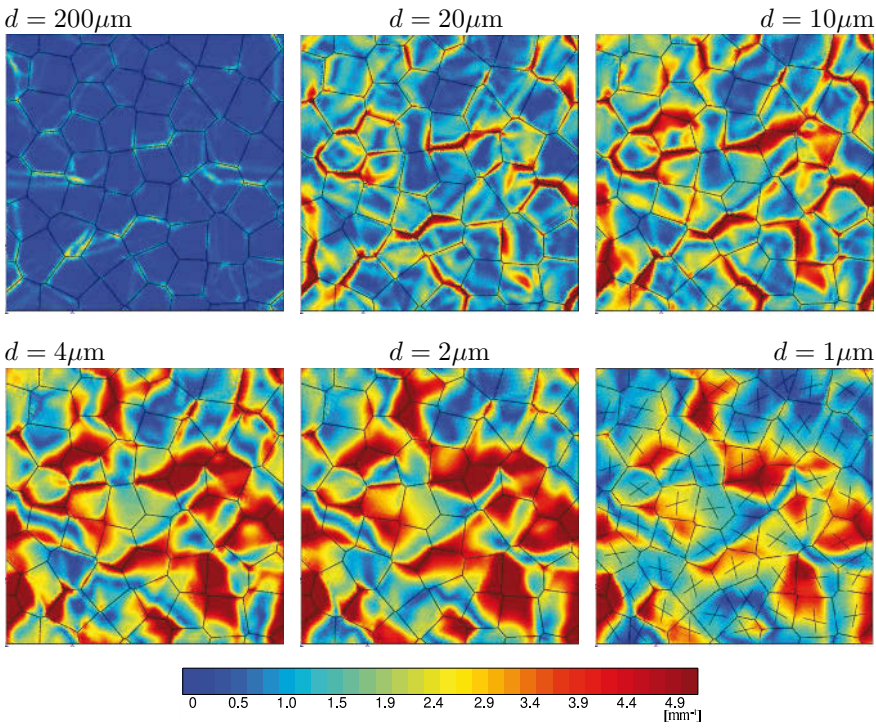

Figure 12. Grain size effect on the norm of the dislocation density tensor. These contour plots are obtained with the 52–grain aggregate for the same mean value of $p = 0.01$. The set of material parameters (g) of Table 3 is used. The pairs of slip plane directions are represented for each grain on the 1μm contour plot.

5 Micromorphic approach vs. phase field models

There are strong links between generalized continuum mechanics and phase field models which are striving in modern field theories of materials. Mindlin's and Casal's second gradient model of mechanics and the Cahn–Hilliard diffusion theory were developed almost simultaneously. More generally, the necessity of introducing additional degrees of freedom in continuum models arose in the 1960s in order to account for microstructure effects on the overall material's response. However, generalized continuum mechanics, with paradigms like Eringen's micromorphic model and Aifantis strain gradient plasticity, developed along an independent track from phase field approach embodied by Khachaturyan's views, for instance.

The links have been seen recently within the context of plasticity and damage mechanics. The computational mechanics community aimed at introducing the evolution of microstructures into their simulations (Ubachs et al., 2004; Ammar et al., 2009a) whereas physicists started introducing plasticity into the thermodynamical setting (Gaubert et al., 2008). Cooperation between these communities becomes necessary when tackling damage mechanics and crack propagation simulation (Aslan and Forest, 2009; Miehe et al., 2010a). First attempts to present a general constitutive framework encompassing classical enhanced mechanical and thermodynamical models have been proposed recently (Forest, 2009; Aslan and Forest, 2011; Miehe, 2011). Such an approach is presented in this chapter and extended to sophisticated descriptions of interactions between viscoplasticity and phase transformations.

The micromorphic model originates from Eringen's introduction of microdeformation tensor at each material point that accounts for the changes of a triad of microstructure vectors. In the present chapter, the micromorphic approach denotes an extension of this theory to other variables than total deformation, namely plastic strain, hardening variables, and even temperature and concentration. The gist of the micromorphic model is to associate a microstructure quantity (e.g. microdeformation) to an overall quantity (e.g. macroscopic deformation). The deviation of the microvariable from the macrovariable and the gradient of the microvariable are sources of stored energy and dissipation. They are controlled by generalized stresses which contribute to the power of internal forces.

On the other hand, the phase field approach has proved to be an efficient method to model the motion of interfaces and growth of precipitates based on a sound thermodynamical formulation including non convex free energy potentials (Finel et al., 2010). The effect of microelasticity on the morphological aspects and kinetics of phase transformation is classically studied but

the occurrence of plasticity is recent (Ubachs et al., 2004; Gaubert et al., 2008, 2010). Beyond plasticity, damage and crack propagation are the subject of both generalized continuum and phase field approaches (Frémond and Nedjar, 1996; Ubachs et al., 2007; Aslan and Forest, 2009; Miehe et al., 2010a,b). Phase field simulations usually rely on finite differences or fast Fourier methods. More recently, the finite element method was also used in order to tackle more general boundary conditions (Ammar et al., 2009a; Miehe et al., 2010a; Rajagopal et al., 2010).

The objective of the present chapter is to formulate a thermomechanical theory of continua with additional degrees of freedom. It is shown in a first part that the theory encompasses available generalized continuum theories and phase field models provided that well–suited free energy and dissipation potentials are selected. The current strain gradient plasticity models are then extended to account simultaneously for plastic strain gradient and plastic strain rate gradient in order to address viscoplastic instabilities occurring in metal plasticity like dynamic strain ageing. The second part of the work exposes how the well–known elastoviscoplastic constitutive framework can be incorporated into the available phase field approach in order to investigate the coupling between viscoplasticity and phase transformation. An original approach is proposed that resorts to standard homogenization techniques used in the mechanics of heterogeneous materials.

5.1 Thermomechanics with additional degrees of freedom

General setting. The displacement variables of mechanics can be complemented by additional degrees of freedom (dof), ϕ, that can be scalars as well as tensor variables of given rank:

$$DOF = \{\underline{\boldsymbol{u}}\,, \quad \phi\}, \tag{151}$$

A first gradient theory is built on the basis of this set of degrees of freedom :

$$STRAIN = \{\underline{\underline{\boldsymbol{\varepsilon}}}, \quad \phi, \quad \boldsymbol{\nabla}\phi\} \tag{152}$$

The strain tensor, $\underline{\underline{\boldsymbol{\varepsilon}}}$, is the symmetric part of the gradient of the displacement field. The main assumption of the proposed theory is that the gradient of the additional degrees of freedom contribute to the work of internal forces in the energy equation, in contrast to internal variables and concentration in diffusion theory. Depending on the invariance properties of the variable ϕ, it can itself contribute to the work of internal forces together with its gradient. It is not the case for the displacement itself which is not an objective vector. The virtual power of internal forces is then extended to the

virtual power done by the additional variable and its first gradient:

$$\mathcal{P}^{(i)}(\underline{\dot{\boldsymbol{u}}}^{\star},\dot{\phi}^{\star}) = -\int_{\mathcal{D}} p^{(i)}(\underline{\dot{\boldsymbol{u}}}^{\star},\dot{\phi}^{\star})\,dV$$

$$p^{(i)}(\underline{\dot{\boldsymbol{u}}}^{\star},\dot{\phi}^{\star}) = \underset{\sim}{\boldsymbol{\sigma}} : \boldsymbol{\nabla}\underline{\dot{\boldsymbol{u}}}^{\star} + a\dot{\phi}^{\star} + \underline{\boldsymbol{b}}.\boldsymbol{\nabla}\dot{\phi}^{\star} \tag{153}$$

where $\mathcal{D}$ is a subdomain of the current configuration Ω of the body. Stars denote virtual fields. The Cauchy stress tensor is $\underset{\sim}{\boldsymbol{\sigma}}$ and a and $\underline{\boldsymbol{b}}$ are generalized stresses associated with the additional dof and its first gradient, respectively. Similarly, the power of contact forces must be extended as follows:

$$\mathcal{P}^{(c)}(\underline{\dot{\boldsymbol{u}}}^{\star},\dot{\phi}^{\star}) = \int_{\mathcal{D}} p^{(c)}(\underline{\dot{\boldsymbol{u}}}^{\star},\dot{\phi}^{\star})\,dV, \quad p^{(c)}(\underline{\dot{\boldsymbol{u}}}^{\star},\dot{\phi}^{\star}) = \underline{\boldsymbol{t}}.\underline{\dot{\boldsymbol{u}}}^{\star} + a^{c}\ \dot{\phi}^{\star} \tag{154}$$

where $\underline{\boldsymbol{t}}$ is the traction vector and a^c a generalized traction. In general, the power of forces acting at a distance must also be extended in the form:

$$\mathcal{P}^{(e)}(\underline{\dot{\boldsymbol{u}}}^{\star},\dot{\phi}^{\star}) = \int_{\mathcal{D}} p^{(e)}(\underline{\dot{\boldsymbol{u}}}^{\star},\dot{\phi}^{\star})\,dV, \quad p^{(e)}(\underline{\dot{\boldsymbol{u}}}^{\star},\dot{\phi}^{\star}) = \rho\underline{\boldsymbol{f}}.\underline{\dot{\boldsymbol{u}}}^{\star} + a^{e}\dot{\phi}^{\star} + \underline{\boldsymbol{b}}^{e}.\boldsymbol{\nabla}\dot{\phi}^{\star} \tag{155}$$

where $\rho\underline{\boldsymbol{f}}$ accounts for given simple body forces and a^e for generalized volume forces. The power of inertial forces also requires, for the sake of generality, the introduction of an inertia I associated with the acceleration of the additional degrees of freedom :

$$\mathcal{P}^{(a)}(\underline{\dot{\boldsymbol{u}}}^{\star},\dot{\phi}^{\star}) = \int_{\mathcal{D}} p^{(a)}(\underline{\dot{\boldsymbol{u}}}^{\star},\dot{\phi}^{\star})\,dV, \quad p^{(a)}(\underline{\dot{\boldsymbol{u}}}^{\star},\dot{\phi}^{\star}) = -\rho\underline{\ddot{\boldsymbol{u}}}.\underline{\dot{\boldsymbol{u}}}^{\star} - I\ddot{\phi}\,\dot{\phi}^{\star} \tag{156}$$

Following (Germain, 1973a), given body couples and double forces working with the gradient of the velocity field, could also be introduced in the theory. The generalized principle of virtual power with respect to the velocity and additional dof, is formulated as

$$\mathcal{P}^{(i)}(\underline{\dot{\boldsymbol{u}}}^{\star},\dot{\phi}^{\star}) + \mathcal{P}^{(e)}(\underline{\dot{\boldsymbol{u}}}^{\star},\dot{\phi}^{\star}) + \mathcal{P}^{(c)}(\underline{\dot{\boldsymbol{u}}}^{\star},\dot{\phi}^{\star}) + \mathcal{P}^{(a)}(\underline{\dot{\boldsymbol{u}}}^{\star},\dot{\phi}^{\star}) = 0,\ \forall\mathcal{D}\subset\Omega, \forall\underline{\dot{\boldsymbol{u}}}^{\star},\dot{\phi} \tag{157}$$

The method of virtual power according to (Maugin, 1980) is used then to derive the standard local balance of momentum equation:

$$\operatorname{div}\underset{\sim}{\boldsymbol{\sigma}} + \rho\underline{\boldsymbol{f}} = \rho\underline{\ddot{\boldsymbol{u}}}, \quad \forall\underline{\boldsymbol{x}}\in\Omega \tag{158}$$

and the generalized balance of micromorphic momentum equation:

$$\operatorname{div}(\underline{\boldsymbol{b}} - \underline{\boldsymbol{b}}^{e}) - a + a^{e} = I\ddot{\phi}, \quad \forall\underline{\boldsymbol{x}}\in\Omega \tag{159}$$

The method also delivers the associated boundary conditions for the simple and generalized tractions:

$$\underline{\boldsymbol{t}} = \underset{\sim}{\boldsymbol{\sigma}}.\underline{\boldsymbol{n}}\,, \quad a^c = (\underline{\boldsymbol{b}} - \underline{\boldsymbol{b}}^{\,e}).\underline{\boldsymbol{n}}\,, \quad \forall \underline{\boldsymbol{x}} \in \partial\mathcal{D} \tag{160}$$

The local balance of energy is also enhanced by the generalized power already included in the power of internal forces (153):

$$\rho\dot{\epsilon} = p^{(i)} - \operatorname{div} \underline{\boldsymbol{q}} + \rho r \tag{161}$$

where ϵ is the specific internal energy, $\underline{\boldsymbol{q}}$ the heat flux vector and r denotes external heat sources. The entropy principle takes the usual local form:

$$-\rho(\dot{\psi} + \eta\dot{T}) + p^{(i)} - \frac{\underline{\boldsymbol{q}}}{T}.\boldsymbol{\nabla} T \geq 0 \tag{162}$$

where it is assumed that the entropy production vector is still equal to the heat vector divided by temperature, as in classical thermomechanics. Again, the enhancement of the theory goes through the enriched power density of internal forces (153). The entropy principle is exploited according to classical continuum thermodynamics to derive the state laws. At this stage it is necessary to be more specific on the dependence of the state functions $\psi, \eta, \underset{\sim}{\boldsymbol{\sigma}}, a, \underline{\boldsymbol{b}}$ on state variables and to distinguish between dissipative and non–dissipative mechanisms. The introduction of dissipative mechanisms may require an increase in the number of state variables. These different situations are considered in the following subsections.

Micromorphic model as a special case. The micromorphic model as initially proposed by Eringen (Eringen and Suhubi, 1964) and Mindlin (Mindlin, 1964) amounts to introducing a generally non compatible microdeformation field:

$$\phi \equiv \underset{\sim}{\boldsymbol{\chi}}$$

where $\underset{\sim}{\boldsymbol{\chi}}$ is a generally non–symmetric second order tensor defined at each material point. When the microdeformation reduces to its skew symmetric part, the Cosserat model is retrieved (Ehlers and Volk, 1998; Forest and Sievert, 2006). The microdeformation is to be compared to the deformation gradient:

$$\underset{\sim}{\boldsymbol{e}} = \underline{\boldsymbol{u}} \otimes \boldsymbol{\nabla} - \underset{\sim}{\boldsymbol{\chi}} \tag{163}$$

If the internal constraint $\underset{\sim}{\boldsymbol{e}} \equiv 0$ is enforced, the microdeformation coincides with the deformation and the micromorphic model reduces to Mindlin's second gradient theory. The free energy density depends of the following state variables:

$$STATE = \{\underset{\sim}{\boldsymbol{\varepsilon}}, \quad \underset{\sim}{\boldsymbol{e}}, \quad \underset{\approx}{\boldsymbol{K}} := \underset{\sim}{\boldsymbol{\chi}} \otimes \boldsymbol{\nabla}, \quad T, \quad \alpha\}$$

where α denotes the set of internal variables required to represent dissipative mechanical phenomena. The Clausius–Duhem inequality (162) becomes, in the isothermal case,

$$(\underset{\sim}{\boldsymbol{\sigma}} - \rho\frac{\partial\psi}{\partial\underset{\sim}{\boldsymbol{\varepsilon}}}) : \dot{\underset{\sim}{\boldsymbol{\varepsilon}}} + (\underset{\sim}{\boldsymbol{a}} - \rho\frac{\partial\psi}{\partial\underset{\sim}{\boldsymbol{e}}}) : \dot{\underset{\sim}{\boldsymbol{e}}} + (\underline{\underline{\boldsymbol{b}}} - \rho\frac{\partial\psi}{\partial\underline{\underline{\boldsymbol{K}}}}) \dot{:} \dot{\underline{\underline{\boldsymbol{K}}}} - (\rho\eta + \rho\frac{\partial\psi}{\partial T})\dot{T} - \rho\frac{\partial\psi}{\partial T}\dot{\alpha} \geq 0 \tag{164}$$

where $\underset{\sim}{\boldsymbol{a}}$ was taken as the stress conjugate to the relative deformation rate $\dot{\underset{\sim}{\boldsymbol{e}}}$ in the power of internal forces, which corresponds to an alternative form for (153). The state laws for micromorphic media are obtained by assuming that the first four contribution are non–dissipative:

$$\underset{\sim}{\boldsymbol{\sigma}} = \rho\frac{\partial\psi}{\partial\underset{\sim}{\boldsymbol{\varepsilon}}}, \quad \underset{\sim}{\boldsymbol{a}} = \rho\frac{\partial\psi}{\partial\underset{\sim}{\boldsymbol{e}}}, \quad \underline{\underline{\boldsymbol{b}}} = \rho\frac{\partial\psi}{\partial\underline{\underline{\boldsymbol{K}}}}, \quad \eta = -\frac{\partial\psi}{\partial T} \tag{165}$$

Elastoviscoplastic micromorphic media are then obtained by a specific choice of the internal variables α and their evolution rules (Forest and Sievert, 2006).

Phase field model as a special case. Enhancing the mechanical power in the energy balance is plausible in the presence of microstructure induced mechanical phenomena, as proposed by Eringen. However, this is also possible in other contexts, namely when the dof ϕ has a more general meaning of an order parameter. Fried and Gurtin (Fried and Gurtin, 1993; Gurtin, 1996) suggested to consider the following reduced state space:

$$STATE = \{\underset{\sim}{\boldsymbol{\varepsilon}}, \quad \phi, \quad \boldsymbol{\nabla}\phi, \quad T, \quad \alpha\} \tag{166}$$

and the following state laws

$$\underset{\sim}{\boldsymbol{\sigma}} = \rho\frac{\partial\psi}{\partial\underset{\sim}{\boldsymbol{\varepsilon}}}, \quad \underline{\boldsymbol{b}} = \rho\frac{\partial\psi}{\partial\boldsymbol{\nabla}\phi}, \quad \eta = -\frac{\partial\psi}{\partial T} \tag{167}$$

so that, in the isothermal case, the dissipation rate reduces to

$$a^v\dot{\phi} + X\dot{\alpha} \geq 0, \quad \text{with} \quad a^v = a - \rho\frac{\partial\psi}{\partial\phi}, \quad X = -\rho\frac{\partial\psi}{\partial\alpha} \tag{168}$$

The choice of a convex potential $\Omega(a^v, X)$ providing the evolution laws:

$$\dot{\phi} = \frac{\partial\Omega}{\partial a^v}, \quad \dot{\alpha} = \frac{\partial\Omega}{\partial X} \tag{169}$$

ensures the positivity of the dissipation rate.
As an illustration, let us consider a quadratic contribution of a^v to the

dissipation potential. We are lead to the following relationships

$$\dot{\phi} = \frac{1}{\beta} a^v = \frac{1}{\beta}(a - \rho \frac{\partial \psi}{\partial \phi}) \tag{170}$$

where β is a material parameter. The latter equation can be combined with the balance law (159), in the absence of volume or inertial forces, and the state law (167) to derive

$$\beta \dot{\phi} = \mathrm{div}\left(\rho \frac{\partial \psi}{\partial \boldsymbol{\nabla} \phi}\right) - \rho \frac{\partial \psi}{\partial \phi} \tag{171}$$

which corresponds to a general Ginzburg-Landau equation.
The authors in (Ubachs et al., 2004) have combined the micromorphic approach and the Cahn–Hilliard approach to diffusion in order to derive an alternative equation to Cahn–Hilliard.

5.2 Constitutive framework for gradient and micromorphic viscoplasticity

We now exploit the established general structure to propose a constitutive framework for elastoviscoplastic materials exhibiting plastic strain gradient. The attention is focused on an isotropic elastoviscoplastic medium characterized by the cumulated plastic strain, p. The proposed formulation encompasses Aifantis–like strain gradient plasticity models and introduces additional strain rate gradient effects. The total strain is split into its elastic and plastic parts: $\underset{\sim}{\boldsymbol{\varepsilon}} = \underset{\sim}{\boldsymbol{\varepsilon}}^e + \underset{\sim}{\boldsymbol{\varepsilon}}^p$. In this context, the additional dof ϕ has the meaning of a microplastic strain (Forest and Aifantis, 2010) to be compared with p itself.

Two variants of the constitutive framework are considered which handle in a slightly different way the dissipative contribution due to the generalized stresses.

Introduction of viscous generalized stresses The free energy density is assumed to depend on the following state variables:

$$STATE = \{\underset{\sim}{\boldsymbol{\varepsilon}}^e, \quad e := \phi - p, \quad p, \quad \underline{\boldsymbol{K}} := \boldsymbol{\nabla}\phi\} \tag{172}$$

The isothermal Clausius–Duhem inequality take the form:

$$(\underset{\sim}{\boldsymbol{\sigma}} - \rho \frac{\partial \psi}{\partial \underset{\sim}{\boldsymbol{\varepsilon}}^e}) : \dot{\underset{\sim}{\boldsymbol{\varepsilon}}}^e + (a - \rho \frac{\partial \psi}{\partial e}) : \dot{e} + (\underline{\boldsymbol{b}} - \rho \frac{\partial \psi}{\partial \underline{\boldsymbol{K}}}) \cdot \dot{\underline{\boldsymbol{K}}} + \underset{\sim}{\boldsymbol{\sigma}} : \dot{\underset{\sim}{\boldsymbol{\varepsilon}}}^p + a\dot{p} - \rho \frac{\partial \psi}{\partial T} \dot{\alpha} \geq 0 \tag{173}$$

The following state laws are adopted

$$\underset{\sim}{\boldsymbol{\sigma}} = \rho \frac{\partial \psi}{\partial \underset{\sim}{\boldsymbol{\varepsilon}}^e}, \quad R = \rho \frac{\partial \psi}{\partial p} \tag{174}$$

To ensure the positivity of the dissipation rate associated with the generalized stress a and $\underline{\boldsymbol{b}}$, we adopt the viscoelastic constitutive equations

$$a = \rho \frac{\partial \psi}{\partial e} + \beta \dot{e}, \quad \underline{\boldsymbol{b}} = \rho \frac{\partial \psi}{\partial \underline{\boldsymbol{K}}} + \kappa \dot{\underline{\boldsymbol{K}}} \tag{175}$$

where β and κ are generalized viscosity coefficients. This viscoelastic formulation amounts to splitting the generalized stresses a and $\underline{\boldsymbol{b}}$ into elastic (reversible) and viscous parts. Regarding viscoplastic deformation, a viscoplastic potential $\Omega(\underset{\sim}{\boldsymbol{\sigma}}, a - R)$ is chosen such that:

$$\dot{\underset{\sim}{\boldsymbol{\varepsilon}}}^p = \frac{\partial \Omega}{\partial \underset{\sim}{\boldsymbol{\sigma}}}, \quad \dot{p} = \frac{\partial \Omega}{\partial a - R} \tag{176}$$

In order to evidence the kind of gradient elastoviscoplastic models we aim at, we illustrate the case of a quadratic free energy potential:

$$\begin{aligned} \rho\psi &= \frac{1}{2} \underset{\sim}{\boldsymbol{\varepsilon}}^e : \underset{\approx}{\boldsymbol{C}} : \underset{\sim}{\boldsymbol{\varepsilon}}^e + R_0 p + \frac{1}{2} H p^2 + \frac{1}{2} H_\phi e^2 + \frac{1}{2} A \underline{\boldsymbol{K}} \cdot \underline{\boldsymbol{K}} \\ \underset{\sim}{\boldsymbol{\sigma}} &= \underset{\approx}{\boldsymbol{C}} : \underset{\sim}{\boldsymbol{\varepsilon}}^e, \quad R = R_0 + Hp, \quad a = H_\phi e + \beta \dot{e}, \quad \underline{\boldsymbol{b}} = A \underline{\boldsymbol{K}} + \kappa \dot{\underline{\boldsymbol{K}}} \end{aligned}$$

The viscoplastic potential is based on the yield function that introduces the equivalent stress measure σ_{eq} and a threshold

$$\Omega(\underset{\sim}{\boldsymbol{\sigma}}, a - R) = \frac{K}{n+1} \left\langle \frac{\sigma_{eq} + a - R}{K} \right\rangle^{n+1}$$

$$\dot{\underset{\sim}{\boldsymbol{\varepsilon}}}^p = \dot{p} \frac{\partial \sigma_{eq}}{\partial \underset{\sim}{\boldsymbol{\sigma}}}, \quad \dot{p} = \left\langle \frac{\sigma_{eq} + a - R}{K} \right\rangle^n$$

where $\langle \cdot \rangle$ denotes the positive part of the quantity in brackets, and K and n are usual viscosity parameters. The decomposition (175) and the generalized balance (159) become

$$a = H_\phi(\phi - p) + \beta(\dot{\phi} - \dot{p}) = \operatorname{div}(A \underline{\boldsymbol{K}} + \kappa \dot{\underline{\boldsymbol{K}}}) \tag{177}$$

We finally obtain the following linear partial differential equation, under the condition of plastic loading, in the absence of volume and inertial forces:

$$H_\phi \phi - A \Delta \phi + \beta \dot{\phi} - \kappa \Delta \dot{\phi} = H_\phi p + \kappa \dot{p} \tag{178}$$

where Δ is the Laplace operator. When the viscous parts are dropped in (175), the Helmholtz type equation used in strain gradient plasticity and damage (Peerlings et al., 2001; Engelen et al., 2003; Forest, 2009) is retrieved. It is classically used for the regularization of strain localization phenomena. The rate dependent part in the previous equation is expected to be useful in the simulation of strain rate localization phenomena which occur for instance in strain ageing materials (Mazière et al., 2010).

Under plastic loading, the equivalent stress can then be decomposed into the following contributions:

$$\sigma_{eq} = R - a + K\dot{p}^{1/n} = R_0 + Hp - A\Delta\phi - \kappa\Delta\dot{\phi} + K\dot{p}^{1/n} \tag{179}$$

If $\kappa = 0$, the micromorphic model is retrieved. If, furthermore, the constraint $\phi \equiv p$ is enforced, Aifantis well–known strain gradient plasticity model is recovered.

Decomposition of the generalized strain measures. It is proposed now to consider the decomposition of the additional dof and its gradient into elastic and plastic parts:

$$\phi = \phi^e + \phi^p, \quad \underline{\boldsymbol{K}} = \underline{\boldsymbol{K}}^{\,e} + \underline{\boldsymbol{K}}^{\,p} \tag{180}$$

The decomposition of ϕ itself is allowed only if it is an objective quantity. This would not apply for instance for $\phi \equiv \underset{\sim}{\boldsymbol{R}}$, the Cosserat microrotation. But it is allowed for a strain variable (Forest and Sievert, 2006). Such generalized kinematic decompositions were proposed in (Forest and Sievert, 2006) for strain gradient, Cosserat and micromorphic media, also at finite deformation. It is generalized here for more general dofs, possibly related to physically coupled phenomena.

The selected state variables then are

$$STATE = \{\underset{\sim}{\boldsymbol{\varepsilon}}^e, \quad \phi^e, \quad \underline{\boldsymbol{K}}^{\,e}, \quad p\} \tag{181}$$

which leads to the following Clausius–Duhem inequality

$$(\underset{\sim}{\boldsymbol{\sigma}} - \rho\frac{\partial\psi}{\partial\underset{\sim}{\boldsymbol{\varepsilon}}^e}) : \dot{\underset{\sim}{\boldsymbol{\varepsilon}}}^e + (a - \rho\frac{\partial\psi}{\partial\phi^e})\dot{\phi}^e + (\underline{\boldsymbol{b}} - \rho\frac{\partial\psi}{\partial\underline{\boldsymbol{K}}^{\,e}})\cdot\dot{\underline{\boldsymbol{K}}}^{\,e} + \underset{\sim}{\boldsymbol{\sigma}} : \dot{\underset{\sim}{\boldsymbol{\varepsilon}}}^p + a\dot{\phi}^p + \underline{\boldsymbol{b}}\cdot\dot{\underline{\boldsymbol{K}}}^{\,p} - R\dot{p} \geq 0 \tag{182}$$

The retained state laws are

$$\underset{\sim}{\boldsymbol{\sigma}} = \rho\frac{\partial\psi}{\partial\underset{\sim}{\boldsymbol{\varepsilon}}^e}, \quad a = \rho\frac{\partial\psi}{\partial\phi^e}, \quad \underline{\boldsymbol{b}} = \rho\frac{\partial\psi}{\partial\underline{\boldsymbol{K}}^{\,e}} \tag{183}$$

The residual dissipation then is

$$\underset{\sim}{\boldsymbol{\sigma}} : \dot{\underset{\sim}{\boldsymbol{\varepsilon}}}^p + a\dot{\phi}^p + \underline{\boldsymbol{b}} \cdot \dot{\underline{\boldsymbol{K}}}^{\,p} - R\dot{p} \geq 0 \tag{184}$$

A simple choice of dissipation potential is

$$\Omega(\underset{\sim}{\boldsymbol{\sigma}}, R, a) = \frac{K}{n+1}\left\langle \frac{\sigma_{eq}+a-R}{K}\right\rangle^{n+1} + \frac{K_a}{m_a+1}\left(\frac{|a|}{K_a}\right)^{m_a+1} + \frac{K_b}{m_b+1}\left(\frac{b_{eq}}{K_b}\right)^{m_b+1}$$

where b_{eq} is a norm of $\underline{\boldsymbol{b}}$ and from which the evolution rules are derived

$$\underset{\sim}{\dot{\boldsymbol{\varepsilon}}}^p = \dot{p}\frac{\partial \sigma_{eq}}{\partial \underset{\sim}{\boldsymbol{\sigma}}}, \quad \dot{p} = -\frac{\partial \Omega}{\partial R} = \left\langle \frac{\sigma_{eq}+a-R}{K}\right\rangle^{n}, \tag{185}$$

$$\dot{\phi}^p = \frac{\partial \Omega}{\partial a} = \dot{p} + \left(\frac{|a|}{K_a}\right)^{m_a} \operatorname{sign} a, \; \underline{\dot{\boldsymbol{K}}}^p = \frac{\partial \Omega}{\partial \underline{\boldsymbol{b}}} = \left(\frac{b_{eq}}{K_b}\right)^{m_b} \frac{\partial b_{eq}}{\partial \underline{\boldsymbol{b}}} \tag{186}$$

The time variation of the additional dof therefore deviates from the cumulated plastic strain rate by a viscous term characterized by the material parameters K_a and m_a. The residual dissipation rate becomes

$$(\sigma_{eq} - R + a)\dot{p} + \frac{|a|^{m_a+1}}{K_a^{m_a}} + \left(\frac{b_{eq}}{K_b}\right)^{m_b} \frac{\partial b_{eq}}{\partial \underline{\boldsymbol{b}}} \cdot \underline{\boldsymbol{b}} \geq 0 \tag{187}$$

which is indeed always positive.

Let us illustrate the type of partial differential equation provided by such a model. For that purpose, a simple quadratic free energy potential is chosen:

$$\rho\psi = \frac{1}{2}\underset{\sim}{\boldsymbol{\varepsilon}}^e : \underset{\approx}{\boldsymbol{C}} : \underset{\sim}{\boldsymbol{\varepsilon}}^e + R_0 p + \frac{1}{2}Hp^2 + \frac{1}{2}H_\phi \phi^{e2} + \frac{1}{2}A\underline{\boldsymbol{K}}^e \cdot \underline{\boldsymbol{K}}^e \tag{188}$$

As a result, the corresponding state laws can be combined with the extra–balance equation (159):

$$a = H_\phi \phi^e = \operatorname{div} \underline{\boldsymbol{b}} = \operatorname{div}(A\underline{\boldsymbol{K}}^e) \tag{189}$$

which leads to the following partial differential equation, under the condition of material homogeneity:

$$H_\phi(\phi - \phi^p) = A\Delta\phi - A \operatorname{div} \underline{\boldsymbol{K}}^p \tag{190}$$

If $K_a = \infty$ (infinite viscosity), equation (186) shows that ϕ^p coincides with p. If, furthermore, $K_b = \infty$, the plastic part of $\underline{\boldsymbol{K}}$ vanishes. The equation (189) then reduces to the Helmholtz–type equation (178) where β and κ are set to zero. An alternative expression of (189) can be worked out by taking the viscous laws into account

$$a = K_a(\dot{\phi}^p - \dot{p}) = \operatorname{div} \underline{\boldsymbol{b}} = \operatorname{div} K_b \underline{\dot{\boldsymbol{K}}}^p \tag{191}$$

which leads to the following partial differential equation

$$K_a(\dot{\phi}^p - \dot{p}) = K_b \,\mathrm{div}\, \dot{\underline{\boldsymbol{K}}}^p \tag{192}$$

When the elastic contributions ϕ^e and $\underline{\boldsymbol{K}}^e$ are neglected, the previous equation reduces to

$$K_a(\dot{\phi} - \dot{p}) = K_b \Delta \dot{\phi} \tag{193}$$

which is identical to (178) after taking $A = H_\phi = 0$.

5.3 Phase field models for elastoviscoplastic materials

In this section, the additional degree of freedom is a phase field variable. We show how the constitutive framework for elastoviscoplastic materials can be embedded in the existing phase field approach which combines diffusion and phase field equations to model the motion of boundaries between phases. The migration of interfaces and growth of precipitates are strongly influenced by the mechanical behaviour of the phases.

One observes in current literature a strong endeavour to develop microstructure evolution simulation schemes coupled with complex mechanical material behaviour ranging from heterogeneous elasticity to general elastoviscoplasticity. The main difficulty of such a task lies in the tight coupling between the complex interface evolutions and the fields, common to many moving boundary problems. The phase field approach has emerged as a powerful method for easily tackling the morphological evolutions involved in phase transformations. Phase field models have incorporated elasticity quite early (Wang et al., 1993) and have succeeded in predicting some complex microstructure evolutions driven by the interplay of diffusion and elasticity. It is only very recently that some phase field models have been enriched with nonlinear mechanical behaviour, extending the range of applications and materials which can be handled by the phase field approach (Ubachs et al., 2004; Gaubert et al., 2008; Ammar et al., 2009b; Gaubert et al., 2010).

There are essentially two ways of introducing linear and nonlinear mechanical constitutive equations into the standard phase field approach:

1. The material behaviour is described by a unified set of constitutive equations including material parameters that explicitly depend on the concentration or the phase variable. Each parameter is usually interpolated between the limit values known for each phase. This is the formulation adopted in the finite element simulations of Cahn–Hilliard like equations coupled with viscoplasticity in (Ubachs et al., 2004, 2007) for tin–lead solders. The same methodology is used in (Gaubert et al., 2008, 2010) to simulate the role of viscoplasticity on

rafting of γ' precipitates in single crystal nickel base superalloys under load.

2. One distinct set of constitutive equations is attributed to each individual phase k at any material point. Each phase at a material point then possesses its own stress/strain tensor $\underset{\sim}{\boldsymbol{\sigma}}_k, \underset{\sim}{\boldsymbol{\varepsilon}}_k$. The overall strain and stress quantities $\underset{\sim}{\boldsymbol{\sigma}}, \underset{\sim}{\boldsymbol{\varepsilon}}$ at this material point must then be averaged or interpolated from the values attributed to each phase. This is particularly important for points inside the smooth interface zone. At this stage, several mixture rules are available to perform this averaging or interpolation. This approach makes possible to mix different types of constitutive equations for each phase, like hyperelastic nonlinear behaviour for one phase and conventional elastic–plastic model with internal variables for the other one. No correspondence of material parameters is needed between the phase behaviour laws. This is the approach proposed in (Steinbach and Apel, 2006) for incorporating elasticity in a multi–phase field model. For that purpose, the authors resort to a well–known homogeneous stress hypothesis taken from homogenization theory in the mechanics of heterogeneous materials (Besson et al., 2009). In the present work, we propose to generalize this procedure to nonlinear material behaviour and to other mixture rules also taken from homogenization theory.

It must be emphasized that the latter procedure is very similar to what has already been proposed for handling diffusion in phase field models by (Kim et al., 1999). Two concentration fields c_α and c_β are indeed introduced, and the real concentration field is obtained by a mixture rule together with an internal constraint on the diffusion potentials. Introducing two concentration fields gives an additional degree of freedom for controlling the energy of the interface with respect to its thickness. If this possibility is not obvious when mechanics is introduced, adding a degree of freedom for describing the stresses/strains within a diffuse interface could be valuable to get rid of some spurious effects due to unrealistic interface thickness.

Coupling with diffusion. In the context of mass diffusion and phase field evolution, the local form of the energy principle is

$$\dot{e} = \underset{\sim}{\boldsymbol{\sigma}} : \dot{\underset{\sim}{\boldsymbol{\varepsilon}}} + a\dot{\phi} + \underline{\boldsymbol{b}} \cdot \boldsymbol{\nabla}\dot{\phi} \tag{194}$$

The total strain is partitioned into the elastic strain $\underset{\sim}{\boldsymbol{\varepsilon}}^e$, the eigenstrain $\underset{\sim}{\boldsymbol{\varepsilon}}^\star$ due to phase transformation and the plastic strain $\underset{\sim}{\boldsymbol{\varepsilon}}^p$:

$$\underset{\sim}{\boldsymbol{\varepsilon}} = \underset{\sim}{\boldsymbol{\varepsilon}}^e + \underset{\sim}{\boldsymbol{\varepsilon}}^\star + \underset{\sim}{\boldsymbol{\varepsilon}}^p \tag{195}$$

According to the thermodynamics of irreversible processes, the second law states that the variation of entropy is always larger than or equal to the rate of entropy flux induced by diffusion:

$$T\dot{\eta} - \boldsymbol{\nabla}.(\mu \underline{\boldsymbol{J}}) \geqslant 0 \tag{196}$$

where $\underline{\boldsymbol{J}}$ is the diffusion flux and μ is the chemical potential. The conservation law for mass diffusion is then

$$\dot{c} = -\boldsymbol{\nabla}.\underline{\boldsymbol{J}} \tag{197}$$

Accordingly, the fundamental inequality containing first and second principles in the isothermal case is written as

$$-\rho\dot{\psi} + \underset{\sim}{\boldsymbol{\sigma}} : \underset{\approx}{\dot{\boldsymbol{\varepsilon}}} + a\dot{\phi} + \underline{\boldsymbol{b}} \cdot \boldsymbol{\nabla}\dot{\phi} + \mu\dot{c} - \underline{\boldsymbol{J}}.\boldsymbol{\nabla}\mu \geqslant 0 \tag{198}$$

Assuming that the free energy density depends on the order parameter ϕ and its gradient, the concentration c, the elastic strain $\underset{\approx}{\boldsymbol{\varepsilon}}^e$ and the set of internal variables V_k associated to material hardening[5]:

$$STATE = \{\phi, \quad \boldsymbol{\nabla}\phi, \quad c, \quad \underset{\approx}{\boldsymbol{\varepsilon}}^e, \quad V_k\}$$

The Clausius-Duhem inequality now becomes:

$$\left(a - \rho\frac{\partial\psi}{\partial\phi}\right)\dot{\phi} + \left(\underline{\boldsymbol{b}} - \rho\frac{\partial\psi}{\partial\boldsymbol{\nabla}\phi}\right)\cdot\boldsymbol{\nabla}\dot{\phi} + \left(\mu - \rho\frac{\partial\psi}{\partial c}\right)\dot{c} + \left(\underset{\sim}{\boldsymbol{\sigma}} - \frac{\partial\psi}{\partial\underset{\approx}{\boldsymbol{\varepsilon}}^e}\right) : \underset{\approx}{\dot{\boldsymbol{\varepsilon}}}^e - \underline{\boldsymbol{J}}.\boldsymbol{\nabla}\mu + \underset{\sim}{\boldsymbol{\sigma}} : \underset{\approx}{\dot{\boldsymbol{\varepsilon}}}^p - \rho\frac{\partial\psi}{\partial V_k}\dot{V}_k \geqslant 0 \tag{199}$$

The following reversible mechanisms and corresponding state laws are chosen:

$$\underline{\boldsymbol{b}} = \rho\frac{\partial\psi}{\partial\boldsymbol{\nabla}\phi}, \quad \mu = \rho\frac{\partial\psi}{\partial c}, \quad \underset{\sim}{\boldsymbol{\sigma}} = \rho\frac{\partial\psi}{\partial\underset{\approx}{\boldsymbol{\varepsilon}}^e}, \quad A_k := \rho\frac{\partial\psi}{\partial V_k} \tag{200}$$

The residual dissipation then is

$$\left(a - \rho\frac{\partial\psi}{\partial\phi}\right)\dot{\phi} - \underline{\boldsymbol{J}}.\boldsymbol{\nabla}\mu + \underset{\sim}{\boldsymbol{\sigma}} : \underset{\approx}{\dot{\boldsymbol{\varepsilon}}}^p - A_k\dot{V}_k \geqslant 0 \tag{201}$$

Three contributions appear in the above residual dissipation rate. The first is the phase field dissipation, associated with configuration changes of atoms and related to the evolution of the order parameter:

$$D_\phi = a^v\dot{\phi} \quad \text{with} \quad a^v = a - \rho\frac{\partial\psi}{\partial\phi} \tag{202}$$

[5]In this section, the notation for internal variables is changed to $(V_k)_{k\in\{\alpha,\beta\}}$ since α is now an index denoting one phase.

where a^v is the chemical force associated with the dissipative processes (Gurtin, 1996). The second contribution is the chemical dissipation due to diffusion, associated with mass transport. The last contribution is the mechanical dissipation, as discussed earlier.

An efficient way of defining the complementary laws related to the dissipative processes and ensuring the positivity of the dissipation for any thermodynamic process is to assume the existence of a dissipation potential $\Omega(a^v, \boldsymbol{\nabla}\mu, \underset{\sim}{\boldsymbol{\sigma}}, A_k)$, which is a convex function of its arguments:

$$\dot{\phi} = \frac{\partial \Omega}{\partial a^v}, \quad \underline{\boldsymbol{J}} = -\frac{\partial \Omega}{\partial \boldsymbol{\nabla}\mu}, \quad \dot{V}_k = -\frac{\partial \Omega}{\partial A_k} \quad , \quad \dot{\underset{\sim}{\boldsymbol{\varepsilon}}}^p = \frac{\partial \Omega}{\partial \underset{\sim}{\boldsymbol{\sigma}}} \tag{203}$$

These equations represent the evolution law for the order parameter, the diffusion flux as well as the evolution laws for the internal variables.

Partition of free energy and dissipation potential. The total free energy is postulated to have the form of a Ginzburg-Landau free energy functional accounting for interfaces through the square of the order parameter gradient. The free energy density ψ is then split into a chemical free energy density ψ_{ch}, a coherent mechanical energy density ψ_{mech}, and the square of the order parameter gradient:

$$\rho\psi(\phi, \boldsymbol{\nabla}\phi, c, \underset{\sim}{\boldsymbol{\varepsilon}}^e, V_k) = \rho\psi_{\text{ch}}(\phi, c) + \rho\psi_{\text{mech}}(\phi, c, \underset{\sim}{\boldsymbol{\varepsilon}}, V_k) + \frac{A}{2}\boldsymbol{\nabla}\phi \cdot \boldsymbol{\nabla}\phi \tag{204}$$

The irreversible part of the behaviour is described by the dissipation potential, which can be split into three parts related to the three contributions in the residual dissipation in Eq.(201): the phase field part $\Omega_\phi(\phi, c, a^v)$, the chemical part $\Omega_c(\phi, c, \boldsymbol{\nabla}\mu)$ and the mechanical dissipation potential $\Omega_{\text{mech}}(\phi, c, \underset{\sim}{\boldsymbol{\sigma}}, A_k)$:

$$\Omega(a^v, \boldsymbol{\nabla}\mu, \phi, c, \underset{\sim}{\boldsymbol{\sigma}}, A_k) = \Omega_\phi(c, \phi, a^v) + \Omega_c(c, \phi, \boldsymbol{\nabla}\mu) + \Omega_{\text{mech}}(\phi, c, \underset{\sim}{\boldsymbol{\sigma}}, A_k) \tag{205}$$

The chemical free energy density ψ_{ch} of a binary alloy is a function of the order parameter ϕ and of the concentration field c. The coexistence of both phases α and β discriminated by ϕ is possible if ψ_{ch} is non–convex with respect to ϕ. Following (Kim et al., 1998), ψ_{ch} is built with the free energy densities of the two phases ψ_α and ψ_β as follows:

$$\psi_{\text{ch}}(\phi, c) = h(\phi)\psi_\alpha(c) + (1 - h(\phi))\psi_\beta(c) + W g(\phi) \tag{206}$$

Here, the interpolating function $h(\phi)$ is chosen as $h(\phi) = \phi^2(3 - 2\phi)$, and $g(\phi) = \phi^2(1-\phi)^2$ is the double well potential accounting for the free energy

penalty of the interface. The height W of the potential barrier is related to the interfacial energy σ and the interfacial thickness δ as $W = 6\Lambda\sigma/\delta$. Assuming that the interface region ranges from θ to $1-\theta$, then $\Lambda = \log((1-\theta)/\theta)$. In the present work $\theta = 0.05$ (Kim et al., 1998; Ammar et al., 2009a).

The densities ψ_α and ψ_β are chosen to be quadratic functions of the concentration only:

$$\rho\psi_\alpha(c) = \frac{k_\alpha}{2}(c-a_\alpha)^2 \quad \text{and} \quad \rho\psi_\beta(c) = \frac{k_\beta}{2}(c-a_\beta)^2 \tag{207}$$

where a_α and a_β are the unstressed equilibrium concentrations of both phases which correspond respectively to the minima of ψ_α and ψ_β in the present model. k_α and k_β are the curvatures of the free energies.

Quadratic expressions are chosen for the chemical dissipation, which ensures the positivity of the dissipation rate:

$$\Omega_\phi(a^v) = \frac{1}{2}(1/\beta)a^{v2} \quad \text{and} \quad \Omega_c(\boldsymbol{\nabla}\mu) = \frac{1}{2}L(\phi)\boldsymbol{\nabla}\mu.\boldsymbol{\nabla}\mu \tag{208}$$

where a^v is given by Eq. (202), β is inversely proportional to the interface mobility and $L(\phi)$ is the Onsager coefficient, related to the chemical diffusivities D_α and D_β in both phases by means of the interpolation function $h(\phi)$ as:

$$L(\phi) = h(\phi)D_\alpha/k_\alpha + (1-h(\phi))D_\beta/k_\beta \tag{209}$$

The state laws and evolution equations for the phase field and chemical contributions can be derived as:

$$\underline{\boldsymbol{b}} = A\boldsymbol{\nabla}\phi, \quad \mu = \rho\frac{\partial\psi_{\text{ch}}}{\partial c} + \rho\frac{\partial\psi_{\text{mech}}}{\partial c} \tag{210}$$

$$\dot{\phi} = \frac{1}{\beta}a^v = \frac{1}{\beta}\left(a - \rho\frac{\partial\psi_{\text{ch}}}{\partial\phi} - \rho\frac{\partial\psi_{\text{mech}}}{\partial\phi}\right), \quad \underline{\boldsymbol{J}} = -L(\phi)\boldsymbol{\nabla}\mu \tag{211}$$

Substituting the previous equations into the balance equations for generalized stresses and mass concentration, the Ginzburg-Landau and usual diffusion equations are retrieved, which represent respectively the evolution equations for order parameter and concentration:

$$\operatorname{div}\underline{\boldsymbol{b}} - a = -\beta\dot{\phi} + \operatorname{div}(A\boldsymbol{\nabla}\phi) - \rho\frac{\partial\psi_{\text{ch}}}{\partial\phi} - \rho\frac{\partial\psi_{\text{mech}}}{\partial\phi} = 0 \tag{212}$$

$$\dot{c} = -\boldsymbol{\nabla}.(-L(\phi)\boldsymbol{\nabla}\mu) = -\boldsymbol{\nabla}.\left(-L(\phi)\left(\boldsymbol{\nabla}\frac{\partial\rho\psi_{\text{ch}}}{\partial c} + \boldsymbol{\nabla}\frac{\partial\rho\psi_{\text{mech}}}{\partial c}\right)\right) \tag{213}$$

Note the coupling of mechanics and diffusion and phase field evolution through the partial derivatives of the mechanical free energy with respect to concentration and order parameter.

Multiphase approach for the mechanical contribution. The second contribution to the free energy density is due to mechanical effects. Assuming that elastic behaviour and hardening are uncoupled, the mechanical part of the free energy density $\rho\psi_{\text{mech}}$ is decomposed into a coherent elastic energy density $\rho\psi_e$ and a plastic part $\rho\psi_p$ as:

$$\rho\psi_{\text{mech}}(\phi, c, \underset{\sim}{\boldsymbol{\varepsilon}}, V_k) = \rho\psi_e(\phi, c, \underset{\sim}{\boldsymbol{\varepsilon}}) + \rho\psi_p(\phi, c, V_k) \tag{214}$$

Moreover, the irreversible mechanical behaviour, related to the dissipative processes, is obtained by a plastic dissipation potential $\Omega_{\text{mech}}(\phi, c, \underset{\sim}{\boldsymbol{\sigma}}, A_k)$. It is assumed to be a function of order parameter, concentration, Cauchy stress tensor as well as the set of thermodynamic force associated variables A_k in order to describe the hardening state in each phase.

In the diffuse interface region where both phases coexist, we propose to use well-known results of homogenization theory to interpolate the local behaviour. The homogenization procedure in the mechanics of heterogeneous materials consists in replacing an heterogeneous medium by an equivalent homogeneous one, which is defined by an effective constitutive law relating the macroscopic variables, namely macroscopic stress $\underset{\sim}{\boldsymbol{\sigma}}$ and strain $\underset{\sim}{\boldsymbol{\varepsilon}}$ tensors, which are obtained by averaging the corresponding non-uniform local stress and strain in each phase. Each material point within a diffuse interface can be seen as a local mixture of the two abutting phases α and β with proportions given by complementary functions of ϕ. The strain and stress at each material point are then defined by the following mixture laws which would proceed from space averaging in a conventional homogenization problem, but which must be seen as arbitrary interpolations in the present case:

$$\underset{\sim}{\boldsymbol{\varepsilon}} = \chi\, \underset{\sim}{\boldsymbol{\varepsilon}}_\alpha + (1-\chi)\, \underset{\sim}{\boldsymbol{\varepsilon}}_\beta \quad \text{and} \quad \underset{\sim}{\boldsymbol{\sigma}} = \chi\, \underset{\sim}{\boldsymbol{\sigma}}_\alpha + (1-\chi)\, \underset{\sim}{\boldsymbol{\sigma}}_\beta \tag{215}$$

where $\underset{\sim}{\boldsymbol{\varepsilon}}_\alpha$, $\underset{\sim}{\boldsymbol{\varepsilon}}_\beta$ are local fictitious strains and $\underset{\sim}{\boldsymbol{\sigma}}_\alpha$, $\underset{\sim}{\boldsymbol{\sigma}}_\beta$ are local fictitious stresses in α and β phases respectively and $\chi(\underline{\boldsymbol{x}}, t)$ is a shape function which must take the value 0 in the β–phase and 1 in the α–phase. The following choice is made in the phase field context:

$$\chi(\underline{\boldsymbol{x}}, t) \equiv \phi(\underline{\boldsymbol{x}}, t) \tag{216}$$

The partition hypothesis, already used for the effective total strain tensor in Eq. (195), requires, in a similar way, a decomposition of the total strain in each phase into elastic, transformation and plastic parts:

$$\underset{\sim}{\boldsymbol{\varepsilon}}_\alpha = \underset{\sim}{\boldsymbol{\varepsilon}}^e_\alpha + \underset{\sim}{\boldsymbol{\varepsilon}}^\star_\alpha + \underset{\sim}{\boldsymbol{\varepsilon}}^p_\alpha \quad \text{and} \quad \underset{\sim}{\boldsymbol{\varepsilon}}_\beta = \underset{\sim}{\boldsymbol{\varepsilon}}^e_\beta + \underset{\sim}{\boldsymbol{\varepsilon}}^\star_\beta + \underset{\sim}{\boldsymbol{\varepsilon}}^p_\beta \tag{217}$$

where each point may depend on the local concentration c, but not on order parameter ϕ. In the proposed model, the elastoplastic and phase

field behaviours of each phase are treated independently and the effective behaviour is obtained using homogenization relation (215). It is assumed that the mechanical state of α and β phases at a given time are completely described by a finite number of local state variables $(\underset{\sim}{\varepsilon}^e_k, V_k)$ defined at each material point. The set of internal variables V_k, of scalar or tensorial nature, represents the state of hardening of phase k: for instance, a scalar isotropic hardening variable, and a tensorial kinematic hardening variable. According to the homogenization theory, the effective elastic and plastic free energy densities are given by the rule of mixtures as follows:

$$\rho\psi_e(\phi, c, \underset{\sim}{\varepsilon}) = \phi\,\rho\psi_{e\alpha}(c, \underset{\sim}{\varepsilon}^e_\alpha) + (1-\phi)\rho\psi_{e\beta}(c, \underset{\sim}{\varepsilon}^e_\beta) \tag{218}$$

$$\rho\psi_p(\phi, c, V_k) = \phi\,\rho\psi_{p\alpha}(c, V_\alpha) + (1-\phi)\rho\psi_{p\beta}(c, V_\beta) \tag{219}$$

Similarly, a mixture rule is used to mix the dissipation potentials of the individual phases:

$$\Omega_{\text{mech}}(\phi, c, \underset{\sim}{\sigma}, A_k) = \phi\,\Omega_{\text{mech}_\alpha}(c, \underset{\sim}{\sigma}_\alpha, A_\alpha) + (1-\phi)\,\Omega_{\text{mech}_\beta}(c, \underset{\sim}{\sigma}_\beta, A_\beta) \tag{220}$$

where the $A_{\alpha,\beta}$ are the thermodynamic forces associated with the internal variables attributed to each phase.

Knowing the free energy and dissipation potentials, the evolution of all variables can be computed. The remaining questions is the way of estimating the previously defined fictitious stress and strain tensors $\underset{\sim}{\varepsilon}_{\alpha,\beta}, \underset{\sim}{\sigma}_{\alpha,\beta}$ from the knowledge of the stress and strain tensors $\underset{\sim}{\varepsilon}$ and $\underset{\sim}{\sigma}$. Several homogenization schemes exist in the literature that can be used to define these new fictitious variables. The most simple schemes are the Voigt/Taylor and Reuss/Static models. We develop the Voigt/Taylor scenario in the sequel.

Voigt/Taylor model coupled phase field mechanical theory. According to Voigt's scheme, the fictitious strains are not distinguished from the local strain. The local stress is then computed in terms of the fictitious stress tensors by averaging with respect to both phases weighted by the volume fractions:

$$\underset{\sim}{\sigma} = \phi\,\underset{\sim}{\sigma}_\alpha + (1-\phi)\,\underset{\sim}{\sigma}_\beta, \quad \underset{\sim}{\varepsilon} = \underset{\sim}{\varepsilon}_\alpha = \underset{\sim}{\varepsilon}_\beta \tag{221}$$

The stresses of both phases $\underset{\sim}{\sigma}_\alpha$ and $\underset{\sim}{\sigma}_\beta$ are given by Hooke's law for each phase:

$$\underset{\sim}{\sigma}_\alpha = \underset{\approx}{C}_\alpha : (\underset{\sim}{\varepsilon}_\alpha - \underset{\sim}{\varepsilon}^\star_\alpha - \underset{\sim}{\varepsilon}^p_\alpha), \quad \underset{\sim}{\sigma}_\beta = \underset{\approx}{C}_\beta : (\underset{\sim}{\varepsilon}_\beta - \underset{\sim}{\varepsilon}^\star_\beta - \underset{\sim}{\varepsilon}^p_\beta) \tag{222}$$

where $\underset{\approx}{C}_\alpha$ and $\underset{\approx}{C}_\beta$ are respectively the tensor of elasticity moduli in α and β phases. As a result,

$$\underset{\sim}{\sigma} = \phi\,\underset{\approx}{C}_\alpha : (\underset{\sim}{\varepsilon}_\alpha - \underset{\sim}{\varepsilon}^\star_\alpha - \underset{\sim}{\varepsilon}^p_\alpha) + (1-\phi)\underset{\approx}{C}_\beta : (\underset{\sim}{\varepsilon}_\beta - \underset{\sim}{\varepsilon}^\star_\beta - \underset{\sim}{\varepsilon}^p_\beta) \tag{223}$$

From the above relation, it follows that the strain-stress relationship in the homogeneous effective medium obeys Hooke's law with the following equation:

$$\boldsymbol{\sigma} = \underset{\approx}{\boldsymbol{C}}_{\text{eff}} : (\underset{\approx}{\boldsymbol{\varepsilon}} - \underset{\approx}{\boldsymbol{\varepsilon}}^{p} - \underset{\approx}{\boldsymbol{\varepsilon}}^{\star})$$

where the effective elasticity tensor $\underset{\approx}{\boldsymbol{C}}_{\text{eff}}$ is obtained from the mixture rule of the elasticity matrix for both phases:

$$\underset{\approx}{\boldsymbol{C}}_{\text{eff}} = \phi\, \underset{\approx}{\boldsymbol{C}}_{\alpha} + (1-\phi)\underset{\approx}{\boldsymbol{C}}_{\beta} \tag{224}$$

and the effective eigenstrain $\underset{\approx}{\boldsymbol{\varepsilon}}^{\star}$ and plastic strain $\underset{\approx}{\boldsymbol{\varepsilon}}^{p}$ vary continuously between their respective values in the bulk phases as follows:

$$\begin{aligned} \underset{\approx}{\boldsymbol{\varepsilon}}^{\star} &= \underset{\approx}{\boldsymbol{C}}_{\text{eff}}^{-1} : (\phi\, \underset{\approx}{\boldsymbol{C}}_{\alpha} : \underset{\approx}{\boldsymbol{\varepsilon}}^{\star}_{\alpha} + (1-\phi)\underset{\approx}{\boldsymbol{C}}_{\beta} : \underset{\approx}{\boldsymbol{\varepsilon}}^{\star}_{\beta}) \\ \underset{\approx}{\boldsymbol{\varepsilon}}^{p} &= \underset{\approx}{\boldsymbol{C}}_{\text{eff}}^{-1} : (\phi\, \underset{\approx}{\boldsymbol{C}}_{\alpha} : \underset{\approx}{\boldsymbol{\varepsilon}}^{p}_{\alpha} + (1-\phi)\underset{\approx}{\boldsymbol{C}}_{\beta} : \underset{\approx}{\boldsymbol{\varepsilon}}^{p}_{\beta}) \end{aligned} \tag{225}$$

In the case of nonhomogeneous elasticity, it must be noted that $\underset{\approx}{\boldsymbol{\varepsilon}}^{\star}$ and $\underset{\approx}{\boldsymbol{\varepsilon}}^{p}$ are not the average of their respective values for each phase.

The proposed approach differs from the one most commonly used in phase field models, as popularized by Khachaturyan and co-workers, e.g. (Khachaturyan, 1983). The latter rely on mixture laws for all quantities within the interface, including the elastic moduli, the transformation and plastic strain. The effect of these different choices on the simulation of moving phase boundaries has been tested in (Ammar et al., 2009b) and (Ammar et al., 2011). In particular, the impact of plasticity on the kinetics of precipitate growth has been evidenced.

6 Summary and Outlook

The general thermomechanical setting for modeling size effects in the mechanics and thermodynamics of materials is based on the main assumption that microstructure effects can be accounted for by the introduction of additional degrees of freedom in addition to displacement, temperature and concentration. The additional dof and its gradient are expected to contribute to the power of internal forces of the medium and to arise in the energy local balance equations and/or entropy inequality. They induce generalized stresses that fulfill an additional balance equation with associated extra boundary conditions. A clear separation between balance equations and constitutive functionals is adopted in the formulation. Constitutive equations derive from the definition of a specific free energy density and dissipation potential.

The crossing of mechanical and physical approaches turns out to be fertile in providing motivated coupling between both kinds of phenomena. As an example, we have shown that the mechanics of heterogeneous materials can be useful to develop a sophisticated and flexible constitutive framework of coupled viscoplasticity and diffusion.

It was not possible to address applications that already exist in this context. In particular, the presented models predict that viscoplasticity affects the morphology and kinetics of precipitate growth in metals or during oxidation (Ammar et al., 2009a; Gaubert et al., 2010; Ammar et al., 2011).

Special attention must now be dedicated to more precise description of coherent vs. incoherent interfaces (Murdoch, 1978; Johnson and Alexander, 1986; Appolaire et al., 2010), and the associated specific interface conditions that can be deduced from asymptotic analysis of phase field models. On the other hand, the targeted applications of strain gradient plasticity are crystal plasticity and grain boundary migration (Cordero et al., 2010; Mayeur et al., 2011; Abrivard, 2009), whereas strain rate gradients are thought to be relevant for ageing materials (Mazière et al., 2010).

Bibliography

Guillaume Abrivard. *A coupled crystal plasticity–phase field formulation to describe microstructural evolution in polycrystalline aggregates*. PhD, Mines ParisTech, 2009.

E.C. Aifantis. On the microstructural origin of certain inelastic models. *Journal of Engineering Materials and Technology*, 106:326–330, 1984.

K. Ammar, B. Appolaire, G. Cailletaud, F. Feyel, and F. Forest. Finite element formulation of a phase field model based on the concept of generalized stresses. *Computational Materials Science*, 45:800–805, 2009a.

K. Ammar, B. Appolaire, G. Cailletaud, and S. Forest. Combining phase field approach and homogenization methods for modelling phase transformation in elastoplastic media. *European Journal of Computational Mechanics*, 18:485–523, 2009b.

K. Ammar, B. Appolaire, G. Cailletaud, and S. Forest. Phase field modeling of elasto-plastic deformation induced by diffusion controlled growth of a misfitting spherical precipitate. *Philosophical Magazine Letters*, 91:164–172, 2011.

B. Appolaire, E. Aeby-Gautier, J. D. Teixeira, M. Dehmas, and S. Denis. Non-coherent interfaces in diffuse interface models. *Philosophical Magazine*, 90:461–483, 2010.

R.J. Asaro. Crystal plasticity. *J. Appl. Mech.*, 50:921–934, 1983.

O. Aslan and S. Forest. Crack growth modelling in single crystals based on higher order continua. *Computational Materials Science*, 45:756–761, 2009.

O. Aslan and S. Forest. The micromorphic versus phase field approach to gradient plasticity and damage with application to cracking in metal single crystals. In R. de Borst and E. Ramm, editors, *Multiscale Methods in Computational Mechanics*, pages 135–154. Lecture Notes in Applied and Computational Mechanics 55, Springer, 2011.

O. Aslan, N. M. Cordero, A. Gaubert, and S. Forest. Micromorphic approach to single crystal plasticity and damage. *International Journal of Engineering Science*, 49:1311–1325, 2011.

V.P. Bennett and D.L. McDowell. Crack tip displacements of microstructurally small surface cracks in single phase ductile polycrystals. *Engineering Fracture Mechanics*, 70(2):185–207, 2003.

J. Besson, G. Cailletaud, J.-L. Chaboche, S. Forest, and M. Blétry. *Non–Linear Mechanics of Materials*. Series: Solid Mechanics and Its Applications, Vol. 167, Springer, ISBN: 978-90-481-3355-0, 433 p., 2009.

B.A. Bilby, R. Bullough, L.R.T. Gardner, and E. Smith. Continuous distributions of dislocations iv: Single glide and plane strain. *Proc. Roy. Soc. London*, A236:538–557, 1957.

P. Cermelli and M.E. Gurtin. On the characterization of geometrically necessary dislocations in finite plasticity. *Journal of the Mechanics and Physics of Solids*, 49:1539–1568, 2001.

Y. Chen and J.D. Lee. Connecting molecular dynamics to micromorphic theory. (I) instantaneous and averaged mechanical variables. *Physica A*, 322:359–376, 2003a.

Y. Chen and J.D. Lee. Connecting molecular dynamics to micromorphic theory. (II) balance laws. *Physica A*, 322:377–392, 2003b.

Y. Chen and J.D. Lee. Determining material constants in micromorphic theory through phonon dispersion relations. *International Journal of Engineering Science*, 41:871–886, 2003c.

W.D. Claus and A.C. Eringen. Three dislocation concepts and micromorphic mechanics. In *Developments in Mechanics, Vol. 6. Proceedings of the 12th Midwestern Mechanics Conference*, pages 349–358, 1969.

W.D. Claus and A.C. Eringen. Dislocation dispersion of elastic waves. *International Journal of Engineering Science*, 9:605–610, 1971.

J.D. Clayton, D.J. Bamman, and D.L. McDowell. A geometric framework for the kinematics of crystals with defects. *Philosophical Magazine*, 85: 3983–4010, 2005.

N.M. Cordero, A. Gaubert, S. Forest, E. Busso, F. Gallerneau, and S. Kruch. Size effects in generalised continuum crystal plasticity for two–phase laminates. *Journal of the Mechanics and Physics of Solids*, 58:1963–1994, 2010.

W. Ehlers and W. Volk. On theoretical and numerical methods in the theory of porous media based on polar and non–polar elasto–plastic solid materials. *Int. J. Solids Structures*, 35:4597–4617, 1998.

R.A.B. Engelen, M.G.D. Geers, and F.P.T. Baaijens. Nonlocal implicit gradient-enhanced elasto-plasticity for the modelling of softening behaviour. *International Journal of Plasticity*, 19:403–433, 2003.

A.C. Eringen and W.D. Claus. A micromorphic approach to dislocation theory and its relation to several existing theories. In J.A. Simmons, R. de Wit, and R. Bullough, editors, *Fundamental Aspects of Dislocation Theory*, pages 1023–1062. Nat. Bur. Stand. (US) Spec. Publ. 317, II, 1970.

A.C. Eringen and E.S. Suhubi. Nonlinear theory of simple microelastic solids. *Int. J. Engng Sci.*, 2:189–203, 389–404, 1964.

Y. Estrin. Dislocation density related constitutive modelling. In *Unified Constitutive Laws of Plastic Deformation*, pages 69–106. Academic Press, 1996.

A. Finel, Y. Le Bouar, A. Gaubert, and U. Salman. Phase field methods: Microstructures, mechanical properties and complexity. *Comptes Rendus Physique*, 11:245–256, 2010.

M. Fivel and S. Forest. *Plasticité cristalline et transition d'échelle : cas du monocristal*. Techniques de l'Ingénieur, M4016, 23 pages, 2004a.

M. Fivel and S. Forest. *Plasticité cristalline et transition d'échelle : cas du polycristal*. Techniques de l'Ingénieur, M4017, 11 pages, 2004b.

S. Forest. The micromorphic approach for gradient elasticity, viscoplasticity and damage. *ASCE Journal of Engineering Mechanics*, 135:117–131, 2009.

S. Forest. Some links between cosserat, strain gradient crystal plasticity and the statistical theory of dislocations. *Philosophical Magazine*, 88: 3549–3563, 2008.

S. Forest and E. C. Aifantis. Some links between recent gradient thermo-elasto-plasticity theories and the thermomechanics of generalized continua. *International Journal of Solids and Structures*, 47:3367–3376, 2010.

S. Forest and R. Sedláček. Plastic slip distribution in two–phase laminate microstructures: Dislocation–based vs. generalized–continuum approaches. *Philosophical Magazine A*, 83:245–276, 2003.

S. Forest and R. Sievert. Elastoviscoplastic constitutive frameworks for generalized continua. *Acta Mechanica*, 160:71–111, 2003.

S. Forest and R. Sievert. Nonlinear microstrain theories. *International Journal of Solids and Structures*, 43:7224–7245, 2006.

S. Forest, F. Barbe, and G. Cailletaud. Cosserat modelling of size effects in the mechanical behaviour of polycrystals and multiphase materials. *International Journal of Solids and Structures*, 37:7105–7126, 2000.

S. Forest, F. Pradel, and K. Sab. Asymptotic analysis of heterogeneous Cosserat media. *International Journal of Solids and Structures*, 38:4585–4608, 2001.

M. Frémond and B. Nedjar. Damage, gradient of damage and principle of virtual power. *Int. J. Solids Structures*, 33:1083–1103, 1996.

E. Fried and M.E. Gurtin. Continuum theory of thermally induced phase transitions based on an order parameter. *Physica D*, 68:326–343, 1993.

A. Gaubert, A. Finel, Y. Le Bouar, and G. Boussinot. Viscoplastic phase field modellling of rafting in ni base superalloys. In *Continuum Models and Discrete Systems CMDS11*, pages 161–166. Mines Paris Les Presses, 2008.

A. Gaubert, Y. Le Bouar, and A. Finel. Coupling phase field and viscoplasticity to study rafting in ni-based superalloys. *Philosophical Magazine*, 90:375–404, 2010.

P. Germain. La méthode des puissances virtuelles en mécanique des milieux continus, première partie : théorie du second gradient. *J. de Mécanique*, 12:235–274, 1973a.

P. Germain. The method of virtual power in continuum mechanics. part 2 : Microstructure. *SIAM J. Appl. Math.*, 25:556–575, 1973b.

P. Grammenoudis and Ch. Tsakmakis. Micromorphic continuum Part I: Strain and stress tensors and their associated rates. *International Journal of Non–Linear Mechanics*, 44:943–956, 2009.

P. Grammenoudis, Ch. Tsakmakis, and D. Hofer. Micromorphic continuum Part II: Finite deformation plasticity coupled with damage. *International Journal of Non–Linear Mechanics*, 44:957–974, 2009.

W. Günther. Zur Statik und Kinematik des Cosseratschen Kontinuums. *Abhandlungen der Braunschweig. Wiss. Ges.*, 10:195–213, 1958.

M.E. Gurtin. A gradient theory of single–crystal viscoplasticity that accounts for geometrically necessary dislocations. *Journal of the Mechanics and Physics of Solids*, 50:5–32, 2002.

M.E. Gurtin. Generalized Ginzburg–Landau and Cahn–Hilliard equations based on a microforce balance. *Physica D*, 92:178–192, 1996.

M.E. Gurtin and L. Anand. Nanocrystalline grain boundaries that slip and separate: A gradient theory that accounts for grain-boundary stress and conditions at a triple-junction. *Journal of the Mechanics and Physics of Solids*, 56:184–199, 2008.

M.E. Gurtin and L. Anand. Thermodynamics applied to gradient theories involving the accumulated plastic strain: The theories of Aifantis and Fleck & Hutchinson and their generalization. *Journal of the Mechanics and Physics of Solids*, 57:405–421, 2009.

C.B. Hirschberger and P. Steinmann. Classification of concepts in thermodynamically consistent generalized plasticity. *ASCE Journal of Engineering Mechanics*, 135:156–170, 2009.

William C. Johnson and J. Iwan D. Alexander. Interfacial conditions for thermomechanical equilibrium in two-phase crystals. *Journal of Applied Physics*, 9:2735–2746, 1986.

A.G. Khachaturyan. *Theory of structural transformations in solids.* John Wiley & Sons, 1983.

S.G. Kim, W.T. Kim, and T Suzuki. Interfacial compositions of solid and liquid in a phase–field model with finite interface thickness for isothermal solidification in binary alloys. *Physical Review E*, 58(3):3316–3323, 1998.

S.G. Kim, W.T. Kim, and T Suzuki. Phase–field model for binary alloys. *Physical Review E*, 60(6):7186–7197, 1999.

E. Kröner. On the physical reality of torque stresses in continuum mechanics. *Int. J. Engng. Sci.*, 1:261–278, 1963.

E. Kröner. Initial studies of a plasticity theory based upon statistical mechanics. In M.F. Kanninen, W.F. Adler, A.R. Rosenfield, and R.I. Jaffee, editors, *Inelastic Behaviour of Solids*, pages 137–147. McGraw-Hill, 1969.

E. Kröner and C. Teodosiu. Lattice defect approach to plasticity and viscoplasticity. In A. Sawczuk, editor, *Problems of Plasticity, International Symposium on Foundations of Plasticity, Warsaw.* Noordhoff International Publishing Leyden, 1972.

M. Lazar and G.A. Maugin. Dislocations in gradient micropolar–I: screw dislocation. *Journal of the Mechanics and Physics of Solids*, 52:2263–2284, 2004.

M. Lazar and G.A. Maugin. On microcontinuum field theories: the eshelby stress tensor and incompatibility conditions. *Philosophical Magazine*, 87: 3853–3870, 2007.

M. Lazar, G.A. Maugin, and E.C. Aifantis. Dislocations in second strain gradient elasticity. *International Journal of Solids and Structures*, 43: 1787–1817, 2006.

J.D. Lee and Y. Chen. Constitutive relations of micromorphic thermoplasticity. *International Journal of Engineering Science*, 41:387–399, 2003.

J. Mandel. Une généralisation de la théorie de la plasticité de W.T. Koiter. *International Journal of Solids and Structures*, 1:273–295, 1965.

J. Mandel. *Plasticité classique et viscoplasticité.* CISM Courses and Lectures No. 97, Udine, Springer Verlag, Berlin, 1971.

J. Mandel. Equations constitutives et directeurs dans les milieux plastiques et viscoplastiques. *Int. J. Solids Structures*, 9:725–740, 1973.

G.A. Maugin. The method of virtual power in continuum mechanics: Application to coupled fields. *Acta Mechanica*, 35:1–70, 1980.

J.R. Mayeur, D.L. McDowell, and D.J. Bammann. Dislocation–based micropolar single crystal plasticity: Comparison if multi– and single cristerion theories. *Journal of the Mechanics and Physics of Solids*, 59:398–422, 2011.

M. Mazière, J. Besson, S. Forest, B. Tanguy, H. Chalons, and F. Vogel. Numerical aspects in the finite element simulation of the portevin-le chatelier effect. *Computer Methods in Applied Mechanics and Engineering*, 199:734–754, 2010.

L. Méric, P. Poubanne, and G. Cailletaud. Single crystal modeling for structural calculations. Part 1: Model presentation. *J. Engng. Mat. Technol.*, 113:162–170, 1991.

C. Miehe. A multifield incremental variational framework for gradient-type standard dissipative solids, in press. *Journal of the Mechanics and Physics of Solids*, 2011.

C. Miehe, F. Welchinger, and M. Hofacker. Thermodynamically–consistent phase field models of fracture: Variational principles and multifield FE implementations. *International Journal for Numerical Methods in Engineering*, 83:1273–1311, 2010a.

C. Miehe, F. Welchinger, and M. Hofacker. A phase field model of electromechanical fracture. *Journal of the Mechanics and Physics of Solids*, 58:1716–1740, 2010b.

R.D. Mindlin. Micro–structure in linear elasticity. *Arch. Rat. Mech. Anal.*, 16:51–78, 1964.

A. I. Murdoch. A thermodynamical theory of elastic material interfaces. *Q. J. Mech. appl. Math.*, 29:245–275, 1978.

J.F. Nye. Some geometrical relations in dislocated crystals. *Acta Metall.*, 1:153–162, 1953.

R.H.J. Peerlings, M.G.D. Geers, R. de Borst, and W.A.M. Brekelmans. A critical comparison of nonlocal and gradient–enhanced softening continua. *Int. J. Solids Structures*, 38:7723–7746, 2001.

A. Rajagopal, P. Fischer, E. Kuhl, and P. Steinmann. Natural element analysis of the cahn-hilliard phase-field model. *Computational Mechanics*, 46: 471–493, 2010.

R.A. Regueiro. On finite strain micromorphic elastoplasticity. *International Journal of Solids and Structures*, 47:786–800, 2010.

C. Sansour, S. Skatulla, and H. Zbib. A formulation for the micromorphic continuum at finite inelastic strains. *Int. J. Solids Structures*, 47:1546–1554, 2010.

Schäfer,H. Eine Feldtheorie der Versetzungen im Cosserat-Kontinuum. *ZAMP*, 20:891–899, 1969.

I. Steinbach and M. Apel. Multi phase field model for solid state transformation with elastic strain. *Physica D*, 217:153–160, 2006.

P. Steinmann. Views on multiplicative elastoplasticity and the continuum theory of dislocations. *International Journal of Engineering Science*, 34: 1717–1735, 1996.

B. Svendsen. Continuum thermodynamic models for crystal plasticity including the effects of geometrically-necessary dislocations. *J. Mech. Phys. Solids*, 50:1297–1329, 2002.

C. Teodosiu. A dynamic theory of dislocations and its applications to the theory of the elastic-plastic continuum. In J.A. Simmons, R. de Wit, and R. Bullough, editors, *Fundamental Aspects of Dislocation Theory*, pages 837–876. Nat. Bur. Stand. (US) Spec. Publ. 317, II, 1970.

C. Teodosiu and F. Sidoroff. A theory of finite elastoviscoplasticity of single crystals. *Int. J. of Engng Science*, 14:165–176, 1976.

R.L.J.M. Ubachs, P.J.G. Schreurs, and M.G.D. Geers. A nonlocal diffuse interface model for microstructure evolution of tin–lead solder. *Journal of the Mechanics and Physics of Solids*, 52:1763–1792, 2004.

R.L.J.M. Ubachs, P.J.G. Schreurs, and M.G.D. Geers. Elasto-viscoplastic nonlocal damage modelling of thermal fatigue in anisotropic lead-free solder. *Mechanics of Materials*, 39:685–701, 2007.

Y. Wang, L.-Q. Chen, and A.G. Khachaturyan. Kinetics of strain-induced morphological transformation in cubic alloys with a miscibility gap. *Acta Metallurgica et Materialia*, 41:279–296, 1993.

A. Zeghadi, S. Forest, A.-F. Gourgues, and O. Bouaziz. Ensemble averaging stress–strain fields in polycrystalline aggregates with a constrained surface microstructure–Part 2: Crystal plasticity. *Philosophical Magazine*, 87:1425–1446, 2007.

Formation of deformation substructures observed in ductile materials

Jan Kratochvíl

Czech Technical University, Faculty of Civil Engineering, Department of Physics, Thákurova 7, 166 29 Prague, and Charles University, Faculty of Mathematics and Physics, Sokolovská 83, 186 75 Prague, Czech Republic

Abstract Deformation substructures control plastic, creep, fatigue and fracture properties of ductile crystalline solids. The key ingredient of a substructure is a spontaneously formed dislocation arrangement – dislocation structure. The present notes provide 5 different, complementary points of view which present the dislocation structure formation as a multi scale phenomenon: (i) The basic concepts of dislocation theory and plasticity of single crystals and polycrystals (Section 2). (ii) A "gallery" of commented pictures of dislocation structures as seen by a transmission electron microscope (Section 3). (iii) Discrete dislocation dynamics (Section 4). (iv) An attempt to formulate statistics of dislocations as a transition from discrete dislocation dynamics to continuum crystal plasticity capable of modeling dislocation structure formation (Section 5). (v) Two continuous models of dislocation structure formation: one dimensional model simulating a formation of vein structure and its transformation into a ladder structure of a persistent slip band (Section 6.1), and a model of misoriented dislocation cells (Section 6.2).

1 Introduction

The most outstanding feature of deformed ductile crystalline solids at microscale is a spontaneous structuralization. The electron micrograph in Fig. 1 displays "fossils" left in a thin foil prepared from a FeSi single crystal specimen exposed to cyclic deformation. We can see "frozen" crystal lattice defects called *dislocations*. A few thin lines are glide dislocations, the short thicker objects are dislocations in a form of dipolar loops. As seen, dislocations tend to cluster into regions of high density separated by regions of low density. This phenomenon which underlines such effects as work hardening

J. Schröder, K. Hackl (Eds.), *Plasticity and Beyond*, CISM International Centre for Mechanical Sciences, DOI 10.1007/978-3-7091-1625-8_4,

and localization of plastic deformation occurs in single crystals as well as in polycrystals.

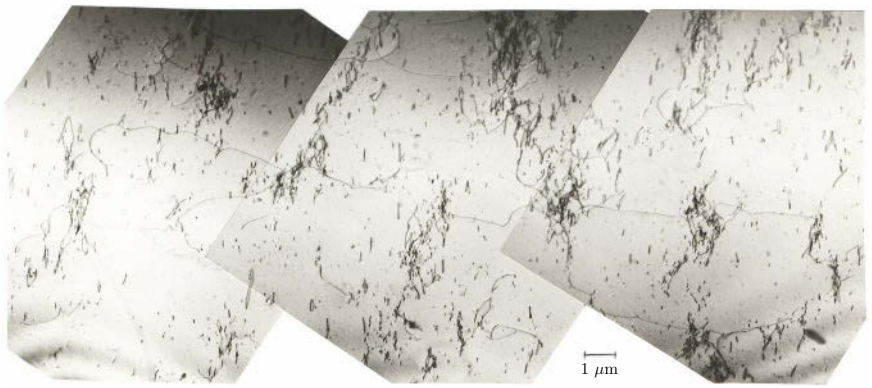

Figure 1. Dislocation pattern in FeSi single crystal deformed by cycling (courtesy of S. Libovický).

The dislocations are generated within the crystal and carry plastic deformation during their short active life. Then they are to a large extent annihilated by mutual interactions leaving dislocation leftovers. Only few of them escape to the surface thus forming the characteristic surface relief. The leftovers, mostly in a form of dislocation loops, are swept into high density regions seen in Fig. 1 as the clusters. This *dislocation pattern* represents a special case of a so called *deformation substructure*. The substructures control plastic, creep, fatigue and fracture properties of ductile materials and depend on a chemical composition of the material, its processing, the thermal treatment and temperature-loading conditions. At the scale of μm there is a broad spectrum of features as in Fig. 1 further enriched by grain boundaries, precipitates, texture, a composite structure of multi-phase alloys, and concentrated plastic strain into shear and kink bands.

General feature of the dislocation pattern formation seems to be similar to a *spontaneous structuralization* of other nonlinear physical systems operating at non-equilibrium thermodynamic conditions (e.g. Benard's cells in fluids, lamellar structures formed during solidification, patterns in chemically reacting systems). In each case an initially homogeneous structure becomes unstable at a critical value of a control parameter and then restabilizes into a complex space configuration. As the control parameter further increases, the system may undergo additional transitions into even more complex states. The successive stages of the formed dislocation patterns

may be understood as a sequence of such restabilized states.

The basic phenomenon underlying the process of plastic deformation at microscale is a large difference between the internal energy of an ideal crystal and a crystal with dislocations deformed by the same amount of strain. The difference creates a thermodynamic driving force which is probably the reason for the highly uncorrelated generation of dislocations by the bursts of activated dislocation sources. This process results in an overproduction of dislocations. Only a small fraction of them is needed to carry plastic deformation, the rest is stored in the crystal. The deformed crystals supersaturated with dislocations tend to decrease the internal energy by the mutual screening of their elastic fields. If dislocations possess a sufficient maneuverability (solids with wavy slip) the leading mechanism is individual screening. The dislocations form dipoles which are partly annihilated and transformed by various mechanisms to dislocation dipolar loops. Observations on a wide range of materials, deformation modes and temperatures show that the dipolar loops are basic building elements of *dislocation dipolar loops arrays*: tangles, veins, walls. The example of the tangles can be seen in Fig. 1. On the other hand, in solids with low dislocation maneuverability (solids with planar slip) the dislocations screen their elastic field collectively forming a quasi regular arrangement which can be roughly modeled as a so called Taylor lattice. The description in the present notes is restricted to the ductile solids with wavy slip character.

A brief simplified view of dislocation pattern evolution includes a progression from *dipolar loops arrays* carried by single slip to the formation of *misoriented dislocation cells* (subgrains) formed by double or multi slip. The cells are separated by dislocation boundaries that have a net crystal lattice rotation across them. Extended nearly planar dislocation boundaries are integral features of the dislocation pattern in advanced stages of deformation. These boundaries separate regions of differing slip and must thereby accommodate the resulting mismatch in lattice rotations. This role has earned them the name *geometrically necessary boundaries* (*GNBs*). One of the most decisive factors influencing substructure formation is the number of activated slip systems, Section 3.4. Observed dislocation patterns arising at single slip are presented in Section 3.1 and 3.2, double slip and multislip is treated in Sections 3.3 – 3.5.

Plastic deformation is a multi-scale phenomenon, where the mechanisms and governing equations at the microscale (the level of order of nm), at the mesoscale (the level of order of μm), and at the macroscale (the level of a specimen size) are strongly interrelated with each other. The current approaches to modeling of plasticity can be roughly divided in five groups: (i) atomistic simulations, (ii) discrete dislocation dynamics,

(iii) mesoscale continuum dislocation-based models of spontaneous structuralization, (iv) phenomenological crystal plasticity theories, possibly endowed with higher plastic strain gradients, and (v) dislocation statistics as an attempt to transfer information among levels (ii)-(iv). The scope of the present notes is limited. I will try to outline the current knowledge on why and how are the dislocation patterns formed and some methods employed in their modeling. The description follows the scheme shown in Fig.2.

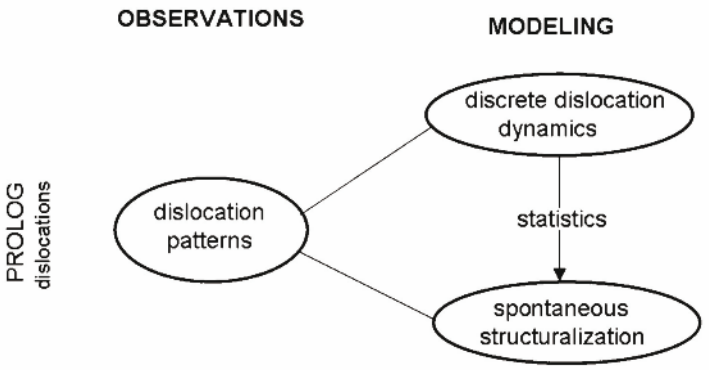

Figure 2. Lecture topics.

Dislocations and plasticity (Section 2). The introductory survey recalls fundamental concepts of the dislocation theory as needed in other sections: slip systems, dislocations, their stress fields, forces and interactions. Additionally, I try to incorporate the concept of dislocations into a broader perspective of inelastic properties of crystalline solids.

Observed dislocation patterns (Section 3). This section is devoted to nearly impossible task: to review the observed dislocation patterns. The short excursion through this vast territory is limited to a few typical examples of dislocation patterns appearing in cubic metals exposed to tension, cycling and severe plastic deformation where most detailed systematic observations were done. Only dislocation patterns formed during deformation carried by dislocation slip are considered. Dislocation climb, which occurs at temperatures above $T_M/3$, where T_M is the melting temperature expressed in the absolute (Kelvin) scale, as well as dislocation patterns directly connected with cracks and surface effects are not considered.

The classical theory of dislocations has led to the understanding of the behavior of individual crystal defects and elementary interactions among them. However, it does not seem to be suitable for the description of complex highly organized behavior of dislocation population under dynamic conditions. For that reason three approaches have emerged: *discrete dislocation dynamics, dislocation statistics, and spontaneous structuralization.* These complementary points of view and mathematical tools employed are confronted with the challenge exposed by the micrographs presented in Section 3.

Discrete dislocation dynamics (Section 4). Discrete dislocation dynamics is an effective tool providing objective guidelines for the modeling of plastic deformation of crystalline materials by studies of the mechanisms of dislocation interactions and patterning. Applications of these models spanned a number of important mesoscale plasticity problems. Let me note, however, that despite recent improvements and ever increasing computing capacity the discrete dislocation dynamics still remains far from an adequate modeling of realistic pattering precesses as seen in the micrographs of Section 3.

Methods developed in discrete dislocation dynamics can be categorized into groups according to the dislocation line discretization scheme and the representation of a general dislocation segment. In Section 4 the method of moving polygons is described in detail and applied to interacting glide dislocations. The dislocations are modeled as planar flexible curves employing the flowing volume method and the method of lines. The evolving positions and shapes of the dislocations are governed by the equation of motion where each dislocation segment is subjected to a line tension, to interactions with segments of other dislocations and to the stress field imposed by loading conditions. As an example the proposed method is employed to evaluate a bowing-out of dislocations from a dislocation wall and their subsequent interactions.

Dislocation statistics (Section 5). Statistical dislocation dynamics represents an attempt to formulate a continuous mesoscale crystal plasticity derived from dislocation dynamics by a statistical treatment of discrete dislocations. The first successful dislocation statistical model considered straight parallel edge dislocations of a single slip system represented by points of intersections of the dislocation lines with the plane of deformation. In this way the problem was transformed to the statistics of point objects, where tools of standard statistical mechanics were employed. However, standard tools of statistical mechanics are not directly applicable to the flexible dislocation lines. It has been

suggested to separate the dislocation population into groups suitable for averaging based on a concept of so called "single valued fields".

In Section 5 a statistical model of straight parallel edge dislocations of double slip is studied in detail. As a next step, the principle ideas of a more sophisticated statistics of a population of flexible dislocations and dislocation loops are outlined. The analysis has revealed one of the main obstacles: an adequate description of the close range correlation among dislocations. In the derived averaged continuous model the correlation results in non-local effects which play a decisive role in modeling of dislocation pattering and size effects. However, an adequate quantification of non-local terms has not been accomplished. Till now the attempts to formulate an adequate statistics of dislocations rises more questions than it gives answers.

Spontaneous structuralization (Section 6). The spontaneous structuralization approach suits well the description of the global cooperative behavior of the dislocation population and the coupling with the stress field. The formation of dislocation structures seems to be governed by two classes of instability transitions accompanied by spontaneous structuralization processes. The first class causes a formation of *dislocation dipolar loops arrays*: tangles, veins, walls. The second class is of the continuum mechanics nature. In the second class two main subclasses can be distinguished: *strain localization* (shear bands, avalanches, persistent slip bands) and/or *misoriented dislocation cells* (subgrains). The bands of localized shear and misoriented cell structures dominate the deformation microstructure at advanced stages of plastic deformation as a prelude to damage and fracture of ductile solids. In Section 6 two models of spontaneous structuralization are presented: (i) the model of formation and disintegration of vein dislocation structure, (ii) the plane strain model of misoriented dislocation cells formed by symmetric double slip.

(i) A qualitative one dimensional model of dislocation structure evolution during cycling is treated as a process of spontaneous structuralization. The main mechanisms of the dislocation structure development are a generation of dipolar loops, their sweeping by glide dislocations to high density regions and their annihilation. The model is described by three equations: the balance law for density of dipolar loops, the local yield condition governing the motion of glide dislocations and the equation controlling the local stress. The results of numerical solution of the model simulate the formation of the dislocation vein structure, its disintegration and formation of dipolar walls in a persistent slip band in a qualitative agreement with the microscopic observations re-

called in Section 3.2.
(ii) Within the framework of continuum mechanics, the formation of the misoriented dislocation cells can be explained as a result of a trend to reduce the energetically costly hardening in multi slip by decreasing locally the number of active slip systems. In the standard (local) approach, the continuum theory predicts an infinitesimally small cell size. The finite size of real cells is controlled by short-range dislocation interactions: (i) the line tension, (ii) the short-range correlation among dislocations. Within the proposed framework the cell size is a result of a compromise: bulk strain and dissipative energy tends to decrease the size, while short-range interactions restrict that tendency. The non-local effects are analyzed using an idealized model of an infinite crystal deformed by symmetric double slip, where plastic strain is carried by straight, parallel, edge dislocations. The constitutive equations for non-local effects are represented by the short-range correlation among dislocations derived from the statistics of dislocations presented in Section 5.

2 Elementary dislocation theory and plasticity of crystalline materials

In a tensile test one observes two distinguished types of a mechanical response. For most materials at sufficiently small strain the stress response is reversible, insensitive to the rate of strain and very little sensitive to temperature and small changes of chemical composition. Above all, the stress response is independent of deformation and thermal history experienced by the material. This mechanical property is called *elasticity*, Fig. 3.

If the strain exceeds a certain limit, then the stress response is quite different. It is irreversible, very often sensitive to the rate of straining, to temperature and to a small change of chemical composition (impurity content, e.g., C in Fe). However, the most distinguished feature is a strong dependence of the response on a previous straining and thermal treatments, the crystalline materials exhibit a peculiar type of memory. This mechanical property is called *inelasticity* and includes the following special cases: creep, visco-plasticity and plasticity, Fig. 4. Further, there is a big practical difference between elasticity and inelasticity. Theory of elasticity, namely the linear isotropic version, is well developed and understood. It is one of the most successful and reliable theoretical tools of engineering. On the other hand, inelasticity is not yet fully understood and its use in engineering depends often on testing, experience and empirical rules. There are many

theories of inelasticity, but their range of validity is uncertain.

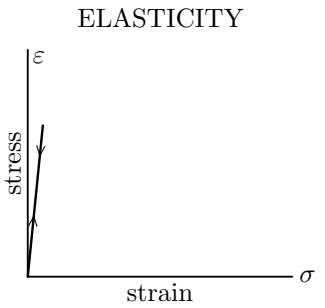

Figure 3.

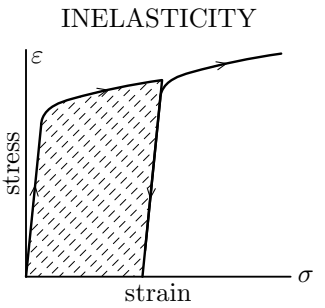

Figure 4.

Irreversibility of inelastic deformation shown in Fig. 4 comes from the fact that inelasticity is an dissipative process: no plastic work, shown as the dashed area, can be recovered. Most of it dissipates to heat and only approximately 5% is stored in the material in a form of structural changes which accompany the inelastic deformation. Therefore, inelastic deformation and thermal effects are always connected. A proper theoretical framework within which inelasticity can be described is irreversible thermodynamics. Inelastic and thermal behavior can be treated separately only approximately at slow deformation processes (at slow processes heat conduction suffices to keep the temperature field uniform and constant). In the course I use this approximation. The theory is then formally simpler.

The inelastic response of crystalline materials is *rate and temperature sensitive*. The inelastic response of some materials in a certain loading and temperature range is nearly rate-independent. Then the stress response depends only on the values of the strain history and not on the rate with which these values have been attained. The following considerations are mostly restricted to the rate (and temperature) independent materials. Such models of materials exclude creep and viscous properties, their response is *elasto-plastic* (rate independent plasticity).

2.1 Mechanism of plastic deformation

In Fig. 5 there is a schematic "close look" at a piece of a crystalline material. It consists of *grains* which are single crystals. In each single crystal grain there is a number of so called *slip systems*. In each slip system there operate *dislocations* which carry plastic deformation.

A polycrystal aggregate:

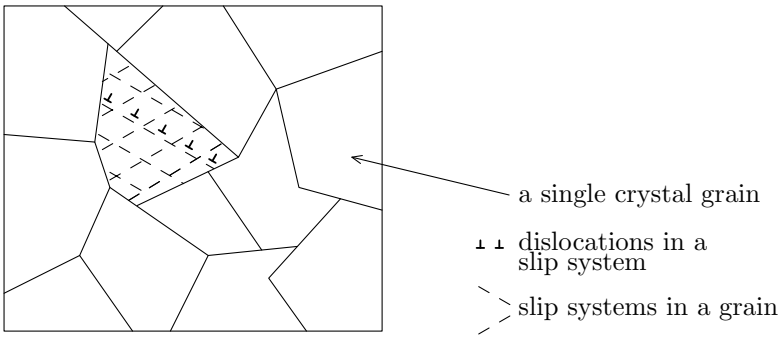

Figure 5. Scheme of a polycrystal

Plastic deformation is controlled at three levels:

1. Interactions among dislocations in a slip system
2. Interactions among slip systems in a single crystal grain
3. Interactions among the single crystal grains within a polycrystal aggregate.

Geometry of slip. The discovery of X-ray diffraction at the beginning of XX-century established that the basic structure of crystalline solids is a periodic array of atoms arranged in a crystal lattice. At the atomic scale the difference between the elastic and plastic deformations is significant. In elastic deformation each atom takes a part and the elastic anisotropy is usually mild, elasticity is a team work. On the other hand in plastic deformation only few atoms participate (i.e. plastic deformation is very inhomogeneous) and the deformation is strongly anisotropic (see Fig. 6)

The *inhomogeneity* and *anisotropy* of plastic deformation at the microscale is connected with the fundamental finding that the crystal structure tends to be preserved during a plastic change of shape (a consequence of energy minimization). This severely limits the number of ways in which the plastic deformation may occur. A common way is *slip* shown in lower part of Fig. 6. The slip (called also glide) occurs in a certain *slip plane* in a certain *slip direction*. A slip plane with a slip direction is called a *slip*

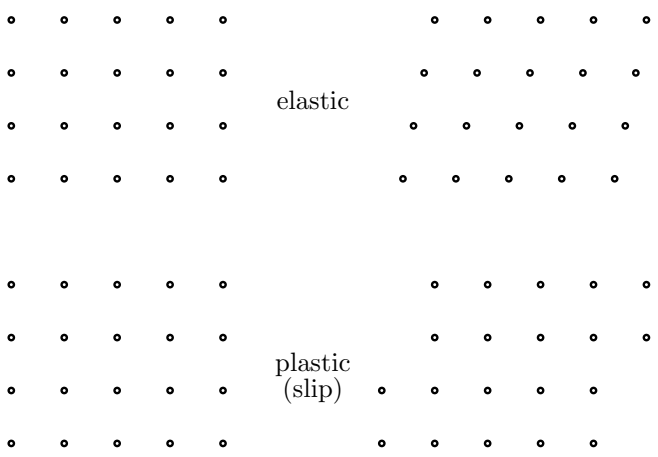

Figure 6. Rearrangement of atoms in elastic and slip deformation

system. The set of slip systems is a characteristic of the material (temperature can change one set of slip systems to another). The slip systems in a crystallographic structure are determined by the simple rule: the slip vector $\vec{b}$, called Burgers vector, is the shortest possible vector between atoms in the crystal structure (this rule is practically always obeyed); the slip direction is a unit vector $\vec{s} = \vec{b}/|\vec{b}|$. The slip plane is mostly a crystallographic plane which has the highest density of atoms and contains the vector $\vec{b}$.
Examples:

a) Cubic face centered structure (e.g. Cu, Al, Ni)

slip vectors	$(a/2)[1,0,1]$	shortest vectors between atoms
slip planes	{1 1 1}	(111 means the vector normal to the slip plane)

there are 4 slip planes, in each 3 slip directions (see Fig. 7) totally: 12 slip systems

b) Cubic body centered structure (e.g. Fe, Nb)

slip vectors	$(a/2)[1,1,1]$
slip planes	{1 1 0}

there are 3 {1 1 0} slip planes, in each 4 slip directions: 12 slip systems (three slip planes of one of the slip directions are shown in Fig. 8). There are other possibilities: 24 {123} and 12 {112} planes with one [111] direction, i.e. additionally 36 systems, for a total of 48.

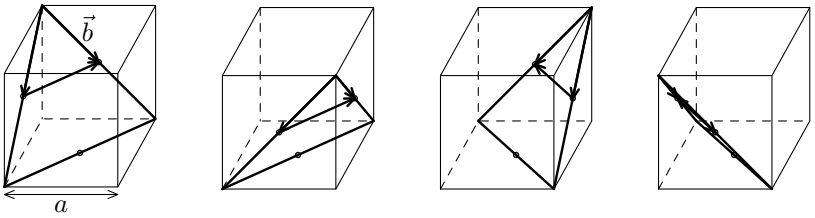

Figure 7. Slip systems in a face centered cubic crystal

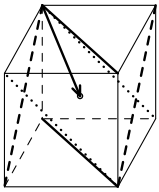

Figure 8. Slip systems in a body centered cubic crystal

Slip strain and macroscopic strain

The scheme of a tensile test of a single crystal where only one slip system is active is shown in Fig. 9. Slip has the discrete character as we know from Fig. 6. Two slip planes S_1 and S_2 which delimit the plastically active part are schematically illustrated in Fig. 9, $\vec{n}$ means the unit normal to the slip plane and $\vec{s}$ denotes the slip direction. In Fig. 10 there is a cross-section through the single crystal in the plane of tensile axis z and $\vec{s}$.

Consider a deformation carried by slip as shown in the lower part of Fig. 6. The elastic strain shown in the upper part of Fig. 6 is usually much smaller than the deformation caused by the slip, therefore in the present consideration it is neglected. Due to the slip δ the material between the slip planes S_1 and S_2 of the distance L_0 in z-direction is elongated to the length L. Therefore, the tensile plastic strain ε^p_{zz} is

$$\varepsilon^p_{zz} = \frac{L - L_0}{L_0}\,, \tag{1}$$

where for small δ there is $L - L_0 = \delta \cos\lambda$, hence

$$\varepsilon^p_{zz} = \frac{\delta \cos\lambda}{L_0}\,. \tag{2}$$

On the other hand, for slip strain γ

$$\gamma = \frac{\delta}{L_0 \cos\phi}\,. \tag{3}$$

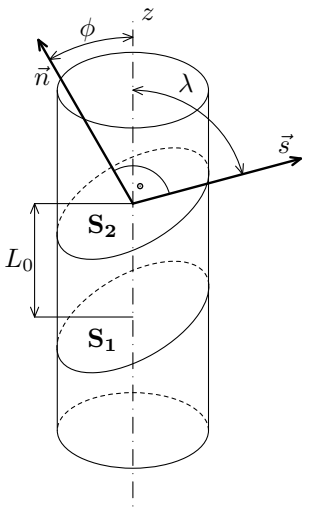

Figure 9.

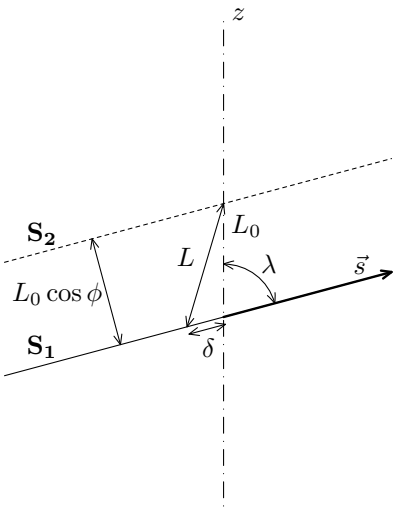

Figure 10.

Combination of (2) and (3) yields

$$\varepsilon^p_{zz} = \gamma \cos\phi \cos\lambda\,, \tag{4}$$

which expresses the relation between the shear strain in the slip system and macroscopic plastic tensile strain in terms of the orientation angles ϕ, λ of the slip systems in the coordinate system of the specimen.

Relation between slip strain and macroscopic strain for general state of strain. We can look at the relation (4) from a more general point of view: $\cos\phi$ is the z-component of the vector $\vec{n}$, i.e. $\cos\phi = n_z$, $\cos\lambda$ is the z-component of $\vec{s}$, i.e. $\cos\lambda = s_z$. Instead of (4)

$$\varepsilon^p_{zz} = \gamma s_z n_z\,, \tag{5}$$

and for the extensions in x and y directions

$$\varepsilon^p_{xx} = \gamma s_x n_x, \quad \varepsilon^p_{yy} = \gamma s_y n_y\,. \tag{6}$$

From a similar consideration as above one gets for the shearing deformation in terms of the displacement vector $\vec{u} = (u_x, u_y, u_z)$

$$\frac{\partial u_x}{\partial y} = \gamma s_x n_y \,, \quad \frac{\partial u_y}{\partial x} = \gamma s_y n_x \,, \quad \text{etc.} \tag{7}$$

For the shear strain (7) yields

$$\varepsilon^p_{xy} = \frac{\gamma}{2}(s_x n_y + s_y n_x) \,. \tag{8}$$

Summarizing (5), (6), (8) and the analogical formula for the strain components $\varepsilon^p_{yz}, \varepsilon^p_{xz}$ one gets: $\alpha, \beta = x, y, z$,

$$\varepsilon^p_{\alpha\beta} = A_{\alpha\beta}\gamma \,, \tag{9}$$

where $A_{\alpha\beta}$ is the so called orientation factor (tensor) of the slip system

$$A_{\alpha\beta} = \frac{1}{2}(n_\alpha s_\beta + s_\alpha n_\beta) \,, \tag{10}$$

in the tensor notation ($\otimes$ means a tensor product of vectors)

$$\mathbf{A} = \frac{1}{2}(\vec{n} \otimes \vec{s} + \vec{s} \otimes \vec{n}) \,, \quad \boldsymbol{\varepsilon}^p = \mathbf{A}\gamma \,. \tag{11}$$

So far only a single active slip system has been considered.

If more slip systems are active simultaneously (*multi slip*) situation is much different, as then only slip rates are physically meaningful. Existence of slip strain γ such as $\dot{\gamma} = \nu$, where the superposed dot means a time derivative and ν is a slip rate, is unique to single slip. Therefore, a generalization of (9) to multi slip reads

$$D^p_{\alpha\beta} = \sum_{i=1}^{N} A^{(i)}_{\alpha\beta}\nu^{(i)} \,, \quad \left(\mathbf{D}^p = \sum_{i=1}^{N} \mathbf{A}^{(i)}\nu^{(i)} \right) , \tag{12}$$

where N is the number of the active slip systems, $A^{(i)}_{\alpha\beta}$ are components of the orientation tensor $\mathbf{A}^{(i)}$ in (i) slip system and $\nu^{(i)}$ is the corresponding slip rate. $\mathbf{D}^p$ is the plastic stretching (kinematics of crystal plasticity is presented in more detail in Section 6.2). The relation (12) can be used approximately also for small slip strain increments $\mathrm{d}\gamma^{(i)}$, i.e.

$$\mathrm{d}\varepsilon^p_{\alpha\beta} = \sum_{i=1}^{N} A^{(i)}_{\alpha\beta}\,\mathrm{d}\gamma^{(i)} \quad \left(\mathrm{d}\boldsymbol{\varepsilon}^p = \sum_{i=1}^{N} \mathbf{A}^{(i)}\,\mathrm{d}\gamma^{(i)} \right) . \tag{13}$$

Response to stress: resolved shear stress

The stress component that does most of work during plastic deformation is the shear stress which acts on the slip plane in the slip direction. This stress component is called the *resolved shear stress* τ. The relation between the tensile stress T_{zz} in a single crystal and τ is seen in Fig. 11.

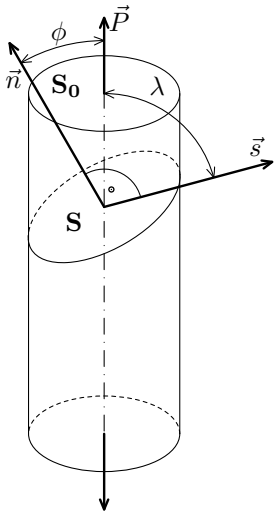

Figure 11.

The force P acting on the cross-section S_0 is

$$P = T_{zz} S_0 \,. \tag{14}$$

The force P_s in the slip direction $\vec{s}$ on the cross-section S of the slip plane is

$$P_s = P \cos\lambda \,. \tag{15}$$

The cross-sections S and S_0 are related by

$$S \cos\phi = S_0 \,. \tag{16}$$

For the resolved shear stress τ equations (14) – (16) yield

$$\tau = \frac{P_s}{S} = T_{zz} \cos\phi \cos\lambda \,, \tag{17}$$

where the value of $\cos\phi \cos\lambda$ is called the Schmid factor.

Note that

$$T_{zz}\,\mathrm{d}\varepsilon_{zz} = \frac{\tau}{\cos\phi\cos\lambda}\cos\lambda\cos\phi\,\mathrm{d}\gamma = \tau\,\mathrm{d}\gamma\,, \tag{18}$$

i.e. incremental work done by the external force equals the plastic work increment done in the slip system (the elastic work is neglected).

The same way as in (5) we can instead of (17) write

$$\tau = T_{zz}s_z n_z \tag{19}$$

and generalized relation (17) for a general stress state

$$\tau = A_{\alpha\beta}T_{\alpha\beta} \quad (\tau = \mathbf{A}\cdot\mathbf{T} = \vec{s}.\mathbf{T}\vec{n})\,, \tag{20}$$

where $\mathbf{A}\cdot\mathbf{T}$ means dot product; the summation convection is employed. For the plastic work increment in the case of the single slip

$$T_{\alpha\beta}\,\mathrm{d}\varepsilon^p_{\alpha\beta} = \tau A^{-1}_{\alpha\beta}A_{\alpha\beta}\,\mathrm{d}\gamma = \tau\,\mathrm{d}\gamma \tag{21}$$

or for more slip systems acting simultaneously (multi slip)

$$T_{\alpha\beta}\,\mathrm{d}\varepsilon^p_{\alpha\beta} = \sum_{i=1}^{N}\tau^{(i)}\,\mathrm{d}\gamma^{(i)}\,. \tag{22}$$

Schmid's law of critical resolved shear stress

One of the main discovery of plasticity of single crystals is Schmid' law: *a slip system begins to operate when the shear stress resolved on its slip plane in its slip direction reaches a critical value.* The critical value is independent of the normal stress in the slip plane.[1]

Schmid's law means that the crystal which contains crystallographically equivalent slip systems (e.g. systems in Figs.7 and 8) all of them having the same initial critical resolved shear stress begins to yield on the slip system with the maximum resolved shear stress. If the critical values of the resolved shear stress are reached on the different slip systems at the same time these systems start to operate simultaneously, the multi slip occurs. Mathematically Schmid's law is expressed in the form of so called *yield criterion*,

$$\text{if} \quad |\tau^{(i)}| = \mathbf{A}^{(i)}\cdot\mathbf{T} < \tau_y^{(i)} \qquad \Rightarrow \qquad \nu^{(i)} = 0, \tag{23}$$

$$\text{if} \quad |\tau^{(i)}| = \mathbf{A}^{(i)}\cdot\mathbf{T} = \tau_y^{(i)} \qquad \Rightarrow \qquad \nu^{(i)} \text{ may be} \neq 0. \tag{24}$$

[1] In a strict sense Schmid's law is valid for rate independent plasticity models. For real materials it represents a convenient approximation.

In (23) , (24), $\tau_y^{(i)}$ means the critical value of the resolved shear stress in the (i) slip system, called *the yield stress*. If the stress in a single crystal is so small that the resolved shear stress in no slip system reaches the critical value, i.e. (23) holds for all slip systems, the crystal is deformed elastically. When at least in a single slip system $\tau^{(i)}$ reaches the critical value $\tau_y^{(i)}$, i.e. (24) is obeyed, plastic deformation may occur, the crystal may start to yield. In plasticity of single crystals and polycrystals the relations (23) and (24) represent an important part of constitutive relations.

However, the main problem of (23), (24) is that $\tau_y^{(i)}$ are not constants and they may be spatially nonuniform; they change due to the slip deformation in a complicated way. A change of $\tau_y^{(i)}$ in the process of plastic deformation (called work hardening or softening) is the main unsolved difficulty of the plastic theory. Sections 4 – 6 concern this problem.

Summary

- Plastic deformation on the microscale is strongly *inhomogeneous and anisotropic*.
- The main mechanism of plastic deformation is the *slip* in the single crystal grains of the material. The slip may occur only in certain crystallographic planes (slip plane) and in the certain crystallographic directions (slip direction) which are both characteristic of the material (*slip plane + slip direction = slip system*).
- The slip is governed by *Schmid's law* (23), (24): a slip system begins to operate when the magnitude of the resolved shear stress $\tau^{(i)}$ reaches the critical value $\tau_y^{(i)}$ – the *yield stress*.
- The main unsolved difficulty of plasticity is a specification of the change of the critical value of the resolved shear stress in a process of plastic deformation.

2.2 Dislocations

The purpose of this section is to indicate why the work hardening of a slip system, i.e. a change of the yield stress with plastic deformation, is such a difficult problem. The reasons are: a complexity of forces acting on dislocations, a dislocation flexibility and a spontaneous arrangement of dislocations into patterns (dislocation structures). Prior to discussion of these problems, which are explained in more detail in Sections 3 – 6, a few basic concepts from the dislocation theory are recalled.

Concept of dislocation

The slip of the crystal shown in the lower part of Fig. 6 is not a result of a sliding of the parts of the crystal as rigid blocks. To carry on such process very large forces would have to be applied. The crystal deforms plastically in much more efficient way. Between a non-slipped and slipped states of the crystal there is an intermediate process, a motion of a dislocation. The net result of the dislocation motion from the left to the right is the slip by a slip vector (Burgers vector) $\vec{b}$, Fig. 12. The dislocation reduces substantially the force needed to cause slip according to a principle that the given amount of work can be done by a small force moved for a large distance, instead of a large force moving for a short distance (the analogy in Fig. 12). Of course, there is a question how dislocations appear in the crystal. Number of them originate during solidification of the material and additionally they multiply easily in a deformation process.

Fig. 12 shows only a special case of the dislocation. The situation in Fig. 13 is more realistic, there the dislocation is presented as a line defect of the crystal lattice. The dislocation is characterized by Burgers vector $\vec{b}$ (slip vector), i.e. *the elementary slip carried by the dislocation*, and *the dislocation line* which determines the position of the dislocation. The unit tangent vector $\vec{t}$ to the dislocation line and the vector $\vec{b}$ determine the slip plane at a given point of the dislocation line, $\vec{b}$ is the same for the whole dislocation, the tangent $\vec{l}$ changes along the dislocation line (the dislocation need not to be a plane curve). If $\vec{l} \perp \vec{b}$ we talk about an *edge orientation* of the dislocation (the case in Fig. 12), $\vec{l}$ is parallel to $\vec{b}$ in a *screw orientation* (the case in Fig. 15). A dislocation segment has a *mixed orientation*, if $\vec{l}$ is neither parallel nor perpendicular to $\vec{b}$. In the edge or mixed orientations the slip plane of the dislocation is uniquely determined. The motion of the dislocation is restricted to this slip plane as the motion perpendic-

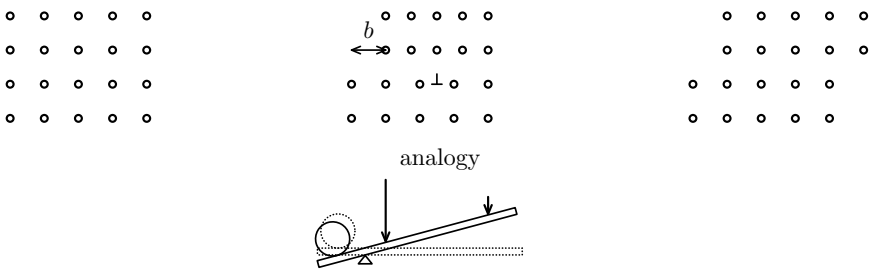

Figure 12. Concept of dislocation

ular to the slip plane requires diffusion of atoms to the dislocation center (available only at higher temperatures). In the screw orientation the slip plane is not uniquely defined; a screw dislocation segment can change the slip planes, so called *cross-slip* may occur. A possibility to change the slip plane of the screw dislocation segment is controlled by the structure of the dislocation center, so called dislocation core. An easy cross-slip provides a high *maneuverability of the dislocation*, the crystal then exhibits so called wavy slip.

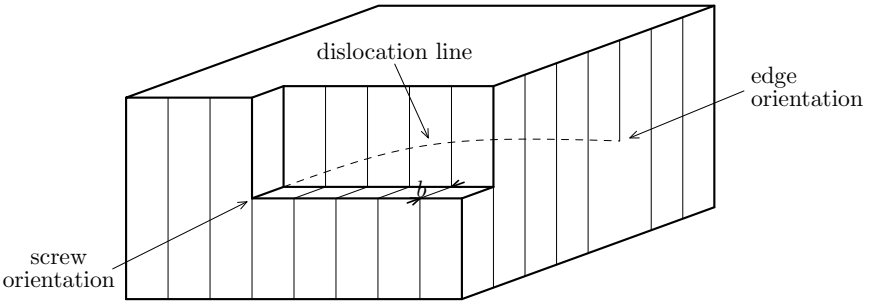

Figure 13. Dislocation line in a crystal

Forces exerted on dislocation

The forces acting on dislocation are of three types: *long range forces* (e.g. force from the external stress field applied to the crystal, the forces between dislocations), *short range forces* (e.g. forces between intersecting dislocations, forces between dislocations and impurities, vacancies, etc.) and *the line tension*. In this section just a brief overview of basic notions is presented. A more detail analysis of the forces is given in Section 4.

Long range forces. Consider a block of a single crystal with a dislocation and the resolved shear stress τ acting on it (Fig. 14). The force on the block is $F = \tau w L$, where w and L are the dimensions of the block as shown in Fig.14. If the dislocation moves the distance $\mathrm{d}x$ the corresponding shear displacement of the block is $\mathrm{d}u = b\,\mathrm{d}x/L$, where $b = |\vec{b}|$ is the magnitude of the Burgers vector. The work done by the force F is then

$$\mathrm{d}W_{\mathrm{ex}} = F\,\mathrm{d}u = \frac{\tau w L b}{L}\,\mathrm{d}x = \tau b\,\mathrm{d}x\,. \tag{25}$$

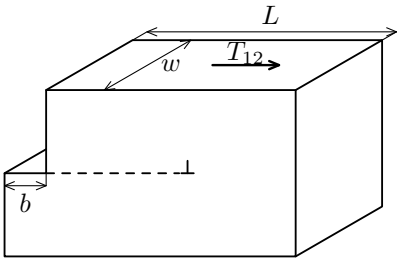

Figure 14. Force exerted on an edge dislocation

The force f per unit length of the dislocation which causes the dislocation to move does the work

$$\mathrm{d}W_{\mathrm{int}} = fw\,\mathrm{d}x\,. \tag{26}$$

The two works have to be equal, i.e. $\mathrm{d}W_{\mathrm{ex}} = \mathrm{d}W_{\mathrm{int}}$, hence, we get from (25) and (26)

$$f = \tau b\,. \tag{27}$$

Since the work associated with the force f is done when the dislocation moves perpendicular to itself (a force parallel to the dislocation line causes no external displacement) the force f is *perpendicular to the dislocation line.*

If more than one stress component is present or if the dislocation line is not parallel to one coordinate axis as in the case of Fig. 13, a more general expression for the force acting on the dislocation is needed (see e.g. Gilman (1969))

$$\vec{f} = \vec{l} \times \vec{P}\,, \qquad P_\alpha = T^D_{\alpha\beta} b_\beta\,, \tag{28}$$

where $\mathbf{T}^D$ is the deviatoric stress tensor $\mathbf{T}^D = \mathbf{T} - \mathrm{tr}\mathbf{T}/3$.

The resolved shear stress in (27) may originate from the external field applied to the crystal according to the equation (20) or it is exerted by other dislocations, as each dislocation has its own stress field. We can see that easily in the case of a screw dislocation (Fig. 15). From the geometry of this figure, we get the shear strain component $\varepsilon_{\theta z}$ at the distance r from the dislocation core

$$\varepsilon_{\theta z} = \frac{b}{2\pi r}\,. \tag{29}$$

(in the case of a screw dislocation the other strain components are equal zero), hence, the stress field of the screw dislocation is

$$T_{\theta z} = \frac{Gb}{\pi r}\,, \tag{30}$$

where G is the shear modulus. Note that the stress field is of a long range character, as it decreases with distance r from the core of the dislocation as $1/r$. If we combine (30), (20) and (27) we see that the force between parallel dislocations can be quite large. Expressions for the stress field derived for other orientations of dislocations are more complex. They are specified in Section 4.

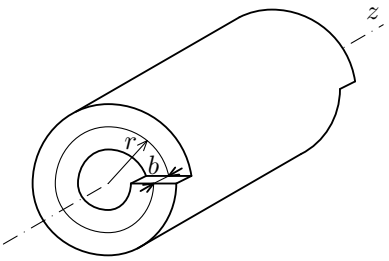

Figure 15. Screw dislocation

Short range forces. The short range forces acting on the dislocations are connected with the properties of the dislocation core. The dislocation core changes its structure during the dislocation motion in the crystal lattice and in interactions with other crystal defects. The change of the atomic structure of the core results in dissipation of energy and causes a friction force (drag) on the dislocation. The cores of the dislocations interact when the dislocations cut each other during the motion in the crystal lattice. The interaction of the core with impurities, vacancies, etc. has the similar character. The short range forces are of interatomic nature. The formula (27) cannot be applied to them as on the atomic scale the concept of stress has no meaning. There is another kind of short range forces. In assembles the long range forces among dislocations mainly screen each other giving a zero overall mean stress field. Then close range interactions among nearby dislocations become important. This type of forces can be modeled by means of higher plastic strain gradients as shown in dislocation statistics in Section 5.

Line tension. The line tension on the dislocation exists because its potential energy is proportional to the length of the dislocation line. Hence, the dislocation tends to be straight if no other forces act on it (the line tension is analyzed in Section 4.2 in more detail). Estimates show that the line tension is relatively small in comparison with other forces acting on the dislocation. As the result dislocations are highly flexible. The dislocation flexibility and

various types of interactions allow an exceedingly large variety of dislocation shapes and configurations to appear: localized irregularities on dislocation lines (kinks, jogs, cusps), multiplication of dislocations (Frank-Read sources, multiple cross-slip), local array of dislocations (dipoles, multipoles, tangles, veins, walls), planar arrays (pile-ups, low angle grain or subgrain boundaries), three-dimensional dislocation networks. Some of the dislocation arrangements are shown in Section 3. Various types of forces acting on dislocations and variety of possible dislocation configurations are far from to be understood. It makes any reliable microscopic estimate of the critical value of the resolved shear stress and its changes during deformation rather difficult.

Summary

- Plastic deformation is caused by the *motion of dislocations*.
- The dislocation motion is controlled by several types of *forces*. Many of them are not well understood at present.
- Uncertainty in the understanding of controlling dislocation forces and dislocation arrangements make any reliable estimate of the critical value of the resolved shear stress (yield stress) and its change during deformation *difficult*, as demonstrated in Sections 4–6.

2.3 Plasticity of single crystals

The knowledge outlined in the previous sections is employed in brief description of plastic behavior of single crystals. In summary, the single crystal plasticity is governed by three rules:

(a) Plastic deformation is caused by motion of dislocations which results in a slip in a particular slip system. The type and number of slip systems is a characteristic of the single crystal material. If $\mathrm{d}\gamma^{(i)}$ and $A^{(i)}$ mean an increment of *slip strain* and *the orientation factor* of a (i) slip system, respectively, then the increase of plastic strain $\mathrm{d}\varepsilon^p$ is (equation (13))

$$\mathrm{d}\boldsymbol{\varepsilon}^p = \mathbf{A}^{(i)}\,\mathrm{d}\gamma^{(i)} \qquad \text{single slip} \tag{31}$$

$$\mathrm{d}\boldsymbol{\varepsilon}^p = \sum_{i=1}^{N} \mathbf{A}^{(i)}\,\mathrm{d}\gamma^{(i)} \qquad \text{multi slip} \tag{32}$$

Throughout the following text we use a convenient convention that the same slip plane with two opposite slip directions forms two slip systems, and the increment of the slip strain is always non-negative

$\mathrm{d}\gamma^{(i)} \geq 0$ (the convention means that the cubic crystallographic structures mentioned in Section 2.1 have now 24 systems each).

(b) A single crystal yields on any particular slip system, if the corresponding resolved shear stress $\tau^{(i)}$ reaches a critical value $\tau_y^{(i)}$. Schmid's law expressed by (23), (24) in a more detailed form reads:

$$\mathbf{A}^{(i)} \cdot \mathbf{T} < \tau_y^{(i)} \quad \text{for each inactive system} \qquad (\mathrm{d}\gamma^{(i)} = 0) \tag{33}$$

$$\mathbf{A}^{(i)} \cdot \mathbf{T} = \tau_y^{(i)} \quad \text{for each active system} \qquad (\mathrm{d}\gamma^{(i)} \geq 0) \tag{34}$$

$$\text{active system remains active}, \mathrm{d}\gamma^{(i)} > 0, \text{if } \mathbf{A}^{(i)} \cdot \mathrm{d}\mathbf{T} = \mathrm{d}\tau_y^{(i)} \tag{35}$$

$$\text{active system becomes inactive}, \mathrm{d}\gamma^{(i)} = 0, \text{if } \mathbf{A}^{(i)} \cdot \mathrm{d}\mathbf{T} < \mathrm{d}\tau_y^{(i)} \tag{36}$$

(c) It is generally accepted that the origin of the *work hardening* in single crystals comes from the long and short range interactions among dislocations and other crystal defects. In mathematical terms, we need to know how the increment in work-hardening $\mathrm{d}\tau_y^{(i)}$ in (35), (36) depends on slip increments $\mathrm{d}\gamma^{(i)}$, $i = 1, .., N$. It should be emphasized that the dislocation interactions cause hardening not only of the active slip system where the slip takes place, but also in other slip systems, the effect is called *latent hardening*, see the constitutive equations (41), (42).

Initial yield surface The rules (a) – (c) may be expressed by means of a geometrical representation called a yield surface (yield locus). For this purpose, it is useful to use a vector representation of the stress and strain:

$$\vec{T} = (T_{11}, T_{22}, T_{33}, T_{12}, T_{13}, T_{23}), \quad \vec{\varepsilon^p} = (\varepsilon^p_{11}, \varepsilon^p_{22}, \varepsilon^p_{33}, 2\varepsilon^p_{12}, 2\varepsilon^p_{13}, 2\varepsilon^p_{23}),$$
$$\vec{A}^{(i)} = (A^{(i)}_{11}, A^{(i)}_{22}, A^{(i)}_{33}, 2A^{(i)}_{12}, 2A^{(i)}_{13}, 2A^{(i)}_{23}), \; i = 1, ..., N.$$

The relations (31), (32) can be rewritten as ($\alpha = 1, \ldots 6$)

$$\mathrm{d}\vec{\varepsilon^p} = \vec{A}^{(i)}\, \mathrm{d}\gamma^{(i)} \qquad (\mathrm{d}\varepsilon^p_\alpha = A^{(i)}_\alpha\, \mathrm{d}\gamma^{(i)}) \qquad \text{single slip,} \tag{37}$$

$$\mathrm{d}\vec{\varepsilon^p} = \sum_{i=1}^{N} \vec{A}^{(i)}\, \mathrm{d}\gamma^{(i)} \qquad (\mathrm{d}\varepsilon^p_\alpha = \sum_{i=1}^{N} A^{(i)}_\alpha\, \mathrm{d}\gamma^{(i)}) \qquad \text{multi slip.} \tag{38}$$

The Schmid's law reads:

$$\vec{A}^{(i)} \cdot \vec{T} < \tau_y^{(i)} \quad (A^{(i)}_\alpha T_\alpha < \tau_y^{(i)}) \;\; \text{inactive system,} \tag{39}$$

$$\vec{A}^{(i)} \cdot \vec{T} = \tau_y^{(i)} \quad (A^{(i)}_\alpha T_\alpha = \tau_y^{(i)}) \;\; \text{active system.} \tag{40}$$

The equation (40) may be interpreted as describing a set of planes (one per each system) in a six dimensional stress space ($\alpha = 1, \ldots, 6$) whose coordinates are the six components of the stress vector $\vec{T}$); $\vec{A}^{(i)}$ is the unit normal determining the orientation of the i-plane of the yield surface in the stress space. The inequality (39) shows that the yield surface which delimits stress states where no slip occurs is the inner envelope of these planes.

The equation (37) shows that the strain increment $\mathrm{d}\vec{\varepsilon}^{p}$ has the direction of the normal $\vec{A}^{(i)}$, hence it is perpendicular to the i-facet of the yield surface in the stress space in the case of single slip. The Schmid's law says nothing about how much plastic strain occurs upon yielding, it only says that it must be positive (or zero) in the direction specified. For multi-slip the situation is different. More slip systems may be activated simultaneously as soon as an edge or a corner on the yield surface is reached. Again Schmid's law does not specify how much slip strain occurs on either system only that it must be positive (or zero) in the direction of the outward normal to each of the facets (38). Thus the plastic strain increment $\mathrm{d}\vec{\varepsilon}^{p}$ may be in any direction contained within the fan of normals at the edge or in the corner of the yield surface. In cubic crystals with 24 slip systems the facets meet in edge states or corner states, where theoretically up to 6 or 8 slip systems can operate simultaneously. As hydrostatic stress has no influence on yield process, the yield surfaces are always extended to infinity in (111000) direction in stress vector space.

Subsequent yield surfaces. The form of the initial yield surface can be deduced from the symmetry of the crystallographic structure and the number of available slip systems. In the initial annealed state, all slip systems have the same critical value of the resolved shear stress. Now there is a question how these initially equal critical values $\tau_y^{(i)}$ change in the process of plastic deformation, i.e. what is the shape of a subsequent yield surface.

The shape of the subsequent yield surface depends on the change of the critical value $\tau_y^{(i)}$ in the active slip system and the changes of the critical values $\tau_y^{(i)}$ in the inactive slip systems. As has been already mentioned, the forces acting on dislocations and dislocation configurations can be roughly divided into the short range and long range forces. Usually, the short range forces of statistical nature and configurations with no preferred orientation (e.g. randomly distributed jogs, three-dimensional dislocation networks) give no preference to any slip system, hardening is isotropic and the critical values $\tau^{(i)_y}$ for all systems change in the same way. On the other hand the long range forces between dislocations and the configurations with preferred directions cause anisotropic work hardening. The presence of both short and long range forces and the various dislocation configurations in the crystal

suggests that the real crystal hardens in a way close to a combination of isotropic and anisotropic (kinematic) hardening.

As changes of the critical values $\tau_y^{(i)}$ and changes of the subsequent yield surface shape are related to changes in slip strains, the rates $\dot{\tau}_y^{(i)}$ can be symbolically expressed in terms of slip rates $\nu^{(j)}$, $i, j = 1, \ldots, N$

$$\dot{\tau}_y^{(i)} = \sum_{j=1}^{N} H^{(ij)} \nu^{(j)} \,, \tag{41}$$

in the incremental form

$$\mathrm{d}\tau_y^{(i)} = \sum_{j=1}^{N} H^{(ij)} \, \mathrm{d}\gamma^{(j)}. \tag{42}$$

The lack of our knowledge is concentrated in the work hardening matrix $H^{(ij)}$ in (41) or (42) and modifications of these hardening constitutive equations. The complexity of the problem is demonstrated by an attempt to construct a hardening constitutive relation by means of statistical treatment of an assemble of discrete dislocations presented in Section 5.

Summary

- Plasticity of single crystals is governed by: *the relation between slip strains and plastic strain* (31), (32), *Schmid's law* (39), (40), and work hardening (41) or (42).
- A convenient concept representing single crystal plasticity is the *yield surface.*
- The *problem of work hardening* is the most difficult, i.e. the specification of the change of the critical values of the resolved shear stresses caused by the slip strains represented in (41) or (42) by the hardening matrix $H^{(ij)}$.

2.4 Plasticity of polycrystals

The schematic picture of a polycrystal has been presented in Fig. 5. There are two main differences between the plasticity of a single crystal and the plasticity of a polycrystal: 1) there is a strong interaction among deformed single crystal grains in the polycrystal, which results in a complex loading conditions in each grain and rotations of grains leading to a texture, 2) in the polycrystal there are grain boundaries, i.e. another type of crystal defects that influence the mechanical properties of polycrystals.

Plastic deformation in a polycrystal starts in the most favorably oriented grains when according to Schmid's law the resolved shear stress in their slip systems reaches the critical value. The deformation of the non-favorably oriented grains remains elastic. The deformation becomes locally inhomogeneous and the internal stresses are developed. In a progress of deformation the internal stresses tend to minimize deformation energy, i.e. to suppress further plastic deformation in already plastically deformed grains and to promote plastic deformation in the non-favorably oriented grains. There is a tendency to smooth the inhomogeneity of deformation caused by the local anisotropy, i.e. to make deformation uniform as much as possible. For instance, the study Hafok and Pippan (2007a) revealed that after severe plastic deformation single crystals with different initial crystallographic orientations and polycrystals develop a similar microstructure and texture. The reason is that a spontaneous structuralization in the grains overshadows the original structure of the material.

One of the main problems of polycrystal plasticity is to evaluate the internal stresses arising due to differences in deformed states of the grains and determine their influence on plastic behavior of the polycrystal. In a simplified sense, one can schematically write

$$\begin{aligned}\text{single crystal plasticity} + \text{internal stress arising due to local anisotropy} \\ + \text{grain boundaries} = \text{polycrystal plasticity}\end{aligned} \tag{43}$$

To illustrate the nature of the internal stresses in a polycrystalline aggregate one of the idealized models proposed by Kröner (1961) and Budiansky and Wu (1962) is recalled.

In an idealized sense a polycrystal can be viewed as an infinite collection of single crystal grains subjected to macroscopically uniform states of stress and strain with the following features:

(a) there is a great number of grains of each crystallographic orientation,
(b) the orientations are randomly distributed, which means that there is overall isotropy, no texture is considered,
(c) there is no correlation among grains, specifically, grains in the vicinity of a given grain are randomly oriented,
(d) the number of surface grains is negligible (note that in a tube of the diameter 20 mm, the thickness of the wall 1 mm and the grain size 0.1 mm, there are 20 % surface grains, due to the free surface the surface grains have a different stress state than a typical grain in the bulk material),
(e) the influence of grain boundaries is neglected.

In Kröner's model of the polycrystal, a grain interacts with its surrounding grains in an average sense. Using the idealization (a) – (e) Kröner assumed that all grains of one crystallographic orientation can be represented as an average spherical single crystal grain of the orientation α. The average surrounding of such grains is modeled by an infinite surrounding matrix in which the spherical single crystal grain is embedded. For this surrounding matrix Kröner assumed isotropic properties.

An external stress applied to the infinite matrix leads to a deformation which is different in the isotropic matrix and the anisotropic average grain. This difference causes the internal stress (the nature of the internal stress in Kröner's idealization of the interaction of grains in the polycrystal is schematically shown in Fig. 16). Hence, the external stress $\mathbf{T}$ and the stress in the grain of the orientation α, $\mathbf{T}^*(\alpha)$ differ from each other. To evaluate

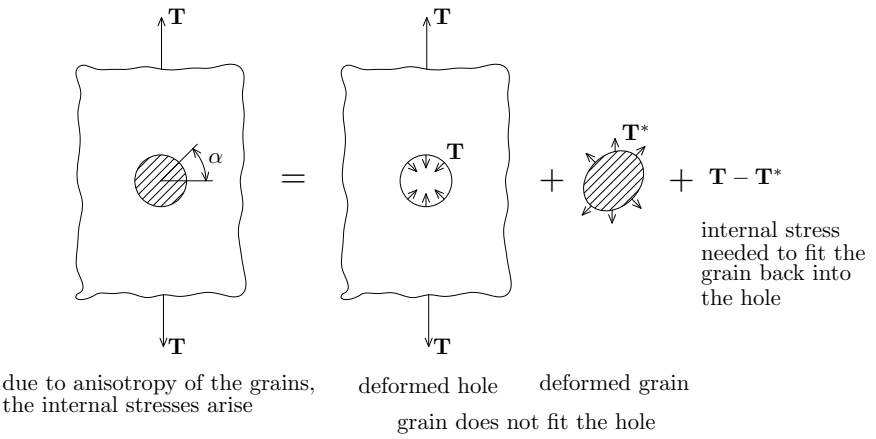

Figure 16. Origin of the internal stress in Kröner's model

$\mathbf{T}^*(\alpha)$, Kröner used the result of Eshelby (1957) that the stress inside the grain of an elliptical shape is uniform and that the internal stress $\mathbf{T}^*(\alpha) - \mathbf{T}$ is directed opposite to the difference between plastic strains of the spherical grain and the isotropic surrounding matrix (Eshelby's result guarantees the equilibrium in this model of the polycrystal)

$$\mathbf{T}^*(\alpha) - \mathbf{T} = -\lambda(\boldsymbol{\varepsilon}^{\mathrm{p}^*}(\alpha) - \boldsymbol{\varepsilon}^{\mathrm{p}}). \tag{44}$$

where $\lambda = 2G(7-5\nu)/[15(1-\nu)] \approx G$ for $\nu = 0.3$; G and ν mean the shear modulus and Poisson's ratio, respectively. From Hooke's law for the grains

and for the polycrystal, and the incremental form of (44), one gets

$$\mathrm{d}\boldsymbol{\varepsilon}^{*}(\alpha) = \mathrm{d}\boldsymbol{\varepsilon} + \left(1 - \frac{\lambda}{2G}\right)\left(\mathrm{d}\boldsymbol{\varepsilon}^{\mathrm{p}^{*}} - \mathrm{d}\boldsymbol{\varepsilon}^{\mathrm{p}}\right). \tag{45}$$

The condition for the active slip in a grain (20),(42), the interaction relation (44) and (32) yield

$$\mathbf{A}^{(i)}(\alpha) \cdot \left[2G\left(\mathrm{d}\boldsymbol{\varepsilon} - \mathrm{d}\boldsymbol{\varepsilon}^{\mathrm{p}}\right) - \lambda\left(\sum_{j=1}^{N}\mathbf{A}^{(j)}(\alpha)\,\mathrm{d}\gamma^{(j)}(\alpha) - \mathrm{d}\boldsymbol{\varepsilon}^{\mathrm{p}}\right)\right] = \sum_{j=1}^{N} H^{(ij)}\,\mathrm{d}\gamma^{(j)}(\alpha). \tag{46}$$

To evaluate the equations (46) of Kröner's model is not straightforward as the slip strains of the grains are interrelated. In the system (46) for unknown slip strain increments $\mathrm{d}\gamma^{(i)}(\alpha)$ we do not know additionally

$$\mathrm{d}\boldsymbol{\varepsilon}^{\mathrm{p}} = \left[\mathrm{d}\boldsymbol{\varepsilon}^{\mathrm{p}^{*}}(\alpha)\right]_{\mathrm{ave}} = \left[\sum_{j=1}^{N}\mathbf{A}^{(j)}(\alpha)\,\mathrm{d}\gamma^{(j)}(\alpha)\right]_{\mathrm{ave}}$$

and therefore the system (46) has to be solved by iterations. From the value of $\mathrm{d}\boldsymbol{\varepsilon}^{\mathrm{p}}_{k}$ of the k-iteration step we must determine $\mathrm{d}\gamma^{\mu}_{k}(\alpha)$ from (46) for each orientation α and the value of $\mathrm{d}\boldsymbol{\varepsilon}^{\mathrm{p}}_{k+1}$ of the next iteration step is given by

$$\mathrm{d}\boldsymbol{\varepsilon}^{\mathrm{p}}_{k+1} = \left[\sum_{j=1}^{N}\mathbf{A}^{(j)}(\alpha)\,\mathrm{d}\gamma^{(j)}_{k}(\alpha)\right]_{\mathrm{ave}}. \tag{47}$$

For $\mathrm{d}\gamma^{(j)}(\alpha)$ established by the iteration we get the stress increment $\mathrm{d}\mathbf{T}$ corresponding to the prescribed strain increment $\mathrm{d}\boldsymbol{\varepsilon}$.

The disadvantage of Kröner's model is that the relation (44) overestimates the interaction among grains, which makes the internal stresses in the polycrystal model too high. The reason is that the parameter λ in (44) being of the order of G represents an elastic interaction between grain and its surrounding in the polycrystal. In reality, this interaction softens when the polycrystal becomes plastic. This disadvantage of Kröner's model was corrected by Hill (1965) (see also Berveiller and Zaoui (1978); Hutchinson (1970)). Kröner's model has been presented as an example of idealized polycrystal shown in Fig. 5. The attempts of this kind encounter two problems.

The first problem is the work hardening of the grains. It is not only the question of which work hardening matrix $H^{(ij)}$ to use in the equations (46), but also the practically important question of a realistic number of available slip systems, as many theoretically possible systems may be effectively blocked by hardening. In general, isotropic hardening will tend to cause a uniform distribution of slips over all activated slip systems, whereas high latent hardening will tend to restrict slips on as few systems as possible. On the other hand, the question of hardening of the grains in the polycrystal need not to be so severe for polycrystal plasticity. Even the first order approximative description of single crystal properties leads to the strong interactions among grains in the polycrystal and the arising internal stresses mask the work hardening behavior of the grains. In this sense polycrystal plasticity is less sensitive to errors in an estimate of the single crystal hardening than single crystal plasticity.

The second problem is that the standard models deal with the ideal polycrystal. In real polycrystals, there are grain boundaries and the grains are deformed inhomogeneously and rotate. This causes at least four additional effects: First, the discrete structure of slip (Fig. 6) leads to a higher work-hardening at the grain boundaries and as a consequence these parts of grains behave as a different material. Second, another inhomogeneity in deformation of the grains arises from an accommodation of a grain to its individual neighbors. This leads to a fragmentation of the grains into domains of more nearly uniform deformation (the grains of the ideal polycrystal are more likely to be these domains). Third, the grain rotations lead to a development of a texture. Fourth, the grain boundaries are very effective obstacles to dislocation motion. The slip distances moved by dislocations are restricted by the grain size, which contribute to hardening. The grain size dependence of hardening, well known experimentally, is not explicitly included in Kröner's or Hill's models. The mentioned effects lead to the conclusion that the properties of a single crystal grain in the polycrystal are different from properties measured on macroscopic single crystal specimens. A grain in the polycrystal has similar plastic anisotropy but the effective hardening properties are modified.

Summary

- One of the most important effects of polycrystal plasticity are the interactions among grains in the polycrystal causing the internal stress demonstrated by Kröner's model.
- Another problem is the work hardening of the grains modified by accommodation of a grain to its individual neighbors and a higher work-hardening at the grain boundaries.

- The distances moved by dislocations are restricted by the grain size. This effect contributes significantly to hardening.

3 Observed dislocation patterns

Plastic properties of ductile solids depend strongly on the evolution of the dislocation arrangement. Deformation substructures are mostly complex and rich in details; a tendency to form a succession of regular dislocation patterns is apparent. The micrographs shown and commented in this section are restricted to metal single crystals and polycrystals of face centered cubic (fcc) or body centered cubic (bcc) crystallographic symmetries (the corresponding slip systems are shown in Fig. 7 and Fig. 8, respectively) where dislocations possess a sufficient maneuverability (solids with wavy slip). Only typical examples of references are cited; they cannot be understood as a survey of the literature in this field. Let me note that reading of the dislocation structure literature requires a knowledge of basic concepts of crystallography and its standard notation. The space reserved for the present notes does not allow to recall these concepts, therefore the following text tries to avoid them.

In micrographs of dislocation structures one can recognize individual dislocations and dislocation clusters, Fig. 1. There are two basic categories of dislocation clusters: (i) dipolar clusters, e.g. Figs. 1, 17–21, and (ii) polar clusters, e.g. Figs. 23, 27–29, 31. They differ in their origin, the dislocation arrangement and their role in the plastic deformation process.

(i) The **dipolar** dislocation clusters contain mostly dislocation dipole loops, dislocation dipoles and multipoles. Their common characteristics is a close to zero total Burgers vector, i.e. in a dipolar cluster the densities of + and - dislocations are nearly the same. The voluminous dipolar loop clusters called variously tangles, braids, veins, dislocation patches (see Figs. 1, 17–19) serve as storage facilities for leftovers of ex-service dislocations; this type is observed namely in initial stages of deformation. In advanced stages the voluminous clusters transform into flat arrangements called walls (Fig. 21) or incidental boundaries, Fig. 23, which serve as annihilation centers of the leftovers and often as sources of fresh glide dislocations.

(ii) The **polar** clusters, mostly in a form of planar arrays, contain excess dislocations of one sign and form a network of boundaries between misoriented regions of the crystal lattice, Figs. 23, 27–29, 31; they are called geometrically necessary dislocation boundaries (GNBs), subgrain boundaries, misoriented cell boundaries. They seem to be of a continuum mechanics origin having the character of an internal buck-

ling, Biot (1965a); Kratochvíl and Orlová (1990); Kratochvíl (1990a); Kratochvíl et al. (2007). According to the continuum mechanics model the misoriented crystal lattice regions with the polar boundaries are formed to avoid energetically costly multi slip (Section 6).

There is another deformation substructure similar to the internal buckling governed by laws of continuum mechanics: **localization of plastic strain**. It is related to the dislocation structure indirectly through the hardening (softening) effect (cf. Section 6.2). In a form of lamellae of localized slip, shear bands or persistent slip bands (see Fig. 21.) it is a prelude of ductile fracture, fatigue or damage of materials. Another form of the deformation substructure of a continuum mechanics origin are **kink bands**. They facilitate the plastic flow as commented at the end of Section 3.3

Using an allegory, a ductile material in a plastic regime tries to build a highway system of misoriented regions and lamellae of localized shear to minimize the energy cost of the plastic traffic. In the system the dipolar clusters serve as service stations which provide fresh carriers of plastic deformation and store or destroy out-of-service carriers (the dipolar clusters provide often a subsidiary service only, as polar boundaries can annihilate and generate glide dislocations as well). The art of metallurgy is to hinder the plastic traffic as much as possible and to allow it only at higher applied stresses and temperatures, but not to stop the traffic entirely. Hindering raises material strength, but stopping it could result in a dangerous brittleness.

Dislocation structures observed in early stages of cyclic or tensile deformation, mostly carried by single slip, are reviewed in Section 3.1. Structures produced by cycling and in tension experiments are commented in Sections 3.2 and 3.3, respectively. A remarkable unifying classification of dislocation structures appearing both in single crystals and in polycrystal at advanced stages of deformation discovered by Winther (2005); Huang and Winther (2007); Winther and Huang (2007) is recalled in Section 3.4. Finally, dislocation structures produced by severe plastic deformation are commented in Section 3.5.

3.1 Early formed dislocation structures

The systematic experimental study of unidirectional (tension and compression) and cyclic plastic deformation of silicon-iron measured at two temperatures 295K and 524K, reported in papers Gemperle et al. (1962); Low and Turkalo (1962); Libovický and Šesták (1983) and summarized in Kratochvíl and Libovický (1986) is recalled here as a typical example:

- At the beginning of plastic deformation of FeSi crystals oriented for

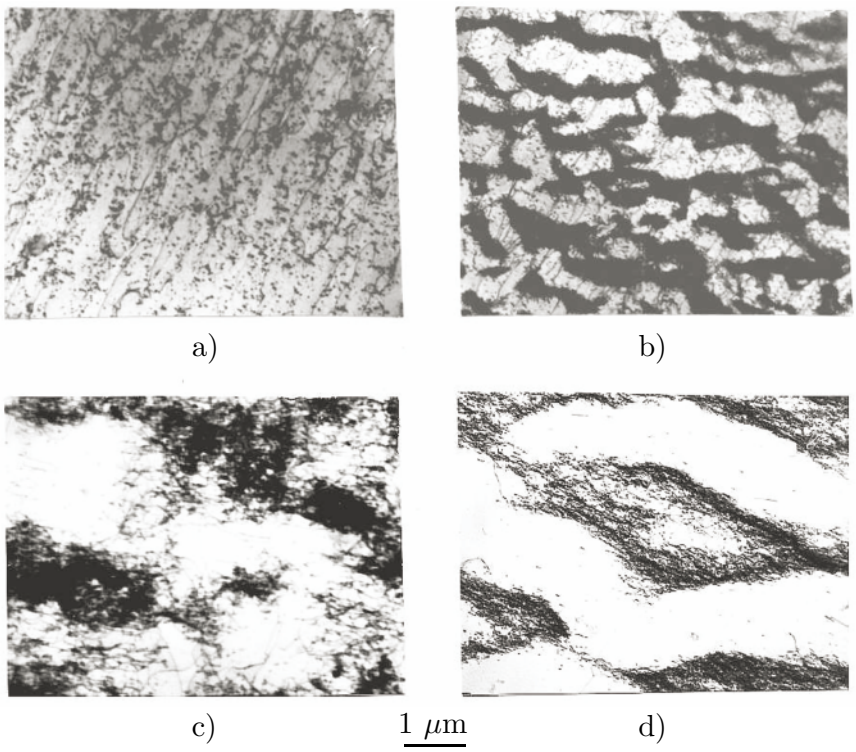

Figure 17. Dislocation pattern in FeSi single crystals oriented for single slip after cyclic (a,b,d) and tension (c) deformation at room temperature 295K. The foils are parallel to the slip plane, the scale is indicated in the figure. (a) Fe-3%Si, cyclic strain amplitude $\triangle\varepsilon = 0.0006$ and cumulative strain $\varepsilon_{cum} = 4$, (b) Fe-3%Si, $\triangle\varepsilon = 0.01$, $\varepsilon_{cum} = 2.3$, (c) Fe-0.9%Si, tension strain $\varepsilon = 0.23$, (d) Fe-0.9%Si, $\triangle\varepsilon = 0.01$, $\varepsilon_{cum} = 9$ (courtesy of S. Libovický).

single slip a homogeneous distribution of dislocations is observed after tension, Gemperle et al. (1962); Low and Turkalo (1962). Nearly the same array of screw dislocations on the background of a homogeneous distribution of dislocation loops of edge character may be also observed in the case of cyclic deformation before clusters of loops are formed (Fig. 17a).

- At higher deformation the dislocations aggregate to clusters in the form of tangles (Fig. 17c) or veins (Fig. 17b and Fig. 17d). Predominantly edge dislocation loops, dislocation dipoles and multipoles are present in the clusters, Libovický and Šesták (1983).
- The density of clusters and their size increase with proceeding deformation. In the relatively free space between the clusters (channels) the low dislocation density remains unchanged.
- In the early stage of deformation there is no principle difference between the dislocation pattern developed during tension (compression) and cycling (compare Fig. 17c and Fig. 17d). Only the surface of the clusters is better defined after cycling than after tension, and there is a higher dislocation density in channels after tension.
- The crystallographic orientation and size of the dislocation structures are the same for both modes of deformation; this is observed at both testing temperatures.
- The size of the structural clusters, however, sharply decreases with increasing silicon content (compare Fig. 17b and Fig. 17d).

In tension (compression) experiments the extension of a specimen is accompanied by a rotation of slip systems, the scheme in Fig. 22. The rotation increases the resolved shear stress which may activate a secondary slip system and as a consequence the close similarity to the single slip cycling dislocation structures is lost. On the other hand, in cycling at sufficiently low strain amplitudes the accompanied rotation remains small and a secondary slip system is not activated and single slip regime is preserved even for high cumulative strain.

3.2 Cyclic deformation

For single slip orientation the dislocation arrangements has been studied in great detail by transmission electron microscopy in cyclically deformed cubic metal single crystals with wavy slip character (Cu, Ni, FeSi) and described in several papers and reviews, e.g. Kuhlmann-Wilsdorf and Laird (1977); Mughrabi (1981); Jin (1989); Holzwarth and Essmann (1993a,b). The complex evolution process proceeds in three main stages, Holzwarth and Essmann (1993a,b, 1994); Mecke et al. (1982):

- *Development of the vein structure.* The homogeneous dislocation distribution is unstable and a pattern of quasi periodically arranged veins is formed. In initial stages of cycling at low plastic strain amplitudes (typically $\Delta\varepsilon < 10^{-3}$) dislocation rich regions form a pattern known as a matrix structure (a very early stage is seen in Fig. 1) consisting of snake-like veins oriented in average along the edge dislocation direction, Fig. 18, e.g. Winter et al. (1981); Ackermann et al. (1984); Jin and Winter (1984); Laird et al. (1986); Šesták et al. (1988); Jin (1989); Basinski and Basinski (1992); Bretschneider and Holste (1998). The veins exhibit irregular cross-sections loosely organized in quasi periodic pattern. An example of the vein cross-section pattern is shown in Fig. 19. With increasing number of cycles the dislocation density in the veins gradually increases. The dislocation density in the channels between the veins nearly does not change.

Figure 18. The snake-like veins in the FeSi crystal oriented for single slip cycled at constant low plastic strain amplitude (courtesy of S. Libovický).

- *The onset of instability.* At a certain stage of cycling the veins become saturated and start to be unstable. As documented by the experiments Holzwarth and Essmann (1993a), the stress amplitude jumps to a maximum value in the first quarter cycle with increased strain

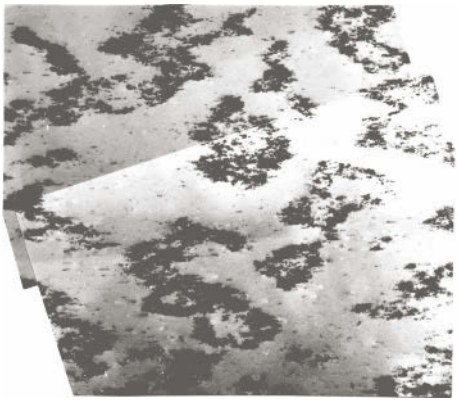

Figure 19. The cross-section through the vein structure shown in Fig. 18 (courtesy of S. Libovický).

amplitude and then declines sharply during further cycling revealing strong dynamic softening. The dislocation vein structure observed after the first two cycles has strongly reduced dislocation density, the veins have lost their compact appearance and become dilapidated. Only small vein fragments remain, it seems they belong preferably to the out-of-center parts of the former veins.

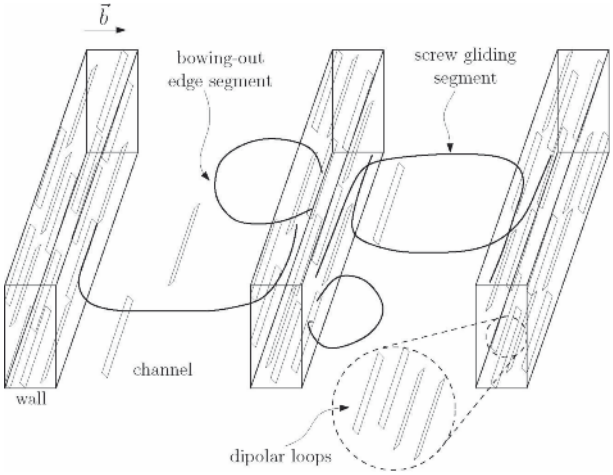

Figure 20. Scheme of PSB

- *Strain localization.* The direct consequence of the onset of the instability of the vein structure is a localization of shear strain into thin lamellae parallel to the primary slip plane called persistent slip bands (PSBs). In the tests on Cu, Holzwarth and Essmann (1993a), the slip bands of localized strain were detected on the surface already during the first two cycles of the increased amplitude, while no evidence of the typical dislocation pattern of PSBs was observed in the bulk. First PSB-like structures comprising up to 10 wall spacings were observed after 20 cycles. The width of these embryonic PSBs, i.e. the extension perpendicular to the primary glide plane, is only about one third of the typical width of a well-developed PSB lamella. After 100 cycles ladder-like wall structures of PSBs become extended. The ladder-like dislocation pattern of the PSBs attains perfection after some 1000 cycles. In the bulk fully developed PSBs consist of the lamellae, typically 1-2 μm high, traversing the specimen in a direction of the active slip plane as shown schematically in Fig. 20. In the case of pure f.c.c. metal crystals deformed by single slip a PSB consists of thin dislocation walls which are arranged in fairly equal spacings perpendicular to the primary slip direction and divide the PSB lamellae into long channels, Fig. 21. The dislocation density in the walls is two orders of magnitude higher than the density in the dislocation-poor channels. The building elements of veins and walls are predominantly edge type dipolar loops. In the channels of PSBs and the matrix structure individual primary screw dislocations dominate.

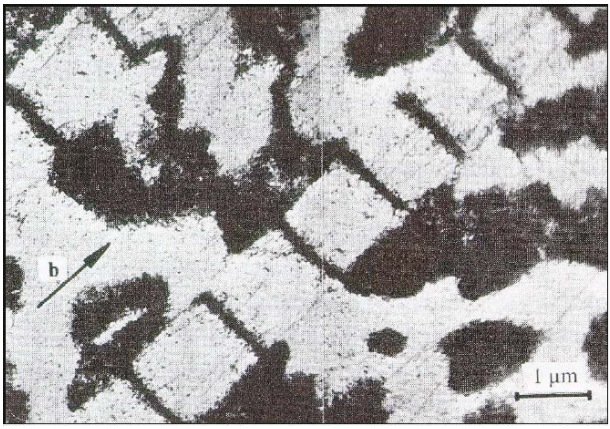

Figure 21. PSB – vein structure (courtesy of H. Mughrabi)

In Kratochvíl (1993); Kratochvíl and Saxlová (1993) it was noted that the formation of the vein structure, its decomposition, the appearance of localized slip and the following evolution of the ladder structure in PSBs can be understood as a sequence of restabilized states resulting in the spontaneous structuralization. One dimensional model adopted for single slip is presented in Section 6.1. It is shown that a vein structure of a characteristic wavelength is developed from an initial perturbation of a homogeneous loop distribution and the dislocation density in veins gradually grows. When the density there reaches a critical level, the annihilation of the dislocations becomes dominant and the vein structure starts to be rebuilt into thinner walls. The simulation of the vein disintegration and the formation of the walls exhibits a marked qualitative resemblance to three evolution stages described above.

3.3 Tensile deformation

As indicated schematically in Fig. 22 the slip systems rotate during a tension test. The rotation causes an increase of the resolved shear stress in a secondary slip system and its activation leads to the increased hardening. Dislocation structures which appear at the onset of the secondary slip activity have been intensively studied e.g. in Basinski (1964); Steeds and Hazzledine (1964); Essmann (1965); Steeds (1966); Essmann and Rapp (1973); Mughrabi (1975); Basinski and Basinski (1979) Moon and Robinson (1967); Pande and Hazzledine (1971a,b); Foxall et al. (1967); Libovický and Šesták (1983), Wasserbach (1986); Karnthaler et al. (1974); Prinz and Argon (1980); Hughes et al. (2001).

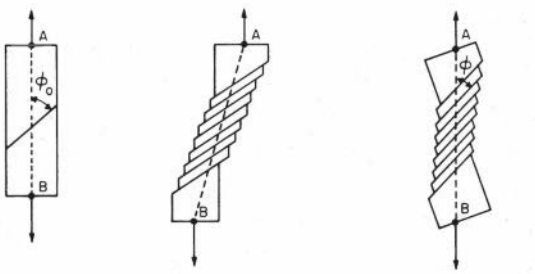

Figure 22. The rotation of the slip systems during a tension test

A misoriented dislocation structure illustrative of the early stages of an arrangement of geometrically necessary dislocations (GNBs), called a slab

structure (layered structure, sheets, carpets), is formed in some cubic metal crystals, originally oriented for single slip, when deformed in tension at sufficiently low temperatures. The GNBs are long planar high density arrays of dislocations, predominantly of one sign, separated by bands filled by some dislocation cells, Hughes et al. (2001). The GNBs frequently tend to form a regular chessboard layered arrangement of pairs made up of dislocations of the opposite sign as seen in Fig. 23 , Libovický and Šesták (1983); the dark regions are misoriented with respect to the rest of the crystal and the GNBs form their boundaries. The layers end, often by becoming narrower and coalescing, or sometimes abruptly. The arrangement is thus probably more accurately described as interleaving slabs, the term used here, rather than layers, Basinski and Basinski (1979). The principal features of the

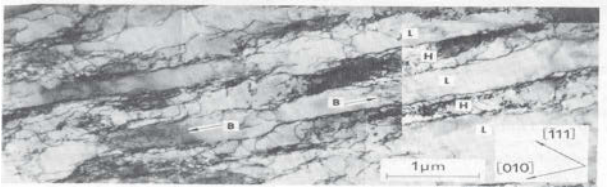

Figure 23. Alternate dislocation slabs in Fe-0.9%Si. There are layers of lower (L) and higher (H) density of secondary dislocations between dislocation sheets. The cross-sections of bundles (incidental boundaries) (B) can be seen in layers of lower density. (courtesy of S.Libovický)

structure of the misoriented slabs can be summarized as follows:

- The **dimension** of the array of misoriented slabs is in the range from several μm^2 to 20 x 20 μm^2, Essmann (1965), Mughrabi (1975); Basinski and Basinski (1979); Pande and Hazzledine (1971a,b). The slabs become narrower with straining Essmann (1965); Mughrabi (1975); Pande and Hazzledine (1971a,b). The minimal critical thickness of slabs observed seems to be comparable with the wavelength of dipolar cell structure, Moon and Robinson (1967). The characteristic ratio of the length of slabs and their thickness is of the order 10, Wasserbach (1986).
- The observations reported reveal that the **misorientation** between slabs increases with strain and reaches about 1° in the most hardened state. It seems to be the same for all materials observed. The axis of rotation is often identified with the edge direction of the primary slip system, e.g. Basinski (1964); Mughrabi (1975); Basinski and Basinski (1979). Sometimes at lower deformation, the twist component about

the normal to the primary slip plane is present, Mughrabi (1975); Basinski and Basinski (1979).

- The slabs which lie parallel to the primary slip plane only approximately are mainly composed of dislocation **grids** (networks). The grids may be looked upon as the consequences of incomplete intersections of primary and secondary forest dislocations just forming attractive junctions. The grids consist of short segments of junction dislocations joined by segments of the dislocations which have reacted to form them. With increasing deformation the networks become denser forming a fine mesh of the order 0.1 μm, Basinski (1964); Essmann and Rapp (1973); Mughrabi (1975); Basinski and Basinski (1979). The short mesh length of the grids does not allow a sufficient dislocation bowing to break down the junctions even at higher stresses.
- It is noteworthy that in the slab structure the plastic deformation is carried by the primary dislocations, Libovický and Šesták (1983). The secondary dislocations seem to assist a construction of the misoriented crystal lattice path for easier primary single slip.

According to Libovický and Šesták (1983) the slab structure is formed in two stages. At the end of the easy glide region the bundles of primary dipolar loops start to dissolve causing avalanches, Fig. 24. The avalanches spread over a distance of several bundles in the direction of primary Burgers vector. At the crossing with the bundles, the density of primary dislocations decreases and bundles are dissolved. During dissolution long parallel primary screw dislocations remain stretched out among the remaining bundles forming warps of one sign only. At the second stage, the secondary

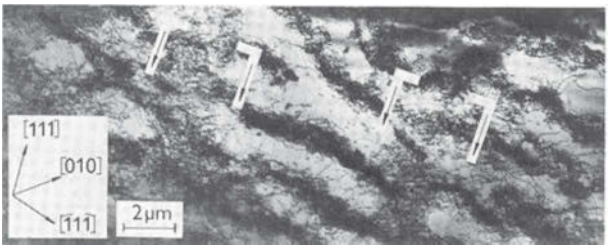

Figure 24. The avalanches in Fe-0.9%Si denoted by the arrows (courtesy of S.Libovický)

dislocations are caught on the warps. That way in the avalanche regions the primary and secondary dislocations interact forming crossed grids, the scheme in Fig. 25. The avalanches and the screw dislocation warps are factors which influence the characteristic size of the slab structure.

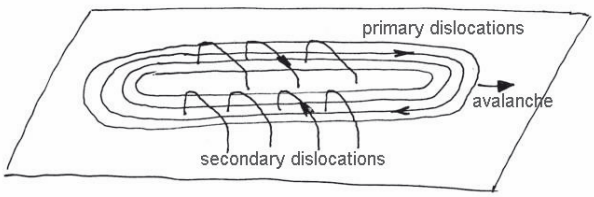

Figure 25. Sketch of an avalanche

As an additional deformation substructure let me recall the detailed microscopic and X-ray observations on copper single crystals subjected to uniaxial tensile or cyclic deformation reviewed by Mughrabi and Obst (2005); Mughrabi (2006a,b). The observed dislocation structures of the type de-

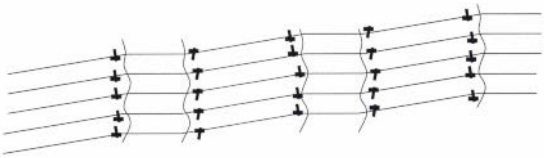

Figure 26. Scheme of shear and kink bands. A micro photograph of such structures can be found e.g. in Mughrabi and Obst (2005)

scribed in this and the previous Section 3.2 may be accompanied by **kink bands** oriented perpendicularly to the primary slip plane as schematically shown in Fig. 26, which is a slight modification of the picture proposed by Mughrabi and Obst (2005). The kink walls representing a GNB have pronounced tilt misorientations around an axis that corresponds roughly to the line direction of the primary edge dislocations. In cycling the misorientation is weaker than in tension. The wavelength of the misorientation related to kink bands is an order of magnitude larger than distances between the tangles and between PSB walls or larger than the widths of PSB and the grid layers. These distances are typically of the order μm, on the other hand, the kink walls have been found to be spaced between about 100 μm and 20 μm., Mughrabi and Obst (2005). In the interpretation proposed in Kratochvíl et al. (2010b) the kink bands arise as a consequence of energy minimization to compensate deviations from an ideal simple shear lattice orientation. The kinks adjust the lattice orientation in an average to the

applied shear and that way facilitate energetically preferred single slip.

3.4 Advanced stage of dislocation structures

At advanced stages of deformation two main categories of dislocation boundaries have been identified, e.g. Kuhlmann-Wilsdorf and Hansen (1991); Hansen (2001); Bay et al. (1992): extended planar geometrically necessary boundaries (GNBs) of the polar nature (type (ii) specified in the introduction of this section) and shorter incidental dislocation boundaries of the dipolar nature (type (i)). Mostly GNBs and IDBs coexist so that GNBs delineate regions in which IDBs are found, Fig. 23. Based on an extended database of microscopic studies of dislocation structures in cubic single crystals and polycrystals deformed at room temperature by tension or cold-rolling to moderate strain $\varepsilon < 1$ Winther (2005); Huang and Winther (2007); Winther and Huang (2007) proposed a universal classification of the dislocation structures. According to the observed GNBs character three types of structures were found. The key parameter controlling the formation of the different structural types is the crystallographic orientation of a crystal or a polycrystalline grain with respect to the loading direction, irrespective of deformation conditions (deformation mode, strain and strain rate) and of material parameters (grain size, impurity). The orientation dependence reflects an underlying correlation to the active slip systems namely to the number of active slip planes. Five slip classes consist of one to four active slip systems, each of them leading to the same type of the dislocation structure. The detail analysis is given in Huang and Winther (2007); Winther and Huang (2007), here a short summary is presented.

The slip classes are correlated with the dislocation structural types according to the following classification scheme:

- **Type 1** structure, Fig. 27, is generated by slip along a single slip plane in a single slip direction, **class 1a**: *single slip*, or generated by slip in a single slip plane along two slip directions laying in this plane, **class 1b**: *coplanar double slip*.
- **Type 2** structure, Fig. 28, is generated by multi slip usually along four slip planes, **class 2**: *multi slip*.
- **Type 3** structure, Fig. 29, is generated by double slip along two slip planes with a common slip direction, **class 3a**: *codirectional double slip*, or by three slip systems: one is coplanar and codirectional, respectively, to the two others, **class 3b**: *dependent coplanar and codirectional slip*.

The type 1 structure (Fig. 27) is formed by GNBs aligned approximately with slip planes. GNBs are straight and parallel and have a well-defined orientation with respect to the loading direction. One set of GNBs is generally

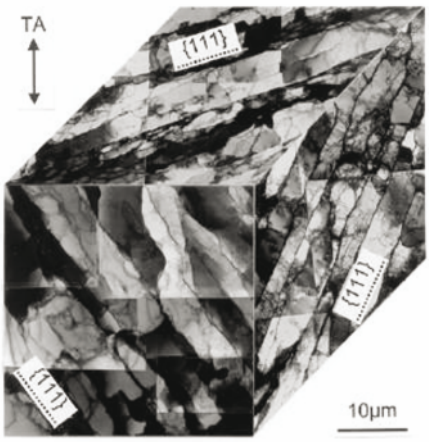

Figure 27. Dislocation structure **Type 1**, TA denotes tensile direction (Huang and Winther (2007)).

related to the slip plane defined by the largest resolved shear stress. The slab structure described in Section 3.3, Fig. 23, is one of typical examples of the type 1, class 1a.

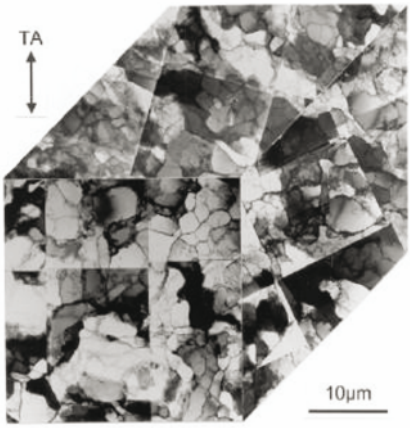

Figure 28. Dislocation structure **Type 2** (Huang and Winther (2007)).

The type 2 structure (Fig. 28) is a cell structure without extended GNBs.

A large scale subdivision occurs characterized by the formation of regions, each of which contains a group of cells of a similar orientation. The cells are approximately equiaxed in shape, however, in some situations the cells are cylindrical and elongated along the loading direction. The regions are associated with relatively large misorientations forming local GNBs between them.

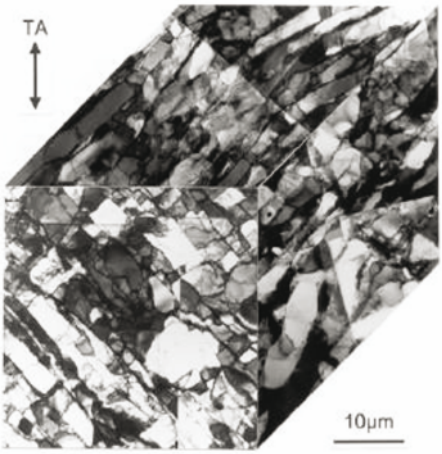

Figure 29. Dislocation structure **Type 3** (Huang and Winther (2007)).

The type 3 structure (Fig. 29) is similar to type 1 with extended straight GNBs, however, GNBs can deviate substantially from the slip planes. More often than in type 1 two sets of GNBs are developed; in some cases one GBN set being aligned closely with a slip plane while one or two another sets being away from slip planes. Also for type 3 the GNBs align with certain crystallographic directions and slip planes – only the relation is more complex than the simple alignment with the slip plane seen for type 1. In the case of the type 3 each GNB consists of a number of long and short segments. The majority of the segments are oriented in similar directions with respect to the loading direction. The types 1 and 3 often coexist.

3.5 Dislocation structures formed by severe plastic deformation

Within the last 20 years it was recognized that severe plastic deformation provides an opportunity for achieving exceptionally fine deformation substructure, often close to the nanometer level, and exceptionally high strength accompanied by relatively good ductility. Several metal forming

processes achieving severe plastic deformation are now available, three procedures receive the most attention at the present: equal-channel angular pressing (ECAP), accumulative roll-bonding (ARB), high-pressure torsion (HPT), e.g. Valiev and Langdon (2006); Zhilyaev and Langdon (2008).

The simplest method to reach severe plastic deformation is HPT. This method allows the application of very high strains without interruption. The strain can be defined approximately as simple shear $\gamma = r\theta/h$, where θ is the twist angle, h is the height of the cylindrical specimen and r is the distance from the torsion axis, Fig. 30. Due to the dependence of γ on r the material is exposed to various amount of strain in different parts of one specimen. For the relatively small size and structural inhomogeneity of the specimens, HTP is less convenient as a practical technological tool. However, for its relative simplicity of loading conditions, the HPT method is suitable for experimental and theoretical studies of the microstructure evolution during severe plastic deformation.

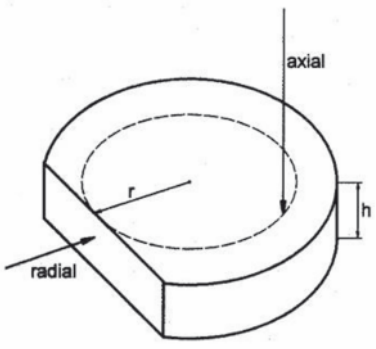

Figure 30. Scheme of HPT specimen

Systematic parameter studies of the microstructure evolution with increasing strain in copper, nickel and Armco iron deformed by conventional and cyclic HPT have been reported in Hebesberger et al. (2005); Wetscher and Pippan (2006); a typical micrograph is shown in Fig. 31. The experiments were directed towards exploring the following basic questions: the way of fragmentation of the original grains into much smaller structural elements, the question of the existence of a saturation in the structural refinement, and how temperature, pressure and cycling affect these phenomena. The results of these measurements provide a base for theoretical analysis and modeling of the fragmentation process.

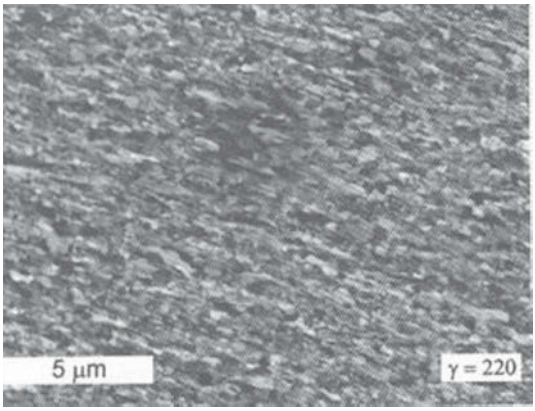

Figure 31. The electron micrograph in the radial direction of Cu specimen deformed by shear strain $\gamma = 220$, the shear direction is horizontal (Hebesberger et al. (2005))

In Hebesberger et al. (2005); Wetscher and Pippan (2006), the microstructure was observed in sections perpendicular to the radial direction and to the axial direction. The observations provide detailed data on the shapes and preferred alignment of the structural elements, their misorientation, size and texture. They can be summarized as follows:

- *Preferred alignment of structural elements.* As reported in Hebesberger et al. (2005), for modest strain (for HPT Cu $\gamma \sim 2$) one sees rather hazily the beginning of the formation of a substructure on the micrometer scale. With increasing strain, the contrasts become more obvious and the scale of substructure decreases. For strain sufficiently high (for HPT Cu $\gamma \sim 55$), there is no further change. A striking feature observed in the radial direction is a preferred alignment of structural elements inclined with respect to the torsion axis, Fig. 31. For moderate strains, their aspect ratio is significantly larger than 1. For larger strains, the observations indicate that the preferred alignment is not a remnant of the original grain structure. It seems that the new smaller equiaxed structural elements are continuously formed during the deformation process. This conclusion is supported by the results of cyclic HPT of nickel and Armco iron where it is observed that the direction of the preferred alignment is changing with the reverse of twist, Wetscher and Pippan (2006).
- *Misorientations.* The misorientation between neighboring structural elements increases with strain and finally reaches a nearly random

distribution. As reported in Hebesberger et al. (2005) for copper observed in axial direction, we can see for $\gamma = 2.1$ slight misorientations, whereas large misorientations on the micrometer scale are observed at $\gamma = 4.7$. Large misorientations appear on a submicrometer scale at $\gamma = 25$. The misorientation does not change appreciably for $\gamma = 75$ and $\gamma = 250$. The misorientation between points which are farther apart than the element size becomes nearly random already at moderate strains. The boundaries between adjacent structural elements are not 'true' grain boundaries; frequently the term 'non-equilibrium boundaries' is used. Even at large misorientation angles, the elements seem to be separated by layers of finite thickness, which might be better described as arrangements of dislocations. With increasing temperature, the steady state boundaries between adjacent elements seem to be better defined. It is only after deformation at elevated temperatures that grain boundaries in the classical sense are observed.

- *Size of structural elements.* As a general feature, the size of the structural elements decreases with increasing strain and reaches a steady-state. The measurements on copper, Hebesberger et al. (2005), showed that in the axial direction, the mean size of the structural elements first decreases with increasing strain and then reaches a saturation value at a strain $\gamma > 10$. In the radial direction, we can see the formation of substructure on a scale well below 1μm, which does not seem to change beyond $\gamma = 27$. With increasing temperature, the steady-state size markedly increases and the steady-state structure is achieved already at a strain $\gamma < 6.8$. An increase in axial pressure leads to a somewhat finer structural size. In cyclic HPT, the strain amplitude determines the resulting structure size. For nickel and Armco iron, the experiments Wetscher and Pippan (2006) demonstrated that after a total equivalent strain larger than approximately 20, no further refinement of the structure occurs. The higher the strain amplitude, the smaller the structural size in the saturation regime. The smallest structure size was measured for monotonously deformed samples.
- *Saturation.* No further work hardening is observed above a certain strain, in many cases there even work softening occurs. In cycling, the saturation is reached earlier in terms of number of cycles for large plastic strain amplitudes; the accumulated strain needed to reach saturation decreases with decreasing amplitude. The highest total strain to reach the saturation is needed for monotonous deformation. In contrast to the saturation in size and the mechanical strength, it seems that the increase in misorientation between neighboring elements does not saturate as fast as the strength. Hence, one can assume that the

mechanical strength is mainly determined by the size of the structural elements and not by the misorientation between these elements. A characteristic feature observed in the saturated state is a pronounced shear texture. The study of Hafok and Pippan (2007a) revealed that HPT nickel single crystals with different crystallographic orientations and nickel polycrystals develop in saturation a similar microstructure and microtexture. A major difference between these two types of materials was that the stable microtexture was achieved earlier in the polycrystalline aggregates.

- *Deformation mechanism.* The guideline for an interpretation has been provided by the observations reported by Hafok and Pippan (2007b). Nickel samples pre-deformed by HPT in a saturated state were sheared by an additional HPT. The observed deformation mechanism was shearing with micro shear bands, which corresponds to the imposed torsion on the sample with no change of the substructure pattern. The width of the bands was about twice that of the average size of the substructure elements. From their observations Hafok and Pippan (2007b) concluded that the deformation was achieved by an intergranular glide. Grain boundary sliding was excluded as the main deformation mechanism in the explored HPT process.

An interpretation of the fragmentation process within the framework of crystal plasticity has been suggested in Kratochvíl et al. (2009, 2010a). Here the considerations are restricted to spatially homogeneous plane-strain, rigid-plastic deformation carried by double slip. A rate-independent material response is considered. Despite of these simplifications, the idealized framework provides a possible explanation of the observations summarized above. The basic feature of the model is a rotation of the slip systems carrying the imposed HPT strain. The slip activity is governed by the shear stress imposed by torsion and by axial compression. It has been suggested that the results of the paper Kratochvíl et al. (2007) summarized in Section 6.2 can be employed in a qualitative analysis of the fragmentation process. The formation of a structural element pattern (misoriented cell pattern) has been explained as a result of a trend to reduce energetically costly multi slip. In the context of HPT, this means that at each orientation of the slip systems, there is a tendency to build the corresponding pattern. The rotation of the slip systems causes a continuous reconstruction of the pattern. The necessary destruction of the previous pattern can be hindered by the high pressure. The effect leads to an increase in the dislocation density and to an enhanced hardening. In the deformation process, the orientation of the slip systems approaches asymptotically a steady state related to the saturation effect.

4 Discrete Dislocation Dynamics

Discrete dislocation dynamics (DDD) is a very useful and effective tool for the modeling of plastic behavior at μm scale. The aim of this section is to illustrate the underlying philosophy of DDD presenting one of the methods of modeling of interacting dislocations. The methods of DDD can be categorized into two groups according to the dislocation line discretization scheme and representation of a general curved dislocation segment. The first group of methods is based on an edge-screw or edge-mixed-screw discretization of the dislocation lines, e.g. Devincre and Kubin (1997); Fivel and Canova (1999); Rhee et al. (1998); Tang et al. (1998). The basic idea of this approach is that the connected line segments of the edge or screw orientation (eventually, of the edge or mixed or screw orientation) jump on a discrete network. The second category of methods simulates dislocations as flexible lines discretized either by curved segments, Ghoniem and Sun (1999); Ghoniem et al. (2002), or by line segments, Minárik et al. (2004); Minárik and Kratochvíl (2007); Křišťan and Kratochvíl (2007a).

In papers Minárik et al. (2004); Minárik and Kratochvíl (2007); Křišťan and Kratochvíl (2007a,b); Beneš et al. (2009); Křišťan et al. (2009); Minárik et al. (2010); Křišťan and Kratochvíl (2010) the method of flexible lines discretized by straight line segments has been applied in the simulation of the following problems: a dislocation moving in a field of dislocation loops, an estimate of a so-called saturation stress in a channel of a persistent band (PSB), and a generation of glide dislocations by the process of bowing-out from PSB walls. In this section the DDD simulations of interacting dislocations modeled as flexible lines are described in detail. A bowing out of dislocations from a dipolar walls of a channel of a persistent slip band (PSB) is presented as an example of an application of the simulation method, Křišťan et al. (2009). The evolving positions and shapes of the dislocations are governed by the equation of motion where each dislocation segment is subjected to a line tension, to interactions with segments of other dislocations and to the stress field imposed by loading conditions. Two different loading regimes approximating boundary conditions are considered: "stress control" and "total strain control".

4.1 Mathematical model

Governing equation. Inspired by papers Gage and Hamilton (1986); Sedláček (1997); Mikula and Ševčovič (2004), a gliding dislocation curve $\Gamma(t)$ at time t is described by a C^1–smooth (not necessarily closed) one dimensional non-self intersecting curve in a plane $\mathbb{R}^2$. It can be parameterized by a smooth vector function $\vec{X}(u,t) : S \times I \to \mathbb{R}^2$, where u is a parameter

from a fixed interval $S = [U_1, U_2]$, $U_2 > U_1$, and $I = [0, T)$ is a time interval; i.e. the dislocation curve is given as

$$\Gamma(t) = \mathrm{Image}(\vec{X}(\cdot, t)) := \{\vec{X}(u, t); u \in S\}$$

and for which the local length $g = |\partial_u \vec{X}| > 0$ ($|\cdot|$ denotes the Euclidean norm in $\mathbb{R}^3$ and $\partial_\xi F = \partial F/\partial\xi$). A motion of a gliding dislocation then corresponds to the family of planar curves $\{\Gamma(t)\}_{t\geq 0}$ evolving from initial configuration $\Gamma^0 = \Gamma(0)$ at $t = 0$. The mapping is shown schematically in Fig. 32. Since at low temperatures the dislocations move along the crystallographic planes, we assume that the set $\{\vec{X}(u, t); (u, t) \in S \times I\}$ is a subset of the corresponding glide plane in the Cartesian coordinate system identified (for simplicity) with the xz–plane.

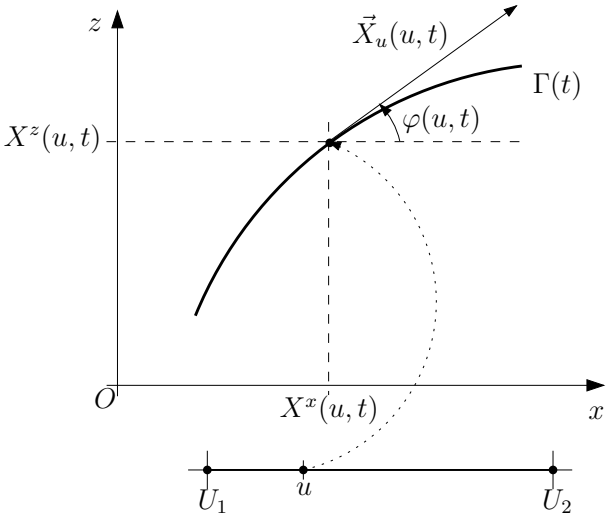

Figure 32. The mapping $\Gamma(t) = \mathrm{Image}(\vec{X}(\cdot, t))$ of the interval $[U_1, U_2]$ into the glide plane xOz.

The tangent and normal vectors to the dislocation line in the glide plane are denoted $\partial_u \vec{X}$ and $\partial_u \vec{X}^\perp$, respectively; the outward normal vector $\partial_u \vec{X}^\perp$ is defined in such a way that the determinant of the 2×2 matrix with column vectors $\partial_u \vec{X}$ and $\partial_u \vec{X}^\perp$, i.e. $\det(\partial_u \vec{X}, \partial_u \vec{X}^\perp) = 1$. A unit arc–length parameterization of the curve Γ is denoted by s and it satisfies $|\partial_s \vec{X}(s, t)| = 1$ for any s and t. Furthermore, the arc–length parameterization is related to the original parameterization u via the equality $\mathrm{d}s = g\,\mathrm{d}u$. The interval of values of the arc–length parameter depends on the curve Γ; more precisely,

$s \in [0, L_\Gamma(t)]$, where $L_\Gamma(t)$ is the total length of the curve Γ at time t. Then $\vec{l} = \partial_s \vec{X}$ and $\vec{m} = \partial_s \vec{X}^\perp$ represent unit tangent and normal vectors to the curve in the glide plane, respectively: $\vec{l} = \partial_s \vec{X} = \partial_u \vec{X}\, \mathrm{d}u/\, \mathrm{d}s = \partial_u \vec{X}/|\partial_u \vec{X}|$ and $\vec{m} = \partial_s \vec{X}^\perp = \partial_u \vec{X}^\perp/|\partial_u \vec{X}|$.

The glide of a planar dislocation segment is governed by a linear viscous law assumed in the form of the standard mean curvature flow equation, Gage and Hamilton (1986); Dziuk (1994),

$$Bv = J\kappa + f\,, \tag{48}$$

where the material constant B is the drag coefficient, $v = v(s,t)$ is the magnitude of the normal velocity $\vec{v}$ of the evolving segment of the curve, $J = J(s,t)$ is the line tension, and the local curvature $\kappa = \kappa(s,t)$ of the curve in the direction $\vec{m}$ at s is defined by Frenét's equation: $\partial_s^2 \vec{X} = \kappa \partial_s \vec{X}^\perp$. The magnitude of the driving force $f = f(s,t)$ in the equation (48) can be written as $f = b\tau_{\mathrm{eff}}$ (a force per unit length of the curve); b is the magnitude of the Burgers vector $\vec{b}$ and τ_{eff} represents the local resolved shear stress acting on the dislocation segment which is specified in the next subsection.

The scalar equation (48), by using $v = \partial_t \vec{X} \cdot \partial_s \vec{X}^\perp$, can be written in the form of an intrinsic diffusion equation,

$$B\partial_t \vec{X} = J\partial_s^2 \vec{X} + f\partial_s \vec{X}^\perp\,. \tag{49}$$

The equation (49) which can be seen in the form $\partial_t \vec{X} = \beta \vec{m}$ is a special case of general geometric equation $\partial_t \vec{X} = \beta \vec{m} + \alpha \vec{l}$; here β and α represent suitable smooth functions. Since for closed curves or curves with pinned end points the presence of a tangential velocity α in the position vector equation has no impact on the shape of the evolving curve, a natural setting $\alpha \equiv 0$ has been chosen for analytical as well as numerical treatment. However, as it was shown in Mikula and Ševčovič (2001), for general curvature driven motions a suitable tangential velocity may significantly stabilize numerical computations. It prevents the Lagrangian algorithm from its main drawbacks, the merging of numerical grid points and it also allows for large time steps without loosing stability.

Commenting the line tension force approximation $J\kappa$ employed in Eqs. (48) and (49) let us note that the curved dislocation feels its own elastic field as a straightening self-force. The self-interaction would require computation of the stress caused by one piece of dislocation at the location of another, so that self-stress effects with logarithmic singularities would occur, see Brown (1964). However, as was shown by Schmid and Kirschner (1988), in the limit of mild curvature the self-stress is proportional to the line tension, which is the approximation introduced by De Witt and Koehler (1959) (a drawback

is that the line tension approximation could negatively influence the shape of dislocation close to the wall where the curvature is the highest). In Foreman (1955) it has been shown that in an elastically anisotropic crystal, the elastic energy E per unit length of a long straight dislocation is given by $E = (Kb^2/4\pi)\ln(R/r_0)$; the distance R has the dimension of the crystal, $r_0 \approx b$ is the inner cut-off radius of the dislocation core and K is a function of the elastic constants of the crystal and the orientation with respect to the crystal axes of both the Burgers vector and the dislocation line. For an elastically isotropic crystal, K can be expressed as a function of the angle φ between the Burgers vector and the dislocation line: $K = G\left(1 - \nu\cos^2\varphi\right)/(1-\nu)$, where G is the shear modulus and ν the Poisson's ratio. To distinguish the edge, screw or mixed character of the dislocation segment the orientation dependent line tension $J = J(\varphi)$, Foreman (1955); De Witt and Koehler (1959), which can be expressed as

$$J(\varphi) = E + \frac{\partial^2 E}{\partial\varphi^2} = \frac{Gb^2}{4\pi}\left(\frac{1-2\nu+3\nu\cos^2\varphi}{1-\nu}\right)\log\frac{R}{r_0}\,. \tag{50}$$

Especially, $J_{\text{screw}} = E_{\text{edge}}(1+\nu)$ and $J_{\text{edge}} = E_{\text{edge}}(1-2\nu)$ are the line tensions for screw and edge dislocation, respectively; $E_{\text{edge}} = E(\varphi = \pi/2)$.

Resolved shear stress. Four contributions to the resolved shear stress are considered:

$$\tau_{\text{eff}} = \tau_{\text{disl}} + \tau_{\text{wall}} + \tau_{\text{app}} + \tau_0\,.$$

τ_{disl} is the resolved shear stress exerted by other gliding dislocations, τ_{wall} represents the wall interaction (treated as the elastic field of rigid edge dipoles) and τ_{app} approximates the stress in the channel determined by the applied boundary conditions (the applied stress). In the present considerations the influence of a friction stress and debris left by shuttling dislocations is incorporated in the term τ_0.

Shear stress exerted by a dislocation. The resolved shear stress in the channel at $\vec{r}$ caused by the elastic field of the curved dislocation Γ can be expressed as (omitting the dependence on time t)

$$\tau_{\text{disl}}(\vec{r}) = \int_\Gamma \tau_{\text{d}}(\vec{r}, s)\,\mathrm{d}s\,. \tag{51}$$

Here, $\tau_{\text{d}}(\vec{r}, s)$ is the resolved shear stress at a point $\vec{r}$ exerted by a dislocation segment $\mathrm{d}s$ of Γ; τ_{d} will be specified in the Section 4.2. The integral is taken along the curve Γ at time t. In the model, a general shape of a dislocation line with no symmetry constraints is considered.

Wall interaction. The long range stress, caused by the different deformability of the walls and the channel, is incorporated into the stress $\tau_{\rm app}$ determined by the boundary conditions. However, there are also short range interactions among the dipolar loops clustered in the walls and parts of dislocations close to the walls. Following Brown (2006), these short range interactions are incorporated in the model as elastic fields of fixed rigid edge dipoles located at the surface of the walls (more realistic walls consisting of dipolar loops has been studied in Křišťan and Kratochvíl (2010)). Segments of gliding dislocations deposited at the walls are trapped in the elastic potential valleys produced by the dipoles parallel to the walls. A sufficiently strong stress can bow-out a dislocation segment from the wall into the channel. Each dipole is formed by the two edge dislocations in a stable equilibrium configuration. For simplicity, the centers of dipoles are placed in the slip planes of dislocations (the effects of the dipolar structure of the walls have been explored in more detail in El-Awady et al. (2007)). The height of individual dipoles, $h_{\rm dip}$, controls the distance of the elastic valleys from the walls as well as their strength. The shear stress field of the dipole consists of the stress field of edge dislocations. The shear stress produced at a point $\vec{r} = (x, y)$ by an infinitely long straight edge dislocation located at the origin along the z–axis is

$$\tau_{\rm edge}(x, y) = \pm \frac{Gb}{2\pi(1-\nu)} \frac{x(x^2 - y^2)}{(x^2 + y^2)^2} \,. \tag{52}$$

The sign "+" or "−" depends on the orientation of the dislocation line representing the corresponding edge dislocation.

Applied stress. Instead of solving the full boundary value problem of the stress distribution in the channel, two simplified limit cases are considered: (i) the "stress controlled regime" in which the applied stress $\tau_{\rm app}$ in the channel is kept uniform, (ii) the "strain controlled regime" in which the total strain $\varepsilon_{\rm tot}$ remains uniform. The reality lies between these two limits.

In the stress-control the elastic strain $\gamma^{\rm e}$ coupled to the stress by Hooke's law $\gamma^{\rm e} = \tau_{\rm app}/G$ remains uniform. Therefore, it cannot adjust to the generally nonuniform plastic strain produced by the dislocation glide (the compatibility of total strain in the channel is violated). Such artificial rigidity causes the stress level to be higher than in reality.

In the strain-control, the total shear strain as the sum of an elastic part $\gamma^{\rm e}$ and a plastic part $\gamma^{\rm p}$, $\varepsilon_{\rm tot} = \tau_{\rm app}/G + \gamma^{\rm p}$, is assumed to be uniform in the channel. It is not required that the stress in the channel satisfies the stress equilibrium; only the equilibrium of the forces exerted on the dislocation lines are guaranteed by the equation of motion (48). Accordingly, the resulting applied stress is smaller than in reality.

To estimate the plastic strain represented by slip γ^{p} the considered dislocations are taken as representatives of glide dislocations in the channel. The rate of slip (at a fixed position in the space) is given by Orowan equation $\partial\gamma^{\mathrm{p}}/\partial t = b\varrho v$; b is the magnitude of the Burgers vector, ϱ density of glide dislocations and v their average velocity. In agreement with the observation that the density ϱ of glide dislocations in PSB channels practically does not change during the deformation process, Mughrabi (1983), ϱ is taken as a material constant. Under these simplifying assumptions the infinitesimal plastic strain $\mathrm{d}\gamma^{\mathrm{p}}$ carried by a dislocation segment of length $\mathrm{d}l$ at a point s of gliding dislocation Γ at time t is

$$\mathrm{d}\gamma^{\mathrm{p}}(s,t) = b\varrho v(s,t)\,\mathrm{d}t\,\mathrm{d}l = b\varrho\ \mathrm{d}S(s,t)\,,$$

and consequently plastic strain carried by dislocation segment $\mathrm{d}l$ during the time interval $[t_0,t]$,

$$\gamma^{\mathrm{p}}(s,t) = b\varrho\int_{t_0}^{t}\mathrm{d}S(s,t) = b\varrho S(s,t_0,t)\,.$$

The integral is taken along the time interval $[t_0,t]$. Initially $\gamma^{\mathrm{p}}(s,t_0)=0$. $S(s,t_0,t)$ denotes the area slipped by the dislocation segment $\mathrm{d}l$ at the point s in the time interval $[t_0,t]$. The applied stress τ_{app} exerted on a dislocation segment of length $\mathrm{d}l$ at the point s and time t can be then explicitly expressed as

$$\tau_{\mathrm{app}}(s,t)\,\mathrm{d}l = G[\varepsilon_{\mathrm{tot}}(t)\,\mathrm{d}l - b\varrho S(s,t_0,t)]\,. \tag{53}$$

Recall that the length $\mathrm{d}l$ of the dislocation segment at s can change during the evolution of a dislocation curve.

4.2 Numerical method

In numerical simulations we employed a semi-implicit scheme and the discretization based on the flowing finite volume approach in space, Mikula and Ševčovič (2001), and the method of lines in time, Dziuk (1994). By discretization in space the governing equations are reduced to a system of ordinary differential equations which are solved by the standard Runge–Kutta method of the fourth order with fixed time step.

Discretization. In the numerical scheme a smooth dislocation curve $\Gamma(t)$ is represented by a M-sided moving polygon $\mathcal{P}(t) = \bigcup_{i=1}^{M}[\vec{X}_{i-1},\vec{X}_i]$, i.e. the curve is approximated by M linear segments $[\vec{X}_{i-1},\vec{X}_i]$, $i=1,\ldots,M$. $M+1$ is a constant number of points on the curve. In the arc–length

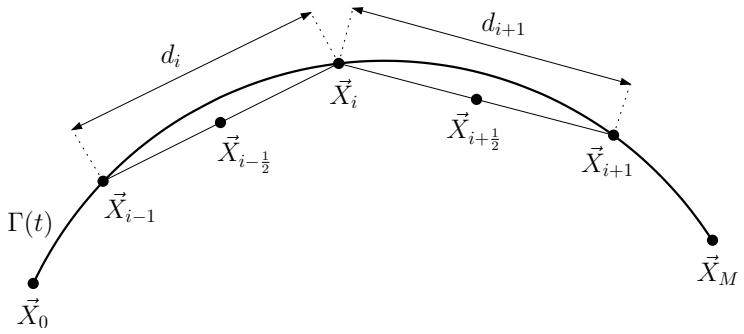

Figure 33. Discretization of the curve by linear segments.

parameterization s the points are denoted by the subindex i, $i = 0, \ldots, M$:

$$\vec{X}_i = \vec{X}_i(t) = \vec{X}(s_i, t)\,; \quad 0 = s_0 < s_1 < \ldots < s_M = L_\Gamma(t)\,,$$

where $L_\Gamma(t)$ is the total length of the curve Γ at time t; see Fig. 33. The linear segments $[\vec{X}_{i-1}, \vec{X}_i]$, $i = 1, \ldots, M$, are called the flowing finite volumes. The corresponding dual volumes $\mathcal{V}_i$ are defined as $\mathcal{V}_i = [\vec{X}_{i-1/2}, \vec{X}_{i+1/2}] \approx [\vec{X}_{i-1/2}, \vec{X}_i] \cup [\vec{X}_i, \vec{X}_{i+1/2}]$ for $i = 1, \ldots, M-1$. For an arbitrary $j = 0, \ldots, M-1$, $\vec{X}_{j+1/2} = \frac{1}{2}(\vec{X}_j + \vec{X}_{j+1})$ denotes a midpoint of the line segment $\vec{X}_j \vec{X}_{j+1}$. Note that $\vec{X}_{(i-1)+1/2} \equiv \vec{X}_{i-1/2}$.

In the considerations we distinguish between different time levels. For that let us introduce the following notation: $\mathcal{P}^j$ is a polygonal approximation of $\Gamma(t)$ at time $t = t_j$, where the time node $t_j = \sum_{k=1}^{j-1} \Delta t_k$ is the j-th time ($t_0 = 0$) with the time step Δt_j. At $t_0 = 0$ the initial $\mathcal{P}^0$ is an approximation of Γ^0. The polygon $\mathcal{P}^j = \bigcup_{i=1}^{M} [\vec{X}_{i-1}^j, \vec{X}_i^j]$ is made by the discrete points $\vec{X}_i^j$; here $i = 1, \ldots, M$, denotes a space discretization and $j = 0, 1, \ldots$, denotes a discrete time stepping.

System of equations. The equation of motion for the point $\vec{X}_i$ is derived from the equation (49). As the interior and the end points of the polygon behave differently, they are treated separately.

Interior points of the polygon. Integrating the evolution equation (49) at time t over a dual volume $\mathcal{V}_i$, $i = 1, \ldots, M-1$, we get

$$B \int_{\mathcal{V}_i} \partial_t \vec{X} \mathrm{d}s = \int_{\mathcal{V}_i} J_i\, \partial_s^2 \vec{X} \mathrm{d}s + b \int_{\mathcal{V}_i} \tau_i\, \partial_s \vec{X}^\perp \mathrm{d}s\,,$$

where the discrete quantities J_i and τ_i are constant over the dual volume $\mathcal{V}_i$ at the corresponding point $\vec{X}_i$; J_i is an approximation of a line tension J, τ_i is an approximation of τ_{eff}. Using the Newton-Leibniz formula we have at any time t:

$$B\,\frac{d_i+d_{i+1}}{2}\,\frac{d\vec{X}_i}{dt} = J_i\,[\partial_s\vec{X}]_{i-\frac{1}{2}}^{i+\frac{1}{2}} + b\tau_i\,[\vec{X}^{\perp}]_{i-\frac{1}{2}}^{i+\frac{1}{2}}\,,$$

where $d_i = |\vec{X}_i - \vec{X}_{i-1}|$ is the distance of the two neighboring points $\vec{X}_i$ and $\vec{X}_{i-1}$ of the polygon. By taking central differences (of the first order) in space we obtain $(\partial_s\vec{X})_{i+1/2} = (\vec{X}_{i+1} - \vec{X}_i)/d_{i+1}$ for $i = 0, \ldots, M-1$. In result, the equation of motion for the corresponding point $\vec{X}_i$ in the dual volume $\mathcal{V}_i$ can be written in the form, $i = 1, \ldots, M-1$,

$$B\frac{\mathrm{d}\vec{X}_i}{\mathrm{d}t} = \frac{2J_i}{d_i+d_{i+1}}\left(\frac{\vec{X}_{i+1}-\vec{X}_i}{d_{i+1}} - \frac{\vec{X}_i-\vec{X}_{i-1}}{d_i}\right) + \frac{2b\tau_i}{d_i+d_{i+1}}\,\frac{\vec{X}_{i+1}^{\perp}-\vec{X}_{i-1}^{\perp}}{2}\,. \tag{54}$$

In the equation (54) we employ the orientation dependent line tension (50) in the form

$$J_i = E_{\text{edge}}\left(1 - 2\nu + 3\nu\cos^2\varphi_i\right),$$

with

$$\cos\varphi_i = (\partial_s\vec{X})_i \cdot \frac{\vec{b}}{b} \approx \frac{\vec{X}_{i+1}-\vec{X}_{i-1}}{d_i+d_{i+1}} \cdot \frac{\vec{b}}{b}\,;$$

the symbol "$\cdot$" stands for the scalar product of vectors.

End points of the polygon. To derive the equations of motion for the end points of the polygon: $\vec{X}_0$ and $\vec{X}_M$, the degenerate dual volumes $\mathcal{V}_0^+ = [\vec{X}_0, \vec{X}_{1/2}]$ for $\vec{X}_0$ and $\mathcal{V}_M^- = [\vec{X}_{M-1/2}, \vec{X}_M]$ for $\vec{X}_M$ are constructed. Integrating the evolution equation (49) in dual volumes $\mathcal{V}_0^+$ and $\mathcal{V}_M^-$, we have

$$B\,\frac{d_0}{2}\,\frac{\mathrm{d}\vec{X}_0}{\mathrm{d}t} = J_0\,[\partial_s\vec{X}]_0^{\frac{1}{2}} + b\tau_0\,[\vec{X}^{\perp}]_0^{\frac{1}{2}}\,,$$

$$B\,\frac{d_M}{2}\,\frac{\mathrm{d}\vec{X}_M}{\mathrm{d}t} = J_M\,[\partial_s\vec{X}]_{M-1/2}^{M} + b\tau_M\,[\vec{X}^{\perp}]_{M-1/2}^{M}\,.$$

Using central differences in space, as above, one gets $(\partial_s\vec{X})_0 = (\vec{X}_1 - \vec{X}_0)/d_1$ and $(\partial_s\vec{X})_M = (\vec{X}_M - \vec{X}_{M-1})/d_M$. Note, that $(\partial_s\vec{X})_0 = (\partial_s\vec{X})_{1/2}$ and $(\partial_s\vec{X})_M = (\partial_s\vec{X})_{M-1/2}$. Therefore, the first terms on the right-hand sides of the last equations vanish. This is in agreement with the fact that for the straight segments $[\vec{X}_0, \vec{X}_{1/2}]$ and $[\vec{X}_{M-1/2}, \vec{X}_M]$ the curvature κ is zero.

Finally, exploiting the definition of the points $\vec{X}_{j+1/2}$ for $j = 0$ and $j = M - 1$, the corresponding equations of motion can be written in the form

$$B\frac{\mathrm{d}\vec{X}_0}{\mathrm{d}t} = \frac{2F_0}{d_1 + d_1}(\vec{X}_1^{\perp} - \vec{X}_0^{\perp})\,; \quad B\frac{\mathrm{d}\vec{X}_M}{\mathrm{d}t} = \frac{2F_M}{d_M + d_M}(\vec{X}_M^{\perp} - \vec{X}_{M-1}^{\perp})\,. \quad (55)$$

The Eqs. (54) and (55) have to be supplemented with initial and boundary conditions. An example of such conditions is given in Section 4.3.

Resolved shear stress. In the numerical implementation of the model the components of the resolved shear stress, i.e. the resolved shear stress exerted by other gliding dislocations τ_{disl}, the wall interaction τ_{wall} and the applied stress τ_{app}, have to be adjusted to the dislocation representation as a moving polygon.

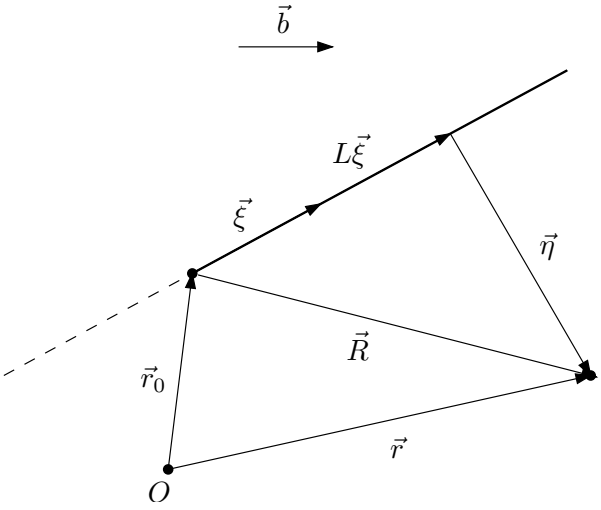

Figure 34. Vectors appearing in the definition of the stress tensor generated by semi–infinite straight dislocation. The unit vector $\vec{\xi}$ is parallel to the dislocation line, $\vec{R}$ is the vectorial distance between a point $\vec{r_0}$ of the dislocation line and an arbitrary point $\vec{r}$ at which the stress produced by the semi–infinite straight dislocation is calculated. $\vec{\eta}$ is the component of $\vec{R}$ perpendicular to $\vec{\xi}$.

Shear stress exerted by a dislocation. In τ_{disl} given by the equation (51) we employ for evaluation of $\tau_{\mathrm{d}}(\vec{r}, s)$ de Wit's formula for the stress field of

finite straight dislocation segment AB, de Wit (1967);

$$\tau_{\mathrm{d}}(\vec{r},s) \approx T_{xy}^{(AB)} = T_{xy}(\vec{r}-\vec{X}_B) - T_{xy}(\vec{r}-\vec{X}_A)\,, \tag{56}$$

where $\vec{X}_A$ and $\vec{X}_B$ are the end points of a straight segment of the polygon at s. T_{ij} are the stress components generated at $\vec{r}$ by the semi-infinite straight dislocation of the Burgers vector $\vec{b}$, with the end point at $\vec{r}_0$, and of a line direction $\vec{\xi}$. Using Devincre's formula (the equation (25) in Devincre (1995)) within isotropic elasticity T_{ij} can be expressed as

$$T_{ij}(\vec{r}-\vec{r}_0) = \tag{57}$$
$$\frac{G}{4\pi}\frac{1}{R(R+L)}\left\{(\vec{b}\times\vec{P})_i\xi_j + (\vec{b}\times\vec{P})_j\xi_i - \frac{1}{1-\nu}\left((\vec{b}\times\vec{\xi})_i P_j + (\vec{b}\times\vec{\xi})_j P_i\right)\right.$$
$$\left. - \frac{(\vec{b}\times\vec{\eta})\cdot\vec{\xi}}{1-\nu}\left[\delta_{ij} + \xi_i\xi_j + (\eta_i\xi_j + \eta_j\xi_i + L\xi_i\xi_j)\,\frac{R+L}{R^2} + \eta_i\eta_j\frac{2R+L}{R^2(R+L)}\right]\right\}$$

The geometrical meaning of the symbols can be seen in Fig. 34. In the equation (57): $i,j \in \{1,2,3\}$ and the following symbols are used: R is the magnitude of the positional vector $\vec{R} = \vec{r} - \vec{r}_0$; η the magnitude of the vector $\vec{\eta} = \vec{R} - L\vec{\xi}$ (which is perpendicular to the straight dislocation); $L = \vec{R}\cdot\vec{\xi}$ is the projection of vector $\vec{R}$ to the dislocation line; P_i and P_j are the components of the vector $\vec{P} = \vec{R} - R\vec{\xi}$; ξ_i and ξ_j the components of the vector $\vec{\xi}$; finally, η_i and η_j are the components of the vector $\vec{\eta}$. δ_{ij} stands for Kronecker delta. The symbols "$\cdot$" and "$\times$" mean the scalar and cross product of vectors, respectively.

In the approximation of $\tau_{\mathrm{d}}(\vec{r},s)$ introduced by the equation (56) the length of straight segments of a polygon can be, in principle, as small as requires the accuracy of the numerical method. However, de Wit's formula (57) is correct only for a semi-infinite dislocation in a homogeneous infinite crystal. The equation (57) should be corrected by image forces at the walls, which are not incorporated in the present version of the model.

In the investigation of mutual interactions of gliding dislocations the stress exerted by other dislocation can be computed as a sum of the stress contributions produced by straight finite segments of its polygon. Therefore, we can use Eqs. (56) and (57). Let the polygons $\mathcal{P}(t) = \bigcup_{i=1}^{M}[\vec{X}_{i-1},\vec{X}_i]$ and $\mathcal{P}'(t) = \bigcup_{i=1}^{M}[\vec{X}'_{i-1},\vec{X}'_i]$ be approximations of the dislocations Γ and Γ', respectively. Then, the shear stress acting at the point $\vec{X}_i$ of the polygon $\mathcal{P}$ is a sum of the stress contributions from all segments $\vec{X}'_j\vec{X}'_{j+1}$ of the

polygon $\mathcal{P}'$ (to simplify the notation, time dependence is omitted):

$$T_{xy}(\vec{X}_i) = \int_{\Gamma'} \tau_{\rm d}(\vec{X}_i, s')\mathrm{d}s' \approx \sum_{j=0}^{M-1} \left(T_{xy}(\vec{X}_i - \vec{X}'_{j+1}) - T_{xy}(\vec{X}_i - \vec{X}'_j) \right). \tag{58}$$

In the above evaluated stress the orientation of the dislocation curves has to be taken into account: if two dislocations have the same line orientations (the dislocations of the same signs) the corresponding interaction shear stress is repulsive; if the dislocations have the opposite line directions (the dislocations of the opposite signs), the shear stress is attractive. The orientations of Γ and Γ', respectively, are specified in the next section.

Wall interaction. As was mentioned in section 4.1, the PSB dislocation walls are modeled as dislocation dipoles. The elastic shear stress field produced by the dipole at a point $\vec{r} = (x, y)$ in the glide plane of a mobile dislocation can be computed by using the equation (52). Let $(\hat{x}_1, \hat{y}_1)$ and $(\hat{x}_2, \hat{y}_2)$ be the relative coordinates between the point $\vec{r}$ and the positions of straight dislocations forming the dipole. By using the equation (52), the expression for the elastic shear stress field at $\vec{r}$ is

$$\tau_{\rm wall}(x, y) = \pm \frac{Gb}{2\pi(1-\nu)} \left(\frac{\hat{x}_1(\hat{x}_1^2 - \hat{y}_1^2)}{(\hat{x}_1^2 + \hat{y}_1^2)^2} - \frac{\hat{x}_2(\hat{x}_2^2 - \hat{y}_2^2)}{(\hat{x}_2^2 + \hat{y}_2^2)^2} \right).$$

The sign, either "+" or "−", depends on the type of dipole.

Applied stress. In the stress-control regime, the applied stress $\tau_{\rm app}$ is uniform at each point of the dislocation line. It is a prescribed function of time and it approximates the stress induced by the loading conditions. In the numerical simulations we explore the case of constant applied stress; i.e. the constant approximation of applied stress $\tau_{\rm app}$ in dual volume $\mathcal{V}_i^j$ at corresponding point $\vec{X}_i^j$ is

$$(\tau_i^j)_{\rm app} = \tau_{\rm app} = \text{const}.$$

In the total strain-control regime, for the evaluation of the applied stress $\tau_{\rm app}$ in the equation (53), one has to specify an area ΔS_i^{j+1} slipped in time interval (t_j, t_{j+1}) by a dual volume $\mathcal{V}_i^j$ in the corresponding point $\vec{X}_i^j$, $i = 1, \ldots, M-1$. For simplicity, the area ΔS_i^{j+1} is replaced by the area of parallelogram with the vertices $\{\vec{X}_{i-1/2}^j, \vec{X}_{i+1/2}^j, \vec{X}_{i-1/2}^{j+1}, \vec{X}_{i+1/2}^{j+1}\}$, Fig. 35. Then the slipped area $\Delta \hat{S}_i^{j+1}$ on a unit length of the dislocation curve can be approximated as

$$\Delta \hat{S}_i^{j+1} \approx |\vec{m}_i^{j+1} \times \vec{l}_i^{j+1}|.$$

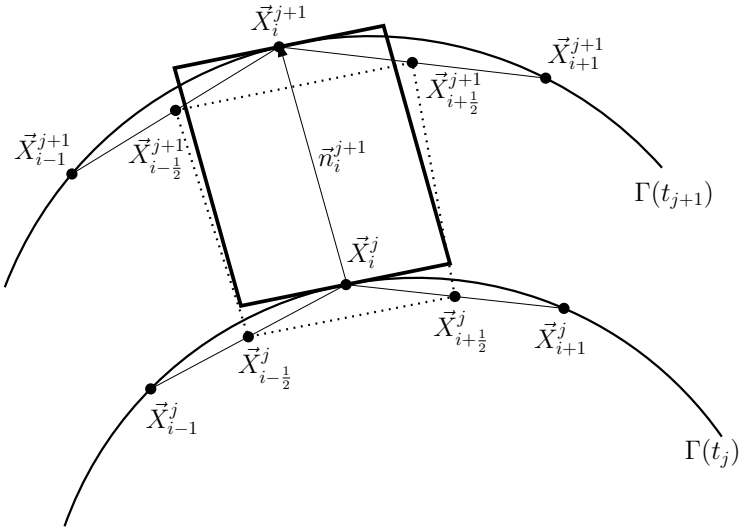

Figure 35. Slipped area by dislocation segment in corresponding dual volume.

The reason for the evaluation of the area on the unit length of the dislocation follows from the equation (59), since the stress $(\tau_i{}^j)_{\text{app}}$ is also outspread on the unit length.

The non-unit normal vector is approximated by $\vec{m}_i^{j+1} = \vec{X}_i^{j+1} - \vec{X}_i^j$ for $i = 1, \ldots, M-1$, and a unit tangent vector by

$$\vec{l}_i^{j+1} \approx \frac{1}{2}\left(\frac{\vec{X}_{i+1}^{j+1} - \vec{X}_{i-1}^{j+1}}{d_{i+1}^{j+1} + d_i^{j+1}} + \frac{\vec{X}_{i+1}^j - \vec{X}_{i-1}^j}{d_{i+1}^j + d_i^j}\right) \quad \text{for} \quad i = 1, \ldots, M-1\,.$$

$d_i^j = |\vec{X}_i^j - \vec{X}_{i-1}^j|$ is the distance of the two neighboring points $\vec{X}_i^j$ and $\vec{X}_{i-1}^j$ of the polygon at time t_j. For $i = 0$ and $i = M$ we set up $\Delta S_i^j = 0$ for all j.

The total area $\hat{S}_i^j$ (on unit length of dislocation) slipped by dual volume $\mathcal{V}_i$ during evolution of dislocation curve from initial time $t_0 = 0$ to current time t_j is $\hat{S}_i^j = \sum_{k=1}^j \Delta\hat{S}_i^k$ and a constant approximation of the applied stress τ_{app} in dual volume $\mathcal{V}_i^j$ at the corresponding point $\vec{X}_i^j$ is

$$(\tau_i{}^j)_{\text{app}} = G[\dot{\varepsilon} t_j - b\varrho\hat{S}_i^j]\,, \tag{59}$$

where $\dot{\varepsilon}$ is a prescribed constant.

4.3 Simulations of a bowing out of dislocations from PSB walls

The geometry of the channel and the walls is shown in Figs. 36 and 37. The model is represented by two originally edge glide dislocations and four edge infinitely-long dipoles. The coordinates of the midpoints of the rigid dipoles in the xy–plane are $(-600, 0)$, $(+600, 0)$, $(-600, h_c = 42)$ and $(+600, h_c = 42)$, respectively (all units are in nm).

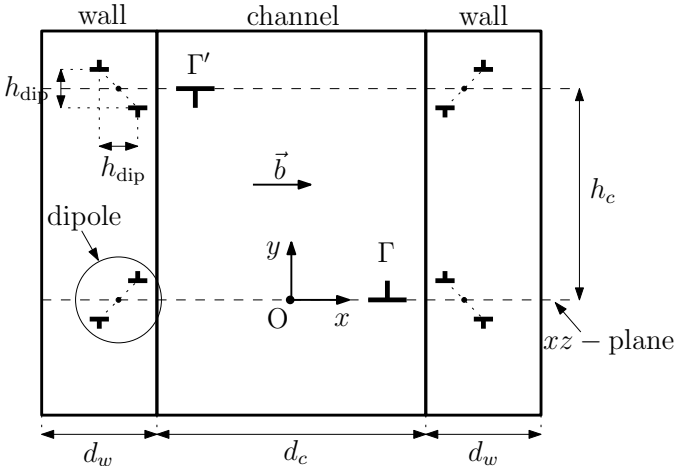

Figure 36. A model of PSB - a perpendicular cut through the channel and the walls.

In Fig. 37 there is a schematic plot of dislocation curves Γ and Γ' which bow-out into the channel from the walls. The dislocations glide in two slip planes which are parallel to the xz–plane. A distance of these planes is $h_c = 42\,\mathrm{nm}$.[2] During the evolution the dislocations are pinned at the end points, in particular in the xyz–system, Γ at $D_1(560, 0, 0), D_2(560, 0, 700)$ and Γ' at $D_1'(-560, 42, -500), D_2'(-560, 42, 0)$, Fig. 37.

If not specified otherwise, the material parameters summarized in Table 1 are used. The height of the wall dipoles $h_{\mathrm{dip}} = 5$ nm is identified with the average height of dipolar loops which are the main building blocks of the walls, Tippelt et al. (1996). The values of the parameters d_c, d_w, b, G and ν correspond to cyclically deformed copper at room temperature, Mughrabi and Pschenitzka (2005); Mughrabi (1981). According to Mughrabi (1981,

[2]The distance of the considered slip planes is equal to the critical separation distance below which the screw dislocations of opposite sign annihilate mutually by cross-slip (the annihilation process is excluded in the present model).

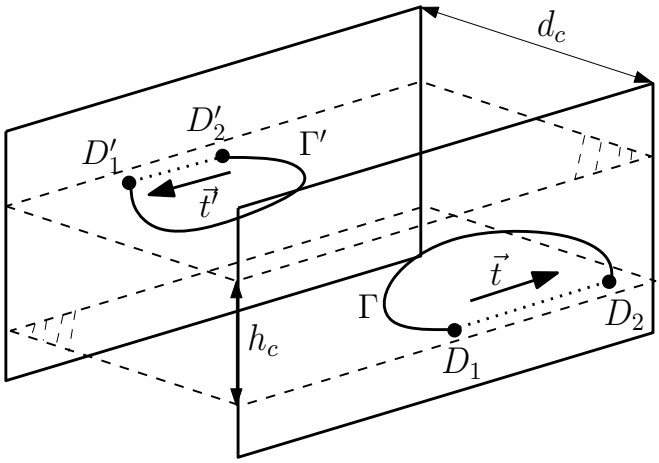

Figure 37. A model of PSB in three-dimensional space.

Table 1. Material parameters (for Cu single crystal cyclically deformed at room temperature) used in the simulations.

Height of wall dipoles	$h_{\mathrm{dip}} = 5$ nm
Width of channel	$d_c = 1200$ nm
Width of dislocation walls	$d_w = 150$ nm
Spacing between slip planes	$h = h_c = 42$ nm
Magnitude of the Burgers vector	$b = 0.256$ nm
Shear modulus	$G = 42.1$ GPa
Poisson ratio	$\nu = 0.33$
Density of glide dislocations	$\varrho \approx 10^{13}$ m^{-2}
Drag coefficient	$B = 1.0 \cdot 10^{-5}$ Pa s
Energy of edge dislocation	$E_{\mathrm{edge}} \approx 2.3$ nJ m^{-1}
Friction stress	$\tau_0 = 5$ MPa

1983) the density of screw dislocations in the PSB–channel $\varrho \approx 10^{13}$ m^{-2}. The energy of edge dislocations $E_{\mathrm{edge}} \approx 2.3$ nJ m^{-1} is chosen in such a way that the line tensions of edge and screw dislocations, $J_{\mathrm{edge}} \approx 0.8$ nN and $J_{\mathrm{screw}} \approx 3.0$ nN, are comparable to the experimental values, Mughrabi (1981, 1983).

Simulations. Initially, in the stress-control regime $\tau_{\mathrm{app}} = 0$ MPa and in the strain-control regime $\varepsilon_{\mathrm{tot}} = 0$. The initial configuration of Γ and Γ'

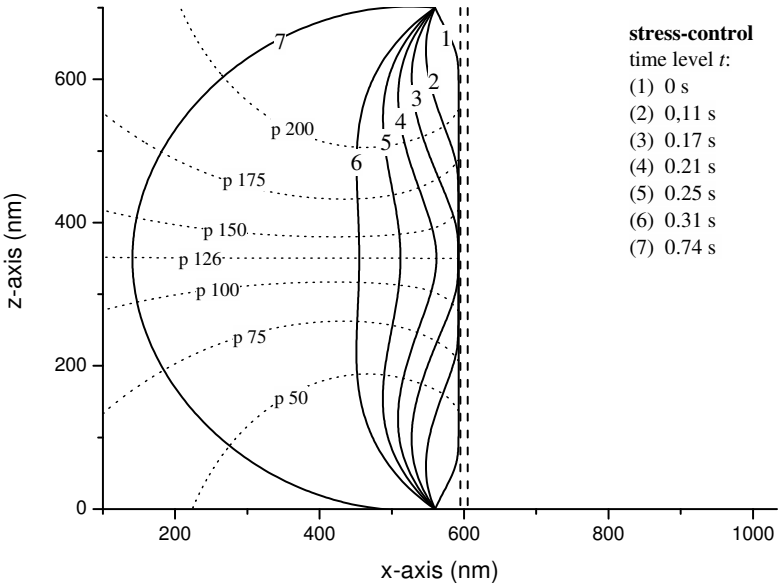

Figure 38. A detail of positions of bowing out curve Γ from the wall in the stress-control regime.

is identified with the linear segments D_1D_2 and $D_1'D_2'$ as shown by dotted lines in Fig. 37. The vectors $\vec{l}$ and $\vec{l}'$ determine the initial orientations of the dislocation curves. These vectors are chosen in such a way that the dislocation dipoles representing the walls attract the dislocation curves inwards to the corresponding walls. These positions of the trapped dislocations are starting positions for the bow-out simulations. A starting position of Γ (at time level $t = 0$), is shown in Fig. 38, the position 1. In a large part of its length, the dislocation segment is straight and parallel to the wall dipoles.

When the dislocations Γ and Γ′ are exposed to a sufficiently strong stress, they bow-out and expand into the channel. We used $\tau_{\text{app}} = 40$ MPa in the stress-control and $\dot{\varepsilon} = 9.3 \cdot 10^{-4}$ s^{-1} in the strain-control. Fig. 38 shows in detail sequential positions of the curve Γ bowing out from the wall in the stress-control; the sequential positions of Γ and Γ′ at the stress control can be seen in Fig. 39. In addition, the trajectories of some selected points of Γ are shown as dotted lines; e.g. $p126$ denotes the midpoint of Γ. In

strain-control regime the sequential positions of both Γ and Γ' can be seen in Figs. 40 (a) and 40 (b).

As long as the dislocations are far from each other, they almost do not feel the elastic field of the other dislocation. On the other hand, if the dislocations are close enough the interaction stress can be very strong. The sequential positions of the dislocations shown in Figs. 39 and 40 for the stress-control and the strain-control, respectively, demonstrate rather big difference in the dislocations' shapes and the extend of their "contact". These upper and lower estimates of the bow-out and passing processes emphasize the need to evaluate correctly the stress field in the channel by solving a boundary value problem. Moreover, the strain-control simulation in Figs. 40 (a) and (b) differ in the starting positions. The simulation in Fig. 40 (a) started at the same positions as in the stress-control, while in the simulation in Fig. 40 (b) the straight segments D_1D_2 and $D_1'D_2'$ were used as the starting positions. The differences seen in Figs. 40 (a) and (b) indicate the sensitivity of the bow-out to details of modeling of the close range interaction between a dislocation and a wall.

As was mentioned in Section 4.1, the tangential velocity of the points of the dislocation lines in a curvature driven motion has no impact on the shape of the evolving curves. Therefore, an introduction of a tangential velocity can provide a convenient redistribution of the grid points X_i of the polygons approximating the dislocations. Two methods have been tested Beneš et al. (2009); Minárik et al. (2010). The first version of the redistribution keeps the grid points equidistant. The method prevents the main drawback of the present simulation that in faster moving parts of the curve the length of the linear segments of the polygon increases faster than in the rest of the curve. Another possibility is to design a redistribution which increases the density of the grid points in the parts of a high curvature. Both methods improve the accuracy of the numerical method, may reduce a computational time and allow larger time steps without loss of stability.

From the computer simulation point of view a higher accuracy and efficiency of the numerical method would be useless without a simultaneous improvement of the model itself. One of such steps would be to formulate and solve the corresponding boundary value problem instead of to estimate the upper and lower limits of the stress field in a PSB–channel by the stress-control and strain-control regimes. The boundary value problem means to consider a PSB sandwiched between two elastic half-spaces which approximate the parts of the crystal filled with a vein structure. Far from the interfaces between the PSB and the vein structure, the half-spaces can be thought of as being exposed to loading conditions of the specimen. The PSB has a composite structure of walls and channels. The plastic prop-

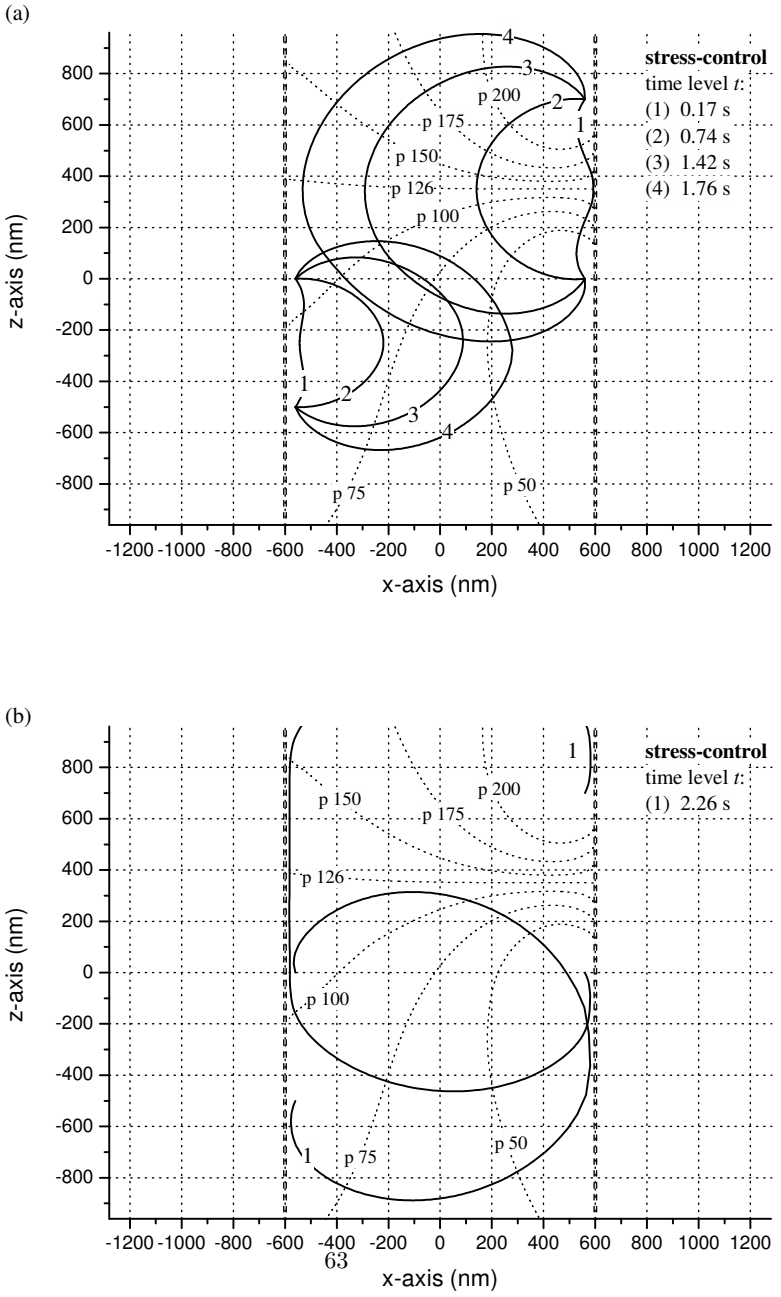

Figure 39. A sequence of positions of the curves in the stress-control.

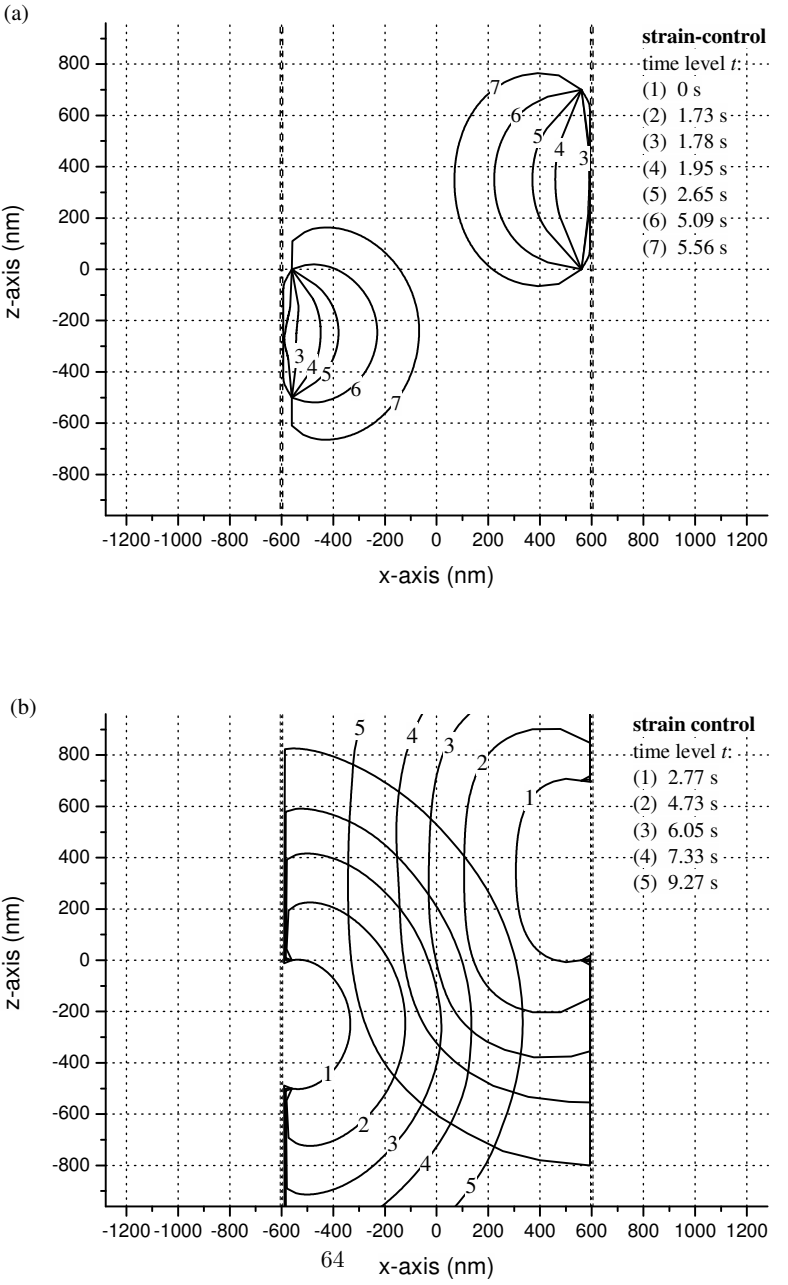

64

Figure 40. A sequence of positions of the curves in the strain-control.

erties of the relatively rigid walls consisting mainly of edge dipolar loops are controlled by polarization of the loops, absorption of dislocations deposited at the walls and the loop and dislocation annihilation. Much softer plastic properties of the channels are governed by dislocation glide. The stress field in the channel is strongly influenced by the dislocation motion. For a computer simulation the specification, formulation and solution of the PSB boundary value problem presents a challenging task. The computation method requires a combination of the discrete dislocation dynamics and the finite element method. The homogenization method for a discrete-continuum simulation of dislocation dynamics Lemarchand et al. (2001) is a promising attempt to design such combination.

4.4 Summary

- The interacting dislocations are modeled in the arc-length parameterization as moving flexible planar curves. The glide of a dislocation segment is governed by a linear viscous law assumed in the form of the standard mean curvature flow equation where each infinitesimal dislocation segment is subjected to the line tension, the interactions with other moving dislocations and the stress field imposed by the loading conditions.
- The presented DDD simulation method is suitable for study of elementary microscopic mechanisms of plastic deformation. We employed an semi-implicit scheme and the discretization based on flowing finite volume approach in space and the method of lines in time. By discretization in space the governing equations are reduced to a system of the ordinary differential equations solved by standard Runge–Kutta method of the fourth order with a fixed time step.
- The proposed simulation method might give a new insight into elementary processes of dislocation interactions in a PSB–channel. It has been employed in modeling of a generation of glide dislocations by the process of bowing out from the PSB walls. The short range interactions among the dislocations and the walls are incorporated in the model as the elastic stress fields of the edge dipoles located at the surface of the walls. Two different physical situations are explored: (i) the stress-control and (ii) the strain-control regime. In the first case the stress in the channel induced by the boundary conditions is assumed to be uniform, in the second case a sum of the elastic and plastic strain is uniform. These two situations roughly substitute a solution of PSB boundary value problem which has not yet been accomplished.

5 Dislocation Statistics

In general, continuous models of discrete systems are very effective tools for description of collective behavior of large assemblies of interacting "particles". In plasticity the "particles" are represented by dislocations. Their collective behavior should enter the continuum mechanics framework as crystal plasticity constitutive equations. It is natural to ask, how to reach such goal by averaging the ensemble of discrete dislocations discussed in Section 4.

The continuum theory of dislocations formulated by Bilby, Kondo, Kröner, Kroupa, Mura, and Kosevich, e.g. Kröner (2001); Kosevich (1979), has been the first attempt to treat rigorously large dislocation ensembles. Most of the early versions of the theory focused on the geometric description of the incompatibility and on the internal stresses arising due to a dislocation distribution. In this sense, the continuum theory of dislocations has became a classical part of theoretical physics. However, despite expectations, the theory has not provided an adequate background for a physically justified theory of plastic properties of solids. The basic problem, already hinted by Kosevich (1965), is how to find a suitable average of the dislocation distribution in deformed crystals. By using the usual averaging, which leads to the standard dislocation density tensor, some factors governing plastic deformation at the mesoscale are lost. Mainly it concerns the dislocation density tensor which is a measure of the local total Burgers vector; dislocations of opposite signs provide zero contribution to it, however, both of them carry a part of plastic deformation. The aim of attempts to formulate dislocation statistics is to find out how to modify and to refine the classical continuum theory of dislocations to provide a constitutive framework of crystal plasticity and explain the observed spontaneous formation of dislocation structures and their transformations.

The first successful dislocation statistics has been proposed by Groma (1997); Groma and Balogh (1999); Groma and Bakó (2000); Zaiser et al. (2001); Groma et al. (2003); Yefimov et al. (2004a); Groma et al. (2007). The idea was to study the idealized plane strain model of straight parallel edge dislocations of a single slip system represented by points of intersection of the dislocation lines with the plane of deformation. In this way the problem was reduced to statistics of point objects, where the tools of standard statistical mechanics were employed. The model revealed one of the main problems: an adequate description of the short range correlations among dislocations. The correlations result in non-local effects which play a decisive role in modeling of dislocation pattering and size effects.

In Section 5.1 Groma's et al. idealized statistical approach is applied to a crystal deformed by plane strain symmetric double slip, Kratochvíl et al.

(2007). The derived constitutive equations are employed in the model of misoriented dislocation cell structure formation presented in Section 6.2.

A statistical treatment of curved glide dislocations outlined in Section 5.2 is far less straightforward. The standard tools of statistical mechanics are not directly applicable to the glide dislocations treated as curved flexible lines. The principal guideline is a refined averaging, Kratochvíl and Sedláček (2008). Dislocations in a deformed material are sorted out into several groups, each of them being averaged separately. The resulting continuum model is formed by superposition of the smoothed out dislocation distribution of the groups. The interaction forces are divided into long range and short range interactions. The long range interactions are incorporated in the mean field approximation directly in the continuum mechanics equations via the solution of the boundary-value problem with eigenstrain. The short range interactions controlled by the short range correlations among dislocations are expressed in integral form as constitutive functionals. The specification and evaluation of the constitutive functionals is the main open problem of the approach.

5.1 Statistics of the idealized double slip

It is assumed that plastic strain is carried by straight parallel edge dislocations. In this idealized model, the nonlocal effects are represented by the short-range correlations only. As a consequence, the self-force of curved dislocations equally important in reality is excluded from the consideration.

Kinematics. A crystal deformed by double slip ($\alpha = 1, 2$) in a plane strain approximation is considered. It is supposed that the crystal contains $N_\alpha(t)$ positive straight edge dislocations with Burgers vector $\vec{b}_\alpha$, and $N_\alpha(t)$ negative straight edge dislocations with Burgers vector $-\vec{b}_\alpha$; the position vectors are $\vec{r}^{\pm}_{\alpha i}(t)$, $i = 1, ..., N_\alpha(t)$, $\alpha = 1, 2$. We assume that the number $N_\alpha(t)$ of $+$ and $-$ dislocations is the same as the dislocations are generated or annihilated in $+$ $-$ pairs.

Following Groma and Balogh (1999) we introduce the discrete densities of positive dislocations $\rho^+_\alpha \geq 0$ and negative dislocations $\rho^-_\alpha \geq 0$, $\alpha = 1, 2$,

$$\rho^+_\alpha(\vec{r}, t) = \sum_{j=1}^{N_\alpha(t)} \delta(\vec{r} - \vec{r}^{+}_{\alpha j}(t)), \qquad \rho^-_\alpha(\vec{r}, t) = \sum_{j=1}^{N_\alpha(t)} \delta(\vec{r} - \vec{r}^{-}_{\alpha j}(t)) \,. \tag{60}$$

$$N_\alpha(t) = \int \rho^{\pm}_\alpha(\vec{r}, t) dV \,, \tag{61}$$

where the integration is carried over the volume of the crystal; $\delta(.)$ means a delta function. The dependence of the densities (60) on time is twofold: (i)

through dislocation motions $\vec{r}^{\pm}_{\alpha i}(t)$, (ii) through the creation/annihilation of dislocations expressed in $N_\alpha(t)$. The rate of change of the total number of $\pm$ dislocations

$$\frac{dN_\alpha(t)}{dt} = \int f_\alpha dV\,, \tag{62}$$

where f_α is introduced as the density of the generation/annihilation rate. Combining (61) and (62)

$$\int f_\alpha dV = \frac{dN_\alpha(t)}{dt} = \frac{d}{dt}\int \rho^{\pm}_\alpha(\vec{r},t)dV = \int [\frac{\partial}{\partial t}\rho^{\pm}_\alpha + \mathrm{div}(\rho^{\pm}_\alpha \vec{v}^{\pm}_\alpha)]dV\,, \tag{63}$$

where $v^{\pm}_\alpha$ represents the dislocation velocity; in the local form

$$\frac{\partial}{\partial t}\rho^{\pm}_\alpha + \mathrm{div}(\rho^{\pm}_\alpha \vec{v}^{\pm}_\alpha) = f_\alpha\,. \tag{64}$$

Equation (64) yields the balance equation for the discrete density of geometrically necessary dislocations, $\kappa_\alpha = \rho^{+}_\alpha - \rho^{-}_\alpha$, $\alpha = 1, 2$

$$\frac{\partial}{\partial t}\kappa_\alpha + \mathrm{div}\left(\vec{v}^{+}_\alpha \rho^{+}_\alpha - \vec{v}^{-}_\alpha \rho^{-}_\alpha\right) = 0\,, \tag{65}$$

and the balance equation for the total discrete dislocation density $\rho_\alpha = \rho^{+}_\alpha + \rho^{-}_\alpha$,

$$\frac{\partial}{\partial t}\rho_\alpha + \mathrm{div}\left(\vec{v}^{+}_\alpha \rho^{+}_\alpha + \vec{v}^{-}_\alpha \rho^{-}_\alpha\right) = 2f_\alpha\,. \tag{66}$$

The alternative derivation of the single slip version of balance equations (65) and (66) was given by Groma and Balogh (1999).

To arrive at a continuous description, the introduced discrete quantities are averaged over an ensemble of statistically equivalent dislocation system (for details of the averaging procedure see Groma and Balogh (1999); Groma (1997); Groma et al. (2003)). The balance equation for the ensemble averaged density $\hat{\kappa}_\alpha = \langle \kappa_\alpha \rangle$ can be deduced from (65)[3]

$$\frac{\partial}{\partial t}\hat{\kappa}_\alpha = -\frac{\vec{b}_\alpha}{b^2_\alpha} \cdot \nabla \nu_\alpha\,, \tag{67}$$

where slip strain rate ν_α is related to the ensemble averaged dislocation flux $\langle \vec{v}^{+}_\alpha \rho^{+}_\alpha - \vec{v}^{-}_\alpha \rho^{-}_\alpha \rangle$, i.e. $\nu_\alpha = \vec{b}_\alpha \cdot \langle \vec{v}^{+}_\alpha \rho^{+}_\alpha - \vec{v}^{-}_\alpha \rho^{-}_\alpha \rangle$. The relation between density $\hat{\kappa}_\alpha$ and the slip strain rate ν_α expressed trough (67) justifies the interpretation of $\hat{\kappa}_\alpha$ as the geometrically necessary dislocation density of slip system α.

[3]There is employed that for constant $\vec{b}_\alpha$, $\nabla(\vec{b}_\alpha \cdot \vec{v}_\alpha) = \vec{b}_\alpha \mathrm{div}\vec{v}_\alpha$.

The balance equation for the ensemble averaged total dislocation density $\hat{\rho}_\alpha = \langle \rho_\alpha \rangle$ follows from (66)

$$\frac{\partial}{\partial t}\hat{\rho}_\alpha = -\frac{\vec{b}_\alpha}{b_\alpha^2} \cdot \nabla \eta_\alpha + 2\hat{f}_\alpha \,, \tag{68}$$

where the difference slip strain rate η_α is related to the ensemble averaged difference dislocation flux $\langle \vec{v}_\alpha^+ \rho_\alpha^+ + \vec{v}_\alpha^- \rho_\alpha^- \rangle$, i.e. $\eta_\alpha = \vec{b}_\alpha \cdot \langle \vec{v}_\alpha^+ \rho_\alpha^+ + \vec{v}_\alpha^- \rho_\alpha^- \rangle$.

To specify the generation/annihilation term $\hat{f}_\alpha = \langle f_\alpha \rangle$ various possibilities has been suggested, Groma and Balogh (1999); Groma (1997); Yefimov et al. (2004a). We accept the assumption proposed in Yefimov et al. (2004a) (equations(16) and (17) there) that $\hat{f}_\alpha$ is proportional slip strain rate ν_α

$$2\hat{f}_\alpha = C|\nu_\alpha| \,, \tag{69}$$

where C is a phenomenological parameter.

Dynamics. The equations for slip strain rates ν_α and η_α are constructed from the equations of motion of discrete dislocations. With the commonly accepted assumption of an over-damped motion the linearized velocity equation for i-the dislocation of α slip system is:
wherever $\tau_{ext}^\alpha + \tau_{int}^\alpha \geq \tau_0$

$$B\vec{v}_\alpha^{\pm}(\vec{r}_i) = \pm\vec{b}_\alpha[\tau^\alpha(\vec{r}_i) - \tau_0] \,, \tag{70}$$

wherever $\tau_{ext}^\alpha + \tau_{int}^\alpha \leq -\tau_0$

$$B\vec{v}_\alpha^{\pm}(\vec{r}_i) = \pm\vec{b}_\alpha[\tau^\alpha(\vec{r}_i) + \tau_0] \,, \tag{71}$$

and wherever $|\tau_{ext}^\alpha + \tau_{int}^\alpha| < \tau_0$

$$B\vec{v}_\alpha^{\pm}(\vec{r}_i) = 0 \,. \tag{72}$$

B is the drag coefficient, $\tau_0 \geq 0$ the friction stress, both assumed to be the same for all dislocations, and $\tau^\alpha(\vec{r}) = \tau_{ext}^\alpha(\vec{r}) + \tau_{int}^\alpha(\vec{r})$ is the resolved shear stress in α slip system at $\vec{r}$; τ_{ext}^α is the local applied resolved shear stress determined by boundary conditions, and τ_{int}^α represents the resolved shear stress in α system at $\vec{r}$ created by + and − dislocations of α and β slip systems, $\alpha, \beta = 1, 2$ (the following summation is carried over all dislocations except i-the one considered in (70)-(72)),

$$\tau_{int}^\alpha(\vec{r}) = \sum_{\beta=1}^{2}\{\sum_{j=1}^{N'_\beta} \tau_{\alpha\beta}(\vec{r} - \vec{r}_{\beta j}^{+}) - \sum_{j=1}^{N'_\beta} \tau_{\alpha\beta}(\vec{r} - \vec{r}_{\beta j}^{-})\} \,. \tag{73}$$

$\tau_{\alpha\beta}(\vec{r})$ is the resolved shear stress in α slip system at $\vec{r}$ created by a positive edge dislocation of β slip system located at the origin, Groma and Bakó (2000)

$$\tau_{\alpha\beta}(\vec{r}) = \frac{Gb_\beta}{2\pi(1-\nu)}\left(\frac{\vec{b}_\alpha}{b_\alpha}\cdot\nabla\right)(\vec{n}_\alpha\cdot\nabla)(\vec{n}_\beta\cdot\nabla)\left[\frac{r^2}{2}\ln(r)\right], \tag{74}$$

where $r = |\vec{r}|$ and $\vec{n}_\alpha$ is a unit vector perpendicular to the α slip plane; G is the elastic shear modulus and ν Poisson's ratio (in the paper Groma and Bakó (2000) the elastic factor $Gb/[2\pi(1-\nu)]$ has been incorporated in the drag coefficient B).

Using the discrete dislocation densities (60), $\alpha = 1, 2$,

$$\sum_{j=1}^{N'_\beta} \tau_{\alpha\beta}(\vec{r} - \vec{r}^{\pm}_{\beta j}) = \int \tau_{\alpha\beta}(\vec{r} - \vec{r'})\rho^{\pm}_\beta(\vec{r'})dV'. \tag{75}$$

For discrete fluxes $\vec{v}^+_\alpha\rho^+_\alpha$ and $\vec{v}^-_\alpha\rho^-_\alpha$, $\alpha = 1, 2$, we get from (70) and (73)–(75):
wherever $\tau^\alpha_{ext} + \tau^\alpha_{int} \geq \tau_0$

$$\vec{v}^+_\alpha\rho^+_\alpha = \frac{\vec{b}_\alpha}{B}\sum_{\beta=1}^{2}\int \tau_{\alpha\beta}(\vec{r} - \vec{r'})[\rho^+_\alpha(\vec{r})\rho^+_\beta(\vec{r'}) - \rho^+_\alpha(\vec{r})\rho^-_\beta(\vec{r'})]dV' + \frac{\vec{b}_\alpha}{B}[\tau^\alpha_{ext} - \tau_0]\rho^+_\alpha(\vec{r}), \tag{76}$$

$$\vec{v}^-_\alpha\rho^-_\alpha = -\frac{\vec{b}_\alpha}{B}\sum_{\beta=1}^{2}\int \tau_{\alpha\beta}(\vec{r} - \vec{r'})[\rho^-_\alpha(\vec{r})\rho^+_\beta(\vec{r'}) - \rho^-_\alpha(\vec{r})\rho^-_\beta(\vec{r'})]dV' - \frac{\vec{b}_\alpha}{B}[\tau^\alpha_{ext} - \tau_0]\rho^-_\alpha(\vec{r})\,. \tag{77}$$

In the case $\tau^\alpha_{ext} + \tau^\alpha_{int} \leq -\tau_0$ the sign at τ_0 is opposite, if $-\tau_0 \leq \tau^\alpha_{ext} + \tau^\alpha_{int} \leq \tau_0$ the fluxes are zero.

The slip strain rate ν_α and the differential slip strain rate η_α are expressed through the ensemble averaged fluxes (the upper signs are valid for ν_α, the lower signs for η_α)

$$\begin{matrix}\nu_\alpha(\vec{r}) \\ \searrow \\ \nearrow \\ \eta_\alpha(\vec{r})\end{matrix} = \vec{b}_\alpha\cdot\langle\vec{v}^+_\alpha\rho^+_\alpha \mp \vec{v}^-_\alpha\rho^-_\alpha\rangle = \tag{78}$$

$$\frac{b_\alpha^2}{B}\sum_{\beta=1}^{2}\int \tau_{\alpha\beta}(\vec{r}-\vec{r'})[\hat{\rho}_{\alpha\beta}^{++}(\vec{r},\vec{r'})-\hat{\rho}_{\alpha\beta}^{+-}(\vec{r},\vec{r'})\pm\hat{\rho}_{\alpha\beta}^{-+}(\vec{r},\vec{r'})\mp\hat{\rho}_{\alpha\beta}^{--}(\vec{r},\vec{r'})]dr'+$$

$$\frac{b_\alpha^2}{B}[\tau_{ext}^{\alpha}-\tau_0]\langle\rho_\alpha^+(\vec{r})\pm\rho_\alpha^-(\vec{r})\rangle$$

where according to previous definitions $\langle\rho_\alpha^+-\rho_\alpha^-\rangle=\hat{\kappa}_\alpha$ and $\langle\rho_\alpha^++\rho_\alpha^-\rangle=\hat{\rho}_\alpha$. The conditions of the validity of (78) that follows from the averaging will be stated after a brief analysis of the terms in that equations.

The two-particle density functions $\hat{\rho}_{\alpha\beta}^{ss'}(\vec{r},\vec{r'})=\langle\rho_\alpha^s(\vec{r})\rho_\beta^{s'}(\vec{r'})\rangle$ may be interpreted as follows: $\hat{\rho}_{\alpha\beta}^{ss'}(\vec{r},\vec{r'})dVdV'$ represents the joint probability to find α-dislocation of sign s in a volume element dV at $\vec{r}$ and β-dislocation of sign s' in a volume element dV' at $\vec{r'}$. The system of equations (67), (68) and (78) represents the double-slip version of the equations derived in Groma et al. (2003) (equations (4) and (5)).

As proposed by Groma et al. (2003) the two-particle density functions $\hat{\rho}_{\alpha\beta}^{ss'}$ can be expressed approximately as the products of the single-particle functions $\hat{\rho}_s^\alpha$ and $\hat{\rho}_{s'}^\beta$ corrected for a short range correlation effects, $\alpha,\beta=1,2$ and $s,s'=+,-$,

$$\hat{\rho}_{\alpha\beta}^{ss'}(\vec{r},\vec{r'})=\hat{\rho}_\alpha^s(\vec{r})\hat{\rho}_\beta^{s'}(\vec{r'})[1+\hat{d}_{\alpha\beta}^{ss'}(\vec{r}-\vec{r'})]\,. \tag{79}$$

As suggested in Groma et al. (2003) the correction $\hat{d}_{\alpha\beta}^{ss'}$ corresponds to the short range arrangement in a homogeneous dislocation system. As a consequence, $\hat{d}_{\alpha\beta}^{ss'}$ depends only on the relative coordinate $\vec{r}-\vec{r'}$.

Introducing (79) in (78) and using the same arguments as in Appendix of Groma et al. (2003) we get

$$\nu_\alpha(\vec{r})=\frac{b_\alpha^2}{B}\hat{\rho}_\alpha(\vec{r})\{\sum_{\beta=1}^{2}[\tau_{sc}^{\alpha\beta}(\vec{r})-\tau_{non}^{\alpha\beta}(\vec{r})-\tau_f^{\alpha\beta}(\vec{r})]+\tau_{ext}^{\alpha}(\vec{r})-\tau_0\}\,, \tag{80}$$

$$\eta_\alpha(\vec{r})=\frac{b_\alpha^2}{B}\hat{\kappa}_\alpha(\vec{r})\{\sum_{\beta=1}^{2}[\tau_{sc}^{\alpha\beta}(\vec{r})-\tau_{non}^{\alpha\beta}(\vec{r})-\tau_f^{\alpha\beta}(\vec{r})]+\tau_{ext}^{\alpha}(\vec{r})-\tau_0\}\,. \tag{81}$$

In (80) and (81)

$$\tau_{sc}^{\alpha\beta}(\vec{r})=\int\tau_{\alpha\beta}(\vec{r}-\vec{r'})\hat{\kappa}_\beta(\vec{r'})dV', \tag{82}$$

$$\tau_{non}^{\alpha\beta}(\vec{r})=-\frac{1}{4}\int\tau_{\alpha\beta}(\vec{r}-\vec{r'})\hat{\kappa}_\beta(\vec{r'})\bar{d}_{\alpha\beta}(\vec{r}-\vec{r'})dV', \tag{83}$$

$$\tau_f^{\alpha\beta}(\vec{r}) = -\frac{1}{4}\int \tau_{\alpha\beta}(\vec{r}-\vec{r'})\hat{\rho}_\beta(\vec{r'})\tilde{d}_{\alpha\beta}(\vec{r}-\vec{r'})dV', \tag{84}$$

where

$$\bar{d}_{\alpha\beta} = \hat{d}_{\alpha\beta}^{++} + \hat{d}_{\alpha\beta}^{+-} + \hat{d}_{\alpha\beta}^{-+} + \hat{d}_{\alpha\beta}^{--}\,, \tag{85}$$

$$\tilde{d}_{\alpha\beta} = \hat{d}_{\alpha\beta}^{++} + \hat{d}_{\alpha\beta}^{+-} - \hat{d}_{\alpha\beta}^{-+} - \hat{d}_{\alpha\beta}^{--}\,. \tag{86}$$

As in (80) and (81) the expressions in the curl brackets are the same, these equations yield ($\hat{\rho}_\alpha$ are assumed non-zero)

$$\eta_\alpha = \frac{\hat{\kappa}_\alpha}{\hat{\rho}_\alpha}\nu_\alpha\,. \tag{87}$$

The stress $\tau_{sc}^{\alpha\beta}$ given by (82) is the part of the resolved shear stress in α slip system caused by all geometrically necessary dislocations belonging to the same, i.e. $\beta = \alpha$, or to the other slip system, i.e. $\beta \neq \alpha$. Through (67) $\tau_{sc}^{\alpha\beta}$ is related to the gradient of plastic strain rate ν_α in both slip systems. Following the analysis of $\tau_{non}^{\alpha\beta}$ and $\tau_f^{\alpha\beta}$ given by Groma et al. (2003) we utilize the results of the discrete dislocation dynamics simulations that the dislocation-dislocation correlation functions $\hat{d}_{\alpha\beta}^{ss'}$ decay to zero within a few dislocation distances, Zaiser et al. (2001). Because of that the density functions $\hat{\kappa}_\beta(\vec{r'})$ and $\hat{\rho}_\beta(\vec{r'})$ in the integrals in (83) and (84) can be approximated by their Taylor expansions around the point $\vec{r}$. Taking into account that $\tau_{\alpha\beta}(\vec{r}) = -\tau_{\beta\alpha}(-\vec{r})$, as follows from (74), and that $\hat{d}_{\alpha\beta}^{ss'}(\vec{r}) = \hat{d}_{\beta\alpha}^{s's}(-\vec{r})$, hence, $\bar{d}_{\alpha\beta}(\vec{r}) = \bar{d}_{\beta\alpha}(-\vec{r})$ and $\tilde{d}_{\alpha\beta}(\vec{r}) = -\tilde{d}_{\beta\alpha}(-\vec{r})$, and keeping only the first non-vanishing terms we arrive at, $\vec{\zeta} = \vec{r} - \vec{r'}$,

$$\tau_{non}^{\alpha\beta}(\vec{r}) = -\frac{1}{4}\nabla\hat{\kappa}_\beta(\vec{r})\cdot\int \vec{\zeta}\tau_{\alpha\beta}(\vec{\zeta})\bar{d}_{\alpha\beta}(\vec{\zeta})d\vec{\zeta}\,, \tag{88}$$

$$\tau_f^{\alpha\beta}(\vec{r}) = -\frac{1}{4}\hat{\rho}_\beta(\vec{r})\int \tau_{\alpha\beta}(\vec{\zeta})\tilde{d}_{\alpha\beta}(\vec{\zeta})d\vec{\zeta}\,. \tag{89}$$

Accepting Groma et al. (2003) interpretation, $\tau_{non}^{\alpha\beta}$ has a diffusion like character. In physical terms this behavior stems from the short range repulsion between individual dislocations of the same sign. Due to (67) $\tau_{non}^{\alpha\beta}$ is related to the second derivative of the plastic strain rate ν_β representing a non-local hardening effect. $\tau_f^{\alpha\beta}$ is interpreted as a friction type stress, called "back" stress, which causes local hardening by + and − dislocations of densities $\hat{\rho}_\beta$; through (68) and (69) the rate $\dot{\tau}_f^{\alpha\beta}$ is related to the rate $|\nu_\beta(\vec{r})|$ and to the gradient $\nabla\eta_\beta$.

It is interesting to note that the short range elastic interactions between individual dislocations are transformed by ensemble averaging into $\tau_{non}^{\alpha\beta}$ and $\tau_f^{\alpha\beta}$ of a dissipative nature. That is reflected in the conditions of the validity of (78) and, hence, of the validity (80) and (81); ν_α and η_α are non-zero only if

$$\sum_{\beta=1}^{2} \tau_{sc}^{\alpha\beta}(\vec{r}) + \tau_{ext}^{\alpha}(\vec{r}) > \sum_{\beta=1}^{2} [\tau_{non}^{\alpha\beta}(\vec{r}) + \tau_f^{\alpha\beta}(\vec{r})] + \tau_0 \tag{90}$$

or only if

$$\sum_{\beta=1}^{2} \tau_{sc}^{\alpha\beta}(\vec{r}) + \tau_{ext}^{\alpha}(\vec{r}) < -\sum_{\beta=1}^{2} [\tau_{non}^{\alpha\beta}(\vec{r}) + \tau_f^{\alpha\beta}(\vec{r})] - \tau_0 \,, \tag{91}$$

otherwise ν_α and η_α are zero.

The attempt to evaluate the integrals in (88) and (89) for the case of single slip from the data of the discrete dislocation dynamics, Groma et al. (2003), was only partly successful (in that case $\tau_{non}^{\alpha\beta}$ and $\tau_f^{\alpha\beta}$ are reduced to τ_b and τ_f, respectively). In the applications τ_f was identified as the macroscopic flow stress and the value of the integral in τ_b was employed as a fitting parameter Groma et al. (2003); Yefimov et al. (2004a,b). According to equation (21) in Groma et al. (2003) $\tau_b = -K\vec{b}.\partial\kappa(\vec{r})/\partial\vec{r}$, where the density of geometrically necessary dislocations $\kappa \approx \hat{\kappa}_\beta$, and the material constant K with total dislocation density $\rho \approx \hat{\rho}_\beta$ is

$$K = \frac{G}{2\pi(1-\nu)} \frac{D}{\rho} \,. \tag{92}$$

From the comparison with the illustrative example of deformation of a constrained channel evaluated by discrete dislocation dynamics in Groma et al. (2003) there was deduced that $D = 0.8$. Expressing an averaged geometry of the correlation among dislocations the factor D is independent of the distances among them. The influence of the distances is introduced in the non-local stress τ_b through the total dislocation density ρ in K. The higher ρ causes the lower τ_b, it means that the total density "overshadows" the effect of GND gradients.

In view of this situation we accept in (80) and (81) the basic structure of the stress terms and express the evolution equations for $\tau_{non}^{\alpha\beta}$ and $\tau_f^{\alpha\beta}$ in the linearized form:

$$\dot{\tau}_{non}^{\alpha\beta}(\vec{r}) = -K_{\alpha\beta}\vec{b}_\alpha \cdot \nabla\dot{\hat{\kappa}}_\beta(\vec{r}) = K_{\alpha\beta}[\vec{b}_\alpha \cdot \nabla][\vec{b}_\beta \cdot \nabla]\nu_\beta(\vec{r})/b_\beta^2 \,, \tag{93}$$

where according to (88)

$$K_{\alpha\beta} = (1/4)\frac{Gb_\beta}{2\pi(1-\nu)b_\alpha}\int[(\vec{\zeta}\cdot\nabla)(\vec{n}_\alpha\cdot\nabla)(\vec{n}_\beta\cdot\nabla)\frac{\zeta^2}{2}\ln(\zeta)]\bar{d}_{\alpha\beta}(\vec{\zeta})d\vec{\zeta}. \quad (94)$$

is the non-local hardening matrix; values of the components are supposed to be of the order of K. In deriving (93) and (94) we employ (67) and utilize that for $\bar{d}_{\alpha\beta}(-\vec{\zeta}) = \bar{d}_{\beta\alpha}(\vec{\zeta})$ the integral

$$\int\vec{\zeta}[(\vec{b}_\alpha\cdot\nabla)(\vec{n}_\alpha\cdot\nabla)(\vec{n}_\beta\cdot\nabla)(\zeta^2/2)\ln(\zeta)]\bar{d}_{\alpha\beta}(\vec{\zeta})d\vec{\zeta} =$$

$$\vec{b}_\alpha\int[(\vec{\zeta}\cdot\nabla)(\vec{n}_\alpha\cdot\nabla)(\vec{n}_\beta\cdot\nabla)(\zeta^2/2)\ln(\zeta)]\bar{d}_{\alpha\beta}(\vec{\zeta})d\vec{\zeta}.$$

Similarly,

$$\dot{\tau}_f^{\alpha\beta}(\vec{r}) = H_{\alpha\beta}\dot{\hat{\rho}}_\beta(\vec{r}) = CH_{\alpha\beta}|\nu_\beta(\vec{r})|\,, \quad (95)$$

where

$$H_{\alpha\beta} = -(1/4)\int\tau_{\alpha\beta}(\vec{\zeta})\tilde{d}_{\alpha\beta}(\vec{\zeta})d\vec{\zeta} =$$

$$-1/4\int[(\vec{b}_\alpha\cdot\nabla)(\vec{n}_\alpha\cdot\nabla)(\vec{n}_\beta\cdot\nabla)(\zeta^2/2)\ln(\zeta)]\tilde{d}_{\alpha\beta}(\vec{\zeta})d\vec{\zeta} \quad (96)$$

is the standard (local) hardening matrix. In the relation (68) it is assumed that the local hardening is dominated by the generation-annihilation term $2\hat{f}_\alpha$ given by (69). The gradient term in (68) expressed through (87), i.e. $\nabla\eta_\alpha = \nabla(\hat{\kappa}_\alpha/\hat{\rho}_\alpha)\dot{\gamma}_\alpha + (\hat{\kappa}_\alpha/\hat{\rho}_\alpha)\nabla\dot{\gamma}_\alpha$, can be understood as a correction to $\tau_{sc}^{\alpha\beta}$ and $\tau_f^{\alpha\beta}$, however, the correction would need further analysis.

Constitutive equations. In summary, the constitutive relations constructed from the equations of motion of discrete dislocations (70)–(72) are represented by the equations (80), (81) for slip strain rates ν_α and η_α

$$\nu_\alpha(\vec{r}) = \frac{b_\alpha^2}{B}\hat{\rho}_\alpha(\vec{r})\{\tau^\alpha(\vec{r}) - \tau_y^\alpha(\vec{r})\}\,, \quad (97)$$

$$\eta_\alpha(\vec{r}) = \frac{b_\alpha^2}{B}\hat{\kappa}_\alpha(\vec{r})\{\tau^\alpha(\vec{r}) - \tau_y^\alpha(\vec{r})\}\,, \quad (98)$$

where it is assumed that plastic strain is carried by parallel + and – straight edge dislocations with Burgers vectors $\pm\vec{b}_\alpha$ of two active slip systems $\alpha = 1, 2$. The slip strain rate ν_α is related to the ensemble averaged dislocation flux: $\nu_\alpha = \vec{b}_\alpha\cdot\langle\vec{v}_\alpha^+\rho_\alpha^+ - \vec{v}_\alpha^-\rho_\alpha^-\rangle$; the difference slip strain rate η_α is related to

the ensemble averaged difference dislocation flux: $\eta_\alpha = \vec{b}_\alpha \cdot \langle \vec{v}_\alpha^+ \rho_\alpha^+ + \vec{v}_\alpha^- \rho_\alpha^- \rangle$, where $\rho_\alpha^\pm$, represent the discrete densities of positive and negative dislocations (60) and $v_\alpha^\pm$ denote their velocities. $\hat{\rho}_\alpha = \langle \rho_\alpha^+ + \rho_\alpha^- \rangle$ is the ensemble averaged total discrete dislocation density; $\hat{\kappa}_\alpha = \langle \rho_\alpha^+ - \rho_\alpha^- \rangle$ represents the ensemble averaged discrete density of geometrically necessary dislocations; B is the drag coefficient assumed to be the same for all dislocations.

$\tau^\alpha(\vec{r})$ denotes the resolved shear stress in α slip system and $\tau_y^\alpha(\vec{r})$ its critical value

$$\tau^\alpha(\vec{r}) = \sum_{\beta=1}^{2} \tau_{sc}^{\alpha\beta}(\vec{r}) + \tau_{ext}^\alpha(\vec{r}), \quad \tau_y^\alpha(\vec{r}) = \sum_{\beta=1}^{2} [\tau_f^{\alpha\beta}(\vec{r}) + \tau_{non}^{\alpha\beta}(\vec{r})] + \tau_0, \quad (99)$$

τ_{ext}^α means the local applied resolved shear stress determined by boundary conditions, and the stress $\tau_{sc}^{\alpha\beta}$ given by (82) represents the part of the resolved shear stress in α slip system caused by all geometrically necessary dislocations belonging to the same, i.e. $\beta = \alpha$, or to the other slip system, i.e. $\beta \neq \alpha$; $\tau_0 \geq 0$ is the friction stress. The stress rate $\dot{\tau}_{sc}^{\alpha\beta}$ is related to the gradient of plastic strain rate ν_α in the slip systems (67).

The validity conditions (90), (91) read:
ν_α and η_α are non-zero if

$$\tau^\alpha(\vec{r}) > \tau_y^\alpha(\vec{r}), \quad (100)$$

or if

$$\tau^\alpha(\vec{r}) < -\tau_y^\alpha(\vec{r}), \quad (101)$$

otherwise ν_α and η_α are zero.

The stress $\tau_{non}^{\alpha\beta}$ given by (88) has a diffusion like character which stems from the short range repulsion between individual dislocations of the same sign. As it is related through (67) to the second derivative of the plastic strain rate ν_β, the stress $\tau_{non}^{\alpha\beta}$ represents a non-local hardening effect. The linearized form (93) reads

$$\dot{\tau}_{non}^{\alpha\beta}(\vec{r}) = K_{\alpha\beta}[\vec{b}_\alpha \cdot \nabla][\vec{b}_\beta \cdot \nabla]\nu_\beta(\vec{r})/b_\beta^2, \quad (102)$$

where $K_{\alpha\beta}$ is the non-local hardening matrix (94).

The stress $\tau_f^{\alpha\beta}$ given by (89) causes local hardening; through (68) and (69) the rate $\dot{\tau}_f^{\alpha\beta}$ is related to the rate $|\nu_\alpha(\vec{r})|$. The linearized form given by (95) reads

$$\dot{\tau}_f^{\alpha\beta}(\vec{r}) = CH_{\alpha\beta}|\nu_\alpha|, \quad (103)$$

where $H_{\alpha\beta}$ is the local hardening matrix (96).

From $(99)_2$, (102) and (103) we get the hardening law, i.e. the evolution equations for the critical resolved shear stresses $\tau_y^\alpha(\vec{r})$

$$\dot{\tau}_y^\alpha(\vec{r}) = \sum_{\beta=1}^{2} \{CH_{\alpha\beta}|\nu_\alpha(\vec{r})| + K_{\alpha\beta}[\vec{b}_\alpha \cdot \nabla][\vec{b}_\beta \cdot \nabla]\nu_\beta(\vec{r})/b_\beta^2\}\,. \tag{104}$$

The constitutive equations (97), (98) (or equivalently (80), (81)) can be further simplified by considering the rate independent limit $B \longrightarrow 0$. Then the constitutive relations are reduced to the yield condition:
the rates ν_α and η_α can be non-zero only if

$$\tau^\alpha(\vec{r}) = \pm\{\sum_{\beta=1}^{2}[\tau_{non}^{\alpha\beta}(\vec{r}) + \tau_f^{\alpha\beta}(\vec{r})] + \tau_0\} = \pm\tau_y^\alpha \tag{105}$$

and ν_α and η_α are zero otherwise.

Introducing the linearized stresses (103) and (102) (or equivalently (95) and (93)) in (105) the hardening constitutive equations can be expressed in the explicit form

$$\dot{\tau}_y^{(1)} = CH_{11}|\nu_1| + CH_{12}|\nu_2| + K_{11}(\vec{s}_1 \cdot \nabla)^2\nu_1 + K_{12}(\vec{s}_1 \cdot \nabla)(\vec{s}_2 \cdot \nabla)\nu_2\,, \tag{106}$$

$$\dot{\tau}_y^{(2)} = CH_{21}|\nu_1| + CH_{22}|\nu_2| + K_{21}(\vec{s}_2 \cdot \nabla)(\vec{s}_1 \cdot \nabla)\nu_1 + K_{22}(\vec{s}_2 \cdot \nabla)^2\nu_2\,. \tag{107}$$

The constitutive equations of hardening (106) and (107) have the format (41) assumed in the plasticity of single crystals presented in Section 2.3 enriched by the higher gradient terms. Despite of high idealization of the model represented by the parallel edge dislocations the non-local hardening matrix (94) suggest a possible interpretation of the higher gradients terms. Through $\bar{d}_{\alpha\beta}$ in (94) they model the short range correlations among dislocations. The described construction and the structure of the hardening matrices $H_{\alpha\beta}$ and $K_{\alpha\beta}$ seen in (94) and (96) reflex the complexity of the hardening problem.

5.2 Note on statistics of curved dislocations

A statistical treatment of curved glide dislocations is far more complicated than the model presented in previous Section 5.1. Here only the main ideas of such statistics are outlined, technical details can be found in the papers cited in the following text. The principle problem is that the connectivity of the dislocation segments forming the dislocation lines must be accounted for, Kratochvíl and Sedláček (2008) (alternative approaches can be found in Malygin (1999); El-Azab (2000a,b); Hochrainer (2006); Zaiser

and Hochrainer (2006); Hochrainer et al. (2007); Ispánovity et al. (2010)). In the model proposed by Kratochvíl and Sedláček (2008) dislocations are sorted out into several groups, each of them being averaged separately. The resulting continuum model is formed by superposition of the smoothed out fields.

As already mentioned, in plastically deforming crystals two types of dislocation populations are observed, with very different characteristic length scale and mobile properties: (i) glide dislocations which carry the plastic deformation, (ii) dislocation debris, mostly in the form of small dipolar dislocation loops, which are the main building elements of dipolar dislocation structures. Segments of glide dislocations may extend over distances of micrometers. They are moved by the resolved shear stress and their density remains nearly the same, being of the order $10^{11} - 10^{14}$ m^{-2}, Mughrabi (1983); a highly localized higher density of geometrically necessary dislocations may appear in boundaries of misoriented cells or subgrains, Bay et al. (1992). On the other hand, the size of the loops is of the order of 10 nm, they are drifted by stress gradients and/or swept by glide dislocations, and during the deformation process their density may increase from zero up to $10^{14} - 10^{16}$ m^{-2} in loop clusters (veins, walls) Mughrabi (1983). Therefore, in the proposed model the glide dislocations and the dipolar loops are treated as different entities.

Being prismatic with their long arms in two neighboring slip planes and short arms in cross slip planes, the loops can move in the slip direction only. Moreover, the computer simulations in Huang et al. (2004) indicate that the changes in the loop size and geometry caused by the stress field of the order of the yield stress are very small. Hence, the dipolar loops may be treated as rigid objects and the statistics of the loops can be formulated as a 3D version of Groma et al. (2003) statistics presented in the Section 5.1. In the model of Kratochvíl and Sedláček (2008) the loop population is treated as a single group. In reality the dipolar loops are of four types: vacancy and interstitial loops, each in two possible stable configurations, cf. Fig. 1 in Verecký et al. (2002); they display a spectrum of sizes. An advanced model of dipolar loop clustering could distinguish this variety. On the other hand, in number of situations, namely at advanced stages of plastic deformation, the deformation substructure is dominated by misoriented dislocation cells or subgrains and/or shear and kink bands, where the spontaneous loop clustering plays only a subsidiary role. Then the effect of the loop population may be modeled as a part of a friction stress and the proposed statistical treatment of the loops can be disregarded.

The standard tools of statistical mechanics are not directly applicable to the glide dislocations treated as curved flexible lines. Therefore the

glide dislocations are first separated into groups suitable for averaging. The model uses the concept of single-valued dislocation fields, originally developed within the framework of continuum theory of dislocations, Kratochvíl and Sedláček (2003); Sedláček et al. (2003). In analogy to standard continuum mechanics, where material points are labeled by their positions in a reference configuration, we should label the glide dislocations in a reference configuration and follow their changes during deformation. To do that, the standard vector space of point positions would have to be replaced by a functional space of parametric curves representing the glide dislocations. To avoid such a complexity and to stay within the framework of the vector space of positions an approximation of single-valued dislocation fields is employed. Roughly speaking, we need to keep information on the connectivity of the segments of glide dislocation lines in the averaged continuum description. It is suggested that in many cases of practical interest, a real dislocation configuration can be approximated by a superposition of single-valued dislocation fields. To achieve this, in a reference configuration the glide dislocations are sorted into groups in such way that, for a sufficiently small volume element, the properties of the segments of the glide dislocations belonging to the same group remain sufficiently close, i.e. they form smooth line bundles, where nearby dislocations are nearly parallel and have the same orientation. One may say that the flow of glide dislocations in each group is 'laminar'. In this way, the quantities averaged over statistically equivalent systems of segments of the dislocations belonging to a given group can be expressed as single-valued fields of the position and time. The membership in a group is preserved during a deformation process. However, if needed, a subsequent configuration can be taken as a new reference configuration in which the dislocation groups can be modified. There are many possibilities to group dislocation populations. One possibility would be to label the dislocation groups according to the sources from which the dislocations were generated. A possibility to group a random chaotic initial dislocation arrangement in an infinite crystal would be to approximate it e.g. by an arrangement of straight dislocations of all orientations. Then the dislocations could be sorted into groups according their initial orientation in the reference configuration. Several other possibilities have been utilized in the papers, e.g. Kratochvíl and Sedláček (2003); Sedláček et al. (2003, 2007).

The statistics of curved dislocations, Kratochvíl and Sedláček (2008), is based on the balance equation for the loop density, the evolution equations for the densities and orientations of glide dislocations for each single-valued field, the conservation law of Burgers vector, and crystal plasticity equations. The equations for the flow of glide dislocations for each single-valued

field and the balance equation for the density of dipolar loops are derived from the discrete equations of motion. The dynamic equations contain constitutive functionals representing short range dislocation interactions. An adequate specification and evaluation of the short range correlations among the dislocations for both the glide dislocations and the loops presents the main obstacle to the quantification of the proposed statistical model.

5.3 Summary

- In my opinion, out of three current approaches to modeling of plasticity outlined in these notes, i.e. discrete dislocation dynamics, dislocation statistics, and mesoscale continuum dislocation-based models of spontaneous structuralization, the statistics is least developed. The main problem is that it is not known how to formulate statistics of interacting flexible lines and how to incorporate in the statistics the connectivity of the segments forming the dislocation lines.
- Groma's et al statistics of the plane strain model of straight parallel edge dislocations is relatively successful. It is represented by points of intersection of the dislocation lines with the plane of deformation. In this way the problem was reduced to statistics of point objects, where the tools of standard statistical mechanics can be employed. However, such statistics is not directly applicable to the glide dislocations treated as curved flexible lines.
- Despite of the drastic simplification, Groma's et al model has revealed the problem of an adequate description of the short range correlations among dislocations. The correlations result in non-local effects which play a decisive role in modeling of dislocation pattering and size effects. The model has exposed the complexity and roughness in the now popular description of these effects by higher plastic strain gradients.

6 Spontaneous structuralization

As has been mentioned in Section 1, the spontaneous structuralization approach suits well a description of the global cooperative behavior of the dislocation population. Two classes of spontaneous structuralization processes are observed: *dislocation dipolar loops arrays* (tangles. veins, walls) and *strain localization* (shear bands, avalanches, persistent slip bands) and/or *misoriented dislocation cells* (sungrains). To illustrate methods used in a description of a spontaneous structuralization each class is represented by a model. We will see that the method of description and mathematical tools employed may be quit different.

In Section 6.1 a one dimensional model of formation and transformation of *dipolar loop array* is presented, Saxlová et al. (1997). The main mechanisms of the dislocation structure development are a generation of dipolar loops, their sweeping by glide dislocations to high dislocation density regions, and their annihilation leading to formation of dislocation walls. Despite of the drastic simplification the results simulate the formation of the dislocation vein structure, its disintegration and formation of dipolar walls in a good qualitative agreement with the available electron microscopic observations as presented in Section 3.

In Section 6.2 a framework of continuum crystal plasticity with higher plastic stain gradients is employed in description of the formation of the *misoriented dislocation cells* (subgrains). The formation is interpreted as a result of a trend to reduce the energetically costly hardening in multi slip by decreasing locally the number of active slip systems. In the standard (local) approach, the continuum theory predicts an infinitesimally small cell size. The finite size of real cells is controlled by short-range dislocation interactions: (i) the line tension, (ii) the short-range correlation among dislocations. Within the proposed framework the cell size is a result of a compromise: bulk strain and dissipative energy tends to decrease the size, while short-range interactions restrict that tendency. The non-local effects are analyzed using an idealized model of an infinite crystal deformed by symmetric double slip, where plastic strain is carried by straight parallel edge dislocations. The constitutive equations for non-local effects are represented by the short-range correlation among dislocations derived from the statistics of dislocations presented in Section 5.

6.1 The model of formation of vein dislocation structure and their transformation into walls

As has been described in Section 3.2, at initial hardening stages of single slip cycling a vein structure appears. The density of edge dipole loops stored in the veins increases with deformation. At a certain stage of cycling the veins become saturated and start to be unstable. Let me recall that detailed study of the electron micrographs reveals three main features of vein disintegration processes Jin (1989); Holzwarth and Essmann (1993a) : (a) The originally thicker veins transform gradually into thinner walls. (b) The interiors of some veins disintegrate locally forming areas free of dislocations. (c) Small dislocation rich clusters can be observed in channels. The disintegration of vein structure is a prelude of the global effect of localization of strain into thin lamellae which penetrate into the whole cross section of the crystal. In the lamellae of concentrated slip (called persistent

slip bands) the characteristic ladder structure of dipolar dislocation walls develops gradually from leftovers of the veins.

In Kratochvíl (1993); Kratochvíl and Saxlová (1993) it was noted that the formation of the cycling dislocation structure can be understood as a sequence of instability transitions accompanied by processes of the spontaneous structuralization. The instability causes dynamical changes of the internal structure consisting of the dislocation population and internal stress and strain fields. Using the highly simplified one dimensional model, Saxlová et al. (1997), it has been shown that from an initial perturbation a vein structure of a characteristic wavelength is developed and the dislocation density in the veins gradually grows. When the density there reaches a critical level, the annihilation of the dislocations becomes dominant and the vein structure starts to be rebuilt into thinner walls. The simulation of vein disintegrations exhibits a marked qualitative resemblance to the three observations (a)-(c) stated above. However, due to the one-dimensional approximation the model considered cannot describe the strain localization. Using a linear stability analysis the localization effect has been studied using a two dimensional version of the model Gregor et al. (1997). For illustration of the basic idea of the spontaneous structuralization method the simpler one dimensional version of the model is presented here, Saxlová et al. (1997).

One dimensional model. The one dimensional approximation with the axis x along the slip direction $\vec{b}$ treats main changes in the vein structure observed in the slip plane. In agreement with experimental results any variation in the glide dislocation density ϱ_m is neglected. Under this simplifying assumption the dislocation displacements $\varphi(x,t)$, representing the resulting slip deformation $\gamma(x,t)$ through the relation $\gamma(x,t) \equiv b\varrho_m\varphi(x,t)$, determine at given time t the representative 'shape' of glide dislocations. As b and ϱ_m are constant, $\gamma(x,t)$ and $\varphi(x,t)$ are equivalent variables of the model. Equally, the slip strain rate $\dot{\gamma}$ is related to the 'speed' $\dot{\varphi}$ of glide dislocations at x and t; $\dot{\gamma}(x,t) \equiv b\varrho_m\dot{\varphi}(x,t)$.

The principal variables of the model considered as evolving fields at the scale of μm are: the density of stored dislocation loops $\varrho(x,t)$, the shape $\varphi(x,t)$ of glide dislocations and the shear stress $\tau(x,t)$ which controls their motions. These variables are governed by three equations: the balance law for stored dislocation loops, the equation of motion of glide dislocations and the equations for the stress and strain.

Equations of the stress and strain. We adopt here a convenient one dimensional approximation essentially the same as in the composite model proposed for PSBs by Mughrabi (1981, 1983). We consider the total shear

strain rate $\dot{\varepsilon_T}$ in the slip plane given by external loading conditions and

$$\dot{\varepsilon}_T = \frac{1}{2G}\dot{\tau}(x,t) + \dot{\gamma}(x,t), \tag{108}$$

where G is elastic shear modulus; $\dot{\tau}/2G$ is the local elastic part of the shear strain rate.

The equation of the motion of glide dislocations. The slip force f acting on a dislocation at x, t consists of resolved shear stress contribution $b\tau(x,t)$ and of the additional force caused by the flexibility of the dislocation line with the line tension J. The dislocation line at a point x will move if the force f exceeds the total friction force consisting of the lattice friction force $\tau_0 b$ and the resistance $\tau_l \varrho b$ caused by the stored loops. The speed $\dot{\varphi}$ of dislocations is taken proportional to the force excess as expressed in the local yield condition:

$$B\frac{\partial \varphi}{\partial t} = \begin{cases} f + \tau_0 b + \tau_l \varrho b & \text{if} \quad f < -\tau_0 b - \tau_l \varrho b \\ 0 & \text{if} \quad f \leq \tau_0 b + \tau_l \varrho b \\ f - \tau_0 b - \tau_l \varrho b & \text{if} \quad f > \tau_0 b + \tau_l \varrho b \end{cases} \tag{109}$$

B is the drag coefficient and

$$f = \tau b + J\frac{\partial^2 \varphi}{\partial x^2}\left[1 + \left(\frac{\partial \varphi}{\partial x}\right)^2\right]^{-3/2},$$

where the second term represents the force caused by the glide dislocation curvature, Kratochvíl and Saxlová (1992).

The balance equation for stored dislocation loops. The density of loops $\varrho(x,\gamma)$ is governed by the balance law written in the standard form

$$\frac{\partial \varrho}{\partial \gamma_{cum}} = -\frac{\partial \Phi}{\partial x} + A, \tag{110}$$

where the cumulative slip strain γ_{cum} is taken as an evolution parameter; $\Phi(x,\gamma)$ and $A(x,\gamma)$ are the flux of loops and the net generation or annihilation of loops produced by the unite slip strain, respectively. The equation (110) means that the rate of accumulation of dipolar loops per the unite slip strain must be equal to the net flux of these loops plus the rate of loop generation or annihilation.

Probably the most efficient part Φ_1 of the flux Φ in (110) is caused by the sweeping of dipolar loops by glide dislocations Kratochvíl et al. (1997). Roughly speaking, the flux Φ_1 is realized by those loops for which the interaction force with the glide dislocation segment exceeds the critical force

needed to slip a loop together with the interacting glide dislocation; $C\varrho$ means the flux which would be caused by a pure edge dislocation segment; a pure screw segment causes no flux. By a convenient interpolation between these two limit cases we get

$$\Phi_1 = -C\varrho \frac{\partial\varphi/\partial x}{\sqrt{1+(\partial\varphi/\partial x)^2}}.$$

The second part of the flux Φ_2 arising from the interaction among dipolar loops is assumed in the 'diffusion' type form, Kratochvíl et al. (1994)

$$\Phi_2 = -H\partial\varrho/\partial x.$$

In the equation (110) the rate A of net generation (annihilation) of loops produced by the unit slip strain is approximately expressed in the form

$$A = A_0 - A_1\varrho^n.$$

The parameters A_0, A_1, n are phenomenological substitutes of the not yet well understood processes of the dislocation generation and annihilation. Their quantification similarly as quantification of parameters in the flux term, C and H, seems to us a rather challenging problem. This deficiency together with one dimensionality of the model cause that the model provides the rough qualitative results only.

Taking time t as the evolution parameter and combining relations stated above one gets the balance equation (110) for the loop density $\varrho(x,t)$ in the form

$$\frac{\partial\varrho}{\partial t} = |\dot\gamma|\frac{\partial}{\partial x}\left[C\varrho\frac{\partial\varphi/\partial x}{\sqrt{1+(\partial\varphi/\partial x)^2}} + H\frac{\partial\varrho}{\partial x}\right] + |\dot\gamma|[A_0 - A_1\varrho^n]. \qquad (111)$$

Results and Discussion. The above system of the model equations is too complicated to be solved analytically, however, it is suitable for numerical simulation of the dislocation structure evolution. For this, it is necessary to choose an appropriate discretization, and boundary and initial conditions. The discretization was done on the regular mesh of equidistant nodes in x and t. In the considered infinite region the periodical boundary conditions were used as a suitable approximation. The initial density of dipole loops at each spatial nodal point was randomly selected from the interval of densities $(\varrho_i, \varrho_i + \Delta\varrho_i)$, where ϱ_i and $\varrho_i + \Delta\varrho_i$ are very low in comparison with the critical dislocation density ϱ_c at which the annihilation of loops starts to

prevail under their generation; $\varrho_c = (A_o/A_1)^{1/n}$. The random dislocation density distribution represents a weak perturbations from which the dislocation pattern develops by spontaneous structuralization. The straight screw orientation $\varphi_i = 0$ is chosen as the initial shape of the glide dislocation. The process of cyclic deformation at the constant plastic strain amplitude ε^p_{amp} is controlled by the total shear strain ε_T. The latter strain is assumed to be a linear function of time t with the slope $\dot{\varepsilon}_T$ which alternates in each half cycle; $|\dot{\varepsilon}_T|$ is taken constant and $\varepsilon_T(t)$ independent of the space coordinate x. The vein evolution is demonstrated by the changes in profiles along x and the corresponding hysteresis loops. The macroscopic response in shear stress $\bar{\tau}(t)$) and plastic strain $\varepsilon_p(t)$ is represented by the volume averages of local stresses $\tau(x,t)$ and slips $\gamma(x,t)$, respectively.

The simulation of Fig. 41. has been done for the following model values of parameters in corresponding units: $C = 0.4$, $H = 0.48$, $A_0 = 10^{-3}$, $A_1 = 10^{-3}$, $n = 10$, $B = 1$, $J = 2.4$, $\tau_0 b = 0$, $\tau_l b = 1.5$, $2G|\dot{\varepsilon_T}|b = 0.05$, $2Gb^2\varrho_m = 10^{-2}$ and $\varepsilon^p_{amp} = 10$.

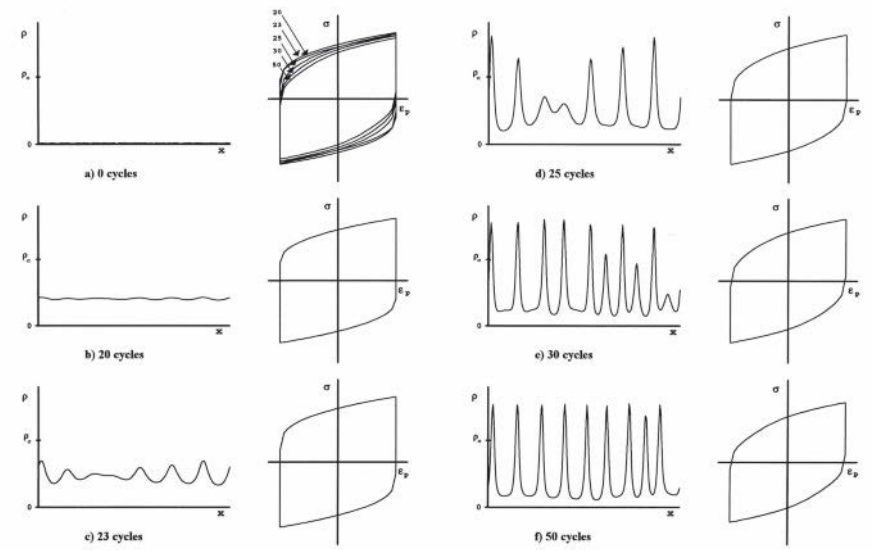

Figure 41. Evolution of vein structure and corresponding hysteresis loops

From the quasi homogeneous loop distribution, Fig. 41 a, the vein structure with a dominant wavelength emerges (1c). The wavelength agrees well with the wavelength of the fastest growing perturbation wave of loop density evaluated by the linear stability analysis of the model Kratochvíl et al.

(1994). The dislocation density in the veins gradually increases and reaches the critical value ϱ_c. Then the loop annihilation becomes significant and veins are disintegrated. The forming of thinner profiles is typical. The series of profiles, Fig. 41 d–f, models the disintegration of veins. The small dislocation rich clusters (called islands in persistent slip bands) are formed, Fig. 41 d and e. The complementary small motion of the walls regulates their distances to an optimum value of the steady state, Fig. 41 f. The results of numerical simulation show the main features of vein disintegration (a)–(c) stated at the beginning of this section qualitatively quite well. For further study a more accurate specification of model parameters is necessary. The main problem is a lack of these parameters. An expectation that DDD and dislocation statistics will provide such data is still far from to be fulfilled.

6.2 Continuous model of misoriented dislocation cell structure formation

Formation of misoriented structural elements, typically in a form of subgrains or misoriented dislocation cells (in the following text we use the short term "subgrains"), is a fundamental process of dislocation patterning accompanying plastic deformation, Bay et al. (1992); Hansen (2001). Subgrains can be found in plastically deformed metals on very different scales, from sub-micron subgrains induced by severe plastic deformation to mm-size subgrains in metals deformed near the melting temperature. The importance of the phenomenon is recognized by considering the process of work hardening, which is clearly correlated with formation of subgrains.

Conventional explanations of formation of subgrains assume either a pre-existing structure of obstacles in the crystal, Orlová and Čadek (1970); Kocks et al. (1980), or use the statistical arguments, Kuhlmann-Wilsdorf and Hansen (1991); Pantleon (1998); Pantleon and Hansen (2001); Pantleon (2005). In the statistical approach misoriented dislocation structures are considered as a random accumulation process of excess dislocations in dislocation boundaries. As was already mentioned in Section 3.4 two types of boundaries are distinguished: the incidental dislocation boundaries (IDB) are assumed to be caused by a statistical mutual trapping of dislocations, whereas a different activation of slip systems is expected on both sides of planar dislocation boundaries termed geometrically necessary boundaries (GDB). As noted in Pantleon (2005), such imbalance in the activation of slip systems between different regions can arise from an intrinsic instability of the deformation process.

As shown in the paper Kratochvíl et al. (2007), the intrinsic instability of

homogeneous plastic flow is driven by energy minimization. The long-range internal stresses which would be set up by deformation of a single volume element are reduced by deformation and rotation of neighboring volume elements Blum (1993); Blum and McQueen (1996); Blum (1996). According to this approach, the dislocations are forced by the laws of non-linear continuum mechanics to arrange themselves into patterns of varying density. From this point of view, the intrinsically developed inhomogeneity of plastic deformation is the basic reason for subgrain formation. The inhomogeneity is caused by the instability in the form of internal buckling, Biot (1963, 1965b,a). This instability is made possible by the inherent anisotropy of plastic deformation. Under certain circumstances, more energy is needed in the uniform plastic deformation than it is required to initiate an internal mode of buckling. In Kratochvíl (1990b); Kratochvíl and Orlová (1990); Kratochvíl and Sedláček (2003); Kratochvíl et al. (2007) it has been shown that the internal buckling leads to the build up of lattice misorientations between neighboring volume elements. The periodic patterns of excess dislocations necessary to accommodate the lattice misorientations were interpreted as the beginning of subgrain formation.

The method is based on mechanics of incremental deformations proposed by Biot (1965a). Biot's theory provides rigorous and completely general equations governing the dynamics and stability of solids and fluids under initial stress in the context of small perturbations. It is applicable to anisotropic, viscoelastic, or plastic media. Biot's approach is employed in an analysis of a strain gradient rigid-plastic model of crystalline solids, Kratochvíl et al. (2007). It provides an insight into an initiation of the subgrain formation and into the mechanism controlling the subgrain size. In order to introduce a physically relevant scale to our problem we assume, following the earlier work Dillon and Kratochvíl (1970), that the energy in the system depends also on the gradient of the plastic variables. The gradient terms represent non-local effects caused by short-range interactions among dislocations. It is not clear, however, which function of the gradients should be used. We refer to Kratochvíl and Sedláček (2008), and to Groma and Bakó (2000) for the attempts to derive a gradient constitutive equation from the statistics of discrete dislocations which reveals the complexity of the problem, as has been shown in Section 5. The constitutive relations of gradient continua are advocated e.g. by Gurtin (2000), Mainik and Mielke (2009), or Conti and Ortiz (2005) and also investigated in Svendsen et al. (2009), mostly in the relation to the so-called size effect. The mathematical theory of a rate-independent isothermal evolution with gradients of plastic variables is developed in Giacomini and Lussardi (2008). An interesting recent contribution by Gurtin and Anand (2009) discusses the flow rules for

rate-independent gradient plasticity proposed by Fleck and Hutchinson. As a key result they showed that the flow rule of Fleck and Hutchinson (1997) is incompatible with thermodynamics unless its nonlocal term is skipped. A physically sound gradient plasticity theory within the framework of small deformations is developed in Gurtin et al. (2007). A survey of non-local models in plasticity appeared in Jirásek and Bažant (2002).

Crystal plasticity

The energetic and incremental methods are based on the crystal plasticity framework introduced in classical papers, e.g. Asaro (1983); Harren et al. (1988) and recalled e.g. in Gurtin (2000). Here the rigid-plastic rate independent approximation to crystal plasticity is considered; this framework seems to be sufficient to catch the essence of the subgrain formation problem.

Each material point of a crystal can be identified by its position in a reference configuration. The point which was at the position $\vec{X}$ in the reference configuration is in the current configuration in time t in the position $\vec{x}(\vec{X},t)$. The difference $\boldsymbol{u} = \vec{x} - \vec{X}$ is the displacement of the material point $\vec{X}$. The deformation of the material is described by the transformation $\boldsymbol{F}$ of an infinitesimal material fiber from the reference to the current configuration,

$$\mathrm{d}\vec{x} = \boldsymbol{F}\mathrm{d}\vec{X}\,. \tag{112}$$

Assuming that $\vec{x}(\vec{X},t)$ is a continuous and differentiable vector field, this transformation can be introduced as the deformation gradient $\boldsymbol{F} = \partial\vec{x}/\partial\vec{X} = \boldsymbol{I} + \partial\vec{u}/\partial\vec{X}$, where $\boldsymbol{I}$ is the second order identity tensor. In the rigid-plastic approximation the crystal lattice can (rigidly) rotate but it is not (elastically) strained. The plastic deformation of a crystal can be decomposed in two steps. First, the material flows through the crystal lattice by shearing along the active slip systems to reach an intermediate configuration. This step is described by the plastic deformation gradient $\boldsymbol{F}^{\mathrm{p}}$, $\det\boldsymbol{F}^{\mathrm{p}} = 1$. Second, the plastic deformation $\boldsymbol{F}^{\mathrm{p}}$ is followed by a rigid rotation $\boldsymbol{R}(\vec{x},t)$ of the lattice representing the elastic part of the deformation gradient[4]. The corresponding decomposition reads

$$\boldsymbol{F} = \boldsymbol{R}\boldsymbol{F}^{\mathrm{p}}\,, \tag{113}$$

hence, $\det\boldsymbol{F} = 1$. The plastic deformation gradient $\boldsymbol{F}^{\mathrm{p}}$ transforms the reference configuration into the lattice (intermediate) configuration, $\boldsymbol{R}$ trans-

[4]In terms of Rajagopal and Srinivasa (2001) $\boldsymbol{R}$ represents the rotation of the crystal lattice from its natural configuration.

forms the lattice configuration to the current configuration, and $\boldsymbol{F}$ transforms the reference configuration into the current configuration.

Unlike $\boldsymbol{F}$, the tensors $\boldsymbol{F}^{\mathrm{p}}$ and $\boldsymbol{R}$ do not generally correspond to a gradient of a vector field, i.e. they may be individually incompatible. In case of inhomogeneous plastic deformation $\boldsymbol{F}^{\mathrm{p}}$, the lattice rotation $\boldsymbol{R}$ can reestablish the compatibility of the overall material deformation. The density of the geometrically necessary dislocations, required for the material to be compatible, can be characterized by the GND density tensor $\boldsymbol{\Lambda} = \boldsymbol{R}^{\mathrm{T}} \operatorname{curl}(\boldsymbol{R}^{\mathrm{T}})$ (an overview and analysis of various measures of GND density is given in Cermelli and Gurtin (2001)). The GND density tensor $\boldsymbol{\Lambda}$ represents the misoriented deformation substructure seen in electron micrographs.

The velocity $\vec{v}$ of a material point is given by the material time derivative of its position, $\vec{v}(\vec{x},t) = \dot{\vec{x}}(\vec{X},t)$. Now we perform the material time derivative of eq. (112),

$$\mathrm{d}\dot{\vec{x}} = \dot{\boldsymbol{F}}\mathrm{d}\vec{X} = \frac{\partial \vec{v}(\partial\vec{x},t)}{\partial \vec{X}}\,\mathrm{d}\vec{X} = \frac{\partial \vec{v}}{\partial \vec{x}}\boldsymbol{F}\boldsymbol{F}^{-1}\mathrm{d}\vec{x} = \boldsymbol{L}\mathrm{d}\vec{x}\,, \tag{114}$$

where $\boldsymbol{L}(\vec{x},t) = \dot{\boldsymbol{F}}\boldsymbol{F}^{-1} = \partial\vec{v}/\partial\vec{x}$ is the velocity gradient. Using eq. (113)

$$\boldsymbol{L} = \boldsymbol{L}^{\mathrm{p}} + \dot{\boldsymbol{R}}\boldsymbol{R}^{T}\,, \tag{115}$$

where $\boldsymbol{L}^{\mathrm{p}}$ is the plastic flow represented by the rate of plastic distortion in the current configuration and $\dot{\boldsymbol{R}}\boldsymbol{R}^{T}$ is the lattice spin.[5]

The flow takes place on prescribed slip systems (i), $i = 1, 2, \ldots, I$. In the current configuration (i)th slip system is defined by the unit vector $\vec{s}^{(i)}$ in the direction of slip and by the unit normal to the glide plane $\vec{n}^{(i)}$. The lattice vectors $\vec{s}^{(i)}$ and $\vec{n}^{(i)}$ rotate rigidly from the lattice configuration into the current configuration, $\vec{s}^{(i)} = \boldsymbol{R}\vec{s}_0^{(i)}$ and $\vec{n}^{(i)} = \boldsymbol{R}\vec{n}_0^{(i)}$ where $\vec{s}_0^{(i)}, \vec{n}_0^{(i)}$ are the unit vectors fixed in the lattice configuration. They are determined by the crystallographic structure of the material.

The plastic flow is governed by slip rates $\nu^{(i)}(\vec{x},t)$ on the individual slip systems via the flow rule

$$\boldsymbol{L}^{\mathrm{p}} = \sum_{i=1}^{I} \nu^{(i)} \vec{s}^{(i)} \otimes \vec{n}^{(i)}\,. \tag{116}$$

[5]In detail: $\boldsymbol{L} = \dot{\boldsymbol{F}}\boldsymbol{F}^{-1} = \boldsymbol{R}\dot{\boldsymbol{F}}^{\mathrm{p}}(\boldsymbol{F}^{\mathrm{p}})^{-1}\boldsymbol{R}^{T} + \dot{\boldsymbol{R}}\boldsymbol{R}^{T}$, where $\dot{\boldsymbol{F}}^{\mathrm{p}}(\boldsymbol{F}^{\mathrm{p}})^{-1}$ is the rate of plastic distortion in the reference lattice, $\boldsymbol{R}\dot{\boldsymbol{F}}^{\mathrm{p}}(\boldsymbol{F}^{\mathrm{p}})^{-1}\boldsymbol{R}^{T} = \boldsymbol{L}^{\mathrm{p}}$ is the rate of plastic distortion rotated with the lattice into the current configuration and $\dot{\boldsymbol{R}}\boldsymbol{R}^{T}$ is the lattice spin.

The slip rate $\nu^{(i)}$ in the current configuration is driven by the resolved shear stress $\tau^{(i)}$,

$$\tau^{(i)} = \vec{s}^{(i)} \cdot (\boldsymbol{T}\,\vec{n}^{(i)})\,, \tag{117}$$

where $\boldsymbol{T}(\vec{x},t)$ is the Cauchy stress tensor. In a quasi static process with no body forces the stress $\boldsymbol{T}$ has to satisfy the equilibrium equation

$$\operatorname{div}\boldsymbol{T} = 0\,. \tag{118}$$

Within the present mechanical framework the second law of thermodynamics is reduced to the requirement that the plastic dissipation be non-negative,

$$\boldsymbol{T}\cdot\boldsymbol{D} = \sum_{i=1}^{I} \tau^{(i)}\nu^{(i)} \geq 0\,, \tag{119}$$

where $\boldsymbol{D} = 1/2(\nabla\vec{v} + (\nabla\vec{v})^T)$ and the equality in (119) follows from (115)-(117). The constitutive relations of the rate-independent rigid-plastic material are represented by the yield condition: the slip system remains active, i.e. $\nu^{(i)}$ may be non-zero, if and only if

$$\tau^{(i)} = \tau_{\mathrm{y}}^{(i)} \operatorname{sign}\nu^{(i)}\,, \tag{120}$$

if $|\tau^{(i)}| < \tau_{\mathrm{y}}^{(i)}$, the rate $\nu^{(i)} = 0$. The critical resolved shear stress $\tau_{\mathrm{y}}^{(i)}(\vec{x},t) \geq 0$ represents local dissipative internal forces that oppose slip. In a rate-independent material, $\tau^{(i)} \leq \tau_{\mathrm{y}}^{(i)}$. The requirement $\tau_{\mathrm{y}}^{(i)} \geq 0$ and the yield condition (120) guarantee the validity of the dissipation inequality (119).

Gurtin (2000) has shown that as a consequence of rate-independence the hardening evolution equation for $\tau_{\mathrm{y}}^{(i)}$ has the form

$$\dot{\tau}_{\mathrm{y}}^{(i)} = \sum_{j=1}^{I} H^{ij}\,|\nu^{(j)}|\,, \tag{121}$$

which was introduced in Section 2.3, equation (41). Here the hardening constitutive equations enriched with the higher gradient terms (106) and (107) and adopted to symmetric double slip will be used in the next subsection.

Symmetric incremental double slip

The crystal plasticity model of symmetric double slip, Fig. 42 , was proposed by Asaro (1979) and considered e.g. by Peirce et al. (1982, 1983). It falls into the class of orthotropic-symmetric models investigated by Biot (1963, 1965b,a) and Hill and Hutchinson (1975). Here it is reviewed the incremental rigid-plastic version of the model which includes higher plastic strain gradients, Kratochvíl et al. (2007).

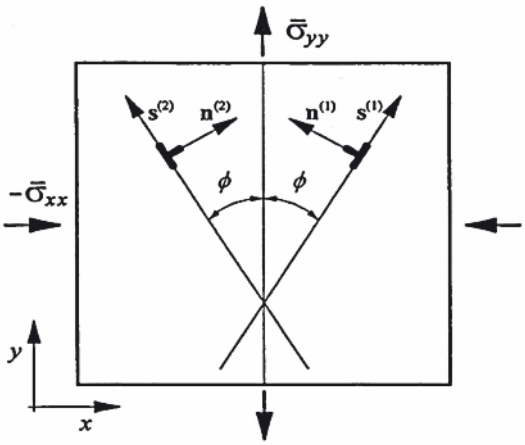

Figure 42. Symmetric double slip

Within the framework of crystal plasticity summarized above the incremental deformation of a pre-stressed crystal deformed in plane strain by symmetric double slip is represented by increments $\nabla \boldsymbol{u}$, $\boldsymbol{\omega}^*$ and $\boldsymbol{\beta}^{\mathrm{p}}$ such that

$$\boldsymbol{F} = \boldsymbol{I} + \nabla \vec{u}\,, \quad \boldsymbol{F}^{\mathrm{p}} = \boldsymbol{I} + \boldsymbol{\beta}^{\mathrm{p}}\,, \quad \boldsymbol{R} = \boldsymbol{I} + \boldsymbol{\omega}^*\,, \tag{122}$$

$\boldsymbol{\beta}^{\mathrm{p}}$ is a plastic distortion which transforms the pre-stressed homogeneous (reference) configuration into the lattice (intermediate) configuration, $\boldsymbol{\omega}^*$ measures the lattice rotation from the lattice configuration into the incremental (current) configuration, and $\nabla \vec{u}$ transforms the reference configuration into the current configuration. With higher order terms neglected the decomposition (113) in the incremental form reads

$$\nabla \vec{u} = \boldsymbol{\beta}^{\mathrm{p}} + \boldsymbol{\omega}^*\,. \tag{123}$$

From (116) for $i = 1, 2$, and from $\boldsymbol{R}\dot{\boldsymbol{F}}^{\mathrm{p}}(\boldsymbol{F}^{\mathrm{p}})^{-1}\boldsymbol{R}^T = \boldsymbol{L}^{\mathrm{p}}$ in footnote 5 the rate of plastic distortion $\dot{\boldsymbol{\beta}}^{\mathrm{p}}$ correct in the first order results in the form $\dot{\boldsymbol{\beta}}^{\mathrm{p}} = \nu^{(1)}\vec{s}^{(1)} \otimes \vec{n}^{(1)} + \nu^{(2)}\vec{s}^{(2)} \otimes \vec{n}^{(2)}$. Assuming that $\boldsymbol{\beta}^{\mathrm{p}} = 0$ initially, the time integration yields

$$\boldsymbol{\beta}^{\mathrm{p}} = \sum_{i=1}^{2} \gamma^{(i)}\vec{s}^{(i)} \otimes \vec{n}^{(i)}\,, \quad \nu^{(i)} = \dot{\gamma}^{(i)}\,, \quad \gamma^{(i)} = 0 \quad \text{initially}\,. \tag{124}$$

Hence, the incremental plastic distortion is expressed as the sum of two incremental single slips. As has been already noted in Section 2.1 the slip

increments $\gamma^{(1)}$ and $\gamma^{(2)}$ have the physical meaning only in this limited sense[6].

In the pre-stressed state the slip systems are characterized by the slip planes with unit normals $\vec{n}^{(1)} = (-\cos\phi, \sin\phi)$, $\vec{n}^{(2)} = (\cos\phi, \sin\phi)$ and slip directions $\vec{s}^{(1)} = (\sin\phi, \cos\phi)$, $\vec{s}^{(2)} = (-\sin\phi, \cos\phi)$; ϕ is the orientation angle of the slip planes with respect to the symmetry axis that coincides with axis y of $x - y$ coordinate system, Fig. 42. The lattice rotation ω^* is related to the material rotation $\omega = \omega_{xy} = (\partial_y u_x - \partial_x u_y)/2$ and plastic rotation $\omega^{\mathrm{p}} = (\gamma(1) + \gamma^{(2)})/2$

$$\omega^* = \omega - \omega^{\mathrm{p}} \,. \tag{125}$$

The density of GNDs $\boldsymbol{\Lambda} = \boldsymbol{R}^{\mathrm{T}} \operatorname{curl}(\boldsymbol{R}^{\mathrm{T}})$ in the incremental form, required for the material deformation to be compatible, is $\boldsymbol{\Lambda} = \operatorname{curl} \boldsymbol{\beta}^{\mathrm{p}} = -\operatorname{curl} \boldsymbol{\omega}^*$. $\boldsymbol{\Lambda}$ can be resolved in the densities $\boldsymbol{\Lambda}^{(i)}$, $i = 1, 2$,

$$\boldsymbol{\Lambda} = \boldsymbol{\Lambda}^{(1)} + \boldsymbol{\Lambda}^{(2)} = \sum_{i=1}^{2} \operatorname{curl}\left(\gamma^{(i)} \vec{s}^{(i)} \otimes \vec{n}^{(i)}\right) \,. \tag{126}$$

If misoriented cell boundaries are present in the crystal, the tensors $\boldsymbol{\Lambda}^{(i)}$ represent their GND composition.

The slip increments $\gamma^{(i)}$ are driven by the resolved shear stress $\tau^{(i)}$ given by (117)

$$\tau^{(i)} = \vec{s}^{(i)} \cdot (\boldsymbol{T}\, \vec{n}^{(i)}) = \vec{s}_0^{(i)} \cdot \boldsymbol{S}\, \vec{n}_0^{(i)} \,, \tag{127}$$

where $\boldsymbol{S} = \boldsymbol{R}^{\mathrm{T}}\, \boldsymbol{T}\, \boldsymbol{R}$ is the stress in the lattice configuration. Assuming the incremental stress $\boldsymbol{\sigma}'$ and rotations to be first order quantities the lattice stress $\boldsymbol{S}$ consists of three contributions[7],

$$\boldsymbol{S} = \bar{\boldsymbol{\sigma}} + \boldsymbol{\omega}^{\mathrm{p}} \bar{\boldsymbol{\sigma}} + \bar{\boldsymbol{\sigma}} (\boldsymbol{\omega}^{\mathrm{p}})^{\mathrm{T}} + \boldsymbol{\sigma}' \,, \tag{128}$$

where we suppose that the pre-stress tensor $\bar{\boldsymbol{\sigma}}$ has only diagonal components $\bar{\sigma}_{xx}$ and $\bar{\sigma}_{yy}$, Fig. 42; we denote $\triangle\bar{\sigma} = \bar{\sigma}_{yy} - \bar{\sigma}_{xx}$. The term $\boldsymbol{\omega}^{\mathrm{p}} \bar{\boldsymbol{\sigma}} + \bar{\boldsymbol{\sigma}} (\boldsymbol{\omega}^{p})^{T}$ is of the geometrical origin caused by rotation of the lattice with respect to the pre-stress configuration; it accounts for so called "geometrical hardening/softening". The incremental stress $\boldsymbol{\sigma}'$ is of the physical nature induced by incremental straining[8]. In the pre-stress configuration the projection of

[6] In this section slip increment is denoted $\gamma^{(i)}$ instead of $\mathrm{d}\gamma^{(i)}$ used in Section 2.

[7] For the increment $\boldsymbol{\sigma}'$ of the pre-stress $\bar{\boldsymbol{\sigma}}$ in the reference configuration one gets to the first order $\boldsymbol{S} = (\boldsymbol{I} + \boldsymbol{\omega}^{\mathrm{p}})(\bar{\boldsymbol{\sigma}} + \boldsymbol{\sigma}')(\boldsymbol{I} + \boldsymbol{\omega}^{\mathrm{p}})^{\mathrm{T}} \doteq \bar{\boldsymbol{\sigma}} + \boldsymbol{\omega}^{\mathrm{p}} \bar{\boldsymbol{\sigma}} + \bar{\boldsymbol{\sigma}} (\boldsymbol{\omega}^{\mathrm{p}})^{\mathrm{T}} + \boldsymbol{\sigma}'$.

[8] The pre-stressed (reference, laboratory), current (material) and lattice configurations relevant to crystal plasticity are analyzed e.g. in Sedláček et al. (2001b,a)

the pre-stress tensor $\bar{\boldsymbol{\sigma}}$ into each slip system has to be equal at yield to the initial value of critical yield stress $\pm\tau_0$, i.e. $\triangle\bar{\sigma}\sin\phi/2 = \pm\tau_0$.

The constitutive relations (120) adjusted to the double slip model are represented by the yield condition: the slip system remains active, i.e. $\dot{\gamma}^{(i)}$, $i = 1, 2$, may be non-zero, if and only if

$$\tau^{(i)} = \tau_{\mathrm{y}}^{(i)} \operatorname{sign} \dot{\gamma}^{(i)} \,. \tag{129}$$

The hardening constitutive equations are taken in the form (106) and (107) derived by the statistical consideration in Section 5.1 adjusted to the symmetric double slip for increments $\tau_{\mathrm{y}}^{(i)} - \tau_0$

$$\tau_{\mathrm{y}}^{(1)} = h\gamma^{(1)} + q\gamma^{(2)} + \tilde{h}(\vec{s}^{(1)} \cdot \nabla)^2\gamma^{(1)} + \tilde{q}(\vec{s}^{(1)} \cdot \nabla)(\vec{s}^{(2)} \cdot \nabla)\gamma^{(2)} + \tau_0 \,, \tag{130}$$

$$\tau_{\mathrm{y}}^{(2)} = q\gamma^{(1)} + h\gamma^{(2)} + \tilde{h}(\vec{s}^{(2)} \cdot \nabla)^2\gamma^{(2)} + \tilde{q}(\vec{s}^{(2)} \cdot \nabla)(\vec{s}^{(1)} \cdot \nabla)\gamma^{(1)} + \tau_0 \,, \tag{131}$$

where an unidirectional incremental loading is considered; $h = H_{11} = H_{22}$ and $q = H_{12} = H_{21}$ are the components of the symmetric matrix of the local hardening, $\tilde{h}$ and $\tilde{q}$ represent nonlocal hardening coefficients, τ_0 is the friction stress.

In analogy to (128) the Cauchy stress $\boldsymbol{T}$ in the current configuration can be expressed in the incremental form

$$\boldsymbol{T} = \bar{\boldsymbol{\sigma}} + \boldsymbol{\omega}\bar{\boldsymbol{\sigma}} + \bar{\boldsymbol{\sigma}}\boldsymbol{\omega}^{\mathrm{T}} + \boldsymbol{\sigma}' \,, \tag{132}$$

hence, the incremental stress tensor $\boldsymbol{\sigma'}$ has to satisfy the condition of the quasi-static stress equilibrium (118) for the pre-stressed sample, Biot (1965a)

$$\partial_x\sigma'_{xx} + \partial_y\sigma'_{xy} + \triangle\bar{\sigma}\partial_y\omega = 0 \,, \qquad \partial_x\sigma'_{xy} + \partial_y\sigma'_{yy} + \triangle\bar{\sigma}\partial_x\omega = 0 \,. \tag{133}$$

A variational formulation of the quasi-static stress equilibrium for a pre-stressed sample has been found in Fürst et al. (2003); Kratochvíl and Sedláček (2004) using the principle of virtual displacements (weak formulation of the problem). The formulation requires that an energy functional $\mathcal{A}$ attains a minimum

$$\delta\mathcal{A} = 0 \,. \tag{134}$$

As has been shown in Kratochvíl et al. (2007), the functional $\mathcal{A}$ in domain Ω can be expressed in the form

$$\begin{aligned}\mathcal{A} = \int_\Omega \{ & h(\gamma^{(1)} + \gamma^{(2)})^2 + 2q\gamma^{(1)}\gamma^{(2)} + 2\tilde{q}(\vec{s}^{(1)} \cdot \nabla\gamma^{(1)})(\vec{s}^{(2)} \cdot \nabla\gamma^{(2)}) \\ & + \triangle\bar{\sigma}\cos 2\phi(\gamma^{(1)} - \gamma^{(2)})(\gamma^{(1)} - \gamma^{(2)} + \omega)/2 \\ & + \tilde{h}[(\vec{s}^{(1)} \cdot \nabla\gamma^{(1)})^2 + (\vec{s}^{(2)} \cdot \nabla\gamma^{(2)})^2]\} \,\mathrm{d}V \,.\end{aligned} \tag{135}$$

In general, the variational formulation leads to a difficult optimization problem deciding which of kinematically admissible instability modes take place in the material under load. The admissible modes are formed by linear combinations of stream functions $\varphi(x+\xi y)$. The stream function φ is related to the displacement $\vec{u}$, so that $u_x = \partial_y\varphi, u_y = -\partial_x\varphi$. The modes represent deformation bands perpendicular to the direction $\xi = \tan\theta$, where θ is the angle between the y-axis and the normal to the band.

To illustrate the proposed incremental variational method a reduced problem has been analyzed in Kratochvíl et al. (2007). The set of deformation modes to be optimized has been restricted to subgrain structures arising from superposition of two periodically arranged sets of parallel deformation bands in a form of lamellae perpendicular to directions ξ and $-\xi$. In each lamella, and hence in each subgrain, the increments $\gamma^{(1)}, \gamma^{(2)}$ and ω are supposed to be uniform. Slip is adjusted so that in the direction perpendicular to the lamellae the incremental slips average to zero. The width L of the lamellae, which specifies the size of the subgrains, is taken to be the same for all the lamellae; for physical reasons it is required that $L > 0$. In this case, the gradient terms $\vec{s}^{(i)}.\nabla\gamma^{(i)}$ are replaced by the difference in slip increments $\gamma^{(i)}$ in the neighboring subgrains divided by the width of the boundary δ. The non-local terms in (135) with $\tilde{h}$ and $\tilde{q}$ thus represent the energy of the subgrain boundaries. The optimization is then reduced to the problem to find out the subgrain structure of a preferred subgrain size L and a preferred orientations $\pm\xi$ which minimize the functional $\mathcal{A}$. With $\vec{s}^{(i)}.\nabla\gamma^{(i)}$ replaced by the jump in $\gamma^{(i)}$ divided by δ and multiplied by the subgrain boundary surface, the functional (135) becomes the function of L and ξ

$$\mathcal{A}_{\mathrm{red}}(L,\xi) = \frac{16V\pi^2a^2}{L^2}\left(\frac{h+q}{\sin^2 2\phi}\xi^2 + \frac{h-q+\triangle\bar{\sigma}\cos 2\phi}{4\cos^2 2\phi}(1-\xi^2)^2 - \frac{\triangle\bar{\sigma}}{4}(1-\xi^4)\right) + \frac{64V\pi^2a^2}{L^3}\left(\frac{\tilde{h}+\tilde{q}}{\sin^2 2\phi}\xi^2 + \frac{\tilde{h}-\tilde{q}}{4\cos^2 2\phi}(1-\xi^2)^2\right), \tag{136}$$

where V is the volume of the domain Ω and a is the amplitude of the incremental displacement in the subgrain boundaries.

The subgrain structure will form if the difference between the function $\mathcal{A}_{\mathrm{red}}$ given by (136) and the corresponding function for the equivalent homogeneous deformation is negative. In that case the non-homogeneous deformation is energetically preferred. As the average incremental deformation is zero, the function for the equivalent homogeneous deformation vanishes and the condition for appearance of the subgrain structure considered is

$\mathcal{A}_{\rm red}(L,\xi) < 0$. For a given orientation of the slip systems ϕ and the pre-stress $\triangle\bar{\sigma}$ the condition $\mathcal{A}_{\rm red} < 0$ delimits instability regions of the material parameters under which the considered deformation substructure may occur. This finding represents an extension of the result for symmetric double slip in plane strain where the non-local effect was excluded, Sedláček et al. (2001b,a).

The necessary conditions $\mathcal{A}_{\rm red} < 0$ for the appearance of subgrains has been expressed in Kratochvíl et al. (2007) in terms of the hardening coefficients

$$\tilde{h} > 0\,, \quad -\tilde{h} < \tilde{q} < \tilde{h}\,, \quad q \leq h + 2\,\triangle\,\bar{\sigma}\cos 2\phi\cos^2\phi\,. \tag{137}$$

To specify sufficient conditions we are looking for $L > 0$, so that $\mathcal{A}_{\rm red} < 0$ is valid. The sufficient conditions expressed in terms of hardening coefficients are cumbersome to write; they are derived and stated in Kratochvíl et al. (2007) together with the bifurcation maps. Let us note that there exist three types of instability regions where both necessary and sufficient conditions are satisfied: A, B and C. The regions A and C correspond to the existence of shear and kink bands (Biot's instability mode of the second kind, Biot (1965a), somewhat modified by nonlocal hardening coefficients), the region B corresponds to Biot's instability mode of the first kind, which represents the internal buckling.

The minimum of $\mathcal{A}_{\rm red}$, with respect to the subgrain size L and the orientation ξ, indicates the most favorable structure formed in a bulk crystal. The conditions $\partial\mathcal{A}_{\rm red}/\partial(\xi^2) = 0$ and $\partial\mathcal{A}_{\rm red}/\partial L = 0$ yield the formulas for L and ξ derived and analyzed in Kratochvíl et al. (2007). Here the results are represented by a sketch of the preferred subgrain structure shown in Fig. 43. The content of the geometrically necessary dislocations in the subgrain boundaries is evaluated from (126).

The subgrain size L can be expressed as $L = R\,g(q/h, \tilde{q}/\tilde{h}, \triangle\bar{\sigma}/h, \phi)$, where g is the function of the parameters of the model specified in Kratochvíl et al. (2007) assuming that $h \neq 0$ and $\tilde{h} \neq 0$. $R = 4\tilde{h}/\delta h$ is the leading factor controlling the size L. The factor R demonstrates the characteristic feature of the model: bulk strain and dissipative energy tend to decrease the size, while short-range dislocation interactions restrict that tendency. The size L grows with non-local effect represented by $\tilde{h}$ (if the non-local effect is neglected, $\tilde{h} \to 0$ and the size $L \to 0$). On the other hand, increasing hardening represented by h decreases the size. As shown in Kratochvíl et al. (2007), the pre-stress has the similar effect; the size L decreases with the absolute value of the pre-stress.

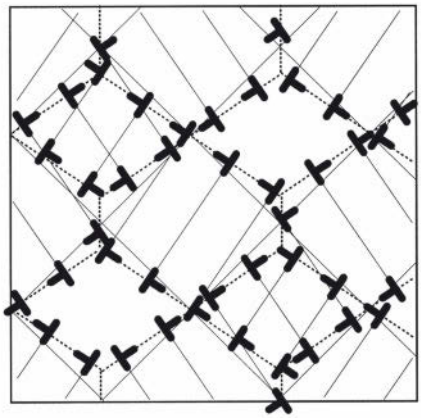

Figure 43. Sketch of the distribution of geometrically necessary dislocation in subgrain boundaries

6.3 Summary and outlook

Any substantial progress in the problem of the dislocation structure formation has to overcome at least three obstacles:

- To formulate crystal plasticity for multi slip. In incremental approach the deformations are assumed small, hence, multi slip can be treated as a sum of single slips. As noted by Gurtin (2000) the existence of a physically meaningful kinematic variable γ whose material time derivative is the slip rate ν is unique to single slip. A multi slip model has to overcome this problem.
- To specify mechanisms controlling the scale represented by the subgrain size. It seems that the size is governed by the short range interactions among dislocations. Unfortunately, it is not clear which plastic variable would describe properly this non-local effect. The current custom is to employ higher gradients of plastic strain. However, the attempt to describe the short range dislocation interactions by averaging an ensemble of discrete dislocations, as shown in Section 5, reveals the complexity of the problem and demonstrates that the gradients represent rather rough approximation.
- To combine the presented crystal plasticity approach with the statistical treatment of subgrain boundaries, Kuhlmann-Wilsdorf and Hansen (1991); Pantleon (1998); Pantleon and Hansen (2001); Pantleon (2005). The approaches seem to express just two aspects of the same reality. As noted by Pantleon (2005), the imbalance in the activation of slip

systems between different regions, which serves as the background of the statistics, can arise from an intrinsic instability of the deformation process. Therefore, it is feasible to propose a joint model combining the deterministic origin of structuralization presented here with the statistical nature of the boundaries.

7 Closing remark

Let me note that the present modeling is not able to explain fully why features like that seen in Fig.1 and in the electron micrographs of Section 3 are formed, what are the mechanisms of their formation, and how they influence the mechanical properties of ductile materials. The current understanding of the sketched scenario is still rather intuitive. Sections 4 to 6 present the examples of the attempts to answer these questions and give a survey of some modeling methods. Section 4 recalls some aspects of discrete dislocation dynamics, two continuum mechanics methods used for modeling of dislocation patterns are presented in Section 6, and dislocation statistics which should provide a transition between discrete and continuous approaches is outlined in Section 5.

There are questions: are all these microscopic details sketched briefly in the notes really necessary for a formulation of theory of plasticity reliable in engineering practice? Are they not averaged out at the macroscopic level? It is important to answer these questions as at present it seems that there is no immediate hope to overcome soon the problem of critical values of the resolved shear stress on microscopic level without a major breakthrough in this field. On the other hand, a purely macroscopic approach based on various extensions of the classical plasticity which disregards the microscopic mechanism of plastic deformation has not be successful. The problem is that there are too many possible extensions of classical plasticity and without some other information they are guide less. In my opinion, there is probably possible to come to a compromise: to use the microscopic analysis to specify the theory of plasticity as realistically as possible and to use meaningful experimental data to complete it. It means, there is lots of work for us to be done.

Acknowledgment. I would like to express my thanks to Dr. G. Winther, Technical University of Denmark, and doc. R. Sedláček, AREVA NP, for their valuable critical comments, to my wife for correcting the final text, and to K. Tůma for the technical handling of the manuscript and the figures. The research has been supported by the grants VZ-MŠMT 6840770003, VZ-MŠMT 6840770021 and GAČR - P201/10/0357.

Bibliography

F. Ackermann, L.P. Kubin, J. Lepinoux, and H. Mughrabi. The dependence of dislocation microstructure on plastic strain amplitude in cyclically strained copper single crystals. *Acta Metallurgica*, 32:715–725, 1984.

R.J. Asaro. Geometrical effects in the inhomogeneous deformation of ductile single crystals. *Acta Metallurgica*, 27:445–453, 1979.

R.J. Asaro. Micromechanics of crystals and polycrystals. *Advances in Applied Mechanics*, 23:1–115, 1983.

S.J. Basinski and Z.S. Basinski. Plastic deformation and work hardening. In Nabarro F.R.N., editor, *Dislocations in Solids*, pages 261–362, Amsterdam, 1979. North-Holland.

Z.S. Basinski. Dislocation distribution in deformed copper single crystals. *Discussions of Faraday Society*, 38:93–101, 1964.

Z.S. Basinski and S.J. Basinski. The cyclic deformation of copper single crystals. *Progress in Materials Science*, 36:89–148, 1992.

B. Bay, N. Hansen, D.A. Hughes, and D. Kuhlmann-Wilsdorf. Evolution of f.c.c. deformation structures in polyslip. *Acta Metallurgica et Materialia*, 40:205–219, 1992.

M. Beneš, J. Kratochvíl, J. Křišťan, V. Minárik, and P. Pauš. A parametric simulation method for discrete dislocation dynamics. *European Physical Journal ST, Special Topics*, 177:061802–061815, 2009.

M. Berveiller and A. Zaoui. Extension of the self-consistent scheme to plastically-flowing polycrystals. *J. Mechanics and Physics of Solids*, 26: 325, 1978.

M.A. Biot. *Mechanics of Incremental Deformations*. John Willey, 1965a.

M.A. Biot. Internal buckling under initial stress in finite elasticity. *Proceedings Royal Society A*, 273:306–328, 1963.

M.A. Biot. Internal instability of anisotropic viscous and viscoelastic media under initial stress. *Journal of the Franklin Institute*, 279:65–82, 1965b.

W. Blum. Dislocation structure evolution and deformation kinetics of pure materials. In *The Johannes Weertman Symposium*, pages 103–117, 1996.

W. Blum. High-Temperature Deformation and Creep of Crystalline Solids. In R.W. Cahn, p. Haasen, and E.J. Kramer, editors, *Materials Science and Technology, volume 6, chapter 8*, pages 359–405, 1993.

W. Blum and H.J. McQueen. Dynamics of recovery and recrystallization. *Materials Science Forum*, 217–222:31–42, 1996.

J. Bretschneider and C. Holste. Cyclic plasticity of fcc single crystals - from nanoscale to macroscale. In J.V. Carstensen et al., editor, *Proceedings of the 19th Risoe Int. Symposium on Material Science: Modelling of Structure and Mechanics of Materials from Microscale to Product*, pages 25–38. Risoe National Laboratory, Roskilde, Denmark, 1998.

L.M. Brown. Dislocation bowing and passing in persistent slip bands. *Philosophical Magazine*, 86:4055, 2006.

L.M. Brown. The self stress of dislocations and the shape of extended nodes. *Philosophical Magazine*, 10:441–466, 1964.

B. Budiansky and T.T. Wu. Theoretical prediction of plastic strain of polycrystals. In *4th Congress Applied Mechanics*, page 1175, 1962.

P. Cermelli and M. Gurtin. On the characterization of geometrically necessary dislocations in finite plasticity. *J. Mechanics and Physics of Solids*, 49:1539–1568, 2001.

S. Conti and M. Ortiz. Dislocationtion microstructures and the effective behavior of single crystals. *Archive of Rational Mechanics and Analysis*, 176:103–147, 2005.

R. de Wit. Some relations for straight dislocations. *physica status solidi*, 20:567–570, 1967.

G. De Witt and J.S. Koehler. Interaction of dislocations with an applied stress in anisotropic crystals. *Physical Review*, 116:1113–1120, 1959.

B. Devincre. Three dimensional stress field expressions for straight dislocation segments. *Solid State Communications*, 93:875–878, 1995.

B. Devincre and L.P. Kubin. Mesoscopic simulations of dislocations and plasticity. *Materials Science and Engineering*, A234-236:8–14, 1997.

O.W. Dillon and J. Kratochvíl. A strain gradient theory of plasticity. *Int. J. Solids and Structures*, 6:1513–1533, 1970.

G. Dziuk. Convergence of a semi discrete scheme for the curve shortening flow. *Mathematical Models and Methods in Applied Sciences*, 4:589–606, 1994.

J.A. El-Awady, N.M. Ghoniem, and H. Mughrabi. Dislocation modelling of localized plasticity in persistent slip bands. In B. Adams and A. Garmestani, editors, *Proc. of the 136th TMS Annual Meeting and Exhibition, Materials Processing and Manufacturing Division Symposium: Mechanics and Materials Modeling and Materials Design Methodologies, Feb. 25 - Mar. 1, 2007, Orlando, Florida*. TMS, 2007.

A. El-Azab. The boundary value problem of dislocation dynamics. *Modelling and Simulation in Materials Science and Engineering*, 8:37–54, 2000a.

A. El-Azab. Statistical mechanics treatment of the evolution of dislocation distributions in single crystals. *Physical Review B*, 61:11956–11966, 2000b.

J.D. Eshelby. The determination of the elastic field of an ellipsoidal inclusion, and related problems. *Proceedings of the Royal Society of London*, 241:376–396, 1957.

U. Essmann. Elektronenmikroskopische Untersuchung der Versetzungsanordnung Verformter Kupfereinkristalle. 2. Die Versetzungsanordnung im Bereich II. *physica status solidi*, 12:723–747, 1965.

U. Essmann and M. Rapp. Slip in copper crystals following weak neutron bombardment. *Acta Metallurgica*, 21:1305–1317, 1973.

M.C. Fivel and G.R. Canova. Developing rigorous boundary conditions to simulations of discrete dislocation dynamics. *Modelling and Simulation in Materials Science and Engineering*, 7:753, 1999.

N.A. Fleck and J.W. Hutchinson. Strain gradient plasticity. *Advances in Applied Mechanics*, 33:295–361, 1997.

A.J.E. Foreman. Dislocation energies in anisotropic crystals. *Acta Metallurgica*, 3:322–330, 1955.

R.A. Foxall, M.S. Duesbery, and P.B. Hirsch. The deformation of niobium single crystals. *Canadian Journal of Physics*, 45:607–629, 1967.

T. Fürst, J. Kratochvíl, and R. Sedláček. Crystal plasticity model of microstructure formation at severe strain. *Materials Science Forum*, 426-432:2759–2764, 2003.

M. Gage and R.S. Hamilton. The heat equation shrinking convex plane curves. *J. Differential Geometry*, 23:69–96, 1986.

A. Gemperle, M. Rozsíval, and B. Šesták. Electron microscope study of dislocations in slip bands of bent Fe-3%Si alloy single crystals. *Czechoslovak Journal of Physics B*, 12:555–560, 1962.

N.M. Ghoniem and L.Z. Sun. Fast sum method for the elastic field of 3-D dislocation ensembles. *Physical Review B*, 60:128–140, 1999.

N.M. Ghoniem, J. Huang, and Z. Wang. Affine covariant-contravariant vector forms for the elastic field of parametric dislocations in isotropic crystals. *Philosophical Magazine Latters*, 82:55–63, 2002.

A. Giacomini and L. Lussardi. Quasi-static evolution for a model in strain gradient plasticity. *SIAM J. Mathematical Analysis*, 40:1201–1245, 2008.

J. Gilman. *Micromechanics of flow in solids*. McGraw-Hill, New York, 1969.

V. Gregor, J. Kratochvíl, and M. Saxlová. Micromechanisms of fatigue of metals. In A. Strejc, editor, *Proceedings of Workshop 97, Prague, January 20-22, 1997*, pages 591–592. Výpočetní centrum ČVUT, 1997.

I. Groma. Link between the microscopic and mesoscopic length-scale description of the collective behavior of dislocations. *Physical Review B*, 56:5807–5813, 1997.

I. Groma and B. Bakó. Dislocation patterning: From micro- to mesoscale description. *Physical Review Letters*, 84:1487–1490, 2000.

I. Groma and P. Balogh. Investigation of dislocation pattern formation in a two-dimensional self-consistent field approximation. *Acta Materialia*, 47:3647–3654, 1999.

I. Groma, F.F. Csikor, and M. Zeiser. Spatial correlations and higher-order gradient terms in a continuum description of dislocation dynamics. *Acta Materialia*, 51:1271–1281, 2003.

I. Groma, G. Györgyi, and B. Kocsis. Dynamics of coarse grained dislocation densities from an effective free energy. *Philosophical Magazine*, 87:1185–1199, 2007.

M. Gurtin. On the plasticity of single crystals: free energy, microforces, plastic strain gradients. *J. Mechanics and Physics of Solids*, 48:989–1036, 2000.

M.E. Gurtin and L. Anand. Thermodynamics applied to gradient theories involving the accumulated plastic strain: the theories of Aifantis and Fleck and Hutchinson and their generalization. *J. Mechanics and Physics of Solids*, 57(3):405–421, 2009.

M.E. Gurtin, L. Anand, and S.P. Lele. Gradient single-crystal plasticity with free energy dependent on dislocation densities. *J. Mechanics and Physics of Solids*, 55(9):1853–1878, 2007.

M. Hafok and R. Pippan. Comparison of single crystalline and polycrystalline behavior under high pressure torsion. *Materials Science Forum*, 550:277–282, 2007a.

M. Hafok and R. Pippan. Post-shear deformation of high pressure torsion-deformed nickel under hydrostatic pressure. *Scripta Materialia*, 56:757–760, 2007b.

N. Hansen. New discoveries in deformed metals. *Metallurgical and Materials Transections A*, 32A:2917–2935, 2001.

S.V. Harren, H.E. Dève, and R.J. Asaro. Shear band formation in plane strain compression. *Acta Metallurgica*, 36:2435–2480, 1988.

T. Hebesberger, H.P. Stüwe, A. Vorhauer, F. Wetscher, and R. Pippan. Structure of Cu deformed by high pressure torsin. *Acta Materialia*, 53: 393–402, 2005.

R. Hill. Continuum micro-mechanics of elastoplastic polycrystals. *J. Mechanics and Physics of Solids*, 13:89–101, 1965.

R. Hill and J.W. Hutchinson. Bifurcation phenomena in the plane tension test. *J. Mechanics and Physics of Solids*, 23:2396–264, 1975.

T. Hochrainer. Evolving systems of curved dislocations: Mathematical foundations of a statistical theory. Master's thesis, University of Karlsruhe, Karlsruhe, November 2006.

T. Hochrainer, M. Zaiser, and P. Gumbsch. A three-dimensional continuum theory of dislocations: Kinematics and mean field formulation. *Philosophical Magazine*, 87:1261–1282, 2007.

U. Holzwarth and U. Essmann. Temperature-induced rearrangement of the dislocation pattern of persistent slip bands in copper single crystals. *J. Applied Physics*, A58:197–210, 1994.

U. Holzwarth and U. Essmann. The evolution of persistent slip bands in copper single crystals. *J. Applied Physics*, A57:131–141, 1993a.

U. Holzwarth and U. Essmann. Transformation of dislocation patterns in fatigued copper single crystals. *Materials Science and Engineering*, A164: 206–210, 1993b.

J. Huang, N.M. Ghoniem, and J. Kratochvíl. On the sweeping mechanism of dipolar dislocation loops under fatigue conditions. *Modelling and Simulation in Materials Science and Engineering*, 12:917–928, 2004.

X. Huang and G. Winther. Dislocation structures. Part I. Grain orientataion dependence. *Philosophical Magazine*, 87:5189–5214, 2007.

D.A. Hughes, S.M.A. Khan, A. Godfrey, and H.M. Zbib. Internal structure of deformation induced planar dislocation boundaries. *Materials Science and Engineering*, A309-310:220–226, 2001.

J.W. Hutchinson. Elastic-plastic behavior of polycrystalline metals and composites. *Proc. Royal Society London A*, 319:242, 1970.

P.D. Ispánovity, I. Groma, G. Györgyi, F.F. Csikor, and D. Weygand. Submicron plasticity: yield stress, dislocation avalanches, and velocity distribution. *Physical Review Letters*, 105:085503, 2010.

N.Y. Jin. Formation of dislocation structures during cyclic deformation of F.C.C. crystals - I. formation of PSBs in crystals oriented for single slip. *Acta Metallurgica*, 37:2055–2066, 1989.

N.Y. Jin and A.T. Winter. Cyclic deformation of copper single crystals oriented for double slip. *Acta Metallurgica*, 32:989–995, 1984.

M. Jirásek and Z.P. Bažant. Nonlocal integral formulation of plasticity and damage: a survey of progress. *J. Engineering Mechanics*, 128:1119–1149, 2002.

H.P. Karnthaler, F. Prinz, and G. Haslinger. Elektronenmikroskopische Untersuchung der Versetzungsstrukturen plastisch verformter Cu-5 at.% Al Einkristalle. *Acta Metallurgica*, 23:155–163, 1974.

U.F. Kocks, T. Hasegawa, and R.O. Scattergood. On the origin of cell walls and of lattice misorientations during deformation. *Scripta Metallurgica*, 14:449–454, 1980.

A.M. Kosevich. Dynamical theory of dislocations. *Soviet Physics - Uspekhi*, 7:837–854, 1965.

A.M. Kosevich. Crystal dislocations and the theory of elasticity. In F.R. Nabarro, editor, *Dislocations in Solids, Volume 1*, pages 33–142, Amsterdam-New York-Oxford, 1979. North-Holland Publishing Company.

J. Kratochvíl. Stability approach to problem of work hardening of metals. *J. Mechanical Behavior of Metals*, 2:353–368, 1990a.

J. Kratochvíl. Instability origin of dislocation cell misorientation. *Scripta Metallurgica et Materialia*, 24:1225–1228, 1990b.

J. Kratochvíl. On the dynamic origin of dislocation structures in deformed solids. *Materials Science and Engineering*, A164:15–22, 1993.

J. Kratochvíl and S. Libovický. Dipole drift mechanism of early stages of dislocation pattern formation in deformed metal single crystals. *Scripta Metallurgica*, 20:1625–1630, 1986.

J. Kratochvíl and A. Orlová. Instability origin of dislocation substructure. *Philosophical Magazine*, A 61:281–290, 1990.

J. Kratochvíl and M. Saxlová. Dislocation pattern formation and strain hardening in solids. *Physica Scripta*, T49:399–404, 1993.

J. Kratochvíl and M. Saxlová. Sweeping mechanism of dislocation pattern formation. *Scripta Metallurgica et Materialia*, 26:113–116, 1992.

J. Kratochvíl and R. Sedláček. Pattern formation in the framework of the continuum theory of dislocations. *Physical Review B*, 67:094105–094114, 2003.

J. Kratochvíl and R. Sedláček. Energetic approach to subgrain formation. *Materials Science and Engineering*, A387-389:67–81, 2004.

J. Kratochvíl and R. Sedláček. Statistical foundation of continuum dislocation plasticity. *Physical Review B*, 77, 2008.

J. Kratochvíl, M. Saxlová, and R.Sedláček. An unified model of sweeping and drift mechanisms of the formation of dipolar dislocation structures. *Key Engineering Materials*, 97-98:479–484, 1994.

J. Kratochvíl, M. Saxlová, B. Devincre, and L.P.Kubin. On the sweeping of dipolar loops by gliding dislocations. *Materials Science and Engineering*, A234-236:318–321, 1997.

J. Kratochvíl, M. Kružík, and R. Sedláček. Statistically based continuous model of dislocation cell structure formation. *Physical Review*, B 75: 064104–14, 2007.

J. Kratochvíl, M. Kružík, and R. Sedláček. A model of ultrafine microstructure evolution in materials deformed by high pressure torsion. *Acta Materialia*, 57:739–748, 2009.

J. Kratochvíl, M. Kružík, and R. Sedláček. Model of structural fragmentation induced by high pressure torsion. *Review of Advance Materials Science*, 25:88–98, 2010a.

J. Kratochvíl, M. Kružík, and R. Sedláček. Crystal plasticity model of shear and kink bands - energetic approach. *Philosophical Magazine A*, 90:3729–3742, 2010b.

E. Kröner. Benefits and shortcomings of the continuous theory of dislocations. *Int. J. Solids and Structures*, 38:1115–1134, 2001.

E. Kröner. Zur plastischen Verformung des Vielkristalls. *Acta Metallurgica*, 9:155, 1961.

D. Kuhlmann-Wilsdorf and N. Hansen. Geometrically necessary, incidental and subgrain boundaries. *Scripta Metallurgica et Materialia*, 25:1557–1562, 1991.

D. Kuhlmann-Wilsdorf and C. Laird. Dislocation behavior in fatigue. *Materials Science and Engineering*, 27:137–156, 1977.

J. Křišťan and J. Kratochvíl. Interactions of glide dislocations in a channel of a persistent slip band. *Philosophical Magazine*, 87:4593–4613, 2007a.

J. Křišťan and J. Kratochvíl. Estimates of stress in the channel of persistent slip bands based on dislocation dynamics. *Materials Science Forum*, 567–568:405–408, 2007b.

J. Křišťan and J. Kratochvíl. Bowing out of dislocations from walls of persistent slip band. *International Journal of Materials Research*, 101: 680–683, 2010.

J. Křišťan, J. Kratochvíl, V. Minárik, and M. Beneš. Simulation of interacting dislocations glide in a channel of a persistent slip band. *Modelling and Simulation in Materials Science and Engineering*, 17:045009–045026, 2009.

C. Laird, P. Charsley, and H. Mughrabi. Low energy dislocation structures produced by cyclic deformation. *Materials Science and Engineering*, 81: 433–450, 1986.

C. Lemarchand, B. Devincre, and L.P. Kubin. Homogenization method for a discrete-continuum simulation of dislocation dynamics. *J. Mechanics and Physics of Solids*, 49:1969, 2001.

S. Libovický and B. Šesták. Development of the dislocation arrangement in Fe-0.9 wt% Si single crystals deformed in tension. *Philosophical Magazine A*, 47:63–78, 1983.

J.R. Low and A.M. Turkalo. Slip band structure and dislocation multiplication in silicon-iron crystals. *Acta Metallurgica*, 10:215, 1962.

A. Mainik and A. Mielke. Global existence for rate-independent gradient plasticity at finite strain. *J. Nonlinear Science*, 19(3):221–248, 2009.

G.A. Malygin. Dislocation self-organization processes and crystal plasticity. *Progress in Physics*, 169:979–1010, 1999.

K. Mecke, C. Blochwitz, and U. Kremling. The development of the dislocation structures during the fatigue process of f.c.c. single crystals. *Crystal Research and Technology*, 17:1557–1570, 1982.

K. Mikula and D. Ševčovič. Evolution of plane curves driven by a nonlinear function of curvature and anisotropy. *SIAM J. Applied Mathematics*, 61: 1473–1501, 2001.

K. Mikula and D. Ševčovič. A direct method for solving an anisotropic mean curvature flow of plane curves with an external force. *Mathematical Methods in Applied Sciences*, 27:1545, 2004.

V. Minárik and J. Kratochvíl. Dislocation dynamics - analytical description of the interaction force between dipolar loops. *Kybernetika*, 43:841–854, 2007.

V. Minárik, J. Kratochvíl, K. Mikula, and M. Beneš. Numerical simulation of dislocation dynamics. In M. Feustauer et al., editor, *5th Eropean Coference on Numerical Mathematics and Advanced Applications ENUMATH 2003*, pages 631–641. Springer Verlag, 2004.

V. Minárik, M. Beneš, and J. Kratochvíl. Simulation of dynamical interaction between dislocations and dipolar loops. *Journal Applied Physics*, 107:841–854, 2010.

D.M. Moon and W.H. Robinson. Dislocation distribution in deformed silver single crystals. *Canadian Journal of Physics*, 45:1017–1030, 1967.

H. Mughrabi. Description of the dislocation structure after unidirectional deformation at low temperatures. In A.S. Argon, editor, *Constitutive Equations in Plasticity*, pages 199–250. M.I.T. Press, Cambridge, Massachusetts and London,. England, 1975.

H. Mughrabi. Cyclic plasticity of matrix and persistent slip bands in fatigued metals. In O. Brulin and R.K.T. Hsieh, editors, *Continuum Models of Discrete Systems*, pages 241–257, Stockholm, 1981. North-Holland.

H. Mughrabi. Dislocation wall and cell structures and long-range internal stresses in deformed metal crystals. *Acta Metallurgica*, 31:1367–1379, 1983.

H. Mughrabi. Dual role of deformation-induced geometrically necessary dislocations with respect to lattice plane misorientations and/or long-range internal stresses. *Acta Materialia*, 54:3417–3427, 2006a.

H. Mughrabi. Deformation-induced long-range internal stresses and lattice plane misorientations and the role of geometrically necessary dislocations. *Philosophical Magazine*, 86:4037–4054, 2006b.

H. Mughrabi and B. Obst. Misorientations and geometrically necessary dislocations in deformed copper crystals: A microstructural analysis of X-ray rocking curves. *Z. Metallkunde*, 96:686–695, 2005.

H. Mughrabi and F. Pschenitzka. Constrained glide and interaction of bowed-out screw dislocations in cofined channels. *Philosophical Magazine*, 85:3029, 2005.

A. Orlová and J. Čadek. On the origin of the dislocation substructure during high-temperature creep. *Philosophical Magazine*, 21:509–518, 1970.

C.S. Pande and P.M. Hazzledine. Dislocation arrays in Cu-Al alloys.I. *Philosophical Magazine*, 24(191):1039–1057, 1971a.

C.S. Pande and P.M. Hazzledine. Dislocation arrays in Cu-Al alloys.II. *Philosophical Magazine*, 24(192):1393–1410, 1971b.

W. Pantleon. Disorientations in dislocation structures. *Materials Science and Engineering*, A 400-401:118–124, 2005.

W. Pantleon. On the statistical origin of disorientations in dislocation structures. *Acta Materialia*, 46:451–456, 1998.

W. Pantleon and N. Hansen. Dislocation boundaries - the distribution function of disorientation angles. *Acta Materialia*, 49:1479–1493, 2001.

D. Peirce, R.J. Asaro, and A. Needleman. An analysis of nonuniform and localised deformation in ductile single crystals. *Acta Metallurgica*, 30: 1087–1119, 1982.

D. Peirce, R.J. Asaro, and A. Needleman. Material rate dependence and localized deformation in crystalline solids. *Acta Metallurgica*, 31:1951–1976, 1983.

F. Prinz and A.S. Argon. Dislocation cell formation during plastic deformation of copper single crystals. *physica status solidi (a)*, 57:741–753, 1980.

K.R. Rajagopal and A.R. Srinivasa. Modeling anisotropic fluids within the framework of bodies with multiple natural configurations. *J. Non-Newtonian Fluid Mechanics*, 99(2-3):109–124, 2001.

M. Rhee, H.M. Zbib, J.P. Hirth, H. Huang, and T. de la Rubia. Models for long-/short-range interactions and cross slip in 3D dislocation simulation of bcc crystals. *Modelling and Simulation in Materials Science and Engineering*, 6:467, 1998.

M. Saxlová, J. Kratochvíl, and J. Zatloukal. The model of formation and disintegration of vein dislocation structure. *Materials Science and Engineering*, A234-236:205–208, 1997.

H. Schmid and H.O.K. Kirschner. Self-stress and equilibrium shapes of dislocation loops. *Philosophical Magazine A*, 58:905–921, 1988.

R. Sedláček. Viscous glide of a curved dislocation. *Philosophical Magazine Letters*, 76:275–280, 1997.

R. Sedláček, W. Blum, J. Kratochvíl, and S. Forest. Subgrain formation during deformation: Physical origin and consequences. *Metallurgical and Materials Transections A*, 32A:1–9, 2001a.

R. Sedláček, J. Kratochvíl, and W. Blum. Plastic instability and misoriented crystal lattice. *physica status solidi*, 186:1–16, 2001b.

R. Sedláček, J. Kratochvíl, and E. Werner. The importance of being curved: bowing dislocations in a continuum description. *Philosophical Magazine*, 83:3735–3752, 2003.

R. Sedláček, C. Schwarz, J. Kratochvíl, and E. Werner. Continuum theory of evolving dislocation fields. *Philosophical Magazine*, 87:1225–1260, 2007.

J.W. Steeds. Dislocation arrangement in copper single crystals as a function of strain. *Proc. Royal Society*, A 292:343–373, 1966.

J.W. Steeds and P.M. Hazzledine. Dislocation configurations in deformed copper and copper 10% (atomic) aluminium alloy. *Discussions of Faraday Society*, 38:103–110, 1964.

B. Svendsen, P. Neff, and A. Menzel. On constitutive and configurational aspects of models for gradient continua with microstructure. *ZAMM, Z. Angewandte Mathematik und Mechanik*, 89(8):687–697, 2009.

M. Tang, L.P. Kubin, and G.R. Canova. Models for long-/short-range interactions and cross slip in 3d dislocation simulation of bcc crystals. *Acta Materialia*, 46:3221, 1998.

B. Tippelt, J. Bretschneider, and C. Holste. Influence of temperature on microstructural parametrs of cyclically deformed nickel single crystals. *Philosophical Magazine Letters*, 74:161–166, 1996.

R.Z. Valiev and T.G. Langdon. Principles of equal-channel angular pressing as a processing tool for grain refinement. *Progress in Materials Science*, 51:881–981, 2006.

S. Verecký, J. Kratochvíl, and F. Kroupa. The stress field of rectangular prismatic dislocation loops. *physica status solidi (a)*, 191:418–426, 2002.

B. Šesták, V. Novák, and S. Libovický. Cyclic deformation of single crystals of iron-silikon alloys oriented for single slip. *Philosophical Magazine A*, A 57:353–381, 1988.

W. Wasserbach. Plastic deformation and dislocation arrangement of Nb-34at.%Ta alloy single crystals. *Philosophical Magazine A*, 53:335–356, 1986.

F. Wetscher and R. Pippan. Cyclic high-pressure torsin of nickel and Armco iron. *Philosophical Magazine*, 86:5867–5883, 2006.

A.T. Winter, O.B. Pedersen, and Rasmussen. Dislocation microstructure in fatigued copper polycrystals. *Acta Metallurgica*, 29:735–748, 1981.

G. Winther. Effect of grain orientation dependent microstructures on flow stress anisotropy modelling. *Scripta Materialia*, 52:995–1000, 2005.

G. Winther and X. Huang. Dislocation structures. Part II. Slip system dependence. *Philosophical Magazine*, 87:5215–5235, 2007.

S. Yefimov, I. Groma, and E. van der Giessen. A comparison of a statistical-mechanics based plasticity model with discrete dislocation plasticity calculations. *J. Mechanics and Physics of Solids*, 52:279–300, 2004a.

S. Yefimov, E. van der Giessen, and I. Groma. Bending of a single crystal: discrete dislocation and nonlocal crystal plasticity simulations. *Modelling and Simulation in Materials Science and Engineering*, 12:1069–1086, 2004b.

M. Zaiser and T. Hochrainer. Some steps towards a continuum representation of 3D dislocation systems. *Scripta Materialia*, 54:717–721, 2006.

M. Zaiser, M.-Carmen Miguel, and I. Groma. Statistical dynamics of dislocation systems: The influence of dislocation-dislocation interactions. *Physical Review B*, 64:224102, 2001.

A.P. Zhilyaev and T.G. Langdon. Using high-pressure torsion for metal processing: Fundamentals and applications. *Progress in Materials Science*, 53:893–979, 2008.

On scale-dependent crystal plasticity models

Mitsutoshi Kuroda

Graduate School of Science and Engineering, Mechanical Engineering, Yamagata University, Jonan 4-3-16, Yamagata 992-8510, Japan
Corresponding author:

Abstract An extended crystal plasticity theory that accounts for the length-scale effects in plastic strain gradient fields is presented. First, foundations and kinematics of crystal plasticity theory is reviewed. Then, experimental evidences for the size-effects in small-sized bent single crystals are presented. Total amounts of apparent strain hardening, which were experimentally observed, are decomposed into isotropic and kinematic hardening components. Physically-based models are formulated to describe the size-dependent isotropic and kinematic hardening behaviors, utilizing possible micromechanical information with respect to dislocations and their motions. Roles of the geometrically necessary dislocations (GNDs) in strain hardening behavior are studied in detail. Furthermore, some aspects of numerical computations of the extended size-dependent crystal plasticity theory are presented. The developed theory involves extra boundary conditions for crystallographic slips and/or the GND densities. Effects of these extra boundary conditions are demonstrated through numerical simulations for some basic boundary value problems. Finally, a phenomenological strain gradient plasticity theory is revisited, based on the knowledge from the present size-dependent crystal plasticity theory.

1 Introduction

In use of phenomenological theories of plasticity, first, mathematical forms of yield function and plastic potential function have to be assumed. Then, values of the parameters included in them are identified using a series of mechanical testing such as uniaxial and biaxial tensile, and/or shearing tests. With such theories, macroscopic material behavior observed in experiments may be efficiently reproduced or simulated. The physical origins of the material behavior, however, are not understood from the simulation results. If our purpose is to understand origins of the material response, contribution of the phenomenological theories is very limited.

J. Schröder, K. Hackl (Eds.), *Plasticity and Beyond*, CISM International Centre for Mechanical Sciences, DOI 10.1007/978-3-7091-1625-8_5,

Efforts to develop material models accounting for microstructural effects will result in deep understanding of the mechanics and physics of the material behavior. The knowledge gained through such modeling may lead to a fountain of ideas for new material designs. Crystal plasticity theory initiated by Taylor (1938) may be a suitable framework for such an advanced modeling strategy. Crystal plasticity is a continuum mechanics-based theory. Therefore, it can be directly applied to large-scale computations such as metal forming simulations (Nakamachi et al. (2001)). Meanwhile, various kinds of micromechanical information with respect to crystal defects (dislocations) can be incorporated into the crystal plasticity framework.

Predictability of realistic material behavior of crystalline materials in a plastic regime rests on ability of the theory to express anisotropy of the material and to describe exact instantaneous plastic straining modes. The former is naturally incorporated in the conventional crystal plasticity theory since slip systems reflecting a realistic crystal structure are directly introduced to the theory. The latter nature is also inherently involved in a standard crystal plasticity model. Generally, crystals are deformed in multi-slip conditions. The loading point in a stress space is positioned at a vertex point on the hyper-polygon constructed by the yield planes for different slip systems. Due to this vertex effect, an abrupt change in the direction of plastic strain rate is allowed with small change in the total stress state, which relates to occurrence of strain localization behavior in the form of shear bands that emerge abruptly from a uniformly straining field. This type of abrupt change in plastic straining mode or strain localization behavior is never predicted by phenomenological theories with a smooth plastic potential and the normality rule. Thus, the crystal plasticity model naturally represents the two distinct features of crystalline materials: (i) anisotropic material behavior due to a specific crystal structure and (ii) vertex effects realized by multi-slip deformations.

At scales of the order of tens of microns or smaller, mechanical responses of metallic materials are significantly dependent on their size. The framework of the conventional crystal plasticity theories, however, does not involve any material length scales.

In this article, an extension of crystal plasticity theory to incorporate length-scale effect is presented. In Section 2, foundations and kinematics of the crystal plasticity theory is reviewed. In Section 3, experimental evidences for the size-effects in small-sized bent copper single crystals are presented. Total amounts of strain hardening, which were observed in the experiments, are decomposed into isotropic and kinematic hardening components. In Section 4, modeling of the size-effects is discussed. Physically-based models are derived to describe the size-dependent isotropic and kine-

matic hardening behaviors, utilizing possible micromechanical information, i.e. knowledge of dislocations and their motions. Spatial gradients of the crystallographic slip correspond to densities of the geometrically necessary dislocations (GNDs), which are considered to be an origin of the size effects. Roles of the GNDs in the strain hardening behavior are studied in detail, and the GND densities are introduced into formulations of the extended crystal plasticity model. In Section 5, some aspects of numerical computations of the scale-dependent crystal plasticity models developed in Section 4 are presented. In Section 6, a phenomenological strain gradient plasticity theory, which was originally formulated by Aifantis (1984), is revisited using the knowledge from the scale-dependent advanced crystal plasticity theory developed in Section 4.

2 Basics of crystal plasticity

The deformation gradient $\boldsymbol{F}$ is assumed to be decomposed into elastic and plastic parts multiplicatively (Kröner (1960); Lee (1969)) as

$$\boldsymbol{F} = \frac{\partial \boldsymbol{x}}{\partial \boldsymbol{X}} = \boldsymbol{F}^{\mathrm{e}} \cdot \boldsymbol{F}^{\mathrm{p}}, \quad \det \boldsymbol{F}^{\mathrm{p}} = 1, \quad \det \boldsymbol{F} \equiv J = \det \boldsymbol{F}^{\mathrm{e}}, \tag{1}$$

where $\boldsymbol{X}$ and $\boldsymbol{x}$ denote the positions of material points in the undeformed and the deformed configurations, respectively, $\boldsymbol{F}^{\mathrm{e}}$ involves small elastic stretches and rigid body rotations of the lattice, $\boldsymbol{F}^{\mathrm{p}}$ involves plastic deformations, J is the ratio of the current volume to the volume at the undeformed state, and it is assumed that all volumetric changes result from elastic stretches in the lattice. Based on Eq. (1), the velocity gradient $\boldsymbol{L}$ is additively decomposed as

$$\left.\begin{array}{c} \operatorname{grad} \boldsymbol{v} \equiv \boldsymbol{L} = \dot{\boldsymbol{F}} \cdot \boldsymbol{F}^{-1} = \boldsymbol{L}^{\mathrm{e}} + \boldsymbol{F}^{\mathrm{e}} \cdot \boldsymbol{L}^{\mathrm{p}} \cdot \boldsymbol{F}^{\mathrm{e}-1}, \\ \boldsymbol{L}^{\mathrm{e}} = \dot{\boldsymbol{F}}^{\mathrm{e}} \cdot \boldsymbol{F}^{\mathrm{e}-1}, \quad \boldsymbol{L}^{\mathrm{p}} = \dot{\boldsymbol{F}}^{\mathrm{p}} \cdot \boldsymbol{F}^{\mathrm{p}-1} \end{array}\right\} \tag{2}$$

where $\boldsymbol{v}$ is the velocity of the material point, grad denotes the spatial gradients with respect to $\boldsymbol{x}$, the superscript -1 denotes the tensor inverse, and a superposed dot denotes the material-time derivative. The plastic flow rate $\boldsymbol{L}^{\mathrm{p}}$ is presumed to be given by the superposition of crystallographic slips on different slip systems (Peirce et al. (1983)), such that

$$\boldsymbol{L}^{\mathrm{p}} = \sum_{\alpha} \dot{\gamma}^{(\alpha)} \boldsymbol{s}^{(\alpha)} \otimes \boldsymbol{m}^{(\alpha)} \tag{3}$$

where $\dot{\gamma}^{(\alpha)}$ are slip rates on the individual slip systems, $\boldsymbol{s}^{(\alpha)}$ and $\boldsymbol{m}^{(\alpha)}$ denote the constant *slip-direction* and *slip-plane* normal unit vectors, respectively,

attached to the lattice space that resides in the intermediate configuration. Substituting Eq. (3) into $(2)_1$ gives

$$\boldsymbol{L} = \boldsymbol{L}^{\mathrm{e}} + \sum_{\alpha} \dot{\gamma}^{(\alpha)} (\boldsymbol{F}^{\mathrm{e}} \cdot \boldsymbol{s}^{(\alpha)} \otimes \boldsymbol{m}^{(\alpha)} \cdot \boldsymbol{F}^{\mathrm{e}-1}) = \boldsymbol{L}^{\mathrm{e}} + \sum_{\alpha} \dot{\gamma}^{(\alpha)} \bar{\boldsymbol{s}}^{(\alpha)} \otimes \bar{\boldsymbol{m}}^{\alpha} \quad (4)$$

with

$$\bar{\boldsymbol{s}}^{(\alpha)} = \boldsymbol{F}^{\mathrm{e}} \cdot \boldsymbol{s}^{(\alpha)}, \quad \bar{\boldsymbol{m}}^{(\alpha)} = \boldsymbol{m}^{(\alpha)} \cdot \boldsymbol{F}^{\mathrm{e}-1} = \boldsymbol{F}^{\mathrm{e}-T} \cdot \boldsymbol{m}^{(\alpha)} \quad (5)$$

Here, $\bar{\boldsymbol{s}}^{(\alpha)}$ and $\bar{\boldsymbol{m}}^{(\alpha)}$ are viewed as $\boldsymbol{s}^{(\alpha)}$ and $\boldsymbol{m}^{(\alpha)}$, respectively, pushed forward from the lattice space to the deformed configuration, and the superscript T denotes the transpose of a tensor. The rate of deformation tensor $\boldsymbol{D}$, which is the symmetric part of $\boldsymbol{L}$, and the continuum spin $\boldsymbol{W}$ being the anti-symmetric part of $\boldsymbol{L}$ are written as

$$\boldsymbol{D} = \boldsymbol{D}^{\mathrm{e}} + \sum_{\alpha} \dot{\gamma}^{(\alpha)} \boldsymbol{P}^{(\alpha)}, \quad \boldsymbol{W} = \boldsymbol{W}^{\mathrm{e}} + \sum_{\alpha} \dot{\gamma}^{(\alpha)} \boldsymbol{W}^{(\alpha)} \quad (6)$$

with

$$\left.\begin{aligned} \boldsymbol{P}^{(\alpha)} &= \tfrac{1}{2}(\bar{\boldsymbol{s}}^{(\alpha)} \otimes \bar{\boldsymbol{m}}^{(\alpha)} + \bar{\boldsymbol{m}}^{(\alpha)} \otimes \bar{\boldsymbol{s}}^{(\alpha)}), \\ \boldsymbol{W}^{(\alpha)} &= \tfrac{1}{2}(\bar{\boldsymbol{s}}^{(\alpha)} \otimes \bar{\boldsymbol{m}}^{(\alpha)} - \bar{\boldsymbol{m}}^{(\alpha)} \otimes \bar{\boldsymbol{s}}^{(\alpha)}) \end{aligned}\right\} \quad (7)$$

Defining the Kirchhoff stress $\boldsymbol{\tau} = J\boldsymbol{\sigma}$ with the Cauchy stress $\boldsymbol{\sigma}$, we introduce the following constitutive relation in terms of the material Jaumann rate of $\boldsymbol{\tau}$ formed on axes that spin with the lattice (Asaro and Needleman (1985)):

$$\overset{\nabla}{\boldsymbol{\tau}}{}^{\mathrm{e}} = \dot{\boldsymbol{\tau}} - \boldsymbol{W}^{\mathrm{e}} \cdot \boldsymbol{\tau} + \boldsymbol{\tau} \cdot \boldsymbol{W}^{\mathrm{e}} = \boldsymbol{C} : \boldsymbol{D}^{\mathrm{e}} = \boldsymbol{C} : \left(\boldsymbol{D} - \sum_{\alpha} \dot{\gamma}^{(\alpha)} \boldsymbol{p}^{(\alpha)} \right) \quad (8)$$

where $\boldsymbol{C}$ is a fourth-order elasticity tensor. This relation can be written in terms of the standard Jaumann rate $\overset{\nabla}{\boldsymbol{\tau}}$ with respect to the continuum spin $\boldsymbol{W}$,

$$\overset{\nabla}{\boldsymbol{\tau}} = \dot{\boldsymbol{\tau}} - \boldsymbol{W} \cdot \boldsymbol{\tau} + \boldsymbol{\tau} \cdot \boldsymbol{W} = \boldsymbol{C} : \boldsymbol{D} - \sum_{\alpha} \dot{\gamma}^{(\alpha)} (\boldsymbol{C} : \boldsymbol{P}^{(\alpha)} + \boldsymbol{W}^{(\alpha)} \cdot \boldsymbol{\tau} - \boldsymbol{\tau} \cdot \boldsymbol{W}^{(\alpha)}) \quad (9)$$

We can further rewrite the relation in terms of the Jaumann rate of the Cauchy stress as

$$\begin{aligned} \overset{\nabla}{\boldsymbol{\sigma}} &= \dot{\boldsymbol{\sigma}} - \boldsymbol{W} \cdot \boldsymbol{\sigma} + \boldsymbol{\sigma} \cdot \boldsymbol{W} \\ &= J^{-1} \boldsymbol{C} : \boldsymbol{D} - \textstyle\sum_{\alpha} \dot{\gamma}^{(\alpha)} (J^{-1} \boldsymbol{C} : \boldsymbol{P}^{(\alpha)} + \boldsymbol{W}^{(\alpha)} \cdot \boldsymbol{\sigma} - \boldsymbol{\sigma} \cdot \boldsymbol{W}^{(\alpha)}) - (\mathrm{tr}\boldsymbol{L})\boldsymbol{\sigma}. \end{aligned} \quad (10)$$

Note that volumetric change resulting from elastic stretch of crystal is usually very small. Therefore, the assumption that $J \approx 1$ (i.e. $\mathrm{tr}\boldsymbol{L} \approx 0$) is generally justified. In most cases, no distinction between the Kirchhoff and Cauchy stresses is needed in practical or engineering computations.

Eq. (3) has been derived on the basis of the kinematics of crystallographic slip. From a viewpoint of plasticity theory, we can assume that plastic slip on a slip system occurs when the shear stress reaches a certain critical value. This is known as Schmid law, which is expressed as,

$$f^{(\alpha)} = |\tau^{(\alpha)}| - \tau_{\mathrm{C}} = 0, \tag{11}$$

where $\tau^{(\alpha)}$ is the resolved shear stress on slip system α, which is given by

$$\tau^{(\alpha)} = \bar{\boldsymbol{s}}^{(\alpha)} \cdot \boldsymbol{\sigma} \cdot \bar{\boldsymbol{m}}^{(\alpha)} = \boldsymbol{\sigma} : \boldsymbol{P}^{(\alpha)} \tag{12}$$

and $\tau_{\mathrm{C}}(> 0)$ is a critical resolved shear stress. The last expression in Eq. (12) is derived using the symmetric character of the Cauchy stress $\boldsymbol{\sigma}$. Eq. (11) is viewed as a yield function for one slip system. Here, we consider an associated flow rule in which the function $f^{(\alpha)}$ is taken as a plastic potential (adopting the last expression in Eq. (12)) and $\dot{\lambda}^{(\alpha)}$ is a positive plastic multiplier, like in a phenomenological plasticity theory. Then, a plastic strain rate tensor for slip system α is given by

$$\boldsymbol{D}^{\mathrm{p}(\alpha)} = \dot{\lambda}^{(\alpha)} \frac{\partial f^{(\alpha)}}{\partial \boldsymbol{\sigma}} = \mathrm{sgn}(\tau^{(\alpha)}) \dot{\lambda}^{(\alpha)} \boldsymbol{P}^{(\alpha)} \tag{13}$$

If $\mathrm{sgn}(\tau^{(\alpha)})\dot{\lambda}^{(\alpha)}$ is identified to the slip rate $\dot{\gamma}^{(\alpha)}$, the summation of Eq. (13) over all active slip systems in a crystal coincides with the plastic part of Eq. $(6)_1$ that is purely derived from the kinematics of crystallographic slips. For single slip deformations, the direction of plastic strain rate is fixed to the *normal* to the yield *plane* represented by Eq. (11). However, in multi-slip deformations, the loading point in a stress space is positioned at a vertex point on the hyper-polygon constructed by the yield planes for different slip systems. This yields vertex effects of plastic deformation, i.e. an abrupt change in the direction of plastic strain rate is allowed without significant change in the direction of the total stress, which relates to occurrence of strain localization in the form of shear bands that emerge abruptly from a uniformly straining field (Peirce et al. (1983); Kuroda and Tvergaard (2001); Kuroda and Tvergaard (2007); Ikawa et al. (2011); an example of shear band analysis will also be presented in Section 5). Crystal plasticity model naturally has the abilities to represent (i) the anisotropic material behavior due to a specific crystal structure and (ii) the vertex effects that lead to strain localization behavior. The conventional framework, however,

does not involve any material length scales. Therefore, they do not represent realistic material behavior at the micron or smaller scales.

3 Size effects in plastic strain gradient field

Metals exhibit size-dependent mechanical responses both under strain-gradient-dominated deformations (e.g. Fleck et al. (1994); Stölken and Evans (1998) Haque and Saif (2003); Shrotriya et al. (2003); Motz et al. (2005); Ehrler et al. (2008); Suzuki et al. (2009); Hayashi et al. (2011)) and under uniform deformations (e.g. Uchic et al. (2004); Dimiduk et al. (2005); Kiener et al. (2008)) at the micron scale. It is known that the plastic strain gradient in a deformed specimen is compensated by *geometrically necessary dislocations* (GNDs) (Ashby (1970); Fleck et al. (1994)). Understanding of how the GNDs affect the mechanical response of metals, however, has not yet been established. The interpretation of the size effect in the absence of the plastic strain gradient is also still at an issue.

Here, we focus on the size effects under strain-gradient-dominated deformations. Two main roles of the GNDs in size effects are considered as follows. One is that the GNDs in a plastic strain gradient field contribute to the slip hardening behavior, in addition to the contribution of the statistically stored dislocations (SSDs). This should yield size-dependent *isotropic hardening*. The other is that, according to the dislocation theory, the configuration of the GNDs produces an internal stress that acts as a backstress and this internal stress affects the mobility of dislocations, which corresponds to the magnitude of slip rate in the context of crystal plasticity. The backstress effect should manifest itself as size-dependent *kinematic hardening*. In experiments with monotonic loading, one cannot know whether the observed strain hardening is isotropic or kinematic one. To ascertain the amounts of these two types of size-dependent hardening, we need to perform reverse or cyclic loading tests for strain-gradient-dominated deformations at the micron scale.

In Hayashi et al. (2011), a series of systematic microbend tests with reversal of the bending direction, as well as uniaxial tensile tests, were conducted on copper foil specimens (nearly single-crystals) with different thicknesses. The results presented below are condensed from this reference.

An oxygen-free copper (99.99% purity) sheet with a thickness of 1.4mm was fully annealed and then cold-rolled to a thickness of about 40μm. Then, the foil was reannealed at 200°C for 30 min. When copper is subjected to such a severe plastic deformation, recrystallization is generally promoted at a rather low temperature (around 200°C) (Yamagishi et al. (2006)). The preferred orientation of recrystallization is (100). Fig. 1 shows {100} poles

of the measured crystal orientations, and all the poles concentrate around a near "cube" orientation, which was rotated clockwise ($\simeq 5^\circ$) about the normal direction (N.D.) of the foil and also slightly inclined from N.D. No explicit grain boundary was detected, although scatter of the poles were observed in Fig. 1. From these data, the foil was considered to be nearly single-crystal. To investigate the size effect on the mechanical response of the material, the foil thickness was reduced to $22-38\mu$m by electropolishing.

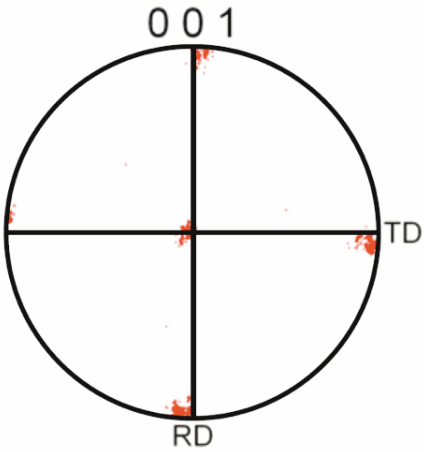

Figure 1. {100} pole figures for the copper foil.

Two specific crystal orientations relative to the loading axis (the direction of tensile stress in tension and bending) were considered in order to investigate whether the size effect is influenced by change in the combination of active slip systems. The first choice was that the longitudinal axis of the specimens was directed counterclockwise at 40° from R.D. Fig. 2_a shows the orientations of the tensile direction in a stereographic triangle. The poles of the tensile direction were scattered within a narrow area in the triangle, and they were positioned close to coplanar double-slip orientations (on $101-111$ side of the triangle). The specimens cut at this direction are referred to as "coplanar double-slip" specimens in brief. As the second choice of the crystal orientation, the specimens were cut at -5° from R.D. Fig. 2_b shows the orientations of the tensile direction in the stereographic triangle. The positions of the tensile direction were close to [001], but not exact one. The specimens cut at this direction are referred to as "multi-planar multi-slip" specimens.

Curves of nominal stress versus nominal strain for uniaxial tensile tests

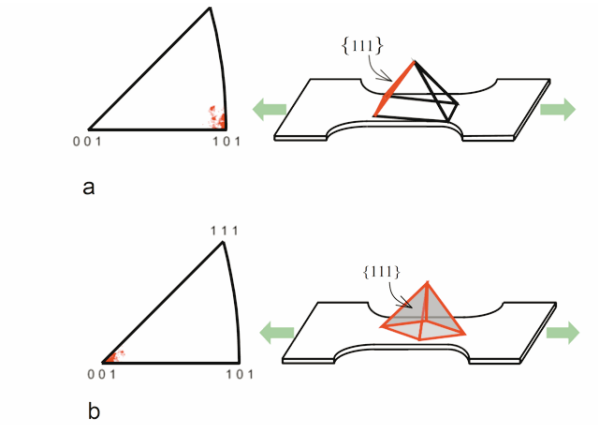

Figure 2. The orientations of the tensile direction in stereographic triangle and schematic diagram of the crystal orientation and the tensile direction: (a) coplanar double-slip specimen; (b) multi-planar multi-slip specimen.

are shown in Fig. 3. Dumbbell-shaped specimens with a width of 4mm were employed in the tests. Any systematic trend of thickness dependence is not observed. In Kiener et al. (2008), the typical size effect, i.e. the smaller is stronger behavior was observed in a copper single-crystal under uniaxial tension for a much smaller range of specimen size (with sectional area of below $8\mu\text{m} \times 8\mu\text{m}$).

The microbend tests were performed following the method and procedure proposed by Stölken and Evans (1998). The specimens for the microbend tests were cut from the foil in a form of strip with 40mm length and 2.5mm width, and then, the strips were further cut into rectangular specimens of 10mm in length. The foil was bent around a cylindrical mandrel into the plastic deformation range. The load required for bending was applied through two profiled dies. Then, the load was removed and elastic springback occured resulting in an increase in the radius of curvature of the foil specimen. In the microbend tests, this springback phenomenon plays a primary role in measuring the applied bending moment M. The microbend test method originally involved a monotonic increase in bending deformation. The method was extended to include a reversal of the bending direction. At the reversal point during loading, the bent specimen was carefully flattened step by step through pressing and rolling using tungsten mandrels with different diameters on a flat table. Then, the microbend test was restarted from the other side of the specimen.

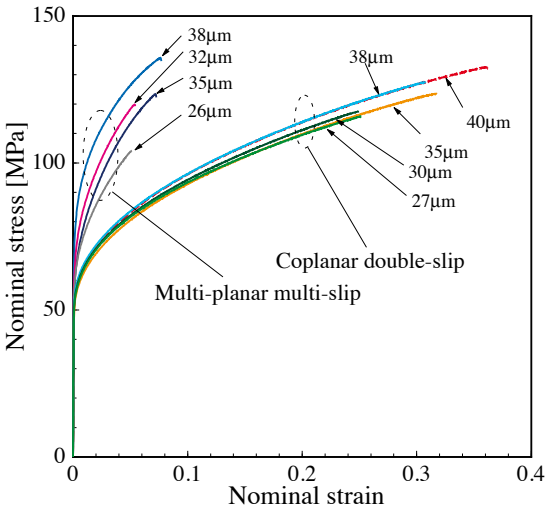

Figure 3. Relationships between nominal stress and nominal strain for tensile tests on single-crystal copper foil specimens with different thicknesses.

In Fig. 4, measured bending moments normalized by BH^2 are plotted as a function of the surface strain, $\varepsilon_s = H/(2R_0)$, for the microbend tests with the reversal of bending. Here, B is the width of the foil specimen, H is the foil thickness, R_0 is the radius of curvature of the foil specimen at the middle of the thickness during plastic loading. Each marker corresponds to an average of experimental values obtained for three different specimens under the same conditions, and the error bars indicate the maximum and minimum values among the three results. Regression lines for the experimental plots, as well as linear elastic loading paths towards the initial yielding, are added to the graphs. Furthermore, the unloading paths just before reversal of bending are also added. As is first seen from Fig. 4, a typical size effect has appeared in the forward bending process. The apparent strain hardening is clearly larger in the thinner foils than in the thicker ones, unlike in the tensile tests where no systematic size effect was detected. The multi-planar multi-slip specimens (Fig. 4_{b}) exhibit a more pronounced size-effect than the coplanar double-slip specimens (Fig. 4_{a}). The heights of the error bars in the multi-planar multi-slip experiments (Fig. 4_{b}) tend to be larger than those in the coplanar double-slip experiments (Fig. 4_{a}). This might be attributed to the uncertainty of the actual active slip systems in the multi-planar multi-slip specimens.

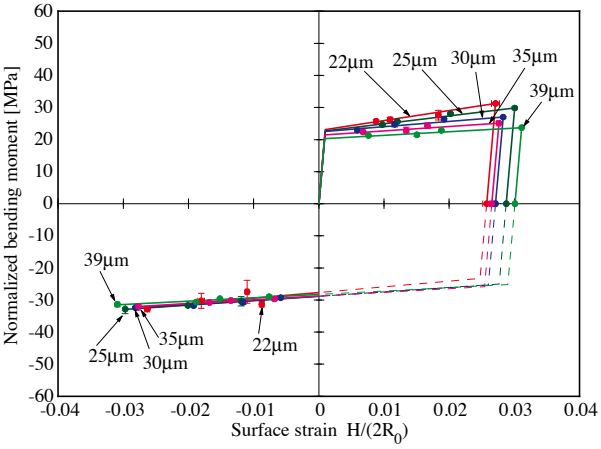

a

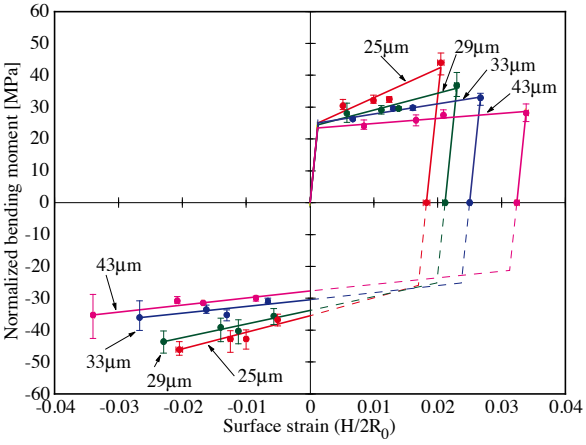

b

Figure 4. Microbend test results: relationship between normalized bending moment and surface strain for specimens with different thicknesses: (a) coplanar double-slip specimens; (b) multi-planar multi-slip specimens.

All the multi-planar multi-slip specimens and some of the coplanar double-slip specimens in the microbend tests exhibited the Bauschinger effect. The

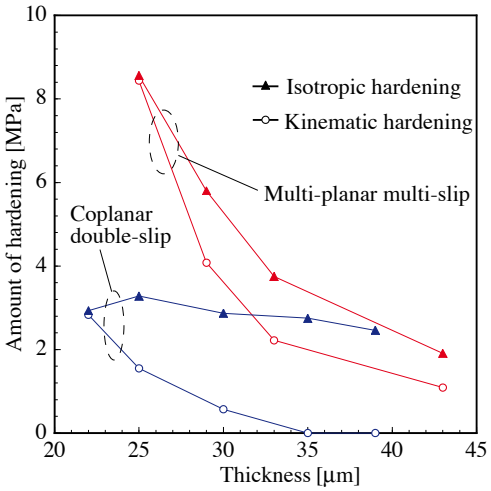

Figure 5. Relationships between amount of hardening at a surface strain of 0.02 and foil thickness

present experiments have confirmed that the Bauschinger effect appears even in single-crystal specimens when the plastic strain gradients exist. Here, the amounts of total hardening in the normalized bending moments during forward loading are divided into isotropic and kinematic components. Curves of the amounts of kinematic hardening and isotropic hardening at a surface strain of 0.02 versus foil thickness are plotted in Fig. 5. Both isotropic hardening and kinematic hardening are strongly size-dependent in the case of multi-planar multi-slip deformation, while in the coplanar double-slip deformation case, isotropic hardening exhibits almost no size dependence, and moderate size dependence is observed for kinematic hardening.

4 Modeling of size-dependent hardening

4.1 Geometrically necessary dislocations

In the context of small strain conditions where geometry changes are neglected, the gradient of the displacement vector $\boldsymbol{u}$ may be additively decomposed into elastic and plastic parts, $\boldsymbol{H}^{\mathrm{e}}$ and $\boldsymbol{H}^{\mathrm{p}}$, as

$$\boldsymbol{u} \otimes \nabla = \boldsymbol{H}^{\mathrm{e}} + \boldsymbol{H}^{\mathrm{p}}, \tag{14}$$

where ∇ is the spatial gradient operator. The geometric properties of dislocation densities may be quantified by a geometric dislocation tensor, often called Burgers tensor (or Nyes tensor after Nye (1953)). This can be expressed by use of the slip gradients (e.g. Gurtin (2002)) as

$$\boldsymbol{G} \equiv \operatorname{curl} \boldsymbol{H}^{\mathrm{p}} = \sum_{\beta} (\nabla \gamma^{(\beta)} \times \boldsymbol{m}^{(\beta)}) \otimes \boldsymbol{s}^{(\beta)} \tag{15}$$

With the tangent line direction of edge dislocation on slip system β,

$$\boldsymbol{l}^{(\beta)} = \boldsymbol{m}^{(\beta)} \times \boldsymbol{s}^{(\beta)}, \tag{16}$$

the geometric dislocation density tensor can also be written in the following form (Kubin et al. (1992); Sun et al. (1998); Sun et al. (2000); Arsenlis et al. (2004); Acharya (2001); Gurtin (2002); Gurtin and Anand (2007))

$$\boldsymbol{G} = b \sum_{\beta} (\rho_{\mathrm{G}(e)}^{(\beta)} \boldsymbol{l}^{(\beta)} \otimes \boldsymbol{s}^{(\beta)} + \rho_{\mathrm{G}(s)}^{(\beta)} \boldsymbol{s}^{(\beta)} \otimes \boldsymbol{s}^{(\beta)}, \tag{17}$$

.

$$\rho_{\mathrm{G}(e)}^{(\beta)} = -\frac{1}{b} \nabla \gamma^{(\beta)} \cdot \boldsymbol{s}^{(\beta)}, \quad \rho_{\mathrm{G}(s)}^{(\beta)} = \frac{1}{b} \nabla \gamma^{(\beta)} \cdot \boldsymbol{l}^{(\beta)} = -\frac{1}{b} \nabla \gamma^{(\beta)} \cdot \boldsymbol{p}^{(\beta)}, \tag{18}$$

where b is the magnitude of the Burgers vector, $\boldsymbol{p}^{(\beta)} = \boldsymbol{s}^{(\beta)} \times \boldsymbol{m}^{(\beta)} = -\boldsymbol{l}^{(\beta)}$[1], and $\rho_{\mathrm{G}(e)}^{(\beta)}$ and $\rho_{\mathrm{G}(s)}^{(\beta)}$ are, respectively, the edge and screw components of the GND densities (henceforth referred to as the edge GND and the screw GND densities). For the finite deformation kinematics, several different expressions have been proposed for the Burgers (geometric dislocation) tensor and the GND densities (Acharya and Bassani (2000); Cermelli and Gurtin (2001); Arsenlis et al. (2004), Evers et al. (2004)). The plastic deformation in the Kröner-Lee decomposition takes place in the lattice space (intermediate configuration) where $\boldsymbol{L}^{\mathrm{p}}$ is defined. Cermelli and Gurtin (Cermelli and Gurtin (2001)) have defined the Burgers tensor as $\boldsymbol{G} \equiv \boldsymbol{F}^{\mathrm{p}} \operatorname{Curl} \boldsymbol{F}^{\mathrm{p}}$ in the lattice space. Gurtin (Gurtin (2006); Gurtin (2008)) showed that the plastically convected rate of $\boldsymbol{G}$ defined by $\overset{\diamond}{\boldsymbol{G}} = \dot{\boldsymbol{G}} - \boldsymbol{L}^{\mathrm{p}} \cdot \boldsymbol{G} - \boldsymbol{G} \cdot \boldsymbol{L}^{\mathrm{p}T}$ can be decomposed in a way similar to Eq. (17) as

$$\overset{\diamond}{\boldsymbol{G}} = b \sum_{\alpha} (-\dot{\rho}_{\mathrm{G}(e)}^{(\alpha)} \boldsymbol{p}^{(\alpha)} \otimes \boldsymbol{s}^{(\alpha)} + \dot{\rho}_{\mathrm{G}(s)}^{(\alpha)} \boldsymbol{s}^{(\alpha)} \otimes \boldsymbol{s}^{(\alpha)}), \tag{19}$$

[1] Different researchers sometimes use different sign conventions for the signed dislocation densities. The reason for introducing $\boldsymbol{p}^{(\beta)}$ here is only to write $\rho_{\mathrm{G}(e)}^{(\beta)}$ and $\rho_{\mathrm{G}(s)}^{(\beta)}$ in the same mathematical form for subsequent convenience.

where $\rho^{(\alpha)}_{\mathrm{G}(e)}$ and $\rho^{(\alpha)}_{\mathrm{G}(s)}$ are the edge and screw GND densities on the individual slip systems in the lattice space[2] and

$$\dot{\rho}^{(\alpha)}_{\mathrm{G}(e)} = -\frac{1}{b}\nabla^{\#}\dot{\gamma}^{(\alpha)} \cdot \boldsymbol{s}^{(\alpha)} = -\frac{1}{b}\mathrm{Grad}\dot{\gamma}^{(\alpha)} \cdot \boldsymbol{s}^{(\alpha)}_{R} = -\frac{1}{b}\mathrm{grad}\dot{\gamma}^{(\alpha)} \cdot \bar{\boldsymbol{s}}^{(\alpha)}, \quad (20)$$

$$\dot{\rho}^{(\alpha)}_{\mathrm{G}(s)} = -\frac{1}{b}\nabla^{\#}\dot{\gamma}^{(\alpha)} \cdot \boldsymbol{p}^{(\alpha)} = -\frac{1}{b}\mathrm{Grad}\dot{\gamma}^{(\alpha)} \cdot \boldsymbol{p}^{(\alpha)}_{R} = -\frac{1}{b}\mathrm{grad}\dot{\gamma}^{(\alpha)} \cdot \bar{\boldsymbol{p}}^{(\alpha)} \quad (21)$$

with

$$\nabla^{\#}\dot{\gamma}^{(\alpha)} = \mathrm{Grad}\dot{\gamma}^{\alpha} \cdot \boldsymbol{F}^{p-1} = \mathrm{grad}\dot{\gamma}^{(\alpha)} \cdot \boldsymbol{F}^{\mathrm{e}}. \quad (22)$$

Here, 'Grad' denotes the spatial gradients with respect to the coordinates $\boldsymbol{X}$ in the undeformed configuration, 'grad' denotes the spatial gradients with respect to the coordinates $\boldsymbol{x}$ in the deformed (current) configuration, $\boldsymbol{s}^{(\alpha)}_{\mathrm{R}} = \boldsymbol{F}^{p-1}\cdot\boldsymbol{s}^{(\alpha)}$, $\boldsymbol{p}^{(\alpha)}_{\mathrm{R}} = \boldsymbol{F}^{p-1}\cdot\boldsymbol{p}^{(\alpha)}$ and $\bar{\boldsymbol{p}}^{(\alpha)} = \boldsymbol{F}^{\mathrm{e}}\cdot\boldsymbol{p}^{(\alpha)}$. Here, $\nabla^{\#}\dot{\gamma}^{(\alpha)}$ can be viewed as the gradient of slip rate in the lattice space, because $\mathrm{Grad}\dot{\gamma}^{(\alpha)}\cdot\boldsymbol{F}^{p-1}$ is interpreted as the material gradient of slip rate pushed forward from the undeformed configuration to the lattice space and $\mathrm{grad}\dot{\gamma}^{(\alpha)}\cdot\boldsymbol{F}^{e}$ is the spatial gradient of slip rate pulled back from the deformed configuration to the lattice space (Gurtin (2008)).

The GND densities in the deformed configuration are written as $\bar{\rho}^{(\alpha)}_{\mathrm{G}(e)} = J^{-1}\rho^{(\alpha)}_{\mathrm{G}(e)}$ and $\bar{\rho}^{(\alpha)}_{\mathrm{G}(s)} = J^{-1}\rho^{(\alpha)}_{\mathrm{G}(s)}$. However, as mentioned in section 2, the volume change is usually negligible for dense metals. Practically, no distinction between $\bar{\rho}^{(\alpha)}_{\mathrm{G}(\cdot)}$ and $\rho^{(\alpha)}_{\mathrm{G}(\cdot)}$ is needed in most cases.

4.2 Isotropic hardening

It is often assumed that the slip resistance $\tau^{(\alpha)}_{\mathrm{C}}$ depends on the GND density through a modified Taylor relation (Fleck et al. (1994); W.D.Nix and H.J.Gao (1998); Han et al. (2005)) as

$$\tau^{(\alpha)}_{\mathrm{C}} = c\mu b\sqrt{\rho^{(\alpha)}_{\mathrm{S}} + ||\rho^{(\alpha)}_{\mathrm{G}}||}, \quad (23)$$

where the superscripted (α) denotes a quantity on the αth slip system, c is an empirical coefficient (of magnitude $0.1 - 1.0$), μ is the elastic shear modulus, $\rho^{(\alpha)}_{\mathrm{S}}$ is the statistically stored dislocation (SSD) density and $||\rho^{(\alpha)}_{\mathrm{G}}||$ denotes the magnitude of the GND density on slip system α , which is defined (Ohashi (2004); Ohashi (2005)) as

$$||\rho^{(\alpha)}_{\mathrm{G}}|| = \sqrt{(\rho^{(\alpha)}_{\mathrm{G}(e)})^2 + (\rho^{(\alpha)}_{\mathrm{G}(s)})^2}. \quad (24)$$

[2]Here, $\boldsymbol{s}^{(\alpha)}$ and $\boldsymbol{p}^{(\alpha)}$ are defined in the lattice space, and $\bar{\boldsymbol{s}}^{(\alpha)}$ and $\bar{\boldsymbol{p}}^{(\alpha)}$ are defined in the deformed configuration (see Eq. (2) - (5)).

Eq. (23) makes it possible to represent size-dependent hardening in the presence of plastic strain gradients. That is, it is assumed that the absolute magnitudes of the GND densities directly augment the slip resistance. Some researchers, however, have questioned this scenario. Mughrabi (2004) argued that the GNDs are not expected to contribute to the self-hardening of the slip system on which they reside. Weertman (2002) suggested that the GNDs primarily contribute to the slip resistance as forest dislocations. The experimental data shown in Fig. 5 exhibited that the amount of isotropic hardening for the coplanar double-slip specimens is nearly independent of the foil thickness, although the specimens with different thicknesses must have different GND densities. This suggests that the GNDs on the active slip plane did not significantly contribute to slip hardening on this slip plane. The arguments by Mughrabi (2004) and Weertman (2002) appear to be consistent with the experimental observation shown in Fig. 5 (Hayashi et al. (2011)).

A slip-hardening model consistent with the above discussion has been proposed by (Ohashi (2004); Ohashi (2005)). In his model, the slip resistance for each slip system is determined solely by the SSD densities through the Taylor relation. However, the mean free path of moving dislocations, which governs the evolution of the SSD densities, is affected by the GNDs that reside on other slip planes since they are considered to act as forest dislocations. That is, in Ohashi's model, $\tau_{\mathrm{C}}^{(\alpha)}$is given by

$$\tau_{\mathrm{C}}^{(\alpha)} = c\mu b \sum_{\beta} \Omega^{(\alpha\beta)} \sqrt{\rho_{\mathrm{S}}^{(\beta)}}, \tag{25}$$

where $\Omega^{(\alpha\beta)}$ is an interaction matrix for dislocations on slip systems α and β. The GND densities are not introduced into the slip hardening law given in Eq. (25), but affect evolution of the SSD density through the mean free path of mobile dislocations, i.e.

$$\dot{\rho}_{\mathrm{S}}^{(\alpha)} = \frac{1}{b}\left(\frac{1}{L^{(\alpha)}} - 2y_{\mathrm{C}}\rho_{\mathrm{S}}^{(\alpha)}\right)|\dot{\gamma}^{(\alpha)}|, \tag{26}$$

where $L^{(\alpha)}$ is the mean free path of moving dislocations on the slip system α , and y_{C} is the critical annihilation length (Essmann and Mughrabi (1979.)). The mean free path is given by

$$L^{(\alpha)} = K \cdot l^{(\alpha)} \tag{27}$$

$$l^{(\alpha)} = \frac{1}{\sqrt{\sum_{\beta}\left(a_1\rho_{\mathrm{S}}^{(\beta)} + a_2||\rho_{\mathrm{G}}^{(\beta)}||\right)}} \tag{28}$$

(no sum over β when the αth and βth systems are coplanar),

where $l^{(\alpha)}$ represents the effective average distance between forest dislocations that obstruct the movement of dislocations on slip system α. In Eq. (28), a_1 and a_2 are parameters that control the contributions from the SSD and GND densities to $l^{(\alpha)}$. The coefficient K in Eq. (27) represents the assumed number of forest dislocations that are cut by a moving dislocation before it ceases to move (usually K is assumed to be in the range of 10 - 100). The existence of the GNDs on one slip plane results in a reduction of the mean free path of moving dislocations on other slip planes. Thus, in the present model, the size-dependent isotropic hardening behavior is reproduced for the *multi-planar multi-slip deformation* case only.

4.3 Kinematic hardening and backstresses

A shear stress at the origin (a material point under consideration) contributed from an edge dislocation at a position (x, y) is given by

$$\tau^{(\alpha)}_{(\mathrm{ind})} = -\frac{\mu b}{2\pi(1-\nu)}\frac{x(x^2-y^2)}{(x^2+y^2)^2}, \tag{29}$$

where the direction of the Burgers vector coincides with that of the coordinate x (e.g. Cottrell (1953)), and the ν is Poisson's ratio. It is assumed that a density of the GNDs near the origin is approximately evaluated with a linearization (Evers et al. (2004)), i.e.

$$\rho^{(\alpha)}_{\mathrm{G}(e)}(x,y) \cong \rho^{(\alpha)}_{\mathrm{G}(e)}(0,0) + \frac{\partial \rho^{(\alpha)}_{\mathrm{G}(e)}}{\partial x}x + \frac{\partial \rho^{(\alpha)}_{\mathrm{G}(e)}}{\partial y}y. \tag{30}$$

Introducing a polar-coordinate system, $x = r\cos\phi$ and $y = r\sin\phi$, and considering Eqs. (29) and (30), a resultant internal shear stress due to the collective dislocations is obtained as

$$\tau^{(\alpha)}_{(\mathrm{disloc})} = \int_0^{r_0}\int_0^{2\pi} \tau^{(\alpha)}_{(\mathrm{ind})}\rho^{(\alpha)}_{\mathrm{G}(e)} r\,d\phi\,dr = -\frac{\mu b r_0^2}{8(1-\nu)}\frac{\partial \rho^{(\alpha)}_{\mathrm{G}(e)}}{\partial x} \tag{31}$$

Here, r_0 is a radius of an integration region to evaluate the internal stress, which is regarded as a length-scale parameter [3]. The effective shear stress, τ_{eff} , to glide dislocations is given by

$$\tau^{(\alpha)}_{(\mathrm{eff})} \equiv \tau^{(\alpha)} + \tau^{(\alpha)}_{(\mathrm{disloc})}, \tag{32}$$

[3] Different definitions for length-scale parameter can be used for dimension consistency, for example, as in Eq. (62).

where $\tau^{(\alpha)}$ is the resolved shear stress (defined in Eq. (12)) and the "$-\tau^{(\alpha)}_{(\mathrm{disloc})}$" is viewed as the backstress, i.e.

$$\tau^{(\alpha)}_{\mathrm{b}} = -\tau^{(\alpha)}_{(\mathrm{disloc})}, \tag{33}$$

$$\tau^{(\alpha)}_{(\mathrm{eff})} = \tau^{(\alpha)} - \tau^{(\alpha)}_{\mathrm{b}}. \tag{34}$$

For the screw GNDs, a relation similar to Eq. (31) can be derived straightforwardly. In the above, the theory of small strain elasticity, which is a basis of the classical dislocation theory, has been adopted. Even in large strain elasto-plastic problems, elastic strains themselves are still small. Thus, a backstress in the deformed configuration, with both the contributions of the edge and screw GND densities, may be written in the form (Kuroda and Tvergaard (2008 b))

$$\tau^{(\alpha)}_{\mathrm{b}} = B\left[\mathrm{grad}\bar{\rho}^{(\alpha)}_{\mathrm{G}(e)} \cdot \bar{\boldsymbol{s}}^{(\alpha)} + \mathrm{grad}\bar{\rho}^{(\alpha)}_{\mathrm{G}(s)} \cdot \bar{\boldsymbol{p}}^{(\alpha)}\right]; \quad B = \frac{\mu b r_0^2}{8(1-\nu)}. \tag{35}$$

Note that the above formulation takes into account only the shear stress component produced by the gradients of the GND density on a slip system α. The model of Eq. (35) may be the simplest model that illuminates the origin of the backstress. In reality, however, the dislocations produce other stress components (c.f. Cottrell (1953)) and the crystal has different slip systems. A generalized formulation with full of these effects has been proposed by Bayley et al. (2006), and a similar model can also be found in Hayashi et al. (2011).

A possible form of the slip rate relation, which involves the backstress effect, may be written as

$$\dot{\gamma}^{(\alpha)} = \dot{\gamma}_0 \,\mathrm{sgn}(\tau^{(\alpha)}_{(\mathrm{eff})}) \left(\frac{|\tau^{(\alpha)}_{(\mathrm{eff})}|}{\tau^{(\alpha)}_{\mathrm{C}}}\right)^{\frac{1}{m}}, \tag{36}$$

where $\dot{\gamma}^{(\alpha)}_0$ is a reference slip rate (a material constant), and m is a slip rate sensitivity parameter. This may be a simple extension of the relation introduced by Peirce et al. (1983) and Asaro and Needleman (1985).

4.4 Formulations of boundary value problems

With neglect of the body force effect, the standard equilibrium and boundary conditions are

$$\left.\begin{array}{ll} \mathrm{div}\boldsymbol{\sigma} = \mathbf{0}, & \\ \boldsymbol{\sigma}^{\mathrm{T}} \cdot \bar{\boldsymbol{n}} = \underline{\boldsymbol{t}} & \text{on } s_t, \\ \boldsymbol{v} = \underline{\boldsymbol{v}} & \text{on } s_u, \end{array}\right\} \tag{37}$$

where $\bar{\boldsymbol{n}}$ is the normal to the surface of the deformed body, $\underline{\boldsymbol{t}}$ denotes prescribed traction on the surface s_t , and $\underline{\boldsymbol{v}}$ is prescribed velocity on the surface s_u , while $s(= s_t + s_u)$ is the surface of the deformed body. Eq. (37) is equivalent to the virtual work principle

$$\int_v \boldsymbol{\sigma} : \delta\boldsymbol{L} dv = \int_{s_t} \underline{\boldsymbol{t}} \cdot \delta\boldsymbol{v} ds, \tag{38}$$

where v is the volume (region) of the deformed body, $\delta\boldsymbol{v}$ is an arbitrary virtual velocity satisfying $\delta\boldsymbol{v} = 0$ on s_u , and $\delta\boldsymbol{L}$ is the corresponding virtual velocity gradient. Since we adopt the rate-type constitutive relation, it is convenient to use a rate-type equilibrium equation and boundary conditions

$$\left.\begin{array}{ll} \mathrm{div}\dot{\boldsymbol{\Pi}} = \mathbf{0}, & \\ \dot{\boldsymbol{\Pi}}^{\mathrm{T}} \cdot \bar{\boldsymbol{n}} = \dot{\underline{\boldsymbol{t}}} & \text{on } s_t, \\ \boldsymbol{v} = \underline{\boldsymbol{v}} & \text{on } s_u, \end{array}\right\} \tag{39}$$

where $\dot{\boldsymbol{\Pi}}$ and $\dot{\underline{\boldsymbol{t}}}$ are the nominal stress rate and nominal prescribed traction rate at the deformed configuration. The relationship between the nominal stress rate defined at the deformed configuration and Cauchy stress rate is given by

$$\dot{\boldsymbol{\Pi}} = \dot{\boldsymbol{\sigma}} - \boldsymbol{L} \cdot \boldsymbol{\sigma} + (\mathrm{tr}\boldsymbol{L})\boldsymbol{\sigma}. \tag{40}$$

The corresponding incremental virtual work principle for an updated Lagrangian formulation takes the form (McMeeking and Rice (1975))

$$\int_v \dot{\boldsymbol{\Pi}}^{\mathrm{T}} : \delta\boldsymbol{L} dv = \int_{s_t} \dot{\underline{\boldsymbol{t}}} \cdot \delta\boldsymbol{v} ds. \tag{41}$$

When only the GND density-dependent isotropic hardening model is taken into account, an updated Lagrangian finite element analysis with scale-dependent crystal plasticity can be performed using the virtual work principle of Eq. (41). The crystal plasticity constitutive relation in the form of

Eq. (10) is substituted into Eq. (40) and the quantity $\tau_{\mathrm{C}}^{(\alpha)}$ in the conventional model is simply replaced by the GND-density-dependent model shown in Eqs. (25)-(28). The boundary conditions that enter boundary value problems are the same as those in the conventional theory, i.e. Eq. $(37)_{2,3}$ (or equivalently, Eq. $(39)_{2,3}$). No extra boundary condition is introduced. This type of theory is classified into the lower-order theories. Numerical computations with the lower-order type theory with Ohashi's mean free path model have been reported in Kuroda et al. (2007).

For the model involving the GND density-dependent backstress, the differential equations for rates of the GND densities (i.e. Eqs. (20) and (21)) can play a role of additional governing equations. When we choose the third expression on the right-hand side of Eq. (20), which is given in terms of the quantities lying in the deformed configuration, i.e. $\mathrm{grad}\dot{\gamma}^{(\alpha)}$ and $\overline{\boldsymbol{s}}^{(\alpha)}$, the weak form of the differential equation takes the form (Kuroda and Tvergaard (2008 b))

$$\int_v \left(\dot{\rho}_{\mathrm{G}(e)}^{(\alpha)} + \frac{1}{b} \mathrm{grad}\dot{\gamma}^{(\alpha)} \cdot \bar{\boldsymbol{s}}^{(\alpha)} \right) \check{\rho}\, dv = 0. \tag{42}$$

Applying the divergence theorem, it becomes

$$\begin{aligned} \int_v \check{\rho}\, \dot{\rho}_{\mathrm{G}(e)}^{(\alpha)} dv = \quad & \tfrac{1}{b} \textstyle\int_v \mathrm{grad}\check{\rho} \cdot \bar{\boldsymbol{s}}^{(\alpha)} \dot{\gamma}^{(\alpha)} dv \\ & + \tfrac{1}{b} \textstyle\int_v \check{\rho}\, \mathrm{div}\bar{\boldsymbol{s}}^{(\alpha)} \dot{\gamma}^{(\alpha)} dv - \tfrac{1}{b} \textstyle\int_s \check{\rho}\, \bar{\boldsymbol{n}} \cdot \bar{\boldsymbol{s}}^{(\alpha)} \dot{\gamma}^{(\alpha)} ds \end{aligned} \tag{43}$$

where 'div' denotes the divergence with respect to $\boldsymbol{x}$ in the deformed configuration.

The second expression on the right-hand side of Eq. (20), which is represented in terms of the quantities lying in the reference configuration, i.e. $\mathrm{Grad}\,\dot{\gamma}^{(\alpha)}$ and $\boldsymbol{s}_{\mathrm{R}}^{(\alpha)}$, also can be used as an additional governing equation instead of the third expression (Kuroda and Tvergaard (2008 b)).

The same arguments as the above are applied to the relations for the screw GND density rates in Eq. (21), replacing $\boldsymbol{s}_{\mathrm{R}}^{(\alpha)}$ and $\overline{\boldsymbol{s}}^{(\alpha)}$ by $\boldsymbol{p}_{\mathrm{R}}^{(\alpha)}$ and $\overline{\boldsymbol{p}}^{(\alpha)}$, respectively.

With the surface integral terms in Eq. (43), microscopic (extra) boundary conditions can be imposed. For example, at a hard interface being impenetrable to dislocations, the boundary condition is given by $\bar{\boldsymbol{n}} \cdot \bar{\boldsymbol{s}}^{(\alpha)} \dot{\gamma}^{(\alpha)} = 0$ in Eq. (43), which means that there is no flow of dislocations through the interface.

The standard incremental virtual work principle, Eq. (41), and the GND density rate relations for the slip systems, Eq. (43), are the governing equations to be solved simultaneously. It is emphasized that these equations

are valid independent of constitutive modeling, but they are connected by the constitutive relations involving the backstresses that are given by the spatial gradients of the GND densities. This type of theory, in which an additional governing differential equation is introduced and extra boundary conditions are accounted for, is classified into the *higher-order* theories.

The present gradient theory does not necessitate introducing concepts of *higher-order stresses* that appear in a work-conjugate type formulations like in Gurtin (2002) and Gurtin (2008).

4.5 Connection to the work-conjugate-type formulations

If a relation for the backstress on each slip system can be expressed with the divergence of a vector quantity, e.g. $\boldsymbol{\xi}^{(\alpha)}$, i.e.

$$\tau_{\mathrm{b}}^{(\alpha)} \equiv -\mathrm{div}\boldsymbol{\xi}^{(\alpha)}, \tag{44}$$

we can rewrite the slip rate relation, Eq. (36), in the form

$$\tau^{\mathrm{p}(\alpha)} - \tau^{(\alpha)} - \mathrm{div}\boldsymbol{\xi}^{(\alpha)} = 0 \tag{45}$$

with

$$\tau^{\mathrm{p}(\alpha)} \equiv \mathrm{sgn}(\tau^{(\alpha)} - \tau_{\mathrm{b}}^{(\alpha)})\tau_{\mathrm{C}}^{(\alpha)} \left(\frac{|\dot{\gamma}^{(\alpha)}|}{\dot{\gamma}_0} \right)^m. \tag{46}$$

In consistent with the kinematics of Eq. (4), we may write the virtual velocity gradient $\delta\boldsymbol{L}$ in Eq. (38) as

$$\delta\boldsymbol{L} \equiv \delta\boldsymbol{L}^{\mathrm{e}} + \sum_{\alpha} \delta\dot{\gamma}^{(\alpha)} \bar{\boldsymbol{s}}^{(\alpha)} \otimes \bar{\boldsymbol{m}}^{(\alpha)}, \tag{47}$$

where $\delta\boldsymbol{L}^{\mathrm{e}}$ is a virtual elastic distortion rate and $\delta\dot{\gamma}^{(\alpha)}$ is a virtual slip rate. Substituting Eq. (47) into the virtual work principle (38) gives

$$\int_v (\boldsymbol{\sigma} : \delta\boldsymbol{L}^{\mathrm{e}} + \sum_{\alpha} \tau^{(\alpha)} \delta\dot{\gamma}^{(\alpha)}) dv = \int_{s_t} \underline{\boldsymbol{t}} \cdot \delta\boldsymbol{v} ds. \tag{48}$$

Using Eq. (45), a relation

$$\mathrm{div}(\boldsymbol{\xi}^{(\alpha)} \delta\dot{\gamma}^{(\alpha)}) = (\mathrm{div}\boldsymbol{\xi}^{(\alpha)}) \delta\dot{\gamma}^{(\alpha)} + \boldsymbol{\xi}^{(\alpha)} \cdot \mathrm{grad}\delta\dot{\gamma}^{(\alpha)}, \tag{49}$$

and the divergence theorem, Eq. (48) can be rewritten as

$$\begin{aligned} &\int_v \boldsymbol{\sigma} : \delta\boldsymbol{L}^{\mathrm{e}} dv + \sum_{\alpha} \int_v (\tau^{\mathrm{p}(\alpha)} \delta\dot{\gamma}^{(\alpha)} + \boldsymbol{\xi}^{(\alpha)} \cdot \mathrm{grad}\delta\dot{\gamma}^{(\alpha)}) dv \\ &= \textstyle\int_{s_t} \underline{\boldsymbol{t}} \cdot \delta\boldsymbol{v} ds + \sum_{\alpha} \int_s \bar{\boldsymbol{n}} \cdot \boldsymbol{\xi}^{(\alpha)} \delta\dot{\gamma}^{(\alpha)} ds \end{aligned} \tag{50}$$

This exactly corresponds to the virtual work principle in Gurtin's theory (Gurtin (2002); Gurtin (2008)). In Gurtin's theory, the vector quantities $\boldsymbol{\xi}^{(\alpha)}$ and the scalar quantities $\bar{\boldsymbol{n}}\cdot\boldsymbol{\xi}^{(\alpha)}$ on the surface are considered as *higher-order microscopic stresses*[4] and *microscopic tractions*, respectively. Eq. (45) is viewed as the additional governing equation, which is called a *microforce balance* equation in Gurtin's theory. But, in the present formulation, this is viewed as a *gradient-dependent yield* function, which is a part of constitutive modeling.

The relation for the backstresses, Eq. (35), which was a simple postulate from the classical dislocation theory, cannot be represented in the form of Eq. (44), because $\bar{\boldsymbol{s}}^{(\alpha)}$ and $\bar{\boldsymbol{p}}^{(\alpha)}$ are not constant, but vary from place to place under finite deformations. If we assume that[5]

$$\begin{aligned}\tau_{\mathrm{b}}^{(\alpha)} \equiv \quad & B[\mathrm{grad}\bar{\rho}_{\mathrm{G}(e)}^{(\alpha)}\cdot\bar{\boldsymbol{s}}^{(\alpha)} + \mathrm{grad}\bar{\rho}_{\mathrm{G}(s)}^{(\alpha)}\cdot\bar{\boldsymbol{p}}^{(\alpha)} \\ & +\bar{\rho}_{\mathrm{G}(e)}^{(\alpha)}\mathrm{div}\bar{\boldsymbol{s}}^{(\alpha)} + \bar{\rho}_{\mathrm{G}(s)}^{(\alpha)}\mathrm{div}\bar{\boldsymbol{p}}^{(\alpha)}],\end{aligned} \tag{51}$$

then the vector quantities satisfying Eq. (44) have to be

$$\boldsymbol{\xi}^{(\alpha)} = -B[\bar{\rho}_{\mathrm{G}(e)}^{(\alpha)}\bar{\boldsymbol{s}}^{(\alpha)} + \bar{\rho}_{\mathrm{G}(s)}^{(\alpha)}\bar{\boldsymbol{p}}^{(\alpha)}]. \tag{52}$$

In Gurtin's theory (Gurtin (2008)), the relation for the microscopic stress, Eq. (52), is derived from the *free-energy inequality* based on the second law. The free-energy is assumed to be augmented by a *defect energy* in the form

$$\Psi = \frac{1}{2}bB\sum_{\alpha}\left[(\rho_{\mathrm{G}(e)}^{(\alpha)})^2 + (\rho_{\mathrm{G}(s)}^{(\alpha)})^2\right]. \tag{53}$$

In Eq. (53), the defect energy is assumed to be a simple quadratic function of the GND densities. In this case, the backstresses are given by the first order gradients of the GND densities. When a different order of the GND densities is introduced in the defect energy formulation, different relations for the microscopic stresses and the backstresses are derived (Gurtin (2008)).

In summary, if the backstress relations can be written in the form of Eq. (44) (i.e. the divergence of a vector quantity), the present gradient crystal plasticity theory is consistent with the work-conjugate type[6] of finite deformation gradient crystal plasticity theory of Gurtin (2008) with quadratic

[4] In Gurtin (Gurtin and Anand (2007)), the microscopic stress is further decomposed into energetic and dissipative parts. In the present study only the energetic part is taken into account.

[5] No interaction between the slip systems is considered here.

[6] This consistency was first discussed in Kuroda and Tvergaard (2006) for small strain single-slip case, and subsequently the discussion was extended to multi-slip and finite strain contexts (Kuroda and Tvergaard (2008 a); Kuroda and Tvergaard (2008 b)).

forms of the defect energy. Eqs. (51) and (52) satisfy the key relation (44), and Eq. (52) is derived from Eq. (53) and the free-energy inequality. Therefore, when the backstress to be used in the slip rate relation (36) is given by Eq. (51), the present theory automatically satisfies the thermodynamic consistency discussed in Gurtin (2002) and Gurtin (2008). However, general heuristic formulations for $\tau_{\mathrm{b}}^{(\alpha)}$ does not necessarily satisfy such a condition.

5 Computational aspects of the theory

For the lower-order theories, the boundary conditions that enter boundary value problems are the same as those in the conventional theory, and no extra boundary condition is needed. By contrast, in the higher-order theories, additional governing equations and corresponding extra boundary conditions are introduced. In this section, numerical aspects of the higher-order theory are presented using some basic problems, including bending of single-crystal foils, which corresponds to the experimental study shown in Section 3. The computational results presented in the subsections (5.2 - 5.4) are condensed from Kuroda (2011), and the results presented in the subsection 5.5 are taken from Hayashi et al. (2011).

5.1 Finite element formulations

A finite element formulation for the theory involving the higher-order effects is presented (Kuroda and Tvergaard (2008 b); Kuroda and Tvergaard (2009); Kuroda (2011)). Finite element equations are derived from the relations (41) and (43), treating the GND density rates as additional nodal degrees of freedom (Kuroda and Tvergaard (2008 b)). The finite element equation based on the conventional virtual work relation, Eq. (41), is in the usual form, and is not repeated here. In the present study, two-dimensional problems are considered. Thus, only the edge GND densities are accounted for in numerical computations. The edge GND density rates are interpolated as

$$\dot{\rho}_{\mathrm{G}(e)}^{(\alpha)} = [N_\rho]\{\dot{\rho}_{\mathrm{G}(e)}^{(\alpha)}\}, \tag{54}$$

where $[N_\rho]$ is a vector-type array of finite element shape functions that do not necessarily coincide with those for the displacement rate field, and $\{\dot{\rho}_{\mathrm{G}(e)}^{(\alpha)}\}$ is a vector-type array of nodal values of the edge GND density rate.

Then, the finite element equation corresponding to Eq. (43) becomes

$$\begin{aligned}\int_v [N_\rho]^{\mathrm{T}}[N_p]dv\{\dot{\rho}^{(\alpha)}_{\mathrm{G}(e)}\} &= \tfrac{1}{b}[B_\rho]^{\mathrm{T}}\{\bar{s}^{(\alpha)}\}\dot{\gamma}^{(\alpha)}dv \\ &+\tfrac{1}{b}\textstyle\int_v [N_\rho]^{\mathrm{T}}\mathrm{div}\bar{\boldsymbol{s}}^{(\alpha)}\dot{\gamma}^{(\alpha)}dv \\ &-\tfrac{1}{b}\textstyle\int_s [N_\rho]^{\mathrm{T}}\bar{\boldsymbol{n}}\cdot\bar{\boldsymbol{s}}^{(\alpha)}\dot{\gamma}^{(\alpha)}ds,\end{aligned} \tag{55}$$

where the matrix $[B_\rho]$ contains the derivatives of each component of $[N_\rho]$ with respect to $\boldsymbol{x}$, and $\{\bar{s}^{(\alpha)}\}$ contains the Cartesian components of $\bar{\boldsymbol{s}}^{(\alpha)}$.

The term $\mathrm{div}\bar{\boldsymbol{s}}^{(\alpha)}$ is evaluated in the following manner: (i) for each element, the values of the components of $\bar{\boldsymbol{s}}^{(\alpha)}$ are extrapolated from the integration points to the nodal points using an approximated plane determined by a least-square method; (ii) the values of the components of $\bar{\boldsymbol{s}}^{(\alpha)}$ associated with a global node are taken to be the averages of the local nodal values of each element which includes that node in its connectivity; (iii) the gradients of $\bar{\boldsymbol{s}}^{(\alpha)}$ at the integration points within an element are computed using the derivatives of the shape functions, and $\mathrm{div}\bar{\boldsymbol{s}}^{(\alpha)}$ is computed as $\partial\bar{s}^{(\alpha)}_1/\partial x_1 + \partial\bar{s}^{(\alpha)}_2/\partial x_2$.

In the present computations, a straightforward linear incremental method is adopted, while carefully choosing small time steps so as to retain stable and convergent solutions. Since we here adopt the viscoplastic constitutive model, the analyses of displacement rates and GND density rates can be decoupled by applying a staggered-type solution scheme for time integration as in Yefimov et al. (2004 b), Yefimov et al. (2004 a), Kuroda and Tvergaard (2006), Kuroda and Tvergaard (2008 a), Kuroda and Tvergaard (2008 b) and Kuroda and Tvergaard (2009).

To obtain relevant solutions at finite strains, a proper choice of finite elements is essential. Here, three types of finite element formulation are adopted (Kuroda (2011)). First, the 8RI-4FI formulation is considered, in which the displacement field is solved using eight-node elements with 2×2 Gauss points (i.e. reduced integration) and the GND density field is solved using four-node elements with 2×2 Gauss points (i.e. full integration). The coordinates of the nodes in the four-node elements are identical to those of the corner nodes in the eight-node elements. The positions of Gauss points in the eight-node and four-node elements do not coincide with each other in a deformed state. Some preliminary computations showed that the effect of this discrepancy on numerical results is negligible, at least, in the problems solved in the following. This was confirmed through a comparison of a solution obtained using the 8RI-4FI formulation with a solution obtained using a *modified* 8RI-4FI formulation in which the biquadratic Jacobian was also used in the four-node elements for the GND density rate field analysis.

The second choice is the '8FI-8FI' formulation, in which both the displacement rate and GND density rate fields are solved using eight-node elements with 3×3 Gauss points (i.e. full integration). The application of reduced integration to Eq. (55) is not suitable, because the matrix $\int_v [N_\rho]^{\mathrm{T}} [N_\rho] dv$ evaluated by the reduced integration carries several zero eigenvalues that result in a singular matrix. The matrix for a rectangular-shaped eight-node element evaluated by 2×2 integration carries four zero eigenvalues. Therefore, the full integration procedure is employed for the GND density rate analysis. The third one is the '4FI-4FI' or '4SRI-4FI' formulation in which the displacement field is solved using four-node elements evaluated by full integration (2×2 Gauss points) or by selectively reduced integration[7] (2×2 Gauss points for the deviatoric part and only a single Gauss point for the volumetric part), depending on whether or not the problem encounters a plastically incompressible difficulty, and the GND density rate field is solved using four-node elements with 2×2 Gauss points (full integration). In computations with the conventional theory, which do not need additional degrees of freedom for $\dot{\rho}^{(\alpha)}_{\mathrm{G}(e)}$, these element types are simply denoted by 8RI, 8FI, and 4FI (or 4SRI).

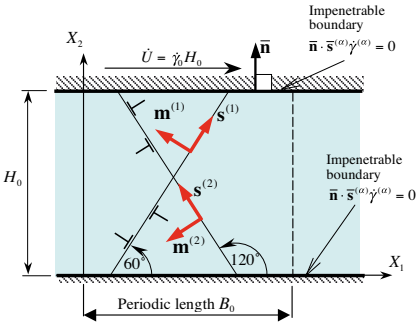

Figure 6. Constrained simple shear problem.

5.2 Constrained simple shear of a double-slip single crystal

In this first example, a thin strip having two-dimensional two slip systems with slip directions of 60° and 120°, specified by angles measured counterclockwise from the X_1 -direction, is considered (Kuroda (2011)), as indicated in Fig. 6. Only the edge dislocations are taken into account; i.e. the direction of dislocation lines always coincides with the X_3 -direction,

[7] The *B-bar* method (Hughes (1980)) is adopted.

$\boldsymbol{p}^{(\alpha)} = \bar{\boldsymbol{p}}^{(\alpha)} = \boldsymbol{e}_3$, where $\boldsymbol{e}_i$ are the Cartesian unit base vectors. The height of the strip is H_0 in the X_2 -direction. This strip is subjected to a simple shear (Fig. 6) under plane strain conditions.

The macroscopic boundary conditions are

$$\left.\begin{aligned} &v_1 = 0, \quad v_2 = 0 \quad \text{along } X_2 = 0; \\ &v_1 = \dot{U} = H_0\dot{\gamma}_0, \quad v_2 = 0 \quad \text{along } X_2 = H_0, \end{aligned}\right\} \tag{56}$$

and the macroscopic shear strain Γ is defined by

$$\Gamma = U/H_0. \tag{57}$$

Using the surface integration term in Eq. (43), the slip rate in the boundary normal directions can be specified. The microscopic boundary condition for the interfaces (at $X_2 = 0$, H_0) being impenetrable to dislocations is adopted as

$$\bar{\boldsymbol{n}} \cdot \bar{\boldsymbol{s}}^{(\alpha)}\dot{\gamma}^{(\alpha)} = 0. \tag{58}$$

This means that there is no outflow of dislocations through the interface.

The strip is assumed to be extended infinitely in the X_1 -direction. Consequently, this problem is essentially one-dimensional, that is, all the quantities vary only in the X_2 -direction. Thus, when formulating the problem in a two-dimensional format, all field quantities are required to be periodic in the X_1 -direction with an *arbitrarily chosen* periodic length B_0 , i.e.

$$\left.\begin{aligned} v_i(0, X_2) \quad &= v_i(B_0, X_2) \\ \dot{\rho}^{(\alpha)}_{\mathrm{G}(e)}(0, X_2) \quad &= \dot{\rho}^{(\alpha)}_{\mathrm{G}(e)}(B_0, X_2) \end{aligned}\right\}. \tag{59}$$

The problem is solved using a model composed of a single column of quadrilateral elements aligned in the X_2 -direction. Here, N is defined as the number of elements aligned in the columnar model.

Isotropic hardening is assumed to be size-independent, i.e.

$$\dot{\tau}^{(\alpha)}_{\mathrm{C}} = \sum_{\beta} h^{(\alpha\beta)}|\dot{\gamma}^{(\beta)}| \,, \quad \tau^{(\alpha)}_{\mathrm{C}}|_{t=0} = \tau_0. \tag{60}$$

The material parameter values are taken as follows: Youngs modulus $E =$ 130 GPa, Poisson's ratio $\nu = 0.3$, $\tau_0 = 50$ MPa, $h^{(\alpha\beta)} = 250$ MPa (linear slip hardening), and $m = 0.02$. A definition of the slip on slip system α ,

$$\gamma^{(\alpha)} \equiv \int_0^t \dot{\gamma}^{(\alpha)} dt, \tag{61}$$

is introduced as a measure of accumulated plastic deformation.

The backtress coefficient B in Eq. (35) is replaced by the following simple expression,

$$B = b\tau_0 l^2, \tag{62}$$

where l is a length scale parameter.

The distributions of $\gamma^{(\alpha)}$ at $\Gamma = 0.24$ for the length scale $l/H_0 = 0.3$ are depicted in Fig. 7. The result for the 4FI-4FI formulation with $N = 40$ has been taken from Kuroda and Tvergaard (2008 b), which was confirmed to be a convergent solution with respect to element discretization. As reported in Kuroda and Tvergaard (2008 b), the solution obtained using 4SRI-4FI is completely identical to that obtained using 4FI-4FI. The 4FI-4FI solution does not exhibit any symptom of locking in this problem. As can be seen in Fig. 7, the 8RI-4FI formulation with $N = 30$ and the 8FI-8FI formulation with $N = 16$ give solutions identical to that for the 4FI-4FI formulation with $N = 40$. For the present problem in which every element is deformed in the simple shear mode along two of the element boundaries, all the element formulations produce satisfactorily accurate solutions with a reasonable element number, at least, for the slips as shown in Fig. 7.

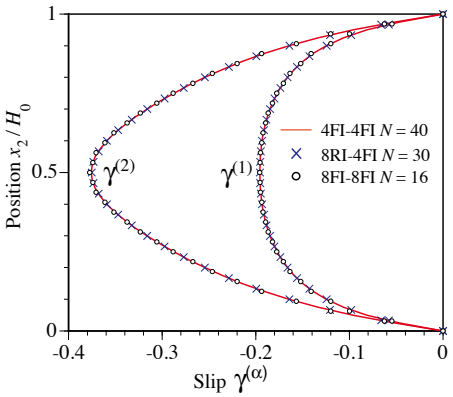

Figure 7. Distributions of slip across the thickness for constrained simple shear problem.

However, stress solutions are not identical. In the present problem, σ_{22} and σ_{12} must be uniform due to the requirement of the equilibrium condition, $\mathrm{div}\boldsymbol{\sigma} = \mathbf{0}$. Only 8FI-8FI exhibited small stress oscillations, which violate the uniformity of σ_{22} and σ_{12}. The mean values of the oscillatory stress distributions completely coincide with the stress solutions obtained

using 4FI-4FI, 4SRI-4FI and 8RI-4FI. Thus, the oscillatory behavior does not relate to global stiffening of the material response.

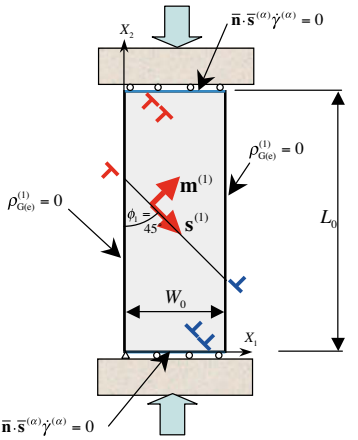

Figure 8. Compression problem of single-slip single crystal with loading surfaces impenetrable to dislocations under plane strain conditions.

5.3 Compression of a single-slip single crystal

A rectangular-shaped single crystal with only one slip system oriented at $\phi_1 = 45°$ relative to the compressive axis is subjected to simple compression under plane strain conditions (Kuroda (2011)) as shown in Fig. 8. The macroscopic boundary conditions are assumed to be

$$\left.\begin{aligned} &v_2 = 0,\ \dot{\hat{t}}_1 = 0 && \text{along } X_2 = 0,\\ &v_2 = \dot{U},\ \dot{\hat{t}}_1 = 0 && \text{along } X_2 = L_0,\\ &\dot{\hat{t}}_1 = \dot{\hat{t}}_2 = 0 && \text{along } X_1 = 0, W_0, \end{aligned}\right\} \tag{63}$$

where L_0 and W_0 are the initial length and width of the specimen, respectively, and $\dot{U}$ is a prescribed end-displacement rate that is taken to be $-\dot{\gamma}_0 \cos\phi_1 \sin\phi_1 L_0$. The aspect ratio of the specimen is $L_0/W_0 = 3$. The nominal compressive strain and nominal stress are respectively defined as $-U/L_0$ and P/W_0, where P is computed from the sum of the nodal forces in the X_2 -direction along $X_2 = 0$.

In addition to the standard displacement/traction boundary conditions, the loading surfaces are assumed to be impenetrable to dislocations (no

plastic flow through the loading surfaces), while plastic straining can occur freely on the left- and right-hand sides of the body, i.e.

$$\left.\begin{array}{ll} \bar{\boldsymbol{n}} \cdot \bar{\boldsymbol{s}}^{(\alpha)} \dot{\gamma}^{(\alpha)} = 0 & \text{along } X_2 = 0, L_0, \\ \rho^{\alpha}_{\mathrm{G}(e)} & \text{along } X_1 = 0, W_0. \end{array}\right\} \tag{64}$$

The material parameter values are taken to be $E = 130$ GPa, $\tau_0 = 50$ MPa, $\nu = 0.3$, $m = 0.05$, and $h^{(\alpha\beta)} = 0$ (no internal hardening). The present problem is the same as that analyzed in Kuroda and Tvergaard (2009). However, they employed 4SRI-4FI only and performed a computation up to a nominal compressive strain of 0.05.

Fig. 9 shows the deformed meshes and contours of the accumulated slip ($\gamma_{\mathrm{a}} \equiv \int_0^t \left|\dot{\gamma}^{(1)}\right| dt$) at a nominal compressive strain of 0.1 obtained using conventional crystal plasticity theory (with zero length scale $l = 0$). All three element formulations predict a similar highly nonuniform deformation mode. Fig. 10 depicts curves of nominal compressive stress versus nominal compressive strain. Beyond a nominal strain of 0.025, 4SRI predicts a slightly stiffer response than the other two element formulations. The deformed meshes and contours of an accumulated slip at a nominal compressive strain of 0.1 for the gradient theory with a length scale of $l/W_0 = 1$ are shown in

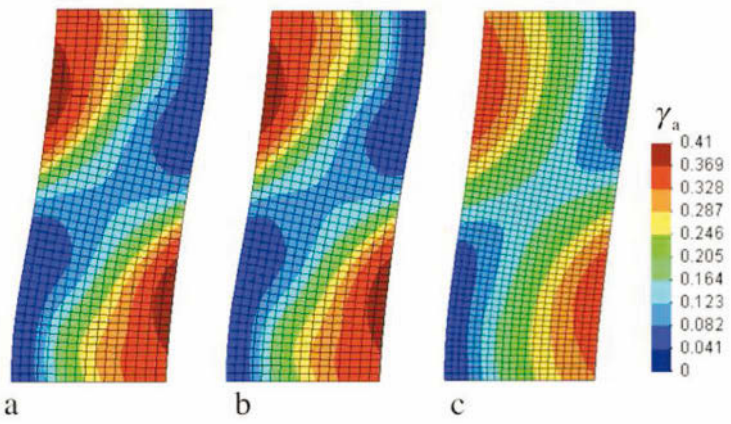

Figure 9. Deformed meshes and contours of accumulated slip γ_{a} a at a nominal compressive strain of 0.1 for the compression problem obtained using conventional crystal plasticity theory: results for (a) 8RI (16×48); (b) 8FI (16×48); (c) 4SRI (20×60).

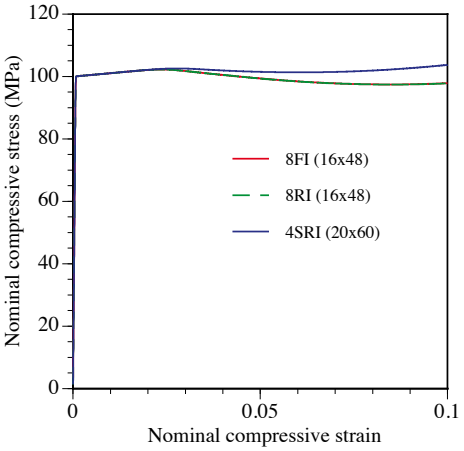

Figure 10. Curves of nominal stress versus nominal strain for compression problem obtained using conventional crystal plasticity theory.

Fig. 11. The deformation mode is significantly different from that for the conventional theory. In the case of 8RI-4FI (Fig. 11_a), the central region of the specimen exhibits uniform simple shear deformation along the slip direction, and the rest of the part (the wedge portions) is hardly deformed. The deformation mode changes abruptly within a single row of elements. In the present problem, there is no constraint on slip on the left- and right-hand sides of the specimen. Thus, the whole diagonal region should be able to deform in the simple shear mode with no constraint, i.e. with no back-stress corresponding to no pile-up at the free side surfaces. The interface between the simple shear region and the hardly deformed region, which is not along element boundaries, is well captured by 8RI-4FI. The deformation behavior predicted by 8FI-8FI (Fig. 11_b) is similar to that predicted by 8RI-4FI. However, a transitional zone between the simple shear region and the hardly deformed region can be seen, which is composed of two to three rows of elements, and also bands with a slightly higher amount of slip can be seen at the upper and lower portions of the simple shear region. The deformation behavior predicted by 4SRI-4FI (Fig. 11_c) is different from those predicted by 8RI-4FI and 8FI-8FI. The amount of accumulated slip gradually increases towards the center of the specimen. This is attributed to the fact that 4SRI-4FI exhibits a stiffer response to shear deformation in directions other than along the edges of the element. The corresponding nominal compressive stress-nominal compressive strain curves are plotted

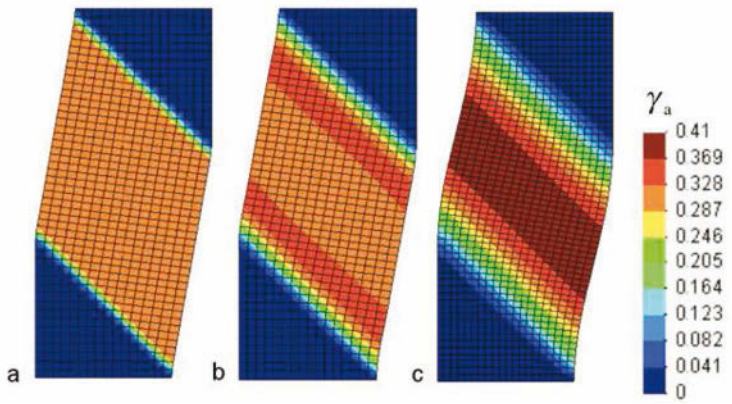

Figure 11. Deformed meshes and contours of accumulated slip γ_a a at a nominal compressive strain of 0.1 for compression problem obtained using gradient-dependent crystal plasticity theory with $l/W_0 = 1.0$: results for (a) 8RI-4FI (16×48); (b) 8FI-8FI (16×48); (c) 4SRI-4FI (20×60).

in Fig. 12. The 4SRI-4FI formulation predicts a larger amount of nominal stress than 8RI-4FI and 8FI-8FI. Comparing Fig. 12 with Fig. 10, it can be seen that the present length scale effect originating from the GND densities does not change the macroscopic yield stresses of the material (they remain at about 100 MPa).

5.4 Tension of single crystal with shear band formation

A rectangular-shaped single crystal having three slip systems whose slip directions are specified by an angle $\phi(= 54.7°)$ (Kysar et al. (2010)) is subjected to tension under plane strain conditions (Kuroda (2011)) (Fig. 13).

The macroscopic boundary conditions are set to be

$$\left.\begin{array}{ll} v_2 = 0,\ \dot{\hat{t}}_1 = 0 & \text{along } X_2 = 0, \\ v_2 = \dot{U},\ \dot{\hat{t}}_1 = 0 & \text{along } X_2 = L_0, \\ \dot{\hat{t}}_1 = \dot{\hat{t}}_2 = 0 & \text{along } X_1 = -\frac{1}{2}(W_0 + \Delta W_0), +\frac{1}{2}(W_0 + \Delta W_0). \end{array}\right\} \quad (65)$$

In this problem, a geometrical imperfection is introduced as

$$\Delta W_0 = W_0[\xi_1 \cos(2\pi x_2/L_0) + \xi_2 \cos(4\pi x_2/L_0)] \quad (66)$$

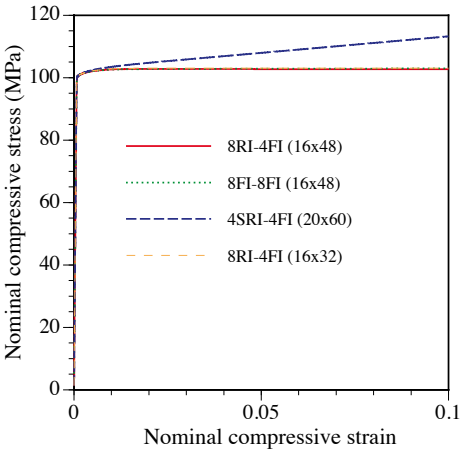

Figure 12. Curves of nominal stress versus nominal strain for compression problem obtained using gradient-dependent crystal plasticity theory with $l/W_0 = 1.0$.

with $\xi_1 = 0.0042$ and $\xi_2 = 0.0024$. The prescribed displacement rate is given by $\dot{U} = 2\dot{\gamma}_0 \cos\phi \sin\phi L_0$ and the aspect ratio of the specimen is $L_0/W_0 = 2$. For all the boundaries, the following GND density-free conditions are applied:

$$\left.\begin{aligned} &\rho^{(\alpha)}_{\mathrm{G}(e)} = 0 \quad \text{along } X_2 = 0, \\ &\rho^{(\alpha)}_{\mathrm{G}(e)} = 0 \quad \text{along } X_2 = L_0, \\ &\rho^{(\alpha)}_{\mathrm{G}(e)} = 0 \quad \text{along } X_1 = -\tfrac{1}{2}(W_0 + \Delta W_0), +\tfrac{1}{2}(W_0 + \Delta W_0). \end{aligned}\right\} \tag{67}$$

The material parameter values are taken to be $E = 1000\tau_0$, $\tau_0 = 60.84$MPa, $\nu = 0.3$, $m = 0.005$, and

$$h^{(\alpha\beta)} = h = h_0 \mathrm{sech}^2\left(\frac{h_0\gamma^{\mathrm{tot}}_{\mathrm{a}}}{\tau_{\mathrm{S}} - \tau_0}\right); \quad \gamma^{\mathrm{tot}}_{\mathrm{a}} = \sum_{\alpha}\int_0^t |\dot{\gamma}^{(\alpha)}|dt, \tag{68}$$

where $h_0 = 8.9\tau_0$ and $\tau_{\mathrm{S}} = 1.8\tau_0$ (Peirce et al. (1983)). The nominal stress and nominal strain used in the nominal stressnominal strain curves are respectively defined as P/W_0 (with P computed from the sum of the nodal forces in the X_2 -direction along $X_2 = L_0$) and U/L_0.

Fig. 14 shows the deformed meshes and contours of the total accumulated slip $\gamma^{\mathrm{tot}}_{\mathrm{a}}$ at a nominal strain of 0.18 obtained using the conventional theory

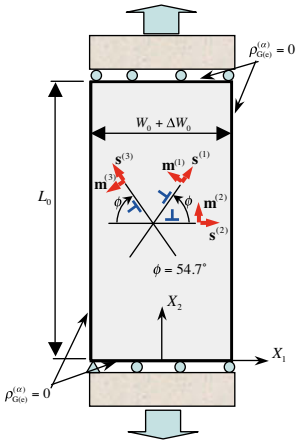

Figure 13. Tension problem of single crystal with dislocation-free surfaces under plane strain conditions.

($l = 0$). For 8RI and 8FI, a mesh of 32×64 quadrilaterals is employed, while for 4SRI a slightly finer mesh (38×76) is used. To observe the mesh dependence of the solution for the conventional theory, the result with a mesh of 16×32 quadrilaterals of 8RI is shown. The mesh of 32×64 for the 8RI formulation predicts the most severe shear band formation. Comparing Figs. 14_a and 14_b, the mesh dependence of the solution can be observed. The 8FI formulation predicts the formation of a little bit weaker shear bands. By contrast, 4SRI predicts a diffuse neck-type deformation mode with broad shear bands, which is significantly different from the deformation model predicted by the other two element formulations.

The corresponding nominal stress-nominal strain curves are plotted in Fig. 15. Only in the case of 8RI (32×64), a noticeable decrease in nominal stress associated with shear band development is seen. The 4SRI formulation predicts a higher nominal stress response associated with less plastic flow localization observed in Fig. 14_d. It appears that 4SRI is not promising for obtaining a relevant prediction of strain localization at finite strain.

Fig. 16 shows deformed meshes and contours of total accumulated slip γ_a^{tot} at a nominal strain of 0.18 for the gradient-dependent solid. The figure shows a comparison between results for two meshes of 16×32 and 32×64 quadrilaterals with the 8RI-4FI formulation. The length scale parameter is here taken to be $l/W_0 = 0.12$. The shear band width spans over several rows of elements. It can be seen that these two meshes give identical deformation

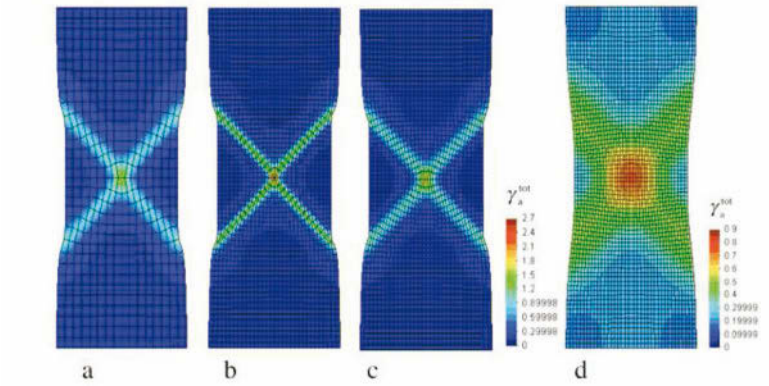

Figure 14. Deformed meshes and contours of total accumulated slip $\gamma_{\mathrm{a}}^{\mathrm{tot}}$ at a nominal strain of 0.18 for tension problem obtained using conventional crystal plasticity theory: results for (a) 8RI (16×32); (b) 8RI (32×64); (c) 8FI (32×64); (d) 4SRI (38×76).

and slip distributions. The solution appears to be mesh-independent, and the result for 32×64 quadrilaterals with the 8RI-4FI formulation is considered to be a convergent solution. The detailed behavior in the gradient-dependent solid with $l/W_0 = 0.12$ modeled by 32×64 quadrilaterals with the 8RI-4FI formulation (at a nominal strain of 0.18) is shown in Fig. 17. The backstress on slip system 1 becomes large along the shear band in which the slip system 3 is the primary system. The effective shear stress $\tau^{(1)} - \tau_{\mathrm{b}}^{(1)}$ becomes almost constant in the band-type region that corresponds to a localized shear zone with a finite width. This stress behavior is unchanged for a coarser mesh of 16×32 quadrilaterals with the 8RI-4FI formulation (not shown here).

It has been confirmed that the backstress relation (51) with an additional term $\bar{\rho}_{\mathrm{G}(e)}^{(\alpha)} \mathrm{div} \bar{\boldsymbol{s}}^{(\alpha)}$ leads to no significant difference in the computational results at least for the three problems demonstrated in sections 5.2, 5.3 and 5.4.

5.5 Bending with reversal of loading direction

In this application, the Ohashi's mean free path model is adopted for the description of size-dependent isotropic hardening, and the generalized backstress model with full stress components (Bayley et al. (2006)) is employed

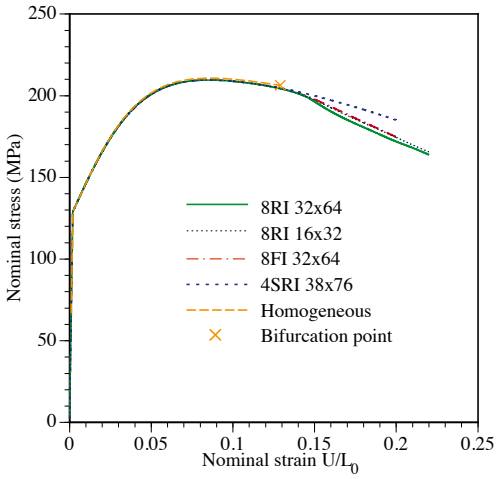

Figure 15. Curves of nominal stress versus nominal strain for tension problem obtained using conventional crystal plasticity theory.

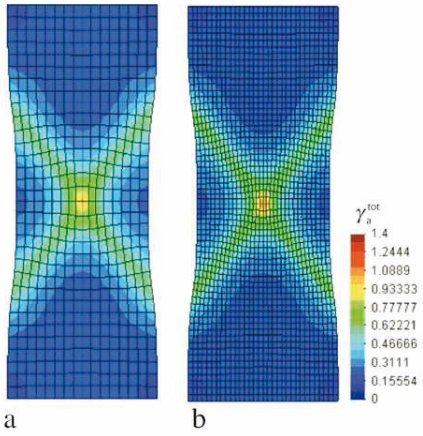

Figure 16. Deformed meshes and contours of total accumulated slip γ_a^{tot} at a nominal strain of 0.18 obtained using gradient-dependent crystal plasticity theory with $l/W_0 = 0.12$: (a) 8RI-4FI (16×32); (b) 8RI-4FI (32×64).

for representing size-dependent kinematic hardening. The results presented here are taken from Hayashi et al. (Hayashi et al. (2011)).

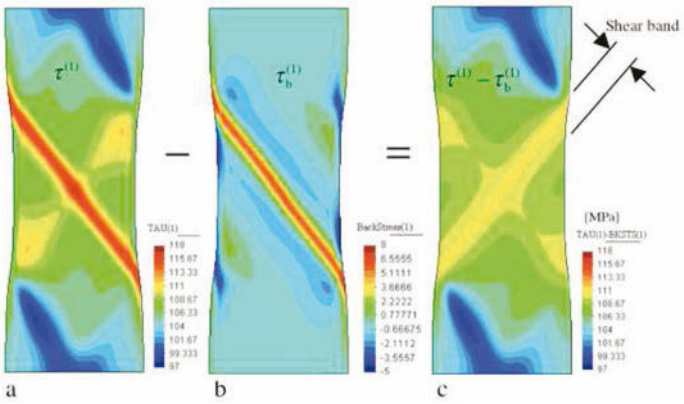

Figure 17. Stress behavior predicted by gradient-dependent crystal plasticity theory with $l/W_0 = 0.12$. (analyzed with the model composed of 32×64 quadrilaterals with the 8RI-4FI formulation).

The ideal cube orientation is assumed in the analysis; i.e., the two crystal axes, [100] and [010], coincide with the direction of tensile stress in bending and the normal direction to the specimen surface. This situation is close to the experimental condition illustrated in Fig. 2_b.

In the problem formulation, taking an arbitrary periodic length of the foil, the pure bending deformation is imposed by rotating both sides of a square shaped analysis region. Plane stress[8] and small strain conditions are assumed. The coordinates x_1 and x_2 are taken to coincide with the directions of length and thickness of the foil, respectively. The 4FI-4FI elements are used, which lead to relevant solutions for plane stress problems at small strains.

Regarding the higher-order boundary conditions, we assume a null GND condition, as a first assumption, at the specimen surfaces. That is, it is postulated that the dislocations can freely exit from the surfaces and no geometrically necessary dislocation is required at the surfaces. This type of higher-order boundary condition is called micro-free condition in previous strain gradient approaches (e.g. Gurtin (2002)). In the microbend experiments, however, contact between the specimen and the mandrel was necessary especially near the end points of the uniform curvature region of the foil. At the flattening step for the reversal of loading, contact be-

[8] We confirmed that the computational results for plane stress and plane strain assumption were similar in the case of the present bending problem.

tween the foil and the tools was also inevitable. But, effects of the contact on the higher-order boundary conditions are not evaluated quantitatively at present. Under such status, the GND-free condition at the specimen surfaces is adopted here as the simplest assumption.

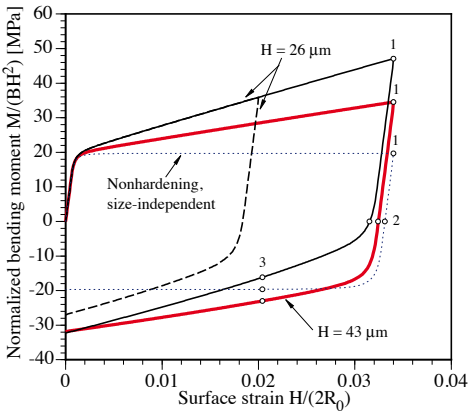

Figure 18. Computed curves of normalized bending moment versus surface strain for pure bending with the reversal of bending direction.

Computed curves of the bending moment normalized by the square of thickness versus surface strain for two different foil thicknesses (43μm and 26μm) are shown in Fig. 18. The size-effect parameter r_0 in Eq. (31) is chosen to be 3.5μm. At the point of zero surface strain after the complete reversal of loading, the curve for the thinner foil has returned to a normalized bending moment slightly larger than, but almost the same as, that for the thicker foil. This means that the size dependence of isotropic hardening is not well described by the present model. In contrast, a pronounced size-dependent kinematic hardening behavior is clearly predicted by the simulations. For comparison purposes and as a reference case, the normalized bending moment-surface strain relation for a nonhardening (with constant $\tau_{\mathrm{C}}^{(\alpha)}$) and size-independent foil ($r_0 = 0$) is also shown in Fig. 18.

Distributions of the normal stress (bending stress), σ_{11} , across the thickness at stages 1, 2 and 3 on the curves in Fig. 18 are shown in Fig. 19. At stage 1 (immediately before unloading), the stresses near the top and bottom surfaces are significantly larger than those in the inner portion[9]. There

[9]The accuracy of the predicted stress near the neutral axis is inherently lower than those near the surfaces, which depends on the finite element mesh discretization, because

appear to be "boundary layers" in stress distribution near the surfaces. As can be seen in Figs. 19_a and 19_b, the width of the boundary layers is constant for the two different foil thicknesses. The effect of the boundary layers on the bending moment should be more dominant in the thinner foil than in the thicker foil. This manifests itself as the "smaller is stronger" behavior observed during forward loading in the curves of normalized bending moment versus surface strain. The boundary layers still remain after the unloading with zero bending moment at stage 2 and the reversal of loading at stage 3. The boundary layers in stress distribution at stage 3 lead to the reduction of bending moment as can be understood from the stress distribution profiles. This stress behavior is seen as the Bauschinger effect in the bending moment-surface strain diagrams. In the nonhardening size-independent case (Fig. 19_c), the stress distributions are almost flat and no boundary layer appears, as expected.

The resolved backstress distributions on slip system 1 are depicted in Fig. 20: the backstress does not change their profiles after the unloading and even after the reversal of loading because it arises from the second-order spatial gradients of slips whose distributions change slowly after the reversal of loading. This nature of backstress is the origin of the observed Bauschinger effect. The boundary layers observed in the distribution profiles of the stress and resolved backstress are attributed to the extra boundary conditions set at the top and bottom surfaces, i.e., the null GND condition at the boundaries.

The model captured the kinematic hardening behavior as well as the Bauschinger effect qualitatively. The assumption of null GND as an extra boundary condition at the free surfaces indeed leads to higher-order spatial gradients of slips in the bent specimens. This resulted in the size-dependent kinematic hardening during forward loading and the Bauschinger effect emerging after the reversal of loading. The size-dependent isotropic hardening behavior (observed in Fig. 4_b and 5), however was not well reproduced in the simulation. One of the reasons for this may be considered as follows. The null GND condition leading to higher-order slip gradients near the surfaces simultaneously causes a sparseness of the GNDs in the same regions (Fig. 21). These regions with low densities of the GNDs correspond to the boundary layers observed in the profiles of the stress and backstress distributions. This sparseness results in a weaker effect of the GNDs on

the spatial gradients of the stress are extremely steep near the neutral axis in bent specimens under plastic deformation. However, the stress values around the neutral axis have only a negligible effect on the bending moment.

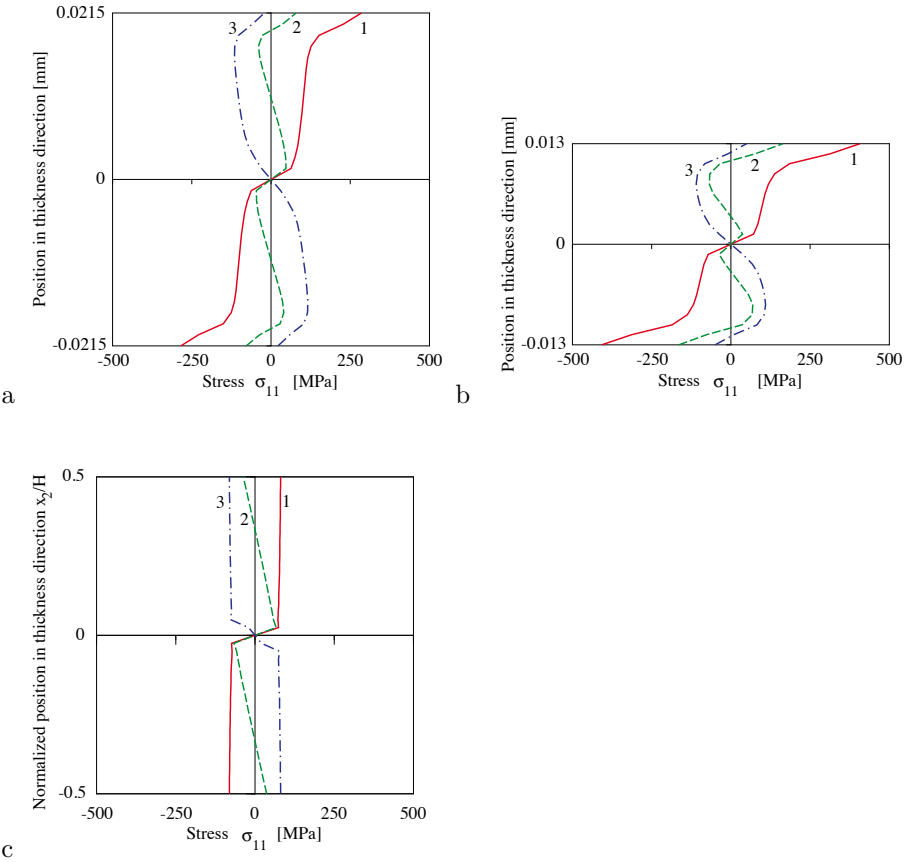

Figure 19. Distributions of the normal stress, σ_{11}, in the thickness direction at stages 1, 2, and 3 on the computed curves in Fig. 18: (a) $43-\mu$m-thick specimen; (b) $26-\mu$m-thick specimen; (c) nonhardening specimen with no length scale.

isotropic hardening.

There may be some question about the physical basis of the extra boundary condition for the GND densities at the top and bottom surfaces. As discussed in Kuroda and Tvergaard (2008 a), formulations of higher-order gradient crystal plasticity models are classified into work-conjugate and non-work-conjugate types. In the former type of formulation proposed by Gurtin

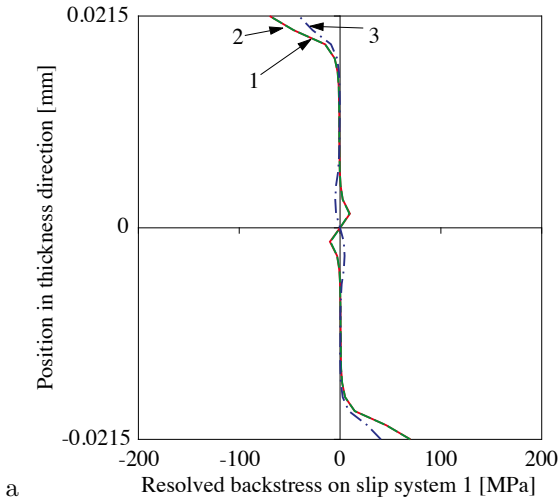

a

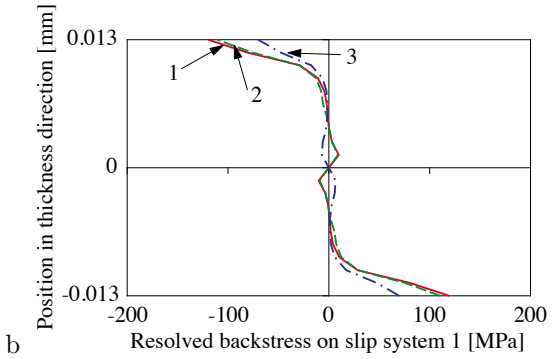

b

Figure 20. Distributions of resolved backstress, τ_{b}, on slip system 1 in the thickness direction at stages 1, 2, and 3 on the computed curves in Fig. 18: (a) $43-\mu$m-thick specimen; (b) $26-\mu$m-thick specimen.

(2002), vector type higher-order stresses are introduced as quantities that are work-conjugate to the slip gradients into an extended virtual work prin-

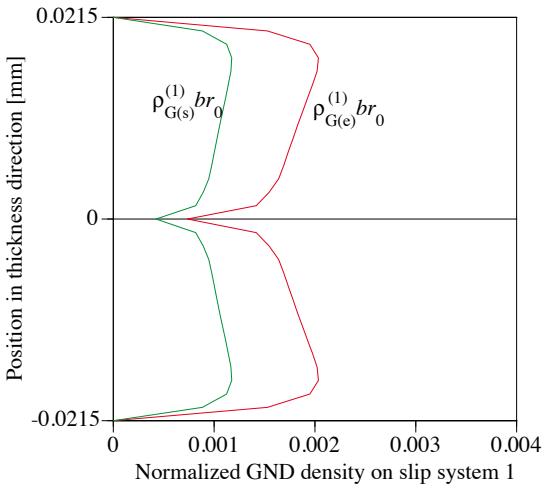

a

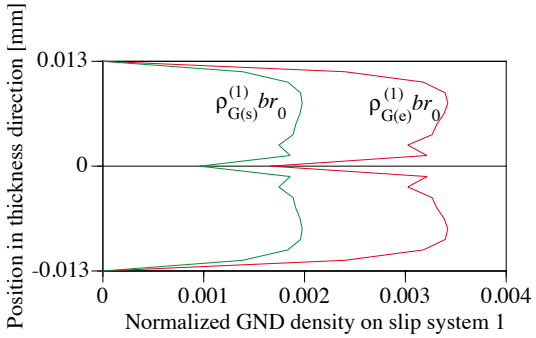

b

Figure 21. Distributions of the GND densities on slip system 1 in the thickness direction at stage 1 on the computed curves in Fig. 18: (a) $43-\mu$m-thick specimen; (b) $26-\mu$m-thick specimen.

ciple. A micro-free condition in which the normal component of higher-order stress at the boundaries is zero corresponds to the null GND condition assumed in the present simulations. A full interpretation of higher-order stress in the mechanics of materials has not yet been provided, and the micro-free condition appears to be a rather mathematical setup.

6 Phenomenological theory

In this section, a phenomenological higher-order strain-gradient plasticity theory is presented through a formulation inspired by the higher-order gradient crystal plasticity discussed above. A physical interpretation of the phenomenological yield condition that involves second-order gradient of the equivalent plastic strain is discussed, applying a dislocation theory-based consideration. The investigation presented here is condensed from Kuroda and Tvergaard (2010).

6.1 Constitutive relations

The theory considered here does not differ much from the conventional plasticity theory. We confine attention to small strain conditions, where geometry changes are neglected. An additive decomposition of the total strain rate $\dot{\boldsymbol{E}}$ is considered as

$$\dot{\boldsymbol{E}} \equiv (\dot{\boldsymbol{u}} \otimes \nabla)_{\mathrm{sym}} = \dot{\boldsymbol{E}}^{\mathrm{e}} + \dot{\boldsymbol{E}}^{\mathrm{e}}, \tag{69}$$

where superscripts e and p denote elastic and plastic parts, and $(\bullet)_{\mathrm{sym}}$ denotes the symmetric part of the tensor. A standard Hooke's law is adopted for elasticity, and a coaxial flow rule is used for plasticity:

$$\dot{\boldsymbol{E}}^{\mathrm{e}} = C^{-1} : \dot{\boldsymbol{\sigma}}; \quad \dot{\boldsymbol{E}}^{\mathrm{p}} = \dot{\phi}\boldsymbol{N}^{\mathrm{p}}; \quad \boldsymbol{N}^{\mathrm{p}} = \frac{\boldsymbol{\sigma}'}{|\boldsymbol{\sigma}'|}, \tag{70}$$

where $\boldsymbol{\sigma}'$ is the deviatoric part of the stress, $|(\bullet)| = \sqrt{(\bullet) : (\bullet)}$, and $\dot{\phi}$ is a plastic multiplier.

Here we introduce the following conventional power law:

$$\dot{\phi} = \dot{\phi}_0 \left(\frac{\sigma_{\mathrm{e}}}{S(\varepsilon^{\mathrm{p}})} \right)^{1/m}, \tag{71}$$

where $\sigma_{\mathrm{e}} = \sqrt{\frac{3}{2}}|\boldsymbol{\sigma}'|$ (the von Mises type of effective stress), $\dot{\phi}_0$ is a reference strain rate, and S represents a strain hardening state that is assumed as a function of an equivalent plastic strain

$$\varepsilon^{\mathrm{p}} = \int_0^t \dot{\varepsilon}^{\mathrm{p}} dt, \quad \dot{\varepsilon}^{\mathrm{p}} = \sqrt{\frac{2}{3}}\dot{\phi} \tag{72}$$

with time t. A simple gradient-enhanced model is introduced as

$$\dot{\phi} = \begin{cases} \dot{\phi}_0 \left(\frac{\sigma_{\mathrm{e}} + \beta\nabla^2\varepsilon^{\mathrm{p}}}{S(\varepsilon^{\mathrm{p}})} \right) & \text{for } \sigma_{\mathrm{e}} + \beta\nabla^2\varepsilon^{\mathrm{p}} > 0, \\ 0 & \text{otherwise,} \end{cases} \tag{73}$$

where β is a positive scalar coefficient and $\nabla^2 (= \nabla \cdot \nabla)$ is the Laplace operator. Although adding the term $\beta \nabla^2 \varepsilon^{\mathrm{p}}$ was first introduced by Aifantis (1984), this also might be motivated by an argument based on the dislocation theory.

Within a uniform field of dislocations with the same sign, dislocations oppositely equidistant from the material point would give opposite stress values to that point (Evers et al. (2004); Bayley et al. (2006)), according to the classical elastic solution for the stress field caused by an isolated dislocation (e.g. Cottrell (1953)). Namely, a resulting internal stress at the material point, which is caused by uniformly distributed GNDs around that point, completely cancels out. Therefore, a dislocation-induced internal stress should arise in response to spatial gradients of the GND density, not to the GND density itself (Groma et al. (2003); Evers et al. (2004); Bayley et al. (2006); Geers et al. (2007); Kuroda and Tvergaard (2006); Kuroda and Tvergaard (2008 a); Suzuki et al. (2009)). This has been discussed in the subsection 4.3[10]. The density of the GNDs corresponds to the spatial gradient of crystallographic slip. Therefore, the internal stresses shall develop in response to the second gradient of the slip. The introduction of the term $\beta \nabla^2 \varepsilon^{\mathrm{p}}$ is consistent with this argument. The coefficient β involves a material length scale. The physical interpretation of the material length scale is still an open question. One may be able to find an appropriate value of β for a specific material through identifying with experimental results as in Fleck et al. (1994), Stölken and Evans (1998), and Suzuki et al. (2009). In the context of crystal plasticity, (Groma et al. (2003)) and Geers et al. (2007) have discussed a physical approach to material length scales, which are set by dislocation densities.

It is noted that the present phenomenological model uses the effective stress σ_{e} and the equivalent plastic strain ε^{p} to describe the external and internal stress effects, respectively. Consequently, the positive or negative direction of the resolved shear stress and the slip, which is appropriately accounted for in the context of crystal plasticity, is not considered. So, the Bauschinger-like effect caused by pile-ups of single-signed dislocations cannot be represented within the present simplified theory.

As shown above, the terms $\sigma_{\mathrm{e}} + \beta \nabla^2 \varepsilon^{\mathrm{p}}$ in Eq. (73) represent a net stress at the material point, i.e. the superposition of the stress caused by external forces and the internal stress due to nonuniform distribution of nonredundant dislocations. This net stress activates plastic straining, i.e. the generation and movement of dislocations. Thus, the plastic dissipation may be evaluated by $\mathcal{D} = (\sigma_{\mathrm{e}} + \beta \nabla^2 \varepsilon^{\mathrm{p}}) \dot{\varepsilon}^{\mathrm{p}} \geq 0$. This consequence is consistent with

[10]The detailed equations have been given in the subsection 4.3.

a recent discussion in Gurtin and Anand (Gurtin and Anand (2009)) that the nonlocal term $\beta\nabla^2\varepsilon^{\mathrm{p}}$ in the Aifantis original theory should be *energetic*.

6.2 Formulations of boundary value problems

With neglect of the body force effect, the standard equilibrium and boundary conditions are

$$\left.\begin{aligned} &\nabla\cdot\boldsymbol{\sigma}=\mathbf{0}, \\ &\boldsymbol{\sigma}\cdot\boldsymbol{n}=\underline{\boldsymbol{t}} \quad \text{on } s_t, \\ &\dot{\boldsymbol{u}}=\underline{\dot{\boldsymbol{u}}} \quad \text{on } s_u, \end{aligned}\right\} \tag{74}$$

where $\boldsymbol{n}$ is the normal to the surface, $\underline{\boldsymbol{t}}$ denotes a prescribed traction on the surface s_t , $\underline{\dot{\boldsymbol{u}}}$ is the prescribed displacement rate on the surface s_u, while $s(=s_t+s_u)$ is the surface of the body, and the underbars, $\underline{\ }$, mean that the values of the quantity are specified on the boundary. Eqs. (74) are equivalent to the incremental virtual work principle

$$\int_v \dot{\boldsymbol{\sigma}}\delta\dot{\boldsymbol{E}}dv=\int_{s_t}\underline{\dot{\boldsymbol{t}}}\cdot\delta\dot{\boldsymbol{u}}ds, \tag{75}$$

where v is the volume (region) of the body, $\delta\dot{\boldsymbol{u}}$ is an arbitrary virtual velocity satisfying $\delta\dot{\boldsymbol{u}}=0$ on s_u , and $\delta\dot{\boldsymbol{E}}$ is the corresponding virtual strain rate. The constitutive relation (70) with Eq. (73), i.e.

$$\dot{\boldsymbol{\sigma}}=\boldsymbol{C}:(\dot{\boldsymbol{E}}-\dot{\phi}\boldsymbol{N}^{\mathrm{p}}) \tag{76}$$

is used together with Eq. (75).

With only the relations introduced above, extra boundary conditions for ε^{p} cannot be imposed. Here, a quantity $\boldsymbol{g}^{\mathrm{p}}$ is introduced, which is defined formally as a solution of the differential equation

$$\boldsymbol{g}^{\mathrm{p}}+\nabla\varepsilon^{\mathrm{p}}=\mathbf{0}. \tag{77}$$

The $\boldsymbol{g}^{\mathrm{p}}$ may be interpreted as a measure of the GND density in a phenomenological sense. Now, a weak form of Eq. (77) is considered as

$$\int_v(\boldsymbol{g}^{\mathrm{p}}+\nabla\varepsilon^{\mathrm{p}})\cdot\check{\boldsymbol{g}}^{\mathrm{p}}dv=0, \tag{78}$$

where $\check{\boldsymbol{g}}^{\mathrm{p}}$ is an arbitrary weighting function. Using a relation $\nabla\cdot(\varepsilon^{\mathrm{p}}\check{\boldsymbol{g}}^{\mathrm{p}})=\nabla\varepsilon^{\mathrm{p}}\cdot\check{\boldsymbol{g}}^{\mathrm{p}}+(\nabla\cdot\check{\boldsymbol{g}}^{\mathrm{p}})\varepsilon^{\mathrm{p}}$ and the divergence theorem, we obtain

$$\int_v\boldsymbol{g}^{\mathrm{p}}\cdot\check{\boldsymbol{g}}^{\mathrm{p}}dv=\int_v\varepsilon^{\mathrm{p}}(\nabla\cdot\check{\boldsymbol{g}}^{\mathrm{p}})dv-\int_s\underline{\varepsilon}^{\mathrm{p}}\boldsymbol{n}\cdot\check{\boldsymbol{g}}^{\mathrm{p}}ds. \tag{79}$$

With the surface integral term in Eq. (79), the extra boundary conditions for ε^{p} can be specified.

In the present treatment of strain-gradient plasticity, the standard incremental virtual work principle Eq. (75) and Eq. (79) are the governing equations to be solved simultaneously. These equations themselves always hold independent of constitutive assumptions, but they are connected by the constitutive relations involving the higher-order gradient term as in Eq. (73).

6.3 Work-conjugate form

Defining a vector quantity,$\boldsymbol{\tau} = -\beta \boldsymbol{g}^{\mathrm{p}}$ (with a constant $\beta(>0)$), and a scalar quantity,

$$\mathcal{Q} = S(\varepsilon^{\mathrm{p}})(\dot{\phi}/\dot{\phi}_0)^m, \tag{80}$$

Eq. (80) may be written as

$$\sigma_{\mathrm{e}} - \mathcal{Q} + \nabla \cdot \boldsymbol{\tau} = 0 \tag{81}$$

It is noted that Eq. (81) for the rate independent limit with $m \to 0$ is identical to the original proposition of Aifantis (1984),

$$\sigma_{\mathrm{e}} = S(\varepsilon^{\mathrm{p}}) - \beta \nabla^2 \varepsilon^{\mathrm{p}}. \tag{82}$$

The form of Eq. (81) itself is the same as the Fleck-Hutchinsons microforce balance equation, but in their theory, different constitutive models have been used for $\mathcal{Q}$ and $\boldsymbol{\tau}$.

Considering Eq. (69) and the relation $\boldsymbol{\sigma} : \dot{\boldsymbol{E}}^{\mathrm{p}} = \sigma_{\mathrm{e}} \dot{\varepsilon}^{\mathrm{p}}$, the standard virtual work relation is rewritten as

$$\int_v (\boldsymbol{\sigma} : \delta \dot{\boldsymbol{E}}^{\mathrm{e}} + \sigma_{\mathrm{e}} \delta \dot{\varepsilon}^{\mathrm{p}}) dv = \int_{s_t} \underline{\boldsymbol{t}} \cdot \delta \dot{\boldsymbol{u}} ds \tag{83}$$

Furthermore, substituting Eq. (81) into Eq. (83) and using a relation $\nabla \cdot (\boldsymbol{\tau} \delta \dot{\varepsilon}^{\mathrm{p}}) = (\nabla \cdot \boldsymbol{\tau}) \delta \dot{\varepsilon}^{\mathrm{p}} + \boldsymbol{\tau} \cdot \nabla \delta \dot{\varepsilon}^{\mathrm{p}}$ together with the divergence theorem, one can reach the relation

$$\int_v (\boldsymbol{\sigma} : \delta \dot{\boldsymbol{E}}^{\mathrm{e}} + \mathcal{Q} \delta \dot{\varepsilon}^{\mathrm{p}} + \boldsymbol{\tau} \cdot \nabla \delta \dot{\varepsilon}^{\mathrm{p}}) dv = \int_{s_t} \underline{\boldsymbol{t}} \cdot \delta \dot{\boldsymbol{u}} ds + \int_s \underline{\chi} \delta \dot{\varepsilon}^{\mathrm{p}} ds \tag{84}$$

with the definition of $\underline{\chi} = \boldsymbol{\tau} \cdot \boldsymbol{n}$. This expression is the same as the extended virtual work principle of Fleck and Hutchinson (2001), which was introduced as a major premise of their theory. As shown in the above, this kind of work-conjugate type strain gradient theory can be recast into the alternative form presented in subsections 6.1 and 6.2, and the latter vice versa.

7 Concluding remarks

In this article, experimental evidences for the size-effects in plastic strain gradient fields and possible modeling of the size-dependent crystal plasticity have been presented. The microbend tests on single-crystal copper foils with reversal of bending direction exhibited a pronounced Bauschinger effect (i.e. kinematic hardening behavior), and this observation suggested that backstresses existed in the bent specimens. Strong size dependence of isotropic hardening was observed for the multi-planar multi-slip deformation. However, the coplanar slip specimens exhibited no size dependence of isotropic hardening. This suggests that the GNDs on the active slip plane, whose densities must increase with reduction of the foil thickness, do not contribute to self-hardening on that slip plane and the GNDs mainly act as forest dislocations that affect hardening on other slip planes. Based on the interpretation for the experimental observations, the GND-density-dependent isotropic hardening model has been introduced, in which the mean free path of moving dislocations is considered to be shortened by the GNDs that act as forest dislocations. For kinematic hardening behavior, relations for the backstress, which are linear in spatial gradients of the GND densities, are derived, using the classical dislocation theory. The advanced crystal plasticity theory with the GND density-gradient-dependent backstress model is a kind of higher-order type theory, which is accompanied by extra boundary conditions for slips or the GND densities.

Numerical aspects of the present advanced theory with extra boundary conditions have been presented. It has been shown that the choice of finite element type is very important to obtain reliable numerical solutions for large strain higher-order crystal plasticity theory. Also, it has been pointed out that relevant boundary conditions for the GND densities at free boundary surfaces are still uncertain and should be subjected to further investigation.

Finally, an alternative treatment for phenomenological higher-order strain-gradient plasticity theory has been presented through a formulation inspired by the higher-order gradient crystal plasticity model.

Acknowledgement

The author thanks Professor Viggo Tvergaard for the long-term collaboration on the present and related research topics.

Bibliography

A. Acharya. A model of crystal plasticity based on the theory of continuously distributed dislocations. *Journal of the Mechanics and Physics of Solids*, 49:761–784, 2001.

A. Acharya and J.L. Bassani. Lattice incompatibility and a gradient theory of crystal plasticity. *Journal of the Mechanics and Physics of Solids*, 48: 1565–1595, 2000.

E.C. Aifantis. On the microstructural origin of certain inelastic models. *Journal of Engineering Materials and Technology*, 106:326–330, 1984.

A. Arsenlis, D.M. Parks, R. Becker, and V.V. Bulatov. On the evolution of crystallographic dislocation density in non-homogeneously deforming crystals. *Journal of the Mechanics and Physics of Solids*, 52:1213–1246, 2004.

R.J. Asaro and A. Needleman. Texture development and strain hardening in rate dependent polycrystals. *Acta Metallurgica*, 33:923–953, 1985.

M.F. Ashby. The deformation of plastically non-homogeneous materials. *Philosophical Magazine*, 21:399–424, 1970.

C.J. Bayley, W.A.M. Brekelmans, and M.G.D. Geers. A comparison of dislocation induced back stress formulations in strain gradient crystal plasticity. *International Journal of Solids and Structures*, 43:7268–7286, 2006.

P. Cermelli and M.E. Gurtin. On the characterization of geometrically necessary dislocations in finite plasticity. *Journal of the Mechanics and Physics of Solids*, 29:1531–1568,, 2001.

A.H. Cottrell. *Dislocations and plastic flow in crystals.* Oxford University Press, London, 1953.

D.M. Dimiduk, M.D. Uchic, and T.A. Parthasarathy. Size-affected single-slip behavior of pure nickel microcrystals. *Acta Materialia*, 53:4065–4077, 2005.

B. Ehrler, X.D. Hou, T.T. Zhu, K.M.Y. Png, C.J. Walker, A.J. Bushby, and D.J. Dunstan. Grain size and sample size interact to determine strength in a soft metal. *Philosophical Magazine*, 25:3043–3050, 2008.

U. Essmann and H. Mughrabi. Annihilation of dislocations during tensile and cyclic deformation and limits of dislocation densities. *Philosophical Magazine*, A40:731–756, 1979.

L.P. Evers, W.A.M. Brekelmans, and M.G.D. Geers. Non-local crystal plasticity model with intrinsic SSD and GND effects. *Journal of the Mechanics and Physics of Solids*, 52:2379–2401, 2004.

N.A. Fleck and J.W. Hutchinson. A reformulation of strain gradient plasticity. *Journal of the Mechanics and Physics of Solids*, 49:2245–2271, 2001.

N.A. Fleck, G.M. Muller, M.F. Ashby, and J.W. Hutchinson. Strain gradient plasticity: theory and experiment. *Acta Metallurgica et Materialia*, 42: 475–487, 1994.

M.G.D. Geers, W.A.M. Brekelmans, and C.J. Bayley. Second-order crystal plasticity: internal stress effects and cyclic loading. *Modelling and Simulation in Materials Science and Engineering*, 16:S133–S145, 2007.

I. Groma, F.F. Csikor, and M. Zaiser. Spatial correlations and higher-order gradient terms in a continuum description of dislocation dynamics. *Acta Materialia*, 51:1271–1281, 2003.

M.E. Gurtin. A gradient theory of single-crystal viscoplasticity that accounts for geometrically necessary dislocations. *Journal of the Mechanics and Physics of Solids*, 50:5–32, 2002.

M.E. Gurtin. The burgers vector and the flow of screw and edge dislocations in finite-deformation single-crystal plasticity. *Journal of the Mechanics and Physics of Solids*, 54:1882–1898, 2006.

M.E. Gurtin. A finite deformation, gradient theory of single-crystal plasticity with free energy dependent on densities of geometrically necessary dislocations. *International Journal of Plasticity*, 24:702–725, 2008.

M.E. Gurtin and L. Anand. A gradient theory for single-crystal plasticity. *Modelling and Simulation in Materials Science and Engineering*, 15: S263–S270, 2007.

M.E. Gurtin and L. Anand. Thermodynamics applied to gradient theories involving the accumulated plastic strain: The theories of aifantis and fleck and hutchinson and their generalization. *Journal of the Mechanics and Physics of Solids*, 57:405–421, 2009.

C.-S. Han, H. Gao, Y. Huang, and W.D. Nix. Mechanism-based strain gradient crystal plasticityi. theory. *Journal of the Mechanics and Physics of Solids*, 53:1188–1203, 2005.

M.A. Haque and M.T.A. Saif. Strain gradient effect in nanoscale thin films. *Acta Materialia*, 51:30533061, 2003.

I. Hayashi, M. Sato, and M. Kuroda. Strain hardening in bent copper foils. *Journal of the Mechanics and Physics of Solids*, 59:1731–1751, 2011.

T.J.R. Hughes. Generalization of selective integration procedures to anisotropic and nonlinear media. *International Journal for Numerical Methods in Engeering*, 15:1413–1418, 1980.

S. Ikawa, M. Asano, M. Kuroda, and K. Yoshida. Effects of crystal orientation on bendability of aluminum alloy sheet. *Materials Science and Engineering*, A 528:40504054, 2011.

D. Kiener, W. Grosinger, G. Dehm, and R. Pippan. A further step towards an understanding of size-dependent crystal plasticity: In situ tension experiments of miniaturized single-crystal copper samples. *Acta Materialia*, 56:580–592, 2008.

E. Kröner. Allegmeine kontinuumstheorie der versetzungen und eigenspannungen. *Arch. Rational Mech. Anal.*, 4:273–334, 1960.

L.P. Kubin, G. Canova, M. Condat, B. Devincre, V. Pontikis, and Y. Brechet. Dislocation microstructures and plastic flow: a 3d simulation. *Solid State Phenomena*, 23-24::445–472, 1992.

M. Kuroda. On large-strain finite element solutions of higher-order gradient crystal plasticity. *International Journal of Solids and Structures*, 48: 3382–3394, 2011.

M. Kuroda and V. Tvergaard. Shear band development predicted by a non-normality theory of plasticity and comparison to crystal plasticity predictions. *International Journal of Solids and Structures*, 38:8945–8960, 2001.

M. Kuroda and V. Tvergaard. Studies of scale dependent crystal viscopalsticity models. *Journal of the Mechanics and Physics of Solids*, 54: 1789–1810, 2006.

M. Kuroda and V. Tvergaard. Effects of texture on shear band formation in plane strain tension/compression and bending. *Internaitonal Journal of Plasticity*, 23:244–272, 2007.

M. Kuroda and V. Tvergaard. On the formulations of higher-order strain gradient crystal plasticity. *Journal of the Mechanics and Physics of Solids*, 56:1591–1608, 2008 a.

M. Kuroda and V. Tvergaard. A finite deformation theory of higher-order gradient crystal plasticity. *Journal of the Mechanics and Physics of Solids*, 56:2573 2584, 2008 b.

M. Kuroda and V. Tvergaard. Effects of microscopic boundary conditions on plastic deformations of small-sized single crystals. *International Journal of Solids and Structures*, 46:4396–4408, 2009.

M. Kuroda and V. Tvergaard. An alternative treatment of phenomenological higher-order strain plasticity theory. *International Journal of Plasticity*, 26:507–515, 2010.

M. Kuroda, V. Tvergaard, and T.Ohashi. Simulations of micro-bending of thin foils using a scale dependent crystal plasticity model. *Modelling and Simulation in Materials Science and Engineering*, 15:S13–S22, 2007.

J.W. Kysar, Y. Saito, M.S. Oztop, D. Lee, and W.T. Huh. Experimental lower bounds on geometrically necessary dislocation density. *International Journal of Plasticity*, 26:1097–1123, 2010.

E.H. Lee. Elastic-plastic deformation at finite strains. *Journal of Applied Mechanics*, 36:1–6, 1969.

R.M. McMeeking and J.R. Rice. Finite-element formulations for problems of large elastic-plastic deformation international. *Journal of Solids and Structures*, 11:601–616, 1975.

C. Motz, T. Schöberl, and R. Pippan. Mechanical properties of micro-sized copper bending beams machined by the focused ion beam technique. *Acta Materialia*, 53:42694279, 2005.

H. Mughrabi. On the current understanding of strain gradient plasticity. *Materials Science and Engineering*, A 387-389:209–213, 2004.

E. Nakamachi, C.L. Xie, and M. Harimoto. Drawability assessment of bcc steel sheet by using elastic/crystalline viscoplastic finite element analyses. *International Journal of Mechanical Sciences*, 43:631–652, 2001.

J.F. Nye. Some geometrical relations in dislocated solids. *Acta Metallurgica*, 1:153–162, 1953.

T. Ohashi, editor. *A new model of scale dependent crystal plasticity analysis*, volume Solid mechanics and its applications vol. 115, 97-106 of *Proceedings of IUTAM Symposium on Mesoscopic Dynamics in Fracture Process and Strength of Materials, Osaka, Japan,*, 2004. Kluwer Academic Publishers, Dordrecht.

T. Ohashi. Crystal plasticity analysis of dislocation emission from micro voids. *International Journal of Plasticity*, 21:2071–2088, 2005.

D. Peirce, R. J. Asaro, and A. Needleman. Material rate dependence and localized deformation in crystalline solids. *Acta Metallurgica*, 31:1951–1976, 1983.

P. Shrotriya, S.M. Allameh, J. Lou, T. Buchheit, and W.O. Soboyejo. On the measurement of the plasticity length scale parameter in liga nickel foils. *Mechanics of Materials*, 35:233243, 2003.

J.S. Stölken and A.G. Evans. A microbend test method for measuring the plasticity length scale. *Acta Materialia*, 45:5109–5115, 1998.

S. Sun, B.L. Adams, C.Q. Shet, S. Saigal, and W. King. Mesoscale investigation of the deformation field of an aluminum bicrystal. *Scripta Materialia*, 39:501–508, 1998.

S. Sun, B.L. Adams, and W. King. Observations of lattice curvature near the interface of a deformed aluminum bicrystal. *Philosophical Magazine*, A80:9–25, 2000.

K. Suzuki, Y. Matsuki, K. Masaki, M. Sato, and M. Kuroda. Tensile and microbend tests of pure aluminum foils with different thicknesses. *Materials Science and Engineering*, A 513-514:77–82, 2009.

G.I. Taylor. Plastic strain in metals. *J. Inst. Metals*, 62:307–325, 1938.

M.D. Uchic, D.M. Dimiduk, J.N. Florando, and W.D. Nix. Sample dimensions influence strength and crystal plasticity. *Science*, 305:986–989, 2004.

W.D.Nix and H.J.Gao. Indentation size effects in crystalline materials: A law for strain gradient plasticity. *Journal of Mechanics and Physics of Solids*, 46:411–425, 1998.

J. Weertman. Anomalous work hardening, non-redundant screw dislocations in a circular bar deformed in torsion, and non-redundant edge dislocations in a bent foil. *Acta Materialia*, 50:673–689, 2002.

K. Yamagishi, R. Takeda, and M. Takeda. The influence of grain size on the flex fatigue property of rolled copper foil. *Copper and Copper Alloys*, 45:27–30, 2006. (in Japanese with English abstract).

S. Yefimov, E. van der Giessen, and I. Groma. Bending of a single crystal: discrete dislocation and nonlocal crystal plasticity simulations. *Modelling and Simulation in Materials Science and Engineering*, 12:10691086, 2004 a.

S. Yefimov, I. Groma, and E. van der Giessen. A comparison of a statistical-mechanics based plasticity model with discrete dislocation plasticity calculations. *Journal of the Mechanics and Physics of Solids*, 52:279–300, 2004 b.

Construction of Statistically Similar Representative Volume Elements

Daniel Balzani [*†], Dominik Brands [*] and Jörg Schröder [*]

[*] Institute of Mechanics, Department of Civil Engineering, Faculty of Engineering, University of Duisburg-Essen

[†] Corresponding author: daniel.balzani@uni-due.de

Abstract In computational homogenization approaches the definition of a representative volume element (RVE) strongly influences the performance of the resulting numerical scheme, not only with respect to its physical accuracy but also with respect to the computational effort required. Here, we propose a method for the construction of *statistically similar* RVEs (SSRVEs), which are characterized by a reduced complexity compared to real microstructures and which therefore lead to computationally less expensive methods. These SSRVEs are obtained by minimizing a least-square functional taking into account differences of statistical measures that characterize the morphology of a real (target) microstructure and the SSRVE. By comparing the mechanical response in a series of numerical investigations it is shown that also the material behavior obtained by considering the real microstructure is well represented by the SSRVEs.

1 Introduction

In many fields of engineering applications the optimization of the material properties with respect to stability and weight reduction becomes more and more important. In this context micro-heterogeneous materials as e.g. advanced high strength steels turn out to excellently match those goals. For the numerical simulation of such materials the incorporation of micromechanics is essential since phenomena occurring at the microscale strongly govern the macroscopic material behavior. Therefore, computational homogenization has attracted interest in the past decade and one prominent method in this context is the direct micro-macro transition approach often referred to as FE^2-method, see e.g. Smit et al. (1998), Miehe et al. (1999), Schröder (2000). This method is based on the solution of microscopic boundary value problems at each macroscopic integration point. These microscopic boundary value problems in turn are based on the definition of a

J. Schröder, K. Hackl (Eds.), *Plasticity and Beyond*, CISM International Centre for Mechanical Sciences, DOI 10.1007/978-3-7091-1625-8_6, © CISM, Udine 2014

suitable representative volume element (RVE) which is typically obtained by considering a sufficiently large substructure of a real micrograph. These RVEs are often characterized by a complex arrangement of individual constituents and therefore a rather high number of finite elements is required for the discretization. This leads to an overall computationally expensive approach making practically relevant boundary value problems difficult to be solved in reasonable time. Therefore, here the focus is on the construction of statistically similar RVEs (SSRVEs), which are characterized by a less pronounced complexity at the microscale such that a lower number of finite elements is required for their discretization enabling more efficient FE^2-calculations. The main idea is to introduce a suitable parameterization for the microstructure in the SSRVE and to minimize a suitable least-square functional with respect to this parameterization, cf. Schröder et al. (2010). The least-square functional takes into account differences of statistical measures describing the microstructure morphology which are computed for a given real (target) microstructure and for the SSRVE. The choice of suitable statistical measures is essential in this context. Various statistical descriptors are summarized and recapitulated in e.g. Exner and Hougardy (1986), Torquato (2002) or Zeman (2003); scalar-valued basic parameters are described in Ohser and Schladitz (2006). In the context of microstructure reconstruction the classical approach is similar to the one considered here because also a least-square functional based on statistical descriptors is minimized. There, the two-point probability functions are often considered, but also e.g. cluster functions proposed in Torquato et al. (1988) are taken into account, see e.g. Capek et al. (2009) or Jiao et al. (2009). A further measure is the lineal-path function proposed in Lu and Torquato (1992) which are used for reconstruction in Manwart et al. (2000). Rather recently, a class of statistical measures based on entropic descriptors is proposed for microstructure reconstruction in Piasecki (2011). A comparative study with respect to different statistical descriptors with application to microstructure reconstruction is given in Li et al. (2012) and with respect to the construction of SSRVEs in Balzani et al. (2010) and Ambrozinski et al. (2012). In this contribution several scalar-valued parameters, the spectral density and the lineal-path function are analyzed with respect to their performance for the construction of SSRVEs. Then numerical examples are provided showing that the SSRVEs lead to a mechanically similar behavior compared with the original target microstructures.

This contribution is organized as follows: After the introduction, Section 2 recapitulates the basic equations for the FE^2-scheme and the finite J_2-plasticity model which is used therein for the individual constituents at the microscale. In Section 3 various statistical measures for the characteri-

zation of microstructures are described and their graphical visualization is explained. Then, Section 4 describes the method for the construction of SSRVEs and details the issue of optimization. Section 5 presents an analysis of SSRVEs which are constructed for an artificially generated random microstructure and includes numerical examples based on the constructed SSRVE. In Section 6 another example focusing on a real DP-steel microstructure is provided which shows the performance of the SSRVE with respect to computational efficiency; Section 7 concludes this paper.

2 Computational Homogenization

In the context of computational homogenization, cf. for more details the contribution by Schröder in this book, continuum mechanical quantities associated to an infinitesimal vicinity of a material point at the macroscale $\overline{\boldsymbol{X}} \in \overline{\mathcal{B}}$ are computed based on informations at the microscale. For the definition of the macroscopic quantities we consider a representative volume element (RVE), parametrized in $\boldsymbol{X} \in \mathcal{B}$, where the microscopic field quantities are determined. In general the macroscopic deformation gradient $\overline{\boldsymbol{F}}$ and the macroscopic first Piola-Kirchhoff stresses $\overline{\boldsymbol{P}}$ are defined by suitable surface integrals, see e.g. Schröder (2000). By application of some technically useful assumptions the macroscopic quantities can be reformulated in terms of the volume averages over their microscopic counterparts, i.e.

$$\overline{\boldsymbol{F}} = \frac{1}{V} \int_{\mathcal{B}} \boldsymbol{F} \, dV \quad \text{and} \quad \overline{\boldsymbol{P}} = \frac{1}{V} \int_{\mathcal{B}} \boldsymbol{P} \, dV \,, \tag{1}$$

respectively. Herein, V denotes the volume of a suitable RVE. In the sequel, macroscopic quantities are denoted as overlined quantities, i.e. $\overline{(\bullet)}$. Different stress measures, the Cauchy- or Kirchhoff stress tensors are then calculated by

$$\overline{\boldsymbol{\sigma}} = (\det \overline{\boldsymbol{F}})^{-1} \overline{\boldsymbol{P}} \, \overline{\boldsymbol{F}}^{T} \quad \text{and} \quad \overline{\boldsymbol{\tau}} = (\det \overline{\boldsymbol{F}}) \overline{\boldsymbol{\sigma}} \,, \tag{2}$$

respectively.

2.1 Boundary Value Problems at Different Scales

Neglecting acceleration terms the balance of linear momentum at the macroscale reads $\mathrm{Div}[\overline{\boldsymbol{P}}] + \overline{\boldsymbol{f}} = \boldsymbol{0}$ in $\overline{\mathcal{B}}$, wherein $\overline{\boldsymbol{f}}$ denotes the macroscopic volumetric force vector. The boundary conditions are given by $\overline{\boldsymbol{u}} = \tilde{\overline{\boldsymbol{u}}}$ on $\partial\overline{\mathcal{B}}_u$ and $\overline{\boldsymbol{t}} = \overline{\boldsymbol{P}} \cdot \boldsymbol{n} = \tilde{\overline{\boldsymbol{t}}}$ on $\partial\overline{\mathcal{B}}_P$, where $\overline{\boldsymbol{u}}$ and $\overline{\boldsymbol{t}}$ denote the macroscopic displacement and traction vectors, respectively. At the microscale

the boundary value problem reads $\mathrm{Div}[\boldsymbol{P}] = \boldsymbol{0}$ in $\mathcal{B}$, where again acceleration terms and volumetric forces are neglected. The boundary conditions are derived from the macro-homogeneity condition, also referred to as Hill–condition, see Hill (1963). It postulates that the macroscopic power is equal to the volumetric average of the microscopic powers. Therefrom, we obtain the three possible types of boundary conditions for the microscopic boundary value problem, (i) the stress boundary condition $\boldsymbol{t} = \overline{\boldsymbol{P}}\boldsymbol{N}$ on $\partial\mathcal{B}$, (ii) the linear boundary displacements $\boldsymbol{x} = \overline{\boldsymbol{F}}\boldsymbol{X}$ on $\partial\mathcal{B}$, and (iii) the periodic boundary conditions

$$\boldsymbol{x} = \overline{\boldsymbol{F}}\boldsymbol{X} + \tilde{\boldsymbol{w}}, \qquad \tilde{\boldsymbol{w}}^{+} = \tilde{\boldsymbol{w}}^{-}, \qquad \boldsymbol{t}^{+} = -\boldsymbol{t}^{-} \qquad \text{on} \qquad \partial\mathcal{B}\,. \tag{3}$$

Note that $\tilde{\boldsymbol{w}}$ denotes fluctuations of the displacement field and that $(\bullet)^{+}$, $(\bullet)^{-}$ characterizes quantities at periodically associated points of the RVE-boundary, for further details we refer to Miehe et al. (1999), Schröder (2000). For a discrete formulation of the coupled micro-macro-transition the basic idea of the FE^2-method is that a standard macroscopic boundary value problem is computed, where at each integration point a microscopic boundary value problem is driven by some of the above mentioned boundary conditions. Focussing on periodic boundary conditions (iii) we solve the microscopic BVP and return the average of the resulting microscopic stresses $\overline{\boldsymbol{P}}$ according to Eq. $(1)_2$ to the macroscale. At the microscale we consider the weak form and its linear increment for a typical finite element

$$G^{e} = \int_{\mathcal{B}^{e}} \delta\tilde{\boldsymbol{F}} \cdot \boldsymbol{P}\, dV \quad \text{and} \quad \Delta G^{e} = \int_{\mathcal{B}^{e}} \delta\tilde{\boldsymbol{F}} \cdot (\mathbb{A} : \Delta\tilde{\boldsymbol{F}})\, dV\,, \tag{4}$$

with the microscopic nominal moduli $\mathbb{A} := \partial_{F}\boldsymbol{P}$. The fluctuation parts of the actual, virtual and incremental deformation gradient can be approximated by using standard ansatz functions for the fluctuation displacements interpolating between the fluctuation parts of displacements $\tilde{\boldsymbol{d}}$, virtual displacements $\delta\tilde{\boldsymbol{d}}$, and incremental displacements $\Delta\tilde{\boldsymbol{d}}$. The resulting nonlinear set of equations is solved by applying a Newton iteration and in the converged state the macroscopic 1st Piola-Kirchhoff stresses are computed as volumetric average over the microscopic ones. For details on deriving the consistent macroscopic moduli we refer to Miehe et al. (1999); Schröder (2000).

2.2 Elasto-Plastic Material Model at the Microscale

For the description of the material behavior of the individual phases on the microscale an isotropic material behavior is assumed. For multiphase steels it seems to be reasonable to use an isotropic finite elastoplasticity

formulation based on the multiplicative decomposition of the deformation gradient $\boldsymbol{F} = \boldsymbol{F}^e \, \boldsymbol{F}^p$ in elastic $\boldsymbol{F}^e$ and plastic $\boldsymbol{F}^p$ parts, see Kröner (1960), Lee (1969). For details of the thermodynamical formulation as well as for the numerical treatment we refer to Simo (1988, 1992), Simo and Miehe (1992), Peric et al. (1992), Miehe and Stein (1992), and Miehe (1993). In the sequel we give a brief summary of the used framework. The basic kinematical quantities are

$$\boldsymbol{b} = \boldsymbol{F} \, \boldsymbol{F}^T = \boldsymbol{F}^e \, \boldsymbol{b}^p \, (\boldsymbol{F}^e)^T \,, \quad \boldsymbol{b}^p = \boldsymbol{F}^p \, (\boldsymbol{F}^p)^T \,, \text{ and } \quad \boldsymbol{b}^e = \boldsymbol{F}^e \, (\boldsymbol{F}^e)^T \,. \tag{5}$$

The spectral decomposition of the elastic finger tensor is considered, i.e. $\boldsymbol{b}^e = \sum_{A=1}^{3} (\lambda_A^e)^2 \boldsymbol{n}_A \otimes \boldsymbol{n}_A$, where $\boldsymbol{n}_A$ denotes the eigenvectors and λ_A^e the eigenvalues of $\boldsymbol{b}^e$. The strain energy function is then assumed to be of the form $\psi = \psi^e(\boldsymbol{b}^e) + \psi^p(\alpha)$, wherein α denotes the equivalent plastic strains. Following Simo (1992) we use a quadratic strain energy function

$$\psi^e = \frac{\lambda}{2}[\epsilon_1^e + \epsilon_2^e + \epsilon_3^e]^2 + \mu[(\epsilon_1^e)^2 + (\epsilon_2^e)^2 + (\epsilon_3^e)^2] \tag{6}$$

in terms of the logarithmic elastic strains $\epsilon_A^e = \log(\lambda_A^e)$; λ and μ are the Lamé constants. In order to model an exponential-type hardening of the individual phases we apply the well-known function

$$\psi^p = y_\infty \alpha - \frac{1}{\eta}(y_0 - y_\infty) \exp(-\eta\alpha) + \frac{1}{2} \, h \, \alpha^2 \,. \tag{7}$$

Herein, y_0 is the initial yield strength, y_∞ and η describe an exponential hardening behavior and h is the slope of a superimposed linear hardening. The yield criterion is given by

$$\phi = ||\mathrm{dev}\boldsymbol{\tau}|| - \sqrt{\frac{2}{3}}\beta \leq 0 \quad \text{with} \quad \beta = \frac{\partial \psi^p(\alpha)}{\partial \alpha} \,. \tag{8}$$

Herein, the Kirchhoff stresses are denoted by $\boldsymbol{\tau}$. The flow rule for the plastic quantity is integrated using an implicit exponential update algorithm, which preserves plastic incompressibility (Weber and Anand (1990), Simo (1992), and Miehe and Stein (1992)). The first Piola-Kirchhoff stresses on the microscale are computed by $\boldsymbol{P} = \boldsymbol{\tau} \, \boldsymbol{F}^{-T}$. For the numerical implementation we follow the algorithmic formulation in a material setting as proposed in Klinkel (2000).

3 Characterization of Microstructure Morphology

For the analysis and reconstruction of microstructures an accurate characterization and mathematical quantification of the microstructure is essential. The basis for such analysis is typically a set of two-dimensional

photographs of surfaces of the material, referred to as micrographs. These micrographs should have a representative character and should therefore be large enough to capture the characteristics of the microstructure. Due to the fact that commonly only two-dimensional micrographs are available, the abstraction of three-dimensional statistical measures from the analysis of two-dimensional ones, referred to as stereology, is an efficient approach to derive measures for the quantification of the real three-dimensional microstructure. Another possibility is to consider a stack of two-dimensional micrographs, construct a three-dimensional geometry and directly calculate three-dimensional statistical measures. Such measurements of stacked micrographs can be done in an automated manner by e.g. the so-called EBSD-FIB technology, see e.g. Konrad et al. (2006), Calcagnotto et al. (2011).
The description of microstructures is based on statistical considerations, see the basic literature in e.g. Beran (1968), Ohser and Mücklich (2000) and Kröner (1971). Various statistical descriptors have been introduced in the last decades, see. e.g. Exner and Hougardy (1986), Zeman (2003), or Torquato (2002) for comprehensive overviews. Such descriptors can be divided into scalar-valued quantities like e.g. some basic parameters such as the volume fraction or the internal surface density, and statistical measures of higher order.

3.1 Scalar-Valued Statistical Descriptors

Many microstructures can be interpreted as a collection of individual features, e.g. the individual inclusions in an inclusion-matrix microstructure. For their characterization feature parameters can be investigated. Not always a detailed analysis of the individual texture components is required and scalar-valued quantities describing the microstructure in an overall manner can be used. In the following sections feature parameters, cf. Exner and Hougardy (1986), and basic field parameters following Ohser and Schladitz (2006) are explained in detail.

Feature Parameters For the description of a feature $\mathcal{B}^{(i)}$ various parameters can be analyzed. First, simple geometrical information such as the volume $V^{(i)} := \int_{\mathcal{B}^{(i)}} dV$, the surface $S^{(i)} := \int_{\partial\mathcal{B}^{(i)}} dS$ or the associated quantities in a two-dimensional cross-section, the cross-section area $A^{(i)} := \int_{\mathcal{B}_C^{(i)}} dA$ and the circumference $L^{(i)} := \int_{\partial\mathcal{B}_C^{(i)}} dL$ can be considered. The individual infinitesimal line, area, surface, and volume elements are denoted by dL, dA, dS, and dV, respectively, see Fig. 1. These parameters describe to some extent the size of the feature in three and two dimensions.

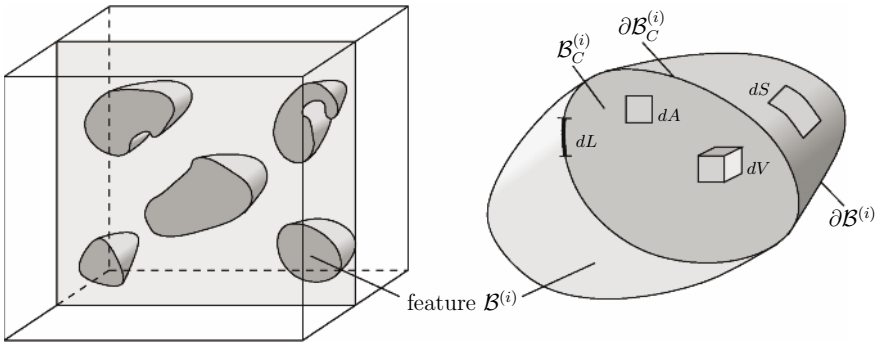

Figure 1. a) Microstructure and b) extraction of one feature $\mathcal{B}^{(i)}$.

An alternative is to consider a representative "diameter" $D^{(i)}$. For this purpose the surface of the particle $S^{(i)}$ may be compared with the surface of a sphere and then we obtain

$$S^{(i)} = \pi (D^{(i)})^2 \quad \Rightarrow \quad D^{(i)} = \sqrt{\frac{S^{(i)}}{\pi}}\,. \tag{9}$$

For the representation of two-dimensional cross-sections further geometrical parameters are often taken into account which are based on projection lengths. These parameters are e.g. the vertical projection, the horizontal projection, the maximal projection or the projection length $\hat{p}$. The projection length $\hat{p} = \sum_j p_j$ takes additionally into account overlapping projections p_j in the projection direction. Features can not only differ with respect to their size, but also with respect to their shape. A rather simple dimensionless parameter to describe a feature's form can be defined as

$$F_{SHP}^{(i)} := \frac{4\pi}{9}\,\frac{(V^{(i)})^2}{(S^{(i)})^3} \quad \text{and} \quad F_{SHP}^{(i)} := 4\pi\,\frac{L^{(i)}}{(A^{(i)})^2}\,, \tag{10}$$

for the three- and two-dimensional case, respectively. A possibility to capture the aspect ratios of a feature can be done in two dimensions by $F_{ASP}^{(i)} := \sqrt{I_1/I_2}$, wherein I_1 and I_2 denote the principle moments of inertia. This measure does not only describe the actual aspect ratio of regular structural elements as e.g. ellipsoids or rectangles but also of features of arbitrary shape. For the description of the compactness of a two-dimensional

feature the comparison of the polar moment of inertia with the one of a circle having the same cross-section yields another reasonable parameter, i.e. $F_{CP}^{(i)} := (2\pi)^{-1}\, A^{(i)}/(I_1 + I_2)$. Another reasonable shape measure characterizes the waviness of the feature by comparing the surface with that part of the surface which is convex. Then the three- and two-dimensional waviness parameter reads

$$F_W^{(i)} := \frac{S_C^{(i)}}{S^{(i)}} \quad \text{and} \quad F_W^{(i)} := \frac{L_C^{(i)}}{L^{(i)}}\,, \tag{11}$$

respectively, wherein $S_C^{(i)}$ and $L_C^{(i)}$ denote the convex part of the surface, i.e. of the circumference. This measure is equal to one for convex features and decreases for features of increasing non-convexity. The characterization of the shape of two-dimensional features may also require symmetry aspects. Then the symmetry parameter

$$F_{SYM,j}^{(i)} := \frac{p_{I_j} - z}{p_{I_j}} \quad \text{with} \quad j = 1, 2\,, \tag{12}$$

can be considered. Herein, p_{I_j} represents the projection length in the direction of the principle axis associated with the moment of inertia I_j whereas z denotes the distance of the other principle axis from its parallel that divides the feature in two sections of the same cross-section area. For symmetric features this parameter is equal to one. Further measures for the characterization of the shape of a feature the curvature $\kappa(\beta) := 1/r(\beta)$ in a certain tangential direction described by β can be taken into account and the two additional feature parameters, the integral of mean curvature $M^{(i)}$ and the integral of total curvature $K^{(i)}$, given by

$$\begin{aligned} M^{(i)} &:= \frac{1}{2}\int_{\partial\mathcal{B}^{(i)}} \left(\min_{\beta}[\kappa] + \max_{\beta}[\kappa]\right) dS, \\ K^{(i)} &:= \int_{\partial\mathcal{B}^{(i)}} \min_{\beta}[\kappa]\, \max_{\beta}[\kappa]\, dS\,, \end{aligned} \tag{13}$$

respectively, are considered. In two dimensions the dependency on the direction angle β vanishes and the latter two feature parameters reduce to

$$\hat{M}^{(i)} := \int_{\partial\mathcal{B}_C^{(i)}} \kappa\, dS \quad \text{and} \quad \hat{K}^{(i)} := \int_{\partial\mathcal{B}_C^{(i)}} \kappa^2\, dS\,. \tag{14}$$

Field Parameters To obtain descriptors for random microstructures consisting of different phases the feature parameters as e.g. the ones explained

above can be considered and related to the observation space. Then, in the general three-dimensional case, four basic parameters are obtained for a phase (P): the volume fraction $\mathcal{P}_V^{(P)} := V^{(P)}/V$, the internal surface density $\mathcal{P}_S^{(P)} := S^{(P)}/V$, the density of the integral of the mean curvature $\mathcal{P}_M^{(P)} := M^{(P)}/V$, and the density of the integral of the total curvature $\mathcal{P}_K^{(P)} := K^{(P)}/V$. Herein the individual quantities represent the summation over all features associated to one phase. Other often investigated quantities are obtained by relating the feature parameters of a phase (P) to the volume taken by the individual phase instead of the total volume. Then the specific internal surface density $\mathcal{P}_{S,V^P}^{(P)} = S^{(P)}/V^{(P)}$, the specific density of the integral of the mean curvature $\mathcal{P}_{M,V^P}^{(P)} = M^{(P)}/V^{(P)}$ and the total curvature are given by $\mathcal{P}_{K,V^P}^{(P)} = K^{(P)}/V^{(P)}$. While the volume fraction describes how the volume of the individual phases assembles the microstructure, the internal surface density is a measure for how fine the individual phases are distributed. Aspects like convexity or non-convexity of the shape of individual phases can be characterized by the density of the integral of the mean and the total curvature.

The above mentioned parameters require information regarding the three-dimensional geometry of the individual phases, which is not available in many applications. Then for some measures the three-dimensional quantities can be statistically estimated based on two-dimensional measurements. The cross-section area fraction $\mathcal{P}_A^{(P)} := A^{(P)}/A^0$ and the point fraction $\mathcal{P}_P^{(P)} := N_p^{(P)}/N_p^0$ of a phase (P) are statistical expectation values for the volume fraction, see Delesse (1848) and Glagolev (1934). Herein, A^0 and N_p^0 denote the analyzed cross-section area and the number of analyzed points, respectively; $A^{(P)}$ is the cross-section area associated to phase (P) and $N_p^{(P)}$ is the number of points which are identified to be located in phase (P) during measurement. This means that the identity $\mathcal{P}_V^{(P)} = \mathcal{P}_A^{(P)} = \mathcal{P}_P^{(P)}$ is valid if the considered cross-section leads to a statistically representative phase cross-section area $A^{(P)}$ or the number of evaluated points is sufficiently large. The internal surface density can also be calculated from one- or two-dimensional measurements. Following Weibel (1980) the internal surface density of a phase (P) is equal to twice of the quotient of intersection points of a measurement line (number of intersection points $N_p^{(P)}$ of a measurement line L^0 with the boundary line of the phase $\mathcal{B}_C^{(p)}$ related to the measurement line), i.e.

$$\mathcal{P}_S^{(P)} = 2\,\frac{N_p^{(P)}}{L^0} = \frac{4}{\pi}\mathcal{P}_L^{(P)} \quad \text{with} \quad \mathcal{P}_L^{(P)} := \frac{L^{(P)}}{A^0}\,. \tag{15}$$

The latter part of the equation shows that also the internal interface length density $\mathcal{P}_L^{(P)}$ is connected with the internal surface density by a factor of $4/\pi$. For the specific internal surface density a connection to the specific internal interface length density $\mathcal{P}_{L,A^p}^{(P)}$ can be shown, too. Please note that these identities are only valid for random microstructures and measurement lines/areas that are large enough to be interpreted as statistically representative.

3.2 Statistical Measures of Higher Order

In this section parameters of higher order are explained which are able to capture more morphological and/or textural information. Many statistical measures of higher order are based on ensemble and volume averages. Ensemble averages represent averages that are calculated for a series of samples at a certain position and volume averages are calculated for only one sample as an average over the positions in this sample. Please note that in this section ensemble averages are denoted by overlined quantities.

Extension of Scalar-Valued Parameters In order to capture direction-dependent information a *set* of scalar-valued parameters can be considered. This set contains the values of simple parameters which are based on line measurements evaluated for different directions. For this purpose a classification of all directions into a set of direction vectors $\boldsymbol{n}_i | i = 1, 2 \ldots n_{\mathrm{dir}}$ is considered with n_{dir} denoting the number of discrete directions to be analyzed. Then, suitable scalar-valued parameters are computed for each discrete direction and included in a set of parameters. For a n_{dim}-dimensional measurement space a $(n_{\mathrm{dim}} - 1)$-dimensional set of parameters is obtained due to the possible parameterization of the directions in polar- or spherical coordinates. Another often used measure is the chord-length density going back to Matheron (1975), see also Torquato and Lu (1993), which is defined as the probability of finding a certain chord length in a phase of interest P. The chord-length describes the sum of all line segments that are inside phase P measured along one line of infinite length.
However, in each direction only one (mean) value can be computed and therefore these one-dimensional (or vector-valued) parameters are of limited applicability when describing complex microstructures.

Orientation Distribution Function In microstructures where different domains are characterized by different orientations (e.g., polycrystals), orientation distribution functions (ODFs) are typically considered to describe the texture. These ODFs are defined as the volume fraction of grains with

a certain direction, i.e. $\mathcal{P}_{ODF}^{(\boldsymbol{n}_g)} := V^{(\boldsymbol{n}_g)}/V$, with the direction vector $\boldsymbol{n}_g$. Typically, for the analysis of polycrystals, Euler angles are used instead of a direction vector and therefore, the ODF leads technically to a 2-/3-dimensional set of parameters for 2-/3-dimensional measurement spaces, respectively. However, since one type of information, here the orientation, is measured this descriptor can also be interpreted as a one-dimensional set of parameters.

***n*-Point Probability Functions** Statistical data of higher order is captured by the n-point probability functions introduced in Brown (1955). Let $D^{(P)}(\alpha)$ denote the domain occupied by the considered phase P in the particular sample α, then the indicator function

$$\chi^{(P)}(\boldsymbol{x}) = \begin{cases} 1, & \text{if } \boldsymbol{x} \in D^{(P)}, \\ 0, & \text{otherwise}, \end{cases} \tag{16}$$

identifies the associated phase in a given microstructure. The indicator function fulfills in every point $\boldsymbol{x}$ the relation $\sum_{P=1}^{n} \chi^{(P)}(\boldsymbol{x}) = 1$ for n phases. The n-point probability function often also referred to as n-point correlation function considers the probability that n points $\boldsymbol{x}_1, \dots \boldsymbol{x}_n$ are located in the phase P. Then the n-point probability function reads

$$\mathcal{S}_n^{(P)}(\boldsymbol{x}_1, \dots \boldsymbol{x}_n) = \overline{\chi^{(P)}(\boldsymbol{x}_1, \alpha)\chi^{(P)}(\boldsymbol{x}_2, \alpha) \dots \chi^{(P)}(\boldsymbol{x}_n, \alpha)}\,. \tag{17}$$

For statistically homogeneous microstructure the n-point probability function does not depend on the absolute position in space and difference vectors between the particular points $\boldsymbol{x}_{1(i+1)} = \boldsymbol{x}_{(i+1)} - \boldsymbol{x}_1 | i = 1 \dots (n-1)$ can be considered. If additionally ergodicity is assumed where the ensemble average over a set of samples can be replaced by the volumetric average over only one sample $\mathcal{B}$ the definition transforms to

$$\mathcal{S}_n^{(P)}(\boldsymbol{x}_{12}, \dots \boldsymbol{x}_{1n}) = \lim_{V \to \infty} \frac{1}{V} \int_{\mathcal{B}} \chi^{(P)}(\boldsymbol{y})\chi^{(P)}(\boldsymbol{y} + \boldsymbol{x}_{12}) \dots \chi^{(P)}(\boldsymbol{y} + \boldsymbol{x}_{1n})\, d\boldsymbol{y}\,. \tag{18}$$

With view to practical applications the analysis of samples with infinite size is impossible and therefore, it is assumed that a sufficiently large sample can be investigated instead. Furthermore, n-point probability functions of lower order are often analyzed in order to keep computational costs low.
The probability function of first order (one-point probability function) is given by

$$\mathcal{S}_1^{(P)}(\boldsymbol{x}) = \overline{\chi^{(P)}(\boldsymbol{x}, \alpha)}\,, \tag{19}$$

representing the probability that a point $\boldsymbol{x}$ is placed in phase P. The one-point probability function coincides with the first basic parameter, the phase

fraction. For ergodic microstructures the alternative expression in terms of volumetric averages reads

$$\mathcal{S}_1^{(P)} = \frac{1}{V} \int_{\mathcal{B}} \chi^{(P)}(\boldsymbol{x})\, d\boldsymbol{x}\,, \tag{20}$$

wherein $\boldsymbol{x}$ represents position vectors to any point in the considered domain $\mathcal{B}$. If a discrete image of $N = N_x \times N_y$ pixels with N, N_x, $N_y \in \mathbb{N}$ of one representative sample of an ergodic microstructure is analyzed and each pixel is linked with its associated physical dimension, then the one-point probability function is computed by

$$\mathcal{S}_1^{(P)} = \frac{1}{N_x N_y} \sum_{p=0}^{N_x-1} \sum_{q=0}^{N_y-1} \chi^{(P)}(p,q) \tag{21}$$

wherein p and q represent the pixel positions in the binary image. The color of each individual pixel is linked with a certain phase P, i.e. for two-phase microstructures binary images may first be generated using standard image processing algorithms. Of course the evaluation of this summation leads to the highest possible accuracy for a given image resolution since all possible positions are evaluated. However, in most cases it is more efficient to only evaluate Eq. (21) at a sufficient number $N^r < N$ with $N^r \in \mathbb{N}$ of random positions and then the equation

$$\mathcal{S}_1^{(P)} = \lim_{N^r \to \infty} \left[\frac{1}{N^r} \sum_{j=0}^{N^r} \chi^{(P)}(p_j, q_j) \right] \tag{22}$$

holds. Herein, the pixel positions for each random generation j are denoted by p_j and q_j. Since the one-point probability is equal to the phase fraction and therefore a scalar-valued quantity it only represents a special case of an n-point probability function providing limited statistical information.
The second-order function (two-point probability or autocorrelation function) is given by the ensemble average

$$\mathcal{S}_2^{(P)}(\boldsymbol{x}_1, \boldsymbol{x}_2) = \overline{\chi^{(P)}(\boldsymbol{x}_1, \alpha)\chi^{(P)}(\boldsymbol{x}_2, \alpha)}\,, \tag{23}$$

which represents the probability that two points are located in phase P. For ergodic microstructures we again replace the ensemble average by the volumetric average and obtain the expression

$$\mathcal{S}_2^{(P)}(\boldsymbol{y}) = \int_{\mathcal{B}} \chi^{(P)}(\boldsymbol{x})\chi^{(P)}(\boldsymbol{x}+\boldsymbol{y})\, d\boldsymbol{x}\,. \tag{24}$$

When evaluating the two-point probability function for discrete two-dimensional image data with a number of $N = N_x \times N_y$ pixels, the function is calculated by

$$\mathcal{P}_{\mathcal{S}_2}^{(P)}(m,k) := \frac{1}{\tilde{N}} \sum_{p=p_m}^{p_M-1} \sum_{q=q_k}^{q_K-1} \chi^{(P)}(p,q)\chi^{(P)}(p+m,q+k) \tag{25}$$

with $m, k \in \mathbb{N}$ and $m \in [-(N_x-1), \ldots (N_x-1)]$, $k \in [0, \ldots N_y-1]$, $\tilde{N} = (p_M - 1 - p_m)(q_K - 1 - q_k)$, and the minimum and maximum values

$$\begin{aligned} p_m &= \max[0,-m] \quad , \quad p_M = \min[N_x, N_x - m]\,, \\ q_k &= \max[0,-k] \quad , \quad q_K = \min[N_y, N_y - k]\,. \end{aligned} \tag{26}$$

As for the one-point probability function a more efficient method for the computation of the second-order probability function with a tolerable deviation is to evaluate only a suitable number of $N^r < N$ random points. If periodic microstructures are to be analyzed it is sufficient to consider only the periodic unitcell, then the two-point probability function for two-dimensional data is computed by

$$\widetilde{\mathcal{P}}_{\mathcal{S}_2}^{(P)}(m,k) = \frac{1}{N_x N_y} \sum_{p=0}^{N_x-1} \sum_{q=0}^{N_y-1} \chi^{(P)}(p,q)\chi^{(P)}(p+m,q+k)\,. \tag{27}$$

For statistically homogeneous and statistically isotropic microstructures the n-point probability function is invariant with respect to the orientation of $\boldsymbol{y}$ and only the magnitudes play a role. Then, the second-order probability function reduces to $\mathcal{S}_2^{(P)}(y)$, wherein y is the length of the translational vector $\boldsymbol{y}$. Then, if the two-point probability function is computed for one representative sample of an ergodic microstructure by evaluating random pairs of points in a discrete sense we consider the representation

$$\mathcal{S}_2^{(P)}(x_{mk}) = \frac{1}{N^r} \sum_{j=1}^{N^r} \chi^{(P)}(p_j,q_j)\chi^{(P)}(p_j+m_j,q_j+k_j)\,. \tag{28}$$

Herein, $x_{mk} := x_{mk}(m_j,k_j)$ denotes a reasonably defined difference magnitude. Typically, the maximum value of the two-point probability function is found for $x_{mk} = 0$, or $m = 0, k = 0$ which represents the value of the one-point probability function $\mathcal{S}_1$, i.e. the phase fraction. For isotropic media it then decays to its asymptotic value of $\mathcal{S}_1^2$.

Spectral Density A strong correlation to the two-point probability function is given by the spectral density for the indicator function defined in Eq. (16). For discrete measurement data in a two-dimensional setting the (discrete) Fourier transform for a phase P is calculated by

$$\mathcal{F}^{(P)}(m,k) = \sum_{p=0}^{N_x-1} \sum_{q=0}^{N_y-1} \exp\left(\frac{2\,i\,\pi\,m\,p}{N_x}\right) \exp\left(\frac{2\,i\,\pi\,k\,q}{N_y}\right) \chi^{(P)}(p,q)\,. \quad (29)$$

The discrete spectral density is then computed by the multiplication of the discrete Fourier-transform with its conjugate complex

$$\mathcal{P}_{SD} := \frac{1}{2\pi\,N}\,|\mathcal{F}|^2\,, \quad (30)$$

wherein the total number of pixels is given by N. It is remarked that the spectral density is correlated with the two-point probability function in terms of the Fourier-transform

$$\mathcal{S}_2^{(P)} = \frac{1}{N}(\mathcal{F}^{(P)})^{-1}[\mathcal{F}^{(P)}[\chi^{(P)}]\overline{\mathcal{F}^{(P)}[\chi^{(P)}(\alpha)]}]\,, \quad (31)$$

cf. Zeman (2003). Herein, $\mathcal{F}^{(P)}$ and $(\mathcal{F}^{(P)})^{-1}$ denote the discrete- and the inverse discrete Fourier transform for phase P. Since direct information concerning the periodicity of a given microstructure is provided by the spectral density, this measure may be of particular interest when the challenge is to simplify a (in general non-periodic) real microstructure by a periodic one. A main advantage of using the spectral density compared to the two-point probability function is that there exist a variety of efficient algorithms for the computation of the discrete Fourier transform as for instance the "FFTW" ("Fastest Fourier Transform in the West") library, developed at the Massachusetts Institute of Technology by M. Frigo and S.G. Johnson.

Lineal-Path Functions The lineal-path functions proposed in Lu and Torquato (1992) describe the probability that a complete line segment $\overrightarrow{\boldsymbol{z}} := \overrightarrow{\boldsymbol{x}_1\boldsymbol{x}_2}$ between two points $\boldsymbol{x}_1$ and $\boldsymbol{x}_2$ is located in the same phase. For its mathematical description we consider the modified indicator function

$$\chi_{LP}^{(P)}(\overrightarrow{\boldsymbol{z}}) = \begin{cases} 1, & \text{if } \overrightarrow{\boldsymbol{z}} \in D^{(P)}, \\ 0, & \text{otherwise}\,, \end{cases} \quad (32)$$

checking if a whole line segment is located in the domain $D^{(P)}$ of phase P. Then the lineal-path function is given by the ensemble average

$$\mathcal{P}_{LP}^{(P)}(\overrightarrow{\boldsymbol{z}}) = \overline{\chi_{LP}^{(P)}(\overrightarrow{\boldsymbol{z}},\alpha)}\,. \quad (33)$$

For statistically homogeneous microstructures the origin of the line segment vanishes and the only dependency is on the orientation and length of the line segment. In this case we are able to reformulate the alternative definition for an arbitrary position $\boldsymbol{x}$ as

$$\mathcal{P}_{LP}^{(P)}(\boldsymbol{y}) = \overline{\chi_{LP}^{(P)}(\overrightarrow{\boldsymbol{x}(\alpha)[\boldsymbol{x}(\alpha)+\boldsymbol{y}]}, \alpha)}\,, \tag{34}$$

wherein $\boldsymbol{y}$ denotes the difference vector governing the line segment. If the microstructure to be analyzed is statistically isotropic the definition reduces to $\mathcal{P}_{LP}^{(P)}(y)$, wherein y is the length of the line segment vector $\boldsymbol{y}$. An important extreme value of $\mathcal{P}_{LP}^{(P)}(y)$ is $\lim\limits_{y\to 0} \mathcal{P}_{LP}^{(P)}(y) = \mathcal{P}_V$, showing that the lineal-path function becomes the phase fraction for vanishing magnitudes y; for the length of the line segment tending to infinity the lineal-path function tends to zero, i.e. $\lim\limits_{y\to\infty} \mathcal{P}_{LP}^{(P)}(y) = 0$. In addition to that, a correlation to the chord-length density is proven in Torquato (2002) for statistically isotropic media. For the calculation of lineal-path functions in discrete representations of statistically homogeneous and ergodic microstructures only one representative sample needs to be analyzed. Then, the lineal-path function is calculated by

$$\mathcal{P}_{LP}^{(P)}(m,k) = \frac{1}{\tilde{N}} \sum_{p=p_m}^{p_M} \sum_{q=q_k}^{q_K} \chi_{LP}^{(P)}(\overrightarrow{\boldsymbol{y}})\,. \tag{35}$$

Herein, the discrete line segment and the total number of pixels are $\overrightarrow{\boldsymbol{y}} = [p+m, q+k]^T$ and $\tilde{N} = (p_M - 1 - p_m)(q_K - 1 - q_k)$. The summation bounds given in Eq. (26) have to be considered. For periodic unitcells the lineal-path function is computed by

$$\tilde{\mathcal{P}}_{LP}^{(P)}(m,k) = \frac{1}{N_x N_y} \sum_{p=0}^{N_x-1} \sum_{q=0}^{N_y-1} \chi_{LP}^{(P)}(\overrightarrow{\boldsymbol{y}})\,. \tag{36}$$

Efficient procedures for the calculation of the lineal-path function can be obtained by defining suitable templates, cf. Zeman (2003). Such a template consists of $T_x \times T_y$ entries characterized by the coordinates (m,k) having either the value one or zero. The value one means that the associated line segment defined by the difference vector from the origin to the associated coordinates (m,k) is part of the analysis, zero means the contrary. Then each line segment defined by the template is compared with the original image for each admissible position (p,q). Lineal-path functions are invariant with respect to reflections of line segments. For discrete images each line

segment to be analyzed has to be defined in an integer manner, which means that for each end position of line segments (m, k) a unique discrete line segment has to be constructed in the template. For this purpose the classical Bresenham algorithm (Bresenham (1965)) can be used. In most cases it is not necessary to compute a complete lineal-path function. The first possibility to improve the efficiency of the algorithm is to reduce the size of the template according to a characteristic maximal particle size. A second possibility is to reduce the number of analyzed line segments; in most cases it will be sufficient to analyze only a certain set of line orientations. As a third possibility it may not be required to evaluate the indicator function for all positions in the original image. It may be sufficient to place the line segments defined in the template at a random position and repeat this process a number of N^r times, then the discrete form of the lineal-path function reads

$$\mathcal{P}_{LP}^{(P)} = \lim_{N_r \to \infty} \frac{1}{N^r} \sum_{j=1}^{N^r} \chi_{LP}^{(P)}(\overrightarrow{\boldsymbol{y}_j}) \,, \tag{37}$$

with the line segments $\overrightarrow{\boldsymbol{y}}_j = [p_j + m, q_j + k]^T$. The random positions represented by the three-dimensional coordinates (p_j, q_j) have to fulfill

$$p_m \leq p_j \leq p_M - 1 \,, \quad q_k \leq q_j \leq q_K - 1 \,, \tag{38}$$

following Eq. (26) for random microstructures and

$$0 \leq p_j \leq N_x - 1 \,, \quad 0 \leq q_j \leq N_y - 1 \,, \tag{39}$$

for periodic unitcells. With a view to practical applications a sufficiently large number of random points N^r that have to be evaluated can be computed from standard statistics.

n-Point Cluster Functions Connectivity between points is not incorporated if lower order point probability functions are considered. The lineal-path function takes into account the connectivity since the affiliation of line segments to a certain phase is analyzed. However, the issue of percolation can not be captured and then the n-point cluster function can be taken into account. For this purpose the indicator function

$$\chi_{CL}^{(P)}(\overrightarrow{\boldsymbol{z}}) = \begin{cases} 1, & \text{if } \overrightarrow{\boldsymbol{z}} \in D^{(P)}, \\ 0, & \text{otherwise}, \end{cases} \tag{40}$$

is considered, which analyzes if the whole connection line $\overrightarrow{\boldsymbol{z}}$ connecting a number of n points $\boldsymbol{x}_1, \boldsymbol{x}_2 \ldots \boldsymbol{x}_n$ is located in the domain $D^{(P)}$ of phase P.

This connection line represents the shortest connection of the points going through phase P if possible. Then the n-point cluster function is defined as the ensemble average of the indicator function

$$\mathcal{C}_n^{(P)}(\overrightarrow{\boldsymbol{z}}) = \overline{\chi_{CL}^{(P)}(\overrightarrow{\boldsymbol{z}}, \alpha)}\,. \tag{41}$$

This function represents the probability that a connection line between a number of n points is located in phase P. For ergodic microstructures the consideration of a volumetric average instead of an ensemble average can be taken into account and the n-point cluster function is given by

$$\mathcal{C}_n^{(P)}(\boldsymbol{x}_1, \boldsymbol{x}_2, \ldots \boldsymbol{x}_n) = \lim_{V\to\infty} \int_{\mathcal{B}} \chi_{LP}^{(P)}\left(\overrightarrow{\boldsymbol{z}}(\boldsymbol{y}+\boldsymbol{x}_1, \boldsymbol{y}+\boldsymbol{x}_2, \ldots \boldsymbol{y}+\boldsymbol{x}_n), \alpha\right)\, d\boldsymbol{y}\,, \tag{42}$$

with $\overrightarrow{\boldsymbol{z}}$ denoting the connection line between the points $\boldsymbol{y}+\boldsymbol{x}_1, \boldsymbol{y}+\boldsymbol{x}_2, \ldots \boldsymbol{y}+\boldsymbol{x}_n$. Herein, $\boldsymbol{y}$ realizes a shift relative to the origin of a considered measurement domain $\mathcal{B}$. For practical applications cluster functions of lower order as e.g., the two-point cluster function as proposed in Torquato et al. (1988) are of particular importance. This function is defined by

$$\mathcal{C}_2^{(P)}(\boldsymbol{x}_1, \boldsymbol{x}_2) = \overline{\chi_{LP}^{(P)}(\overrightarrow{\boldsymbol{z}}(\boldsymbol{x}_1, \boldsymbol{x}_2), \alpha)}\,, \tag{43}$$

and for ergodic microstructures where the ensemble average over a set of samples is replaced by a volumetric average over only one sample we obtain

$$\mathcal{C}_2^{(P)}(\boldsymbol{x}_1, \boldsymbol{x}_2) = \lim_{V\to\infty} \int_{\mathcal{B}} \chi_{LP}^{(P)}\left(\overrightarrow{\boldsymbol{z}}(\boldsymbol{y}+\boldsymbol{x}_1, \boldsymbol{y}+\boldsymbol{x}_2)\right)\, d\boldsymbol{y}\,. \tag{44}$$

For the calculation in discrete representations of statistically homogeneous and ergodic microstructures the two-point cluster function is calculated by

$$\mathcal{P}_{CL}^{(P)}(m,k) = \frac{1}{\tilde{N}} \sum_{p=p_m}^{p_M-1} \sum_{q=q_k}^{q_K-1} \chi_{CL}^{(P)}\left(\overrightarrow{\boldsymbol{y}}(p+m, q+k)\right)\,. \tag{45}$$

Herein, $\tilde{N} = (p_M - 1 - p_m)(q_K - 1 - q_k)$ denotes the total number of elements, typically pixels, and the summation bounds are given by Eq. (26). The connection lines $\rightarrow \boldsymbol{y}$ are computed from points located at $[p, q]$ to points located at $[p+m, q+k]$. For periodic unitcells the cluster function is computed by

$$\tilde{\mathcal{P}}_{CL}^{(P)}(m,k) = \frac{1}{N_x N_y} \sum_{p=0}^{N_x-1} \sum_{q=0}^{N_y-1} \chi_{LP}^{(P)}\left(\overrightarrow{\boldsymbol{y}}(p+m, q+k)\right)\,. \tag{46}$$

With contrast to the lineal-path function the definition of templates is not possible since the connection lines are not unique for every combination of points. Therefore, the calculation of the connection lines is typically computationally expensive and requires rather sophisticated algorithms. One possibility to decrease computational costs is to reduce the number of analyzed point combinations. As a further possibility the evaluation for all positions in the original image may not be required. Then a sufficiently large number of N^r random positions can be evaluated and the two-point cluster function reads

$$\mathcal{P}_{CL}^{(P)} = \lim_{N_r \to \infty} \frac{1}{N^r} \sum_{j=1}^{N^r} \chi_{CL}^{(P)} \left(\overrightarrow{\boldsymbol{y}_j}(\boldsymbol{x}_{1j}, \boldsymbol{x}_{2j}) \right) \tag{47}$$

wherein the random positions $\boldsymbol{x}_{1j} = [p_j, q_j]^T$ and $\boldsymbol{x}_{2j} = [p_j + m_j, q_j + k_j]^T$ have to fulfill the conditions given in Eq. (38) for random microstructures and Eq. (39) for periodic unitcells. For two-dimensional microstructures the associated bounds have to be considered. Regarding practical applications a sufficiently large number of random points N^r has to be considered.

Graphical Visualization Different visualization schemes are considered for the individual statistical measures of higher order. The visualization of two-dimensional data sets is explained by means of an example focusing on the oversimplified academic unitcell of a periodic microstructure shown in Fig. 2a. The image is parameterized by the index pair $[p, q]$ and its size is $N_x \times N_y = 10 \times 10$ pixels; the phase fraction of the inclusion phase $P = I$ is $\mathcal{P}_V^{(I)} = (13\,\text{pixels})/(100\,\text{pixels}) = 0.13$. The spectral density, the complete two-point probability function and the complete lineal-path function are computed, see Fig. 2c,d,b, respectively. Please note that the horizontal and vertical axis in the visualizations of the statistical measures are associated with the index m and k. The origin of the coordinate system is located in the center for the spectral density and in the lower center for the two-point probability and the lineal-path function. The results are depicted as normalized values: for the lineal-path function $(\tilde{\mathcal{P}}_{LP}^{(I)}(m,k)/\mathcal{P}_V^{(I)})$ and the two-point probability function $(\tilde{\mathcal{P}}_{\mathcal{S}_2}^{(I)}(m,k)/\mathcal{P}_V^{(I)})$ the distributions are normalized with respect to their maximum value which is always equal to the phase fraction and always located at the origin $m = 0$, $k = 0$. For the spectral density first the trivial entry at $m = 0$, $k = 0$ is deleted because the spectral density provides relative information, i.e. the individual entries give the weights for the individual frequencies, and thus, the trivial entry does not provide information. Then, the remaining distribution is normalized

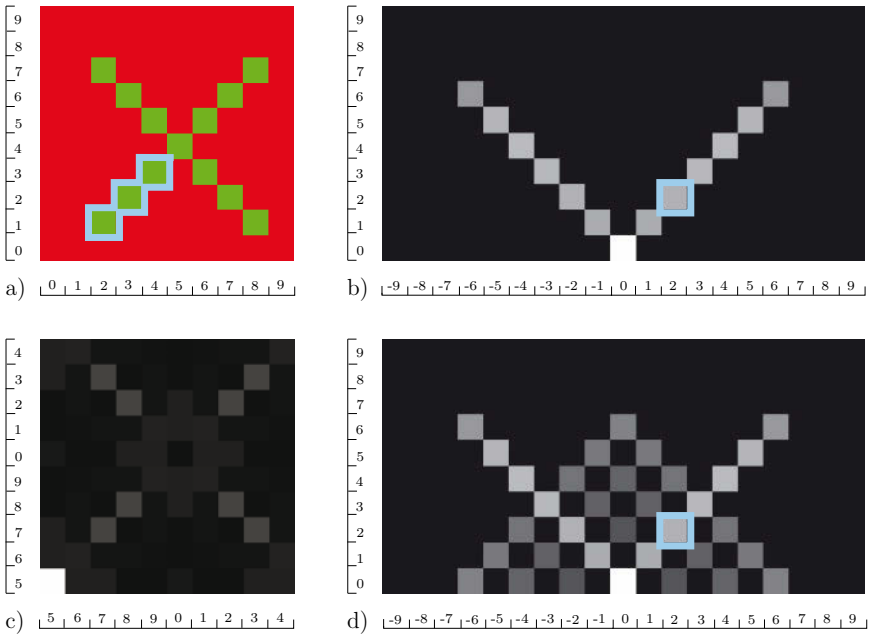

Figure 2. Example for statistical measures calculated for the inclusion phase ($P = I$) morphology: a) Binary dataset of microstructure; graphical illustrations of the normalized b) lineal-path function, c) spectral density and d) two-point probability function.

with respect to its maximum value, i.e. $\mathcal{P}_{SD}^{(I)}(m,k)/\max[\mathcal{P}_{SD}^{(I)}(m,k)]$. The visualization of the results is color-coded in greyscale where white represents the limit value 1 and black the limit value 0.

As an example for the interpretation of the statistical measures we consider the line segment $m = 2$, $k = 2$ exemplarily marked in Fig. 2a. Its associated value of the lineal-path function is then marked in Fig. 2b. Since the given line segment can be found 5 times in the microstructure the associated value of the lineal-path function is $\tilde{\mathcal{P}}_{LP}^{(I)}(2,2) = 5/100$ which corresponds to a normalized value of $5/13 \approx 0.39$ which in turn corresponds to a medium grey color. This means that the probability of finding a line segment with $m = 2$, $k = 2$ in the microstructure is approximately 40 %.

The associated value of the two-point probability is marked in Fig. 2d and now the number of pairs of pixels in the inclusion phase with a distance of $m = 2$, $k = 2$ is also 5. Therefore the color is the same in the plot of the two-point probability function as the one for the lineal-path function and the probability of finding that particular pair of pixels is again

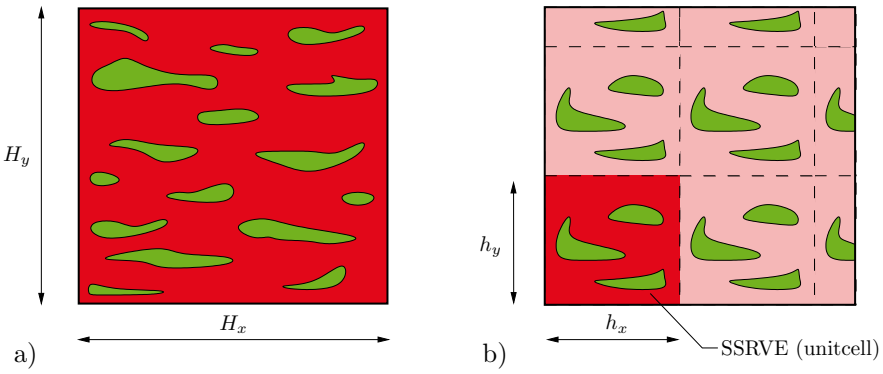

Figure 3. a) complex (non-periodic) RVE for a two-phase microstructure with arbitrary inclusion morphology and b) simplified periodic microstructure with SSRVE.

approximately 0.4. The difference between those two statistical measures becomes clear by noticing that for the lineal-path function (Fig. 2b) only non-vanishing entries are observed in diagonal direction. This is obvious since connected line segments with a length larger than 2 pixels are only found in the original image (Fig. 2a) in diagonal direction as well. When comparing this with the two-point probability function we observe that further non-vanishing entries exist also in directions differing from the diagonal one. This directly results from the fact that repeating pixels in different directions exist. For instance, the upper and lower two pixels of the inclusion in Fig. 2 are the only two pairs of pixels that have a horizontal distance of 6 pixels. This oriented distance $(m = 6, k = 0)$ is able to be detected twice. Hence, the probability of finding this distance in a microstructure of the dimension 10×10 pixels is $\tilde{\mathcal{P}}^{(I)}_{\mathcal{S}_2}(6, 0) = 2/100 = 0.02$.

4 Statistically Similar RVEs

In the context of computational homogenization schemes the challenging task is the estimation and identification of a representative volume element (RVE). In most cases a usual RVE for a random inclusion/matrix-microstructure is determined by the smallest possible sub-structure which still leads to a qualitatively and quantitatively realistic macroscopic material behavior. However, such RVEs are typically too complex for efficient cal-

culations. Thus, the construction of statistically similar RVEs (SSRVEs), which are characterized by a lower complexity than the smallest possible random sub-structures, is described here for the reduction of computational costs, cf. Schröder et al. (2010). The basic idea in this context is to replace an in general non-periodic RVE with an arbitrary complex inclusion morphology by a periodic one composed of optimal periodically arranged unit cells, see Fig. 3. The main effort is that in FE^2 calculations only the periodic unit cell needs to be considered as a RVE provided that periodic boundary conditions are applied. The lower complexity of the unit cell then leads to a lower number of degrees of freedom in the finite element discretization and reduces the computational cost.

For the construction of such SSRVEs the approach proposed here is based on the ideas for microstructures with circular inclusions presented in Povirk (1995). There, the position of the circular inclusions with constant and equal diameters is optimized by the minimization of a least-square functional taking into account the side condition that the spectral density of the periodic RVE should be as similar as possible to the one of the non-periodic microstructure. Motivated by this approach we consider a reasonable parameterization $\boldsymbol{\gamma}$ of the inclusion phase in the SSRVE. Then, the optimal SSRVE defined by the parameterization $\widetilde{\boldsymbol{\gamma}}$ is calculated by minimizing a least-square functional such that

$$\widetilde{\boldsymbol{\gamma}} = \arg \left\{ \min_{\boldsymbol{\gamma}} \left[\sum_{L=1}^{n_{sm}} \omega_{(L)} \, \mathcal{L}_{(L)}(\boldsymbol{\gamma}) \right] \right\} , \tag{48}$$

wherein the individual least-square functionals for different statistical measures L are computed by

$$\mathcal{L}_{(L)}(\boldsymbol{\gamma}) = \left(\mathcal{P}_{(L)}^{real} - \mathcal{P}_{(L)}^{SSRVE}(\boldsymbol{\gamma}) \right)^2 , \tag{49}$$

cf. Balzani et al. (2009). A number of n_{sm} statistical measures $\mathcal{L}_{(L)}$ describing the inclusion morphology is taken into account. The individual least-square functionals take into account the squares of differences of the individual statistical measures $\mathcal{P}_{(L)}^{real}$ and $\mathcal{P}_{(L)}^{SSRVE}(\boldsymbol{\gamma})$ computed for a real (complex) microstructure, referred to as target structure, and for the SSRVE, respectively. The weighting factors $\omega_{(L)}$ levels the influence of the individual measures. Here, splines are used for the two-dimensional parameterization of the inclusion phase morphology, and thus, the coordinates of the sampling points enter the general vector $\boldsymbol{\gamma}$, i.e.

$$\boldsymbol{\gamma} := [\hat{x}_1 \ , \ \hat{y}_1 \ , \ \hat{x}_2 \ , \ \hat{y}_2 \ , \ \dots \ \hat{x}_{n_{sp}} \ , \ \hat{y}_{n_{sp}}]^T \tag{50}$$

with the number of sampling points n_{sp}.

4.1 Optimization Method

Due to the discrete character of the statistical measures entering the minimization problem (48), the energy surface is not smooth and therefore, typically no gradient-based optimization method can be applied. To overcome these difficulties the moving frame algorithm described in Balzani et al. (2010) is applied. For this purpose random initial sampling point coordinates $x_{0,k}, y_{0,k}$ are generated first, which direct to the sampling point $M_{0,k}$. Then further n_{mov} random points $M_{j,k}(x_{j,k}, y_{j,k})$ with $j = 1 \dots n_{mov}$ in a frame of the size $2a \times 2a$ are generated, see Fig. 4a, and the objective function is evaluated for each generated sampling point. Then the initial sampling point moves to the sampling point $M_{0,k+1}$ defined by the lowest value of $\mathcal{L}$ and the iteration counter is initialized $l_{iter} = 0$, see Fig. 4b. If the frame center remains unaltered, i.e. no lower value of $\mathcal{L}$ is found in this iteration step ($M_{0,k+1} = M_{0,k+2}$), we set $l_{iter} = l_{iter} + 1$, see Fig. 4c. If the stopping criterion $l_{iter} = l_{itermax}$ is reached, the actual minimal value of $\mathcal{L}$ is interpreted as local minimum associated to the starting value. In addition, this procedure is repeated a predefined number of cycles with different random starting values. If a high fraction of minimizers of the individual optimization cycles leads to similar sampling point coordinates, then we choose this result as an appropriate solution. In order to improve the method the frame size a can be modified depending on the difference $|\boldsymbol{d}|$ and l_{iter}. Furthermore, a combination with a line-search algorithm is implemented, where $\mathcal{L}$ is also evaluated at a number of n_{line} points interconnecting the frame center point M_0 with the random points $M_1, M_2, \dots M_{n_{mov}}$.
Different possibilities for the solution of non-smooth optimization problems can be found in e.g. Kolda et al. (2003), Conn et al. (2009) and Mäkelä and Neittaanmäki (1992).

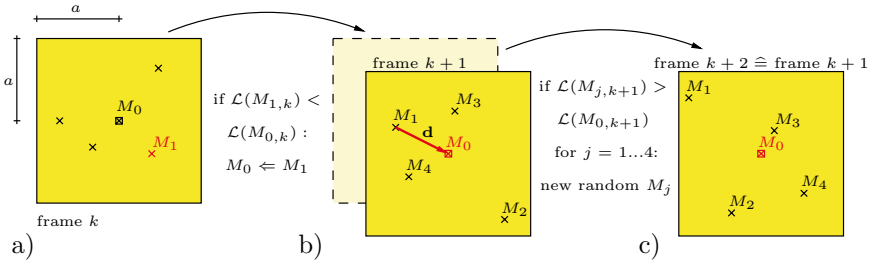

Figure 4. Moving frame algorithm: optimization frames a) k, b) $k+1$ and c) $k+2$, cf. Balzani et al. (2009).

4.2 Mechanical Verification

In order to incorporate microstructure information mainly governing the macroscopic response, no macroscopic mechanical measures are taken into account in the least-square functional (48). Since the degree of microstructure complexity in the SSRVE is a priori unknown different complexity levels need to be considered. Then for each resulting SSRVE a mechanical verification has to be performed in order to estimate the required degree of complexity. For this purpose a mechanical multiscale error analysis is considered where the macroscopic mechanical response of the individual SSRVE realizations is compared with the response of the target structure. Three different two-dimensional macroscopic virtual experiments are considered in the x-y-plane: (i) horizontal uniaxial tension, (ii) vertical uniaxial tension and (iii) simple shear. At the microscale a discretization by triangular Finite Elements with quadratic ansatz functions for the displacements are considered. Furthermore, plain stress conditions and periodic boundary conditions are applied. Based on the resulting macroscopic stress-strain response we define the relative errors r_x, r_y and r_{xy} for each individual evaluation point i, i.e.

$$r_j^{(i)} = \frac{\overline{\sigma}_{j,i}^{real} - \overline{\sigma}_{j,i}^{SSRVE}}{\overline{\sigma}_{j,i}^{real}} \quad \text{with} \quad j = x, y, xy\,, \tag{51}$$

where only values with non-vanishing denominators are taken into account. In addition to that, the average errors over the total number of evaluation points n_{ep} for each experiment

$$\widetilde{r}_j = \sqrt{\frac{1}{n_{ep}} \sum_{i=1}^{n_{ep}} [r_j^{(i)}]^2} \quad \text{with} \quad r_j^{(i)} := r_j \left(\tfrac{i}{n} \triangle l_{\max}/l_0 \right) \tag{52}$$

and the overall comparative measure

$$\widetilde{r}_{\varnothing} = \sqrt{\tfrac{1}{3}(\widetilde{r}_x^2 + \widetilde{r}_y^2 + \widetilde{r}_{xy}^2)} \tag{53}$$

are taken into account for quantitative statements with respect to the performance of the individual SSRVEs.

5 Analysis of SSRVEs for a Virtual Target Structure

To show the performance of the proposed method and to analyze the influence of individual statistical measures, SSRVEs are constructed first for a virtually generated target microstructure. This target structure is constructed such that an oriented inclusion morphology is obtained which leads

to a macroscopically anisotropic response. Then, the mechanical response of the SSRVEs is compared in simple virtual experiments with the response of the target structure. To provide quantitative estimations for the accuracy of the individual considered least-square functionals, a mechanical error analysis is performed.

The virtual target structure is obtained by applying the Boolean method, where a certain two-dimensional space of interest is first completely filled with the inclusion material. Then, ellipsoids with the semi-axis a_x and a_y of predefined aspect ratios, here $a_x/a_y = 14.3$, and random semi-axis $a_x \in [3, 6]\mu$m are randomly placed in the space of interest. This process is stopped if a certain phase fraction of $\mathcal{P}_V = 0.1872$ is reached. The resulting binary image is shown in Fig. 5a. Subsequently, the boundaries of the inclusion phase are smoothened and a Finite-Element discretization is automatically constructed, see Fig. 5b. Here, 14,982 triangular Finite Elements with quadratic ansatz functions for the displacements are taken into account.

For the mechanical analysis we consider a simple J_2-plasticity model with isotropic hardening at the microscale for the description of the mechanical behavior of the individual constituents. This model uses an exponential von Mises type hardening law and is described in Section 2. Fig. 6 shows the used material parameters and the macroscopic mechanical response of the target structure in the three virtual experiments. The results of the tension tests show the macroscopic anisotropic behavior of the target structure.

5.1 Analysis of Basic Parameters and Spectral Density

Four different types of SSRVEs are considered: one convex inclusion parameterized by three sampling points (type I), one inclusion with four sampling

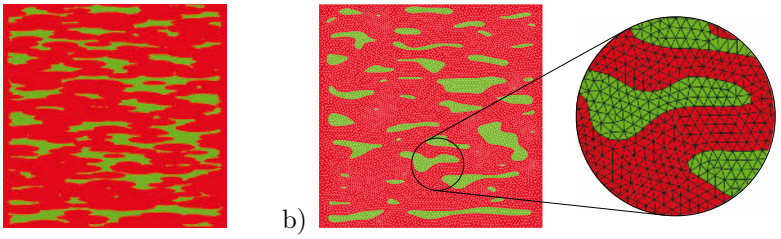

a) $a_x/a_y = 14.3,\ a_x \in [3, 6]$ b) $\mathcal{P}_V = 0.1872\,,\ n_{ele} = 14{,}982\,,\ n_{dof} = 60{,}410$

Figure 5. Considered target microstructure: a) result of the Boolean method and b) smoothened inclusion phase boundaries with FE-discretization.

	matrix	inclusion
λ [MPa]	118,846.2	
μ [MPa]	79,230.77	
y_0 [MPa]	260.0	1000.0
y_∞ [MPa]	580.0	2750.0
η [-]	9.0	35.0
h [-]	70.0	10.0

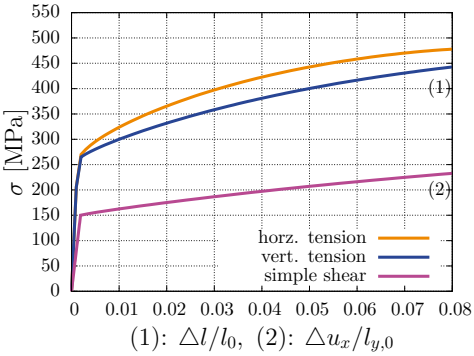

Figure 6. Material parameters of the individual constituents (left) and the macroscopic mechanical response of the target structure in the three virtual experiments (right).

points (type II), and two inclusions with three and four sampling points each (type III and type IV), respectively. Illustrations of these types are shown in Fig. 7. During the optimization process the inclusions are constricted to be located inside the frame of the unitcell such that no spline intersects the limits of the unitcell. First, the significance of several statistical measures on their influence on the quality of the SSRVEs is analyzed. In detail, separately the specific internal surface, the specific integral of mean curvature and the spectral density are considered as statistical measures. In all cases the phase fraction is additionally taken into account. Please note that due to the fact that two-dimensional analysis are performed the two-dimensional counterparts of the scalar-valued basic parameters are calculated.

Specific internal surface For the incorporation of the phase fraction $\mathcal{P}_V$ and the specific internal surface $\mathcal{P}_S$ as statistical measures the least-square

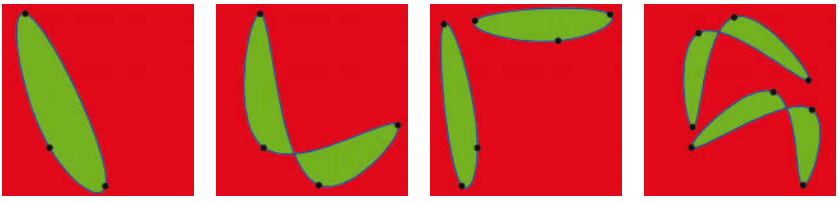

I: $n_{sp} = 3$ II: $n_{sp} = 4$ III: $n_{sp} = 6$ IV: $n_{sp} = 8$

Figure 7. Considered SSRVE types with spline sampling points .

functional

$$\mathcal{L}_1(\boldsymbol{\gamma}) = \omega_V \left(1 - \frac{\mathcal{P}_V^{SSRVE}(\boldsymbol{\gamma})}{\mathcal{P}_V^{target}}\right)^2 + \omega_S \left(1 - \frac{\mathcal{P}_S^{SSRVE}(\boldsymbol{\gamma})}{\mathcal{P}_S^{target}}\right)^2 \tag{54}$$

is considered. The weighting factor ω_V and ω_S are set to one. The results of the optimization process are shown in Fig. 8. Decreasing values of the minimized value of the objective function with an increasing number of sampling points is observed. This is reasonable since the number of sampling points somehow correlates with the complexity of the SSRVE type. On the other hand, this also induces a higher quantity of finite elements in the discretization with an increasing number of sampling points.
In order to study the SSRVE's capability to reflect the mechanical response of the target structure we compare the mechanical errors described in Section 4.2. The error values and their standard deviations for the virtual experiments based on the SSRVEs constructed by $\mathcal{L}_1$ are shown in Table 1. Note, that the rows are sorted by the two categories of convex and non-convex inclusions, i.e. the first two rows show the SSRVE types with convex inclusions and the following rows the ones with the non-convex inclusions. As we can see the results for the horizontal tension test show significantly higher mechanical errors than for the vertical tension. This also shows the theoretical impossibility of the specific internal surface density to characterize oriented microstructures that lead to a macroscopically anisotropic response. The overall comparative mechanical error $\widetilde{r}_{\varnothing}$ decreases in the two categories with an increasing number of finite elements, which seems to be physically reasonable. Furthermore, it is observed that the mechanical response of even the most complex SSRVE type IV deviates by approximately 4 %.

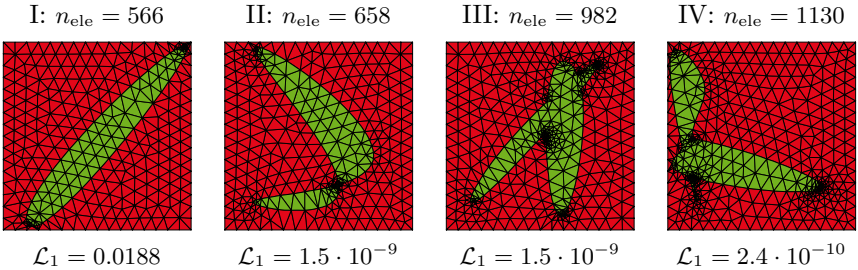

Figure 8. Discretizations of the SSRVEs resulting from the minimization of $\mathcal{L}_1$.; n_{ele} denotes the number of finite elements in the discretization.

Table 1. Values of the objective function $\mathcal{L}_1$ and the errors $\widetilde{r}$ using the SSRVEs shown in Fig. 8.

SSRVE	$\mathcal{L}_1$	n_{dof}	$\widetilde{r}_x$ [%]	$\widetilde{r}_y$ [%]	$\widetilde{r}_{xy}$ [%]	$\widetilde{r}_{\varnothing}$ [%]
I	0.0188	2394	12.44 ± 2.83	0.39 ± 0.40	9.18 ± 3.18	8.93
III	$1.5{\cdot}10^{-9}$	4058	9.12 ± 2.09	4.68 ± 1.35	2.16 ± 1.12	6.05
II	$1.5{\cdot}10^{-9}$	2762	9.67 ± 2.18	0.27 ± 0.16	2.23 ± 1.09	5.73
IV	$2.4{\cdot}10^{-10}$	4650	6.52 ± 1.43	3.00 ± 0.85	0.66 ± 0.17	4.16

Specific Integral of Mean Curvature Now the specific integral of mean curvature in combination with the phase fraction is investigated. The associated least-square functional reads

$$\mathcal{L}_2(\boldsymbol{\gamma}) = \omega_V \left(1 - \frac{\mathcal{P}_V^{SSRVE}(\boldsymbol{\gamma})}{\mathcal{P}_V^{target}}\right)^2 + \omega_M \left(1 - \frac{\mathcal{P}_M^{SSRVE}(\boldsymbol{\gamma})}{\mathcal{P}_M^{target}}\right)^2 , \qquad (55)$$

where $\mathcal{P}_M$ denotes the specific integral of mean curvature. The weighting factors ω_V and ω_M are set to one again. The resulting realizations of SSRVEs are depicted in Fig. 9.

We notice that again the horizontal tension test shows rather large mechanical errors in contrast to the vertical tension. Thereby, it is again shown that also the specific integral of mean curvature is not able to represent the main anisotropy directions. The overall mechanical error $\widetilde{r}_{\varnothing}$ is comparable with the ones obtained for the specific internal surface density and no significant improvement can be observed. However, a strange behavior is observed for the category with the non-convex inclusions since here an increase of $\widetilde{r}_{\varnothing}$ is observed for an increasing number of inclusions and thereby a higher complexity.

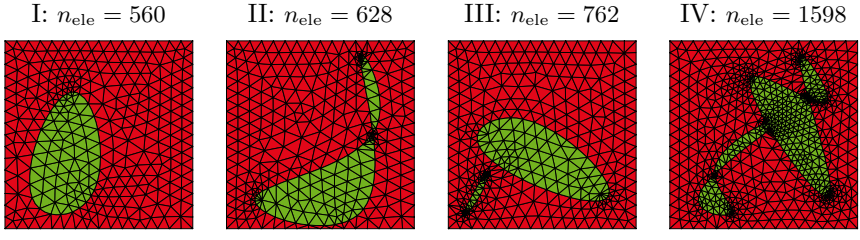

Figure 9. Discretization of the SSRVEs resulting from the minimization of $\mathcal{L}_2$. n_{ele} denotes the number of finite elements in the discretization.

Table 2. Values of the objective function $\mathcal{L}_2$ and the errors $\widetilde{r}$ using the SSRVEs shown in Fig. 9.

SSRVE	$\mathcal{L}_2$	n_{dof}	$\widetilde{r}_x$ [%]	$\widetilde{r}_y$ [%]	$\widetilde{r}_{xy}$ [%]	$\widetilde{r}_{\varnothing}$ [%]
I	0.2648	2370	11.58 ± 2.66	0.33 ± 0.20	2.40 ± 0.65	6.83
III	$8.5{\cdot}10^{-4}$	3178	9.79 ± 2.21	2.65 ± 0.57	0.84 ± 0.19	5.88
II	$8.5{\cdot}10^{-4}$	2642	9.02 ± 2.00	0.58 ± 0.31	0.85 ± 0.18	5.24
IV	$8.5{\cdot}10^{-4}$	6522	10.20 ± 2.32	1.22 ± 0.54	1.99 ± 0.90	6.04

Spectral Density The results from the previous analyses show that statistical measures need to be incorporated that at least also capture the main anisotropy directions of the microstructure. Therefore, additionally the (discrete) spectral density (SD) for the inclusion phase is considered. In order to end up in a more efficient optimization procedure a relevant area of the spectral density is defined. For this purpose the complete spectral density of the target structure is computed and normalized before optimization. Since the target structure consists of 200×200 pixels the number of entries in the complete spectral density is 200×200. Then the spectral density is rebinned to the size 20×20, which seems to be reasonable because the important characteristics of the spectral density are maintained by rebinning. For a further enhancement of the numerical procedure, the minimal rectangular sub-area of the rebinned spectral density is identified, where no entry higher than a predefined threshold value of 0.02 is placed outside of the relevant area. Then only this rebinned relevant area of the spectral density with the size 4×12 enters the least-square functional. The

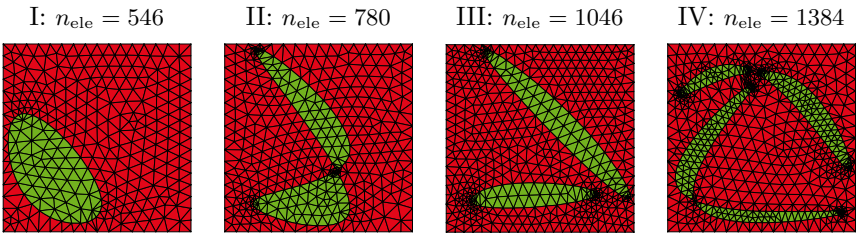

Figure 10. Discretization of the SSRVEs resulting from the minimization of $\mathcal{L}_3$. n_{ele} denotes the number of finite elements in the discretization.

Table 3. Values of the objective function $\mathcal{L}_3$ and the errors $\widetilde{r}$ using the SSRVEs shown in Fig. 10.

SSRVE	$\mathcal{L}_3$ $[10^{-2}]$	n_{dof}	$\widetilde{r}_x$ [%]	$\widetilde{r}_y$ [%]	$\widetilde{r}_{xy}$ [%]	$\widetilde{r}_{\varnothing}$ [%]
I	1.44	2314	11.80 ± 2.70	1.35 ± 0.30	1.53 ± 0.35	6.91
III	1.27	4350	7.85 ± 1.74	1.24 ± 0.25	5.83 ± 2.37	5.69
II	1.33	3250	9.48 ± 2.15	0.96 ± 0.54	0.78 ± 0.41	5.52
IV	1.00	5666	5.04 ± 1.14	0.59 ± 0.25	4.52 ± 1.84	3.92

associated least-square functional reads

$$\mathcal{L}_3(\boldsymbol{\gamma}) = \omega_V \, \mathcal{L}_V(\boldsymbol{\gamma}) + \omega_{SD} \, \mathcal{L}_{SD}(\boldsymbol{\gamma}) \tag{56}$$

wherein the individual least-square functionals for the phase fraction $\mathcal{P}_V$ and the spectral density $\mathcal{P}_{SD}$ are given by

$$\begin{aligned} \mathcal{L}_V &= \left(1 - \frac{\mathcal{P}_V^{SSRVE}(\boldsymbol{\gamma})}{\mathcal{P}_V^{target}} \right)^2 \\ \mathcal{L}_{SD} &= \frac{1}{N_x \, N_y} \sum_{m=1}^{N_x} \sum_{k=1}^{N_y} \left(\mathcal{P}_{SD}^{target}(m,k) - \mathcal{P}_{SD}^{SSRVE}(m,k,\boldsymbol{\gamma}) \right)^2 , \end{aligned} \tag{57}$$

respectively. Herein, N_x and N_y denote the number of pixels in the relevant area. The weighting factors ω_V and ω_{SD} are set to one again.
In Fig. 10 the resulting SSRVEs from the optimization process are shown. Again the three virtual experiments are performed and the mechanical errors are computed. Table 3 shows the corresponding values. As can be seen for the horizontal- and the vertical tension tests a reasonable decreasing mechanical error is observed with an increasing number of sampling points. This is however not the case for the simple shear test such that the overall mechanical error $\widetilde{r}_{\varnothing}$ does not show a significant improvement again. It seems that although the spectral density turns out to be a statistical measure suitable for the description of directional information it seems not to be sufficient for a characterization of a random microstructure.

5.2 Enhanced Construction Method

Since the results of the analysis in the previous section turn out to be unsatisfying an enhancement may be obtained by modifying the technical construction method of the SSRVE itself. First, the previous SSRVEs are allowed to interpenetrate themselves or other inclusions and therefore untypical inclusions as shown in Fig. 7 for Type II and IV are obtained. This

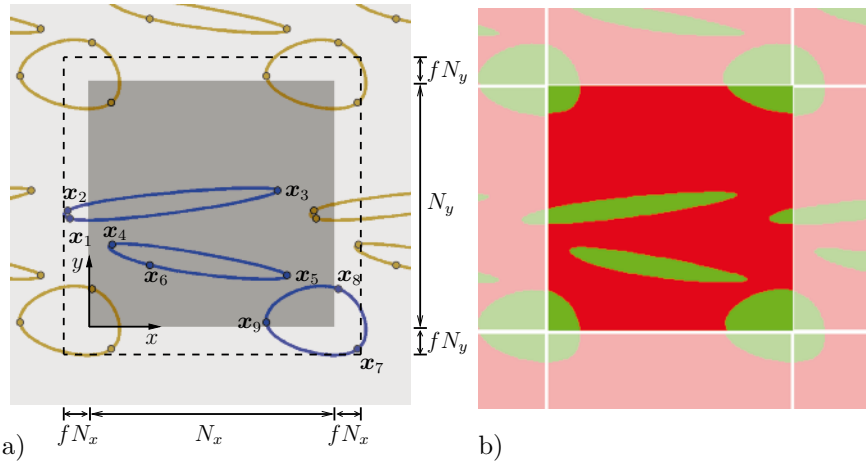

Figure 11. Illustration of improved SSRVE-construction method ensuring periodic extensibility: a) required splines with the sampling points and b) resulting binary SSRVE image (center) with the periodic expansion (transparent).

leads also to Finite Element discretizations with singularities at the intersection points which should be avoided for numerical reasons. Second, it might be too restrictive to assume that no inclusion crosses the unitcell boundaries.

Therefore, now SSRVEs are constructed ensuring that no intersections of splines with themselves and each other occur via checking admissible coordinates and/or a penalty approach. Consequently, inclusion geometries as shown in Fig. 7 for Type II and IV are not permitted. Additionally, inclusions are enabled to be located at the SSRVE's boundaries. This requires a construction which ensures periodic extensibility. For this purpose the construction procedure is as follows: The sampling point coordinates are allowed in a specified space $((N_x + 2\,f\,N_x) \times (N_y + 2\,f\,N_y))$ where a certain spatial overlap factor f with respect to the SSRVE space of interest $(N_x \times N_y)$ is taken into account. This means that the sampling point coordinates have to match

$$x_i \in [-fN_x, N_x{+}fN_x]\,, \quad y_i \in [-fN_y, N_y{+}fN_y] \quad \text{for} \quad i = 1 \ldots n_{sp}\,. \tag{58}$$

In the analysis performed in this contribution the overlap factor is set to $f = 0.1$ and a SSRVE-resolution of $N_x \times N_y = 60 \times 60$ pixels is considered. The resulting splines are shown exemplarily in Fig. 11a as dark (blue) splines. Then, the SSRVE is periodically expanded by inserting the gen-

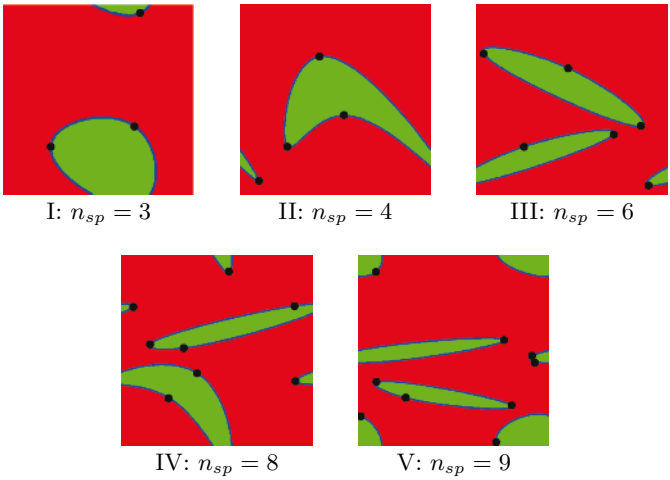

Figure 12. Five considered SSRVE-types with spline sampling points.

erated splines at the periodic positions, cf. the lighter (brown) splines in Fig. 11a. In order to preclude inclusions that intersect with themselves or with others, this construction procedure is repeated until a permitted unitcell is obtained and a resulting binary image of the SSRVE as shown in Fig. 11b is constructed. Furthermore, we consider an additional SSRVE type containing three inclusions with three sampling points each. A total number of five different SSRVE types are therefore analyzed, see Fig. 12.
Another aspect is the incorporation of an additional statistical measure of higher-order. In preceding investigations (Balzani et al. (2009, 2010)) it appears, that the spectral density seems to be a suitable measure capturing information concerning periodicity as well as direction-depended information and it is relatively efficient to be computed compared to the complete two-point probability function. Therefore, the spectral density as well as the phase fraction are considered further on. Even if "only" a three-point probability function is considered as an additional measure, the procedure will likewise be very expensive to be computed since the three-point probability function has a much higher dimension of solution space than the two-point probability function. Therefore, the lineal-path function may be a further reasonable statistical measure since it has the same solution space as the two-point probability function and it captures further information with respect to the type of connectivity of points and therefore the connectedness of inclusions. This information is rather not covered by the spectral density. Conversely, information regarding relative distances between the inclusions can not be represented by the lineal-path function, but it is one of the main

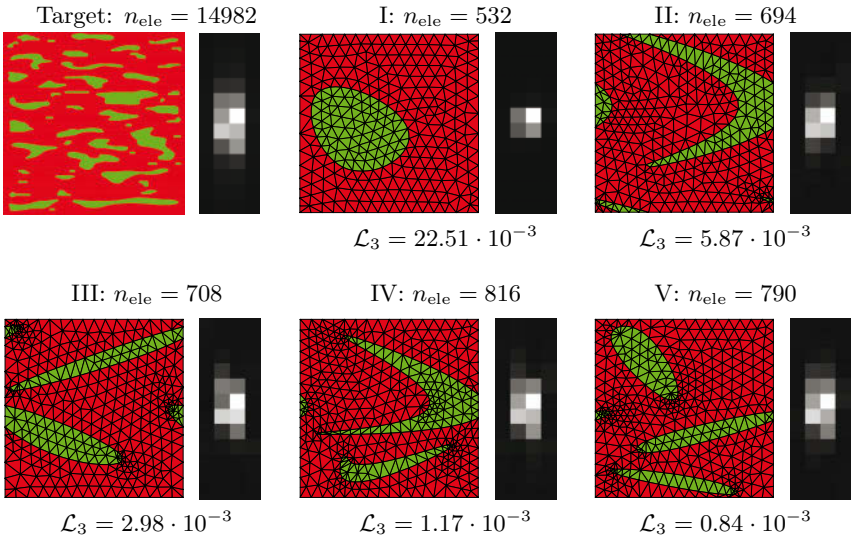

Figure 13. Target structure and discretization of the SSRVEs with corresponding relevant area of the spectral density (right) resulting from the minimization of $\mathcal{L}_3$.

features of the spectral density. Consequently, in the sequel we analyze the improvements eventually achieved by the modified construction technique and/or by incorporating additionally the lineal-path function. The same artificial target structure shown in Fig. 5 is considered.

Spectral Density The least-square functional including the phase fraction and the spectral density is considered first, see Eq. (56) and again the weighting factors are set to one. Minimizing the functional with respect to the sampling point coordinates of the splines yields the SSRVEs whose discretization is shown in Fig. 13. It can be observed that the number of finite elements n_{ele}, that is required for a suitable discretization, increases with increasing complexity of the SSRVE. In addition to that, the value of the computed minimum of the objective function is decreasing from $\mathcal{L}_3 = 22.51 \cdot 10^{-3}$ for Type I to $\mathcal{L}_3 = 0.84 \cdot 10^{-3}$ for Type V. This is kind of obvious since an increasing complexity of the inclusion morphology coincides more or less with an increase of the number of sampling points, which liberates the optimization problem given in Eq. (48). For the visual comparison the rebinned relevant areas of the spectral density are provided on the right hand side of the microstructure images. The spectral density of Type V obviously matches the spectral density of the target structure most

Table 4. Values of the objective function $\mathcal{L}_3$ and the errors $\widetilde{r}$ using the SSRVEs shown in Fig. 13, n_{dof} denotes the number of global degrees of freedom of the finite element discretization.

SSRVE	$\mathcal{L}_3$ [10^{-3}]	n_{dof}	$\widetilde{r}_x$ [%]	$\widetilde{r}_y$ [%]	$\widetilde{r}_{xy}$ [%]	$\widetilde{r}_{\varnothing}$ [%]
I	22.51	2254	8.44 ± 1.96	0.66 ± 0.22	0.95 ± 0.22	4.92
III	2.98	2962	2.43 ± 0.86	1.72 ± 0.40	5.06 ± 2.07	3.39
V	0.84	3290	0.14 ± 0.15	0.09 ± 0.06	3.08 ± 1.24	1.78
II	5.87	2914	2.56 ± 1.29	0.54 ± 0.26	9.12 ± 3.40	5.48
IV	1.17	3402	1.14 ± 0.39	0.97 ± 0.44	4.38 ± 1.85	2.67

accurately, significantly more than Type I. For the mechanical comparison of the SSRVEs with the target structure the three virtual experiments are calculated using the FE^2-scheme. For a better quantitative comparative analysis, the average errors, together with their standard deviation, and the overall mechanical comparative measures are given in Table 4.

First, it is observed that the order of magnitude of the least-square function regarding the phase fraction $\mathcal{L}_V$ is twice to four times lower than the one regarding the spectral density $\mathcal{L}_{SD}$. Since we are interested in SSRVEs where the phase fraction matches very well with the phase fraction of the target structure the choice of $\omega_V = \omega_{SD} = 1$ seems to be reasonable. Second, it can be observed that with increasing complexity in each category (convex- and non-convex inclusions) the overall comparative error decreases in general and Type V turns out to yield the best mechanical correspondence to the response of the target structure. However, when analyzing the individual average errors for the three virtual experiments a relatively high value of $\widetilde{r}_{xy} = 3.08$ is obtained for the simple shear test. Although the other two experiments of SSRVE Type V fit rather well the response of the target structure, the simple shear test is only partly represented accurately. In turn, the rather simple SSRVE Type I provides the best representation of the simple shear test, but the horizontal tension test is reflected less accurately such that the overall comparative measure is $\widetilde{r}_{\varnothing} = 4.92$. We conclude that an improvement in the individual tests can be observed but the overall results of the SSRVEs are still not satisfying.

Spectral Density and Lineal-Path Function The objective function given in Eq. (56) is extended by the lineal-path function in order to incorporate further statistical measures of higher order. This leads to the objective function

$$\mathcal{L}_4(\boldsymbol{\gamma}) = \omega_V \, \mathcal{L}_V(\boldsymbol{\gamma}) + \omega_{SD} \, \mathcal{L}_{SD}(\boldsymbol{\gamma}) + \omega_{LP} \, \mathcal{L}_{LP}(\boldsymbol{\gamma}) \,, \tag{59}$$

with the additional least-square function for the lineal-path function

$$\mathcal{L}_{LP}(\boldsymbol{\gamma}) = \frac{1}{N_x\, N_y} \sum_{m=1}^{N_x} \sum_{k=1}^{N_y} \left(\tilde{\mathcal{P}}_{LP}^{target}(m,k) - \tilde{\mathcal{P}}_{LP}^{SSRVE}(m,k,\boldsymbol{\gamma}) \right)^2 . \qquad (60)$$

The weighting factors are set such that the order of magnitude of the individual least-square function values are in a reasonable range. From that we end up with $\omega_V = \omega_{SD} = 1$ and $\omega_{LP} = 10$. To achieve an efficient optimization procedure the definition of a relevant area is used for the spectral density again. Due to the fact that computing the lineal-path function demands even more operations than computing the spectral density, an improved calculation method is required here, too. Therefore, only a number of 40 line orientations distributed uniformly between the horizontal and the vertical direction is taken into account by an appropriate definition of the template, cf. Fig. 14b. Furthermore, the size of the template which is considered for the computation of the lineal-path function of the SSRVEs can be significantly reduced by considering the typical length of inclusions in the target structure. For this purpose, the complete lineal-path function taking into account a template size $T_x \times T_y = 399 \times 200\,\mathrm{px}^2$ is computed for the target structure before optimization, see Fig. 14a. Then, all values which are lower than a specified threshold value of 0.1 are set to zero. This defines the relevant template analogous to the way the relevant spectral density is identified. This leads to the fact that the size of the lineal-path function and the template size coincide and the specific size $T_x \times T_y = 63 \times 9\,px^2$ is considered for the analysis performed here. In Fig. 14 blue boxes mark the relevant regions of the lineal-path function and the template.

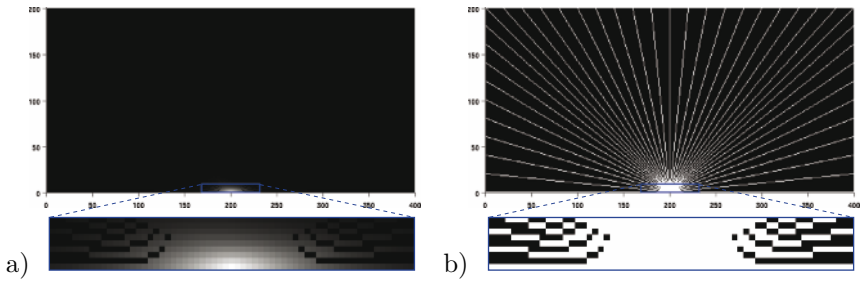

Figure 14. a) Lineal-path function of the target structure and b) the used template in order to improve the computational performance. The blue boxes mark the relevant region taking into account during the optimization procedure.

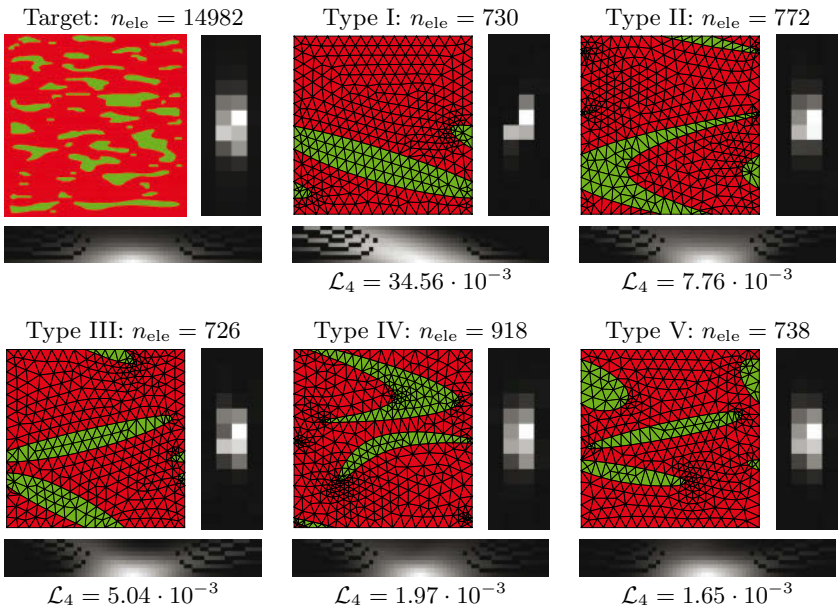

Figure 15. Target structure and discretization of SSRVEs with corresponding relevant area of the spectral density (right) and the lineal-path function (bottom) resulting from the minimization of $\mathcal{L}_4$.

The objective function (59) is minimized with respect to $\boldsymbol{\gamma}$ and the SSRVEs as illustrated in Fig. 15 are obtained. Again, a similar behavior of the objective function is observed. For an increasing complexity of the SSRVE-type the value of the minimized objective function decreases from $\mathcal{L}_4 = 34.56 \cdot 10^{-3}$ for Type I to $\mathcal{L}_4 = 1.65 \cdot 10^{-3}$ for Type V. Obviously, the absolute values of the minimized objective functions for the individual SSRVE types is now slightly higher than for $\mathcal{L}_3$, because an additional least-square functional is taken into account. For a comparative analysis of the mechanical response the average mechanical errors as well as the overall comparative measures are given in Table 5.

The most suitable SSRVE with the lowest overall comparative error is Type V. Although Type I also leads to a rather low value of $\widetilde{r}_{\varnothing}$, the average error for the horizontal tension test is rather high with $\widetilde{r}_x = 4.11$. In turn, SSRVE Type V yields low average errors for all three virtual experiments and yields the best approximation of the overall mechanical behavior of the target structure. Moreover it is observable, that the SSRVE types based on a convex inclusion interface, i.e. 3 sampling points for each inclusion, show better results compared to the corresponding SSRVE types with 4 sampling

Table 5. Values of the objective function $\mathcal{L}_4$ and the errors $\widetilde{r}$ using the SSRVEs shown in Fig. 15, n_{dof} denotes the number of global degrees of freedom of the FE-discretization.

SSRVE	$\mathcal{L}_4$ [10^{-3}]	n_{dof}	$\widetilde{r}_x$ [%]	$\widetilde{r}_y$ [%]	$\widetilde{r}_{xy}$ [%]	$\widetilde{r}_{\varnothing}$ [%]
I	34.56	3054	4.11 ± 1.28	1.05 ± 0.30	0.49 ± 0.30	2.47
III	5.04	3042	1.87 ± 0.67	0.89 ± 0.20	3.03 ± 1.29	2.12
V	1.65	3082	0.32 ± 0.21	0.49 ± 0.13	1.47 ± 0.70	0.91
II	7.76	3238	7.74 ± 1.92	0.73 ± 0.32	6.39 ± 2.81	5.81
IV	1.97	3814	3.20 ± 0.78	0.86 ± 0.35	3.78 ± 1.58	2.90

points for each inclusion. Compared to the results obtained from minimizing $\mathcal{L}_3$, we can conclude that the incorporation of statistical measures of higher order seems to be promising, since the additional incorporation of the lineal-path function yields significantly improved SSRVEs.

5.3 Analysis of Macroscopically Inhomogeneous Problems

In this section the most suitable SSRVE, which is constructed in the previous section, is applied to macroscopically inhomogeneous FE^2-simulations to show the applicability of SSRVEs in more realistic engineering problems. These computations are performed using FEAP with an embedded self-written FE^2-environment, whereby the solution of the microscopic boundary value problem is achieved by the application of the direct solver SuperLU (Vers. 3.1), for details see Demmel et al. (1999).

Radially Loaded Circular Disc As a first example a macroscopically inhomogeneous FE^2-simulation based on the SSRVE at the microscale is compared with the one obtained by using the complex target structure at the microscale. The considered problem is a radially expanded circular disc with a hole, see Fig. 16a for the macroscopic boundary value problem. The outer radius is $r_o = 3.0\,\text{cm}$ and the inner radius is $r_i = 0.5\,\text{cm}$. The disk is discretized with 244 triangular elements with quadratic ansatz functions and plain strain conditions are considered. During the simulation the outer radius is driven by a radially orientated displacement condition from $\overline{u}(t = 0) = 0\,\text{mm}$ up to $\overline{u}(t = t_{max}) = 1.725\,\text{mm}$. At the microscale periodic boundary conditions are applied and at first the target structure is considered where a discretization with 5452 quadratic triangular elements (21930 degrees of freedom) is taken into account, see Fig. 16b. Second, the SSRVE Type V constructed by minimizing the objective function $\mathcal{L}_4$ is considered at the microscale, where a discretization with 738 quadratic triangular elements (3082 degrees of freedom) is considered. In Fig. 16c

the finite element mesh of the considered SSRVE (regular colors) with its periodic expansion (transparent colors) of comparable size is shown. It is emphasized that for the FE^2-simulation only the unitcell of the periodic microstructure is considered as the SSRVE (regular colors) and taken into account by applying periodic boundary conditions.
First, the macroscopic response of both simulations is compared. Therefore, Fig. 17 shows the stress distributions $\overline{\sigma}_{11} = \overline{\sigma}_{xx}$, $\overline{\sigma}_{22} = \overline{\sigma}_{yy}$ and $\overline{\sigma}_{33} = \overline{\sigma}_{zz}$ in the radially expanded disk at the final load step. When comparing the response of the second simulation, where the SSRVE is considered at the microscale (second row), with the first one based on the target structure (first row), a qualitatively and quantitatively similar stress response is observed at the macroscale. To get a quantitative estimation of the accordance the relative deviation

$$r_{\sigma_{ii}}(\overline{\boldsymbol{x}}) = \left| \left[\overline{\sigma}_{ii}^{target}(\overline{\boldsymbol{x}}) - \overline{\sigma}_{ii}^{SSRVE}(\overline{\boldsymbol{x}}) \right] \Big/ \max_{\overline{\boldsymbol{x}}} \left[\overline{\sigma}_{ii}^{target}(\overline{\boldsymbol{x}}) \right] \right| \tag{61}$$

with $i = 1, 2, 3$ is defined as a function of the position $\overline{\boldsymbol{x}}$ in the disk. This relative error describes the difference of the macroscopic stresses between both simulations relative to the maximal stress of the target structure at each macroscopic point. From the corresponding plots in the third row of Fig. 17 a relative deviation lower than 5% for all three stress components is observed. However, the maximum values of the relative deviation are rather localized, thus, a similar behavior of the macroscopic stress response can be concluded when comparing the response obtained for the SSRVE with the one based on the target structure. It is worthwhile mentioning that the

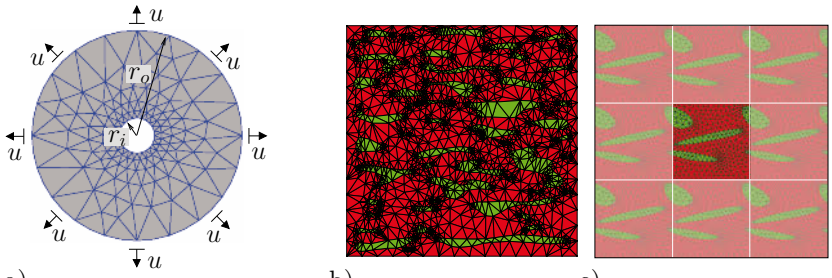

Figure 16. a) Macroscopic BVP: radially expanded circular disk with a hole discretized with 244 quadratic triangular elements under plain strain conditions; discretization of the b) target structure with a reduced number of $n_{ele} = 5452$ finite elements and c) of the SSRVE Type V based on $\mathcal{L}_4$ (with its periodic expansion).

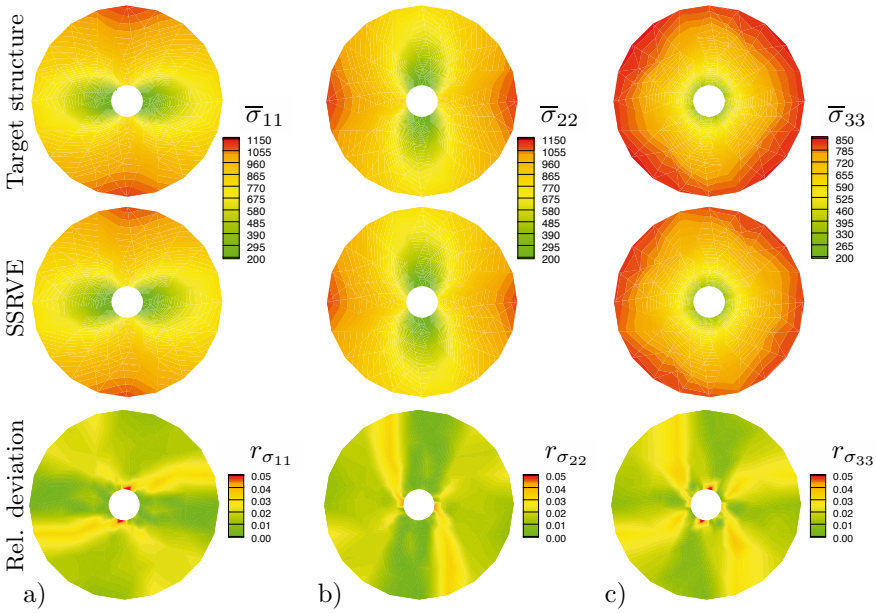

Figure 17. Macroscopic stress distribution for a) $\overline{\sigma}_{11}$, b) $\overline{\sigma}_{22}$ and c) $\overline{\sigma}_{33}$ of the FE^2-simulations based on the target structure (first row) and the SSRVE (second row), and the relative deviations a) $r_{\sigma_{11}}$, b) $r_{\sigma_{22}}$ and c) $r_{\sigma_{33}}$ comparing these two results (third row), taken from Brands (2012).

macroscopic stress response shows a relatively low anisotropic character, although the virtual experiments in the last section show a significantly different behavior for the horizontal- and the vertical tension test. In Fig. 17c the contour plot of $\overline{\sigma}_{33}$ is quite close to a rotational-symmetric distribution. A more pronounced anisotropic response can be expected for larger expansions.

Nevertheless, when comparing the microscopic stress distributions at different positions in the disk, a rather strong anisotropic character may be observed. To show this, Fig. 18 provides the von Mises stress distribution at the final load step in the disk ($\overline{\sigma}_{vM}$) as well as in the microstructures (σ_{vM}) at different macroscopic positions. For this multiscale comparison three different macroscopic points are considered, which are located at the same distance from the inner boundary close to the inner radius of the disk. The symbols in the upper right corner of the images for the microscopic response represent the link to the macroscopic position and the grey area behind the microstructure indicates the undeformed configuration. The maximum stress levels at the analyzed microstructures differ at the individ-

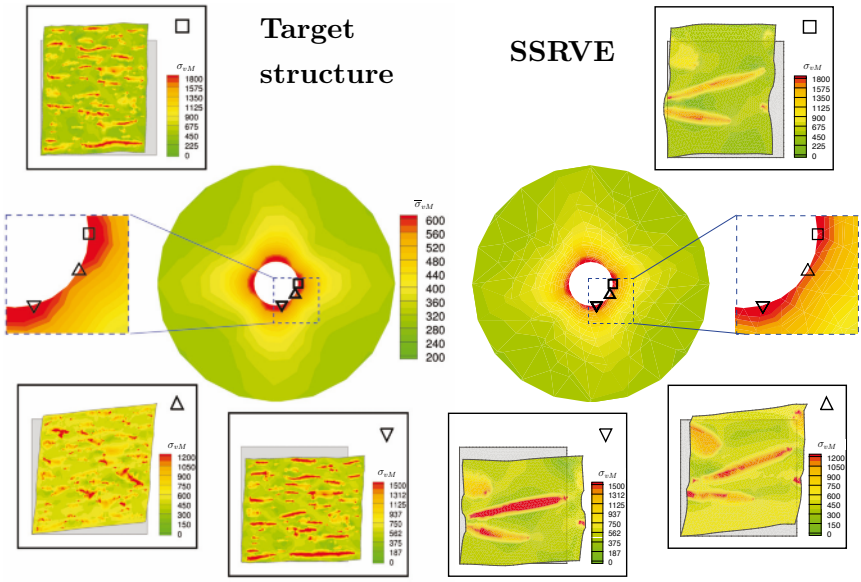

Figure 18. Results of the FE^2-simulations based on a) the target structure and b) the SSRVE with the von Mises stress distributions in the deformed microstructures for three selected positions, taken from Brands (2012).

ual macroscopic points significantly from approximately 1200 MPa to 1800 MPa due to the anisotropy of the RVEs. This represents a rather anisotropic character at the microscale although the macroscopic von Mises stress distribution is close to a rotational-symmetric one. In addition to that, the maximal stress levels at the microscales are significantly larger than the ones at the macroscale. The latter two issues may play an important role with respect to failure initialization analysis, since the microscopically observable orders of magnitude and positions of maximum stress levels can not be observed in purely macroscopic simulations.

If we compare the microscopic results related to the same macroscopic point of the simulation based on the SSRVE with the one based on the target structure, again similar stress levels are observed. Furthermore, the qualitative response at the microscale is similar, too. This accentuates the performance of the SSRVE and shows that it seems to be possible to approximate the response of random microstructures by much simpler SSRVEs.

Finally, the profit with respect to the costs of data storage of the history variables is enormous when using SSRVEs compared with the chosen target structure. In the proposed approach the required data storage capacity

is approximately reduced about 95 %, for the considered coupled micro-macro boundary value problem and the computation time is significantly reduced. These are of course only rough estimates based on the considered discretizations.

Deep-Drawing of a Hat-Profile As a second example the deep-drawing of a sheet metal made of a micro-heterogeneous steel is simulated here. During a deep-drawing process the sheet metal is stretched into the desired part shape by pushing a tool on the sheet and forcing it into a die. The plastic deformations resulting from the tensile strain enable that the desired shape remains after removing the tools. Structural components made by this method can be found in many fields, e. g. automotive bodies and fuel tanks as well as kitchen sinks, cans and cups.
Before the forming process starts the sheet metal is clamped by a blank holder over the drawing die. The die has a cavity representing the desired outer shape of the part. By pushing the punch into the sheet, the material is drawn into the die cavity. After reaching the final loading position the clamping is released by removing the blank holder and the punch is moved out of the sheet. In Fig. 19 the loading and unloading is schematically shown including the aforementioned schedule for the releasing of the sheet metal. In contrast to the multiscale analysis presented in the previous section here no simulation is performed on basis of the target microstructure. Although the number of integration points at the macroscopic boundary value problems does not differ strongly from the radially loaded circular disc, the simulation here exhibits a higher complexity due to the application of the contact formulation and requires a higher number of load steps. Here, the focus is to show that SSRVEs can be used to make such more realistic and practically relevant multiscale simulations computable in rather reasonable time.

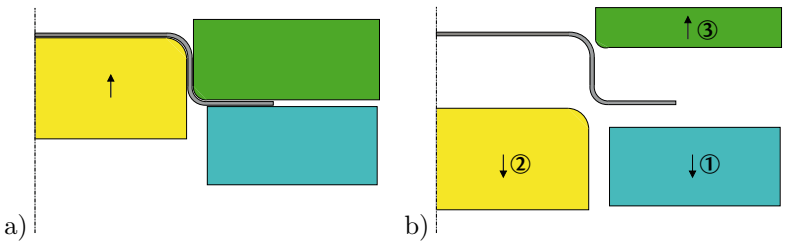

Figure 19. a) deep-drawing and b) unloading steps of a deep-drawing process of a hat profile; the numbers represent the order of tool release.

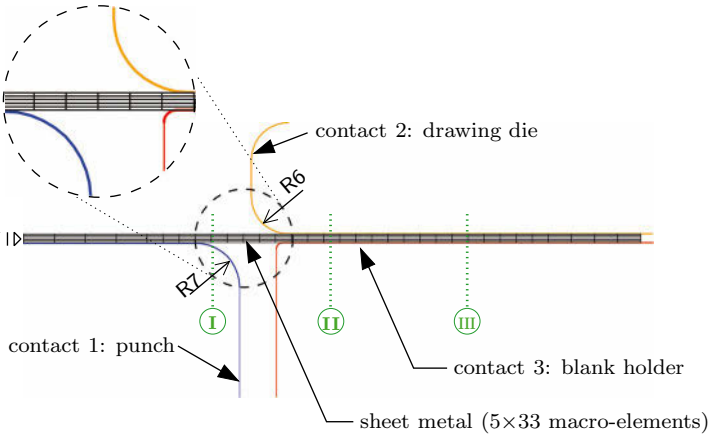

Figure 20. Discretization of the macroscopic BVP with 165 linear quadrilateral elements under plain strain condition.

For the computation the process is simplified to a two-dimensional boundary value problem with plain strain conditions and furthermore exploit symmetry of the problem. In Fig. 20 the macroscopic discretization of the sheet metal based on 165 linear quadrilateral elements using a 4-Gauss-point quadrature is depicted. Horizontal displacement boundaries are applied to the nodes at the left end of the sheet representing the symmetry condition. For a detailed view on the results of the microscale we consider three different locations along the sheet. In the final state they should be located near the punch radius (I), in the vertical section (II) and near the die radius (III), see Fig. 20. The contact of the tools are realized through a frictionless penalty contact. For the analyzed hat profile we consider a punch radius of 7 mm, a die radius of 6 mm and a drawing depth of 45.7 mm. The sheet has a half width of 100 mm and a thickness of 1.4 mm. In order to perform an efficient computation we use the most suitable SSRVE obtained in the previous section at the microscale. The discretization of the SSRVE is shown in Fig. 16c and it consists of 738 quadratic triangular elements and 3082 degrees of freedom. Applying periodic displacement boundary conditions to its edges we achieve the boundary value problem at the microscale, which is solved at each macroscopic integration point during the nonlinear FE-simulation. For each locations along the sheet three points at different thickness positions are considered: near the i) top side (□), ii) center (◯) and iii) bottom side (△). For these overall nine macroscopic points we analyze the microscopic results at the final load and unload step.

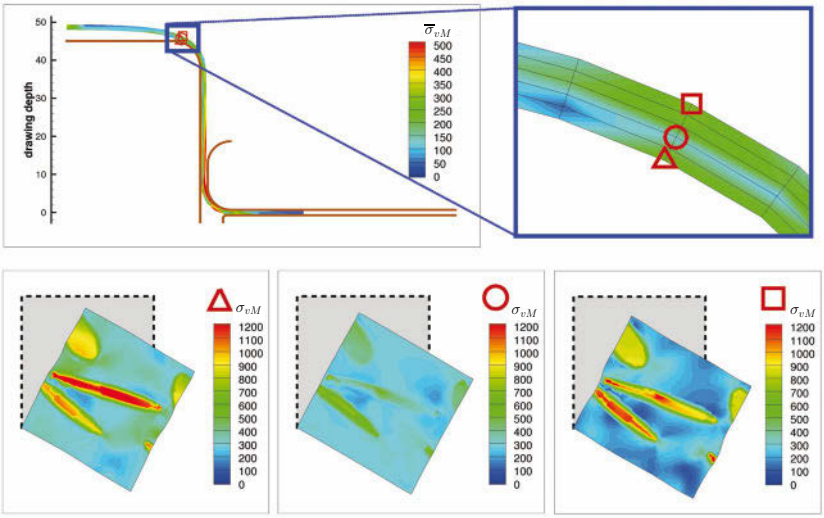

Figure 21. Location I, final load step: distribution of the von Mises stresses at the macroscopic and three microscopic boundary value problems, taken from Brands (2012).

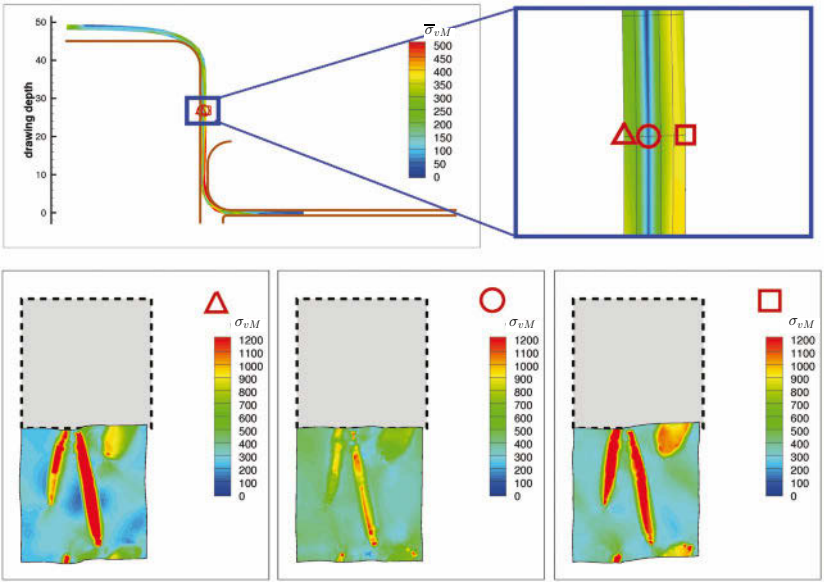

Figure 22. Location II, final load step: distribution of the von Mises stresses at the macroscopic and three microscopic boundary value problems, taken from Brands (2012).

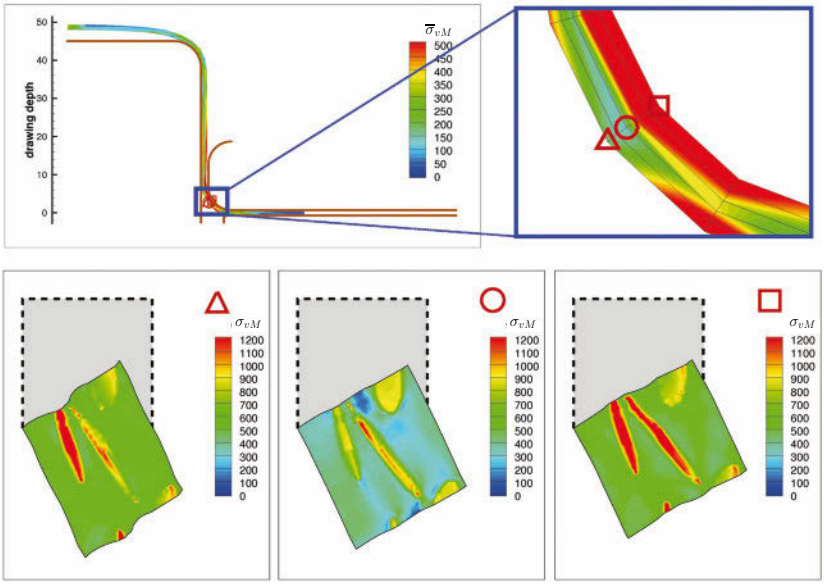

Figure 23. Location III, final load step: distribution of the von Mises stresses at the macroscopic and three microscopic boundary value problems, taken from Brands (2012).

After the deep-drawing is finished, see Fig. 21, we observe a different stress distribution in the three microstructures at location I. This aspect can be addressed to the different loading states within the sheet in direction of thickness due to the bending by the punch radius. Consequently, near the bottom side a compression zone arises, which can be observed by a shortening of the horizontal edge length of the associated RVE (△). The opposite – a tension zone – can be observed near the top side, since the edge of the RVE (◯) is longer in the deformed configuration. Since near the center of the sheet the neutral axis should appear, the RVE located near this location (◯) shows a lower stress maximum compared to both the other positions. At location II (Fig. 22) we also observe different stress distributions in the related microstructures but all three RVEs show a similar elongation of the edges, which are orientated in longitudinal direction. The differences in the stresses may result from the previous forming process by the die radius and the related plastic deformation. But with further progress the formed shape is rolled back to a straight sheet and, consequently, the differences in the length are removed. The final load state at location III and the associated results at the microscale are shown in Fig. 23. Therein, we observe qualitatively similar deformation and stress states at the different positions along the sheet thickness. Again we measure compression in

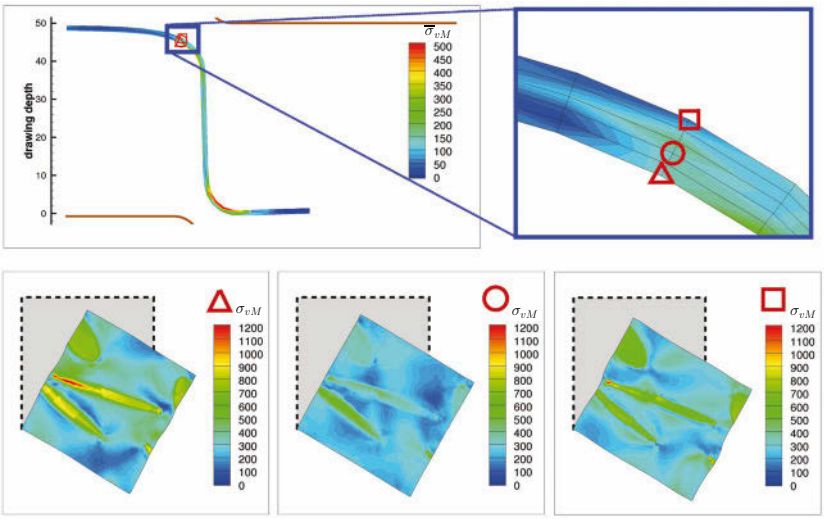

Figure 24. Location I, unloaded situation: distribution of the von Mises stresses at the macroscopic and three microscopic boundary value problems, taken from Brands (2012).

the RVE associated to the position close to the die radius and tension at the opposite side of the sheet. One possible explanation can be a similar bending characteristic, which is applied to the sheet during the forming process by the die radius. Summarizing, at all locations we observe a strong discrepancy between the maximal stress level at the microscale and the related macroscopic location. This aspect is important with respect to failure analysis, where the initialization of crack propagation at the microscale is to be investigated.

In Fig. 24, 25 and 26 the stress distribution in the released sheet and the related microstructures are shown. All stress states are relaxed compared to their counterpart at the final load step in Fig. 21-23, but the discrepancy of the maximal stress levels between macro- and microscale still remains. From the deformation state of the macroscopic BVP we observe a typical phenomenon, the spring back behavior, which occurs typically in many metal forming processes after the release of the specimen. The right end of the sheet is moved up, cf. upper left subframe in Fig. 24, compared to its deformed shape in the final load step, cf. upper left subframe in Fig. 21. This behavior is explained by the release of the elastic deformations, which were stored in the sheet during the loading. In many research fields the spring back is a crucial topic, since the final shape of the deformed specimen is strongly influenced by this phenomenon.

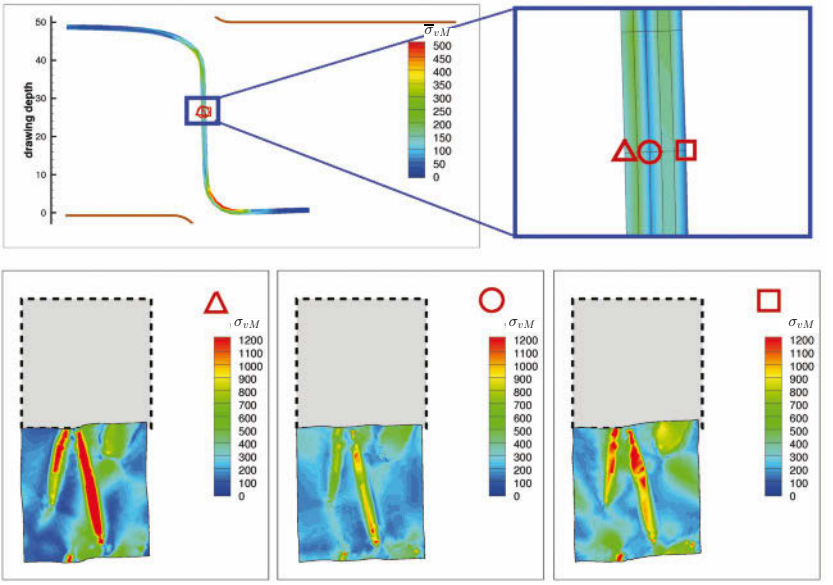

Figure 25. Location II, unloaded situation: distribution of the von Mises stresses at the macroscopic and three microscopic boundary value problems, taken from Brands (2012).

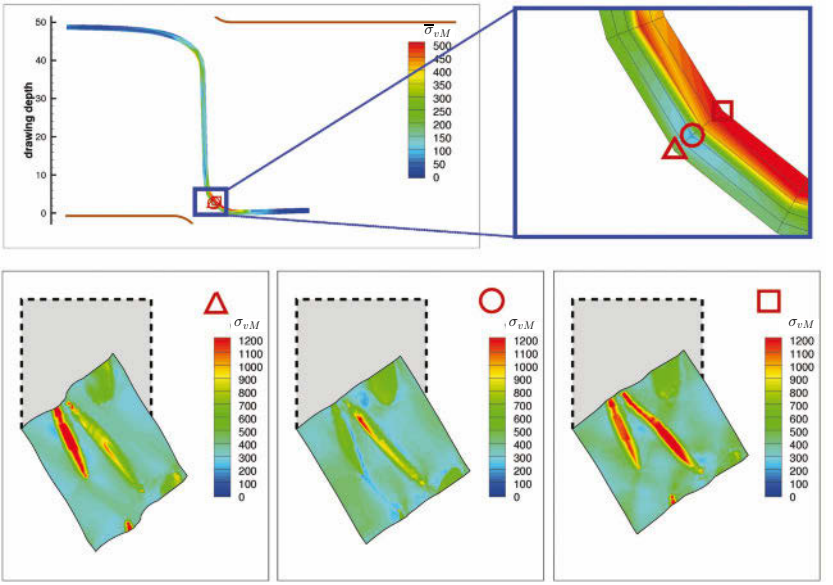

Figure 26. Location III, unloaded situation: distribution of the von Mises stresses at the macroscopic and three microscopic boundary value problems, taken from Brands (2012).

If we measure the deformations of the three microstructures at location I along their horizontal reference axis we again observe the aforementioned elongation of the RVE at the top side located structure, a nearly unchanged RVE at the center and a compressed one at the bottom side. As also mentioned before, this behavior is addressed to the nearly pure bending at this location of the sheet. Whereas at the location II we observe a shear in the microstructure at the top and bottom side of the sheet. In the center shear is only slightly observable. At location III similar states arise compared to those at location I. However, a significantly higher stress level at the macroscale and the microscale occurs compared to the other locations. This could be caused by either the smaller die radius and/or the higher tensile force at this location in the sheet.

6 SSRVEs for a DP Steel Microstructure

In the previous section we analyze the construction of SSRVEs based on an artificial target structure of a two-phase material leading to a macroscopically anisotropic material response. Here, we study the applicability of the proposed method to a real microstructure of a two-phase material. Advanced high strength steels are important with respect to automotive constructions due to their higher stability and formability at a lower weight compared to common steels. The material behavior of these steels is mainly governed by the microstructure which in case of DP-steels consists of a ferritic matrix and a martensitic inclusion phase. Fig. 27a shows the binary image of a characteristic DP-steel microstructure.

6.1 Construction of SSRVEs for a Real Microstructure

The micrograph of a DP-steel as shown in Fig. 27a serves as target structure in the following analysis. For the constitutive modeling of the individual constituents we use again the finite J_2-plasticity model with a von Mises type hardening law described in Section 2. The material parameters given in the table in Fig. 6 are used for the matrix and the inclusion phase. For the SSRVE construction that least-square functional is used which turns out in the last section to yield the "best" results in the mechanical tests. Consequently, we use the functional given by Eq. (59), where the volume fraction, the spectral density and the lineal-path function is taken into accout and consider the weighting factors $\omega_V = \omega_{SD} = 1$, $\omega_{LP} = 10$. Since the enhancements discussed in Section 5.2 show satisfying results in the previous section, those construction principles are taken into account here, too. Consequently, five different SSRVE types (I-V) are considered, which

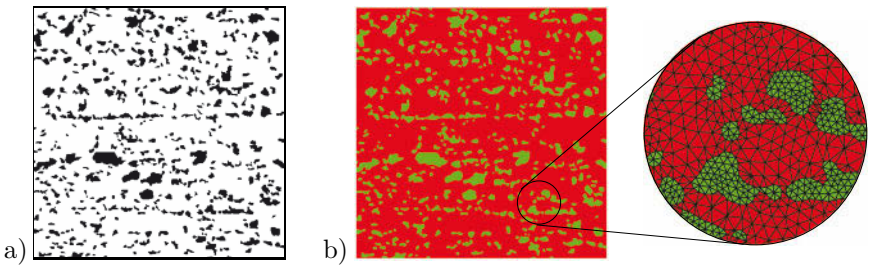

Figure 27. a) Real microstructure of a dual phase steel and b) the discretization of the structure by 38,594 triangular finite elements with quadratic ansatz functions.

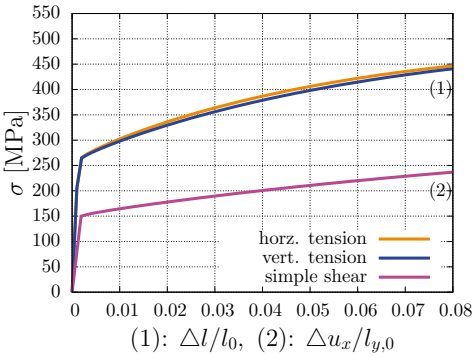

Figure 28. Macroscopic mechanical response of the real microstructure in the three virtual experiments.

preclude any intersections of the splines and enable the periodic extensibility for splines located at the SSRVE's boundaries. The minimization of the least-square functional with respect to $\boldsymbol{\gamma}$ for the five different SSRVEtypes results in the structures depicted in Fig. 29. Again, for each category of SSRVEtypes (convex and non-convex inclusions) a decreasing value of the objective function minimum from $\mathcal{L}_4 = 39.41 \cdot 10^{-3}$ to $\mathcal{L}_4 = 4.22 \cdot 10^{-3}$ is observed with an increase of inclusions (and finite elements). For a comparision of the mechanical response first the stress-strain response in the three macroscopically homogeneous virtual experiments investigated in the previous section are considered, cf. Fig. 28.
As it is observed in the previous section the overall comparative error $\widetilde{r}_{\varnothing}$ shows that SSRVE type V appears to be the "best" SSRVE, see Table 6. There it can be seen that also the overall comparative mechanical error decreases with an increase of inclusions and finite elements.

Table 6. Values of the objective function $\mathcal{L}_4$ and the errors $\widetilde{r}$ using the SSRVEs shown in Fig. 29, n_{dof} denotes the number of global degrees of freedom of the FE-discretization.

SSRVE	$\mathcal{L}$ [10^{-3}]	n_{dof}	$\widetilde{r}_x$ [%]	$\widetilde{r}_y$ [%]	$\widetilde{r}_{xy}$ [%]	$\widetilde{r}_{\varnothing}$ [%]
I	39.41	2254	1.16 ± 0.29	1.58 ± 0.39	3.34 ± 0.91	2.24
III	8.66	2962	0.26 ± 0.20	2.24 ± 0.52	0.41 ± 0.22	1.32
V	4.22	3290	1.12 ± 0.35	0.92 ± 0.26	1.10 ± 0.23	1.05
II	9.29	2914	8.24 ± 2.10	2.10 ± 0.31	7.45 ± 2.87	6.53
IV	3.70	3402	2.22 ± 0.80	4.89 ± 1.24	2.43 ± 1.22	3.40

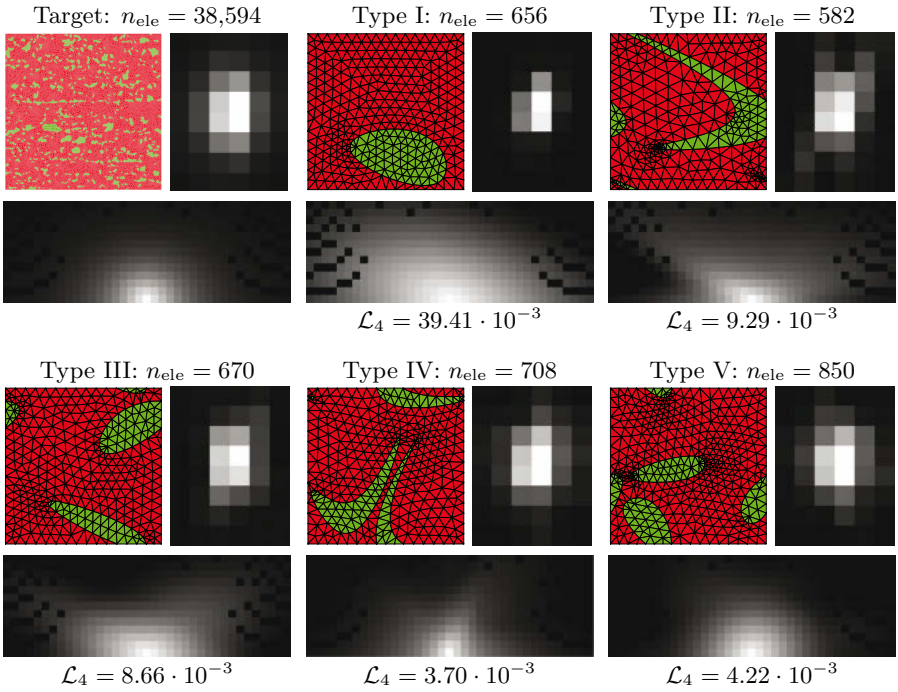

Figure 29. Target structure (real micrograph) and discretization of SSRVEs with corresponding relevant area of the spectral density (right hand side of each microstructure) and the lineal-path function (beneath the microstructure images) resulting from the minimization of $\mathcal{L}_4$; n_{ele} denotes the number of finite elements.

6.2 Analysis of the Bauschinger Effect

Typically the Bauschinger effect is observed for DP-steels, which results from a kinematic hardening observed at the macroscale. Thus, a virtual cyclic compression test is analyzed where the mechanical response of the "best" SSRVE (Type V) from above is compared with the response of the target structure. In the literature several parameters are defined which quantify the Bauschinger effect. Here, a suitable Bauschinger factor is defined as

$$\overline{f}_B = \left(|\overline{\sigma}^I| - \overline{\sigma}^{II}\right) \Big/ |\overline{\sigma}^I| \tag{62}$$

cf. Fig. 30. This factor is zero for the case where no kinematic hardening occurs and increases for an increasing kinematic hardening. The setup of the

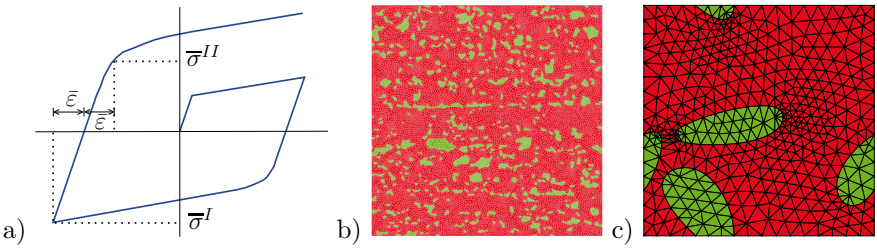

Figure 30. a) Illustration for the calculation of the Bauschinger factor, b) the real (target) microstructure and c) the SSRVE type V.

boundary value problem is almost identical to the horizontal tension test, introduced in Section 4.2, however the load scenario involves compression up to $\Delta\overline{l}/\overline{l}_0 = -0.05$, tension back to $\Delta\overline{l}/\overline{l}_0 = 0$ and then further tensile loading. The resulting stress-strain diagrams are displayed in Fig. 31 and from that we compute the Bauschinger factors

$$\overline{f}_B^{real} = \frac{447 - 328}{447} = 0.27 \quad \text{and} \quad \overline{f}_B^{SSRVE} = \frac{440 - 348}{440} = 0.21\,. \tag{63}$$

As can be observed the stress-strain response as well as the Bauschinger factor of the SSRVE is similar to the one of the target structure. Interestingly, a significant macroscopic kinematic hardening is observed although no kinematic hardening is considered in the individual phases. This is a result of the complex interactions between the different phases showing a different plastic behavior. At the microscale the distribution of the σ_{11}-stress is compared for the two different microstructures, see Fig. 32. At the size level of a typical inlusion in the real RVE the stress distribution is also similar

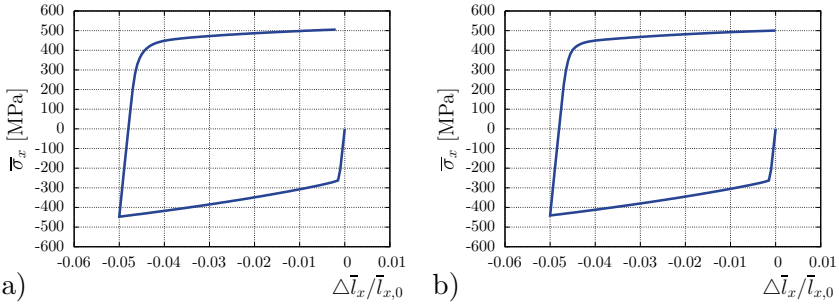

Figure 31. Stress-strain response of the a) real (target) microstructure ($\overline{f}_B^{real} = 0.27$) and b) SSRVE type V ($\overline{f}_B^{SSRVE} = 0.21$) in the compression-tension test.

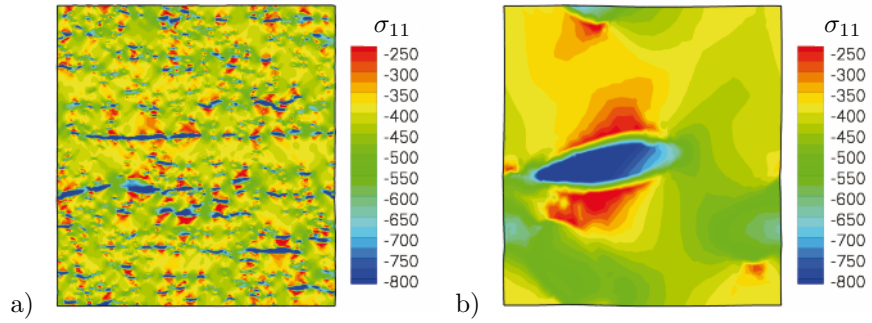

Figure 32. Distribution of the σ_{11}-stress in the a) real (target) microstructure and b) SSRVE type V at maximum compression.

compared with the distribution in the SSRVE. We summarize that not only a similar mechanical response is observed at the macroscale but also at the microscale.

6.3 Application to Inhomogeneous Boundary Value Problem

To show the capability of the "best" SSRVE in a macroscopically inhomogeneous FE^2-simulation a radially loaded circular disk with a hole is calculated. The disk is discretized by 252 triangular elements with quadratic ansatz functions and plain strain conditions are considered. The outer radius of the disk is $r_o = 4\,\text{cm}$ and the inner radius is $r_i = 2\,\text{cm}$, see Fig. 33a. The load is applied on the inner side of the disk as Dirichlet condition which pull the inner border radially inwards up to a displacement of $u = 0.35\,\text{cm}$.

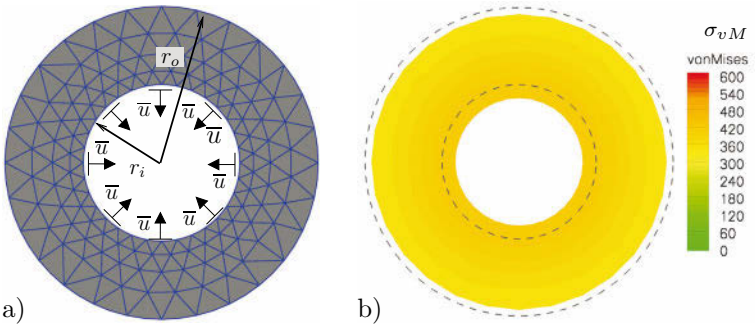

Figure 33. Radially loaded circular disc: a) macroscopic boundary value problem and b) the von Mises stress distribution resulting from a purely macroscopic calculation.

λ [MPa]	115,384.6
μ [MPa]	76,923.1
y_0 [MPa]	230.0
y_∞ [MPa]	436.0
η [-]	16.7
h [-]	7.0

a)

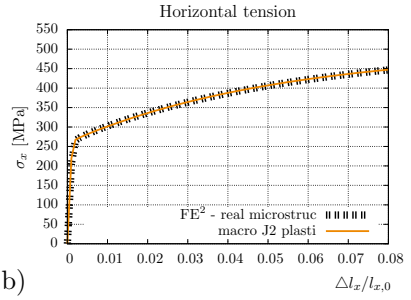

b)

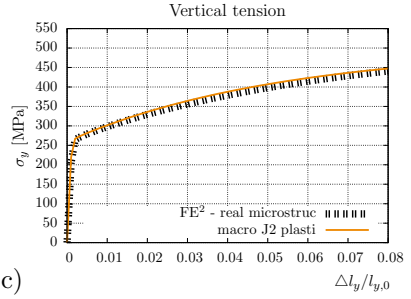

c)

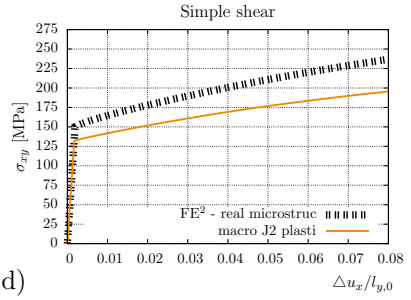

d)

Figure 34. a) Material parameters for the finite J_2-plasticity model applied at the macroscale, comparision of the mechanical behavior resulting from the purely macroscopic calculation with the response resulting from the FE^2-simulation based on the target microstructure for the three virtual tests: b) horizontal tension, c) vertical tension and d) simple shear test.

In a first simulation a purely macroscopic computation is analyzed where the phenomenological elasto-plastic material model described in Section 2 is applied. The material parameters are adjusted such that the mechanical behavior in the three virtual experiments matches the macroscopic response of the target structure as similarly as possible. The material parameters are provided in Fig. 34a. A comparision of the mechanical response of the FE^2 computation using the real (target) microstructure and the purely macroscopic computation is shown in Fig. 34b-d. It is observed that not all tests can be represented by the simple purely macroscopic material law, which shows the complexity of the mechanical behavior of the micro-heterogeneous material. The resulting von Mises stress distribution in the disk from the purely macroscopic calculation is depicted in Fig. 33b and only a slightly graded stress distribution with a range about 350 MPa at the outer side to 430 MPa at the inner side is observed. These results are now compared with the FE^2-simulation using the SSRVE TypeV at the microscale.

In Fig. 35 the results of this FE^2-simulation are depicted, where the macroscopic response is shown on the top at the left hand side. The stresses range at the macroscale from about 400 MPa at the outer side to 630 MPa at the inner side. This distribution shows a wider range with higher maximum stress values compared with the purely macroscopic calculation. Furthermore Fig. 35 shows the distributions of von Mises stresses inside the SSRVEs for three different macroscopic locations, which are designated by the symbols ($\square$,$\triangle$,$\triangledown$). The maximum stress level of approximately 1000 MPa is significantly higher at the microscale than at the macroscale. This shows one of the advantages of a FE^2-simulation because it offers a more critical view on the (maximal) stress levels since it incorporates the stress distributions at the microscale. This is important with respect to the initialization of failure.

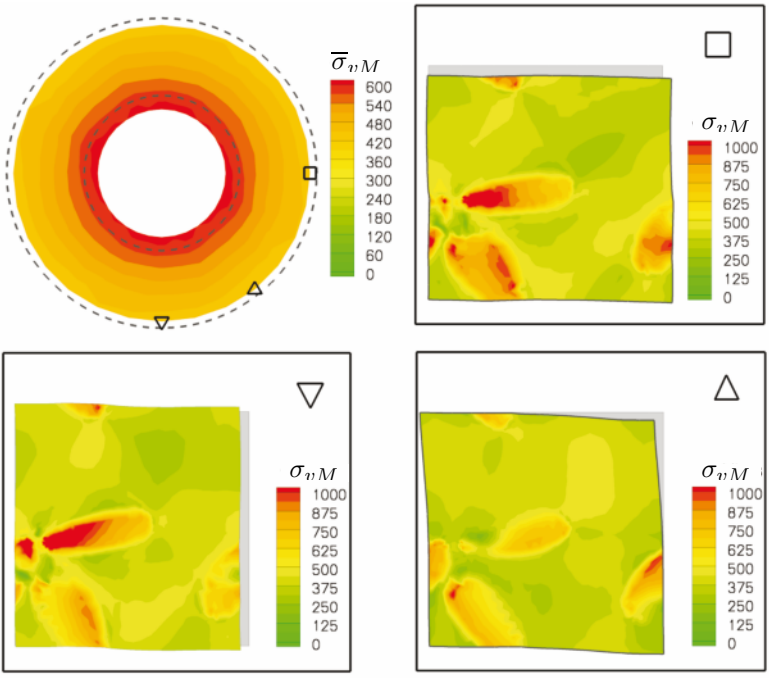

Figure 35. Results of the FE^2-simulation based on SSRVE Type V with the von Mises stress distributions in the deformed macroscopic disc and in the deformed microstructures of three different macroscopic locations.

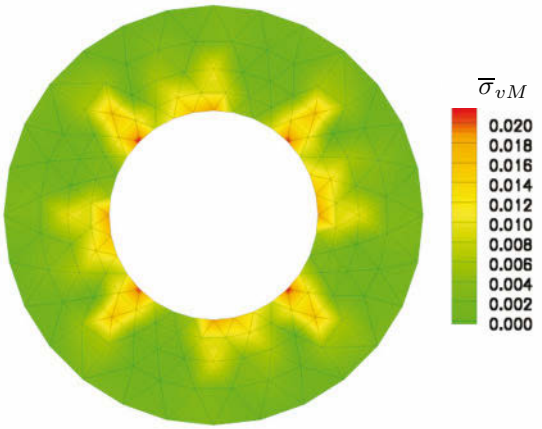

Figure 36. Distribution of the relative error $\overline{r}_{\sigma_{vM}}$ defined in Eq. (64) regarding the von Mises stresses at an inner radial displacement $\overline{u} = 0.0012\,\text{cm}$.

Finally, the above FE^2-simulation is compared with a simulation where the target structure is considered at the microscale. Since this leads to a computationally highly expensive calculation a lower radial displacement of $\overline{u} = 0.0012$ cm is prescribed at the inner boundary. For the comparison of the mechanical response of both calculations the relative error

$$\overline{r}_{\overline{\sigma}_{vM}}(\overline{\boldsymbol{x}}) = \left| \frac{\overline{\sigma}_{vM}^{target}(\overline{\boldsymbol{x}}) - \overline{\sigma}_{vM}^{SSRVE}(\overline{\boldsymbol{x}})}{\max\limits_{\overline{\boldsymbol{x}}} \left[\overline{\sigma}_{vM}^{target}(\overline{\boldsymbol{x}})\right]} \right| , \tag{64}$$

is defined. The resulting distribution of this relative error is depicted in Fig. 36. The maximum error is approximately 2% and in most of the domain lower than 1%. Thus, we conclude that also the FE^2-simulation of the macroscopically inhomogeneous boundary value problem using the SSRVE at the microscale leads to satisfying results compared to those based on the real microstructure. However, the computation time is dramatically reduced for the SSRVE-based calculation: the calculation based on the real microstructure is 200 times slower than the simulation based on the SSRVE.

7 Conclusion

In this contribution a method for the construction of statistically similar representative volume 0 (SSRVEs) was described. These SSRVEs serve as

more efficient RVEs compared to typically used RVEs since the geometrical complexity and therefore the number of finite elements required for the discretization at the microscale have been significantly reduced. The basic assumption of this method was that the macroscopic mechanical response of the considered material is strongly governed by the morphology of the microstructure. Starting from that, the SSRVEs were constructed based on the minimization of an objective function considering the differences of statistical measures computed for a random microstructure and for the SSRVE. The method was applied to different (target) microstructures in order to show the applicability of the thereby constructed SSRVEs. In a first sensitivity study some basic scalar-valued parameters turned out to be not sufficient for an the construction of appropriate SSRVEs, and statistical measures of higher order (spectral density and lineal-path function) were analyzed. Macroscopically inhomogeneous FE^2-simulations were performed including the deep-drawing procedure of a hat profile where the SSRVE was used at the microscale. By constructing a SSRVE for a real microstructure of a DP-steel and by comparing with calculations based on the original real microstructure it was shown that the presented method yields also reasonable results regarding real microstructures. In this example the computation time resulting from the calculation where the SSRVE was used was 200 times faster than the calculation based on the target structure. Summarizing, the proposed method enables the construction of SSRVEs which capture the main attributes of random microstructures and which still show a similar mechanical response. However, such SSRVEs have a less complex microstructure and require therefore a lower number of finite elements for the discretization at the microscale increasing significantly the computational efficiency.

Acknowledgements: The authors greatly appreciate the Deutsche Forschungsgemeinschaft (DFG) for the financial support under the research grant SCHR 570/8-2 within the research group 797 on the "Analysis and Computation of Microstructure in Finite Plasticity".

Bibliography

M. Ambrozinski, K. Bzowski, L. Rauch, and M. Pietrzyk. Application of statistically similar representative volume element in numerical simulations of crash box stamping. 12:126–132, 2012.

D. Balzani, J. Schröder, and D. Brands. FE^2-simulation of microheterogeneous steels based on statistically similar RVE's. In *Proceedings of the IUTAM Symposium on Variational Concepts with applications to the mechanics of materials, September 22-26, 2008, Bochum, Germany*, 2009.

D. Balzani, D. Brands, J. Schröder, and C. Carstensen. Sensitivity analysis of statistical measures for the reconstruction of microstructures based on the minimization of generalized least-square functionals. *Technische Mechanik*, 30:297–315, 2010.

M. Beran. *Statistical continuum theories*. Wiley, 1968.

D. Brands. *Geometrical Modeling and Numerical Simulation of Heterogeneous Materials*. Dissertation, Universität Duisburg-Essen, 2012.

J.E. Bresenham. Algorithm for computer control of a digital plotter. *IBM Systems Journal*, 4(1):25–30, 1965. reprinted in Interactive Computer Graphics, Herbert Freeman ed., 1980, and Seminal Graphics: Pioneering Efforts That Shaped The Field, Rosalee Wolfe ed., ACM SIGGRAPH, 1998.

W.F. Brown. Solid mixture permettivities. *Journal of Computational Physics*, 23:1514–1517, 1955.

M. Calcagnotto, Y. Adachi, D. Ponge, and D. Raabe. Deformation and fracture mechanisms in fine- and ultrafine-grained ferrite/martensite dual-phase steels and the effect of aging. *Acta Materialia*, 59:658–670, 2011.

P. Capek, V. Hejtmanek, L. Brabec, A. Zikanova, and M. Kocirik. Stochastic reconstruction of particulate media using simulated annealing: Improving pore connectivity. *Transport in Porous Media*, 76(2):179–198, 2009.

A.R. Conn, K. Scheinberg, and L.N. Vicente. *Introduction to derivative-free optimization*, volume 8 of *MPS/SIAM Series on Optimization*. Society for Industrial and Applied Mathematics (SIAM), Philadelphia, PA, 2009. ISBN 978-0-898716-68-9.

A. Delesse. Procédé méchanique pour déterminer la composition des roches. *Annales des Mines*, 13:379, 1848.

J.W. Demmel, S.C. Eisenstat, J.R. Gilbert, X.S. Li, and J.W.H. Liu. A supernodal approach to sparse partial pivoting. *SIAM J. Matrix Analysis and Applications*, 20(3):720–755, 1999.

H.E. Exner and H.P. Hougardy. *Einführung in die quantitative Gefügeanalyse*. Deutsche Gesellschaft für Metallkunde, 1986.

A.A. Glagolev. Quantitative analysis with the microscope by the point method. *Engineering and Mining Journal*, 135:399, 1934.

R. Hill. Elastic properties of reinforced solids: some theoretical principles. *Journal of the Mechanics and Physics of Solids*, 11:357–372, 1963.

Y. Jiao, F.H. Stillinger, and S. Torquato. A superior descriptor of random textures and its predictive capacity. *Proceedings of the National Academy of Sciences of the United States of America*, 106(42):17634–17639, 2009.

S.O. Klinkel. *Theorie und Numerik eines Volumen-Schalen-Elementes bei finiten elastischen und plastischen Verzerrungen*. PhD thesis, Universität Fridericiana zu Karlsruhe, 2000.

T.G. Kolda, R.M. Lewis, and V. Torczon. Optimization by direct search: new perspectives on some classical and modern methods. *SIAM Rev.*, 45 (3):385–482 (electronic), 2003. ISSN 0036-1445.

J. Konrad, S. Zaefferer, and D. Raabe. Investigation of orientation gradients around a hard laves particle in a warm rolled Fe3Al-based alloy by a 3d EBSD-FIB technique. *Acta Materialia*, 54:1369–1380, 2006.

E. Kröner. Allgemeine Kontinuumstheorie der Versetzung und Eigenspannung. *Archive of Rational Mechanics and Analysis*, 4:273–334, 1960.

E. Kröner. Statistical continuum mechanics. In *CISM Courses and Lectures*, volume 92. Springer-Verlag, Wien, New-York, 1971.

E.H. Lee. Elasto-plastic deformation at finite strains. *Journal of Applied Mechanics*, 36:1–6, 1969.

D.S. Li, M.A. Tschopp, M. Khaleel, and X. Sun. Comparison of reconstructed spatial microstructure images using different statistical descriptors. *Computational Materials Science*, 51:437–444, 2012.

B.L. Lu and S. Torquato. Lineal-path function for random heterogeneous materials. *Physical Reviews A*, 45:922–929, 1992.

M.M. Mäkelä and P. Neittaanmäki. *Nonsmooth Optimization: Analysis and Algorithms with Applications to Optimal Control*. World Scientific Publishing Co. Inc., 1992. ISBN 981-02-0773-5.

C. Manwart, S. Torquato, and R. Hilfer. Stochastic reconstruction of sandstones. *Physical Review E*, 62:893–899, 2000.

G. Matheron. *Random Sets and Integral Geometry*. Wiley, New York, 1975.

C. Miehe. *Kanonische Modelle multiplikativer Elasto-Plastizität. Thermodynamische Formulierung und Numerische Implementation.* 1993. Habilitationsschrift.

C. Miehe and E. Stein. A canonical model of multiplicative elasto-plasticity formulation and aspects of the numerical implementation. *European Journal of Mechanics, A/Solids*, 11:25–43, 1992.

C. Miehe, J. Schröder, and J. Schotte. Computational homogenization analysis in finite plasticity. simulation of texture development in polycrystalline materials. *Computer Methods in Applied Mechanics and Engineering*, 171:387–418, 1999.

J. Ohser and F. Mücklich. *Statistical analysis of microstructures in materials science*. J Wiley & Sons, 2000.

J. Ohser and K. Schladitz. *Image Processing and Analysis*. Clarendon Press Oxford, 2006.

D. Peric, D.R.J. Owen, and M.E. Honnor. A model for finite strain elasto-plasticity based on logarithmic strains: Computational issues. *Computer Methods in Applied Mechanics and Engineering*, 94:35–61, 1992.

R. Piasecki. Microstructure reconstruction using entropic descriptors. *Proceedings of the Royal Society of London, Series A : Mathematical, Physical and Engineering Science*, 467:806–820, 2011.

G.L. Povirk. Incorporation of microstructural information into models of two-phase materials. *Acta Metallurgica*, 43/8:3199–3206, 1995.

J. Schröder. *Homogenisierungsmethoden der nichtlinearen Kontinuumsmechanik unter Beachtung von Instabilitäten.* Bericht aus der Forschungsreihe des Instituts für Mechanik (Bauwesen), Lehrstuhl I, Universität Stuttgart, 2000. Habilitationsschrift.

J. Schröder, D. Balzani, and D. Brands. Approximation of random microstructures by periodic statistically similar representative volume elements based on lineal-path functions. *Archive of Applied Mechanics*, 81: 975–997, 2010.

J.C. Simo. A framework for finite strain elastoplasticity based on maximum plastic dissipation and the multiplicative decomposition: Part i. continuum formulation. *Computer Methods in Applied Mechanics and Engineering*, 66:199–219, 1988.

J.C. Simo. Algorithms for static and dynamic multiplicative plasticity that preserve the classical return mapping schemes of the infinitesimal theory. *Computer Methods in Applied Mechanics and Engineering*, 99:61–112, 1992.

J.C. Simo and C. Miehe. Associative coupled thermoplasticity at finite strains: Formulation, numerical analysis and implementation. *Computer Methods in Applied Mechanics and Engineering*, 96:133–171, 1992.

R.J.M. Smit, W.A.M. Brekelmans, and H.E.H. Meijer. Prediction of the mechanical behavior of nonlinear heterogeneous systems by multi-level finite element modeling. *Computer Methods in Applied Mechanics and Engineering*, 155:181–192, 1998.

S. Torquato. *Random heterogeneous materials. microstructure and macroscopic properties.* Springer, 2002.

S. Torquato and B. Lu. Chord-length distribution function for two-phase random media. *Physical Review E*, 47:2950–2953, 1993.

S. Torquato, J.D. Beasley, and Y.C. Chiew. Two-point cluster function for continuum percolation. *Journal of Computational Physics*, 88:6540–6547, 1988.

G. Weber and L. Anand. Finite deformation constitutive equations and a time integration procedure for isotropic, hyperelastic-viscoelastic solids. *Computer Methods in Applied Mechanics and Engineering*, 79:173–202, 1990.

E.R. Weibel. *Stereological Methods, Vol. 2: Theoretical Foundations.* Academic Press, London, New York, Toronto, Sydney, San Francisco, 1980.

J. Zeman. *Analysis of Composite Materials with Random Microstructure.* PhD thesis, University of Prague, 2003.